SPRINGER SERIES ON CHEMICAL SENSORS AND BIOSENSORS 05

Series Editor O. S. Wolfbeis
Volume Editors C. Steinem · A. Janshoff

Piezoelectric Sensors

Springer

5
Springer Series on Chemical Sensors and Biosensors

Methods and Applications

Series Editor: O. S. Wolfbeis

Springer Series on Chemical Sensors and Biosensors

Series Editor: O. S. Wolfbeis

Recently Published and Forthcoming Volumes

Piezoelectric Sensors
Volume Editors: Steinem C., Janshoff A.
Vol. 5, 2006

Surface Plasmon Resonance Based Sensors
Volume Editor: Homola J.
Vol. 4, 2006

Frontiers in Chemical Sensors
Novel Principles and Techniques
Volume Editors: Orellana G., Moreno-Bondi M. C.
Vol. 3, 2005

Ultrathin Electrochemical Chemo- and Biosensors
Technology and Performance
Volume Editor: Mirsky V. M.
Vol. 2, 2004

Optical Sensors
Industrial, Environmental and Diagnostic Applications
Volume Editors: Narayanaswamy R., Wolfbeis O. S.
Vol. 1, 2003

Piezoelectric Sensors

Volume Editors: Claudia Steinem · Andreas Janshoff

With contributions by

M. A. Cooper · L. Daikhin · D. Johannsmann · F. L. Dickert
F. Eichelbaum · H. Furusawa · E. Gileadi · G. G. Guilbault
V. Heitmann · F. Höök · A. Janshoff · D. Johannsmann · B. Kasemo
P. A. Lieberzeit · R. Lucklum · K. A. Marx · M. Mascini
M. Minunni · T. Mori · T. Nihira · Y. Okahata · B. Reiß
C. Steinem · S. Tombelli · V. Tsionsky · M. Urbakh
R. D. Vaughan · J. Wegener

Springer

Chemical sensors and biosensors are becoming more and more indispensable tools in life science, medicine, chemistry and biotechnology. The series covers exciting sensor-related aspects of chemistry, biochemistry, thin film and interface techniques, physics, including opto-electronics, measurement sciences and signal processing. The single volumes of the series focus on selected topics and will be edited by selected volume editors. The Springer Series on Chemical Sensors and Biosensors aims to publish state-of-the-art articles that can serve as invaluable tools for both practitioners and researchers active in this highly interdisciplinary field. The carefully edited collection of papers in each volume will give continuous inspiration for new research and will point to existing new trends and brand new applications.

Library of Congress Control Number: 2006935375

ISSN 1612-7617
ISBN-10 3-540-36567-2 Springer Berlin Heidelberg New York
ISBN-13 978-3-540-36567-9 Springer Berlin Heidelberg New York
DOI 10.1007/b100347

Springer is a part of Springer Science+Business Media

springer.com

Cover design: WMXDesign GmbH, Heidelberg
Typesetting and Production: LE-TEX Jelonek, Schmidt & Vöckler GbR, Leipzig

Printed on acid-free paper 02/3100 YL – 5 4 3 2 1 0

Series Editor

Prof. Dr. Otto S. Wolfbeis

Institute of Analytical Chemistry,
Chemo- and Biosensors
University of Regensburg
93040 Regensburg, Germany
otto.wolfbeis@chemie.uni-regensburg.de

Volume Editors

Prof. Dr. Andreas Janshoff

University of Mainz
Institute of Physical Chemistry
Welder Weg 11
55128 Mainz
Germany
janshoff@uni-mainz.de

Prof. Dr. Claudia Steinem

Georg August University
Institute of Organic and Biomolecular Chemistry
Tammannstr. 2
37077 Göttingen
Germany
claudia.steinem@chemie.uni-goettingen.de

Springer Series on Chemical Sensors and Biosensors Also Available Electronically

For all customers who have a standing order to Springer Series on Chemical Sensors and Biosensors, we offer the electronic version via SpringerLink free of charge. Please contact your librarian who can receive a password or free access to the full articles by registering at:

springerlink.com

If you do not have a subscription, you can still view the tables of contents of the volumes and the abstract of each article by going to the SpringerLink Homepage, clicking on "Browse by Online Libraries", then "Chemical Sciences", and finally choose Springer Series on Chemical Sensors and Biosensors.

You will find information about the

- Editorial Board
- Aims and Scope
- Instructions for Authors
- Sample Contribution

at springer.com using the search function.

Preface

Demand for in situ surface analysis tools has increased considerably with the advent of nanotechnology and the rapid development of life sciences and chemical sensors. Investigating surface reactions in physics, chemistry, and biology is rewarding and demanding at the same time. In particular, non-invasive techniques are required to study subtle effects as they occur at cellular membranes. The detection and quantification of subtle shifts in mechanical properties comprising viscoelastic properties of soft matter, friction on small length scales, adsorption of biomolecules, and interfacial forces created by molecular contacts are desirable measurements for understanding processes occurring at the solid liquid and solid gas interface.

In the last few years, acoustic resonators have leaped forward, meeting many of the demands of interfacial sensors. Among them, thickness shear mode (TSM) resonators are the most widespread and versatile acoustic resonators capable of studying viscoelastic properties of soft matter, adsorption of molecules down to the picogram regime, motility of living cells just to name a few prominent achievements. The beauty of this approach is that the information content goes beyond most optical techniques comprising information about mass density, contact mechanics, dynamics of interfacial processes, surface roughness, and viscoelasticity of many layer systems. Acoustic sensor technology is a highly interdisciplinary field. Researchers from different areas ranging from electrical engineering to cell biology have contributed valuable technological concepts, theoretical insights and applications to the use and development of thickness shear mode resonators as extremely sensitive, robust and versatile sensors, which are discussed in this book.

The book is intended to give a state-of-the-art overview of the recent achievements in the area of piezoelectric sensors. The focus lies on TSM resonators, since this class of piezoelectric devices is most frequently used in physical and chemical sensor and biosensor applications, and they are largely commercially available. The book is divided into three parts. The first four chapters cover the physical background of piezoelectric devices. While Ralf Lucklum and Frank Eichelbaum discuss different interface circuits to drive a TSM resonator in the first chapter, Diethelm Johannsmann provides a comprehensive picture of how to treat different load situations of the quartz crystal microbalance (QCM) in the second, including rather new development in the area of con-

tact mechanics in the fourth chapter. The third chapter, written by Michael Urbakh and coworkers, the solid/liquid interface, as probed by the QCM, is discussed focusing on the impact of surface roughness and interfacial friction. The second part of the book then presents a variety of possible applications of the QCM and surface acoustic wave (SAW) sensors. The chapter by Franz Dickert and Peter Lieberzeit describes how functionalization of a QCM and SAW sensor surface with imprinted polymers allow monitoring very different analytes ranging from simple organic molecules to bacteria and cells. The next two chapters by Marco Mascini and coworkers and Robert Vaughan and George G. Guilbault, respectively, provide an overview of nucleic acid biosensors and immunosensors based on QCM techniques. In the eighth chapter we show that, besides pure analytical applications, the combination of QCM with atomic force microscopy measurements, and Monte-Carlo simulations allow for a better understanding of the formation process of solid supported membranes (SSMs) on quartz resonator surfaces and the interaction of proteins with SSMs. Joachim Wegener and coworkers demonstrate in the ninth chapter that, due to the sensitivity of a TSM resonator to changes in viscoelasticity, the QCM is an invaluable tool to monitor and understand the interface between cells and the resonator's surface, which makes it possible to use this device in whole cell biosensor applications.

This aspect is also discussed in the chapter written by Kenneth Marx, who not only describes recent applications of the QCM to study thin polymer films, electron transfer systems, biological macromolecules, and cells, but also the application of the electrochemical QCM. This chapter is one of four of the third part of this book, which is devoted to advanced QCM techniques. Yoshio Okahata and coworkers demonstrate that a 27 MHz quartz plate enables one to monitor the action of enzymes online, while Matthew Cooper gives an overview on resonant acoustic profiling (RAP^{TM}) and rupture event scanning (REVS^{TM}) realized by a QCM at Akubio. Fredrik Höök and Bengt Kasemo point out the applicability of the QCM-D technique to biological questions pronouncing that there is more than pure microgravimetry involved in interfacial processes.

We hope that the reader will find these contributions from leading scientists working in the field of piezoelectric sensors stimulating.

Finally, we would like to express our gratitude to all the authors who have contributed to this book, to Britta Wecker for her able handling of the manuscripts, and to Otto S. Wolfbeis for his invitation to edit a book on this cutting-edge topic in sensor development for this series and to Springer for their professionalism in producing this book.

October 2006

Andreas Janshoff
Claudia Steinem

Contents

Part A
Physical Aspects of QCM-Measurements

Springer Ser Chem Sens Biosens (2007) 5: 3–47
DOI 10.1007/5346_023

Published online: 11 August 2006

Interface Circuits for QCM Sensors

Ralf Lucklum (✉) · Frank Eichelbaum

Institute for Micro- and Sensor Systems (IMOS),
Otto-von-Guericke-University Magdeburg, 39106 Magdeburg, Germany
ralf.lucklum@e-technik.uni-magdeburg.de

Abstract Oscillators are the standard interface circuits for quartz crystal resonator sensors. When applying these sensors in gases a large set of circuits is available, which can be adapted to particular applications. In liquid applications viscous damping accompanied by a significant loss in the *Q* factor of the resonator requires specific solutions. We summarize major design rules and discuss approved solutions. We especially address the series resonance frequency and motional resistance determination and parallel capacitance compensation. We furthermore introduce recent developments in network analysis and impulse excitation technique for more sophisticated applications. Impedance analysis especially allows a more complete characterization of the sensor and can nowadays be

realized with sensor interface circuitry. The performance of electrical circuitry depends essentially on the stability of the acoustic device. We therefore begin with a discussion of selected quartz crystal properties, disturbances from temperature and mechanical stress, and analyze AT and BT cut from the sensor point of view.

Keywords Quartz crystals · Resonance frequencies · Oscillators · Network analysis

Abbreviations

A	Gain
A	Amplifier
a, b, c	Acoustic modes
ALC	Automatic level control
B	Susceptance
BAW	Bulk acoustic wave
C	Capacitance
C_0	Parallel capacitance
C_c	Equivalent capacitance
C_{ext}	External (stray) capacitance
C_q	Equivalent (motional) capacitance of bare quartz crystal
c_{26}	Element of piezoelectric tensor
c_{66}	Element of mechanical stiffness tensor
$\tilde{c}_q$	Effective complex shear modulus of quartz crystal
c_q	Piezoelectrically stiffened shear modulus of quartz crystal (real part)
D	Dissipation
D	Diode
d	Plate thickness, crystal thickness
DA	Differential amplifier
DDS	Direct digital synthesizer
DT	Diamond transistor
E	Power source
$e_q \equiv e_{26}$	
f	Frequency
f_0	Mechanical resonance frequency
f_{osc}	Oscillator frequency
f_{pb}	Plate-back frequency
f_s, f_r, f_m	Series resonance frequencies of quartz crystal
f_p, f_a, f_n	Parallel resonance frequencies of quartz crystal
f_V	VCO frequency
FM	Frequency modulation
FPGA	Field programmable gate array
G	Conductance
$G(s)$	Transfer function
$g(t)$	Impulse response
HPF	High pass filter
I	Current
I	Integrator
$j \equiv \sqrt{-1}$	
k	Feedback factor
k	Network parameter

$\tilde{K}_q^2$	Electromechanical coupling factor (complex value)
K_q^2	Electromechanical coupling factor ($\eta_q = 0$)
L	Inductance
$L_q(L_L)$	Equivalent (motional) inductance of bare quartz crystal (acoustic load)
$L\{\}$	Laplace transform
LPF	Low pass filter
M	Multiplier
N	Number of samples
n	Harmonic number
OSC	Auxiliary oscillator
PI	Proportional-integral
PLL	Phase-locked loop
PR	Peak rectifier
PS	Phase shifter
Q	Quality factor
QCM	Quartz crystal microbalance
QCR	Quartz crystal resonator
R	Resistance
$R_q(R_L)$	Equivalent (motional) resistance of bare quartz crystal (acoustic load)
r	Voltage ratio
r_E	Internal dynamic emitter resistance
r_q	Electrode radius
$s \equiv \sigma + j\omega$	Laplace variable
SAW	Surface acoustic wave
T	Temperature
T	Period
t	Time
V	Voltage
v	Acoustic velocity
V_D	DC voltage representing acoustic energy dissipation
VCA	Voltage-controlled amplifier
VCO	Voltage-controlled oscillator
X	Reactance
Y	Electrical admittance
Z	Electrical impedance
Z_L	Acoustic load (impedance)
Z_q	(Characteristic) acoustic impedance of quartz
α	Resistance ratio
α_q	Acoustic phase shift in quartz crystal
χ_{mk}	kth Root of Bessel function of order m
ε_{22}	Element of permittivity tensor
$\varepsilon_q \equiv \varepsilon_{22}$	
η	(Effective) viscosity
φ	Phase angle
φ, θ	Crystal cut angles
κ	Design parameter of circular quartz discs
ρ	Density
τ	Time constant
ω	Angular frequency

Indices

c	Index for coating
el	Index for electrical
H	Index for high frequency
i	Counting index
IF	Index for intermediate frequency
L	Index for low frequency
L	Index for load
liq	Index for (Newtonian) liquid
n, *m*, *k*	Indices for acoustic modes in circular plate
m	Index for motional
p	Index for parallel
off	Index for offset
open	Index if $Z \to \infty$
out	Index for output
q	Index for quartz
ref	Index for reference
s	Index for series
short	Index if $Z = 0$
$*$	Index for sum of lumped elements
$\hat{}$	Index for peak value

1 Introduction

There has been remarkable progress in the development and application of the quartz crystal microbalance (QCM) principle in sensitive devices for the detection and concentration measurement of specific molecules in gaseous and liquid media [1]. Since the behavior of quartz crystal resonator (QCR) sensors in gases is similar to quartz crystals technically used as frequency standards, a large set of circuit configurations is available, whose known properties can merely be adapted to particular applications [2–5]. In many cases quartz crystals used in electronic circuitry, sometimes even from mass production, are employed.

However, for chemical sensing applications these generally sealed devices have to be opened and their surface functionalized with a chemically sensitive coating. Just open the case reduces the quality factor, *Q*, by 1/3, and the aging is 100–1000 times larger [6]. Viscoelastic properties of macromolecular coating materials can have a strong impact on the vibration behavior of the crystal and diminish the *Q* factor.

When using QCM sensors in liquid media one faces a considerably more involved situation. The behavior of QCRs under these conditions diverges essentially from that in vacuum or gaseous media. Most important is the significant dissipation of acoustic energy due to liquid contact, which translates to energy lost from the electrical circuit. The oscillation is significantly

damped and the *Q* factor is significantly reduced. This effect has two consequences: Firstly, proofed circuit configurations for standard applications cannot be applied anymore. Secondly, the zero-phase series resonance frequency deviates notably from the series resonance frequency at in-phase admittance maximum. This deviation is important, since the latter is the only straightforward value when applying QCRs for sensing applications.

These facts must be taken into account when designing the sensor system. We will therefore start with some considerations related to the quartz crystal as transducer element. We will continue with an analysis of standard quartz oscillators. We will give a survey on suitable circuit configurations and will outline their advantages and drawbacks. Finally, a few interesting developments will be presented in more detail.

2
Crystals

2.1
Temperature and Force Sensitivity

The performance of oscillators depends essentially on the stability of the acoustic device [7–9] no matter if working as electromechanical resonator or delay line. Because of its extraordinary importance we will concentrate further on resonators, namely quartz crystal resonators. However, the analysis is descriptive also for other piezoelectric materials and partly for delay line elements as well.

In a very fundamental way the principle of resonators must be described on the basis of a traveling wave in a confined structure. Resonance in a vibrating system is always associated with a standing wave. The frequency is jointly determined by the velocity of the traveling wave and the dimensions of the confinement structure. In the case of a bulk acoustic wave (BAW) resonator, an acoustic wave is confined by the substrate surfaces. The eigenfrequencies can be mechanically and/or electrically perturbed, wanted or unwanted, by either a change in the dimension of the resonator or by a change in the wave velocity. Considering a complex wave vector those perturbations can also cause a change of the acoustic wave amplitude, reflected in values of practical interest: a change of the phase slope or in the *Q* factor of the device.

In its original application as timing reference, special care has been taken to minimize the perturbations on frequency of the selected mode of vibration caused by unavoidable variations in the environment, first of all temperature and acceleration. The breakthrough of quartz crystal resonators in timekeeping is very much correlated to the existence of a specific crystal cut, at which the device resonance frequency provides a zero temperature coefficient of frequency at 25 °C and a remarkable temperature stability around room

temperature [10]. Operated in the thickness shear mode, this so called AT-cut quartz utilizes having two almost equal, but opposite temperature coefficients of elastic stiffness compensating each other. This temperature insensitivity is also favorable for sensor applications where variations in temperature are usually a common concomitant. However, the temperature insensitivity of the AT-cut is limited to bare crystals.

Applying a coating on one or the two main surfaces of the quartz disc reduces the temperature stability considerably, because acoustic properties of the coating material usually depict much larger temperature sensitivities. The overall temperature sensitivity of the sensor can be roughly estimated taking the ratio of crystal and coating thickness into account. The temperature sensitivity is significantly increased when operating the crystal in a liquid. A shear wave evanescently penetrates into the liquid, thereby probing liquid density and viscosity. The latter value can vary by an order of magnitude or more with temperature and hence it governs the temperature coefficient of the sensor signal. The temperature dependence of liquid viscosity defines the requirements of temperature maintenance of the experimental or measurement setup. Applying a reference sensor for temperature effect compensation is a passable way; however, the design of a reference element is a challenging task.

As a second important fact, the coating required for (bio)chemical sensing also tends to introduce mechanical stress into the system. For obvious reasons the development concentrates on chemical sensitivity and selectivity. Mechanical and thermal properties should not be underestimated. They strongly determine sensor reproducibility. On the one hand, stress from different thermal expansion coefficients contributes to the overall temperature sensitivity of the sensor in an indirect way. On the other hand, the coating procedure must be considered to generate a noticeable amount of initial stress. One example is a polymer film preparation from solution, where the solvent evaporates more or less quickly and a solid polymer film remains on the crystal surface. At the beginning of solvent evaporation the relaxation time describing the time necessary for the macromolecule to realize conformational changes is short enough to completely release the stress resulting from volume reduction accompanying solvent evaporation. With continuously decreasing solvent content the relaxation time increases and the coating might not be able to release the generated stress within preparation time. A certain amount of stress is “frozen” in the film and slowly released. Under those circumstances the resonance frequency tends to show a long-term drift. This relaxation phenomenon must not be mixed up with the viscoelastic response of the coating to acoustic wave perturbations of the equilibrium state, as discussed in Sect. 2. Due to the different time scales the coating can behave rigidly without significant damping of the acoustic wave at the elevated ultrasonic frequencies, and at the same time act like a viscoelastic fluid in response to the quasi-static stress introduced during preparation. The same holds for thermal stress when temperature varies.

The force–frequency effect was first observed by Bottom in 1947 [11]. Since then, broad effort has been put into the design of piezoelectric resonators for time-keeping purposes to reduce the effect of forces, mostly to make the devices immune to acceleration. The initial emphasis of these activities was driven by military applications. With the advent of satellite communications systems, sensitivity to mechanical stress, mostly generated from acceleration, is an important specification for commercial hardware as well. The sensitivity of piezoelectric transducers to acceleration has been critically reviewed in [12]. Kosinski's analysis also provides conclusions for sensor development although advances achieved in resonator design get partly lost when using them as sensor elements [13]. The driving factor behind frequency shifts caused by a mechanical bias is deformation of the resonator. The effect can be investigated based on Tiersten's perturbation approach [14]. Changes in the wave velocity are primarily a result of the non-linear elastic behavior of the piezoelectric substrate; changes in the confinement dimensions is primarily a linear mechanical effect. The frequency shift caused by wave velocity changes is typically substantially larger than that caused by changes in the resonator dimensions, hence the effect is sometimes thought of in a purely non-linear manner. However, the linear part also causes an asymmetry in the effective material constants [15]. The important consequence is that different mechanical phenomena must be analyzed for the way in which they act as deformation drivers. Acceleration sensitivity is hence a reaction to a force against the mounting structure, planar stress sensitivity a result of interfacial stress at the substrate/electrode/coating interfaces, and aging a relaxation phenomenon of the composite resonator and the mounting structure. The practical implication for sensor development is that techniques that reduce the generic deformation sensitivity will improve the immunity to all of these parameters simultaneously [12].

Minimization of the resonator deformation is a basic structural engineering problem. It has the advantage of achieving improvements without regard to fabrication tolerances. On the one hand, plate thickness obviously governs normal deformation, but on the other hand, plate thickness is the frequency-determining value for BAW resonators. In consequence, a net $1/f$ dependence of BAW resonator sensitivity on acceleration has been found for scaled designs [12]. Scaled design means a similar crystal diameter- and electrode-to-thickness ratio. Furthermore, the BAW acceleration sensitivity dependence has been found experimentally to initially decrease with increasing harmonic number and later to be essentially constant or slightly increased [16]. In sensor applications, especially those which require liquid medium contact on one side of the crystal only, special attention must be paid to the mounting structure, which in addition to sealing must minimize the resonator deformation. An optimized mounting structure is symmetric with respect to the top and bottom of the disc. A viscoelastic mount and a set of rigid support posts should be advantageous to release both in-plane and normal stress [12]. Iso-

lation of the crystal from external vibrations is less effective due to the direct impact of the analyte on the crystal. Pressure variations originated, e.g., from a peristaltic pump must be reduced with advanced sensor system design, for example a fluidic low-pass filter [17]. Static pressure, e.g., hydrostatic pressure from a liquid column acting on one side of the crystal, must be avoided, carefully compensated or at least kept constant. For example, a simple dipping experiment with a sensor, whose second surface is protected from liquid contact by casing may fail if the immersion depths and the immersion angle are not carefully controlled.

2.2 Crystal Cuts

The only design criterion of thickness–shear mode resonators for frequency control is frequency stability. The AT-cut is most appropriate. AT-cut quartz crystals are also typically used as sensor elements, although the requirements for sensor applications are more complex. If part of the temperature insensitivity of AT-cut quartz crystal resonators is lost anyway in sensor applications, it is worth considering other crystal cuts. Each cut of a piezoelectric crystal supports three bulk acoustic modes, each having different phase velocity, different polarization, and different piezoelectric coupling. The modes are usually ordered in terms of the wave velocity, with "*a*" having the highest and "*c*" having the lowest velocity [18]. The *a*-mode is called quasi-longitudinal, since the largest component is in the direction of wave propagation. The *b*- and the *c*-modes are termed fast quasi-thickness shear and slow quasi-thickness shear, respectively, since the dominant component is shear. The existence of crystal orientations having a purely transverse *b*- and *c*-mode is an important feature when designing a sensor. The resonators are called thickness-shear mode (TSM) sensors. The absence of a longitudinal component makes TSM sensors attractive for sensor applications, especially in liquids. Acoustic energy is trapped within the device and an extremely thin liquid layer adjacent to the resonator – the shear wave is evanescent in viscous fluids – whereas energy from longitudinal waves is radiated into the fluid[1]. This radiation loss must be considered as loss of acoustic energy stored in the transducer and has the same adverse consequences as acoustic energy dissipation.

Plates whose lateral dimensions are much larger than their thickness can be approximated as a thin plate with infinite extension. With two electrodes placed onto the main surfaces the three acoustic modes that can be excited in principle are those associated with wave propagation in the direction of the plate normal. Given that the specific cut has a non-zero coupling factor,

[1] Classical SAW devices utilize a Rayleigh wave, which has a normal component. Therefore SAWs face significant insertion loss when operating in liquids due to radiation of acoustic waves into the liquid.

an applied AC voltage will induce an acoustic wave at the frequency of excitation. The boundary conditions established at the top and bottom of the plate together with the sound velocity in the plate define the frequencies of resonance[2]. Remember, the mechanical resonance frequencies must not be mixed up with the resonance frequencies of quartz crystal oscillator circuits, although the quartz crystal is the frequency-determining element.

Coherent reflections at the top and bottom boundaries of the plate give way for a set of standing acoustic waves between the two main surfaces of the plate. Due to the piezoelectric nature of quartz two sets of resonance frequencies exist for each mode, depending on the electrical boundary conditions. The first set corresponds to a plate with open-circuit boundary conditions. From the physical point of view charges will be collected on the electrodes building up a potential difference and hence an electrical field; from the electrical point of view the electrodes are unconnected. This resonance is termed anti-resonance in the piezoelectric literature and parallel resonance in electronics literature. The second set of resonance frequencies corresponds to a plate with short-circuit boundary conditions. The electrodes are connected and a potential difference cannot be built up. The respective names are resonance in piezoelectric and series resonance in electronics literature. The differences arise from piezoelectric stiffening accompanied by differences in the sound velocity. The anti-resonance (parallel) frequencies of each of the three acoustic modes are completely decoupled giving:

$$f_m = n\frac{v_m}{2d_\mathrm{q}}\,. \tag{1}$$

where index m denotes the mode, v_m is the respective mode velocity, d_q is the plate thickness, and n is the harmonic number and an odd integer; odd only, because even harmonics cannot be excited under symmetric load conditions. By contrast, the (series) resonance frequencies of each mode are coupled and cannot be given in a closed form. The practical consequence is that n is not exactly an (odd) integer [19] (see also Fig. 7 later in this chapter).

Vetelino et al. [20] have studied the properties of singly and doubly rotated cuts from the sensor application point of view. The crystal orientation that defines the cut is determined by two angles, φ and θ. Due to the symmetry of quartz, varying θ from $-90°$ to $90°$ and φ from $0°$ to $30°$ encompasses all the unique cuts possible [21]. Common cuts are AT ($\theta = -35.25°$, $\varphi = 0°$), BT ($\theta = 49.20°$, $\varphi = 0°$), DT ($\theta = 52°$, $\varphi = 0°$), FC ($\theta = -34.33°$, $\varphi = 15°$), IT ($\theta = -34.08°$, $\varphi = 19.10°$), SC ($\theta = -33.93°$, $\varphi = 21.93°$), LC ($\theta = -9.39°$, $\varphi = 11.17°$), and RT ($\theta = 34.50°$, $\varphi = 15°$).

[2] The electrodes are assumed here to be infinitesimally thin and provide just an area of equipotential. From the mechanical point of view the surfaces are assumed to be stress-free. These assumptions are not generally required; they just provide the simplest form of the transducer element.

The main criterion for the selection of an appropriate crystal cut for liquid application is the absence of longitudinal displacements, i.e., to find a cut with pure shear modes or at least a dominant shear mode. This restriction eliminates all *a*-modes. The rotated *Y*-cut family of cuts corresponds to $\varphi = 0$, i.e., a rotation of the *y*-axis about the crystallographic *x*-axis. All *Y*-cuts share the beneficial property of having a single mode that is purely shear. Due to its importance, sensor device key properties are repeated here in Figs. 1, 2, and 3 [20]. The data points were calculated using Matlab and the material constants were taken from Salt's book [21]. Figure 1 shows the wave velocity of the *b*- and the *c*-mode, Fig. 2 the coupling factor, and Fig. 3 the temperature coefficient of frequency.

The acoustic velocity reaches its minimum of about 3316 ms^{-1} at $\theta = -32°$ and its maximum of about 5107 ms^{-1} at $\theta = 58°$. At $\theta = 24°$ the velocities of *b*- and *c*-modes are equal; the shear modes switch between "*b*" and "*c*". The coupling factor has its maximum of about 13.6% in mode "*c*" around $\theta = -5°$.

The two most important cuts, AT and BT, provide a zero temperature coefficient of frequency. Actually, when departing from 25 °C the frequency of AT-cut crystals varies in a cubic manner with respect to temperature. The temperature dependence of BT-cut crystals is quadratic. This second-order response to temperature is larger than the cubic variation of AT-cut quartzes.

The acoustic velocity of the shear mode in AT-cut quartz is not far from the minimum acoustic velocity of the *c*-mode, whereas the BT-cut is next to the maximum of the *b*-mode. Only one of the three modes can be electrically

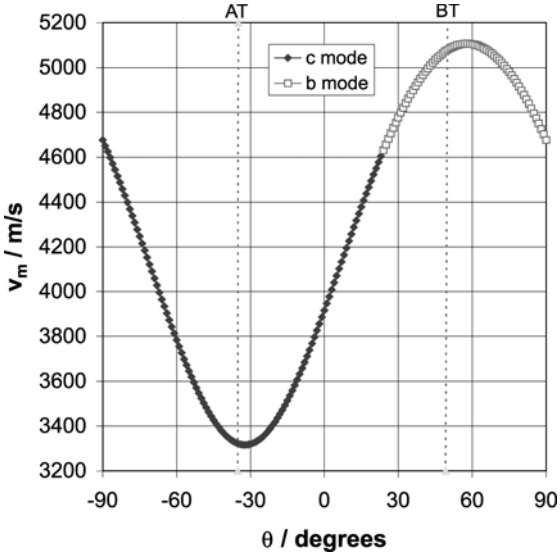

Fig. 1 Acoustic wave velocity for pure shear mode of rotated *Y*-cut quartz (courtesy of J. Vetelino [20])

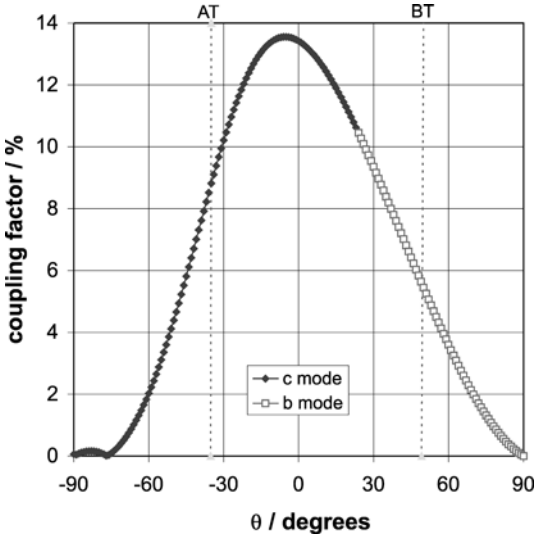

Fig. 2 Coupling factor for pure shear mode of rotated *Y*-cut quartz (courtesy of J. Vetelino [20])

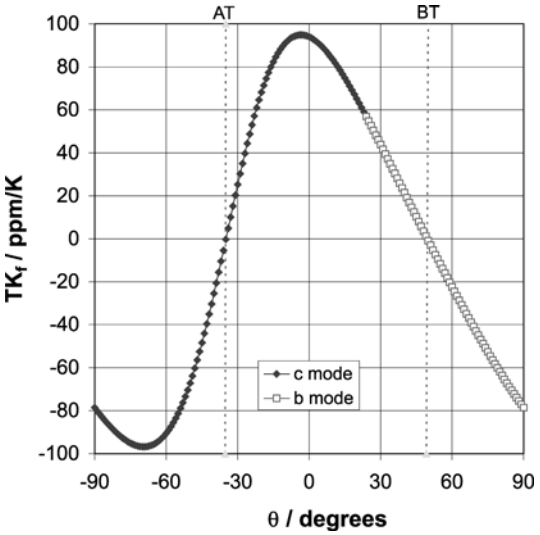

Fig. 3 Temperature coefficient of frequency for pure shear mode of rotated *Y*-cut quartz (courtesy of J. Vetelino [20])

excited. The coupling coefficients of the other two are zero. This reduces the occurrence of spurious modes to those which owe their existence to the finite lateral dimensions of a real crystal and the necessity of mechanical clamps. The piezoelectric coupling of AT-cut crystals is reasonably high with 8.8%

and moderate for BT-cut quartzes with 5.5%. A larger coupling factor allows for excitation of the device with lower voltages.

For discussion of the consequences of acoustic wave velocity and coupling factor for sensor applications we recall the electrical impedance, Z_{el}, as it can be derived from the one-dimensional transmission line model [22, 23]:

$$Z_{el} = \frac{1}{j\omega C_0}\left(1 - \frac{K_q^2}{\alpha_q}\cdot\frac{2\tan\frac{\alpha_q}{2} - j\frac{Z_L}{Z_q}}{1 - j\frac{Z_L}{Z_q}\cot\alpha_q}\right). \tag{2}$$

Equation 2 can be rewritten in a way that Z_{el} can be presented as a parallel arrangement of C_0, the only genuine electrical parameter in Eq. 2 (formed by the two electrodes with quartz as dielectric), and a so-called motional impedance, $Z_m : Z_{el} = C_0 \| Z_m$ (Fig. 4a). Z_m contains two elements in series. The first summand, Z_{mq}, includes only crystal parameters and describes the motional impedance of the quartz crystal as a function of frequency $\omega = 2\pi f$. The second summand expresses the "transformation" of the acoustic load, Z_L, into the (electrical) motional load impedance, Z_{mL}. We therefore call the fraction in front of Z_L transformation factor. Applying some assumptions reasonable in most sensor applications Z_m becomes:

$$Z_m \approx \frac{j}{\pi C_0}\frac{d_q}{v_q}\left(\frac{\alpha^2 - \pi^2}{8\tilde{K}_q^2} - 1\right) + \frac{d_q}{4C_0\cdot\rho_q\cdot\tilde{K}_q^2 v_q^2}Z_L\,, \tag{3}$$

$\tilde{K}_q^2 = \frac{e_q^2}{\varepsilon_q \tilde{c}_q}$ is the electromechanical coupling coefficient with $\tilde{c}_q \equiv c_{66} + \frac{e_{26}^2}{\varepsilon_{22}} + j\omega\eta_q \equiv c_q + j\omega\eta_q$, $e_q \equiv e_{26}$ and $\varepsilon_q \equiv \varepsilon_{22}$ with c_{66}, e_{26}, and ε_{22} being components of the material property tensors for mechanical stiffness, piezoelectric constant, and permittivity, respectively, and η_q being the effective quartz crystal viscosity. α_q is the acoustic phase shift in the quartz crystal, ρ_q is the quartz density, and $Z_q = \rho_q v_q$ is the characteristic acoustic impedance of quartz. Index q has been introduced to denote material properties of the quartz crystal. By contrast, Z_L is the acoustic load (impedance) generated from coatings, liquids, etc. and acts at the surface of the crystal. Z_{mL} is the electrical representation of Z_L and therefore carries all information relevant for sensing.

Consequently, the second term in Eq. 3 is the important one for sensor applications. Obviously a small coupling factor and a small wave velocity increase the electrical representation of the acoustic load. On the other hand, the quartz motional impedance also alters upon changes in v_q and $\tilde{K}_q^2$. It is therefore helpful to rewrite Eq. 3 for our purposes:

$$Z_m \approx \underbrace{\frac{\pi^2\eta_q}{8e_q^2\kappa d_q} + j\omega\frac{\rho_q d_q}{8e_q^2\kappa} + \frac{1}{j\omega\frac{8e_q^2\kappa d_q}{\pi^2 c_q}} + \frac{1}{j\omega(-C_0)}}_{Z_{mq}} + \underbrace{\frac{1}{4e_q^2\kappa}Z_L}_{Z_{mL}} \tag{4}$$

where $\kappa = \pi(r_q/d_q)^2$ is a design parameter for circular quartz discs and electrodes, which implies the ratio between electrode radius, r_q, and thickness of the quartz disc, d_q. The first three summands introduce the lumped elements, R_q, L_q, and C_q, respectively (Fig. 4b). The fourth summand is a straightforward result of the transmission line model and must not be neglected. With Eq. 4 one can define the already empirically found elements, known from the Butterworth–Van Dyke (BVD) equivalent circuit of a quartz crystal (Fig. 4c)[3]:

$$R_q = R_s = \frac{\pi^2 \eta_q}{8 e_q^2 \kappa d_q}$$

$$L_q = L_s = \frac{\rho_q d_q}{8 e_q^2 \kappa} \tag{5}$$

$$C_q = \frac{8 e_q^2 \kappa d_q}{\pi^2 c_q} \quad C_s = \frac{C_0 C_q}{C_0 - C_q} = \frac{8 e_q^2 \kappa d_q}{c_q \left(\pi^2 - 8K_q^2\right)},$$

with $K_q^2 = e_q^2/(\varepsilon_q c_q)$.

In the approximation Eq. 4, the transformation factor $1/(4e_q^2\kappa)$ does not contain wave velocity or coupling coefficient and is therefore independent of the quartz cut; neither does it include the frequency. The transformation factor is real and constant if the electrode radius–thickness ratio is constant. Therefore the real part of Z_L directly determines the real part of Z_{mL}, whereas the imaginary part of Z_L defines the imaginary part of Z_{mL}. In a narrow frequency range one can represent $\mathrm{Re}(Z_m)$ as R_L and $\mathrm{Im}(Z_L)$ as ωL_L. In general, $R_L = R_L(\omega)$ and $L_L = L_L(\omega)$ remain frequency-dependent due to $Z_L = Z_L(\omega)$ (not linear).

Fig. 4 depicts Eqs. 2–Eq. 5 in an electrical circuit.

The resistance increase is consequently independent of the quartz cut:

$$\Delta R = R_L = \frac{1}{4e_q^2\kappa}\mathrm{Re}\left(Z_L\right). \tag{6}$$

The calculation of the frequency shift requires the inductance L_q. Figure 4c delivers for the series resonance frequency $\omega_{sL} = 1/\sqrt{(L_q + L_L)\, C_s} = \omega_s/\sqrt{1 + L_L/L_q} \approx \omega_s(1 - L_L/2L_q)$ and therefore:

$$\frac{\Delta f_s}{f_s} \approx -\frac{L_L}{2L_q}, \tag{7}$$

[3] In consequence of – C_0, the series resonance frequency at conductivity maximum, G_{max}, (with $Y = G + jB$) is $\omega_s = \left(L_q \frac{C_0 C_q}{C_0 - C_q}\right)^{-1/2} = \sqrt{\frac{1}{L_q C_q}\left(1 - \frac{8K_q^2}{\pi^2}\right)}$ whereas $\omega_p = \sqrt{\frac{1}{L_q C_q}}$ is the parallel frequency at resistance maximum, R_{max} ($Z = R + jX$). Because of $C_s = C_q/\left(1 - \frac{8K_q^2}{\pi^2}\right)$ the definitions are obviously consistent with Eq. 14, which uses the nomenclature of electronic literature. Series and parallel resonance frequencies lie close together with differences decreasing with larger coupling factor.

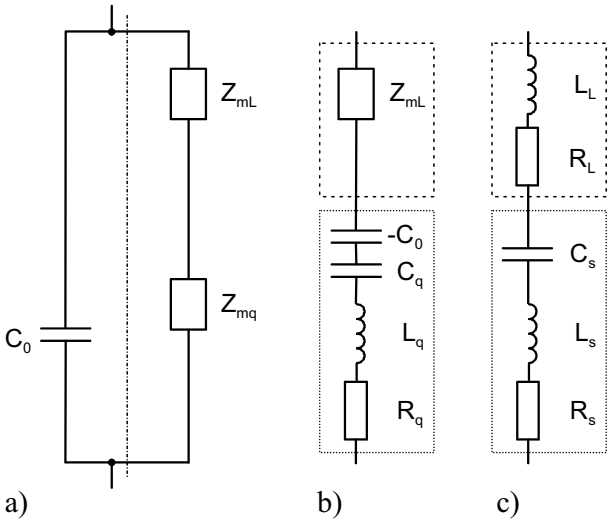

Fig. 4 Equivalent circuit representation of Eq. 2 (**a**), Eqs. 3, 4 (**b**), and Eq. 5 (**c**)

or with Eqs. 4 and Eq. 5:

$$\Delta f_s = -\frac{1}{2\pi\rho_q d_q}\mathrm{Im}\left(Z_L\right). \tag{8}$$

Obviously the factor relating $\mathrm{Im}(Z_L)$ to Δf_s is proportional to $1/d_q$ and, at the first glance, independent of the crystal cut. Δf_s is independent of κ and hence of the electrode diameter[4] as well. As consequence of $v_q = 2d_q f_0$ the frequency shift remains dependent on v_q. The effect of wave velocity on the sensor's frequency sensitivity is dependent upon whether a certain resonance frequency or a certain crystal thickness is the (experimentally) given value. It can be easily demonstrated in the simplest case of pure mass sensitivity ($Z_L = j\omega\rho_c d_c$ holds). Following Sauerbrey, the frequency sensitivity can be rewritten as:

$$\frac{\Delta f}{\rho_c d_c} \approx -\frac{2f_0^2}{\rho_q v_q} = -\frac{v_q}{2\rho_q d_q^2}. \tag{9}$$

Obviously a small wave velocity in the crystal improves the mass sensitivity of the sensor for a given mechanical resonance frequency f_0, whereas a large wave velocity increases the mass sensitivity if thickness of the crystal must not fall below a specific value. Table 1 illustrates these basic findings for AT-cut (exemplarily for a small v_q) and BT-cut quartz (exemplarily for a high v_q) for two cases: a 100 nm rigid film (Sauerbrey case) and a semi-infinite liquid with a viscosity of 1 cP (Kanazawa case).

[4] Note, that these conclusions are based on a one-dimensional approximation based on $d_q \ll r_q$. The smaller the electrode diameter, the more effects like fringing fields come into play, which are not considered in the model.

Table 1 Some example data for AT-and BT-cut quartz crystals

	AT		BT	
v_q/ms^{-1}	3322		5071	
K_q^2	0.0078		0.00335	
f_0/MHz	10	15.265	10	15.265
d_q/μm	166.1	108.8	253.5	166.1
r_q/mm	3	2	3.3	3
f_s/MHz	9.968	15.216	9.986	15.244
R_q/Ω	8	12	5	8
L_q/mH	5.914	3.874	9.0274	5.914
C_q/pF	0.043	0.028	0.028	0.018
C_0/pF	6.778	4.440	10.347	6.778
Q factor	46 562	30 502	108 497	71 076
Δf_{100}/kHz	2.3	5.3	1.5	3.5
Δf_{1cP}/Hz	2.0	3.8	1.3	2.5
ΔR_{1cP}/Ω	150	186	150	186
$\Delta R_{1cP}/\Delta f_{1cP}$/Ω/kHz	74	49	113	74

Indices 100 and 1 cP denote the cause of the signal shift: a rigid 100 nm thick film or a semi-infinite liquid of 1 cP, respectively

A vast majority of (bio)chemical QCM sensors involve AT-cut quartz. Experiments are usually performed at a certain frequency and AT-cut crystals provide the larger frequency shift. However, BT-cut quartz can be considered as an interesting alternative, if, e.g., a certain crystal thickness is required for mechanical stability. As discussed already, the limited temperature insensitivity of BT-cut crystals plays a minor role in sensor applications because temperature maintenance is usually required anyway.

When applying quartz crystal resonators outside Sauerbrey's limitations in the so-called non-gravimetric regime, material properties come into play. The electrical admittance (impedance) of the coated quartz crystal gives access to the determination of material properties of the coating. The crystal cut can again be used for optimization of the sensor performance. If mechanical stability is an issue (e.g., lateral stress induced during the experiment) BT-cut crystals are favorable.

2.3 High Frequency Crystals

An increase in the sensor sensitivity can be realized when decreasing d_q. A minimal thickness around 55 μm to limit mechanical fragility results in a fundamental frequency of 30 MHz [24]. The application of photolitho-

graphy and wet etching processes has been found to be a promising approach to push this limit down to smaller thicknesses and to fabricate mechanically stable quartz membranes with higher resonance frequencies and smaller diameters in a supporting quartz frame [25]. This technique also allows the fabrication of sensor arrays on one quartz wafer (Fig. 5) [26]. Mechanical cross-talk between the array elements can be minimized by a proper design.

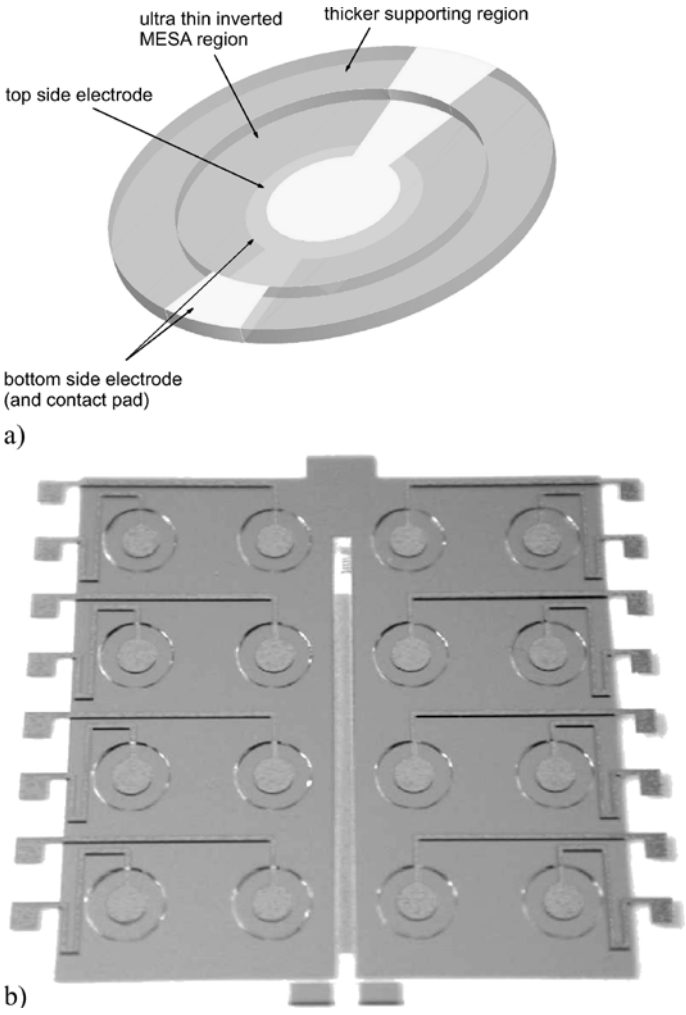

Fig. 5 Scheme of inverted MESA quartz crystal (**a**) and realized 4×4 quartz crystal sensor array (**b**). The membrane of each sensor element has been thinned with wet etching. The resonance frequency of each sensor could be elevated to frequencies up to 50 MHz. The analyte usually faces the flat (bottom) surface

The challenging task of high frequency resonators arises from inharmonic modes, often called spurious modes or spurs. These are characterized by movement of particles in several regions of the quartz disc in antiphase. If the frequency separation between the harmonic and inharmonic modes is not sufficiently large, modes can efficiently be coupled. Frequency jumps of quartz oscillators are an unwanted effect that impedes a reliable frequency measurement. Spurious modes, especially those which lie close to the resonance frequency, enhance the challenges of oscillator design.

The eigenfrequencies of a circular plate have been found to be [27]:

$$f_{nmk} = f_{n01}\left[1 + \frac{\chi_{mk}^2}{2n^2\pi\kappa}\right], \tag{10}$$

with $n = 1, 3, 5, \ldots$, $m = 0, 1, 2, \ldots$, $k = 1, 2, 3, \ldots$ and χ_{mk} being the kth root of the Bessel function of order m, and f_{n01} being the frequency of the nth harmonic mode. The second term in the brackets of Eq. 10 corresponds to the frequency difference between harmonic and inharmonic modes. This difference increases with decreasing κ, i.e., with decreasing electrode radius–quartz crystal thickness ratio. Consequently the electrode size must be reduced when increasing the resonance frequency. Energy trapping [28], e.g., based on MESA shaped structures [29], or contouring [27], or beveling [30] can be employed to suppress or shift the unwanted modes to higher frequencies. The latter two procedures are not feasible for wet etching processes. A rule of thumb for the design is given by the so-called plate-back frequency, Δf_{pb}. With $\chi_{11} = 3.832$ one gets:

$$\Delta f_{\mathrm{pb}} < f_0 \frac{2.337}{n^2\kappa} \tag{11}$$

to suppress the first mode ($n11$) and all higher modes. In practice, the bare device is etched to a thickness that corresponds to a frequency somewhat above the wanted resonance frequency, f_0. The electrodes are then applied, reducing the frequency to f_0. This plate-back frequency should fulfill Eq. 11 to suppress inharmonic modes. Considering that Δf_{pb} is caused by the mass per area of the electrodes, the maximum electrode thickness can be derived by comparison of Eqs. 9 and Eq. 11. This thickness is proportional to h_{q}/κ. Hence thinning the quartz crystal thickness would reduce Δf_{pb}, therefore κ cannot kept constant. Figure 6 shows a plot of diameter versus thickness of gold electrodes for three different resonance frequencies. Considering furthermore that the electrode thickness cannot be reduced below a certain value without reducing electrical conductivity, the only free design parameter is the electrode diameter.

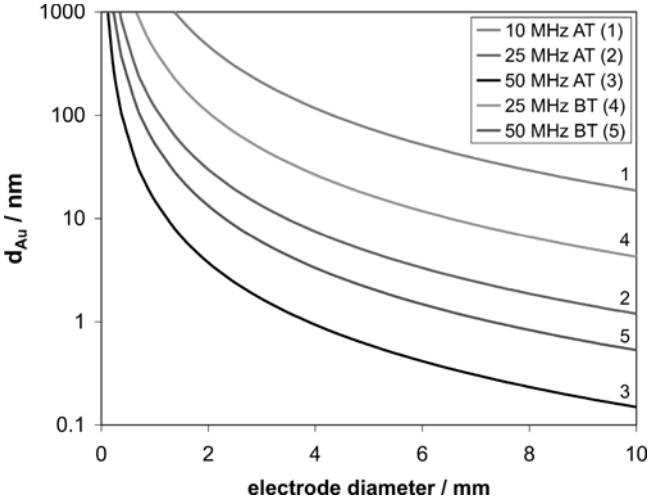

Fig. 6 Relation between geometrical gold electrode parameters for suppressing spurs for AT-and BT cut quartz crystals

An unavoidable consequence of crystal thinning is a reduction of the Q factor. Applying Eq. 5 the Q factor is:

$$Q = \frac{\omega L_q}{R_q} = \frac{\rho_q v_q d_q}{\pi \eta_q} = \frac{\rho_q v_q^2}{\omega_0 \eta_q} . \tag{12}$$

It decreases linearly with decreasing d_q or is inversely proportional to f_0 (assuming the effective viscosity does not change with the crystal dimensions). A large wave velocity improves the Q factor, hence the BT-cut provides enhanced properties. Note that Eq. 12 does not contain κ; hence the Q factor of the crystal does not depend on the electrode diameter in a direct manner. However, η_q is an effective value and tends to increase with decreasing r_q. As part of electronic circuitry an increase of R_q may also reduce the signal-to-noise ratio.

In liquid applications the Q factor is given by:

$$Q = \frac{\omega \left(L_q + L_{liq}\right)}{R_q + R_{liq}} \approx \frac{\pi \rho_q v_q}{\sqrt{2\omega \rho_{liq} \eta_{liq}}} . \tag{13}$$

The additive contributions to L_q and R_q are similar due to similar real and imaginary parts of Z_L. Because $L_q \gg L_{liq}$ and $R_q \ll R_{liq}$ holds, Q changes approximately inversely with $\sqrt{f_0}$. This behavior is reflected in the plot of the real part of electrical admittance, G, of a quartz crystal with single side contact to water, Fig. 7. Both maximum and slope continuously decrease with

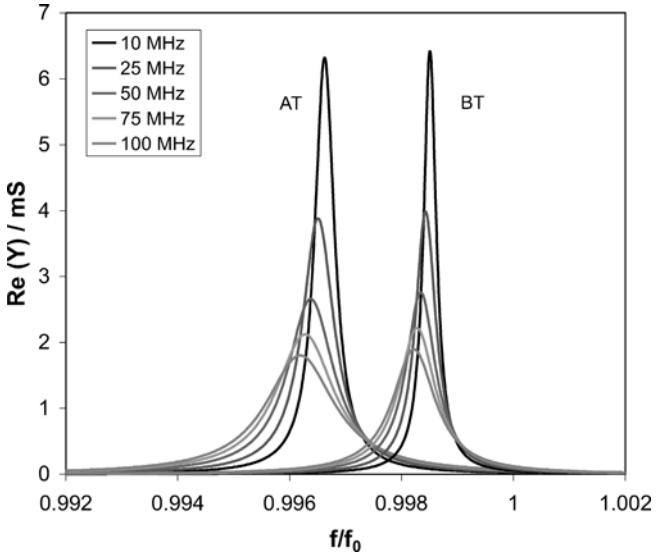

Fig. 7 Plot of real part admittance, G ($Y = G + jX$), against reduced frequency for AT-and BT-cut quartz crystals for different fundamental frequencies, f_0

frequency. The same holds for phase and phase slope, which makes oscillator design more involved. The differences between AT- and BT-cut are less pronounced due to liquid load.

In summary, when looking for the optimal sensor design several conflictive rules have to be taken into account. Only maximum frequency shift is not an appropriate measure. A better value is the limit of detection, which depends on the signal-to-noise ratio. Crystals with a higher resonance frequency supply a larger signal. AT-cut crystals are the better choice when working at a specific resonance frequency. They provide a smaller resistance change to frequency shift ratio in liquid applications as well. The Q factor is an important value governing frequency stability. Here, quartz resonators with a lower resonance frequency are favorable. With respect to $Q \cdot \Delta f$ the frequency dependence becomes approximately linear for a rigid coating. BT or other crystal cuts with large wave velocity offer advantageous properties.

Temperature dependence is a second major issue. It is small for AT-cut crystals; however, temperature fluctuations cause fluctuations in R_q inversely proportional to Q [7]. This effect is small compared to temperature effects having their origin in properties of the measurand. In liquid applications, the most temperature-sensitive value is the liquid viscosity. Here, temperature-induced variations in frequency increase with $\sqrt{\omega}$, whereas mass sensitivity increases with ω. Therefore, an elevated resonance frequency is helpful.

Sensitivity to mechanical perturbations is a third major problem. It is smaller for thicker crystals, i.e., lower resonance frequencies. BT-cut crystals are favorable due to their larger thickness at a given resonance frequency.

Finally, noise and systematic errors introduced by the electronic circuitry must be also taken into account, especially when standard instruments are used. An analysis has been performed in [31]. For driving the crystal in an oscillator circuit a small equivalent resistance of the resonator is beneficial. A large electrode diameter is advised; however, separation of harmonic from spurious modes defines a maximum diameter, which decreases with frequency.

3
Fundamentals of Oscillators

3.1
Quartz Crystal Resonator

3.1.1
Equivalent Circuit of Quartz Crystal in Vacuum

As shown in the previous section, the mechanical properties of a quartz crystal close to resonance frequency can be expressed by means of a motional impedance. To complete the equivalent circuit of a quartz crystal, the capacitance, C_0, must be added in parallel to the motional impedance. It results in the Butterworth–Van Dyke (BVD) equivalent circuit of a quartz crystal, as shown again in Fig. 8 for an unloaded quartz crystal [32]. In this notation common in electronic literature, L_s is the dynamic inductance and is understood here as a representation of the oscillating mass of the quartz crystal. C_s is the dynamic capacitance and reflects the elasticity of the oscillating body. R_s is the dynamic resistance and returns friction of the quartz slice as well as all kinds of acoustic damping.

The plot of impedance[5] $Z = R + jX$ with $R = R_s$ and $X = j\left(\omega L_s - \frac{1}{\omega C_s}\right)$ is shown in terms of impedance magnitude, $|Z| = \sqrt{R^2 + X^2}$, and phase, $\tan\varphi = X/R$ in Fig. 9. The values given in Table 1 for a 10 MHz AT-cut quartz crystal have been taken for computation. The quartz impedance is inductive (phase shift + 90°) between f_s and f_p, and capacitive (phase shift – 90°) outside this interval. The phase shift is very steep.

L_s, C_s, R_s, and C_0 determine resonance frequencies of the crystal. Considering Fig. 8, the series resonance frequency, f_s^{el}, and the parallel resonance

[5] We switch to electrical impedance as common in electronic literature, we furthermore renounce the index el.

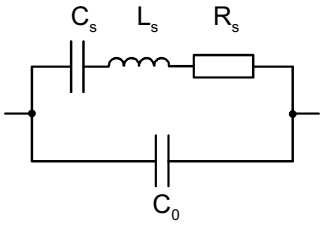

Fig. 8 Electrical equivalent circuit of a quartz crystal in vacuum

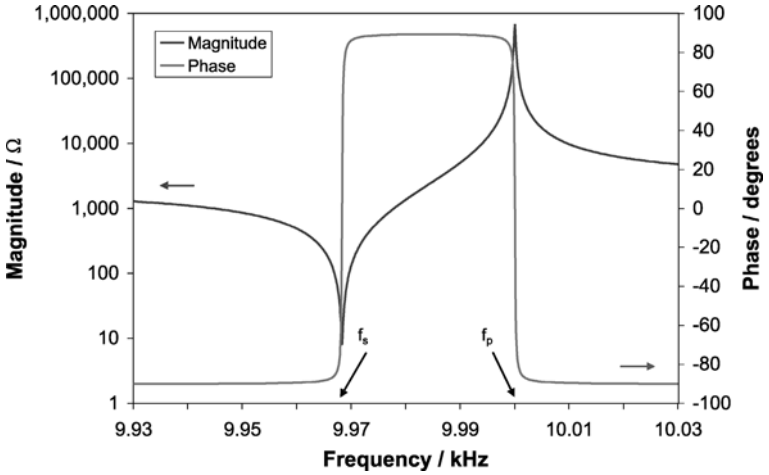

Fig. 9 Impedance and phase of a quartz crystal

frequency, f_p^{el}, can be found as follows:

$$f_s^{el} = \frac{1}{2\pi\sqrt{L_s C_s}} \tag{14}$$

$$f_p^{el} = \frac{1}{2\pi\sqrt{L_s C^*}}, \quad \text{with} \quad C^* = \frac{C_s C_0}{C_s + C_0}. \tag{15}$$

3.1.2 Equivalent Circuit for Under-Liquid Sensing

The equivalent circuit of a liquid-immersed quartz crystal, Fig. 10, consists of the same basic components. The motional acoustic impedance caused by a (sensing) rigid film and the liquid load can be separated into an inductance, L_c, (coating), an inductance, L_{liq}, and a resistance, R_{liq}, (liquid). All additional elements are in series to the quartz motional elements. C_{liq} and G_{liq} account

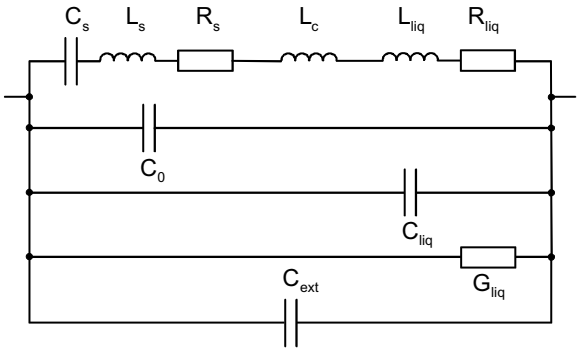

Fig. 10 Electrical equivalent circuit for under-liquid sensing with a rigid coating

for permittivity and conductivity of the liquid. In the case of single-side contact of the liquid to the grounded electrode C_{liq} and G_{liq} can be neglected [33]. However, an external capacitance, C_{ext} accounts for (not fully compensated) contributions from the measurement setup (cables, measurement cell).

The plots shown in Fig. 11 are based on the same values as above. One crystal surface is loaded with a 100 nm rigid film and is in contact with water. This combined load causes a shift of the complete impedance plot to lower frequencies. Changes in both impedance magnitude and phase are smoother than for the bare quartz crystal (Fig. 9). The result of an external capacitance, C_{ext}, parallel to C_0 has been presented as well. A rigid coating alone does

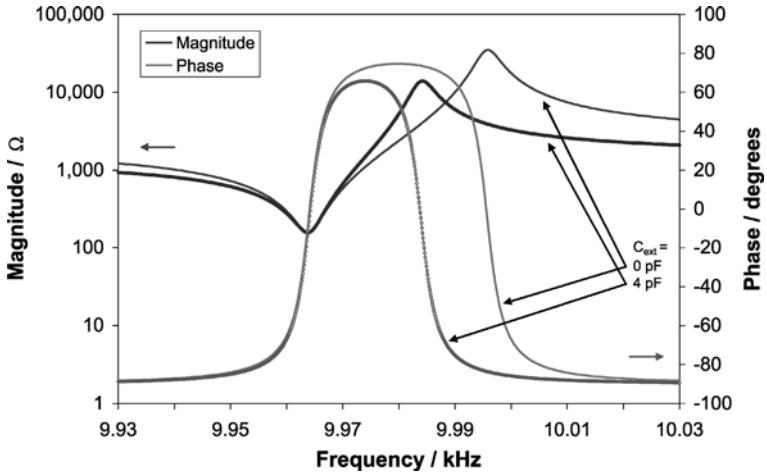

Fig. 11 Impedance and phase curve of a 10 MHz quartz crystal coated with a rigid 100 nm thick film in contact with water on one side (liq). The influence of an external capacitance is also shown

not change the shape of impedance plot; the curves are only shifted to lower frequencies.

3.2 Characteristic Resonance Frequencies

For definition of the different characteristic resonance frequencies, the locus of impedance $Z = R + jX$ (a) and admittance $Y = 1/Z = G + jB$ (b) of a bare quartz crystal are shown in Fig. 12 (for better distinction R_s has been set to 160 Ω here, a typical value for single-side liquid load). The definitions are summarized in Table 2 [34].

The separation between the resonance frequencies is very small for very small R_s while it becomes obvious and cannot be neglected for higher R_s. The major challenge for sensor electronics design arises from the fact that the acoustically relevant frequency for sensing purposes is f_s, whereas oscillators work at a certain phase angle, usually $\varphi = 0$, i.e., at f_r in case of an ideal series oscillator. Applying the respective definitions one finds:

$$f_s = \frac{1}{2\pi\sqrt{L_s C_s}} = f_s^{el} \tag{16}$$

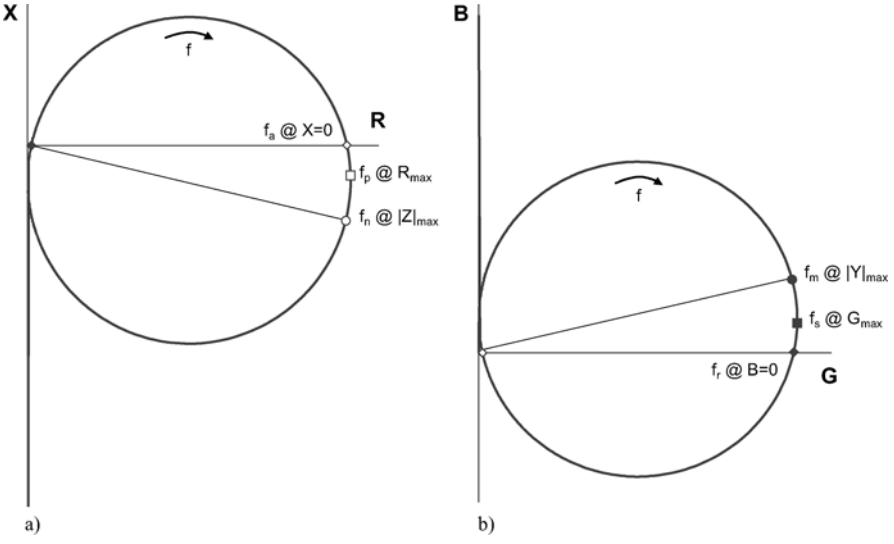

Fig. 12 Characteristic resonance frequencies of quartz crystal resonators, shown in the locus of impedance, $Z = R + jX$ (**a**), and admittance, $Y = G + jB$ (**b**). □ is the parallel resonant frequency f_p at R_{max}, ◇ is the parallel resonant frequency f_a at $X = 0$, ○ is the parallel resonant frequency f_n at $|Z|_{max}$, ■ is the series resonance frequency f_s at G_{max}, ◆ is the series resonant frequency f_r at $B = 0$, and ● is the series resonant frequency f_m at $|Y|_{max}$

Table 2 Definition of characteristic resonant frequencies and example data of frequency shifts generated from a rigid coating (density 1 g cm^{-3}, thickness 100 nm) alone and with an additional semi-infinite Newtonian liquid (density 1 g cm^{-3}, viscosity 1 cP) on top. Furthermore the effect of an external capacitance is considered (values in *brackets*)

	Definition	Frequency C_{ext} = 0 (4) pF (MHz)	Frequency shift 100 nm rigid film C_{ext} = 0 (4) pF (Hz)	Frequency shift 100 nm film + liquid C_{ext} = 0 (4) pF (HZ)
f_s	$G \rightarrow$ Max	9 968 304 (9 968 304)	2271 (2271)	4299 (4299)
f_r	$B = 0$ ($\varphi = 0$)	9 968 304 (9 968 304)	2271 (2270)	4155 (4068)
f_m	$\|Y\| \rightarrow$ Max	9 968 304 (9 968 304)	2271 (2272)	4442 (4525)
f_p	$R \rightarrow$ Max	10 000 000 (9 988 260)	2271 (2270)	4296 (4297)
f_a	$X = 0$ ($\varphi = 0$)	10 000 000 (9 988 260)	2271 (2271)	4440 (4528)
f_n	$\|Z\| \rightarrow$ Max	10 000 000 (9 988 260)	2271 (2271)	4153 (4072)

and with some approximations reasonable for small R_s[6]:

$$f_r \approx \frac{1}{2\pi}\sqrt{\frac{1}{L_s C_s} + \frac{R_s^2 C_0}{L_s^2 C_s}}\,. \tag{17}$$

Equation Eq. 17 clearly explains the dilemma of f_r; the series resonance frequency at zero phase depends on the equivalent resistance.

In a sensor experiment (e.g., in a typical biochemical experiment) the sensor has been functionalized with a sensitive film, which is in contact with an analyte containing buffer solution. The new resonance frequencies f^* can be calculated when replacing L_s and R_s by $L_s^* = L_s + L_c + L_{liq}$ and $R_s^* = R_s + R_{liq}$, respectively (neglecting C_{liq} and G_{liq}). Usually frequency shifts are determined and of interest only. Some example data are added to Table 2. Series and parallel resonance frequency shifts vary by a few percent. All the parallel resonance frequencies are very much affected by external capacitance (values in brackets). The same holds for all frequency shifts in a liquid except f_s. Oscillators based on parallel resonance should not be used because stray capacitance is hardly to avoid and hardly to keep constant in an experimental setup. Deviations of f_r and f_m from f_s are also amplified by external capacitance.

The liquid may exhibit constant properties (R_{liq} and L_{liq} are constant). Only in those cases are differences in frequency shifts caused by mass accumulation in/on the sensitive film (small ΔL_c) reasonably equivalent for all resonance frequencies.

[6] The difference between the exact solution within the BVD model and the approximation Eq. 17 for a 10 MHz quartz crystal and an equivalent resistance R_s = 200 Ω is only 2 Hz.

4
Sensor Interface Circuits

4.1
Oscillators

The application of oscillator circuits as sensor interface for QCM is the most common method. Since a quartz crystal is a resonant element, stable oscillation can be excited by quite simple circuits. They deliver a frequency analog output signal, which can be easily processed in digital systems. Two oscillation conditions can be formulated assuming approximately linear behavior and not considering the pre-oscillation process:

$$\text{Amplitude condition:} \quad |kA| \geq 1 \tag{18}$$

$$\text{Phase condition:} \quad \varphi = 0,\ 2\pi, \ldots,\ n2\pi \tag{19}$$

where A is the open loop gain and k is the feedback factor. The electronic circuitry must provide deattenuation to get undamped oscillation. In order to generate stable oscillations the oscillator circuit must excite the quartz crystal with respect to a frequency where a sharp phase slope occurs. In gases, this condition is fulfilled at the zero-phase resonance frequencies f_r and f_a. Phase slope of an ordinary 10 MHz quartz crystal is about 2 Hz/degree. The phase slope decreases in water to about 37 Hz/degree. Therefore, extreme phase stability of the circuit must be obtained, which becomes the deciding criterion for frequency stability of the oscillator. Since the phase slope decreases further with increasing (viscous) damping accompanied by shift of the largest phase gradient to phase angles smaller than zero degrees (i.e., the absence of phase zero crossing at strong damping) phase correction according to Eq. 19 is required. A phase-shifter should not deteriorate the phase stability in the neighborhood of the resonance frequency. An automatic level control (ALC) is advantageous, because the ALC controls the amplitude condition of the oscillator so that $|kA| = 1$. The output of the ALC can be employed as a measure for quartz damping.

The operation principle of quartz crystal oscillators can be reduced to two variants: series and parallel resonance oscillators [35]. The latter rarely operate at parallel resonance, Eq. 15, since classic LC-oscillator configurations are used applying the quartz as a high quality inductance. Parallel resonance oscillators in fact oscillate slightly below parallel resonance frequency. Practically, this is no disadvantage because the oscillator circuit only has to guarantee high frequency stability. The oscillation frequency may vary due to unavoidable production tolerance of quartz crystals; the exact oscillation frequency can be adjusted by additional electronic components. Series oscillators theoretically work at zero phase; again, a problem arises with real oscillator circuits. They produce phase shifts slightly different from theory so

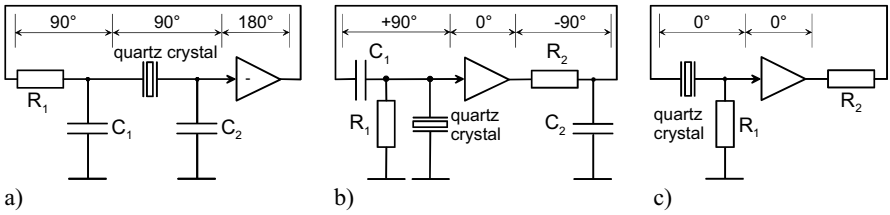

Fig. 13 Oscillator circuit with inverting amplifier (**a**), with a Colpitts structure (**b**), and with non-inverting amplifier (**c**)

that the quartz will not oscillate exactly at zero phase. Figure 13 shows the two basic oscillator principles. The Pierce oscillator in Fig. 13a uses an inverting amplifier so that its phase of 180° must be shifted to 360° by the feedback network (R_1, C_1 and quartz crystal, C_2) in order to fulfill the phase condition. The circuit, Fig. 13b, with an operation principle like Colpitts, forms a capacitive three point connection, where the quartz crystal acts as inductance of high quality. The oscillator principle, in which the quartz behaves inductively is generally named parallel resonance oscillator.

The oscillator circuit in Fig. 13c, applying a non-inverting amplifier, works as a series resonance oscillator where the quartz fulfils the phase condition at series resonance frequency.

Because of the parallel capacitance the zero phase frequency deviates from the series resonance frequency, Eq. 14, as discussed in Sect. 3.1.1, therefore series resonance oscillators oscillate at a frequency $f_{\mathrm{osc}} \neq f_{\mathrm{s}}$. The series resonance frequency f_{s} is not accessible with standard oscillator concepts without compensation of the parallel capacitance, C_0[7]. The phase of a quartz crystal with compensation of C_0 becomes $\varphi_{\mathrm{m}} = \frac{\mathrm{Im}(Z_{\mathrm{m}})}{\mathrm{Re}(Z_{\mathrm{m}})} = \frac{\omega L_{\mathrm{s}}^* - 1/\omega C_{\mathrm{s}}^*}{R_{\mathrm{s}}^*}$, where * again symbolizes the sum of all respective series elements in the motional arm of the modified BVD circuit (Fig. 10). The definition of f_{s} ($G \rightarrow \mathrm{Max}$) is equivalent to $\mathrm{Im}(Z_{\mathrm{m}}) = 0$ (i.e., $\varphi_{\mathrm{m}} = 0$) hence an ideal series resonance oscillator now vibrates at f_{s}. Figure 14 displays the difference between φ and φ_{m} for a 10 MHz quartz crystal with single side in contact with water in the region around series resonance. The plot of φ_{m} has an offset of 144 Hz with respect to φ (see also Table 2), the slope of both curves is almost equivalent. The plot of G has been added for comparison.

The quartz crystal should be operated in the neighborhood of its series resonance frequency, since alterations in C_0 or C_{ext} have much lower effects on resonance frequency than on parallel resonance (Table 2). Another essential reason for operating at series resonance is that the quartz impedance is in the range of RF-technique impedance (50 Ω), which minimizes the effect of interference signal coupling.

[7] If an external capacitance C_{ext} parallel to C_0 exists, i.e., $C_0 \rightarrow C_0^* = C_0 + C_{\mathrm{ext}}$, C_0^* must be compensated.

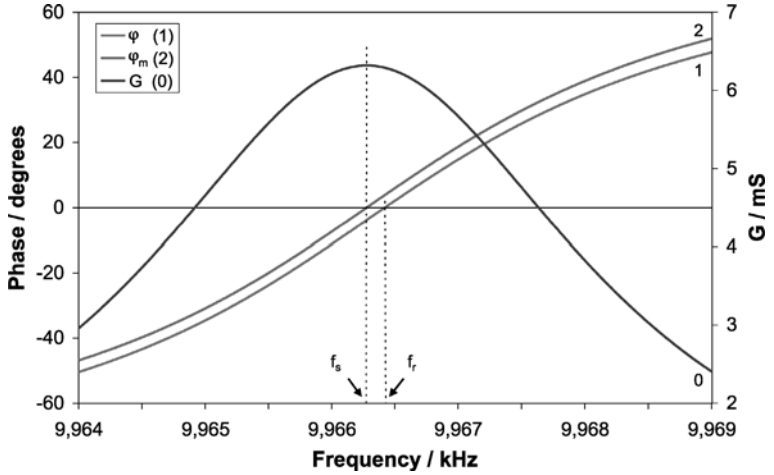

Fig. 14 Phase of impedance $Z(\varphi = X/R)$ and phase of motional impedance Z_m ($\varphi_m = \mathrm{Im}(Z_m)/\mathrm{Re}(Z_m)$) and conductivity G of a 10 MHz blank quartz crystal with one surface in contact with water

Due to the reduced Q factor of the quartz crystals in liquids, and therefore decreased phase slope, the requirements of the circuit with respect to phase (frequency dependence, noise, temperature dependence), to amplification linearity, and to temperature constancy are much higher. One electrode of the quartz crystal should be grounded to minimize parasitic effects and to allow operation of quartz arrays in conductive liquids. The increased damping of the oscillator should be overcome by automatic level control. The control variable in the amplitude control loop can be used as an independent measurement value. It also allows for calibration of f_{osc} with respect to f_s [36].

4.2 Network Analysis

The aim of network analysis is the investigation of the amplitude and phase response of a two- or four-port network. Impedance analysis determines the complex impedance or admittance of a device. This method is appropriate for quartz resonators in order to obtain more complete information than is conceivable by merely considering the shift of the resonance frequency. The method especially allows the determination of the equivalent circuit elements (BVD) presented in Fig. 8. Actually many commercial instruments directly provide this information. Determination of the physical parameters, or their effective values, for accurate modeling of the sensor behavior based on Eq. 5 requires mathematical procedures which fit the calculated curves (e.g., with Eq. 2) to the experimentally measured values. It is recommended to include an external capacitance parallel to C_0 to account for uncompensated para-

sitic capacitance, even if the crystal interacts with the surroundings only on one surface. An external capacitance shifts the parallel frequency to lower values but it does not change the elements of the motional arm, Fig. 4. It accounts for deviations between series and parallel frequency from $1 - 8K_q^2/\pi^2$, see Footnote 3.

Impedance analysis is also suggested when properties of an attached film, a liquid, or interfaces are of interest. Due to the weak frequency dependence[8] of the acoustic load within a typical measurement range of some 10 kHz at fundamental mode, one measurement point would be sufficient to calculate Z_L (Eq. 2). An effective method to decrease statistical errors is to first fit a theoretical curve to the experimental curve or a specific segment, secondly to calculate Z_L from the fit, and finally to extract (material) parameters of interest using separate models describing how the acoustic load is generated [37].

Due to passive operation of the quartz crystal it is possible to minimize parasitic influences from the experimental setup, i.e., to almost eliminate their effects by calibration. If the interface behaves like a linear network, most electrical parameters relevant for the measurement can be implicitly obtained and the influence of the network can be eliminated. Calibration of the measurement setup is one of the important advantages of network analysis and must be performed with care.

The ratiometric method treats the sensor interface as a network with four ports (Fig. 15) [38].

The interface is powered by a source E. The measurement voltages V_1 and V_2 depend on an impedance Z. In this model the inner resistance of the voltage source E, the cable connecting Z to the circuit, and the measurement channels for V_1 and V_2 belong to the network itself and do not produce systematic errors. As a consequence of assumed linearity the voltage ratio:

$$\frac{V_1}{V_2} = r(Z) = \frac{k_0 + Z}{k_1 Z + k_2} \tag{20}$$

depends on the measurement impedance Z and on three as yet unknown network parameters k_0, k_1, and k_2. In order to determine these constants three calibration standards, open ($Z \to \infty$), short ($Z = 0$), and a reference resistor ($Z = R_{ref}$) are required, which deliver three voltage ratios, r_{open}, r_{short}, and r_{ref}, respectively. Solving Eq. 20 for the unknown measurement impedance Z and expressing $k_{0,1,2}$ by their dependencies on r_{open}, r_{short}, and r_{ref} delivers:

$$Z = R_{ref} \frac{r_{open} - r_{ref}}{r_{ref} - r_{short}} \frac{r_{short} - r(Z)}{r(Z) - r_{open}} . \tag{21}$$

$r(Z)$ is measured with the unknown impedance Z connected. In this way Z is independent of the unknown linear network properties of the sensor

[8] Under certain circumstances the acoustic load may exhibit a noticeable frequency dependence, e.g., near the so-called film resonance.

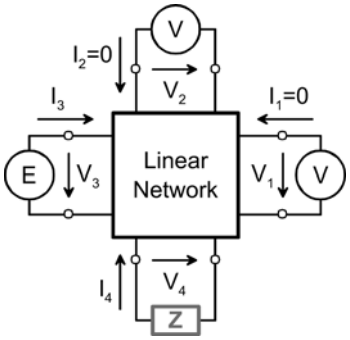

Fig. 15 Network model for the measurement of impedance Z

interface. Since the behavior of the sensor interface is generally frequency-dependent, the above calibration should be performed for every frequency ω in the spectrum $Z(\omega)$ to be acquired.

The ratiometric measurement principle is independent of the configuration of the input stage, which therefore can be adapted to the specific sensor application. The impedance range is restricted by stray capacitance in general and by the input capacitance of the measurement channels in particular.

The essential drawbacks of network analysis are the high costs and large dimensions of commercial equipment, which has to satisfy the requirements of universal application such as large frequency range and different measurement principles. Acoustic sensors as a particular application case do not require many of those instrument functions. The specific requirements have been realized in new network analyzer-based sensor interface circuitry.

4.3 Impulse Excitation

After excitation with an ideal impulse, the quartz resonator will carry out damped oscillations solely influenced by the acoustic properties of the resonator. The effect of the sensor interface circuit with a proper design is negligible. At a first glance, the advantage of impulse excitation is the oscillation of the quartz resonator at its mechanical resonance frequency, i.e., the oscillation frequency depends only on the motional elements. The decay of oscillation is defined by mechanical damping. In analogy to the discussion of oscillators, the motional elements of the quartz crystal can be replaced by those with * in case of a sensor application; the generic principle does not change.

In control theory the impulse response, $g(t)$, is the response of a (linear) system to a Dirac delta input. The Laplace transform of the delta function is

1, hence the system's transfer function is equivalent to the Laplace transform of the impulse response:

$$G(s) = L\{g(t)\} = \int_0^\infty g(t)\mathrm{e}^{-st}\,\mathrm{d}t\,, \tag{22}$$

where $s \equiv \sigma + j\omega$ is the Laplace variable. Obviously impulse excitation delivers the inverse Laplace transform of the system's transfer function in a (theoretically) infinite frequency range. Since the resonator comprises several modes, including spurious modes near fundamental (or overtone) modes, signal processing and analysis is more involved if high accuracy in absolute values is required.

4.4 Comparison

Table 3 summarizes the advantages and drawbacks of the above sensor interface concepts. Oscillators are the best solution for most chemical sensor applications. Low expenses of circuitry and a frequency analog output signal

Table 3 Survey on advantages and drawbacks of sensor interfaces

Sensor interface	Advantages	Drawbacks
Oscillator	• Low expenses for circuitry • Direct frequency output with high resolution • Acoustic energy dissipation measurement possible	• High stability of circuit necessary • Extremely high phase stability required • $f_{osc} \neq f_s$ without C_0-compensation • Restricted to single mode
Network analysis	• Provides complete impedance spectrum • Calibration of measurement setup; reduction of parasitic effects • Access to acoustic parameters	• High expenses for circuitry • Data processing necessary to select characteristic values • Complex measurement setup and measurement routines
Impulse excitation	• Provides sensor transfer function • Other kinds of excitation possible • Direct access to resonant frequency and acoustic energy dissipation	• Impulse generation not appropriate in liquid applications • Limited range for precise frequency and damping measurement • High expenses for circuitry

are the crucial advantages. Oscillators allow per se high accuracy of frequency measurement, however, f_{osc} may significantly deviate from f_s. The necessity of parallel capacitance compensation increases the efforts in oscillator development. The same holds when a lower Q factor of the sensor must be expected. Automatic level control and evaluation of the control signal as a measure of acoustic energy dissipation is strongly recommended since this value provides independent information.

Network analysis is the preferred concept under more complex experimental conditions and is approved during sensor development to analyze and optimize sensor signal generation, especially for (bio)sensors if effects other than pure mass effects contribute to the signal. Measurement at different harmonics is easily established. Modern sensor interface concepts are about to combine the advantages of precision measurement with reasonable expenses for circuitry.

Determination of the sensor transfer function, unperturbed by the interface electronics, is a major advantage of impulse excitation. Other forms of excitation have been proven to overcome limitations when applied to liquid analytes. Access to harmonic analysis of the resonator is an inherent feature of this method.

5
Examples for Sensor Interface Circuits

5.1
Quartz Crystal Oscillators

5.1.1
Pierce and Colpitts Oscillator

The simplest oscillator circuits for QCM apply solutions according to Pierce or Colpitts–Miller. The Pierce oscillator (Fig. 13a) does not meet the requirement of a quartz crystal with one electrode grounded. The operation principle of the Colpitts oscillator (Fig. 13b) applies the quartz crystal as an inductance of high quality. In order to fulfill the phase condition the oscillator operates at a frequency at which the quartz crystal has a phase of 90°. As shown in Fig. 11, a quartz crystal in contact with water is not able to reach this phase, hence additional frequency-dependent feedback components are used to enable the circuit to oscillate. Since the quartz crystal is part of the feedback network, alterations of its equivalent parameters cause a shift of the phases in this network, which means a shift of the resonance point along the phase curve depending on damping. Therefore, the oscillator frequency is strongly influenced by the acoustic load.

5.1.2
Lever Oscillator

The Lever oscillator [39], Fig. 16, allows the application of series resonance configurations with one-side quartz electrode grounding. Since the effect of parasitic capacitance is minimized and simple shielding is possible, this circuit configuration is especially suited for under-liquid QCM. Besides the series resonance frequency, the series resonance resistance R_s can be measured. For this purpose the Lever oscillator allows a largely transistor current gain-independent measurement of the resistance. An automatic level control provides a signal proportional to R_s.

The practical realization with discrete transistor circuits may offer some problems caused by a strong influence of their parasitic capacitance to the phase curve. Best results could be achieved in the lower MHz range.

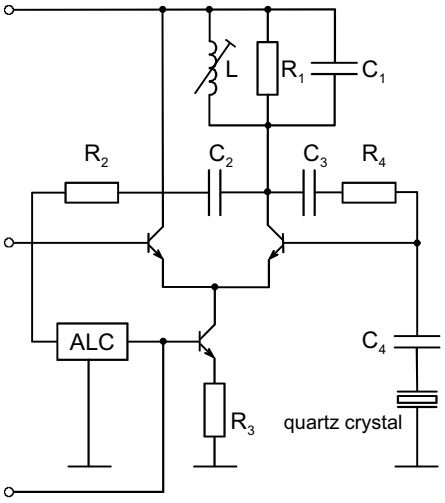

Fig. 16 Simplified circuit of the Lever oscillator [39]

5.1.3
Emitter Coupled Oscillator

The emitter coupled oscillator (Fig. 17) is a circuit also providing one quartz crystal electrode grounded. For practical realization as a series resonance oscillator, a signal proportional to the current through the quartz crystal is amplified and fed back as a voltage. Since least gain is necessary for low impedance resonance, the resonance with the smallest impedance will preferably be excited. Phase condition is fulfilled for a frequency where the quartz crystal behavior is real, i.e., for f_r.

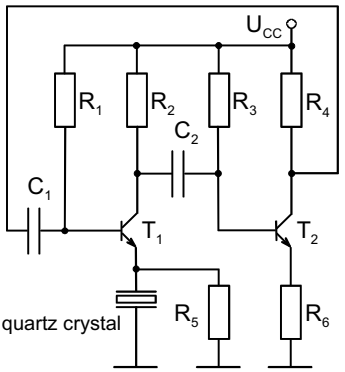

Fig. 17 Emitter-coupled oscillator (example)

The properties of discrete transistors, their non-linear amplification characteristic, parasitic capacitance, and the problematic adjustment of a stabile operating point are uncomfortable drawbacks.

5.1.4 Quartz Oscillator with OTA

5.1.4.1 OTA as Amplifier

In contrast to the traditional operational amplifier (OPA) an operational transconductance amplifier (OTA), Fig. 18, has a mode of operation where the non-inverting input is high ohmic whilst the inverting input is low ohmic. Here, the input current controls a current source, which affects transconductance and thus generates the output voltage [40, 41].

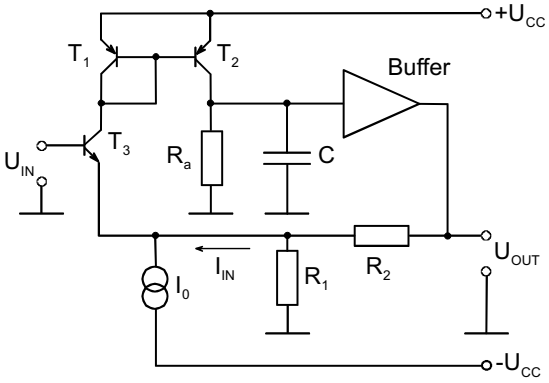

Fig. 18 Amplifier with OTA and current feedback (simplified circuit)

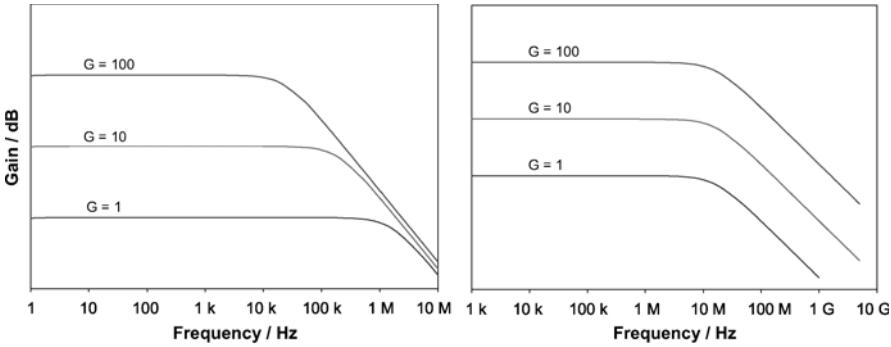

Fig. 19 Frequency response: **a** voltage feedback, **b** current feedback

In contrast to common OPAs a low ohmic current source reloads internal parasitic capacitance, which determines the upper cut-off frequency. Consequently a much higher slew rate becomes possible. Gain for both voltage and current feedback OPA circuits is:

$$A = 1 + \frac{R_2}{R_1}. \tag{23}$$

Figure 19 demonstrates the advantage of current feedback (OTA) over voltage feedback. Bandwidth in the case of current feedback is almost independent of gain, and also the phase shift is constant over a wide frequency range. The OTA bandwidth is determined by R_2, where constancy of bandwidth–gain–product is not given. Nevertheless, the feedback voltage divider R_1, R_2 should be low ohmic in order to minimize low-pass behavior of R_2 together with parasitic capacitance.

Current feedback amplifiers always consist of a diamond transistor (DT) and a buffer stage internally connected. The OPA660 [42] or its replacement OPA860 [43] allows separated access to both circuit parts so that a voltage-controlled current source (OTA) at a bandwidth of 90 MHz and a buffer stage at a bandwidth of 700 MHz are available. In contrast to normal transistors the diamond transistor, whose temperature-stabile operating point is internally determined, allows four-quadrant operation. The OTA provides the required almost-ideal transistor to design an emitter-coupled oscillator.

5.1.4.2 Circuitry

Fig. 20 shows the practical realization of a quartz oscillator concept [44] utilizing an OTA.

Bias current and thus maximal current slew rate of DT_1 must be adjusted with R_1, R_5, and R_6 to suppress high frequency parasitic effects; R_3 generates

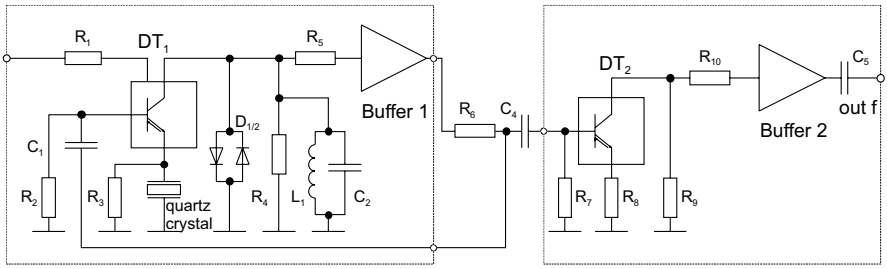

Fig. 20 Quartz crystal oscillator with OTA and amplitude limiting

an emitter DC potential. Gain is to be charged as follows:

$$A = \frac{R_4}{(Z \| R_3) + r_E}, \tag{24}$$

where Z is the electrical impedance of the quartz crystal and r_E is the internal dynamic emitter resistance [42].

Amplitude stabilization is provided by means of antiparallel connected low capacitance Schottky diodes D_1 and D_2. Thus gain is maximal at small amplitudes and the oscillator begins to oscillate even at strong quartz damping. The R_2, C_1 high-pass partially compensates for the phase-shift of the circuit resulting from loop transit time, internal OPA860 phase-shift, and low-pass behavior of the entire configuration. The phase at resonance frequency can be adjusted in the range – 25° to – 60° depending on bias current (R_1-determined), gain (R_4-determined) and C_1,R_2 high-pass. The L_1,C_2 parallel oscillating circuit damped by R_4 avoids parasitic oscillation above quartz crystal resonance.

The frequency signal is coupled out via DT_2 and buffer 2, amplified and adapted to the coaxial cable impedance. The circuit is adjusted to a resonance frequency near f_r. However, driving the quartz crystal at a phase of – 40° has been found to be optimal for under-liquid sensing [44]. Temperature dependence of the circuit is essentially due to the temperature dependence of the quartz crystal. Dependence on voltage supply of approximately 20 Hz V^{-1} has been found for a quartz crystal in air and 80 Hz V^{-1} in water [45]. Thus common stabilizing methods for current supply are sufficient.

For measurement of quartz crystal damping the amplitude limiting can be replaced by an automatic level control (ALC). For this purpose the oscillator, Fig. 21, must be modified by opening the feedback loop and inserting a variable gain amplifier. The control variable effecting the loop gain is proportional to the series resonance resistance R_s.

For designing an ALC, a precision rectifier, a comparator, a proportional-integral (PI) controller, and a gain-controllable amplifier are required. The block diagram of the quartz crystal oscillator with ALC is depicted in Fig. 21

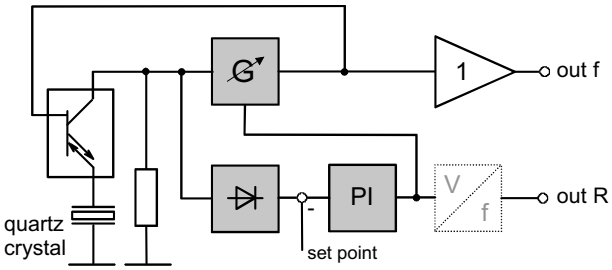

Fig. 21 Scheme of a quartz crystal oscillator with automatic level control. The *gray* components belong to the automatic level control [36]

with the new components marked gray. A realization of this oscillator allowed under-liquid measurement up to a resonance frequency of 30 MHz and a damping equivalent value of $R_s = 800\ \Omega$ [44].

5.1.5 PLL-Based Oscillators

PLL-based oscillators are characterized by a loop with phase detection of two signals in a sensor and reference path. A circuit based on a phase-locked loop (PLL) configuration has been introduced in [46]. The core of this solution is a sensor circuit consisting of a reference and a sensor path. It is essential for the working principle to maintain an identical structure in the sensor and the reference path, in order to minimize systematic differences between them. A phase frequency detector measures the phase difference between the sensor and reference path. An adjustable capacitance in the reference path allows for C_0-compensation. The oscillator can therefore work at f_s.

The concept behind the design of the oscillator shown in Fig. 22 ensures continuous measurement and automatic compensation of the parallel capacitance C_0^*, while the quartz crystal is simultaneously and independently driven at its zero-phase frequency [47, 48]. Provided that the capacitance compensation is effective, the zero-phase frequency is always equal to the sensor series resonance frequency f_s, irrespective of the load.

For that purpose, the quartz crystal is simultaneously excited at two frequencies. The response at the lower frequency is processed by a feedback loop dedicated to measure and automatically compensate C_0^*. The response at the higher frequency is processed by a phase-locked loop that continuously maintains and tracks oscillations at f_s. The voltage waveform V_{HL} is the sum of the two sinusoidal signals V_H, with frequency f_H generated by the voltage controlled oscillator VCO, and V_L, with frequency f_L lower than f_H, generated by the auxiliary oscillator OSC. The frequency f_H of the signal V_H is taken as the output frequency f_{out} of the whole circuit. In the frequency domain, the ex-

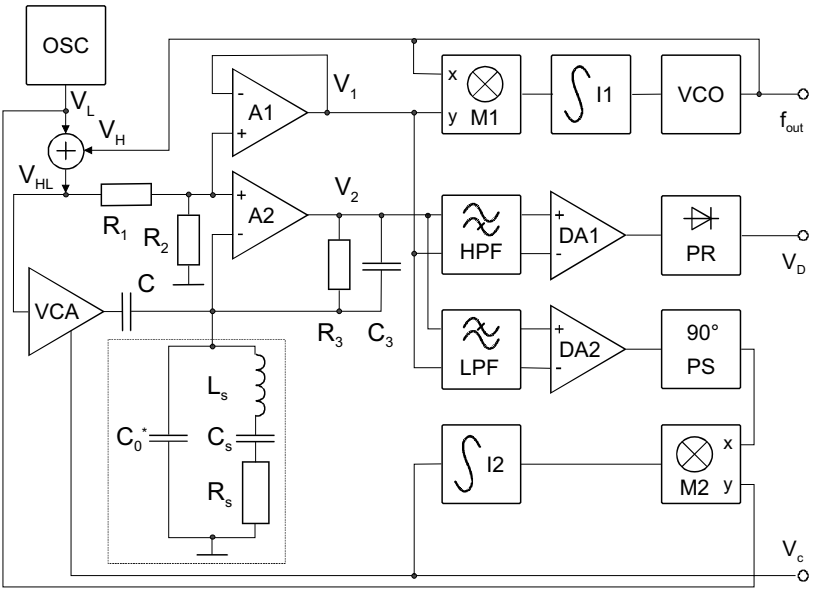

Fig. 22 Block diagram of the automatic capacitance compensation oscillator. Adapted from [48] with kind permission of V. Ferrari

pression of the differential voltage ($V_2 - V_1$) at the output of the amplifiers A1 and A2 is:

$$V_2 - V_1 = V_{\mathrm{HL}} Z_3 \alpha \left[Y_\mathrm{s} + j\omega C_0^* - j\omega C_\mathrm{C} \right], \tag{25}$$

where $Z_3 = \frac{R_3}{1+j\omega R_3 C_3}$, $\alpha = \frac{R_2}{R_1+R_2}$, $C_\mathrm{C} = \left[\frac{A}{\alpha} - 1\right] C$, and $Y_\mathrm{s} = \left[j\omega L_\mathrm{s} + R_\mathrm{s} + \frac{1}{j\omega C_\mathrm{s}} \right]^{-1}$.

As shown in Eq. 25, the equivalent capacitance C_C, that is dependent on the gain A of the voltage-controlled amplifier VCA, becomes subtracted from the sensor parallel capacitance C_0^*. Therefore, C_C effectively behaves as a voltage-controlled compensating capacitance. The values of R_3 and C_3 are properly chosen so that their parallel impedance Z_3 is dominated by R_3 at the low frequency f_L, and by C_3 at the high frequency f_H. Therefore, Eq. 25 can be simplified in two ways. At f_L the sensor is far from the resonance, therefore its equivalent circuit reduces to the parallel capacitance C_0^* and Eq. 25 becomes:

$$V_2 - V_1 = j\omega V_\mathrm{L} R_3 \alpha \left[C_0^* - C_\mathrm{C} \right]. \tag{26}$$

According to Eq. 26 $V_2 - V_1 = 0$ if $C_\mathrm{C} = C_0^*$. The circuit section including low pass differential filter (LPF), differential amplifier (DA2), phase shifter (PS), multiplier (M2), integrator (I2), and the equivalent capacitance C_C automatically maintain the compensation condition by forming a feedback loop so

that $V_2 - V_1$ is constantly kept zero. The LPF extracts the low-frequency component from $V_2 - V_1$ at f_L. The DC voltage V_c at the output of I2 adjusts the gain A of the voltage-controlled amplifier (VCA) and, in turn, modifies the equivalent compensating capacitance C_C to be equal to the sensor parallel capacitance C_0^*. The integrator output voltage V_c can be taken as an additional output providing the value of C_0^*.

At f_H, due to the automatic compensation of C_0^*, Eq. 25 becomes:

$$V_2 - V_1 = \frac{\alpha V_H}{j\omega C_3}\left[j\omega L_s + R_s + \frac{1}{j\omega C_s}\right]^{-1}. \tag{27}$$

M1, I1 and the VCO form a phase-locked loop feedback system. The multiplier makes a synchronous detection of $(V_2 - V_1)$ at the frequency f_H. The output of I1 drives the VCO so that the output frequency f_H constantly adjusts to the frequency where the admittance of the motional arm Y_s of the sensor is real, i.e., to the series resonance frequency f_s. Therefore, the oscillator output frequency $f_{out} = f_H$ is continuously tracking f_s.

The high-pass differential filter (HPF), DA1, and peak rectifier (PR) form a section dedicated to the measurement of the sensor damping at resonance. The HPF extracts from $(V_2 - V_1)$ the high frequency component at $f_H = f_s$. The rectifier then detects the amplitude and provides a DC voltage V_D, which is proportional to $1/R_s$ and a measure of acoustic energy dissipation at resonance:

$$V_D = \frac{\alpha \hat{V}_H}{j\omega_s C_3}\frac{1}{R_s}. \tag{28}$$

A different way of C_0-compensation is schematically shown in Fig. 23 [49, 50].

This approach is dedicated to the measurement of liquid viscosity by determining the real part of the sensor admittance at series resonance frequency. According to this concept, one terminal of the sensor is fed with the (constant-level) output of a VCO. The resonator current I is measured by connecting a transimpedance amplifier at the second terminal. Due to the low input impedance of the transimpedance amplifier, the entire VCO output voltage is applied to the sensor. Parasitic capacitances from the sensor terminals to ground (e.g., due the shielding of the connection cables) are on one side

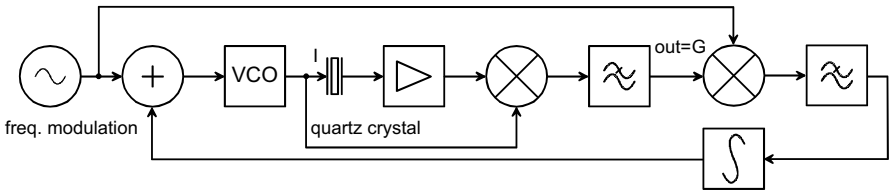

Fig. 23 Oscillator circuit self-tuning to f_s and evaluating G. Adapted from [49] with kind permission of B. Jacoby

shorted by the low input impedance of the transimpedance amplifier, while they are fed by a low impedance source (VCO output) on the other side, so that they do not affect the measurement. The amplitude of the in-phase contribution of I (with respect to the phase of the VCO output voltage) is then determined by means of a synchronous detector (demodulator) consisting of a mixer and a low pass filter yielding an output signal G according to

$$\hat{V}_1 \sin(\omega t) \cdot \hat{V}_2 \sin(\omega t + \varphi) = \frac{\hat{V}_1 \hat{V}_2}{2} \left[\cos(-\varphi) - \cos(2\omega t + \varphi)\right]. \tag{29}$$

With the latter summand in the brackets suppressed by the low pass filter and with $\hat{V}_2(\omega) \propto \hat{V}_1/Z_q$, $\varphi(\omega) = \mathrm{Im}(Z_q)/\mathrm{Re}(Z_q)$ Eq. 29 yields

$$\left| \frac{\hat{V}_1 \hat{V}_2}{2} \cos\varphi \right| \propto \frac{\mathrm{Re}\left(Z_q\right)}{\left|Z_q\right|^2} = G. \tag{30}$$

If the VCO frequency f_V is tuned to the series resonance frequency f_s $G(f)$ shows a maximum value. In order to tune f_V to f_s, the resonance peak in $G(f)$ needs to be detected. This is achieved by means of a control loop applying a frequency modulation (FM) to the VCO signal using a low-frequency modulating signal, e.g., a sinusoidal signal (or a triangular waveform). For $f_V < f_s$, the FM-induced amplitude variations in G are in phase with the FM signal, for $f_V < f_s$ they are out of phase, Fig. 24. These phase shifts can be detected by means of another synchronous detector whose output signal is used as the input of a controller (integrator) tuning the center frequency of the VCO, f_V, to f_s. In the case of $f_V = f_s$, the tuning signal vanishes.

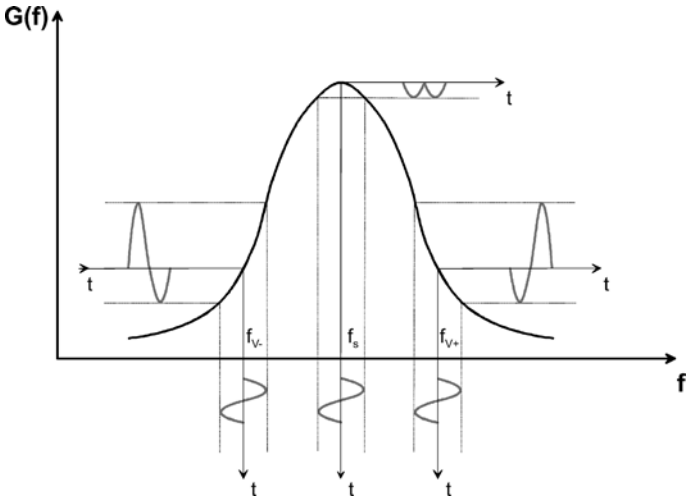

Fig. 24 Tuning principle. Adapted from [49] with kind permission of B. Jacoby

5.2 Network Analysis

5.2.1 Analog Interface

A miniaturized realization of an analog network analysis interface is shown in Fig. 25 [38, 51].

The input stage of the impedance analyzer is a voltage divider formed by the quartz crystal and the series resistor R_V. The quartz crystal is grounded to meet the requirements of sensor applications in liquids. The voltage divider is powered by a direct digital synthesizer (DDS 1) at a programmable frequency f for acquiring an impedance spectrum. The synthesizer applied here is clocked at 100 MHz and controlled with a 4×8 bit frequency tuning word which gives a resolution of $100\,\text{MHz}/2^{32} = 0.02$ Hz. The DDS is set by a field-programmable gate array having an identical clock to the DDS. The DDS output signal is a staircase sine wave with a typical pulse amplitude modulation spectrum containing the desired frequency, f, and, additionally, artifacts at $100\,\text{MHz} \pm f$. These artifacts are suppressed with a fourth-order Cauer filter, thus obtaining a harmonic excitation signal for the voltage divider. The filter is optimized for a measurement frequency of $f = 10$ MHz, having two notches at 90 and 110 MHz for suppressing the first two artifacts. The voltage divider is fed at adjustable amplitude and the voltage across the

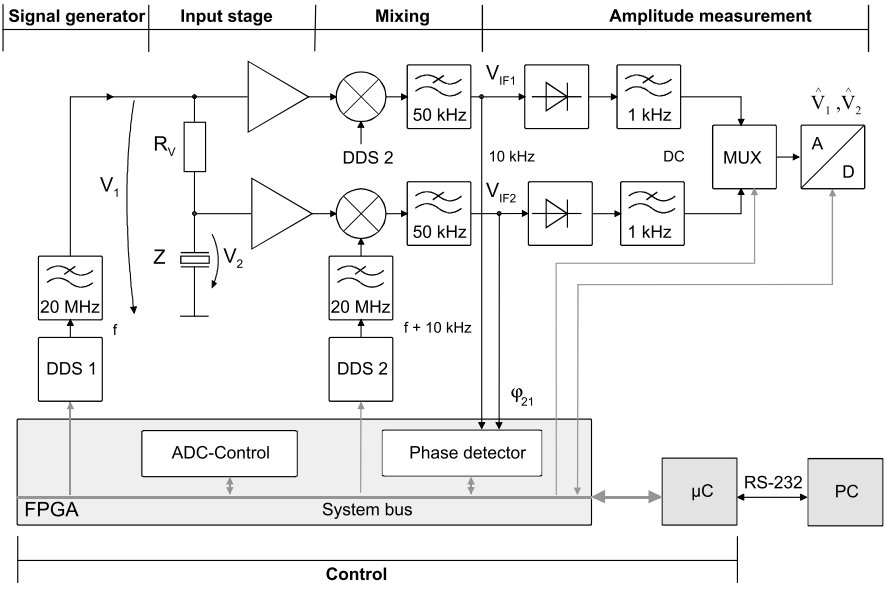

Fig. 25 Interface with analog measurement of (quartz crystal) sensor impedance

frequency-dependent sensor impedance varies between 1.5 V and 70 mV. The resulting voltages V_1 and V_2 are to be measured referring to amplitudes and phase difference.

For the improvement of precision, $V_1(f)$ and $V_2(f)$ are transformed into the low frequency range by mixing each with a sine wave from a second DDS at a frequency f + 10 kHz. A mixed signal consists of a harmonic component at the intermediate frequency of 10 kHz and a second component at $2f$ + 10 kHz that is suppressed by low-pass filtering. Consequently, intermediate signals V_{IF1} and V_{IF2} are obtained at a 10 kHz intermediate frequency retaining the amplitude and phase information of V_1 and V_2. The value of 10 kHz is constant while the measurement frequency f increases stepwise when acquiring an impedance spectrum.

The amplitudes of the intermediate signals are measured by two-way rectification according to the principle of the "ideal diode" having zero threshold. The error of the output voltage due to the thresholds of applied diodes is reduced by the factor of the open-loop gain of the employed amplifier. The 20 kHz signals resulting from a rectification of 10 kHz sine waves are composed of two positive half-cycles whose mean value is determined by averaging with fourth-order Butterworth low-pass filters. Due to the cut-off frequency of 1 kHz, signals require a settling time of 1 ms which limits the measurement rate of this analog interface. Finally, the amplitude information $\hat{a}_1$ and $\hat{a}_2$ is obtained as two DC voltages. The use of two individual analog-to-digital converters (ADCs) for simultaneous sampling could imply temperature dependence. Consequently, amplitudes are subsequently measured by a single 12 bit-ADC, which is multiplexed by the FPGA.

The phase shift φ_{12} between the intermediate signals V_{IF1} and V_{IF2} is measured with the FPGA counting the time Δt_{12} elapsing between zero crossings of V_{IF1} and V_{IF2}. Because of their constant period (T = 100 µs) the phase shift becomes

$$\varphi_{21} = 360^\circ \frac{\Delta t_{21}}{T} . \tag{31}$$

Zero crossings are detected by fast comparators. Since their thresholds diverge from 0 V a zero crossing will be detected too early or too late, resulting in time measurement errors Δt_1 and Δt_2. Assuming that these errors are the same for the positive and negative slopes of the signal, they can be compensated by counting the time between the positive and negative edges of the comparators 1 and 2. Since the shift register S is refreshed every 40 ns the phase resolution is $360^\circ \times 40\ \text{ns}/100\ \mu\text{s} = 0.14^\circ$.

The impedance Z can be calculated according to Eq. 20, using a computer. An impedance spectrum with 1000 frequencies can be acquired within 5 s, including data transfer.

With a similar concept, real and imaginary parts of the admittance, instead of magnitude and phase of impedance, can also be determined [52]. In this

case, the DDS must provide two signals phase-shifted by 90 degrees. Multiplication with the sensor signal followed by low pass filtering provides two voltages that contain the essential information.

5.2.2 Digital Interface

The digital interface shown in Fig. 26 employs a fast analog-to-digital converter for directly sampling the voltages V_1 and V_2 at their original frequency $\omega = 2\pi f$. The method of direct sampling aims at calculating amplitudes and phase shifts by a sine wave fitting of acquired signal probes [38, 53, 54].

The time dependence of the voltage signals $V_1(t)$ and $V_2(t)$ considering an unavoidable offset V_{off} is given by:

$$V(t) = \hat{V}\sin(\omega t + \varphi) + V_{\text{off}} = \hat{V}_s \sin(\omega t) + \hat{V}_c \cos(\omega t) + V_{\text{off}}, \tag{32}$$

where $\hat{V}_s = \hat{V}\cos(\varphi)$ and $\hat{V}_c = \hat{V}\sin(\varphi)$, $\hat{V} = \sqrt{(\hat{V}_s^2 + \hat{V}_c^2)}$, and $\varphi = \arctan(\hat{V}_c/\hat{V}_s)$.

A least mean square fitting of N samples:

$$\sum_{i=1}^{N} \left(\hat{V}_s \sin\left(\omega t_i\right) + \hat{V}_c \cos\left(\omega t_i\right) + V_{\text{off}} - V_i\right)^2 \rightarrow \min \tag{33}$$

is necessary to achieve the required accuracy of the unknown parameters $\hat{V}_s$, $\hat{V}_c$, and V_{off}. In order to run the digital interface independent of a computer this sine fitting is performed by an onboard FPGA in real time. The final computation is done by an onboard microcontroller via a standard routine for matrix inversion. This procedure delivers the amplitudes $\hat{V}_1$ and $\hat{V}_2$ and

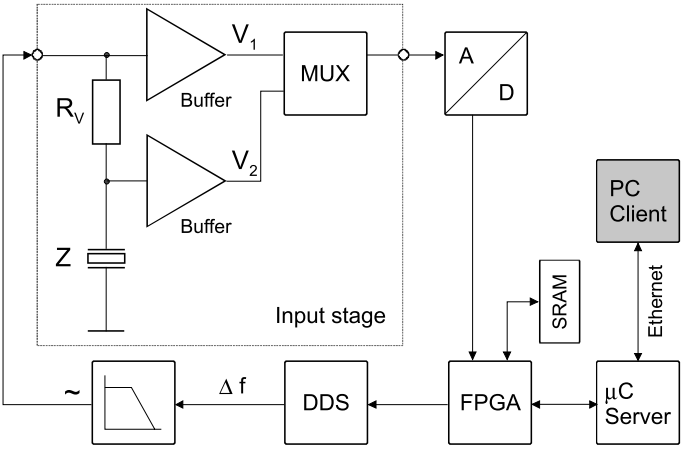

Fig. 26 Digital interface based on direct sampling and sine fitting with an FPGA

phase angles φ_1 and φ_2. Note that offset voltages V_{off} do not influence these results since they are fitted as well. The measurement time for both voltages including multiplexing is 60 µs compared to 3 ms for the analog interface.

5.3 Impulse Excitation

The practical application of this measurement principle is the QCM-D technique (quartz crystal microbalance with dissipation monitoring), patented by Q-Sense [55]. The QCM-D technique extracts frequency, f, and dissipation, $D = R_s/(\omega L_s)$, or the respective changes Δf and ΔD (see Chap. 12 in this volume).

The measuring principle is based on an abrupt decoupling of the sensor driving circuitry from the resonator and monitoring the decay of the quartz sensor oscillation, Fig. 27. The influence of electrical load on the crystal is both minimized and independent of the mechanical load on the crystal. It is possible to measure the resonance frequency for parallel oscillation mode, f_p, the resonance frequency for series oscillation mode, f_s, the decay constant for parallel oscillation mode, D_p, and the decay constant for series oscillation mode, D_s.

The oscillation decays is with a time constant τ inversely proportional to D:

$$V(t) = \hat{V}e^{-t/\tau}\sin(\omega t + \varphi) + \text{constant}, \quad t \geq 0\,. \tag{34}$$

The QCM-D technique allows measurement of these parameters several times per second and the performance of measurements on quartz crystals either in vacuum, gaseous, or liquid environment. Additionally it is possible to switch between fundamental frequency and overtones [56].

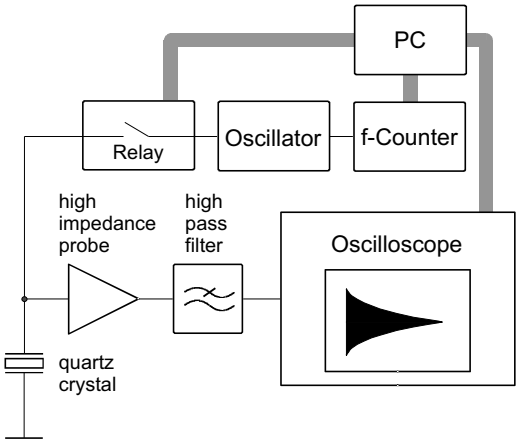

Fig. 27 Principal circuitry for QCM-D [55]

References

1. Lucklum R, Hauptmann P (2006) Anal Bioanal Chem 384:667
2. Matthys RJ (1992) Crystal oscillator circuits, revised edn. Krieger, Malabar
3. Rhea RW (1995) Oscillator design and computer simulation, 2nd edn. McGraw-Hill, New York
4. Gottlieb IM (1997) Practical oscillator handbook. Newnes, Oxford
5. Graf RF (1997) Oscillator circuits. Newnes, Boston
6. Kim Y, Vig JR (2001) IEEE Int Frequ Contr Symp Proc, p 551
7. Walls FL, Vig JR (1995) IEEE Trans Ultrason Ferroelectr Freq Control 42:576
8. Howe DA (2000) IEEE Trans Ultrason Ferroelelectr Freq Control 47:1102
9. Vig JR, Walls FL (2000) IEEE/EIA Int Frequ Contr Symp Proc, p 30
10. Lack FR, Willard GW, Fair IE (1934) Bell Syst Tech J 13:453
11. Bottom VE (1947) Am Mineral 32:590
12. Kosinski JA, Pastore RA (2001) IEEE Trans Ultrason Ferroelectr Freq Control 48:1426
13. EerNisse EP, Clayton LD, Watts HD (1990) IEEE Trans Ultrason Ferroelectr Freq Control 37:571
14. Tiersten HF (1978) J Acoust Soc Amer 64:832
15. Tiersten HF (1996) IEEE Int Freq Contr Symp Proc, p 449
16. Filler RL, Kosinski JA, Vig JR (1983) 37th Annu Symp Freq Contr Proc, p 265
17. Borngräber R (2001) Quarzresonanzsensoren für flüssige Medien – Systemdesign und Anwendung. Shaker, Aachen
18. Ballato A (1977) Doubly rotated thickness mode plate vibrators. In: Mason WP, Thurston RN (eds) Physical acoustics: principles and methods, vol XIII. Academic, New York
19. Auld BA (1990) Acoustic fields and waves. In: Solids, vol 1+2. Krieger, Melbourne
20. Schmidt RF, Allen JW, Vetelino JF, Parks J, Zhang C (2001) Sensors Actuators B 76:95
21. Salt D (1987) Hy-Q handbook of quartz crystal devices. Van Nostrand Reinhold, New York
22. Behling C, Lucklum R, Hauptmann P (1997) Sensors Actuators A 61:260
23. Lucklum R, Hauptmann P (2003) Meas Sci Technol 14:1854
24. Lin Z, Yip CM, Joseph IS, Ward MD (1993) Anal Chem 65:1546
25. Zimmermann B, Lucklum R, Hauptmann P, Rabe J, Büttgenbach S (2001) Sensors Actuators B 76:47
26. Rabe J, Büttgenbach S, Schröder J, Hauptmann P (2003) IEEE Sensors J 3:361
27. Bottom VE (1982) Introduction to quartz crystal unit design, Van Nostrand Reinhold, New York, p 165
28. Shockley W, Curran DR, Koneval DJ (1966) J Acoust Am Soc 41:981
29. Lu F, Lee HP, Lim SP (2005) Smart Mater Struct 14:272
30. Bechmann R (1952) J Sci Instr 29:73
31. Schröder J (2003) Miniaturisierter Impedanzanalysator und hochfrequente Sensorarrays für die Quarzmikrobalance in Flüssigkeiten. Shaker, Aachen
32. Rosenbaum JF (1988) Bulk acoustic wave theory and devices. Artech, Boston
33. Auge J, Hauptmann P, Eichelbaum F, Rösler S (1994) Sensors Actuators B 18–19:518
34. Gerber EA, Ballato A (ed) (1985) Precision frequency control, vol II: oscillators and standards. Academic, New York
35. Barnes C (1991) Sensors Actuators A 29:59
36. Borngräber R, Schröder J, Lucklum R, Hauptmann P (2002) IEEE Trans Ultrason Ferroelectr Freq Control 49:1254

37. Behling C, Lucklum R, Hauptmann P (1999) IEEE Trans Ultrason Ferroelectr Freq Control 46:1431
38. Schröder J, Borngräber R, Lucklum R, Hauptmann P (2001) Rev Sci Instr 72:2750
39. Wessendorf KO (1993) 47th Freq Contr Symp Proc, p 711
40. Baker B (1996) Tuning in amplifiers (AB-105). Burr-Brown, Tucson
41. Henn Ch (1993) New ultra high-speed circuit techniques with analog ICs (AB-183). Burr-Brown, Tucson
42. (1995) Data Sheet OPA660 (PDS-1072E) Burr-Brown, Tucson
43. (2005) Data Sheet OPA860 (SBOS331) Texas Instruments, Dallas
44. Rösler S, Lucklum R, Borngräber R, Hartmann J, Hauptmann P (1998) Sensors Actuators B 48:415
45. Eichelbaum F, Borngräber R, Schröder J, Lucklum R, Hauptmann P (1999) Rev Sci Instr 70:2537
46. Arnau A, Sogorb T, Jiménez Y (2000) Rev Sci Instr 71:2563
47. Arnau A, Sogorb T, Jiménez Y (2002) Rev Sci Instr 73:2724
48. Ferrari V, Marioli D, Taroni A (2003) IEEE Sensors 2003 Proc 2:849
49. Jacoby B, Art G, Bastemeijer J (2003) IEEE Sensors 2003 Proc 2:839
50. Jacoby B, Art G, Bastemeijer J (2005) IEEE Sensors 5:1106
51. Schröder J, Doerner S, Schneider T, Hauptmann P (2004) Meas Sci Technol 15:1271
52. Schnitzer R, Reiter C, Harms KC, Benes E, Groschl M (2004) IEEE Sensors 2004 Proc 2:798
53. Doerner S, Schneider T, Schröder J, Hauptmann P (2003) IEEE Sensors 2003 Proc 1:596
54. Schneider T, Richter D, Doerner S, Fritze H, Hauptmann P (2005) Sensors Actuators B 111–112:187
55. Rohdal M, Höök F, Krozer A, Kasemo B (1996) WO Patent WO9635103
56. Edvardsson M, Rodahl M, Kasemo B, Höök F (2005) Anal Chem 77:4918

Springer Ser Chem Sens Biosens (2007) 5: 49–109
DOI 10.1007/5346_024

Published online: 8 September 2006

Studies of Viscoelasticity with the QCM

Diethelm Johannsmann

Institute of Physical Chemistry, Clausthal University of Technology,
Arnold-Sommerfeld-Str. 4, 38678 Clausthal-Zellerfeld, Germany
johannsmann@pc.tu-clausthal.de

Abstract The chapter summarizes the standard model of how acoustic multilayers interact with a quartz crystal microbalance (QCM). In a first step, it is shown how the three formulations around (the mathematical description, the description in terms of acoustic reflectivities, and the equivalent circuit) model correspond to each other. Special emphasis is given to the small-load approximation, which states that the shifts of frequency and bandwidth are about equal to the real and the imaginary parts of the stress–speed ratio (the load) at the crystal surface. The (laterally averaged) stress–speed ratio can be computed for many types of samples (including anisotropic and heterogeneous materials). The small-load approximation is therefore of outstanding importance when employing the QCM in complex environments. The second part of the chapter provides the predictions of the standard model for various geometries. This includes the discussion of slip, of the comparison of optical and acoustic thickness, of electrode effects, of the frequency dependence of the viscoelastic parameters, and of the consequences of a finite contact area. Viscoelastic modeling of QCM data has some pitfalls, which are pointed out. A separate section is devoted to the shortcomings of the small-load approximation (which can be very noticeable) and the amendments to the model accounting for these.

Keywords Acoustic multilayers · Equivalent circuits · Quartz crystal microbalance · Quartz crystal resonator · Viscoelasticity

Abbreviations

A	Area
a	Amplitude of oscillation at the crystal surface
b_s	Slip length
c	Speed of sound, $c = (G/\rho)^{1/2}$
C_1	Motional capacitance
C_0	Electrical (parallel) capacitance
D	Dissipation, $D = Q^{-1}$
d	Thickness
d_e	Thickness of the electrode
d_f	Thickness of the film
d_q	Thickness of the crystal, $d_q = c_q/(2f_f)$
d_{26}	Piezoelectric strain coefficient, $d_{26} = 3.1 \times 10^{-12}$ m V^{-1}
e_{26}	Piezoelectric stress coefficient, $e_{26} = d_{26}G_q = 9.65 \times 10^{-2}$ C m^{-2}
e	as an index: Electrode
F	Force
F_{ex}	External force
f	as an index: Film (exception: f_f, frequency of the fundamental)
f	Frequency
f_r	Resonance frequency (real part)
f_0	Resonance frequency in reference state
$\tilde{f}_r$	Resonance complex frequency, $\tilde{f}_r = f_r + i\Gamma$
$\tilde{f}_0$	Resonance complex frequency in reference state
f_f	A parameter close to the resonance frequency of the fundamental
G	Shear modulus, $G = G' + iG''$
G_q	Shear modulus of AT-cut quartz, $G_q \approx 29.3 \times 10^9$ Pa
h_q	Half of the thickness of the crystal, $h_q = d_q/2$
h	Half of the thickness of a layer
I_{el}	Electrical current

J Shear compliance, $J = 1/G$, $J = J' - \mathrm{i}J''$
k Wave vector, $k = \omega/c = \omega(\rho/G)^{1/2}$, $k = k' - \mathrm{i}k''$
liq as an index: Liquid
L_1 Motional inductance
m_e Areal mass density of the electrode
m_f Areal mass density of the film
m_p Mass of resonating system; m_p is not an areal mass density, it is a mass
m_q Areal mass density of the crystal, $m_q = \rho_q d_q = \rho_q c_q/(2f_f) = Z_q/(2f_f)$
n Overtone order, $n \approx f_r/f_f$
q as an index: Quartz
Q Q factor, $Q = f_r/(2\Gamma)$
R_1 Motional resistance
t Time
u Lateral displacement
$\dot{u}$ Lateral speed, $\dot{u} = \mathrm{i}\omega u$
$u^{\pm}$ Wave traveling to the left (+) or to the right (–)
$u^{\pm,0}$ Amplitudes of waves
U_{el} Electrical voltage
x Spatial coordinate in the surface plane
y Spatial coordinate in the surface plane
z Spatial coordinate perpendicular to the surface plane
$z_{j,j+1}$ Location of interface between layers j and $j + 1$
Z Acoustic impedance, $Z = \rho c = (\rho G)^{1/2}$, $Z = Z' + \mathrm{i}Z''$
Z_{el} Electric impedance
Z_k Circuit element related piezoelectric stiffening
Z_{liq} Acoustic impedance of a liquid, $Z_{liq} = (\mathrm{i}\omega\eta\rho)^{1/2}$
Z_m Mechanical impedance, $Z_m = F/\dot{u} = A\sigma/\dot{u}$
Z_q Acoustic impedance of AT-cut quartz, $Z_q = 8.8 \times 10^6\ \mathrm{kg\,m^{-2}\,s^{-1}}$
Z_L Load impedance, $Z_L = \sigma/\dot{u}$
β' Power law exponent of viscoelastic dispersion, $J'(f) = J'(f_{ref}) \cdot (f/f_{ref})^{\beta'}$
β'' Power law exponent of viscoelastic dispersion, $J''(f) = J''(f_{ref}) \cdot (f/f_{ref})^{\beta''}$
$\Delta\tilde{f}$ Complex frequency shift
Δf Frequency shift
$\Delta\Gamma$ Shift of half bandwidth at half maximum
$\Delta\varphi$ Phase shift induced by the sample
γ Decay constant, $\gamma = \xi_p/m_p$
Γ Half-band-half-width of a resonance, HBH width, “bandwidth” for short
ϕ Factor for conversion between current and speed, $\phi = Ae_{26}/d_q$, $I_{el} = \phi\dot{u}$
φ Phase shift for one round-trip
η Viscosity, $\eta = G/(\mathrm{i}\omega)$
κ_p Spring constant of a resonator
κ Piezoelectric coupling coefficient, $\kappa^2 = e_{26}^2/(\varepsilon\varepsilon_0 G_q)$
λ Wavelength
μ_e Dimensionless parameter describing the mass of the electrode, $\mu_e = m_e/m_q$
μ_f Dimensionless parameter describing the mass of the film, $\mu_f = m_f/m_q$
ρ Density
σ Stress
ω Radial frequency
ω_r Radial frequency on resonance

ω_0 Radial frequency on resonance in the reference state or eigenfrequency of a resonator, $\omega_0 = (\kappa_p/m_p)^{1/2}$
ξ_p Drag coefficient, $\xi_p = F/\dot{u}$
ξ_{liq} Dimensionless parameter describing the viscosity of liquid
ζ_e Dimensionless parameter describing the compliance of the electrode
ζ_f Dimensionless parameter describing the compliance of the film

1 Introduction

The quartz crystal microbalance (QCM) is a well-known tool to measure film thicknesses in the nanometer range [1–3]. It is difficult to imagine a device which is simpler than a quartz crystal resonator, and simplicity is one of the principal advantages of the QCM. A QCM is a disk of crystalline quartz. The disk displays acoustic resonances like any other three-dimensional body. As a resonator, it distinguishes itself from other resonators by a number of features:

- Since crystalline quartz is weakly piezoelectric, the acoustic resonances can be probed by electrical means. Otherwise, piezoelectricity is of minor importance.
- There are a number of acoustic modes, which can be well approximated by standing plane waves with the k vector perpendicular to the crystal surface. For these plane-wave modes, the crystal can be considered as laterally infinite. The only dimension of interest is the dimension perpendicular to the surface. One-dimensional models apply [4].
- For certain crystal cuts the motion is of the thickness-shear type. Since the motion at the crystal surface is then in the surface plane, these modes do not emit longitudinal sound (or at least not very much of it). The weak acoustic coupling to the environment increases the Q factor of the resonances to rather exceptional levels. The bandwidth is orders of magnitude smaller than the resonance frequency, which greatly simplifies the data analysis.

The classical sensing application of quartz crystal resonators is microgravimetry [1, 5]. Many commercial instruments are around. These devices exploit the Sauerbrey relation (Eq. 28). For thin films, the resonance frequency is—by and large—inversely proportional to the total thickness of the plate. The latter increases when a film is deposited onto the crystal surface. Monolayer sensitivity is easily reached. However, when the film thickness increases, viscoelastic effects come into play, as was for instance recognized by Lu and Lewis, who derived a refined version of the Sauerbrey equation [6]. These authors mainly intended to improve the microweighing procedure. Actually measuring viscoelastic properties with the QCM was not a major issue

at the time. In the late 1980s, it was recognized that the QCM can also be operated in liquids, if proper measures are taken to overcome the large damping [7, 8]. The ensuing questions and their discussion contributed much to the increased interest in nongravimetric applications of the QCM.

Today, microweighing is only one out of many uses of the QCM (Fig. 1). The QCM can be viewed as an acoustic reflectometer, as a high-frequency interfacial rheometer, or as a micromechanical probe. In view of this diverse set of applications, it is helpful to describe the acoustic interaction between the crystal and the sample in a general way. This entails a certain mathematical effort. However, there are intuitive views for most cases. Regardless of the complexity occurring in the intermediate steps of the calculation, simple relations are eventually found which can be readily programmed in any of the standard software packages for data analysis. For instance, if the sample is a thin film in air, an advanced analysis (Eq. 72) can yield the viscous compliance of the film, $J_f''(\omega)$. If the film is in a liquid environment, the elastic compliance of the film, $J_f'(\omega)$, is derived (Eq. 85). Equations 72 and 85 are limiting cases to a viscoelastic model, which today is well established. Note that the "nongravimetric" QCM is by no means an alternative to the conventional QCM. Viscoelastic modeling deepens our understanding of the conventional QCM and enhances the information derived from physical, chemical, or biological sensors based on quartz crystal resonators.

Although this chapter is mainly concerned with modeling, we briefly address a few experimental issues:

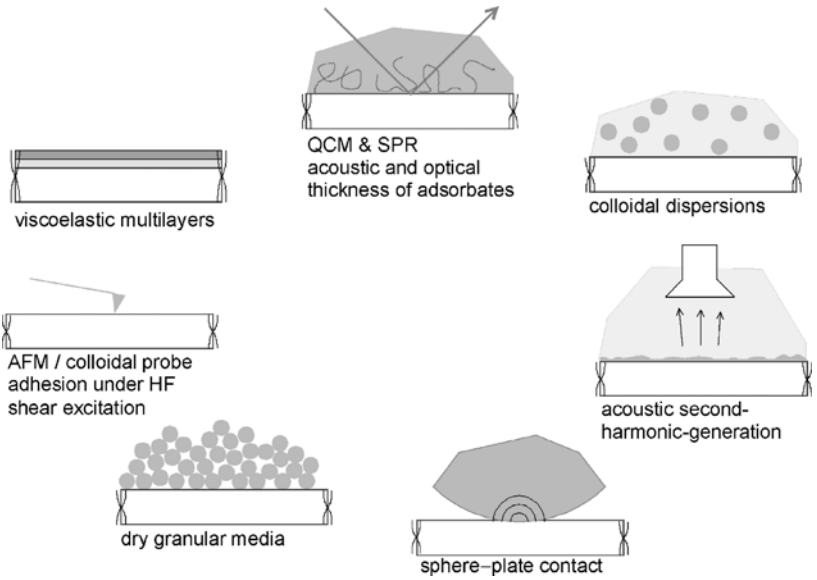

Fig. 1 Different uses of the QCM

- Impedance analysis (Fig. 2), whereby the resonance curves are passively mapped out with a network analyzer, has in many ways laid the experimental ground for the viscoelastic modeling [9, 10]. With impedance analysis, both the frequency and the bandwidth of the resonance are accessible on a number of different overtones. Ring-down has been recently introduced as an alternative to impedance analysis [11]. This technique (Sect. 2) also provides frequency and bandwidth and can do so on a number of harmonics.
- Oscillator circuits are a cost-efficient alternative to impedance analysis and ring-down [12, 13]. Naturally, most sensors run on oscillator circuits. Some advanced circuits provide a measure of the dissipation (such as the peak resistance, R_1, see Sect. 6) in addition to the frequency. Most oscillators operate on one harmonic only. Oscillators can be more stable than ring-down and impedance analysis because the latter two techniques periodically turn the crystal on and off in one way or another, whereas oscillators just run quietly on one fixed frequency. If the signal-to-noise ratio is the primary concern, no technique can beat oscillators. There is one pitfall with the use of oscillators worth mentioning: the theory below pertains to the series resonance frequency (simply called resonance frequency). The output frequency of an oscillator circuit, on the other hand, usually is *not* the series resonance frequency (Fig. 2). For instance, phase-locked-loop oscillators keep the phase constant. Many oscillators run at the zero-phase frequency ($B \equiv 0$, Fig. 2). Importantly, the difference between the zero-phase frequency and the series resonance frequency changes if the bandwidth or the parallel capacitance change (Sect. 6). The

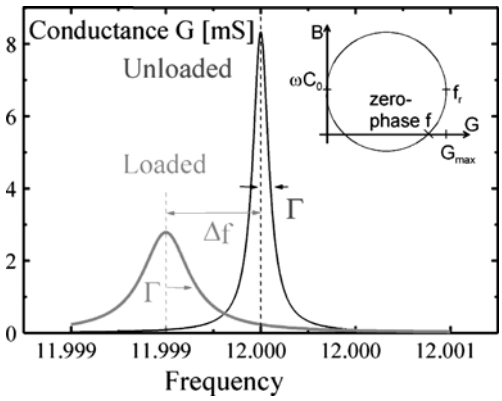

Fig. 2 Impedance analysis is based on the conductance curve of the crystal. The central parameters of measurement are the resonance frequency, f_r, and the half-band-half-width, Γ. The *insert* shows the admittance diagram in the complex plane of the admittance $Y(\omega) = G(\omega) + iB(\omega)$. The series resonance frequency, f_r, corresponds to the peak of the conductance. The frequency corresponding to $B = 0$ is the zero-phase frequency

latter may happen as a consequence of fluctuating stray capacitances. Changes in bandwidth or parallel capacitance therefore induce a change in the frequency of oscillation that is not related to a shift of the (series) resonant frequency. This cross-sensitivity easily leads to misinterpretations.

- Because the QCM is so tremendously sensitive, factors of influence come into play that can safely be ignored in other fields of physics. The correct interpretation of an experiment is often a challenge and supplemental information in addition to the frequency shift is helpful. Such information can, for instance, come from the comparison of the shifts of frequency and bandwidth at the different harmonics. The combination of the QCM with other surface-analytical techniques like electrochemical cyclovoltammetry [14–16], optical reflectometry [17], atomic force microscopy [18, 19], or the colloidal probe [20, 21] has been pursued for the same reason. Particularly advanced is the electrochemical QCM (EQCM) [14].
- While a stability of $\delta f/f < 10^{-9}$ and better is achieved with sealed resonators as they are usually employed in timing and frequency-control applications, a typical stability for resonators exposed to the environment is in the range of 10^{-8}–10^{-7}.
- The best agreement between theory and experiment is reached with planar, optically polished crystals for overtone orders between $n = 5$ and $n = 13$. On low harmonics, energy trapping [22] is insufficient, while on high harmonics, anharmonic side bands interfere with the main resonance [23].
- Admittedly, some of the amazing simplicity of quartz crystal resonators is lost once the surfaces are covered with electrodes and the crystal is inserted into a holder. In this chapter, we mostly stick to an idealistic view and describe the modeling as if there were none of these complications. We do not touch upon compressional waves [24, 25], effects of varying temperature or stress [26, 27], anharmonic side bands [23], roughness [28, 29], bubbles and slip [30], or effects of a variable dielectric environment [31, 32].

Although this chapter is concerned with bulk acoustic wave (BAW) devices, some of the concepts apply to shear horizontal surface acoustic wave (SH-SAW) devices in a similar way [33, 34]. When modeling SH-SAW devices, one usually decomposes the wave vector into a vertical and a lateral component. The vertical component obeys similar laws as the shear wave in a BAW resonator. This being said, we confine the discussion to BAW devices (also termed thickness-shear resonators) in the following.

The most popular BAW resonator is the QCM. The name QCM correctly suggests that its main use is microgravimetry. However, many researchers who use quartz resonators for other purposes have continued to call the quartz crystal resonator “QCM”. We will follow this usage and call all quartz crystal resonators QCMs. Actually, the term “balance” makes sense even for

nongravimetric applications if it is understood in the sense of a force balance. The force exerted on the crystal by the sample is balanced by the force originating from the shear gradient inside the crystal. This is the essence of the small-load approximation (Eq. 51). Crystalline α-quartz is by far the most important material for thickness-shear resonators. Langasite ($La_3Ga_5SiO_{14}$, "LGS") and gallium orthophosphate ($GaPO_4$) are investigated as alternatives to quartz, mainly (but not only) for use at high temperatures [35, 36]. We also call these devices "QCMs", even though they are not made out of quartz (and may or may not be used for gravimetry).

2 Complex Resonance Frequencies

We use complex resonance frequencies, where the real part, f_r, is the series resonance frequency and the imaginary part, Γ, is half the bandwidth at half maximum of the resonance (half-band-half-width, HBH width, also termed "bandwidth" for short). In the following, we comment on why—and under what conditions—the imaginary part of the resonance frequency is equal to the half-band-half-width [37].

Consider a forced resonator obeying the force-balance equation:

$$m_p \frac{d^2x(t)}{dt^2} + \xi_p \frac{dx(t)}{dt} + \kappa_p x(t) = F_{ex}(t) \tag{1}$$

with m_p the mass, ξ_p the drag coefficient, κ_p the spring constant, and F_{ex} the external force. Introducing the decay constant $\gamma = \xi_p/m_p$ and the eigenfrequency $\omega_0 = \left(\kappa_p/m_p\right)^{1/2}$, and also considering the Fourier transforms $x(\omega)$ and $F_{ex}(\omega)$, this reads:

$$\frac{m_p x(\omega)}{F_{ex}(\omega)} = \frac{1}{\omega_0^2 - \omega^2 + i\gamma\omega}\,. \tag{2}$$

We now introduce the variables $f = \omega/2\pi$, $f_r = \omega_0/2\pi$, and $\Gamma = (1/2)\gamma/(2\pi)$. The factor of 1/2 in the latter definition is essential. Assuming that the resonance is narrow ($\Gamma \ll f_r$), one may approximate $2i\Gamma f$ by $2i\Gamma f_r$ and write:

$$\begin{aligned}\frac{4\pi^2 m_p x(f)}{F_{ex}(f)} &\approx \frac{1}{f_r^2 - f^2 + 2i\Gamma f} \approx \frac{1}{f_r^2 - f^2 + 2i\Gamma f_r} \approx \frac{1}{f_r^2 - f^2 + 2i\Gamma f_r - \Gamma^2} \\ &= \frac{1}{\left(f_r + i\Gamma\right)^2 - f^2} = \frac{1}{\tilde{f}_r^2 - f^2}\,.\end{aligned} \tag{3}$$

The small term Γ^2 has been added to the denominator in step 3. As Eq. 3 shows, the bandwidth can been absorbed into a complex resonance frequency, $\tilde{f}_r$, if one chooses the real part as f_r and the imaginary part as Γ. Since the crystal cannot be excited with a complex frequency, the denominator al-

ways remains nonzero and the amplitude $x(f)$ remains finite. Allowing for complex resonance frequencies is a convenient way to include the bandwidth in all equations.

It is instructive to go through a similar set of equations in the time domain. Assume that the excitation of the resonance is carried out with a radiofrequency pulse (rather than a continuous sine wave). After the excitation has been turned off, the resonator rings down according to a decaying complex exponential:

$$x(t) = x_0 \exp\left(\mathrm{i}\tilde{\omega}_\mathrm{r} t\right) = x_0 \exp\left(2\pi \mathrm{i} \tilde{f}_\mathrm{r} t\right) \exp\left(-2\pi\Gamma t\right) \ . \tag{4}$$

Since $F_\mathrm{ex} = 0$, Eq. 1 requires that:

$$\left(-m_\mathrm{p}\tilde{\omega}_\mathrm{r}^2 + \mathrm{i}\xi_\mathrm{p}\tilde{\omega}_\mathrm{r} + \kappa_\mathrm{p}\right)\left(x_0 \exp(2\pi \mathrm{i}\tilde{\omega}_\mathrm{r} t)\right) = 0 \tag{5}$$

and further, since $x_0 \neq 0$:

$$\tilde{\omega}_\mathrm{r}^2 - \mathrm{i}\gamma\tilde{\omega}_\mathrm{r} - \omega_0^2 = 0 \ , \tag{6}$$

which, for $\gamma \ll \omega_0$, is solved by

$$\tilde{\omega}_\mathrm{r} = \frac{\mathrm{i}\gamma}{2} \pm \sqrt{\frac{-\gamma^2}{4} + \omega_0^2} \approx \pm\omega_0 + \frac{\mathrm{i}\gamma}{2} \ . \tag{7}$$

Again, the imaginary part of $\tilde{\omega}_\mathrm{r}$ is *one half* of the decay constant, γ, provided that the resonance is sharp. Sharp resonances are always found for the QCM. A quick estimate shows that the error caused by neglecting $\gamma^2/4$ in comparison to ω_0^2 in Eq. 7 is negligible in all cases of practical interest. The complex resonance frequency, $\tilde{f}_\mathrm{r}$, also describes the ring-down of a freely oscillating resonator. Since the decay time, τ, is equal to $(2\pi\Gamma)^{-1}$, Γ can be determined by ring-down experiments (see the chapter by F. Höök and B. Kasemo, 2006, in this volume) just as well as by mapping out the resonance curve with an impedance analyzer.

The time-domain description and the frequency-domain description are connected via the Greens function formalism. Solving Eq. 1 for an arbitrary tune sequence of the external force $F_\mathrm{ex}(t)$ by means of the Greens function shows that the crystal "remembers" the ariving conditions of a tune equal to $(2\pi\Gamma)^{-1}$. The Greens function formalism is of importance in the context of advanced pulse sequences for driving the crystal [40]. Note, however, that a response to a change in the crystal properties (for example a change in κ_p caused by a contact with an external object) is instantaneous. The parameters κ_p, m_p, and ξ_p in Eq. 1 (and, as a consequence, $\tilde{f}_\mathrm{r}$) then acquire an explicit time dependence. The output of the QCM responds almost instantaneously to changes in its resonance parameters, whereas it responds more slowly to changes in its driving conditions. This issue is of importance in the context of fast measurements [38, 39].

In this chapter, the half-band-half-width, Γ, is used to quantify dissipation.[1] Other common parameters are the quality factor, Q, and the dissipation [11] $D = Q^{-1}$. Q is defined as:

$$Q = \frac{f_r}{2\Gamma} , \tag{8}$$

which implies that:

$$D = \frac{2\Gamma}{f_r} . \tag{9}$$

These other measures of dissipation are completely equivalent to the bandwidth. It is entirely a matter of taste which variable to use.

The motional resistance, R_1 (Sect. 6), is also used as a measure of dissipation. R_1 is an output parameter of some instruments based on advanced oscillator circuits. However, experiments based on impedance analysis show that R_1 usually is *not* strictly proportional to the bandwidth (although it should be, according to the Butterworth–van Dyke (BvD) circuit, Appendix A). Also, in absolute terms, R_1—being an electrical quantity and not a frequency—is affected by calibration problems much more than the bandwidth. In the author's opinion, Γ or D are better measures of dissipation than R_1.

Even though getting used to a complex resonance frequency takes some exercise, one is rewarded later on with a reduction in the number of equations by a factor of two. Just about every single equation below (concerning load, impedance, speed of sound, wave vector, resonance frequency, shear modulus, or shear compliance) can be formulated with complex parameters, where the imaginary part quantifies a loss of energy. Consistently using complex variables (including complex resonance frequencies) much simplifies the algebra.

At this point, we introduce a convention: a traveling wave $u(z, t)$ shall be of the form

$$u^{\pm}(z, t) = u^{\pm,0} \exp\left(+ \mathrm{i}(\omega t \pm kz)\right) + \text{c.c.} , \tag{10}$$

where "c.c." denotes the complex conjugate and is usually omitted. We could equally well have written $u^{\pm}(z, t) = u^{\pm,0} \exp\left(- \mathrm{i}(\omega t \pm kz)\right) + \text{c.c.}$ because after adding the complex conjugate, it does not matter whether the time dependence has the form $\exp(\mathrm{i}\omega t)$ or $\exp(- \mathrm{i}\omega t)$. However, it is helpful to stick to $\exp(+ \mathrm{i}\omega t)$ and to certain other sign conventions as well, in order to ensure that dissipative processes always increase the entropy and never decrease it. These sign conventions are: $G = G' + \mathrm{i}G''$ for the shear modulus, $J = J' - \mathrm{i}J''$ for the shear compliance, $Z = Z' + \mathrm{i}Z''$ for the acoustic impedance, $\varepsilon = \varepsilon' - \mathrm{i}\varepsilon''$ for the dielectric constant, $k = \pm k' - \mathrm{i}k''$ for the wave vector, $c = c' + \mathrm{i}c''$ for

[1] Note that Γ denotes the half-band-*full*-width in [28] and other publications by this group.

the speed of sound, and $\eta = \eta' - i\eta''$ for the viscosity. Using the above conventions, all quantities with two primes are positive as long as the corresponding processes comply with the second law of thermodynamics.[2]

In the following, all variables which are connected to viscoelasticity in one way or another (such as G, J, k, c, or Z) are considered complex. Exceptions are the parameters G_q, k_q, c_q, and Z_q, which pertain to the quartz crystal. These parameters, as well as the frequency of the fundamental, f_f, are considered to be real in order to conform to the current usage in the literature. One can also define them as complex (which they are, in principle, although the imaginary parts are much smaller than the real parts). When any of the parameters G_q, k_q, c_q, and Z_q are meant to be complex, they attain a tilde ($\tilde{}$). Even when they are complex, the ratios $\tilde{c}_q/(2\tilde{f}_f)$ and $\tilde{Z}_q/(2\tilde{f}_f)$ (leading to the thickness of the crystal, d_q, and the mass per unit area of the crystal, m_q) are real. Frequencies and spring constants are real, unless they have a tilde ($\tilde{f}_r$, $\tilde{f}_0$, $\tilde{\omega}_r$, $\Delta\tilde{f}$, $\tilde{\kappa}_p$). The overtone order, n, is never complex. The overtone order is meant to be the nearest integer to $\tilde{f}_r/f_f$. In some cases, it makes sense to define n as the *real part* of $\tilde{f}_r/f_f$. Since overtones are always slightly displaced from the exact integer multiples of the fundamental, $\tilde{f}_r/f_f$ is not exactly an integer [41]. The deviation is small and, further, the context will make it clear whether accuracy can be gained by considering n a real number (close to an integer), rather than an integer.

3
Assumptions of the Standard Model

A standard model has emerged for the calculation of the resonance frequencies of quartz crystal resonators coated with planar layers [37, 42–45]. We first summarize the assumptions entering the model:

1. The resonator and all cover layers are laterally homogeneous and laterally infinite.
2. The distortion of the crystal is given by a transverse plane wave with the k vector perpendicular to the surface normal (thickness-shear mode). There are neither compressional waves [24] nor flexural contributions to the displacement pattern [46]. There are no nodal lines in the plane of the resonator. The standard model ignores anharmonic side bands (spurious modes) [23].
3. All stresses are proportional to strain. Linear viscoelasticity holds [47].
4. The voltage across the crystal is a boundary condition controlled by the experimentalist. The current through the electrodes is the primary parameter of the measurement.

[2] For the viscosity, the *primed* quantity (η') is related to dissipation rather than the quantity with double primes.

These assumptions deserve a few comments. Assumptions 1 and 2 are interrelated and not fulfilled in practice. In order to be able to mount the crystal in a holder touching its rim, "energy trapping" [22] is employed. One confines the oscillating region to the center of the plate by making the crystal slightly thicker in the center than at the rim. The resonator then acts as a small acoustic lens, which focuses the acoustic beam to the center of the plate. An increased thickness at the center can, for instance, be achieved with keyhole-shaped back electrodes or, alternatively, with plane-convex crystals. There is an analytical treatment of energy trapping with plane-convex crystals by Stevens and Tiersten [48]. Finite element calculations are being done [49], but their routine use at this point seems difficult. Importantly, energy trapping induces flexural contributions to the pattern of motion as well as compressional waves [50, 51], which is a problem with the use of the QCM in liquids. Because laterally heterogeneous samples are of tremendous importance in practice, we treat them briefly in Sect. 8.1.1 (see also D. Johannsmann, 2006, in this volume).

Assumptions 1 and 2 constitute a practical requirement for the construction of resonators in the sense that resonators perform poorly if the width-to-thickness ratio is less than about 30. This condition severely restricts the design options when it comes to miniaturization and array sensors. Violations of assumptions 1 and 2 are tolerable only to a certain extent.

Linear viscoelasticity (assumption 3) is obeyed as long as the driving voltage is small enough. In air, a drive level of – 5 dBm (170 mV_{rms}) usually is safe.[3] In liquids, higher drive levels (resulting in a better signal-to-noise ratio) can be tolerated because the motion is more strongly damped and the peak amplitude is not as high as in air. The main source of a drive-level dependence of the resonance parameters is an elastic anharmonicity of the crystal [47, 52]. Heating also plays a role. Linear viscoelasticity is often violated in contact mechanics experiments (D. Johannsmann, 2006, in this volume) because interfacial friction is a strongly nonlinear phenomenon.

Assumption 4 is not fulfilled in practice, because the electrical circuitry probing the crystal has finite output and input impedance. Nevertheless, since the calculations provide the electrical impedance of the crystal, the electrical circuitry can be accounted for by using an appropriately extended equivalent electrical circuit of the crystal (Sect. 6) in the analysis.

When employing impedance analysis, proper calibration of the impedance analyzer takes care of the additional electric circuit elements to a large extent.[4] It turns out to be advantageous to interface the crystal to an elec-

[3] A drive level of DL = 0 dBm corresponds to a power of $P = 1$ mW. With an impedance of the cable of $R = 50$ ohms, this translates to a voltage $U_{el} = (RP)^{1/2} = (50 \times 10^{-3})^{1/2} V(rms) \times \exp(DL/(20\,dBm)) = 223.6\,mV(rms) \times \exp(DL/(20\,dBm))$. The amplitude of the voltage is equal to the rms voltage multiplied by $2^{1/2}$.

[4] Most network analyzers use three-term calibration, which is good enough in the sense that the resonance curves look correct after calibration. Evidently, three-term calibration only accounts for sufficiently simple electrical elements between the analyzer and the crystal. Three-term calibration is described in the EIA Standard 512.

tronic circuitry with *low* impedance. Because of piezoelectric stiffening (Sect. 6) the crystal responds rather sensitively to stray capacitances between the electrodes. The influence of stray capacitances can be lowered by connecting the two electrodes across a small resistor (typically 14.2 ohms). The resistor short-circuits the stray capacitances. Such an electrical separation from the environment is achieved by means of a π network [53]. However, the π network also short-circuits the connection between the crystal and the driving electronics to some extent (effectively acting as a 15-dB attenuator), thereby decreasing the signal-to-noise ratio.

4 Wave Equations and Continuity Conditions: The Mathematical Approach

The following section describes the canonical mathematical way of finding the resonance frequencies of coated quartz crystals. The method is described in detail in [54]. The wave equations for the different layers and the boundary conditions at the interfaces between the layers form a homogeneous system of linear equations, which can only be solved if the determinant of the system is zero. Since the determinant depends on frequency, the zeros of the determinant lead to the resonance frequencies.

Figure 3 illustrates the geometry. There are a total of N layers, where the semi-infinite media to the left and to the right of the layer stack have the indices 0 and $N + 1$. Later on, the crystal will usually be layer 1 and the index 1 will be replaced by q. Each layer j is characterized by the thickness, d_j, an acoustic impedance, Z_j, and a speed of sound, c_j. Both the impedance Z_j and the speed of sound c_j are complex. They are given by:

$$c_j = \sqrt{\frac{G_j}{\rho_j}} = \sqrt{\frac{G'_j + iG''_j}{\rho_j}} \tag{11}$$

$$Z_j = \rho_j c_j = \sqrt{\rho_j G_j} = \sqrt{\rho_j \left(G'_j + iG''_j\right)}, \tag{12}$$

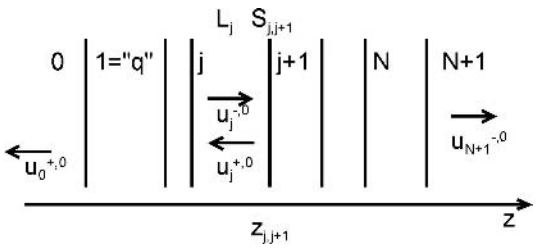

Fig. 3 Layer system and definition of variables

where ρ is the density and G is the shear modulus. Each layer supports two waves of the form $u_j^{\pm} = u_j^{\pm,0} \exp\left(\mathrm{i}(\omega t \pm k_j z)\right)$, where the "+" and "–" signs denote the direction of propagation; u_j^- is the wave traveling from left to right, $k_j = \omega/c_j$ is the wave vector, and $u_j^{\pm,0}$ is the amplitude. Unless the crystal is operated as a microphone [55] (which is not considered here), the semi-infinite media to the left and to the right each only support one wave, which propagates outwards. The amplitudes $u_0^{-,0}$ and $u_{N+1}^{+,0}$ are zero, leaving us with a set of $2N + 2$ nontrivial amplitudes. The N layers are bounded by $N + 1$ interfaces. Both the displacement, u, and the stress, $G\partial u/\partial z$, are continuous at the interface. The continuity of displacement is expressed as:

$$u_j^+\left(z_{j,j+1}\right) + u_j^-\left(z_{j,j+1}\right) = u_{j+1}^+\left(z_{j,j+1}\right) + u_{j+1}^-\left(z_{j,j+1}\right) , \tag{13}$$

where $z_{j,j+1}$ is the location of the interface between layers j and $j + 1$. Adopting the definition that:

$$\begin{aligned} u_j^{\pm}\left(z_{j-1,j}\right) &= u_j^{\pm,0} \\ u_j^{\pm}\left(z_{j,j+1}\right) &= u_j^{\pm,0} \exp\left(\pm \mathrm{i} k_j d_j\right) , \end{aligned} \tag{14}$$

Eq. 13 translates to:

$$u_j^{+,0} \exp\left(\mathrm{i} k_j d_j\right) + u_j^{-,0} \exp\left(-\mathrm{i} k_j d_j\right) = u_{j+1}^{+,0} + u_{j+1}^{-,0} . \tag{15}$$

The continuity of stress is expressed as:

$$\mathrm{i} G_j k_j \left[u_j^+\left(z_{j,j+1}\right) - u_j^-\left(z_{j,j+1}\right)\right] = \mathrm{i} G_{j+1} k_{j+1} \left[u_{j+1}^+\left(z_{j,j+1}\right) - u_{j+1}^-\left(z_{j,j+1}\right)\right] . \tag{16}$$

Using Eqs. 14 and 15 as well as $k = \omega/c = \omega(\rho/G)^{1/2} = \omega Z/G$, Eq. 16 can also be written as:

$$Z_j \left[u_j^{+,0} \exp\left(\mathrm{i} k_j d_j\right) - u_j^{-,0} \exp\left(-\mathrm{i} k_j d_j\right)\right] = Z_{j+1} \left[u_{j+1}^{+,0} - u_{j+1}^{-,0}\right] . \tag{17}$$

Equation 17 illustrates why the acoustic impedance is of such tremendous importance in the physics of the QCM. The acoustic impedance governs the condition of stress continuity, and thereby the reflectivity at acoustic interfaces.

Equations 15 and 17 constitute a homogeneous system of $2N + 2$ linear equations. A nontrivial solution for the set of amplitudes $\{u_j^{\pm,0}\}$ only exists if the determinant of this equation system vanishes. The search for the zeros of the determinant as a function of frequency will in general be carried out numerically. The zeros define the resonance frequencies. Since, for a real material, the shear modulus always contains a dissipative component, G'', the resonance frequencies are complex (where the imaginary part is the half-band-half-width, Γ).

Let us consider a simple example. For the bare crystal in air, the number of layers is equal to 1 and the adjacent bulk media have vanishing impedance ($Z_0 = 0$, $Z_2 = 0$). Here and in the following, we neglect the impedance of air

and treat air and vacuum as the same. We use the index "q" instead of "1" because the first layer is the quartz crystal. The resulting set of equations is:

$$u_0^{+,0} = u_q^{+,0} + u_q^{-,0} \tag{18}$$

$$0 = \tilde{Z}_q \left[u_q^{+,0} - u_q^{-,0} \right] \tag{19}$$

$$u_q^{+,0} \exp\left(i\tilde{k}_q d_q\right) + u_q^{-,0} \exp\left(-i\tilde{k}_q d_q\right) = u_2^{-,0} \tag{20}$$

$$\tilde{Z}_q \left[u_q^{+,0} \exp\left(i\tilde{k}_q d_q\right) - u_q^{-,0} \exp\left(-i\tilde{k}_q d_q\right) \right] = 0\,. \tag{21}$$

In matrix notation this reads as:

$$\begin{bmatrix} -1 & 1 & 1 & 0 \\ 0 & \tilde{Z}_q & -\tilde{Z}_q & 0 \\ 0 & \exp\left(i\tilde{k}_q d_q\right) & \exp\left(-i\tilde{k}_q d_q\right) & -1 \\ 0 & \tilde{Z}_q \exp\left(i\tilde{k}_q d_q\right) & -\tilde{Z}_q \exp\left(-i\tilde{k}_q d_q\right) & 0 \end{bmatrix} \begin{bmatrix} u_0^{+,0} \\ u_q^{+,0} \\ u_q^{-,0} \\ u_2^{-,0} \end{bmatrix} = 0\,. \tag{22}$$

Requiring that the determinant of this system be zero amounts to:

$$\tilde{Z}_q^2 \exp\left(i\tilde{k}_q d_q\right) - \tilde{Z}_q^2 \exp\left(-i\tilde{k}_q d_q\right) = 0 \tag{23}$$

or equivalently:

$$\tilde{k}_q = \frac{\tilde{\omega}_r}{\tilde{c}_q} = \frac{n\pi}{d_q}\,, \tag{24}$$

where the overtone order, n, is an integer.[5] Equation 24 is the well-known resonance condition for a bare plate in vacuum. The displacement pattern is given by a standing wave with antinodes at the surfaces. For the fundamental, the wavelength is twice the crystal thickness. The surfaces are stress-free with vanishing gradients $\partial u/\partial z$. The overtone order may be even or odd. However, only odd harmonics can be excited electrically.[6]

For later use, we rewrite Eq. 24 in two different ways. Calling the frequency of the fundamental $\tilde{f}_f$ ($n = 1$), we find:

$$d_q = \frac{1}{2}\frac{\tilde{c}_q}{\tilde{f}_f} \tag{25}$$

and

$$m_q = \rho_q d_q = \frac{1}{2}\frac{\rho_q \tilde{c}_q}{\tilde{f}_f} = \frac{1}{2}\frac{\tilde{Z}_q}{\tilde{f}_f}\,, \tag{26}$$

[5] The overtone order may turn into a noninteger number if piezoelectric stiffening and energy trapping are taken into account. This does not change the structure of the equations.

[6] A resonance can be excited electrically if there is a difference between the displacement of the two electrodes (inducing a polarization and a current). Harmonics with even overtone order can, under certain conditions, also be electrically excited. The displacement pattern has to be slightly asymmetric. This may be the case if one side of the crystal is heavily loaded whereas the other side is empty.

where m_q is the mass per unit area of the crystal, and ρ_q is its density. In the context of viscoelastic modeling, the combination of parameters Z_q and f_f usually encodes the mass of the crystal. For the reasons stated in [41], the resonance frequency at the fundamental is not the best choice for the parameter f_f. This resonance frequency is also affected by piezoelectric stiffening and energy trapping. Some accuracy can be gained by using the high-frequency limit $f_0(n)/n$ (where $f_0(n)$ is the frequency of the bare crystal at overtone order n) for the parameter f_f, rather than the frequency of the fundamental. The two are not exactly the same.

Let us assume that a thin film of thickness $d_f \ll d_q$ has been coated onto the crystal surface. Let the film have the same acoustic properties as the crystal ($\rho_f = \rho_q$, $\tilde{c}_f = \tilde{c}_q$). Adding a film of identical properties amounts to a thickening of the plate. This system may still be modeled as a single layer. If the properties of the film were to be different from the properties of the crystal, we would need to repeat the full analysis with two layers instead of one. The discussion of a viscoelastic film with arbitrary acoustic properties is deferred to Sect. 8.2.

For a film which has exactly the same acoustic properties as the crystal, the shift in resonance frequency is predicted as:

$$\frac{\Delta\tilde{f}}{\tilde{f}_0} \approx -\frac{d_f}{d_q} = -\frac{m_f}{m_q}\,. \tag{27}$$

Here and in the following, $\tilde{f}_0$ is the resonance frequency of the crystal in the reference state (which usually is the uncoated state)[7]; m_f and m_q are the areal mass densities (mass per unit area) of the film and the crystal, respectively. The relation $d_f/d_q = m_f/m_q$ evidently requires that the density of the film and the crystal are the same. It will turn out that the fractional frequency shift is the same as the ratio of m_f and m_q for all thin films, regardless of their acoustic properties. Therefore, one may memorize the relation $\Delta\tilde{f}/\tilde{f}_0 = -\,m_f/m_q$ right here. Note that this "Sauerbrey limit" only holds for films much thinner than the wavelength of sound, λ.

Using Eq. 26 for the parameter m_q, we arrive at the famous Sauerbrey equation:

$$\frac{\Delta\tilde{f}}{f_f} \approx -\frac{2\tilde{f}_0}{Z_q} m_f \tag{28}$$

or, equivalently,

$$\Delta\tilde{f} \approx -\frac{2\tilde{f}_0 f_f}{Z_q} m_f \approx -\frac{2nf_f^2}{Z_q} m_f\,. \tag{29}$$

[7] For reasons which are stated in [56] and [41], the reference frequency at the nth overtone is never strictly equal to nf_f.

Z_q is the acoustic impedance of AT-cut quartz; its value is 8.8×10^6 kg m^{-2} s^{-1}. Strictly speaking, Z_q is a complex quantity $Z_q' + iZ_q''$, where Z_q'' accounts for internal friction. Z_q is often considered to be real. When this happens, the fundamental frequency f_f must also be a real number (see end of Sect. 2). The Sauerbrey equation fails to account for viscoelasticity and also, when applied in liquids, cannot distinguish between the adsorbed material itself and solvent trapped inside the adsorbed film. When a mass is derived by means of the Sauerbrey equation, the interpretation of this mass parameter is sometimes difficult. The terms "Sauerbrey mass" and "Sauerbrey thickness" are used in order to indicate that the respective parameters have been calculated by the simple Sauerbrey equation.

The derivation above ignores piezoelectricity (Sect. 6). The theory of the piezoelectric plate has been worked out by Tiersten [56]. Kanazawa has applied this theory rigorously to the case of a crystal loaded with a liquid or a viscoelastic film [54]. These treatments are equivalent to the treatment with equivalent circuits (Sect. 6), and we therefore defer the discussion of piezoelectricity to that section.

5
The QCM as an Acoustic Reflectometer: The Optical Approach

The procedure described in Sect. 4 is mathematically straightforward, but somewhat technical. Applying the formalism to multilayers leads to awkwardly large determinants (Eq. 22). Searching the zeros of these determinants certainly is possible, at least numerically. On the other hand, the procedure is tedious and somewhat obscures the underlying physics. Two other formulations are around. These make use of an analogy to the theory of optical reflectivities and of electrical circuits, respectively. With regard to the outcome, these theories are completely equivalent to the strictly mathematical formulation. It is just a matter of language and graphical representation. The

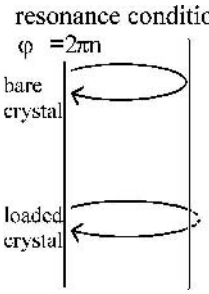

Fig. 4 The frequency shift depends on the acoustic reflectivity at the quartz–sample interface

alternative formulations provide an intuitive insight and we therefore discuss them both.

Within an optics-type approach, one considers the resonator as an acoustic cavity. The term "acoustic" in this context always pertains to shear waves, never to longitudinal waves. This distinction is important: in liquids, shear waves rapidly decay because the elastic part of the shear modulus is zero. Shear waves therefore provide for *surface specificity*. Longitudinal waves, on the contrary, propagate because the elastic component of the compressional modulus is nonzero.

Resonances occur if the time required for one round-trip is an integer multiple of the period of oscillation. If this is the case, there is constructive interference and the amplitude becomes large. In order to calculate the time needed for one round-trip, we need to know the set of layer thicknesses, $\{d_j\}$, wave vectors, $\{k_j\}$, and reflectivities at the interfaces (Fig. 3). Let us calculate the reflectivity $r_{a,b} = u_a^{+,0}/u_a^{-,0}$ of a single interface between media termed "a" and "b". We have $u_a^{-,0} = 1$ and $u_b^{+,0} = 0$. The analogs of Eqs. 13 and 17 are:

$$u_a^{+,0} + u_a^{-,0} = u_b^{-,0} \tag{30}$$

$$Z_a \left[u_a^{+,0} - u_a^{-,0}\right] = Z_b u_b^{-,0} \,. \tag{31}$$

Eliminating $u_b^{-,0}$, one finds:

$$r_{a,b} = \frac{u_a^{+,0}}{u_a^{-,0}} = \frac{Z_a - Z_b}{Z_a + Z_b} \,. \tag{32}$$

This relation is reminiscent of the reflectivity of optical waves impinging vertically onto a dielectric interface. The optical reflectivity r is given by $r = (n_a - n_b)/(n_a + n_b)$, where n_a and n_b are the indices of refraction. In acoustics, the acoustic impedance, $Z = (\rho G)^{1/2}$, takes the role of the refractive index. Note, however, that this analogy has its limitations. In optics, the refractive index governs both the reflectivity at interfaces and the speed of light. This happens because the magnetic permeability (the analog of the density) is about equal to unity at optical frequencies. In acoustics, it is not quite as easy. Also, strictly speaking, n is not the optical impedance, but the ratio of the optical impedances of vacuum and of the medium. Finally, refractive indices typically vary by a few percent. Typical optical reflectivities (of—let's say—the water surface) therefore are also in the range of a few percent. The acoustic shear impedance, on the other hand, can easily vary by a factor of 10 or more because the shear modulus may vary by orders of magnitude. As a consequence, acoustic reflectivities easily approach unity even for rather similar materials (Sect. 8.3.2).

Let us apply the optical approach to a single plate in vacuum. The amplitude of the wave after one round-trip, $u^{(1)}$, is given by:

$$u^{(1)} = u^{(0)} \exp\left(-\mathrm{i}\tilde{k}_\mathrm{q} d_\mathrm{q}\right) r_{\mathrm{q},2} \exp\left(-\mathrm{i}\tilde{k}_\mathrm{q} d_\mathrm{q}\right) r_{\mathrm{q},0} \,, \tag{33}$$

where $u^{(0)}$ is the initial amplitude and r is the reflectivity. Since both Z_0 and Z_2 vanish, we have $r_{\mathrm{q},2} = r_{\mathrm{q},0} = 1$ and the condition of constructive interference is:

$$\begin{aligned} u^{(0)} \equiv u^{(1)} &= u^{(0)} \exp\left(-2\mathrm{i}\tilde{k}_\mathrm{q} d_\mathrm{q}\right) = u^{(0)} \exp\left(\frac{-2\mathrm{i}\tilde{\omega}_\mathrm{r}}{\tilde{c}_\mathrm{q}} d_\mathrm{q}\right) \\ &= u^{(0)} \exp\left(\frac{-4\pi\mathrm{i}\tilde{f}_\mathrm{r}}{\tilde{c}_\mathrm{q}} d_\mathrm{q}\right) = u^{(0)} \exp\left(\frac{-4\pi\mathrm{i}\tilde{f}_\mathrm{r}\sqrt{\rho_\mathrm{q}}}{\sqrt{\tilde{G}_\mathrm{q}}} d_\mathrm{q}\right) \\ &= u^{(0)} \exp\left(\frac{-4\pi\mathrm{i}\tilde{f}_\mathrm{r}\rho_\mathrm{q}}{\tilde{Z}_\mathrm{q}} d_\mathrm{q}\right) . \end{aligned} \tag{34}$$

The argument of the exponential (the phase shift, $-\mathrm{i}\varphi$) must be an integer multiple of $-2\pi\mathrm{i}$, leading to:

$$\tilde{f}_\mathrm{r} = \frac{n\tilde{c}_\mathrm{q}}{2d_\mathrm{q}} = \frac{n}{2}\sqrt{\frac{\tilde{G}_\mathrm{q}}{\rho_\mathrm{q}}}\frac{1}{d_\mathrm{q}} = \frac{n\tilde{Z}_\mathrm{q}}{2\rho_\mathrm{q} d_\mathrm{q}} = \frac{n\tilde{Z}_\mathrm{q}}{2m_\mathrm{q}} \,, \tag{35}$$

which is the familiar resonance condition.

Now let us assume that the reflectivity at the front surface, $r_{\mathrm{q},2}$, is slightly different from unity. The absolute value may be smaller than unity because some energy may be dissipated inside the sample. Also, there may be a phase shift because a certain part of the wave enters the sample, returns, and superimposes itself onto the wave reflected at the crystal surface (Fig. 4). The resonance condition then is:

$$1 \equiv r_{\mathrm{q},2} \exp\left(-\frac{4\pi\mathrm{i}\tilde{f}_\mathrm{r} d_\mathrm{q}}{\tilde{c}_\mathrm{q}}\right) . \tag{36}$$

If we assume that $r_{\mathrm{q},2}$ is close to unity, we may write $\tilde{f}_\mathrm{r} = \tilde{f}_0 + \Delta\tilde{f}$ with a small complex frequency shift $\Delta\tilde{f}$. Since $4\pi\tilde{f}_0 d_\mathrm{q}/\tilde{c}_\mathrm{q} = 2\pi n$, we can write:

$$\begin{aligned} 1 &\equiv r_{\mathrm{q},2} \exp\left(-\frac{4\pi\mathrm{i}\tilde{f}_0 d_\mathrm{q}}{\tilde{c}_\mathrm{q}}\right) \exp\left(-\frac{4\pi\mathrm{i}\Delta\tilde{f}\mathrm{d}_\mathrm{q}}{\tilde{c}_\mathrm{q}}\right) \\ &= r_{\mathrm{q},2} \exp\left(-\frac{4\pi\mathrm{i}\Delta\tilde{f} d_\mathrm{q}}{\tilde{c}_\mathrm{q}}\right) \approx r_{\mathrm{q},2}\left(1 - \frac{4\pi\mathrm{i}\Delta\tilde{f} d_\mathrm{q}}{\tilde{c}_\mathrm{q}}\right) , \end{aligned} \tag{37}$$

which leads to the expression:

$$\frac{4\pi\mathrm{i}\Delta\tilde{f} d_\mathrm{q}}{\tilde{c}_\mathrm{q}} = 2\pi\mathrm{i}\frac{\Delta\tilde{f}}{\tilde{f}_\mathrm{f}} \approx 2\pi\mathrm{i}\frac{\Delta\tilde{f}}{f_\mathrm{f}} \approx \frac{r_{\mathrm{q},2} - 1}{r_{\mathrm{q},2}} \approx r_{\mathrm{q},2} - 1 \tag{38}$$

or equivalently:

$$\frac{\Delta\tilde{f}}{\tilde{f}_f} \approx \frac{i}{2\pi}\left(1 - r_{q,2}\right) . \tag{39}$$

$\Delta\tilde{f}/\tilde{f}_f$ is small whenever $r_{q,2}$ is close to one. Conversely, since the QCM only works well when the normalized frequency shift $\Delta\tilde{f}/\tilde{f}_f$ is small, it makes sense to assume $r_{q,2} \approx 1$. Equation 39 shows that quartz crystals are acoustic reflectometers. The results of QCM measurements can therefore be easily compared to data obtained with other forms of ultrasonic reflectometry [57, 58]. It is well known from optical techniques such as ellipsometry [59] or surface plasmon resonance (SPR) spectroscopy [60] that a film thickness can be inferred from a measurement of the reflectivity. The same applies to acoustics.

Let us assume that the crystal has been coated with a thin film of thickness d_f. Let the film have the same acoustic properties as the crystal. In this case, the entire acoustic wave enters the sample. Evaluating $r_{q,2}$ as the ratio $u_q^+(z_{q,2})/u_q^-(z_{q,2})$, we find the modulus $|r_{q,2}|$ as unity. There is a phase shift $\Delta\varphi = -2k_f d_f$ which the wave acquires while traveling through the film. We find:

$$\frac{\Delta\tilde{f}}{\tilde{f}_f} \approx i\frac{1 - \exp(-2ik_f d_f)}{2\pi} \approx \frac{-2k_f d_f}{2\pi} = \frac{-\tilde{\omega}_r d_f}{\pi\tilde{c}_q} = \frac{-2\tilde{f}_r d_f}{\tilde{c}_q} = \frac{-2\tilde{f}_r}{\tilde{Z}_q} m_f , \tag{40}$$

which is again the Sauerbrey equation.

In the presence of multilayers, the coefficient of reflectivity $r_{q,2} = u_q^+(z_{q,2})/u_q^-(z_{q,2})$ can be derived in the same way as in optics. There is a choice between the matrix formalism [61] and an iterative scheme [59]. In the following, we briefly describe the matrix formalism.

The amplitudes are written as a two-dimensional vector $(u_j^{+,0}, u_j^{-,0})$. There is no reflected wave in the last, semi-infinite medium on the right-hand side. The transmitted wave in this medium, $u_{N+1}^{-,0}$, is normalized to unity. The vector of amplitudes in this medium therefore is (0,1). The vector $(u_j^{+,0}, u_j^{-,0})$ at any other location is related to the amplitudes at the right end of the layer system via transfer matrices (Fig. 3). There are transfer matrices for the layers (L_j) and for the interfaces ($S_{j,j+1}$). The amplitudes are calculated as:

$$\begin{pmatrix} u_j^{+,0} \\ u_j^{-,0} \end{pmatrix} = L_j \cdot S_{j,j+1} \cdot \ldots \cdot S_{N,N+1} \cdot \begin{pmatrix} 0 \\ 1 \end{pmatrix} . \tag{41}$$

For the matrix L_j, one has:

$$L_j = \begin{pmatrix} \exp(-ik_j d_j) & 0 \\ 0 & \exp(ik_j d_j) \end{pmatrix} , \tag{42}$$

where k_j is the wave vector and d_j is the thickness. $S_{j,j+1}$ takes care of reflection at interfaces. One has:

$$S_{j,j+1} = \frac{1}{2}\begin{pmatrix} 1 + Z_j/Z_{j+1}\, 1 - Z_j/Z_{j+1} \\ 1 - Z_j/Z_{j+1}\, 1 + Z_j/Z_{j+1} \end{pmatrix}, \tag{43}$$

where $Z_j = (\rho_j G_j)^{1/2}$ is the acoustic impedance of the respective medium. Applying $S_{j,j+1}$ to the vector $\left(u_{j+1}^{+,0}, u_{j+1}^{-,0}\right)$, one reproduces Eqs. 13 and 17. The vector $(u_q^+(z_{q,2}), u_q^-(z_{q,2}))$ is computed as:

$$\begin{pmatrix} u_q^+(z_{q,2}) \\ u_q^-(z_{q,2}) \end{pmatrix} = S_{q,2} \cdot L_2 \cdot \ldots \cdot S_{N,N+1} \cdot \begin{pmatrix} 0 \\ 1 \end{pmatrix}. \tag{44}$$

Finally, using $r_{q,2} = u_q^+(z_{q,2})/u_q^-(z_{q,2})$, the reflectivity of an arbitrary layer system can be obtained.

6 Equivalent Circuits: The Electrical Approach

Electrical engineers also deal with waves. In electrical engineering, the waves are usually confined to cables and different cables are interconnected to form networks. When calculating the properties of such networks, one makes use of the Kirchhoff laws. The first Kirchhoff law states that the sum of all the currents entering a junction is equal to the sum of all the currents leaving the same junction. The second law states that the sum of voltages encountered in a complete traversal of any closed loop is zero. With a little exercise, one can get an intuitive feeling for a network by just looking at its graphical representation. For instance, when a capacitance, C, and an inductance, L, are placed in series, the total impedance of the two vanishes at a resonance frequency equal to $(LC)^{-1/2}$.

Naturally, electrical engineers have designed "equivalent circuits" for non-electrical wave phenomena. The waves may or may not be confined to cables. For simple propagating waves, the equivalent circuits are often called transmission line models. The transmission line has two ports representing input and output. The input–output relation can be predicted by applying the Kirchhoff laws to the set of elements located in between.[8] The circuit elements may be simple resistors or capacitors, but their electrical impedance may also be a more complicated function of frequency (see, for instance, Fig. 6)

Can acoustic phenomena be described by electrical circuits? Yes, they can, by means of the electromechanical analogy, that maps forces onto voltages

[8] While a certain equivalent circuit uniquely predicts the input–output relation, the same input–output relation can be represented by more than one equivalent circuit. It is a bit of an art to find the simplest one. For example, the Norton transformation (Fig. 13b) links two networks which are equivalent to each other with regard to the input–output relation.

and speeds onto currents. The ratio of force and speed is termed "mechanical impedance". Nota bene: speed here means the derivative of a displacement, not the speed of sound. There is also an electroacoustic analogy, within which stresses (rather than forces) are mapped onto voltages. In acoustics, forces are normalized to area. With regard to the terminology, there is a complication: the ratio of stress and speed cannot be called "acoustic impedance" (in analogy to the mechanical impedance) because this term is already in use for the material property Z (which only under certain conditions is equal to the stress–speed ratio, see below). We call the stress–speed ratio "load impedance". It is also called "surface impedance" [30] and "acoustic load" [62].

The electromechanical analogy provides for simple equivalents of a resistor, an inductance, and a capacitance, which are the dashpot (quantified by the drag coefficient, ξ_p), the point mass (quantified by the mass, m_p), and the spring (quantified by the spring constant, κ_p). The ratio of force and speed is the mechanical impedance, Z_m. For a dashpot, the impedance by definition is $Z_\mathrm{m} = F/\dot{u} = \xi_\mathrm{p}$ (with F the force and $\dot{u}$ the speed). For a point mass undergoing oscillatory motion $u(t) = u_0 \exp(\mathrm{i}\omega t)$ we have $Z_\mathrm{m} = \mathrm{i}\omega m_\mathrm{p}$. Finally, the spring obeys $Z_\mathrm{m} = \kappa_\mathrm{p}/(\mathrm{i}\omega)$.

Piezoelectric coupling is depicted as a transformer. It is characterized by a "ratio of the number of loops", ϕ. While ϕ is dimensionless for usual transformers, it has the dimension of current/speed here. The transformer separates the electrical and the acoustic branch of the network. The following equations hold [4]:

$$\begin{aligned} I_\mathrm{el} &= \phi\dot{u} \\ U_\mathrm{el} &= \frac{1}{\phi}F = \frac{1}{\phi}A\sigma \\ Z_\mathrm{el} &= \frac{U_\mathrm{el}}{I_\mathrm{el}} = \frac{1}{\phi^2}\frac{A\sigma}{\dot{u}} = \frac{1}{\phi^2}Z_\mathrm{m} \\ \phi &= \frac{Ae_{26}}{d_\mathrm{q}}\,. \end{aligned} \tag{45}$$

The parameter A is the effective area of the crystal, σ is the stress, d_q is the thickness of the quartz plate, and e_{26} is the piezoelectric stress coefficient [63]. Its value is $9.65 \times 10^{-2}\,\mathrm{C\,m^{-2}}$ for AT-cut quartz. Actually, putting down a number for the effective area of a quartz crystal, A, is not an easy task (end of Appendix A). The effective area is less than the total area of the plate because of energy trapping [22].

There is a pitfall with the application of the electromechanical analogy, which has to do with how we draw networks. When a spring pulls onto a dashpot, we would usually draw the two elements in series. However, when applying the electromechanical analogy, we have to draw the two elements *in parallel*. For two parallel electrical elements the *currents* are additive. Since

the speeds add when placing a spring *behind* a dashpot, this assembly has to be represented by a parallel network (Fig. 5).

Figure 6a shows the transmission line representing a viscoelastic layer [64]. Every layer is represented by a "T". The application of the Kirchhoff laws to the Ts reproduces the wave equation and the continuity of stress and strain. The detailed proof is provided in [4]. To the left and to the right of the circuit are open interfaces (ports). These can be exposed to external shear waves. They can also be connected to the ports of neighboring layers (Fig. 6b). Alternatively, they may just be short-circuited, in case there is no stress acting on this surface (left-hand side in Fig. 6c). Finally, if the stress–speed ratio Z_L (the load impedance, see below) of the sample is known, the port can be short-circuited across an element of the form AZ_L, where A is the active area (right-hand side in Fig. 6c). Figure 6c shows a viscoelastic layer which is also piezoelectric. This equivalent circuit was first derived by Mason [4, 55]. We term it the Mason circuit. The capacitance, C_0, is the electric capacitance between the electrodes. The port to the right-hand side of the transformer is the electrical port. The series resonance frequency is given by the condition that the impedance of the acoustic part (the stress–speed ratio, $\sigma/\dot{u}$) be zero, where the "acoustic part" comprises all elements connected to the left-hand side of the transformer.

Even though $\sigma/\dot{u}$ is an entirely acoustic quantity, the series resonance frequency is affected by the value of the electrical capacitance, C_0, because of the element $Z_k = -\phi^2/(i\omega C_0)$, which introduces piezoelectric stiffening into the acoustic branch. Piezoelectricity adds a negative capacitor into the mechanical branch of the circuit.

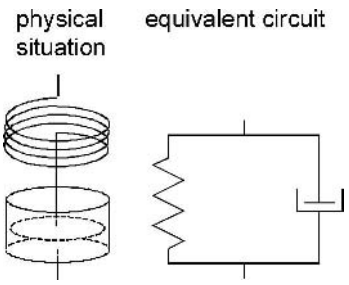

Fig. 5 When representing mechanical elements with equivalent circuits, elements which are placed in series to each other, physically, have to be drawn as parallel elements in the circuit representation because currents (speeds) are additive for parallel electrical elements. Conversely, mechanical elements which are physically placed in parallel have to be represented in series because the voltage (force) is additive for electrical elements placed in series. In the literature on polymer rheology, springs and dashpots are depicted as on the *right-hand side*, but connected to each other as on the *left-hand side*. This convention differs from the convention chosen here. It amounts to a different set of Kirchhoff rules

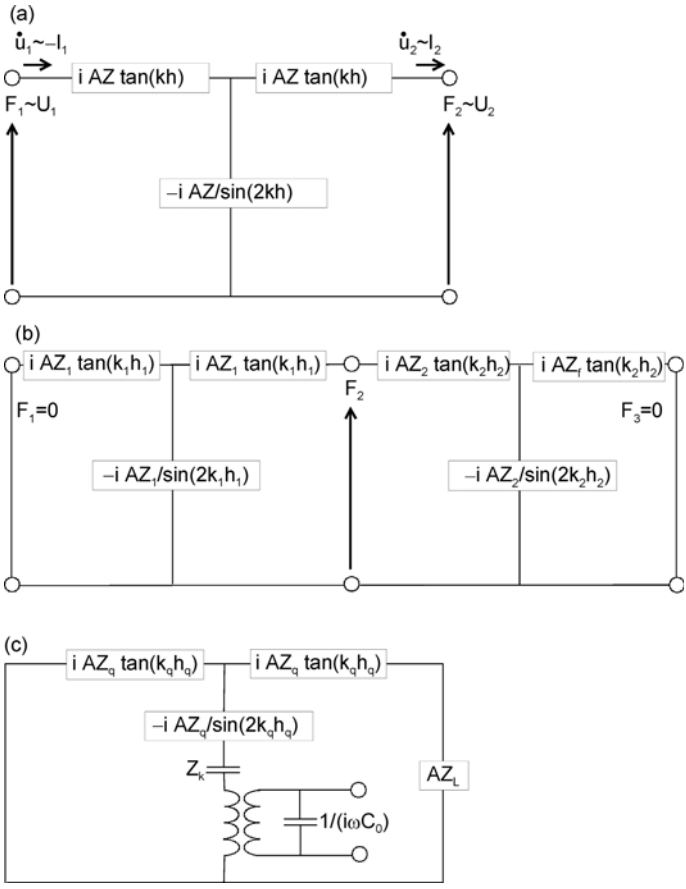

Fig. 6 Equivalent circuits of **a** a viscoelastic layer of thickness $2h$, **b** two viscoelastic layers of thickness $2h_1$ and $2h_2$ (where 1 denotes the quartz crystal and 2 denotes the film), and **c** a piezoelectric plate loaded on one side with a load AZ_L. The parameter h is half of the thickness of the respective layer

When applying the Kirchhoff laws to such a network, one finds the same resonance conditions as with the mathematical and the optical approaches.[9] Why should one bother going through these transformations if the results are the same? There are important benefits tied to the use of equivalent circuits:

- All acoustic, electric, and piezoelectric parameters can be displayed in a single graph, which is not just a cartoon. The graph, in conjunction with the Kirchhoff laws, predicts the behavior of the resonator. Anyone who can

[9] In this section, the Mason circuit does account for piezoelectric stiffening, whereas piezoelectric stiffening is neglected in Sects. 4 and 5. In order to find exact equivalence between the three models, the element Z_k (dealing with piezoelectric stiffening) must be deleted from the Mason circuit.

master the Kirchhoff laws can also calculate the impedance across the electrical port and search the zeros of this impedance. This can be done for arbitrarily complicated layer systems. It is easy to add more layers to the model. Every new layer is represented by another "T", as in Fig. 6b [65]. If the crystal is immersed in a viscoelastic liquid, the mechanical port on the right-hand side is not just short-circuited (as in air), but connected across a circuit element, AZ_{liq}, which is the product of the area A and the acoustic impedance of the liquid, Z_{liq}. A load impedance Z_{L} (see below) is treated in the same way as the acoustic impedance of a liquid.

- In the vicinity of resonances, the somewhat complicated algebraic form of the circuit elements can be approximated in such a way that they can be represented by resistors, capacitors, and inductances. If this is the case, one can intuitively understand the circuit. The famous Butterworth–van Dyke (BvD) circuit [66] (Fig. 7) can be derived from the Mason circuit. While the general form of the BvD circuit can be guessed without going back to the Mason circuit, the values of its elements can only be determined by the full derivation (Appendix A).
- Piezoelectricity and piezoelectric stiffening are rigorously accounted for in the Mason circuit. This is not the case for the mathematical and optical approaches at the level of detail presented here.

Apart from these practicalities, there is an important new concept contained in the equivalent circuit representation, which is the load impedance, Z_{L}. The load impedance in this context is the ratio of the stress, σ, and the speed, $\dot{u}$, at the crystal surface. The load impedance is normalized to area (unlike the mechanical impedance).

The load impedance, Z_{L}, in general is not equal to the material constant $Z = \rho c = (G\rho)^{1/2}$. Only for propagating plane waves in an infinite medium are the values of Z_{L} and Z the same. The ratio of stress and speed in this case is given as

$$Z_{\mathrm{L}} = \frac{\sigma}{\dot{u}} = \frac{G\partial u/\partial z}{\partial u/\partial t} = \frac{Giku}{i\omega u} = \frac{G}{c} = \sqrt{G\rho} = Z\,. \tag{46}$$

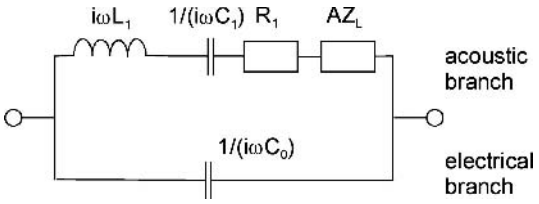

Fig. 7 Butterworth–van Dyke equivalent circuit

For a propagating wave in an infinite medium the stress–speed ratio is the same everywhere and equal to the acoustic impedance. This is not true for more complicated displacement patterns. For instance, if two waves u^+ and u^- travel in opposite directions, the analog of Eq. 46 reads:

$$Z_L = \frac{\sigma}{\dot{u}} = \frac{Gik\left(u^+(z) - u^-(z)\right)}{i\omega\left(u^+(z) + u^-(z)\right)} \tag{47}$$

and there is no way to further specify Z_L without knowledge of the amplitudes and the relative phase of the two waves. One can show that the fractional frequency shift of a quartz crystal resonator is proportional to the load impedance. This important result is further elaborated in Sect. 7.

The Mason circuit is a necessary level of complication (and a safe ground, as well) if any of the following conditions are encountered:

- Both sides of the crystal are loaded.
- The behavior of the crystal far away from the resonances matters.
- The linearizations used in the derivation of the Butterworth–van Dyke circuit (Fig. 7) are not accurate enough (Sect. 9).
- The amplitude of shear motion is of interest (end of Appendix A).

A word of caution is appropriate with regard to an over-interpretation of the Mason circuit: in principle, one might attempt to calculate the complete admittance spectrum of a crystal directly from the Mason circuit. However, this possibility is of little practical use, because the electrical admittance cannot be measured accurately enough in experiment. In order to allow for a comparison with the prediction from the Mason circuit, the admittance would have to be measured as precisely as the resonance frequency (relative error of 10^{-7}), which is impossible. The strength of the QCM lies in its tremendous accuracy with regard to frequency measurements. Unfortunately, this extreme accuracy is limited to the frequency of the peak conductance; it does not extend to the conductance (or, more generally, the complex admittance) itself.

For frequencies close to the resonance, the Mason circuit can be simplified to the Butterworth–van Dyke (BvD) circuit shown in Fig. 7. The values of its elements are:

$$\begin{aligned}
C_1 &= 4\phi^2 \frac{1}{\bar{\kappa}_p} = \frac{8Ae_{26}^2}{d_q(n\pi)^2 G_q}\left(1 - \frac{8\kappa^2}{(n\pi)^2}\right)^{-1} \\
L_1 &= \frac{1}{4\phi^2} m_p = \frac{\rho_q d_q^3}{8Ae_{26}^2} \\
R_1 &= \frac{1}{4\phi^2}\xi_p = \frac{d_q^2}{8Ae_{26}^2} Z_q n\pi \tan(\delta) = \frac{d_q}{8Ae_{26}^2}(n\pi)^2 \eta_q \,.
\end{aligned} \tag{48}$$

The derivation is provided in Appendix A; $\bar{\kappa}_\mathrm{p}$, m_p, and ξ_p represent a (piezoelectrically stiffened) spring, a mass, and a dashpot. The parameter κ is a dimensionless measure of piezoelectric coupling (see Appendix A). The BvD circuit is frequently used. For instance, the admittance diagram of a quartz crystal (insert in Fig. 2) can be easily understood from the BvD circuit. Given that the width of any given resonance is small, the susceptance of the parallel capacitance, ωC_0, can be considered constant over the frequency range of an individual resonance. It adds to the susceptance of the motional branch and therefore just displaces the admittance curve along the vertical scale. The conductance (the real part of the admittance) is unaffected by C_0. The admittance curve of the motional branch is a circle, where the series resonance frequency corresponds to the point with the largest conductance.

A few other comments on the Mason circuit and the BvD circuit are provided in the Appendix. Here, we move on and discuss the role of the load impedance in data analysis.

7 Relation Between the Frequency Shift and the Load Impedance

The load impedance is the ratio of stress and speed at the crystal surface. From the BvD circuit, one can read how the resonance frequency responds to the load. Below we derive a relation between the frequency shift and the stress–speed ratio. We use a complex spring constant, $\tilde{\kappa}_\mathrm{p} = \bar{\kappa}_\mathrm{p} + \mathrm{i}\omega\xi_\mathrm{p}$, and a complex eigenfrequency of the bare crystal, $\tilde{\omega}_0 = (\tilde{\kappa}_\mathrm{p}/m_\mathrm{p})^{1/2}$, for computational convenience. From Fig. 14b one reads the resonance condition as:

$$
\begin{aligned}
0 &= \mathrm{i}\tilde{\omega}_\mathrm{r} m_\mathrm{p} + \frac{\tilde{\kappa}_\mathrm{p}}{\mathrm{i}\tilde{\omega}_\mathrm{r}} + AZ_\mathrm{L} = \mathrm{i}\sqrt{\tilde{\kappa}_\mathrm{p} m_\mathrm{p}}\left(\frac{\tilde{\omega}_\mathrm{r}}{\tilde{\omega}_0} - \frac{\tilde{\omega}_0}{\tilde{\omega}_\mathrm{r}}\right) + AZ_\mathrm{L} \\
&= \mathrm{i}\sqrt{\tilde{\kappa}_\mathrm{p} m_\mathrm{p}}\frac{\left(\tilde{\omega}_\mathrm{r} + \tilde{\omega}_0\right)\left(\tilde{\omega}_\mathrm{r} - \tilde{\omega}_0\right)}{\tilde{\omega}_0\tilde{\omega}_\mathrm{r}} + AZ_\mathrm{L} \approx \mathrm{i}\sqrt{\tilde{\kappa}_\mathrm{p} m_\mathrm{p}}\frac{2(\tilde{\omega}_\mathrm{r} - \tilde{\omega}_0)}{\tilde{\omega}_0} + AZ_\mathrm{L} \qquad (49) \\
&\approx \mathrm{i}A\widetilde{Z}_\mathrm{q}\frac{n\pi}{2}\frac{2\Delta\tilde{f}}{\tilde{f}_0} + AZ_\mathrm{L}\,,
\end{aligned}
$$

where the relation $(\tilde{\kappa}_\mathrm{p} m_\mathrm{p})^{1/2} = \left((\bar{\kappa}_\mathrm{p} + \mathrm{i}\omega\xi)m_\mathrm{p}\right)^{1/2} \approx A\widetilde{Z}_\mathrm{q} n\pi/2$ was used (Eq. 115). Equation 49 also made use of the approximation $\omega_0 + \omega_\mathrm{r} \approx 2\omega_0$, which requires $\Delta f/f_0 \ll 1$. Further using $\tilde{f}_0 = n\tilde{f}_\mathrm{f}$, we obtain:

$$
\frac{\Delta\tilde{f}}{\tilde{f}_\mathrm{f}} \approx \frac{\mathrm{i}}{\pi\widetilde{Z}_\mathrm{q}} Z_\mathrm{L} = \frac{\mathrm{i}}{\pi\widetilde{Z}_\mathrm{q}}\frac{\sigma}{\dot{u}}\,. \qquad (50)
$$

Since the phase angles of $\tilde{Z}_q$ and $\tilde{f}_f$ are the same, one has $\tilde{Z}_q/\tilde{f}_f = Z_q/f_f$ and one can also write:

$$\frac{\Delta\tilde{f}}{f_f} = \frac{\Delta f + i\Delta\Gamma}{f_f} \approx \frac{i}{\pi Z_q} Z_L = \frac{i}{\pi Z_q}\frac{\sigma}{\dot{u}} . \tag{51}$$

Equation 51 shows that Δf and $\Delta\Gamma$ are proportional to the imaginary and the real part of the load, respectively. Using $\tilde{Z}_q = 2m_q\tilde{f}_f$, this can be further rewritten as:

$$\Delta\tilde{f} = \Delta f + i\Delta\Gamma \approx \frac{i}{2\pi m_q} Z_L . \tag{52}$$

Equation 52 shows that the areal mass density of the crystal is the only parameter connecting the load and the frequency shift, as long as the latter is small. The stiffness of the crystal (and piezoelectric stiffening, in particular) is of no influence at this level of approximation. Comparing Eqs. 51 and 39, we find:

$$1 - r_{q,2} \approx 2\frac{Z_L}{Z_q} , \tag{53}$$

which provides the link between the optical and the equivalent circuit formulation.

We briefly convince ourselves that the same result is found without recurrence to equivalent circuits in case the sample is a semi-infinite liquid ($Z_L = Z_{liq}$ with $Z_{liq} \ll Z_q$ a materials constant). For such a situation we have using (Eq. 32):

$$\begin{aligned} 1 - r_{q,2} &= 1 - \frac{Z_q - Z_{liq}}{Z_q + Z_{liq}} \approx 1 - \frac{1 - Z_{liq}/Z_q}{1 + Z_{liq}/Z_q} \\ &\approx 1 - \left(1 - Z_{liq}/Z_q\right)\left(1 - Z_{liq}/Z_q\right) \approx 1 - \left(1 - 2Z_{liq}/Z_q\right) = \frac{2Z_{liq}}{Z_q} , \end{aligned} \tag{54}$$

which is equivalent to Eq. 53.

Since Eq. 51 is of such fundamental importance, we briefly re-derive it in the frame of the mathematical approach. According to Eqs. 13 and 16, the displacement and the stress must both be continuous at the crystal surface. The equation for displacement is given as:

$$u_q^+\left(z_{q,2}\right) + u_q^-\left(z_{q,2}\right) = \exp\left(i\tilde{k}_q d_q\right) u_q^{+,0} + \exp\left(-i\tilde{k}_q d_q\right) u_q^{-,0} = u_{sample}^{tot} , \tag{55}$$

where $z_{q,2}$ is the location of the crystal surface and u_{sample}^{tot} is the total displacement at the crystal surface. Note that $u_j^{\pm}(z)$ is always defined to be equal to $u_j^{\pm,0}$ on the *left-hand side* of each layer j (Eq. 14). The condition that the stress at the back of the crystal (the left-hand side in Fig. 3) vanishes, reads:

$$i\tilde{G}_q\tilde{k}_q\left[u_q + \left(z_{q,0}\right) - u_q^-\left(z_{q,0}\right)\right] = i\omega\tilde{Z}_q\left[u_q^{+,0} - u_q^{-,0}\right] = 0 , \tag{56}$$

where $z_{q,0}$ is the location of the back of the crystal. The stress continuity at the front surface requires that the stress originating from the shear gradient inside the crystal is balanced by the stress from the sample, where the latter is $-Z_L \dot{u}^{tot}_{sample} = -Z_L i\omega u^{tot}_{sample}$:

$$\begin{aligned} & i\omega\tilde{Z}_q \left[u_q^+ (z_{q,2}) - u_q^- (z_{q,2}) \right] \\ & = i\omega\tilde{Z}_q \left[\exp\left(i\tilde{k}_q d_q\right) u_q^{+,0} - \exp\left(-i\tilde{k}_q d_q\right) u_q^{-,0} \right] = -i\omega Z_L \, u^{tot}_{sample} \\ & = -i\omega Z_L \left[\exp\left(i\tilde{k}_q d_q\right) u_q^{+,0} + \exp\left(-i\tilde{k}_q d_q\right) u_q^{-,0} \right] . \end{aligned} \tag{57}$$

From Eq. 56 we know that $u_q^{+,0} = u_q^{-,0}$. Using this result, Eq. 57 can be simplified to read:

$$\tilde{Z}_q \left[\exp\left(i\tilde{k}_q d_q\right) - \exp\left(-i\tilde{k}_q d_q\right) \right] = -Z_L \left[\exp(i\tilde{k}_q d_q) + \exp(-i\tilde{k}_q d_q) \right] \tag{58}$$

or, equivalently:

$$\begin{aligned} -\frac{Z_L}{\tilde{Z}_q} &= i \tan\left(\tilde{k}_q d_q\right) = i \tan\left(2\pi \left(\tilde{f}_0 + \Delta\tilde{f}\right) \frac{d_q}{\tilde{c}_q}\right) \\ &= i \tan\left(2\pi \Delta\tilde{f} \frac{d_q}{\tilde{c}_q}\right) = i \tan\left(\pi \frac{\Delta\tilde{f}}{\tilde{f}_f}\right) . \end{aligned} \tag{59}$$

Equation 25 as well as the relation $\tan(n\pi + \varepsilon) = \tan(\varepsilon)$ have been used. Taylor-expanding $\tan(x)$ as $\tan(x) \approx x$ we find Eq. 50 confirmed. The perturbation analysis (Sect. 9) will start out from Eq. 59.

When using the small-load approximation below, the load will always be evaluated at the reference frequency, f_0. For instance, for the load given by a Sauerbrey film, one uses $i\omega m = 2\pi i f_0 m$ (as opposed to $2\pi i(f_0 + \Delta f)m$). Using the latter expression would turn Eq. 51 into an implicit equation in Δf and that is exactly what must be avoided at this level of approximation. Within the perturbation analysis, one makes peace with implicit equations and therefore also evaluates the load at the true resonance frequency, rather than the reference frequency. The perturbation analysis cures both the problems resulting from approximating $\tan(x)$ as x and the problems resulting from evaluating the load at f_0 rather than f.

Equation 51 is the most important equation of the physics of the QCM. As long as the frequency shift is small compared to the frequency, the complex frequency shift is proportional to the load impedance at the crystal surface. We term Eq. 51 the *small-load approximation*. At this point, we have not made any statement on the nature of the sample. We have only stated how the frequency shift depends of the stress–speed ratio at the crystal surface.

Under certain conditions, this statement can also be applied in an *average sense*.[10] [67]

Assume that the sample does not consist of planar layers, but instead of a sand pile, a froth, an AFM tip, an assembly of spheres or vesicles, a cell culture, a droplet, or any other kind of heterogeneous material. There are many interesting samples of this kind. The frequency shift induced by such objects can be estimated from the average ratio of stress and speed at the crystal–sample interface. The latter is the load impedance of the sample. The concept of the load impedance tremendously broadens the range of applicability of the QCM. The load impedance is the conceptual link between the QCM and complex samples. If we want to predict the frequency shift induced by a complex sample, we must ask for the average stress–speed ratio. If this ratio can be estimated in one way or another, a quantitative analysis of the experimental QCM data is in reach. Otherwise, the analysis must remain qualitative.

8
Layered Systems within the Small-Load Approximation

In the previous sections, we have assembled the tools needed to calculate the frequency shifts based on acoustic modeling. In following, we apply these equations to calculate the complex frequency shift for a number of different planar geometries.

8.1
Semi-infinite Viscoelastic Medium

For the semi-infinite medium, there is only one wave traveling outwards with an amplitude $u^{-,0}$. The stress exerted onto the crystal surface is:

$$\begin{aligned}\sigma &= -G_{\mathrm{liq}}\frac{\partial u}{\partial z} = -G_{\mathrm{liq}}(-\mathrm{i}k)u^{-,0} = \mathrm{i}G_{\mathrm{liq}}\frac{\omega}{c_{\mathrm{liq}}}u^{-,0} \\ &= \mathrm{i}\omega G_{\mathrm{liq}}\sqrt{\frac{\rho_{\mathrm{liq}}}{G_{\mathrm{liq}}}}u^{-,0} = \mathrm{i}\omega Z_{\mathrm{liq}}u^{-,0}\,, \end{aligned} \tag{60}$$

where the index liq denotes the liquid. For the frequency shift, $\Delta\tilde{f}$, one finds:

$$\begin{aligned}\frac{\Delta\tilde{f}}{f_{\mathrm{f}}} &= \frac{\mathrm{i}}{\pi Z_{\mathrm{q}}}\frac{\sigma}{\dot{u}} = \frac{\mathrm{i}}{\pi Z_{\mathrm{q}}}Z_{\mathrm{liq}} = \frac{\mathrm{i}}{\pi Z_{\mathrm{q}}}\sqrt{\rho_{\mathrm{liq}}\mathrm{i}\omega\eta} \\ &= \frac{1}{\pi Z_{\mathrm{q}}}\frac{-1+\mathrm{i}}{\sqrt{2}}\sqrt{2\pi n f_{\mathrm{f}}\rho_{\mathrm{liq}}\left(\eta' - \mathrm{i}\eta''\right)} \end{aligned} \tag{61}$$

[10] Heterogeneous samples will, in general, lead to scattering of acoustic waves and a modified energy trapping, which is not captured by just calculating the average stress.

which was independently derived by Stockbridge [68], Borovikov [69], and Kanazawa [70]. (The Borovikov reference misses a factor of 2 in Eqs. 1, 2, and 3. Otherwise, the result is the same as the Kananazawa result.) A related version applying to torsional resonators was derived by Mason in the early days of acoustic sensing [71]. For Newtonian liquids ($\eta' = \text{const.}$, $\eta'' = 0$), Δf and $\Delta\Gamma$ are equal and opposite. They scale as the square root of the overtone order, $n^{1/2}$. For non-Newtonian liquids ($\eta' = \eta'(\omega)$, $\eta''(\omega) \neq 0$), the complex viscosity can be obtained by inversion of Eq. 61 as:

$$\eta' = -\frac{\pi Z_q^2 f}{\rho_{liq}} \frac{\Delta f \Delta\Gamma}{f_f^2}$$

$$\eta'' = \frac{1}{2} \frac{\pi Z_q^2 f}{\rho_{liq}} \frac{\left(\Delta\Gamma^2 - \Delta f^2\right)}{f_f^2} . \tag{62}$$

Note that viscoelasticity always entails viscoelastic dispersion in the sense that η' and η'' are themselves a function of frequency [72]. The $n^{1/2}$ scaling therefore no longer holds. Contrary to intuition, a finite elastic component increases the bandwidth more than it increases the negative frequency shift. An ideally elastic medium leads to $\Delta f = 0$ and to a nonzero $\Delta\Gamma$, because energy is withdrawn from the crystal in the form of elastic waves.

Compressional waves, surface roughness, and slip cause systematic errors in the determination of the viscosity on the order of about 10%. For reasons which are not entirely understood, the imaginary part of the viscosity, η'', often is derived as slightly negative when applying Eq. 62 to the experimental data [73]. This clearly contradicts the second law of thermodynamics and points to a systematic shortcoming of Eq. 62. Roughness and slip may play a role [28]. These issues are covered in more detail in Chapter by M. Urbakh et al. 2006, in this volume. The values for η' found by application of Eq. 62 to the experimental data tend to be larger than the literature values, which may be related to compressional waves [24].

Importantly, the QCM only probes the region close to the interface. The shear wave evanescently decays into the liquid according to:

$$\frac{u(z)}{u_0} = \exp\left(-\mathrm{i}(k' - \mathrm{i}k'')z\right) = \exp\left(-\frac{\mathrm{i}\omega}{\tilde{c}}z\right) = \exp\left(-\frac{\sqrt{\mathrm{i}\rho_{liq}\omega}}{\sqrt{(\eta' - \mathrm{i}\eta'')}}z\right) . \tag{63}$$

For Newtonian liquids ($\eta'' = 0$), this amounts to:

$$\frac{u(x)}{u_0} = \exp\left(-(1 + \mathrm{i})\frac{z}{\delta}\right) \tag{64}$$

with $\delta = \sqrt{2\eta' / \left(\rho_{liq}\omega\right)}$, the penetration depth. Using $\omega = 2\pi \cdot 5$ MHz and the viscosity of water ($\eta \approx 10^{-3}$ Pa s), the penetration depth is found to be about

250 nm. For the general case of viscoelastic materials, one writes:

$$\delta = \left(k''\right)^{-1} = -\left(\mathrm{Im}\sqrt{\frac{\rho_{\mathrm{liq}}\omega}{\mathrm{i}\left(\eta' - \mathrm{i}\eta''\right)}}\right)^{-1} . \tag{65}$$

8.1.1 The Sheet-Contact Model

Equation 62 is very attractive for the study of adhesion between polymers and solid surfaces, since it allows for the determination of the viscoelastic constants of the adhesive in the immediate vicinity of the contact. Unfortunately, the QCM does not work well with semi-infinite media when the viscosity, η, is larger than about 50 cP. The bandwidth in this case is too large. Most polymers exceed this limit. If, however, the contact area can be confined to a small spot in the center of the crystal the measurement becomes feasible [74]. Such a small contact area can, for instance, be established with a JKR tester [75]. The area of contact can be determined by optical microscopy. Of course, this kind of sample is laterally heterogeneous and the applicability of simple models may be questioned. Experiment shows that the finite contact area can be reasonably well accounted for by modifying as:

$$\frac{\Delta f}{f_{\mathrm{f}}} = \frac{\mathrm{i}}{\pi Z_{\mathrm{q}}} K_{\mathrm{A}} \frac{A_{\mathrm{c}}}{A} Z_{\mathrm{L}} , \tag{66}$$

where A_{c} is the contact area and K_{A} is a "sensitivity factor". For more details see Sect. 4.2 by D. Johannsmann, 2006, in this volume.

8.1.2 Nematic Liquid Crystals

Nematic liquid crystals (LCs) are a classical example of complex fluids. If we trust the small-load approximation as well as the matured theory of nematodynamics [76], we must be able to predict the frequency shift induced by nematic LCs. The theory of nematic LCs in contact with the QCM has been worked out in detail by people who did not know about the QCM as a tool to probe these phenomena. These authors performed ultrasonic reflectometry. As we know from Sect. 5, the results of these studies can be transported to the QCM in a straightforward way by just using Eq. 39.

In nematic liquid crystals, the viscosity depends on the relative orientation between the shear gradient and the orientation of the nematic phase. Close to a surface, the orientation is usually governed by surface orientational anchoring [77]. Anchoring transitions, for instance induced by the adsorption of an analyte molecule to the surface [78], can therefore be easily detected with the QCM [79, 80]. This reorientation induced by adsorption amounts to an amplification scheme: the expected shift in the resonance frequency and bandwidth

due to reorientation is much larger than the frequency shift induced by the adsorption in the Sauerbrey sense.

The physics of shear waves in nematic liquid crystals is rather complicated. Because shear couples to reorientation, there are two separate modes—termed "hydrodynamic" and "orientational"—emanating from the oscillating crystal surface. The hydrodynamic mode mainly transports vorticity. This mode is known from simple liquids. The orientational modes mainly transport rotation of the director with regard to the background fluid. The penetration depth of the orientational mode is much smaller than the penetration depth of the hydrodynamic mode. While the amplitude of the orientational mode strongly depends on the strength of surface anchoring, the amplitude of the hydrodynamic mode does not [76].

The quantitative description has been worked out by Kiry and Martinoty [81]. They discuss the director orientations perpendicular to the surface ("*c*"), along the direction of shear ("*b*"), and in-plane and perpendicular to the direction of shear ("*a*"). Tilted orientation is not covered. Their experiments were based on ultrasonic reflectometry [82] rather than quartz crystal resonators. Generally speaking, the topic is somewhat academic because the theory involves no less than five independent parameters, which are usually unknown. Interestingly, Kiry and Martinoty predict the effective viscosities, η_b and η_c, to be the same, which was confirmed by their experiments on the liquid crystal 4-*n*-pentyl-4′-cyanobiphenyl (5CB). This finding has gotten some attention because it constitutes the only experimental proof of the Parodi relation [83]. Parodi has used the Onsager theorem to reduce the number of independent parameters of nematodynamics from six to five.

8.1.3 Colloidal Dispersions

The flow behavior of colloidal dispersions at interfaces is of paramount importance in many branches of industry [84]. The effective high-frequency viscosity of such materials is of interest in this context because there are qualitative differences between the low-frequency and the high-frequency rheology [85–87]. A considerable amount of literature on this topic has been accumulated by authors employing torsional resonators. Apart from the frequency range (which is around 100 kHz for torsional resonators) the principles established in these works apply to the QCM as well. Three different timescales come into play, which are the Brownian diffusion time $\tau_R \sim a^2/D_0$ (a is a characteristic length such as the particle radius and D_0 the self-diffusion coefficient), the hydrodynamic retardation time $\tau_H \sim d^2/\nu$ (d is the interparticle distance and ν the kinematic viscosity), and the momentum relaxation time $\tau_B \sim m/\xi$ (m is the mass of the particle and $\xi = 6\pi\eta R$ the drag coefficient) [88]. Time–temperature superposition [72] does not hold for colloidal dispersions. Theories exist for excitation frequencies larger than τ_R^{-1},

but smaller than τ_H^{-1} and τ_B^{-1} [86, 88]. Filling in numbers, one finds that the particle size must be in the range of 10 nm or less in order for these conditions to hold in the megahertz range.

8.2 Viscoelastic Film in Air

8.2.1 Purely Inertial Loading

Before going into the details of the calculation for thin films, we briefly come back to a statement made earlier with regard to the proportionality of frequency shift and *added mass* (as opposed to film thickness). This proportionality is the essence of the Sauerbrey relation. The frequency shift–mass proportionality holds for all thin films, regardless of their viscoelastic properties. It even applies to laterally heterogeneous samples as long as these are so thin that viscoelasticity can be ignored. In the latter case, the areal mass density of course is an average mass density.

We now prove the Sauerbrey equation (Eq. 28) based on the small-load approximation (Eq. 51): the stress induced by a very thin film is caused by inertia only and is given as $\sigma = -\omega^2 u_0 m_f$, where u_0 is the amplitude of oscillation and m_f is the (average) mass per unit area. Inserting this result into the small-load approximation (Eq. 51), one finds:

$$\frac{\Delta f}{f_f} \approx \frac{i}{\pi Z_q} \frac{-\omega^2 u_0 m_f}{i\omega u_0} = -\frac{2f}{Z_q} m_f , \tag{67}$$

which is the Sauerbrey relation.

8.2.2 Viscoelastic Film

If we now drop the thin-film condition and instead consider viscoelastic films of arbitrary thickness, we find:

$$\begin{aligned} \sigma = -G_f \frac{\partial u}{\partial z} &= -G_f \left(-ik_f\right) \left(u_f^{-,0} - u_f^{+,0}\right) \\ &= iG_f \frac{\omega}{c_f} \left(u_f^{-,0} - u_f^{+,0}\right) \\ &= i\omega Z_f \left(u_f^{-,0} - u_f^{+,0}\right) , \end{aligned} \tag{68}$$

where $u_f^{-,0}$ and $u_f^{+,0}$ are the amplitudes of the waves traveling away from the crystal and toward the crystal, respectively. The index f labels the film. Since the reflectivity at the film–air interface is $r_{f,a} = 1$, the parameter $u_f^{+,0}$ is given

by:

$$u_f^{+,0} = \exp\left(-2ik_f d_f\right) u_f^{-,0} = \exp\left(-\Delta\varphi\right) u_f^{-,0}\,, \tag{69}$$

where $\Delta\varphi$ is the phase shift induced by the film. The frequency shift induced by the film is:

$$\begin{aligned}\frac{\Delta\tilde{f}}{f_f} &= \frac{i}{\pi Z_q}\frac{i\omega Z_f\left(u_f^{-,0} - u_f^{+,0}\right)}{i\omega\left(u_f^{-,0} + u_f^{+,0}\right)} = \frac{i}{\pi Z_q} Z_f \frac{1 - \exp\left(-2ik_f d_f\right)}{1 + \exp\left(-2ik_f d_f\right)} \\ &= \frac{i}{\pi Z_q} Z_f \frac{\exp\left(ik_f d_f\right) - \exp\left(-ik_f d_f\right)}{\exp\left(ik_f d_f\right) + \exp\left(ik_f d_f\right)} \\ &= \frac{-1}{\pi Z_q} Z_f \tan\left(k_f d_f\right)\,. \end{aligned} \tag{70}$$

The first pole of the tangent ($k_f d_f = \pi/2$) defines the film resonances [6, 37, 89]. Higher order film resonances corresponding to $k_f d_f = m\pi/2$ with m an odd integer should exist, in principle, but have rarely been observed in experiment. At the film resonance one has $d_f = \lambda/4$. Note that the frequency shift is not small right at the film resonance and that the small-load approximation used in the derivation of Eq. 70 breaks down. Cernosek et al. have developed an equivalent circuit for the film resonance which also holds right at the film resonance [90]. According to this circuit (and also to a more rigorous numerical calculation based on the Mason circuit), the frequency shift does not go to infinity at the film resonance. Rather, there are two resonances in parallel, which correspond to a symmetric and an antisymmetric motion of the crystal and the film, respectively. The quantitative agreement between the experimental data and this more rigorous theory still is not impressive. This is one manifestation of the general rule that the QCM does not work well when the frequency shifts become large. It is instructive to write Eq. 70 in a slightly different form:

$$\begin{aligned}\frac{\Delta\tilde{f}}{f_f} &= \frac{-1}{\pi Z_q} Z_f \tan\left(k_f d_f\right) \\ &= \frac{-Z_f}{\pi Z_q}\tan\left(\frac{\omega}{c_f} d_f\right) = \frac{-Z_f}{\pi Z_q}\tan\left(\frac{\omega\sqrt{\rho_f}}{\sqrt{G_f}} d_f\right) = \frac{-Z_f}{\pi Z_q}\tan\left(\frac{\omega}{Z_f}\rho_f d_f\right) \\ &= \frac{-Z_f}{\pi Z_q}\tan\left(\frac{\omega}{Z_f} m_f\right)\,, \end{aligned} \tag{71}$$

which shows that the acoustic properties of a film are fully specified by two parameters: its acoustic impedance, Z, and its mass per unit area, m. Equation 70 misleadingly suggests that there might be three parameters (Z, k, and d), but these three parameters are not independent. As a consequence, one

can never hope to independently derive the thickness, density, and viscoelastic parameters of a film from acoustic measurements alone. This statement holds for multilayers and films in contact with a liquid in the same way.

8.2.3 Derivation of Viscoelastic Constants

In principle, viscoelastic constants can be extracted from the experimental data by fitting Eq. 70 (or any of the more complicated equations below) to the data. For a small film thickness, certain approximations hold which make the derivation more transparent. If $k_f d_f$ is much less than unity, the tangent in Eq. 70 can be Taylor-expanded to third order as $\tan(x) \approx x + 1/3x^3$, resulting in:

$$\begin{aligned}\frac{\Delta\tilde{f}}{f_f} &= \frac{-1}{\pi Z_q} Z_f \tan\left(k_f d_f\right) \approx \frac{-1}{\pi Z_q} Z_f \left(k_f d_f + \frac{1}{3}\left(k_f d_f\right)^3\right) \\ &= \frac{-1}{\pi Z_q} Z_f k_f d_f \left(1 + \frac{1}{3}\omega^2 \frac{\rho_f}{G_f}\frac{m_f^2}{\rho_f^2}\right) = \frac{-1}{\pi Z_q}\omega m_f \left(1 + \frac{1}{3} J_f \frac{Z_q^2}{\rho_f}\left(\frac{m_f}{m_q} n\pi\right)^2\right) \\ &= \frac{-1}{\pi Z_q}\omega m_f \left(1 + \frac{1}{3}\frac{Z_q^2}{Z_f^2}\left(\frac{m_f}{m_q} n\pi\right)^2\right), \end{aligned} \tag{72}$$

where the relation $\omega = 2\pi n f_f = \pi n Z_q / m_q$ has been used. J_f is the complex compliance $J_f = G_f^{-1} = J_f' - \mathrm{i}J_f''$. A large elastic compliance, J_f', tends to decrease the frequency, whereas a large viscous compliance, J_f'', increases the bandwidth. For small m_f (neglecting the second term inside the brackets) this expansion reproduces the Sauerbrey equation. For slightly larger film thicknesses, there is a viscoelastic correction proportional to n^2. In principle, both J_f' and J_f'' can be extracted from the dependence of the frequency shift on the overtone order. However, there are certain caveats to be kept in mind:

- Unless the film is very soft, Eq. 72 should be replaced by the corresponding equation derived from perturbation theory (Eq. 99) for the reasons stated in Sect. 9. The difference is noticeable if the compliance of the film is of the same order of magnitude as the compliance of the crystal.
- J_f' and J_f'' often depend on frequency f. Since the experimentally accessible range of frequencies is narrow (usually less than a decade), it is fair to assume that J_f' and J_f'' depend on f according to a power law with power law exponents β' and β'':

$$\begin{aligned} J_f'(f) &\approx J_f'(f_{ref}) \left(\frac{f}{f_{ref}}\right)^{\beta'} \\ J_f''(f) &\approx J_f''(f_{ref}) \left(\frac{f}{f_{ref}}\right)^{\beta''}, \end{aligned} \tag{73}$$

where f_{ref} is a reference frequency (typically in the center of the accessible frequency range).

In standard polymer rheology, there are no inertial effects and β' is always negative [72]. The choice of the exponents β' and β'' does affect the derived values of the compliance. Generally speaking, viscoelastic dispersion applies to all viscoelastic parameters, not just the compliance of the film. However, for the crystal and the electrodes, the viscoelastic dispersion is often weaker than for polymer films.

Not all choices for J_f', J_f'', β', and β'' are equally plausible, because $J_f'(f)$ and $J_f''(f)$ are interrelated by the Kramers–Kronig relations [72]. For illustration, consider the simplest model for a viscoelastic solid depicted in Fig. 8. If the spring on the left-hand side is small, the material behaves like a Maxwell fluid ($J'' \ll J'$, $\beta' \approx -2$, $\beta'' \approx -1$). The Maxwell fluid is characterized by its relaxation time $\tau = \xi/\kappa$. Simple liquids like water have relaxation times in the gigahertz range. For more complex liquids, there is a broad spectrum of relaxation times, usually also covering the megahertz range. The other extreme is given by the viscoelastic solid in the Voigt sense ($J'' \gg J'$, $\beta' \approx 0$, $\beta'' \approx -1$). Voigt-based modeling [92] with frequency-independent parameters G' and η only makes sense if G' is significantly larger than $\omega\eta(\omega\tau)$. However, $\omega\tau$ is often comparable to unity in the megahertz range, and G' and $\omega\eta$ are often comparable as well. This is the essence of viscoelasticity. If G' works out to be of the same order of magnitude as $\omega\eta(\omega\tau)$, $G'(\omega)$ must increase with frequency.

Electrode effects are very important in the determination of J_f' from experimental data (Fig. 11). Unless the electrode thickness is precisely known, the derivation of J_f' is difficult. The viscous compliance, J_f'', can be derived much

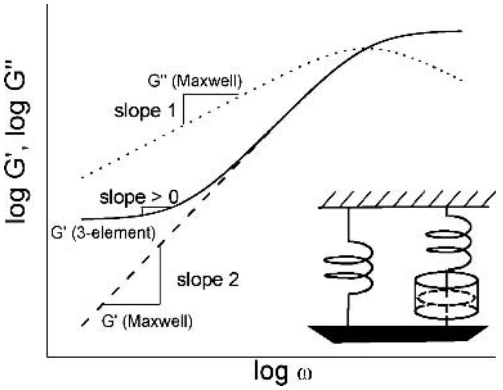

Fig. 8 Three-element network describing a viscoelastic solid. Leaving out the spring on the *right-hand side* leads to the Voigt model [92]. However, this model predicts infinite stress at infinite frequency. Since the frequency of the QCM is high, the Voigt model misses an essential bit of the picture

more reliably. Even the frequency dependence of J_f'' can be determined. This applies to experiments *in air*.

The Voigt modes is represented by Fig. 8 if the spring on the *right-hand side* is omitted. Omission of the spring is dangerous because it leads to an infinite stiffness at infinite frequencies. The Voigt model only makes sense in the low-frequency limit.

8.3 Viscoelastic Film in Liquid

As usual, we start the calculation from the small-load approximation. Equation 68 still applies, but the coefficient of reflection at the outer interface of the film now is not unity but $(Z_f - Z_{liq})/(Z_f + Z_{liq})$ instead. The amplitude $u_f^{+,0}$ is given by:

$$u_f^{+,0} = \exp\left(-2ik_f d_f\right) \frac{Z_f - Z_{liq}}{Z_f + Z_{liq}} u_f^{-,0} \,. \tag{74}$$

Inserting Eq. 74 into Eq. 68, we arrive at [91–93]

$$\frac{\Delta\tilde{f}}{f_f} = \frac{i}{\pi Z_q} Z_f \frac{1 - \exp\left(-2ik_f d_f\right)\frac{Z_f - Z_{liq}}{Z_f + Z_{liq}}}{1 + \exp\left(-2ik_f d_f\right)\frac{Z_f - Z_{liq}}{Z_f + Z_{liq}}} = \frac{-Z_f}{\pi Z_q} \frac{Z_f \tan\left(k_f d_f\right) - iZ_{liq}}{Z_f + iZ_{liq}\tan\left(k_f d_f\right)} \,. \tag{75}$$

At the pole of the tangent one again has a film resonance [91]. The Chalmers group (F. Höök and B. Kasemo, 2006, in this volume) have derived an equivalent equation, which they term "Voigt model" [92]. Expanding Eq. 75 to first order in d_f, one finds:

$$\frac{\Delta\tilde{f}}{f_f} \approx \frac{i}{\pi Z_q}\left[Z_{liq} + iZ_f d_f k_f \left(1 - \frac{Z_{liq}^2}{Z_f^2}\right)\right] \,. \tag{76}$$

The frequency shift is usually determined with respect to a reference state, where the quartz is already immersed in liquid. When the film is absent, one has $Z_L = Z_{liq}$. Referencing the measurement to the bare quartz in liquid by means of subtraction of Eq. 61 from Eq. 76, one obtains [94–96]:

$$\begin{aligned}\frac{\Delta\tilde{f}}{f_f} &\approx \frac{i}{\pi Z_q}(Z_{tot} - Z_{liq}) = \frac{-1}{\pi Z_q} Z_f k_f d_f \left(1 - \frac{Z_{liq}^2}{Z_f^2}\right) = \frac{-\omega m_f}{\pi Z_q}\left(1 - \frac{Z_{liq}^2}{Z_f^2}\right) \\ &= \frac{-\omega m_f}{\pi Z_q}\left(\frac{Z_f^2 - Z_{liq}^2}{Z_f^2}\right) \,,\end{aligned} \tag{77}$$

where Z_{tot} is the load of the entire sample. Apart from the term in brackets, Eq. 77 is equivalent to the Sauerbrey equation. The term in brackets is a viscoelastic correction, dealing with the fact that highly dilute and soft layers lead to a smaller Sauerbrey thickness than rigid layers.

Because Eq. 77 is linear in mass, it also holds in an integral sense [97]:

$$\frac{\Delta\tilde{f}}{f_f} \approx -\frac{-\omega}{\pi Z_q}\int_0^\infty \left[\frac{Z_f^2(z) - Z_{liq}^2}{Z_f^2(z)}\right]\rho(z)\,dz \approx -\frac{\rho\omega}{\pi Z_q}\int_0^\infty \left[\frac{G_f(z) - G_{liq}}{G_f(z)}\right]dz\,, \tag{78}$$

where $\rho(z)$ was assumed to be about constant and equal to ρ. The integral formulation would be used when the viscoelastic properties vary with distance from the crystal surface.

8.3.1 Physical Interpretation of the Sauerbrey Thickness

The correct interpretation of the frequency shift from QCM experiments in liquids is a challenge. Practitioners often just apply the Sauerbrey equation (Eq. 28) to their data and term the resulting areal mass density "Sauerbrey mass" and the corresponding thickness "Sauerbrey thickness". Even though the Sauerbrey thickness can certainly serve to compare different experiments, it must not be naively identified with the geometric thickness. Here is a list of considerations:

1. The QCM always measures an areal mass density, never a geometric thickness (cf. the remarks below Eq. 71). The conversion from areal mass density to thickness usually requires the physical density as an independent input. A density of 1 g cm^{-3} is often *assumed* in soft matter experiments. Given the other uncertainties (see below), this is in many cases a fair approximation.
2. It is difficult to infer the viscoelastic correction (brackets in Eq. 77) from QCM data. However, if the correction factor is significantly different from unity, it may be expected that it also affects the bandwidth, $\Delta\Gamma$, and also that it depends on overtone order. If, conversely, such effects are absent ($\Delta\Gamma \ll \Delta f$, Sauerbrey thickness same on all overtone orders) one may assume $(1 - Z_{liq}^2/Z_f^2) \approx 1$.
3. When the viscoelastic correction as discussed in (2) is insignificant, this by no means implies that the film is not swollen in the solvent. It only means that the (swollen) film is much more rigid than the ambient liquid. The amount of swelling can only be inferred from a comparison of the wet and dry thicknesses. QCM data taken on the wet sample alone do not allow the degree of swelling to be inferred (Sect. 8.3.2).
4. Complex samples are often laterally heterogeneous. The models presented here do not capture lateral heterogeneities, for example caused by roughness (M. Urbakh et al. 2006, in this volume).
5. Complex samples often have fuzzy interfaces. Again, the QCM can never quantitatively determine such a fuzziness. However, a "fluffy" interface will lead to a viscoelastic correction and, as a consequence, to a nonzero

$\Delta\Gamma$ as well as an overtone-dependent Sauerbrey mass. In the absence of such effects, one may conclude that the outer interface of the film is sharp.

6. Last but not least, let it be mentioned that the competing techniques for thickness determination in liquids have their own problems. For AFM measurements, one worries about the influence of the tip on the film. Neutron reflectometry [98] certainly is very accurate, but not easily available on a routine basis. With optical measurements, there is the unknown refractive index of the film. The output of SPR measurements is often reported in terms of the shift of the coupling angle (rather than in terms of thickness) for that reason. The conversion from the shift in coupling angle (or from "RUs" [99]) to percent coverage must be done for every adsorbate separately, based on a calibration to be carried out on this particular system.

8.3.2 Comparison of Optical and Acoustic Reflectometry

It is instructive to compare Eq. 78 with the corresponding equation applied in the context of SPR spectroscopy. For the shift of the coupling angle, θ_c, we have [17, 100, 101]:

$$\Delta\left(\sin\theta_c\right) \approx \frac{2\pi}{n_r\lambda}\left(\frac{\varepsilon_q\varepsilon_{liq}}{\varepsilon_q+\varepsilon_{liq}}\right)^2 \frac{1}{\sqrt{-\varepsilon_q\varepsilon_{liq}}}\int_0^\infty \frac{\varepsilon_f(z)-\varepsilon_{liq}}{\varepsilon_f(z)}\,dz\,, \tag{79}$$

where n_r is the refractive index, λ is the wavelength, and $\varepsilon = n_r^2$ is the dielectric permittivity of the medium. The index q in this case denotes the substrate, rather than the quartz crystal. The structure of Eqs. 78 and 79 is very similar. Since both techniques are based on reflectometry, this is not at all a coincidence.

Comparing Eqs. 78 and 79, and one might assume that the information contained in surface plasmon resonances and quartz crystal resonances is essentially the same. However, this is very often not the case, which has to do with the fact that the contrast obtained with acoustic shear waves is usually much larger than the contrast in optics. While refractive indices typically vary in the range of a few percent, shear moduli may easily vary by orders of magnitude even for rather dilute adsorbates. In optics the weight function (the integrand in Eq. 79) is much smaller than unity and roughly proportional to the concentration. Therefore, the shift of the coupling angle is approximately proportional to the *adsorbed amount*. In acoustics, on the contrary, the weight function (integrand in Eq. 78) easily saturates to a value of unity even for dilute adsorbates if the shear modulus of the adsorbate is much higher than the shear modulus of the liquid [91]. As a consequence, the Sauerbrey thickness (also termed acoustic thickness) approaches the *geometric thickness* even for rather dilute polymer layers. If the adsorbate drags some

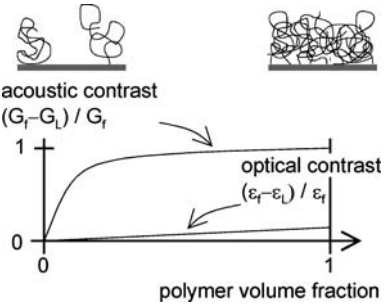

Fig. 9 The acoustic contrast easily saturates. The figure shows a sketch of the contrast function (integrands in Eqs. 78 and 79) as a function of the polymer volume fraction of an adsorbed polymer film. It is assumed that both the shear modulus G_f and the dielectric constant ε_f are roughly proportional to the polymer concentration. However, G_f increases much more strongly than ε_f. If, for instance, a swollen polymer film contains 50% water, this will not appreciably decrease the apparent acoustic thickness because the modulus of the film is still much larger than the modulus of water and $(G_f - G_{liq})/G_f$ remains about unity. This is different in optics because the contrast is roughly proportional to the concentration. As a consequence, the apparent optical film thickness is proportional to the product of concentration and thickness, which is the adsorbed amount. In acoustics, the apparent thickness is close to the geometric thickness. Trapped water appears as part of the film in acoustics

solvent along in its shear movement, the trapped solvent appears as part of the film, as far as the acoustic properties are concerned. However, the trapped solvent does *not* increase the optical thickness (Fig. 9). Swelling therefore increases the acoustic thickness, while it affects the optical thickness to a much lesser extent [102]. The ratio of acoustic and optical thickness gives an estimate of the degree of swelling. For adsorbed proteins, this amounts to an estimate of the degree of hydration.

Evidently, the fact that the acoustic contrast is much higher than the optical contrast is beneficial for sensing. The advantage which the QCM has over the competing optical techniques is most strongly felt for dilute adsorbates. The QCM responds very sensitively to these because—pictorially speaking—a few polymer strands suffice to turn the film into a solid-like object.

8.3.3 Information Contained in the *D*/*f* Ratio

The term in brackets in Eq. 77 is a viscoelastic correction to the Sauerbrey equation. The viscoelastic correction is independent of film thickness in a liquid environment. This is in contrast to films in air or vacuum, where the viscoelastic correction scales as the square of the mass (Eq. 72). In air, the film surface is stress-free. The film only shears under its own inertia and in the limit of vanishing film thickness, the shear strain goes to zero. As a conse-

quence, the shear compliance drops out of the equations in the thin-film limit. This is different in liquids: here the film is "clamped" by the liquid on its outer side, regardless of how thin it is.

In most cases, the viscoelastic correction cannot be directly extracted from the frequency shift because the mass, m_f, is not known independently. The frequency shift contains the product of the mass and the real part of the term in brackets in Eq. 77. The two contributions cannot be disentangled. Note, however, that the mass *can* be eliminated by considering the ratio of the shift in half-band-half-width, $\Delta\Gamma$, and the negative frequency shift, $-\Delta f$ (the "*D*/*f* ratio", where the *D* stands for dissipation). One has:

$$\frac{\Delta\Gamma}{-\Delta f} = \frac{-\,\mathrm{Im}\left(1 - Z_{liq}^2/Z_f^2\right)}{\mathrm{Re}\left(1 - Z_{liq}^2/Z_f^2\right)} . \tag{80}$$

In the following, we assume that the liquid is Newtonian with a density, ρ_{liq}, and a viscosity, η. The acoustic impedance then is:

$$Z_{liq} = \sqrt{\mathrm{i}\omega\rho_{liq}\eta} . \tag{81}$$

For the film we use:

$$Z_f = \sqrt{\rho_f G_f} = \sqrt{\frac{\rho_f}{J_f}} . \tag{82}$$

Inserting Eqs. 81 and 82 into Eq. 80, we find:

$$\frac{\Delta\Gamma}{-\Delta f} = \frac{-\,\mathrm{Im}\left(1 - \mathrm{i}\omega\rho_{liq}\eta J_f/\rho_f\right)}{\mathrm{Re}\left(1 - \mathrm{i}\omega\rho_{liq}\eta J_f/\rho_f\right)} = \frac{\omega\rho_{liq}\eta J_f'}{\rho_f - \omega\rho_{liq}\eta J_f''} . \tag{83}$$

Equation 83 is exact to first order in d_f. Further simplifying assumptions can be made with regard to the right-hand side. Firstly, the densities in soft matter experiments usually are similar. Assuming $\rho_f \approx \rho_{liq}$ yields:

$$\frac{\Delta\Gamma}{-\Delta f} \cong \frac{\omega\eta J_f'}{1 - \omega\eta J_f''} . \tag{84}$$

Secondly, most films of interest are substantially more rigid than the ambient liquid. Even films which are statically soft will often appear rigid at megahertz frequencies. The denominator in Eq. 83 can be rewritten as $1 - J_f''/J_{liq}''$, where $J_{liq}'' = (\omega\eta)^{-1}$ is the viscous compliance of the liquid. The elastic compliance of the liquid is infinite. If the film is much more rigid than the liquid, the denominator is close to unity and one has [97]:

$$\frac{\Delta\Gamma}{-\Delta f} \approx \eta\omega J_f' = 2\pi n f_f \eta J_f' . \tag{85}$$

If the density of the film and the liquid are not the same, one can still neglect the second term in the denominator in Eq. 83, leading to:

$$\frac{\Delta\Gamma}{-\Delta f} \approx \frac{\rho_{\mathrm{liq}}}{\rho_{\mathrm{f}}}\eta\omega J'_{\mathrm{f}} = \frac{\rho_{\mathrm{liq}}}{\rho_{\mathrm{f}}}2\pi n f_{\mathrm{f}}\eta J'_{\mathrm{f}} = \mathrm{Re}\left(\frac{\left|Z^2_{\mathrm{liq}}\right|}{Z^2_{\mathrm{f}}}\right) . \tag{86}$$

Detailed investigation shows that Eqs. 85 and 86 require films with a thickness of not more than a few nanometers in order to yield fair agreement with the full equation. Still, it holds quite generally that the shift in bandwidth is mostly affected by the *elastic* compliance of the film, rather than its viscous compliance. This contrasts to the situation in air, where $\Delta\Gamma$ is dominated by the viscous compliance of the film.

8.3.4 Slip

The issue of slip at the solid–liquid interface has been a topic of much debate [103]. The influence of slip on the frequency of the QCM is discussed in detail in the chapter by M. Urbakh et al. 2006, in this volume. Slip can be very easily integrated into the framework of the multilayer formalism and we briefly show this connection. We represent slip by a layer close to the solid surface (a "film") with a reduced viscosity. Inside this layer, the shear gradient is increased, leading to the flow profile indicated in Fig. 10. The slope of the profile $\mathrm{d}v(z)/\mathrm{d}z$ is proportional to $\eta^{-1}(z)$. The slip length, b_{s}, is the difference between the location of the surface and the extrapolated plane of zero shear. One can show that the slip length, b_{s}, is given by:

$$b_{\mathrm{s}} = \left[\frac{\eta_{\mathrm{liq}}}{\eta_{\mathrm{f}}} - 1\right] d_{\mathrm{f}} , \tag{87}$$

where η_{f} is the viscosity inside the film and d_{f} is the thickness of the layer with reduced viscosity (solid line in Fig. 10). Since this relation is linear in d_{f}, it also holds for continuous profiles $\eta(z)$ (dashed line in Fig. 10) in an integral

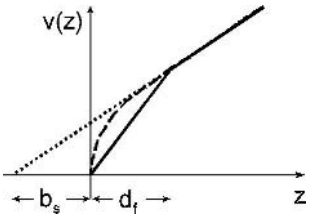

Fig. 10 Flow profile above a solid surface with slip. *Dashed line*: the viscosity $\eta(z)$ increases continuously from a small value at the surface to a somewhat higher value in the bulk. At the surface, the shear gradient is correspondingly increased. *Solid line*: the viscosity is reduced inside a hypothetical discrete layer of thickness d_{f}

sense:

$$b_s = \int_0^\infty \left[\frac{\eta_{liq}}{\eta(z)} - 1 \right] dz \,. \tag{88}$$

For quantitative analysis, we may treat the layer with reduced viscosity like a thin film. As in Eq. 78, we can use an integral formulation:

$$\begin{aligned} \frac{\Delta f}{f_f} &= -\frac{2f}{Z_q} \int_0^\infty \left(1 - \frac{Z_{liq}^2}{Z_f^2(z)} \right) \rho(z)\, dz \\ &= -\frac{2f}{Z_q} \int_0^\infty \left(1 - \frac{i\omega\rho_{liq}\eta_{liq}}{i\omega\rho(z)\eta(z)} \right) \rho(z)\, dz \\ &\approx \frac{2f}{Z_q}\rho_{liq} \int_0^\infty \left(\frac{\eta_{liq}}{\eta(z)} - 1 \right) dz = \frac{2f}{Z_q}\rho_{liq} b_s \,, \end{aligned} \tag{89}$$

where $\rho(z) \approx \rho_{liq}$ has been used.

To the experimentalist, slip looks like a negative Sauerbrey mass, where the slip length is equal to the negative Sauerbrey thickness. This model ignores roughness and lateral heterogeneities, which presumably play a role in most practical situations where slip is observed.

8.3.5 Roughness at the Film–Liquid Interface

Roughness, generally speaking, is not easily incorporated into the multilayer formalism because it violates the assumption of lateral heterogeneity. On the other hand, it is certainly essential. The chapter (M. Urbakh et al. 2006, in this volume) describes various ways to deal with roughness. Roughness may very well occur not only at a quartz–liquid interface, but also at a film–liquid interface. There is a logical extension of the formalism treated to the case of multilayers (M. Urbakh et al. 2006, in this volume). One uses an impedance of the liquid of the form:

$$Z_{liq} \approx \sqrt{\frac{\rho_{liq}\omega\eta}{2}} \left[\left(1 + 2\frac{h_r^2}{\delta^2} \right) + i \left(1 + 3\sqrt{\pi}\frac{h_r^2}{l_r\delta} - 2\frac{h_r^2}{\delta^2} \right) \right] . \tag{90}$$

The term in front of the bracket is the well-known Kanazawa expression (Eq. 61). The correction terms inside the brackets take care of roughness at the interface of the liquid; l_r is the lateral correlation length of roughness (where the spectrum of spatial frequencies is assumed to be Gaussian), h_r is the root-mean-square roughness, and $\delta = (2\eta/(\rho\omega))^{1/2}$ is the penetration

depth. Both l_r and h_r must be much smaller than δ for Eq. 90 to hold. Also, h_r must be much less than l_r (shallow roughness). For details, see (M. Urbakh et al. 2006, in this volume)

8.4 Two Viscoelastic Films in Air

For two films in air, the matrix formalism yields:

$$\frac{\Delta\tilde{f}}{f_f} = \frac{-1}{\pi Z_q} \frac{Z_f \tan\left(k_f d_f\right) + Z_e \tan\left(k_e d_e\right)}{1 - Z_f/Z_e \tan\left(k_f d_f\right) \tan\left(k_e d_e\right)} \,. \tag{91}$$

The indices e and f denote the electrode (the lower film, in general) and the film (the upper film, in general), respectively. Electrode effects can be very noticeable, particularly when Eq. 91 is used to derive the elastic properties of a film. For thin films ($\tan(x) \approx x$), the effects of both films are additive in the sense that:

$$\frac{\Delta\tilde{f}}{f_f} = \frac{-\omega}{\pi Z_q} \left(m_e + m_f\right) \,. \tag{92}$$

8.5 Two Viscoelastic Films in Liquid

For two films in a semi-infinite medium (liquid) the matrix formalism yields:

$$\frac{\Delta\tilde{f}}{f_f} = \frac{-Z_e}{\pi Z_q} \frac{Z_f \left(Z_e \tan\left(k_e d_e\right) + Z_f \tan\left(k_f d_f\right)\right) + \mathrm{i} Z_{liq} \left(Z_e \tan\left(k_f d_f\right) \tan\left(k_e d_e\right) - Z_f\right)}{Z_f \left(Z_e - Z_f \tan\left(k_f d_f\right) \tan\left(k_e d_e\right)\right) + \mathrm{i} Z_{liq} \left(Z_e \tan\left(k_f d_f\right) + Z_f \tan\left(k_e d_e\right)\right)} \,. \tag{93}$$

The indices e, f, and liq denote the electrode (the lower film, in general), the film (the upper film, in general), and the liquid, respectively. While Eq. 93 seems long and complicated, it definitely is of practical relevance. It has to be used when films in liquids are investigated and electrode effects not be neglected.

9 Perturbation Analysis

In Sect. 8 we have used the small-load approximation to derive frequency shifts for various geometries. Evidently, the linearization in Δf, which was applied in order to derive the small-load approximation, has its limits of

validity. These limits are felt not only when large frequency shifts are encountered, but also when one looks into the details of the dependence of the frequency shift on the overtone order n. This one would do in order to derive viscoelastic parameters such as the compliances J' and J''. These viscoelastic effects are typical second-order effects in the sense that a linearization of the equations can easily produce wrong results.

For an illustration of this shortcoming, assume that the film has the exact same acoustic properties as the quartz crystal. In this case the fractional frequency shift must be strictly the same on all overtone orders:

$$\frac{\Delta f}{f_0} \equiv - \frac{d_\mathrm{f}}{d_\mathrm{q}} \equiv - \frac{m_\mathrm{f}}{m_\mathrm{q}} \,. \tag{94}$$

Equation 94 holds regardless of the overtone order and is a simple result. However, Eq. 94 is not reproduced when applying the small-load approximation (Eq. 51) and using the load impedance of a viscoelastic film as expressed in Eq. 72:

$$\frac{\Delta \tilde{f}}{f_\mathrm{f}} \approx \frac{-1}{\pi Z_\mathrm{q}} \omega m_\mathrm{f} \left(1 + \frac{1}{3} \frac{Z_\mathrm{q}^2}{Z_\mathrm{f}^2} \left(\frac{m_\mathrm{f}}{m_\mathrm{q}} n\pi \right)^2 \right) = - \frac{m_\mathrm{f}}{m_\mathrm{q}} \left(1 + \frac{1}{3} J_\mathrm{f} \frac{Z_\mathrm{q}^2}{\rho_\mathrm{f}} \left(\frac{m_\mathrm{f}}{m_\mathrm{q}} n\pi \right)^2 \right) . \tag{95}$$

Unless the compliance of the film, J_f, is zero (which is physically impossible) there is a nontrivial dependence of $\Delta \tilde{f}$ on overtone order, contradicting Eq. 94. This error occurs because the term $-2\mathrm{i}AZ_\mathrm{q} \cot(\tilde{k}_\mathrm{q} \tilde{h}_\mathrm{q})$ in Eq. 113 was *linearized* in $f - f_\mathrm{r}$ (Appendix A), whereas the impedance of the load was expanded to *third* order in thickness (Sect. 8.2.3). In order to do the derivation consistently, we have to omit the linearization in $\Delta \tilde{f} = f - f_\mathrm{r}$. Requiring that the mechanical impedance on resonance, Z_m, be zero amounts to an implicit equation in $\Delta \tilde{f}$. The entire equation has to be Taylor-expanded in $\Delta \tilde{f}/f$ and solved iteratively. In the following, we sketch the argument. The full derivation is given in [104].

We neglect piezoelectric stiffening and base the analysis on Eq. 59:

$$Z_\mathrm{L} = - \mathrm{i} \widetilde{Z}_\mathrm{q} \tan \left(\pi \frac{\Delta \tilde{f}}{\tilde{f}_\mathrm{f}} \right) = - \mathrm{i} \widetilde{Z}_\mathrm{q} \tan \left(n\pi \frac{\Delta \tilde{f}}{\tilde{f}_0} \right) \equiv Z_\mathrm{cr} \,, \tag{96}$$

where the last identity only serves to define the parameter Z_cr. In the following, we neglect the difference between $\tilde{f}_0$ and f_0. Both sides of Eq. 96 can be Taylor-expanded in $\Delta \tilde{f}/f_0$ as:

$$Z_\mathrm{L}^{(0)} + Z_\mathrm{L}^{(1)} \frac{\Delta \tilde{f}}{f_0} + Z_\mathrm{L}^{(2)} \left(\frac{\Delta \tilde{f}}{f_0} \right)^2 + \ldots \approx Z_\mathrm{cr}^{(1)} \frac{\Delta \tilde{f}}{f_0} + Z_\mathrm{cr}^{(2)} \left(\frac{\Delta \tilde{f}}{f_0} \right)^2 + \ldots \,. \tag{97}$$

Superscripts in brackets ($^{(n)}$) denote the respective coefficient of the Taylor expansion. Importantly, the zeroth-order term on the right-hand side van-

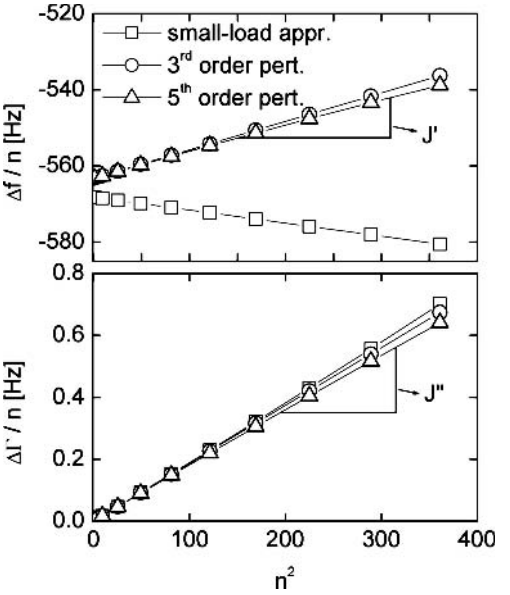

Fig. 11 Illustration of the effects of electrodes for a film in air. The figure shows the frequency shift scaled by overtone order $\Delta f/n$ induced by a 100-nm polymer film ($\rho = 1\,\mathrm{g/cm^3}$, $G' = 1$ GPa, $G'' = 0$) as a function of the square of the overtone order (Eq. 99). □: Small-load approximation, no electrode effects; ○: 200-nm gold electrodes ($\rho_e = 19\,\mathrm{g/cm^3}$, $G'_e = 29$ GPa); third-order perturbation same as ○; △: fifth-order perturbation. The slope in the *upper panel* strongly depends on the electrode thickness

ishes. Solving Eq. 97 to first order in $\Delta\tilde{f}/f$, we find:

$$\left(\frac{\Delta\tilde{f}}{f_0}\right)^{[1]} \approx \frac{Z_L^{(0)}}{Z_{cr}^{(1)} - Z_L^{(1)}} \approx \frac{Z_L^{(0)}}{Z_{cr}^{(1)}} \,. \tag{98}$$

In the next step we write $\Delta\tilde{f}/f_0$ as $(\Delta\tilde{f}/f_0)^{[1]} + (\Delta\tilde{f}/f_0)^{[2]}$, insert this expression into Eq. 97, linearize in $(\Delta\tilde{f}/f_0)^{[2]}$, and solve for $(\Delta\tilde{f}/f_0)^{[2]}$. Superscripts in square brackets denote the perturbation order. This step is iterated until the desired accuracy is reached. This procedure cures, for instance, the problem outlined below Eq. 95. After going through the perturbation analysis to third order, one finds:

$$\begin{aligned}\frac{\Delta\tilde{f}}{f_f} &= -\frac{2\tilde{f}_0}{Z_q} m_f \left(1 + \frac{1}{3}\left(\frac{Z_q^2}{Z_f^2} - 1\right)\left(\frac{m_f}{m_q}\pi n\right)^2\right) \\ &\approx -\frac{2\tilde{f}_0}{Z_q} m_f \left(1 + \frac{1}{3}\left(J_f \frac{Z_q^2}{\rho_f} - 1\right)\left(\frac{m_f}{m_q}\pi n\right)^2\right) \,. \end{aligned} \tag{99}$$

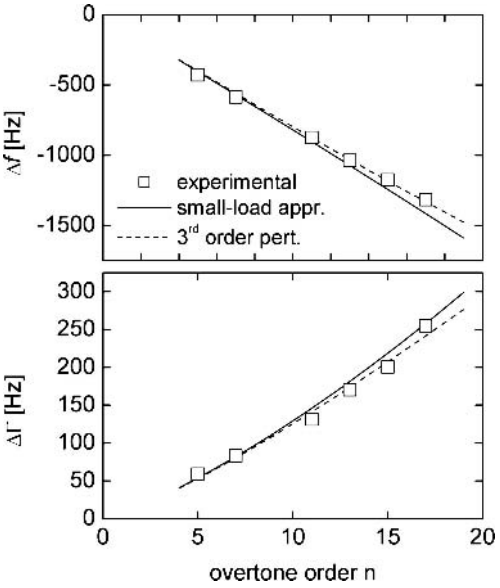

Fig. 12 Illustration of the difference between the small-load approximation and the perturbation analysis for a film in liquid. □: Experimental data obtained with an adsorbed protein layer in buffer. *Dashed line*: fit with third-order perturbation analysis. Fit parameters: $d_f = 14$ nm, $J'_f = 13\,300$ GPa^{-1}, and $\beta' = -1$; gold electrodes as in Fig. 11. The viscosity of the buffer was 0.96 cP. *Solid line*: simulation with the small-load approximation and the same model parameters as the input to the *dashed line*. There is a systematic difference. (Experimental data kindly provided by I. Reviakine)

Clearly, the viscoelastic correction (second term in brackets) vanishes if the film and the crystal have identical properties ($Z_f = Z_q$).

We introduce the following new variables:

$$\mu_e = \frac{m_e}{m_q}\,, \qquad \mu_f = \frac{m_f}{m_q}\,,$$

$$\zeta_e(\omega) = \frac{Z_q^2}{Z_e^2(\omega)} - 1 = \frac{J_e(\omega)}{\rho_e} Z_q^2 - 1\,, \quad \zeta_f(\omega) = \frac{Z_q^2}{Z_f^2(\omega)} - 1 = \frac{J_f(\omega)}{\rho_f} Z_q^2 - 1\,,$$

$$\xi_{liq}(\omega) = \frac{Z_{liq}(\omega)}{Z_q}\,. \tag{100}$$

The parameter μ is a dimensionless measure of the film thickness. The parameter ζ is a dimensionless measure of the shear compliance, and the parameter ξ_{liq} is a dimensionless measure of the viscosity of the liquid. Strictly speaking, the parameters ζ_e, ζ_f, and ξ_{liq} of course are measures of the acoustic impedances of these materials. In soft matter experiments, the density often

is about constant and the impedance is governed by the viscoelastic parameters. The parameters μ_e, μ_f, and ξ_{liq} are considered small in the perturbation calculation. The perturbation therefore can only cover the thin-film limit.

The full equations are lengthy and therefore not reproduced here. They are available from the author on request. As an example, we provide the fifth-order perturbation result for a film in liquid:

$$\begin{aligned}\frac{\Delta\tilde{f}}{f_0} \approx & \frac{i\xi_{liq}}{n\pi} + \frac{i\xi_{liq}^3}{3n\pi} + \frac{i\xi_{liq}^5}{5n\pi} \\ & + \left(-1 - \frac{i\xi_{liq}}{n\pi} + \zeta_f\xi_{liq}^2 + \frac{\left(-5i + 15i\zeta_f\right)\xi_{liq}^3}{15n\pi} + \zeta_f\xi_{liq}^4 \right)\mu_f \\ & + \left(1 + \left(\frac{i}{n\pi} + in\pi\zeta_f\right)\xi_{liq} - 4\zeta_f\xi_{liq}^2 \right. \\ & \quad \left. + \frac{\left(5i - 45i\zeta_f\right)}{15n\pi} + \frac{\left(15i\pi^2\zeta_f - 15i\pi^2\zeta_f^2\right)}{15n\pi}\xi_{liq}^3 \right)\mu_f^2 \\ & + \left(-1 - \frac{1}{3}n^2\pi^2\zeta_f + \left(-\frac{i}{n\pi} - 4in\pi\zeta_f\right)\xi_{liq} \right. \\ & \quad \left. + \left(10\zeta_f + \frac{n^2\left(-10\pi^3\zeta_f + 20\zeta_f^2\right)}{15\pi}\right)\xi_{liq}^2 \right)\mu_f^3 \\ & + \left(1 - \frac{4}{3}n^2\pi^2\zeta_f + \left(\frac{i}{n\pi} + 10in\pi\zeta_f + \frac{n^3\left(-5\pi^4\zeta_f + 10\pi^4\zeta_f^2\right)}{15\pi}\right)\xi_{liq} \right)\mu_f^3 \\ & + \left(-1 - \frac{10}{3}n^2\pi^2\zeta_f - \frac{1}{15}n^4\pi^4\zeta_f\left(-1 + 2\zeta_f\right) \right)\mu_f^5 . \end{aligned} \tag{101}$$

Note that the reference state is always the bare crystal. Should the crystal in the reference state already have a load (such as an electrode or a buffer solution) the proper subtractions have to be carried out. For instance, if the reference state is the crystal immersed in liquid without a film, one applies Eq. 101 setting $\mu_f = 0$ and subtracts this result from the full result in order to compare with the experimental frequency shift.

In order to properly treat electrode effects, it is essential to use the perturbation formalism. The small-load approximation gives the wrong results. The situation is particularly dangerous in dry environments. In liquids, the shortcomings of the small-load approximation are less severe.

Equation 101 also clarifies which viscoelastic parameters are easily determined from experiments, and which are not. A typical situation where

Eq. 101 would be employed is adsorption from solution, such as typically occurs in biosensing. In this case, the reference state is usually the QCM inserted in the buffer. Also, the films are usually so thin that only the first-order term in μ_f is of importance. Subtracting the contribution from the pure liquid and omitting terms proportional to μ_f^2 and μ_f^3 one arrives at:

$$\frac{\Delta\tilde{f}}{f_0} \approx -\mu_f\left(1+\frac{i\xi_{liq}}{n\pi}-\zeta_f\xi_{liq}^2\right)\mu_f \tag{102}$$

$$= -\frac{m_f}{m_q}\left(1-\frac{Z_{liq}^2}{Z_f^2}+\frac{Z_{liq}^2}{Z_q^2}+\frac{i\sqrt{i\omega\rho_{liq}\eta}}{n\pi Z_q}\right).$$

In order to make the comparison with Eq. 77, we normalize to the frequency of the fundamental f_f, rather than to f_0. Further, we neglect the last two terms on the right-hand side. These are small because they have the quantity Z_q in the denominator. Finally, we assume a Newtonian liquid ($\eta'(\omega) = \text{const.}$, $\eta'' = 0$) and separate the real and the imaginary parts, leading to:

$$\frac{\Delta f}{f_f} \approx -\frac{2f_0}{Z_q}m_f\left(1-J_f''\frac{\omega\rho_{liq}\eta}{\rho_f}\right)$$

$$\frac{\Delta\Gamma}{f_f} \approx \frac{2f_0}{Z_q}m_f\left(J_f'\frac{\omega\rho_{liq}\eta}{\rho_f}\right). \tag{103}$$

Equation 103 shows that—at this level of approximation—only the quantity J'' (the viscous compliance) enters the frequency shift, whereas only the quantity J' (the elastic compliance) enters the bandwidth. This has far-reaching consequences in the data analysis. Because the thickness and the viscous compliance *additively* enter the frequency shift, it is difficult to derive the viscous compliance without independent knowledge of the thickness. J' cannot be inferred from the n-dependence of Δf because the n-dependence of J' is unknown. The elastic compliance, on the other hand, can be derived with fair accuracy, because the mass only enters the bandwidth as a prefactor. Even its frequency dependence (Eq. 73) is obtained.

The situation becomes much more complicated when moduli (or the viscosity) are used for the analysis, rather than compliances. Moduli and compliances are interrelated in the following way:

$$G'(\omega) = \text{Re}\left(\frac{1}{J(\omega)}\right) = \frac{J'(\omega)}{J'^2(\omega)+J''^2(\omega)}$$

$$G''(\omega) = \text{Im}\left(\frac{1}{J(\omega)}\right) = \frac{J''(\omega)}{J'^2(\omega)+J''^2(\omega)}$$

$$\eta'(\omega) = \frac{1}{\omega}G''(\omega) = \frac{1}{\omega}\frac{J''(\omega)}{J'^2(\omega)+J''^2(\omega)}. \tag{104}$$

When using moduli (or an elastic modulus and a Newtonian viscosity) one has parameters which are combinations of J' and J''. Since only J' is well determined, the solutions found in the fitting procedure will not be unique. However, it will be difficult to find the cross correlations, because J' and J'' both contribute. Fitting with J' and J'' is more transparent. Figures 11 and 12 illustrate that perturbation indeed is of practical relevance.

10 Concluding Remarks

This chapter has focused on applications of the QCM which go beyond microweighing. The analysis has relied on the small-load approximation and has led to a comprehensive picture covering a wide variety of configurations. From a practical point of view, the main benefits of this analysis can be summarized as follows:

- The frequency-dependent viscous compliance $J''(\omega)$ can be determined for thin films in air.
- The frequency-dependent elastic compliance $J'(\omega)$ can be determined for thin films in a liquid environment.
- Interfacial viscoelastic spectroscopy on soft elastomers is possible by virtue of the sheet-contact model.

On the other hand, there are numerous experiments which cannot easily be interpreted within this frame. Here are some examples:

- Electrical fringe fields often *do* penetrate into the sample. The sample's dielectric properties affect the parallel capacitance, C_0, and thereby the frequency shift. The QCM can probe dielectric properties and viscoelastic properties at the same time.
- The laws of linear acoustics are violated at high amplitudes of oscillation. Studying nonlinear interactions between the crystal and the sample should be useful in the context of tribology and adhesion.
- Many interesting samples are not laterally homogeneous. The calculation of the average shear-induced stress is not an easy task, but it seems feasible in some cases. High-frequency fluid dynamics calculations should be helpful.

It is to be hoped that the established models describing the QCM can be extended to cover these more complicated—but also more interesting—samples as well.

Acknowledgements The author is indebted to I. Reviakine and R. Lucklum for critical reading of the manuscript.

Appendix

A
Derivation of the Butterworth–van Dyke Equivalent Circuit

In the following, we derive the Butterworth–van Dyke (BvD) equivalent circuit (Fig. 7) from the Mason circuit (Fig. 6c). The Mason circuit itself is derived in detail in [4]. The BvD circuit approximates the Mason circuit close to the resonances. The BvD circuit accounts for piezoelectric stiffening and can also be extended in a simple way to include an acoustic load *on one side of the crystal*. In the derivation of the BvD circuits, one assumes small frequency shifts as well as small loads and applies Taylor expansions in the frequency shift (or the load) whenever these variables occur. The condition of $\Delta f/f \ll 1$ is fulfilled as long as the load impedance of the sample, Z_L, is much smaller than the impedance of crystalline quartz, Z_q (where the latter, as opposed to Z_L, is a material constant). Z_q sets the scale of the impedances contained in the Mason circuit. Generally speaking, the QCM only works properly if $Z_L \ll Z_q$.[11]

In a first step, we set the load on the back side of the crystal (left-hand side in Fig. 6a) to zero and short-circuit the respective port. In a second step we apply the "Norton transformation" (Fig. 13b). The circuit from Fig. 13c is fully equivalent to the circuit shown in Fig. 13a. The equivalence of Figs. 13c and 13d is based on the relation:

$$\tan(x) + \cot(x) = \frac{2}{\sin(2x)} \,. \tag{105}$$

In the following we neglect the small element $4Z_k$ for notational convenience. Accounting for the term $4Z_k$ does not introduce essential changes. We put the term $4Z_k$ back into the equations when introducing the piezoelectrically stiffened spring constant $\bar{\kappa}_p$ (Eq. 117). On resonance, the total impedance across the electrical port (which is now located on the left-hand side) vanishes. This happens close to a frequency where $\cot(\tilde{k}_q h_q)$ is zero. Since $\tan(\tilde{k}_q h_q)$ is large at this frequency and since we have assumed the element AZ_L (in parallel to $\mathrm{i}AZ_q \tan(\tilde{k}_q h_q)$) to be small, we may omit the element $\mathrm{i}AZ_q \tan(\tilde{k}_q h_q)$ close to resonance.

We first consider the resonance in the absence of the sample ($Z_L = 0$). On resonance, $\cot(\tilde{k}_q h_q)$ is zero, which implies:

$$\tilde{k}_q h_q = \frac{2\pi \tilde{f}_0}{\tilde{c}_q} h_q = \frac{n\pi}{2} \,, \quad n = 1, 3, 5, \ldots \tag{106}$$

[11] This is a statement based on practical experience. The theory itself is not limited to small loads. However, the agreement between theory and experiment is unsatisfactory for large loads.

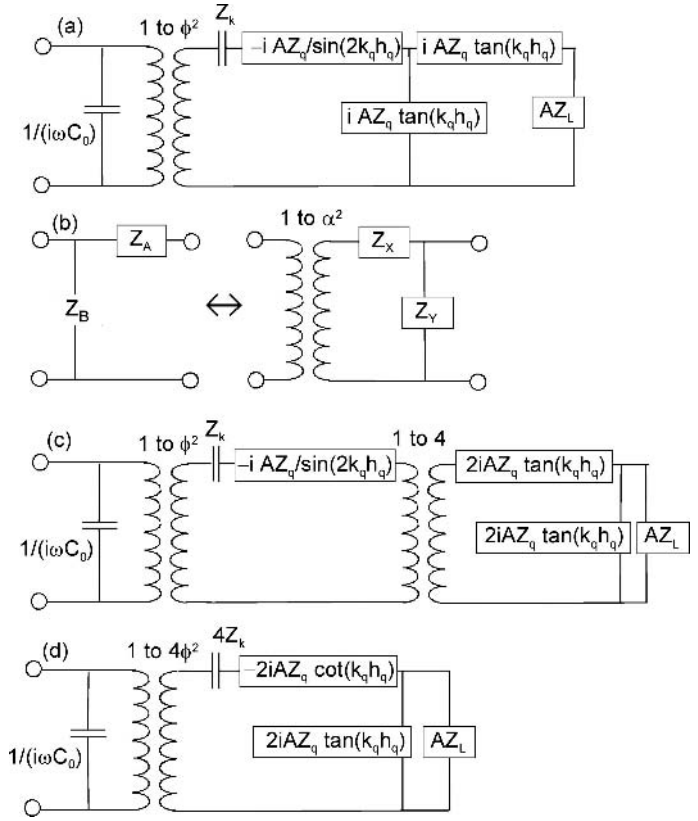

Fig. 13 Steps in the derivation of the Butterworth–van Dyke circuit. **a** Same as Fig. 6c with the circuit elements rearranged. **b** Norton equivalence: $Z_X = \alpha Z_A$, $Z_Y = \alpha Z_B$, $\alpha = (Z_A + Z_B)/Z_B$. **c** Norton equivalence applied to **b**. **c** Same as **c** where the relation $-2/\sin(2x) + \tan(x) = -\cot(x)$ has been used. The two transformers have been merged

and

$$\tilde{f}_0 = f_0 + \mathrm{i}\Gamma_0 = \frac{n\tilde{c}_\mathrm{q}}{4h_\mathrm{q}} = \frac{n\tilde{c}_\mathrm{q}}{2d_\mathrm{q}}, \quad n = 1, 3, 5, \ldots . \tag{107}$$

Here, the overtone order, n, is odd to ensure an antisymmetric pattern of motion. Otherwise, there is no current through the electrodes. Symmetric acoustic resonances cannot be excited electrically. Neither the mathematical approach (Eq. 24) nor the optical approach (Eq. 35) captures this fact because they do not account for piezoelectricity. Separating the real and imaginary parts of Eq. 107, we find:

$$f_0 = \frac{nc'_\mathrm{q}}{2d_\mathrm{q}}, \quad n = 1, 3, 5, \ldots \tag{108}$$

and

$$\Gamma_0 = \frac{n\pi\, c_q''}{2d_q} = f_0 \frac{c_q''}{c_q'} = f_0 \frac{\sqrt{G_q''}}{\sqrt{G_q'}} = f_0 \sqrt{\tan(\delta)} \approx f_0 \frac{1}{2} \tan(\delta) \ , \tag{109}$$

where $\tan(\delta) = G_q''/G_q'$ is the loss tangent. Note that the approximation $(\tan(\delta))^{1/2} \approx \tan(\delta)/2$ requires $\tan(\delta) \ll 1$, which is certainly fulfilled for quartz.

For the Q factor, we find:

$$Q = \frac{f_0}{2\Gamma_0} = \frac{1}{\tan(\delta)} \ . \tag{110}$$

We now consider a frequency close to the resonance frequency $f = f_0 + \mathrm{d}f$ rather than the resonance frequency itself. Here $\mathrm{d}f$ is a small difference between the driving frequency and the resonance frequency (as opposed to a shift of the resonance frequency). We write:

$$\tilde{k}_q h_q = k_q' h_q - \mathrm{i}\, k_q'' h_q \approx \frac{n\pi}{2} \left(1 + \frac{\mathrm{d}f}{f_0} - \mathrm{i} \frac{\tan(\delta)}{2} \right) \ . \tag{111}$$

Separation of $\cot(\tilde{k}_q h_q)$ into its real and imaginary part yields

$$\begin{aligned} \cot\left(\left(k_q' - \mathrm{i} k_q'' \right) h_q \right) = & - \frac{\sin\left(2k_q' h_q \right)}{\cos\left(2k_q' h_q \right) - \cosh\left(2k_q'' h_q \right)} \\ & - \mathrm{i} \frac{\sinh\left(2k_q'' h_q \right)}{\cos\left(2k_q' h_q \right) - \cosh\left(2k_q'' h_q \right)} \ . \end{aligned} \tag{112}$$

Using Eq. 111 and Taylor-expanding Eq. 112 to first order in the small terms $\mathrm{d}f/f_0$ and $\tan(\delta)$, we find:

$$-2\mathrm{i} A Z_q \cot\left(\tilde{k}_q h_q \right) \approx n\pi A Z_q \left(\frac{\tan(\delta)}{2} + \mathrm{i} \frac{\mathrm{d}f}{f_0} \right) \ . \tag{113}$$

In order to find the equivalent mass, m_p, the equivalent spring constant, κ_p, and the equivalent dashpot, ξ_p, we need to write down the impedance of such an equivalent circuit (Fig. 14b). By comparing the coefficients with the coefficients in Eq. 113, we determine the values of m_p, κ_p, and ξ_p. When placing a mass, a spring, and a dashpot in series (in the electrical sense, Fig. 5) the

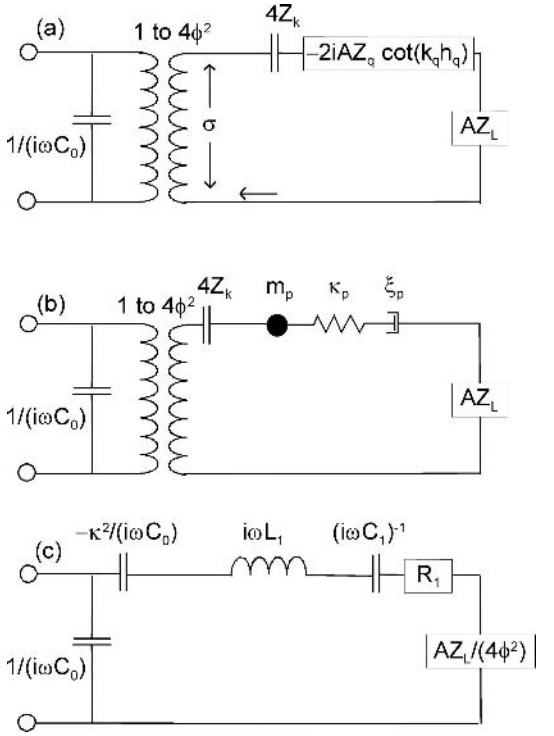

Fig. 14 Simplified Mason circuit (**a**) close to Fig. 13d. Since $\tan(k_q h_q)$ is large close to the resonance and, further, since this element is in parallel to the small load AZ_L, it may be neglected. **b** Close to resonance we have $\cot(k_q h_q \approx 0)$ and the element $-2iAZ_q \cot(k_q h_q)$ can be approximated by a spring, a mass, and a dashpot. **c** Using the electromechanical analogy, the spring, the mass, and the dashpot may also be represented as a motional capacitance, C_1, a motional inductance, L_1, and a motional resistance, R_1

total impedance is:

$$
\begin{aligned}
\mathrm{i}\omega m_\mathrm{p} + \frac{\kappa_\mathrm{p}}{\mathrm{i}\omega} + \xi_\mathrm{p} &= \mathrm{i}\sqrt{\kappa_\mathrm{p} m_\mathrm{p}} \left(\frac{\omega}{\omega_0} - \frac{\omega_0}{\omega} \right) + \xi_\mathrm{p} \\
&= \mathrm{i}\sqrt{\kappa_\mathrm{p} m_\mathrm{p}} \left(\frac{(\omega + \omega_0)(\omega - \omega_0)}{\omega_0 \omega} \right) + \xi_\mathrm{p} \\
&\approx \mathrm{i}\sqrt{\kappa_\mathrm{p} m_\mathrm{p}} \left(\frac{2(\omega - \omega_0)}{\omega_0} \right) + \xi_\mathrm{p} \\
&\approx \mathrm{i}\sqrt{\kappa_\mathrm{p} m_\mathrm{p}} \left(\frac{2\,\mathrm{d}f}{f_0} \right) + \xi_\mathrm{p} \,, \qquad (114)
\end{aligned}
$$

where the relations $\omega_0 = (\kappa_p/m_p)^{1/2}$ and $\omega + \omega_0 \approx 2\omega$ have been used. Comparison with Eq. 113 shows that:

$$\sqrt{\kappa_p m_p} = \frac{\kappa_p}{\omega_0} = AZ_q\frac{n\pi}{2}$$

$$\xi_p = AZ_q\frac{n\pi}{2}\tan(\delta) = \frac{\sqrt{\kappa_p m_p}}{Q}\,. \tag{115}$$

Using $2\pi f_r = (\kappa_p/m_p)^{1/2} = 2\pi n c_q/(4h_q)$ we find:

$$\kappa_p = \sqrt{\kappa_p m_p}\,2\pi f_r = AZ_q\frac{n\pi}{2}\frac{c_q}{h_q}\frac{n\pi}{2} = \frac{AG_q}{d_q}\frac{(n\pi)^2}{2} = \kappa_{q,stat}\frac{(n\pi)^2}{2}$$

$$m_p = \frac{\sqrt{\kappa_p m_p}}{2\pi f_0} = AZ_q\frac{h_q}{c_q} = \frac{A\rho_q d_q}{2} = \frac{1}{2}Am_q$$

$$\xi_p = AZ_q\frac{n\pi}{2}\tan(\delta)\,, \tag{116}$$

where $\kappa_{q,stat}$ is the static shear stiffness of the crystal. As expected, κ_p is related to the static stiffness, but the relation is not trivial. The same is true for the mass parameter, m_p, and the mass of the crystal, Am_q.

We now put the term $4Z_k$ back into the equations, thereby accounting for piezoelectric stiffening. The elastic energy contained in a strained crystal depends on whether or not the strain-induced polarization is compensated by an external potential (supplied by the electric circuit). If the polarization is not compensated, then there is an electrical contribution to the strain energy and the restoring force pushing the crystal back into its original shape is stronger than in the case of compensation. Piezoelectric stiffening is more effective on higher harmonics than on lower ones because the displacement pattern on high harmonics contains antinodes in the center of the plate, whereas the fundamental only has antinodes at the surfaces. A polarization close to the surface is more efficiently compensated by the external electric field emanating from the electrodes than a polarization at the center.

This stiffening is one of two reasons why the resonance frequencies on the various overtone orders do not strictly scale as the overtone order, n [41, 105]. In the context of timing applications, one actually takes advantage of piezoelectric stiffening in order to electrically pull the resonance frequency of a crystal [106]. By inserting a capacitor in series with the crystal, one can shift the resonance frequency within certain limits. Stray capacitances between the electrodes and the sample also pull the frequency, which—most of the time—is an undesired perturbance. One way to diminish the influence of stray capacitances is to connect the two electrodes across a small resistor (see end of Sect. 3). A second countermeasure is good grounding of the front electrode. If no such measures are taken, piezoelectricity opens a box of interesting phenomena [31, 32] which are, in fact, highly relevant to sensing.

Given the functional form of the term related to piezoelectric stiffening, one can define a new complex spring constant, $\bar{\kappa}_\mathrm{p}$, taking piezoelectric stiffening into account. Remembering that $Z_\mathrm{k} = \phi^2/(\mathrm{i}\omega C_0)$, one writes:

$$\bar{\kappa}_\mathrm{p} = \kappa_\mathrm{p} - 4\phi^2 \frac{1}{C_0} = \frac{AG_\mathrm{q}}{d_\mathrm{q}} \frac{(n\pi)^2}{2} - \frac{4A^2 e_{26}^2}{d_\mathrm{q}^2} \frac{d_\mathrm{q}}{A\varepsilon\varepsilon_0}$$

$$= \frac{AG_\mathrm{q}}{d_\mathrm{q}} \frac{(n\pi)^2}{2} \left(1 - \frac{8e_{26}^2}{G_\mathrm{q}\varepsilon\varepsilon_0} \frac{1}{(n\pi)^2}\right) = \kappa_\mathrm{p} \left(1 - \frac{8}{(n\pi)^2}\kappa^2\right) , \tag{117}$$

where $\kappa = [e_{26}^2/(\varepsilon\varepsilon_0 G_\mathrm{q})]^{1/2}$ is a dimensionless coefficient of piezoelectric coupling. Its value is $\kappa = 0.089$ for AT-cut quartz. The spring constant drops out from the resonance conditions when the latter is linearized in $\Delta\tilde{f}/f_\mathrm{f}$ (Eq. 52). Within the linearized theory, piezoelectric stiffening may be ignored. This is not true in the same way for the perturbation analysis (Sect. 9). Neglecting piezoelectric stiffening in the perturbation theory amounts to an approximation, which *does* change the outcome of the calculation to some extent.

Equations 114–116 can be written down in terms of an electrical capacitance, C_1, an inductance, L_1, and a resistance, R_1, as well (Fig. 14c). In order to find the values for C_1, L_1, and R_1, one needs the conversion factor between electrical and mechanical impedances. We have:

$$Z_\mathrm{el} = \frac{1}{4\phi^2} Z_\mathrm{m} = \left(\frac{d_\mathrm{q}}{2\, e_{26} A}\right)^2 Z_\mathrm{m} , \tag{118}$$

where the factor of 4 (Eq. 45) is a consequence of the Norton transformation (Fig. 13b). We have for the Butterworth–van Dyke circuit elements:

$$C_1 = 4\phi^2 \frac{1}{\bar{\kappa}_\mathrm{p}} = \frac{8Ae_{26}^2}{d_\mathrm{q}(n\pi)^2 G_\mathrm{q}} \left(1 - \frac{8\kappa^2}{(n\pi)^2}\right)^{-1}$$

$$L_1 = \frac{1}{4\phi^2} m_\mathrm{p} = \frac{\rho_\mathrm{q} d_\mathrm{q}^3}{8Ae_{26}^2}$$

$$R_1 = \frac{1}{4\phi^2} \xi_\mathrm{p} = \frac{d_\mathrm{q}^2}{8Ae_{26}^2} Z_\mathrm{q} n\pi \tan(\delta) = \frac{d_\mathrm{q}}{8Ae_{26}^2} (n\pi)^2 \eta_\mathrm{q} = \sqrt{\frac{L_1}{C_1}} \frac{1}{Q} , \tag{119}$$

where the relations $\tan(\delta) = G_\mathrm{q}''/G_\mathrm{q}' = \omega\eta_\mathrm{q}/G_\mathrm{q}'$ and $d_\mathrm{q} Z_\mathrm{q}\omega/G_\mathrm{q}' = d_\mathrm{q} Z_\mathrm{q} 2\pi n f_\mathrm{r}/G_\mathrm{q}' = n\pi Z_\mathrm{q} c_\mathrm{q}/G_\mathrm{q}' = n\pi$ have been used. The parameter η_q quantifies internal damping of the crystal. It is not a Newtonian viscosity: η_q depends on frequency in a nontrivial way.

The load, AZ_L, can also be introduced into effective BvD parameters in analogy to Eq. 117. For instance, one could write $m_\mathrm{p} = A(m_\mathrm{q}/2 + m_\mathrm{f})$ in the Sauerbrey case. The author prefers to use the BvD parameters for the un-

loaded crystal according to Eq. 119 and calculate the frequency shift with the small-load approximation (Eq. 52). This, again, is a matter of taste.

The amplitude of motion and the effective area can be calculated rather straightforwardly from the Mason circuit. One has:

$$a = \frac{4}{(n\pi)^2} d_{26} Q U_{\mathrm{el}} \,. \tag{120}$$

Here, $d_{26} = e_{26}/G_{\mathrm{q}} = 3.1 \times 10^{-12}\,\mathrm{m\,V^{-1}}$ is the piezoelectric strain coefficient. Note that the derivation assumes laterally infinite resonators; it does not account for energy trapping. Equation 120 is therefore expected to miss a numerical factor of order unity. Inputting values ($d_{26} = 3.1\,\mathrm{pm\,V^{-1}}$), we arrive at:

$$\frac{a}{QU_{\mathrm{el}}} = \frac{4}{(n\pi)^2} d_{26} = \frac{1.25}{n^2} \frac{\mathrm{pm}}{\mathrm{V}} \,. \tag{121}$$

This compares well with the experimental value of $1.4\,\mathrm{n^{-2}\,pm\,V^{-1}}$, where the latter has been extracted from the blurring of a scanning tunneling microcopy (STM) image (taken of the electrode of a quartz crystal), which occurred when the oscillation was turned on [107]. Kanazawa finds a similar value by numerically solving the full Mason circuit [108]. The agreement between Eq. 120 and experimentally derived values of the amplitude is often bad on the fundamental, whereas it is fair on overtones with $n = 3$ and higher.

The direction of oscillation can be experimentally determined with a polarizing microscope in the conoscopic mode. Colored rings are observed. The direction of curvature points perpendicular to the x-axis of the crystal, that is, perpendicular to the direction of oscillation.

The drive level is often quoted in dBm, where 0 dBm corresponds to a power of 1 mW. The conversion is:

$$U_{\mathrm{el}} = 0.317 \times 10^{(\mathrm{power[dBm]}/20)} \,, \tag{122}$$

where U_{el} is the amplitude (half of the peak-to-peak voltage).

From the comparison of the resistance R_1 and the Q factor one can infer the effective electrode area as:

$$A = \frac{1}{32 f_{\mathrm{f}}^2 Z_{\mathrm{q}} d_{26}^2} \frac{n\pi}{R_1 Q} \,. \tag{123}$$

When the resonance parameters are probed via impedance analysis, the parameter R_1 is routinely determined as the inverse of the peak conductance, G_{max}. The effective area is proportional to the peak conductance, $G_{\mathrm{max}} = R_1^{-1}$, because a large active area draws a large current. Being an electric quantity, the parameter R_1 is susceptible to calibration problems and electrical imperfections. Also, Eq. 123 does not account for energy trapping and is therefore expected to miss a factor of the order of unity. The active area may vary with overtone order due to energy trapping. By routinely measuring the effective

electrode area, one can check for the electrical contact of the electrodes with the holder.

References

1. Lu C, Czanderna AW (1984) Applications of piezoelectric quartz crystal microbalances. Elsevier, Amsterdam
2. Arnau A (ed) (2004) Piezoelectric transducers and applications. Springer, Berlin Heidelberg New York
3. Grate JW (2000) Chem Rev 100:2627
4. Thurston RN (1984) In: Truesdell C (ed) Mechanics of solids, vol 4. Springer, Berlin Heidelberg New York, Chap 36, p 257
5. Sauerbrey G (1959) Z Phys 155:206
6. Lu CS, Lewis O (1972) J Appl Phys 43:4385
7. Bruckenstein S, Shay M (1985) Electrochim Acta 30:1295
8. Ward MD, Buttry DA (1990) Science 249:1000
9. Beck R, Pittermann U, Weil KG (1988) Ber Bunsenges Phys Chem 92:1363
10. Bruschi L, Delfitto G, Mistura G (1999) Rev Sci Instrum 70:153
11. Rodahl M, Kasemo B (1996) Rev Sci Instrum 67:3238
12. Horowitz P, Hill W (1989) The art of electronics, 2nd edn. Cambridge University Press, New York
13. Arnau A, Sogorb T, Jimenez Y (2002) Rev Sci Instrum 73:2724
14. Schumacher R (1990) Angew Chem Int Ed Engl 29:329
15. Bruckenstein S, Shay M (1985) J Electroanal Chem Interfacial Electrochem 188:131
16. Buttry DA, Ward MD (1992) Chem Rev 92:1335
17. Laschitsch A, Menges B, Johannsmann D (2000) Appl Phys Lett 77:2252
18. Kim JM, Chang SM, Muramatsu H (1999) Appl Phys Lett 74:466
19. Bund A, Schneider O, Dehnke V (2002) Phys Chem Chem Phys 4:3552
20. Ducker WA, Senden TJ, Pashley RM (1991) Nature 353:239
21. Butt HJ (1991) Biophys J 60:1438
22. Bottom VE (1982) Introduction to quartz crystal unit design. Van Nostrand Reinhold, New York
23. Goka S, Okabe K, Watanabe Y, Sekimoto H (2000) Jpn J Appl Phys 1 39:3073
24. Lin ZX, Ward MD (1995) Anal Chem 67:685
25. Eggers F, Funck Th (1987) J Phys E Sci Instrum 20:523
26. EerNisse EP (2001) Jpn J Appl Phys 1 40:3479
27. Heusler KE, Grzegozewski A, Jäckel L, Pietrucha J (1988) Ber Bunsenges Phys Chem 1218:92
28. Daikhin L, Gileadi E, Katz G, Tsionsky V, Urbakh M (2002) Anal Chem 74:554
29. Martin SJ, Frye GC, Ricco AJ (1993) Anal Chem 65:2910
30. McHale G, Lucklum R, Newton MI, Cowen JA (2000) J Appl Phys 88:7304
31. Zhang C, Vetelino JF (2003) Sens Actuators B 91:320
32. Shana ZA, Josse F (1994) Anal Chem 66:1955
33. Martin F, Newton MI, McHale G, Melzak KA, Gizeli E (2004) Biosens Bioelectron 19:627
34. Gulyaev YV (1998) IEEE Trans Ultrason Ferroelectr Freq Control 45:935
35. Fritze H, Tuller HL (2001) Appl Phys Lett 78:976
36. Elam JW, Pellin MJ (2005) Anal Chem 77:3531

37. Johannsmann D, Mathauer K, Wegner G, Knoll W (1992) Phys Rev B 46:7808
38. Pax M, Rieger J, Eibl RH, Thielemann C, Johannsmann D (2005) Analyst 130:1474
39. Berg S, Johannsmann D (2003) Phys Rev Lett 91:145505
40. Edvardsson M, Rodahl M, Kasemo B, Hook F (2005) Anal Chem 77:4918
41. Reviakine I, Morozov AN, Rosetti FF (2004) J Appl Phys 95:7712
42. Nakamoto T, Moriizumi T (1990) Jpn J Appl Phys 29:963
43. Bandey HL, Martin SJ, Cernosek RW, Hillman AR (1999) Anal Chem 71:2205
44. Lucklum R, Behling C, Hauptmann P (1999) Anal Chem 71:2488
45. Benes E (1984) J Appl Phys 56:608
46. Friedt JM, Choi KH, Francis L, Campitelli A (2002) Jpn J Appl Phys 1 41:3974
47. Borovikov VV, Dialnyan RA, Shmyt'ko IM (1987) Sov Phys Tech Phys 32:325
48. Stevens SD, Tiersten HF (1986) J Acoust Soc Am 79:1811
49. Wu DH, Chien WT, Tsai YJ (2005) IEEE Trans Ultrason Ferroelectr Freq Control 52:480
50. Lin ZX, Ward MD (1995) Anal Chem 67:685
51. Schneider TW, Martin SJ (1995) Anal Chem 67:3324
52. Thurston RN, McSkimin HJ, Andrea CP (1966) J Appl Phys 37:267
53. IEC standard 60444-1
54. Reed CE, Kanazawa KK, Kaufmann JH (1990) J Appl Phys 68:1993
55. Mason WP (1948) Piezoelectric crystals and their applications to ultrasonics. Van Nostrand, Princeton
56. Tiersten HF (1963) J Acoust Soc Am 35:234
57. Alig I, Lellinger D, Sulimma J, Tadjbakhsch S (1997) Rev Sci Instrum 68:1536
58. Mason WP, Baker WO, McSkimin HJ, Heiss JH (1949) Phys Rev 75:936
59. Azzam RMA, Bashara NM (1987) Ellipsometry and polarized light. Elsevier, Amsterdam
60. Knoll W (1997) In: Hummel RE, Wißmann P (eds) Handbook of optical properties, vol II. CRC, Boca Raton, p 373
61. Satomaki M, Loikas K, Kankare J (2003) Anal Chem 75:5895
62. Lucklum R, Hauptmann P (2003) Meas Sci Technol 14:1854
63. Munn RW (1973) J Phys C Solid State Phys 6:3213
64. Rosenbaum JF (1988) Bulk acoustic wave theory and devices. Artech House, Boston, p 376
65. Bandey HL, Martin SJ, Cernosek RW, Hillman AR (1999) Anal Chem 71:2205
66. Henderson J (1991) Electronic devices, concepts, and applications. Prentice Hall, New Jersey, p 357
67. Laschitsch A, Johannsmann D (1999) J Appl Phys 85:3759
68. Stockbridge CD (1966) Vacuum microbalance techniques, vol 5. Plenum, New York
69. Borovikov AP (1976) Instrum Exp Tech 19:223
70. Kanazawa KK, Gordon JG II (1985) Anal Chim Acta 99:175
71. Mason WP (1948) J Colloid Sci 3:147
72. Ferry JD (1980) Viscoelastic properties of polymers. Wiley, New York
73. Du B, Gubaidoulline I, Johannsmann D (2004) Langmuir 20:10614
74. Flanigan CM, Desai M, Shull KR (2000) Langmuir 16:9825
75. Shull KR (2002) Mater Sci Eng R 36:1
76. de Gennes JP, Prost J (1993) The physics of liquid crystals, Chap. 5.2.2. Oxford University Press, Oxford
77. Jérôme B (1991) Rep Prog Phys 54:391
78. Gupta VK, Skaife JJ, Dubrovsky TB, Abbott NL (1998) Science 279:2077
79. Muramatsu H, Iwasaki F (1995) Mol Cryst Liq Cryst 258:153

80. Domack A, Johannsmann D (2002) Appl Phys Lett 80:4750
81. Kiry F, Martinoty P (1977) J Phys Paris 38:153
82. Martinoty P, Candau S (1971) Mol Cryst Liq Cryst 14:243
83. Parodi O (1970) J Phys Paris 31:581
84. Huang JS, Varadaraj R (1996) Curr Opin Colloid Interface Sci 1:535
85. Bell J, Köhler T, Woermann D (1997) Ber Bunsenges Phys Chem 101:879
86. Lionberger R, Russel WB (1994) J Rheol 38:1885
87. Fritz G, Pechhold W, Willenbacher N, Wagner NJ (2003) J Rheol 47:303
88. Wagner NJ (1993) J Colloid Interface Sci 161:169
89. Granstaff VE, Martin SJ (1994) J Appl Phys 75:1319
90. Martin SJ, Bandey HL, Cernosek RW, Hillman AR, Brown MJ (2000) Anal Chem 72:141
91. Domack A, Prucker O, Rühe J, Johannsmann D (1997) Phys Rev E 56:680
92. Voinova MV, Rodahl M, Jonson M, Kasemo B (1999) Phys Scripta 59:391
93. Kunze M, Shull KR, Johannsmann D (2006) Langmuir 22:169
94. Johannsmann D (1999) Macromol Chem Phys 200:501
95. Voinova MV, Jonson M, Kasemo B (2002) Biosens Bioelectron 17:835
96. Kankare J (2002) Langmuir 18:7092
97. Du B, Johannsmann D (2004) Langmuir 20:2809
98. Russell TP (1990) Mater Sci Rep 5:171
99. Myszka DG (2000) Methods Ezymol 323:325
100. Pockrand I (1978) Surf Sci 72:577
101. Plunkett MA, Wang Z, Rutland MW, Johannsmann D (2003) Langmuir 19:6837
102. Voinova MV, Jonson M, Kasemo B (2002) Biosens Bioelectron 17:835
103. Neto C, Evans DR, Bonaccurso E, Butt HJ, Craig VS (2005) Rep Prog Phys 68:2859
104. Johannsmann D (2001) J Appl Phys 89:6356
105. Cady WG (1946) Piezoelectricity. McGraw Hill, New York
106. http://www.ieee-uffc.org/freqcontrol/quartz/vig/vigtoc.htm
107. Borovski B, Mason BL, Krim J (2000) J Appl Phys 88:4017
108. Kanazawa KK (1997) Faraday Discuss 107:77

Springer Ser Chem Sens Biosens (2007) 5: 111–149
DOI 10.1007/5346_025

Published online: 15 July 2006

Probing the Solid/Liquid Interface with the Quartz Crystal Microbalance

M. Urbakh (✉) · V. Tsionsky · E. Gileadi · L. Daikhin

School of Chemistry, Raymond and Beverly Sackler Faculty of Exact Sciences,
Tel-Aviv University, 69978 Ramat-Aviv, Israel
urbakh@post.tau.ac.il

Abstract In this chapter we discuss the results of theoretical and experimental studies of the structure and dynamics at solid–liquid interfaces employing the quartz crystal microbalance (QCM). Various models for the mechanical contact between the oscillating quartz crystal and the liquid are described, and theoretical predictions are compared with the experimental results. Special attention is paid to consideration of the influence of slippage and surface roughness on the QCM response at the solid–liquid interface. The main question, which we would like to answer in this chapter, is what information on

the structure and dynamics at the solid–liquid interface can be extracted from the QCM measurements. In particular, we demonstrate that the quartz crystal resonator acts as a true microbalance only if, in the course of the process being studied, the nature of the interface (its roughness, slippage, the density and viscosity of the solution adjacent to it, and the structure of the solvent in contact with it) is maintained constant.

So far most of the QCM data were analyzed on a qualitative level only. The next step in QCM studies requires a quantitative treatment of the experimental results. Theoretical basis for the solution of this problem already exists, and has been discussed in this review. Joint experimental and theoretical efforts to elevate the QCM technique to a new level present a challenge for future investigators.

Keywords Quartz crystal microbalance · Roughness · Slippage · Thin films

Abbreviations

a	Ratio of the slip length to the liquid decay length, b_s/δ
AFM	Atomic force microscope
C_m	Mass sensitivity of the QCM, $\frac{2f_0^2}{\sqrt{\mu_q \rho_q}}$
C_η	Sensitivity of the QCM operating in contact with a liquid, $\frac{f_0^{3/2}}{\sqrt{\pi \mu_q \rho_q}}$
d	Thickness of the quartz crystal
EQCM	Electrochemical quartz crystal microbalance
f	Frequency
f_0	Fundamental frequency of the resonator
$g(\boldsymbol{K})$	Correlation function for surface roughness
h	Root mean square height of a roughness
k	Wave vector of shear waves in quartz, $\omega\sqrt{\rho_q/\mu_q}$
l	Correlation length of surface roughness
d_f	Thickness of the liquid film
L	Thickness of interfacial layer
MD	Molecular dynamics
$P(\boldsymbol{r}, \omega)$	Pressure in a liquid
QCM	Quartz crystal microbalance
R	Hydrodynamic roughness factor
$\tilde{R}$	Electrochemical roughness factor
$\boldsymbol{r} = (z, \boldsymbol{R})$	Coordinates (normal and lateral)
SFA	Surface force apparatus
STM	Scanning tunneling microscope
$u(z, \omega)$	Amplitude of the shear displacements of the quartz
$u_f(\omega)$	Displacements of the homogeneous surface film
$v_f(t)$	Film velocity
$v_{f0}(\omega)$	Amplitude of film velocity
$v_q(t)$	Velocity of the quartz surface
$v_{q0}(\omega)$	Amplitude of the quartz surface velocity
$v_a(\omega)$	Velocity of absorbed later
$v_l(\omega)$	Liquid velocity at the interface
Z_L	Mechanical impedance of the contacting medium
Z_q	Mechanical impedance of quartz crystal
$\Delta\Gamma$	Half-width of the resonance

$\Delta\Gamma_l$	Half-width of the resonance for quartz crystal resonator contacting a semi-infinite liquid
Γ_a, Γ_m	Surface excess and maximum surface excess of adsorbate
δ	Velocity decay length in a liquid, $\delta = \sqrt{\eta/\pi\rho f_0}$
$\Delta\gamma$	Change of surface tension
Δf	Resonant frequency shift
Δf_m	Mass-induced resonant frequency shift
Δf_η	Viscosity-induced resonant frequency shift
Δf_P	Pressure-induced resonant frequency shift
Δf_R	Roughness-induced resonant frequency shift
Δf_{sl}	Slippage-induced resonant frequency shift
Δf_T	Resonant frequency shift due to change of temperature
Δf_l	Frequency shift for quartz resonator contacting a semi-infinite liquid
Δm_f	Surface mass density of a film
Δm_a	Average surface density of the adsorbed atoms
$\overline{\Delta m_f}$	Average surface mass density
Δm_1	Root mean square deviation of the mass distribution
$\varepsilon_{ls}, \varepsilon_{ll}$	Energy of liquid–substrate and liquid–liquid interactions
$\varepsilon_{la}, \varepsilon_{aa}, \varepsilon_{as}$	Energy of adsorbate–liquid, adsorbate–adsorbate and adsorbate–substrate interactions
η	Viscosity of a liquid
η_f	Viscosity of the liquid film
b_s	Slip length
b_s^{eff}	Effective slip length
λ_q	Wave length of shear-mode quartz oscillations
μ_q	Shear modulus of the quartz crystal
$\xi(\boldsymbol{R})$	Surface profile
ξ_H	Permeability of interfacial layer
ρ	Density of a liquid
ρ_q	Density of the quartz crystal
ρ_f	Density of the liquid film
ρ_s	Density of solid
τ_s	Slip time
ϕ	Porosity of interfacial layer
χ	Coefficient of sliding friction
ω	Angular frequency
ω_0	Fundamental angular frequency, $\omega_0 = 2\pi f_0$

1 Introduction

The literature concerning the quartz crystal microbalance (QCM) and its electrochemical analog, the electrochemical EQCM, is wide and diverse. Many reviews are available in the literature, discussing the fundamental properties of this device and its numerous applications, including its use in electrochemistry [1–7]. In this chapter we focus on the effect of interfacial properties on the QCM response, specifically when the device is immersed in a liquid.

When the quartz crystal microbalance was first introduced in 1959 [8], it represented a major step forward in our ability to weigh matter. Until then, routine measurements allowed a sensitivity of 0.1 mg, and highly sensitive measurements could be made with an accuracy limit of 0.03 μg, under well-controlled experimental conditions [9]. The QCM extended the sensitivity by two or three orders of magnitude, into the sub-nanogram regime.

Even when used in vacuum or in an inert gas at ambient pressure, the QCM acts as a balance only under certain conditions, as discussed below. Under these conditions the change of mass caused by adsorption or deposition of a substance from the gas phase can be related directly to the change of frequency, by the simple equation derived by Sauerbrey [8].

Generally this is not the case, and the frequency shift observed could more appropriately be expressed by a sum of terms of the form:

$$\Delta f = \Delta f_{\mathrm{m}} + \Delta f_{\eta} + \Delta f_{\mathrm{P}} + \Delta f_{\mathrm{R}} + \Delta f_{\mathrm{sl}} + \Delta f_{\mathrm{T}} \,, \tag{1}$$

where the different terms on the right hand side of this equation represent the effects of mass loading; viscosity and density of the medium in contact with the vibrating crystal; the hydrostatic pressure; the surface roughness; the slippage effect, and the temperature, respectively, and the different contributions can be interdependent. These effects become of major importance particularly when small changes of frequency, associated with sub-monolayer phenomena, are considered. Some of these factors will be discussed in this chapter.

1.1 Applications of the Quartz Crystal Microbalance

The most common commercial use of the QCM is as a thickness gauge in thin-layer technology. When used to monitor the thickness of a metal film during physical or chemical vapor deposition, it acts very closely as a nanobalance, providing a real-time measurement of the thickness. Indeed, devices sold for this purpose are usually calibrated in units of thickness (having a different scale for each metal, of course), and claim a sensitivity of less than 0.1 nm, which implies a sensitivity of less than a monolayer.

The other common application of the QCM is as a nanosensor proper, made sensitive to one gas or another by suitable surface treatment. Selecting the suitable coating on the electrodes of the QCM can determine selectivity and enhance sensitivity. It is not our purpose to discuss sensors in the present review. It should only be pointed out that any such sensor would have to be calibrated, since the Sauerbrey equation would not be expected to apply quantitatively.

1.2 Applications for Gas-Phase Adsorption

The high sensitivity of the QCM should make it an ideal tool for the study of adsorption from the gas phase. We note that the number of sites on the surface of a metal is typically of the order of 10^{15} cm^{-2}, hence a monolayer of a small adsorbate, occupying a single site, would be about 2 nmol cm^{-2}. A monolayer of water would therefore weigh about 40 ng cm^{-2}, while a monolayer of pyridine would weigh 30–60 ng cm^{-2}, depending on its orientation on the surface. Comparing these numbers with the sensitivity of 2 ng cm^{-2} shows that adsorption isotherms could be measured in the gas phase, employing the QCM. This has not been done properly until relatively recently, mainly because the device was treated as a microbalance, i.e., it was assumed that the Sauerbrey equation could be applied, and several important terms in Eq. 1 were ignored. Obtaining adsorption isotherm one has to change the pressure over a wide range. Therefore the changes of properties of the surrounding gas cannot be ignored. This shortcoming was overcome by the present authors [10] who developed the *supporting gas method*. When this method is employed, the overall pressure is maintained constant by a large excess of an inert gas, and the frequency shift of the QCM is measured as a function of the partial pressure of the material being investigated. In this manner all terms in Eq. 1, other than Δf_m, are essentially zero and the device acts as a true nanobalance.

1.3 Use of the QCM in Liquids

It was not initially obvious that the quartz crystal resonator would operate in liquids, until this was proven experimentally [11, 12]. The term associated with the influence of the viscosity, η, and density, ρ, of liquid in Eq. 1 can be written [13] as:

$$\Delta f_\eta = - C_\eta \left(\eta\rho\right)^{1/2} \ . \tag{2}$$

Since the product of $\sqrt{\eta\rho}$ in liquids is about two orders of magnitude higher than in gases at ambient pressure, the crystal is heavily loaded when transferred from the gas phase into a liquid.

Once the door had been opened to its use in liquids, the potential of the QCM for interfacial electrochemistry was obvious, and the EQCM became popular.

When a QCM, with fundamental frequencies 6–10 MHz, is placed in contact with a dilute aqueous solution, the frequency should shift to lower values by about 0.8–1.2 kHz according to Eq. 2. In practice the observed shift is larger by 1–2 kHz, depending on the surface roughness. The effect of roughness is also related indirectly to viscosity and density, since the hydrodynamic

flow regime at the surface is altered as a result of roughness [14–16]. Roughness is a major issue in the interpretation of the response of the QCM in liquids, and it is discussed in some detail in the following sections.

1.4 Impedance Spectrum of the EQCM

In early studies of the QCM and the EQCM, only the resonance frequency was determined, and conclusions were drawn, based on the shift of frequency. Unfortunately, in many cases this shift was attributed to mass loading alone, and it was used to calculate the weight added or removed from the surface, disregarding other factors that affect the frequency. In the past decade more and more laboratories expanded such studies to include measurements of the impedance spectrum of the crystal [17–28]. This provides an additional experimental variable that can obviously yield further information and deeper understanding of the structure of the interface. For instance, a variation of the resonance width provides an unambiguous proof that mechanisms other than mass loading are also involved.

The properties of the impedance spectrum are discussed in detail in Chap. 2 in this volume. Here we present only a relation between the resonant frequency and the mechanical impedance of the medium contacting the quartz surface, Z_L. The latter is defined as the ratio of the shear stress acting on the contact medium to the surface velocity [6]. Under the experimental conditions when the surface loading is relatively small, the shift of the resonant frequency with respect to the resonant frequency of the unloaded quartz crystal, f_0, can be written as [14, 29]:

$$\Delta\tilde{f} \equiv \Delta f + i\Delta\Gamma = i\frac{f_0}{\pi}\frac{Z_L}{Z_q}, \tag{3}$$

where Z_q is the acoustic impedance of an AT-cut quartz.

It should be noted that the frequency shift $\Delta\tilde{f}$ can be a complex number, and its imaginary part, $\Delta\Gamma$, reflects the half-width of the resonance. Equation 3 shows that the complex frequency shift $\Delta\tilde{f}$ contains the same information as the mechanical impedance Z_L.

In order to analyze the influence of the different loading mechanisms on the QCM response one has to model a dependence of the mechanical impedance Z_L or the complex resonance frequency shift on the chemical and physical properties of the contacting medium. Various models for the mechanical contact between the oscillating quartz crystal and the outer medium are discussed below. The QCM is now so widely and extensively used that, in the framework of this chapter, it is not possible to review all the available literature. Hence we limited ourselves here to a review of the experimental data and theoretical ideas concerning the studies of structure and interaction at solid–liquid interface. Furthermore, we did not present here studies on

adsorption, metal deposition, and kinetics with the help of the QCM. These topics are well described in previous reviews ([1, 2, 6], and in many articles published in readily accessible journals). The problems of the interpretation of the QCM response caused by changes taking place at the solid–liquid interface are obviously of first priority, especially for studies in electrochemistry.

2
Effect of Thin Surface Films

2.1
Film Rigidly Attached to the Surface

First we consider the effect of a thin film, rigidly attached to an ideally flat crystal surface, on the response of the quartz crystal resonator (Fig. 1).

For a homogeneous thin film with a thickness smaller than the wavelength of the shear oscillations, the shift of the resonance frequency can be expressed in terms of the change in surface mass density of the film, Δm_f, (in units g cm^{-2}). This was given by Sauerbrey [8] as:

$$\Delta f = - C_m \Delta m_f \,, \tag{4}$$

where $C_m = 2f_0^2/(\mu_q \rho_q)^{1/2}$ and ρ_q and μ_q are the density and shear modulus of quartz. Equation 4 can be derived by supplementing the wave equation, which describes displacements in the quartz crystal, with the Newtonian equation of motion for the surface film [6]. Equation 4 shows that the addition of mass rigidly attached to the surface of the quartz crystal resonator leads to a decrease of the resonant frequency, but it does not influence the width of

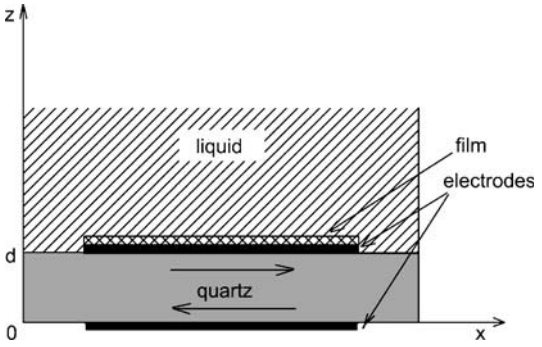

Fig. 1 Schematic presentation of the quartz crystal resonator in contact with a liquid. The contacting medium is a thin film rigidly attached to the crystal surface from one side, at $z = d$. The opposite surface of the crystal ($z = 0$) is unconstrained. d is the thickness of the quartz crystal

the resonance. The constant C_m in Eq. 4 can differ from the theoretical value given above due to effects of non-uniform mass distribution, roughness, etc. Therefore one is well advised to calibrate the QCM.

It should be noted that Eq. 4 is valid only for thin films for which the thickness is much smaller than the wave length of the shear mode oscillations. In this case the frequency shift is determined by the inertial force of the film acting on the quartz surface. For thicker films effects of elasticity or viscoelasticity become important and Eq. 4 should be modified essentially [30].

A question arises whether an inhomogeneous mass distribution would lead to an additional shift of frequency and/or to a broadening of the resonance, compared to the result given by the Sauerbrey equation? It was shown [6] that in the case of inhomogeneous mass distribution splitting of the resonant frequency can occur, and the frequency shift can be estimated as:

$$\Delta f = - \frac{2f_0^2}{\sqrt{\rho_q \mu_q}} [\overline{\Delta m}_f \pm \Delta m_1] , \tag{5}$$

where Δm_1 is the root mean square deviation of the mass density from the average value $\overline{\Delta m}_f$. In contrast to the case of uniform mass loading, where $\Delta m_1 = 0$, two values of the resonance frequency are derived. This effect can be simulated by a simple equivalent circuit consisting of two Butterworth–Van Dyke [31–33] circuits in series with the inductances corresponding to the two different values of the surface mass densities, $\overline{\Delta m}_f + \Delta m_1$ and $\overline{\Delta m}_f - \Delta m_1$. Due to overlap of these two resonance states, splitting can lead to an apparent broadening of the resonance, which will have an effective half-width of the order of $f_0^2 \Delta m_1 / \pi (\mu_q \rho_q)^{1/2}$. For the 6 MHz quartz resonator this broadening effect becomes important when the correlation length of the mass distribution is larger than 0.02 cm.

2.2 Slippage at the Interface Between a Thin Film and a Solid

The Sauerbrey equation shows that a thin uniform film rigidly attached to the quartz surface does not influence the width of the mechanical resonance. However, it was experimentally shown for a number of systems that adsorption on the quartz surface produced both a shifts of frequency and an increase of the width of the resonance [34–38]. This phenomenon can be explained, assuming slippage at the adsorbate–substrate interface.

Slippage occurs as a result of the force of inertia acting on the adsorbate during the vibrational motion of the crystal. The force of inertia, $\boldsymbol{F}$, is extremely weak ($\sim 10^{-13}$ dyne per atom) [39] and cannot, by itself, move an adsorbed species over the lateral energy barriers of the adsorbate–substrate potential [39]. However, this force decreases the barriers in the direction of $\boldsymbol{F}$ that leads to a thermally activated drift of the adsorbate in the direction oppo-

site to the motion of the crystal surface. As a result, the instantaneous velocity in the adsorbate layer can differ from the velocity of the surface of the quartz crystal resonator.

The slippage at the interface between a thin film of density Δm_f and the substrate is usually described in terms of an interfacial friction coefficient ("coefficient of sliding friction"), χ. This coefficient determines the stress acting between the film and the substrate, which move at different velocities. An infinite value of χ implies that the non-slip (sticking) boundary condition is applicable. When the interfacial friction coefficient equals zero, the film is free to slide with no energy dissipation.

The motion of the adsorbed film on the oscillating quartz surface can be described by Eq. 6:

$$\Delta m_f \frac{d}{dt} v_f(t) = -\chi [v_f(t) - v_q(t)] , \tag{6}$$

where $v_q(t) = v_{q0}(\omega) \exp(i\omega t))$ and $v_f(t) = v_{f0}(\omega) \exp(i\omega t)$ are the velocities of the crystal surface and of the film. Simultaneous solution of the wave equation in the quartz crystal and the equation of motion (Eq. 6) for the adsorbed film yields the following expressions for the changes of the frequency, Δf, and the half-width of the resonance,$\Delta \Gamma$:

$$\Delta f = -\frac{2f_0^2 \Delta m_f}{\sqrt{\rho_q \mu_q}} \left[\frac{\chi^2}{\chi^2 + (2\pi f_0 \Delta m_f)^2} \right] \tag{7}$$

$$\Delta \Gamma = \frac{2f_0^2 \Delta m_f}{\sqrt{\rho_q \mu_q}} \left[\frac{2\pi f_0 \Delta m_f \chi}{\chi^2 + (2\pi f_0 \Delta m_f)^2} \right] . \tag{8}$$

Note that:

$$\frac{\Delta \Gamma}{\Delta f} = -2\pi f_0 \frac{\Delta m_f}{\chi} . \tag{9}$$

Thus, the interfacial friction can be evaluated from measurement of $\Delta \Gamma$ and Δf. This procedure has been applied to a number of systems in which weak physical adsorption occurs, such as the adsorption of Xe, Kr, N_2 on Au, and of H_2O and C_6H_{12} on Ag [34–38]. In all the above cases slippage was observed, and the ratio of the coefficient of sliding friction to the mass density was of the order $\chi/\Delta m_f = (10^8 - 10^9)\,s^{-1}$. As an example, the frictional stress acting on the monolayer Xe film sliding on a Ag(111) surface at a velocity $v = 1\,cm\,s^{-1}$, $F = \chi v$, equals about $10\,Nm^{-2}$ [40]. It is much smaller than typical shear stresses involved in sliding of a steel block on a steel surface under boundary lubrication condition (Eq. 6), which is of order $\approx 10^8\,Nm^{-2}$ [39].

The effect of slippage at a substrate–film interface can also be described in terms of slip time [39]. To understand the physical meaning of the slip time, one can consider an adsorbate film on a substrate, moving at constant velocity. If the substrate stops, the velocity and momentum of the film decay exponentially, and the time constant of this process is the slip time. If this process is very rapid, i.e., we have a rigidly adsorbed film, the time constant will be close to zero, and there will be no noticeable slip. The slip time is related to the interfacial friction coefficient through the equation [39]:

$$\tau_s = \Delta m_f / \chi \, . \tag{10}$$

In a recent paper [41] the dependence of the slip time, τ_s, on the amplitude of the crystal surface oscillations, A, and on the surface coverage was investigated. The results refer to the absorption of krypton atoms on gold at 85 °K. It was found that there is a step-like transition between a low-coverage region, where slippage exists at the solid–film interface, and a high-coverage region where the film is locked to the surface. The transition occurs at different coverage depending on the amplitude, A. Independent of coverage, the film is attached rigidly to the surface for $A \leq 0.18$ nm and slides for $A > 0.4$ nm. In the region of sliding at small coverages the values of the slip time are in the interval 2–10 ns, for $0.18 \text{ nm} < A < 0.4$ nm.

3
Quartz Crystal Operating in Contact with a Liquid

3.1
General Considerations

When a quartz crystal resonator operates in contact with a liquid, the shear motion of the surface generates motion in the liquid near the interface. The velocity field, $\boldsymbol{v}(\boldsymbol{r}, \omega)$, related to this motion in a semi-infinite Newtonian liquid is described by the linearized Navier–Stokes equation:

$$i\omega\rho\boldsymbol{v}(\boldsymbol{r}, \omega) = -\nabla P(\boldsymbol{r}, \omega) + \eta\Delta\boldsymbol{v}(\boldsymbol{r}, \omega) \, , \tag{11}$$

where $P(\boldsymbol{r}, \omega)$, η and ρ are pressure, viscosity, and density of the liquid. Under the typical conditions of the QCM experiments, where the shear velocities are much smaller than the sound velocity in the liquid, the displacement of the crystal does not generate compressional waves and a liquid can be considered to be incompressible. If the surface is sufficiently smooth, the quartz oscillations generate plane-parallel laminar flow in the liquid, as shown in Fig. 2. The velocity field obtained as the solution of Eq. 11 for a flat surface has the form:

$$v_x(z) = v_{q0}(\omega) \exp[-(1 + i)z/\delta] \, , \tag{12}$$

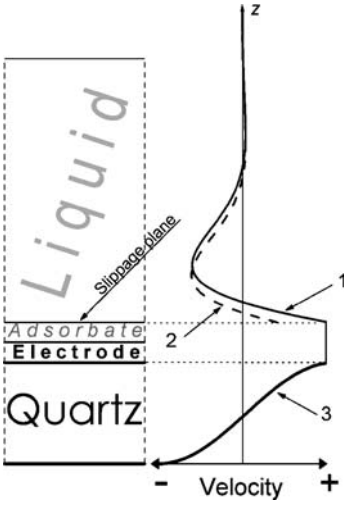

Fig. 2 System geometry and velocity profiles. *Curves 1* and *2* represent the velocity distributions at the liquid–adsorbate interface without and with slippage, respectively. *Curve 3* is the velocity distribution in the quartz. The thickness of various layers is not drawn to scale

where $v_{q0}(\omega)$ is the velocity of the liquid at the surface, and $\delta = \sqrt{2\eta/\omega_0\rho}$. Equation 12 represents a damped shear wave radiating into the liquid from the surface of the oscillating resonator. δ is the velocity decay length of this shear wave, which lies between 250 and 177 nm for dilute aqueous solutions at room temperature, for crystals having a fundamental frequency in the range 5–10 MHz. Damping of the shear wave has a number of important consequences. First, it ensures that the quartz crystal can operate in liquids, the losses in the liquid being limited by the finite depth of penetration. Secondly, a small portion of the liquid is coupled to the crystal motion and a frequency decrease is observed. Thirdly, the viscous nature of motion gives rise to energy losses, which are sensed by the resonator, both as a decrease in frequency and as an increase in the width of the resonance.

3.2
Non-slip Boundary Condition

The response of the QCM at the solid–liquid interface can be found by matching the stress and the velocity fields in the medium in contact. It is usually assumed that the relative velocity at the boundary between the liquid and the solid is zero. This corresponds to the non-slip boundary condition. Strong experimental evidence supports this assumption on the macroscopic scales [42, 43]. In this case the frequency shift, Δf_l, and the half-width of the

resonance, $\Delta\Gamma_l$, can be written as follows [12, 13]:

$$\Delta f_l = -\frac{f_0^{3/2}\sqrt{\rho\eta}}{\sqrt{\pi\rho_q\mu_q}} \tag{13}$$

$$\Delta\Gamma_l = \frac{f_0^{3/2}\sqrt{\rho\eta}}{\sqrt{\pi\rho_q\mu_q}}\,. \tag{14}$$

Equations 13 and 14 show that the generation of a damped laminar flow in the liquid causes a decrease in the resonance frequency and an increase in the resonance width, which are both proportional to $\sqrt{\rho\eta}$. In contrast to the case of the mass loading where Δf is proportional to f_0^2, the liquid-induced response of the QCM is proportional to $f_0^{3/2}$.

It is interesting to note that for both a surface film rigidly attached to the resonator and a liquid in contact with the surface of the quartz crystal, the shift of the resonant frequency can be written in the same form, as:

$$\Delta f = -f_0\frac{\rho}{\rho_q}kh_{\text{eff}}\,. \tag{15}$$

Where $k = \omega_0\sqrt{\rho_q/\mu_q}$, ρ is the bulk density of the medium in contact with the vibrating surface of the solid, a film or a liquid, and h_{eff} is the thickness of the layer that responds to the quartz oscillations. In the case of the film, h_{eff} coincides with the thickness. For a semi-infinite liquid, h_{eff} presents a thickness of liquid involved in the motion and it should be taken as equal to $\delta/2$. The difference in the frequency dependence of the QCM response in the two cases is a result of the frequency dependency of δ. However, in contrast to the case of pure mass loading, the effect of a liquid results not only in a frequency shift but also in a broadening of the resonance.

3.3 Effect of a Thin Liquid Film at the Interface

The properties (the effective viscosity and density) of the liquid layer in close vicinity to the interface can differ from their bulk values. There are various reasons for these phenomena. For example, the structuring of a liquid induced by the substrate and a non-uniform distribution of species in the liquid near the substrate can influence significantly the properties of the liquid at the interface. The liquid properties change with distance from the interface, until the values corresponding to the bulk of solution have been reached. In order to simplify the description of this non-uniformity on the QCM, we assume here that a thin film of liquid, having different values of η_f and ρ_f, exists at the interface [44]. To calculate the effect of this film on the frequency shift,

one has to solve the wave equation for the elastic displacements in the quartz crystal simultaneously with the linearized Navier–Stokes equation for the velocities in the film and in the bulk liquid under standard non-slip boundary conditions.

Then the shift of the resonant frequency and the half-width of the resonance can be written as:

$$\Delta f = -\frac{f_0^{3/2}\sqrt{\rho\eta}}{\sqrt{\pi\mu_q\rho_q}} - \frac{2f_0^2}{\sqrt{\mu_q\rho_q}}\left[\rho(1-\frac{\eta}{\eta_f}) + (\rho_f - \rho)\right] d_f \tag{16}$$

$$\Delta\Gamma = \frac{f_0^{3/2}\sqrt{\rho\eta}}{\sqrt{\pi\mu_q\rho_q}} + \frac{2f_0^2}{\sqrt{\mu_q\rho_q}}\left[\rho(1-\frac{\eta}{\eta_f}) + (\rho_f - \rho)\right] \frac{d_f^2}{\delta}\,. \tag{17}$$

Here d_f and ρ_f are the thickness and the density of the film. These equations are valid in a particular case, when $d_f \ll \delta$. The general case for arbitrary d_f was given in [44]. The first terms in Eqs. 16 and 17 yield the liquid-induced frequency shift and half-width of the resonance in the absence of a film. The terms in brackets describe the influence of the viscosity and density of a film of thickness d_f. According to Eqs. 16 and 17, the ratio of the film-induced half-width to the film-induced frequency shift is proportional to d_f/δ. Thus, for $d_f/\delta \ll 1$, the contribution of the thin interfacial film to the width is much smaller than its contribution to the frequency shift. For $\eta_f \gg \eta$ the film acts as though it were rigidly attached to the surface: it causes a shift in frequency equal to that caused by its mass. The thin film model has been successfully used to describe the QCM response in electrochemical systems, which arises due to the effect of electrostatic adsorption of ions and the effect of electric field on viscosity inside the diffuse layer [44].

3.4
Slip Boundary Conditions

3.5
Slippage at Solid–Liquid Interface

Although the non-slip boundary condition has been remarkably successful in reproducing the characteristics of liquid flow on the macroscopic scale, its application for a description of liquid dynamics in microscopic liquid layers is questionable. A number of experimental [45–52] and theoretical [53, 54] studies suggest the possibility of slippage at solid–liquid interfaces. Recent reviews [55–57] summarize the results of these works. Here we focus on the effect of slippage on the QCM response.

The boundary condition is controlled by the extent to which the liquid "feels" a spatial corrugation in the surface energy of the solid. This depends

on a number of interfacial parameters, including the strength of the liquid–liquid and liquid–solid interactions, the commensurability of the substrate and the liquid structures, substrate and liquid densities, and also the roughness of the interface. In order to quantify the slippage effect, the slip length, b_s, is usually introduced [53, 58, 59]. The traditional non-slip boundary condition is replaced by:

$$\left.\frac{dv(z,\omega)}{dz}\right|_{z=0} = \frac{1}{b_s}(v(0,\omega) - v_{q0}(\omega)) , \tag{18}$$

where $v(z,\omega)$is the velocity in the liquid and $v_{q0}(\omega)$ is the velocity of the quartz crystal surface, $z = 0$. Equation 18 expresses the discontinuity of the velocity across the interface. For $b_s = 0$, Eq. 18 is reduced to the usual non-slip boundary condition: $v(d,\omega) = v_{q0}(\omega)$. The physical meaning of the slip length can be clarified by comparing velocity profiles for the non-slip and slip boundary conditions. These two profiles coincide when the non-slip boundary condition is imposed at the surface shifted inside the solid by the distance b_s with respect to the actual interface.

Basically two different types of experimental approaches have been used to study the boundary slip: local (direct) [45, 60] and effective (indirect) methods [49–52, 61]. The first group of methods is based on application of optical techniques using tracer particles or molecules to determine the flow field. These techniques have a resolution of less than 100 nm, so they cannot distinguish small differences in slip lengths. The effective methods assume the boundary conditions (Eq. 18) or similar ones to hold at the substrate surface and infer the slip length by measuring macroscopic quantities. These methods have been the most popular so far and they include atomic force microscopy (AFM), surface force apparatus (SFA), capillary techniques, and QCM.

The experimental studies involving different techniques report slip effects varying over more than two orders of magnitude, and with qualitatively different shear-rate dependence, for similar systems [55, 56]. Drastically different behaviors are reported for liquids wetting atomically smooth surfaces [45, 49, 55, 56, 62], for the influence of surface roughness [63, 64], and for the amplitude and rate dependence of boundary slip on hydrophobic surfaces [48–52]. There is no clear understanding why such large differences are obtained. A possible reason for the disagreement between the results obtained by different groups is a contamination of substrate surfaces by nanoparticles [49, 65]. Another parameter of obvious importance, which may explain such variability, is surface roughness. We discuss the effect of roughness on slippage in Sect. 5 of this chapter.

Within the QCM measurements the slip boundary condition (Eq. 18) results in the following equations for the resonant frequency shift and the

half-width of the resonance:

$$\Delta f = -\frac{f_0^2 \rho \delta}{\sqrt{\rho_q \mu_q}} \left[\frac{1}{(1 + b_s/\delta)^2 + (b_s/\delta)^2} \right] \approx -\frac{f_0^2 \rho \delta}{\sqrt{\rho_q \mu_q}} \left[1 - \frac{2 b_s}{\delta} \right] \tag{19}$$

$$\Delta \Gamma = \frac{f_0^2 \rho \delta}{\sqrt{\rho_q \mu_q}} \left[\frac{1 + 2\lambda/\delta}{(1 + b_s/\delta)^2 + (b_s/\delta)^2} \right] \approx \frac{f_0^2 \rho \delta}{\sqrt{\rho_q \mu_q}} \left[1 - \frac{2 b_s^2}{\delta^2} \right], \tag{20}$$

where the right hand side equalities are valid for small values of the slip length, $b_s/\delta \ll 1$. Equations 19 and 20 show that the influence of the slippage on the response of the QCM in liquid is determined by the ratio of the slip length b_s to the velocity decay length, δ. Even for a small value of $b_s \approx 1$ nm the slippage-induced correction to the frequency shift, Δf_{sl}, will be of the order of 6.5 Hz for the fundamental frequency of $f_0 = 5$ MHz. This value far exceeds the resolution of the QCM, but it is difficult to separate it from the overall QCM signal.

It should be noted that in QCM measurement interfacial properties are determined by averaging over the length scale δ. As a result one cannot distinguish between a true slip on the molecular level and an apparent hydrodynamic slip, which can arise from a shear thinning of the liquid near the surface. The latter leads to a steep velocity profile at the surface that appears as a slip, although the velocity is continuous at the surface. Indeed, a comparison between Eqs. 19–20 and Eqs. 16–17, which describe the effects of slip and surface film on the resonant frequency respectively, allow a relationship to be established between the apparent slip length and the film properties that give the same QCM response:

$$\frac{b_s}{\delta} = \left(\frac{\eta}{\eta_f} - \frac{\rho_f}{\rho} \right). \tag{21}$$

According to Eq. 21 the apparent boundary slip can be observed if the viscosity and/or density depends on the composition ($\eta \neq \eta_f$, $\rho \neq \rho_f$) and the less viscous and less dense fraction of the liquid wets the substrate better than the more viscous and the more dense one ($\eta > \eta_f$, $\rho > \rho_f$). It is also clear that there are two ways to obtain a large slip length. The first is by having a macroscopically thick boundary layer, since the slip length has the same order of magnitude as the thickness of this layer. The second is by providing large values of the viscosity and/or density contrast. Similar conclusions were reached in [66] for the Couette flow of liquid.

There were attempts [39] to estimate the slip length at the solid–liquid interface on the basis of QCM experiments for adsorbed liquid layers. The slip length can be expressed in terms of the coefficient of sliding friction, χ, at the

interface:

$$b_s = \frac{\eta}{\chi} . \tag{22}$$

Using the sliding friction coefficient $\chi = 3\,\mathrm{g\,cm^{-2}\,s^{-}}$, which is obtained for a monolayer of water on Ag in [35] and on Au in [67], a surprisingly high slip length of $b_s = 6 \times 10^4$ nm is obtained. Using this value for the interface between Au and bulk water, Eq. 19 yields for $f_0 = 5$ MHz a value of $\Delta f \approx 7 \times 10^{-3}$ Hz, which turns out to be smaller than that observed experimentally by a factor of 10^5. This inconsistency is most likely caused by a roughness of the electrode surface that reduces the effective slip length. Another reason could be the difference between friction at the solid–adsorbed layer and the solid–liquid interfaces. For example, a decrease of the slip length with increasing film thickness has been observed recently in QCM studies of Kr films on gold electrodes [41].

From a theoretical point of view, molecular dynamics simulations (MD) have shown [53, 66, 68] that the slip length is mostly determined by the ratio of characteristic energies of liquid–substrate, ε_{ls} and liquid–liquid ε_{ll} interactions, $b_s = f(\varepsilon_{ls}/\varepsilon_{ll})$. For the simple Lennard–Jones liquids wetting an atomically smooth surface, $\varepsilon_{ls}/\varepsilon_{ll} \geq 1$, slip length is negligible except at very high shear rate when the hydrodynamic boundary condition becomes nonlinear [53, 68]. It grows with the decrease of the parameter $\varepsilon_{ls}/\varepsilon_{ll}$. Substantial slip develops in non-wetting situations when the contact angle is larger than 90°, with slip lengths reaching 10–50 molecular sizes, and it depends on the pressure [59]. It should also be noted that, for a given value of $\varepsilon_{ls}/\varepsilon_{ll}$, the slip length is minimal when substrate and liquid molecules are of the same size, and increases with the increase of incommensurability of the sizes. For smaller coupling between the liquid and the substrate or incommensurability of their sizes, the spatial corrugation in the interfacial energy is weaker and interfacial slip can develop.

MD simulations and mode-coupling calculations [59, 68, 69] have shown that the magnitude of the hydrodynamic slippage can be correlated to the wettability of surfaces, which is characterized by a contact angle θ [59]:

$$\cos(\theta) = -1 + 2\frac{\rho_s}{\rho}\frac{\varepsilon_{ls}}{\varepsilon_{ll}} , \tag{23}$$

where ρ_s and ρ are the density of the solid and the liquid, respectively. Thus, the contact angle may be interpreted as a measure of the strength of interaction between the liquid and the solid, ε_{ls}. One expects a large value of the slip length for a non-wetting situation ($\cos(\theta) \to -1$), when ε_{ls} becomes much smaller than ε_{ll}. This conclusion is in agreement with several experimental observations [45, 70] reporting large slip lengths for partially wetting liquids.

An early model for molecular slip based on wetting properties has been suggested by Tolstoi [71] and extended in later publications [72]. This model

predicts a relation between the slip length and the contact angle in the form

$$b_s/\sigma = \exp\left[\alpha\sigma^2\gamma\left(1-\cos\theta\right)/k_BT\right]-1\,, \tag{24}$$

where σ is the molecular size, γ is the surface tension at the substrate–liquid interface and α is a geometric parameter of order one. According to Eq. 24 the slip length increases with the contact angle and can be orders of magnitude above the molecular length. However, the values predicted by Eq. 24 are usually much smaller than those measured experimentally. As well, Eq. 24 does not account for surface roughness or other surface properties.

The authors of [16, 73, 74] showed that surface treatments affecting liquid contact angle influence the response of quartz crystal resonator: resonant frequency changes caused by liquid loading were consistently smaller for surfaces having large liquid contact angles. These results were interpreted as arising from the onset of slippage at the solid–liquid interface: the solid–liquid interaction becomes sufficiently weak on a hydrophobic surface and shear displacement becomes discontinuous at the interface. However, this interpretation was called into question by a series of experiments, in which the effect of a hydrophobic monolayer was examined on devices with various surface roughness [14].

3.6
Slippage at the Adsorbate–Electrolyte Interface

Slippage is very sensitive to the molecular structure of the interface, as we have already discussed. Thus, adsorption can strongly influence this phenomenon. In order to describe the effect of adsorption, let it be assumed that the adsorbed layer is rigidly attached to the surface, and slippage occurs at the adsorbate–liquid interface, see Fig. 2. Then the equation of motion of the adsorbed layer can be written as [61]:

$$i\omega\Delta m_a v_a(\omega) = -\mu_q\frac{du(z)}{dz} - \chi(v_a(\omega)-v_l(\omega))\,,\quad \text{at}\quad z=d\,, \tag{25}$$

where $v_a(\omega)$ is the velocity of the adsorbed layer and Δm_a is its mass per unit area, while $v_l(\omega)$ is the velocity of the liquid at the interface, $z = d$. The first term on the right hand side of Eq. 25 describes the driving force acting on the adsorbed layer from the quartz crystal, while the second term accounts for the friction at the adsorbate–liquid interface.

The velocity fields in the crystal and the liquid are given by the solutions of the wave equation in the crystal and the linearized Navier–Stokes equation in the liquid, respectively. The solution of these equations and Eq. 25, with the boundary conditions for shear stresses and velocities, leads to the following equation for the shift of the resonant frequency, Δf, and the change of the

half-width of the resonance, $\Delta\Gamma$:

$$\Delta f = -\frac{2f_0^2\Delta m_a}{(\rho_q\mu_q)^{1/2}} - \frac{f_0^{3/2}(\rho\eta)^{1/2}}{(\pi\rho_q\mu_q)^{1/2}}\left[\frac{1}{(1+a)^2+a^2}\right] \tag{26}$$

$$\Delta\Gamma = \frac{f_0^{3/2}(\rho\eta)^{1/2}}{(\pi\rho_q\mu_q)^{1/2}}\left[\frac{(1+2a)}{(1+a)^2+a^2}\right]. \tag{27}$$

Writing Eqs. 26 and 27 we introduced a dimensionless parameter $a = \eta/\chi\delta = b_s/\delta$, which is the ratio of the slip length, $b_s = \eta/\chi$, and the velocity decay length in the liquid, δ. Equations 26 and 27 include both the interfacial (adsorption) and the bulk solution contributions to the response of the QCM, given by Eqs. 13 and 14. The latter remains constant in adsorption studies, and can be subtracted from the overall change given by Eqs. 26 and 27. As a result, the shift of the resonant frequency and the change of the half-width due to adsorption, which are measured experimentally, are given by the equations:

$$\Delta f - \Delta f_l \equiv \Delta f_m + \Delta f_{sl} = -\frac{2f_0^2\Delta m_a}{(\rho_q\mu_q)^{1/2}} + \frac{f_0^{3/2}(\rho\eta)^{1/2}}{(\pi\rho_q\mu_q)^{1/2}}\left[\frac{a(a+1)}{(1+a)^2+a^2}\right] \tag{28}$$

$$\Delta\Gamma - \Delta\Gamma_l = -\frac{2f_0^{3/2}(\rho\eta)^{1/2}}{(\pi\rho_q\mu_q)^{1/2}}\frac{a^2}{(1+a)^2+a^2}. \tag{29}$$

Equation 28 shows that there are two different contributions to the frequency shift, Δf_m and Δf_{sl}, which originate from: (i) a change of the mass of the adsorbed layer rigidly coupled to the surface (first term on the right hand side of Eq. 28), and (ii) partial decoupling between the quartz crystal oscillations and the solution, caused by slippage at the adsorbate–liquid interface (second term on the right hand side of Eq. 28). It should be stressed here that, in contrast to adsorption from the gas phase, adsorption from liquid phase can result in either a decrease or an increase of the resonant frequency, depending on its effect on the mass of the layer rigidly coupled to the surface and on changes of the coefficient of sliding friction, χ, which determined the slip length, according to Eq. 22.

Consider the effect of adsorption on the parameters Δm_a and χ. The layer adsorbed at the electrode–electrolyte interface contains two types of molecules: adsorbate and solvent. In the framework of mean field approximation, the effective interaction between the liquid and the adsorbed layer can be characterized by the energy $\varepsilon_{ls} \approx \varepsilon_{la}\boldsymbol{\Gamma}_a/\boldsymbol{\Gamma}_m + \varepsilon_{ll}(1 - \boldsymbol{\Gamma}_a/\boldsymbol{\Gamma}_m)$, where ε_{la} is the characteristic energy of the adsorbate–liquid interaction $\boldsymbol{\Gamma}_a$ and $\boldsymbol{\Gamma}_m$ are the surface excess and the maximum surface excess of the adsorbate, respectively. As a result, the slip length at the adsorbed layer–liquid interface can be

expressed as

$$b_s = f[(\varepsilon_{la}/\varepsilon_{ll})\boldsymbol{\Gamma}_a/\boldsymbol{\Gamma}_m + (1 - \boldsymbol{\Gamma}_a/\boldsymbol{\Gamma}_m)] \approx f(\varepsilon_{la}/\varepsilon_{ll})\boldsymbol{\Gamma}_a/\boldsymbol{\Gamma}_m\,, \tag{30}$$

showing an increase of b_s with $\boldsymbol{\Gamma}_a$ for $\varepsilon_{la}/\varepsilon_{ll} < 1$. Equation 30 is the interpolation formula that describes correctly the behavior of b_s for small $\boldsymbol{\Gamma}_a/\boldsymbol{\Gamma}_m$ and for $\boldsymbol{\Gamma}_a/\boldsymbol{\Gamma}_m = 1$. We note that, when the liquid and the adsorbate molecules are of significantly different size, the incommensurability between the structures of the adsorbed layer and the liquid grows with $\boldsymbol{\Gamma}_a$, which may lead to an additional enhancement of the slip length. What is important here is a relation between scales of corrugations of the potential energy in the solvent and the adsorbate molecules, rather than their physical size.

The foregoing discussion shows that for $\varepsilon_{la}/\varepsilon_{ll} < 1$ the parameter $a = b_s/\delta$, in Eqs. 28 and 29, characterizing the effect of slippage on the response of the QCM increases with $\boldsymbol{\Gamma}_a$. For instance, for $\varepsilon_{la}/\varepsilon_{ll} \approx 0.5$, it may reach values as high as $a \approx 10^{-2}$, for $\boldsymbol{\Gamma}_a \approx \boldsymbol{\Gamma}_m$. Correspondingly, the adsorption-induced slippage leads to a positive frequency shift, which grows with $\boldsymbol{\Gamma}_a$. This contribution can be larger than the effect of added weight. As a result, the overall frequency shift due to adsorption can be positive and increases with $\boldsymbol{\Gamma}_a$ [61]. It should be noted that, for small values of the parameter a, the effect of slippage on the resonance frequency shift is much larger than its effect on the width of the resonance (Eqs. 28 and 29). Also, slippage will always cause a decrease in the width of the resonance. Thus, if a positive shift of frequency with adsorption is to be associated with enhanced slippage, it should also be exhibited as a reduction of the width of the resonance, although the latter may be hard to detect experimentally.

The approach described above has been applied to treat experimental data on adsorption of pyridine from the electrolyte solutions [61]. Using Eq. 28 made it possible to determine the slip length as a function of surface excesses of pyridine. In agreement with the theoretical prediction, it was found that b_s grows with $\boldsymbol{\Gamma}_a$. The values of b_s did not exceed 0.3 nm and 1.2 nm for adsorption from butanol and water solutions, respectively. The dependence of slip length on surface excess was essentially linear (Eq. 30) for pyridine adsorption from butanol solution, but deviated from linearity for pyridine adsorption from water. The deviation was attributed to a reorientation of adsorbed pyridine molecules at the Au surface.

Above, we discussed the situation where the adsorbed layer is rigidly attached to the oscillating crystal surface, and there is finite slippage at the adsorbate–liquid interface. An alternative model, based on the assumption that slippage occurs at the crystal-adsorbed interface and non-slip boundary conditions apply to the adsorbate–liquid interface, can also be considered. For a small slip length, $b_s \ll \delta$, this model leads to the same results for the shift of the complex resonance frequency as the model discussed above and measurements employing the QCM cannot distinguish between them. How-

ever, in the case of specific adsorption, the assumption of slippage at the crystal-adsorbed layer interface is hard to justify, since the characteristic energy of adsorbate–substrate interactions, ε_{as}, is larger than the energy of adsorbate–adsorbate interactions, ε_{aa}, hence the corresponding slip length $b_s = f(\varepsilon_{as}/\varepsilon_{aa})$ is expected to be very small.

4
Quartz Crystals with Rough Surfaces Operating in Liquids

4.1
Theoretical Approaches

When the surface of a quartz crystal resonator is rough, the liquid motion generated by the oscillating surface becomes much more complicated than for the smooth surface. A variety of additional mechanisms of coupling between the acoustic waves in the solid and the motion in the liquid can arise. These may include generation of non-laminar motion, the conversion of in-plane surface motion to motion normal to the surface, and trapping of liquid by cavities and pores. It has been experimentally demonstrated [14, 17, 75–79] that the roughness-induced response of the QCM includes both the inertial and viscous contributions. Measurements of the complex shear mechanical impedance [14] were used to analyze different contributions to the roughness-induced response of the quartz resonator, and to correlate the experimental results with the surface roughness of the quartz resonator. Nevertheless, this subject is poorly developed, and the interpretation of experimental results can often be ambiguous.

The dependence of the QCM response on the morphology of the interface is determined by the relation between the characteristic sizes of roughness and the length scales of the shear modes in the liquid and the quartz resonator. The length scales in the liquid (the velocity decay length, δ) and in the crystal (wave length of the shear-mode oscillations, λ_q) are defined by the Navier–Stokes equation and by the wave equation for elastic displacement, respectively. For typical frequencies used in QCM experiments, $f_0 \approx 5$–10 MHz, the lengths $\delta = (\eta/\pi f_0 \rho)^{1/2}$ and $\lambda_q = (\mu_q/\rho_q)^{1/2} f_0^{-1}$ are of the order 0.177–0.25 μm and 0.03–0.1 cm, respectively.

The surface profile may be specified by a single valued function $z = \xi(\boldsymbol{R})$ of the lateral coordinates $\boldsymbol{R}$ that defines a local height of the surface with respect to a reference plane ($z = 0$). The latter is chosen so that the average value of $\xi(\boldsymbol{R})$ will equal zero. Surfaces used in QCM experiments may have various scales of roughness. In order to clarify this point, let us consider the two limiting cases: *slight* and *strong* roughness structures, which are schematically shown in Fig. 3. For the slight roughness (Fig. 3a) the "amplitude" of deviation from the reference plane $z = 0$ is much less than the lateral charac-

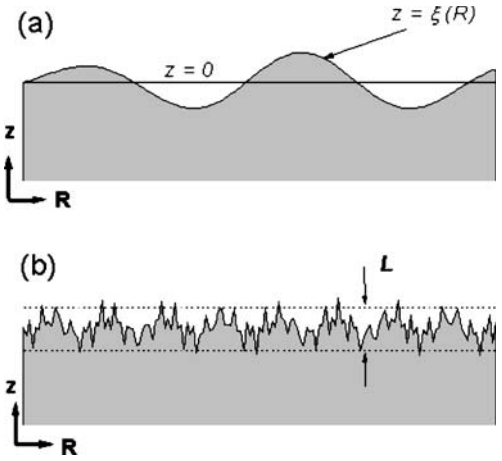

Fig. 3 Schematic representation of a slight (**a**) and a strong (**b**) roughness. The profile of slight roughness is described by the function $z = \xi(\boldsymbol{R})$. L is the effective thickness of the "porous" film that represents strong roughness. (From [27])

teristic length. In the case of strong roughness (Fig. 3b), the "amplitude" and "period" of repetitions are of the same order of magnitude.

In order to stress the multiscale nature of roughness, the profile function can be written as the sum of the functions that characterize the profile of the specific scale i:

$$\xi(\boldsymbol{R}) = \sum_i \xi_i(\boldsymbol{R}) \,. \tag{31}$$

For the calculation of the response of the QCM, the height–height pair correlation function is needed [80]. When rough structures having different scales do not correlate, the total correlation function can be written in the form:

$$\langle \xi(\boldsymbol{R}')\xi(\boldsymbol{R}' - \boldsymbol{R})\rangle = \sum_i \langle \xi_i(\boldsymbol{R}')\xi_i(\boldsymbol{R}' - \boldsymbol{R})\rangle \,, \tag{32}$$

where $\langle \xi_i(\boldsymbol{R}')\xi_i(\boldsymbol{R}' - \boldsymbol{R})\rangle$ is the correlation function for the scale i and $\langle \quad \rangle$ means averaging over the lateral coordinates. Usually one assumes that the correlation function $\langle \xi_i(\boldsymbol{R}')\xi_i(\boldsymbol{R}' - \boldsymbol{R})\rangle$ has a Gaussian form $\langle \xi_i(\boldsymbol{R}')\xi_i(\boldsymbol{R}' - \boldsymbol{R})\rangle = h_i^2 \exp(-|\boldsymbol{R}|^2 / l_i^2)$, where h_i is the root mean square height of the roughness and l_i is the lateral correlation length, which represents the lateral scale. Thus, the morphology of the rough surface can be characterized by a set of lengths [81].

It is impossible at the present time to provide a unified description of the response of the QCM for non-uniform solid–liquid interfaces with arbitrary geometrical structure. Below we summarize results obtained for the limiting cases of slight and strong roughness.

4.1.1 Slight Roughness

For slightly rough surfaces, the problem was solved in the framework of perturbation theory with respect to the parameters $|\nabla\xi(\boldsymbol{R})| \ll 1$ and $h/\delta \ll 1$, where h is the root mean square height of the electrode surface [80, 82]. The first condition means that the local slope of the interface is small, i.e., the height, h, is less than the lateral characteristic length (i.e., the correlation length, l) of the roughness.

For roughness described by a one-scale correlation function, the shift in the resonant frequency and the half-width of the resonance can be written in the following form [80, 82]:

$$\Delta f = -\frac{f_0^2\rho\delta}{(\rho_q\mu_q)^{1/2}}\left[1+\frac{h^2}{l^2}F(l/\delta)\right] \tag{33}$$

$$\Delta\Gamma = \frac{f_0^2\rho\delta}{(\rho_q\mu_q)^{1/2}}\left[1+\frac{h^2}{l^2}\Phi(l/\delta)\right]. \tag{34}$$

The scaling functions $F(l/\delta)$ and $\Phi(l/\delta)$ are expressed through the Fourier components of the height–height correlation function of the roughness $g(\boldsymbol{K})$ [82], which can be defined as:

$$h^2 g(\boldsymbol{K}) = \int \mathrm{d}\boldsymbol{R}\exp(-i\boldsymbol{K}\boldsymbol{R})\langle\xi(\boldsymbol{R}')\xi(\boldsymbol{R}'-\boldsymbol{R})\rangle\,. \tag{35}$$

The correlation function provides the most detailed characterization of the surface structure. Sometimes the surface roughness is described by an integral parameter, the roughness factor, R, which is the ratio between the true and the apparent (geometrical) surface area. For slight roughness, the roughness factor is expressed through the correlation function [82] as:

$$R = 1+\frac{h^2}{2}\int\frac{\mathrm{d}\boldsymbol{K}}{(2\pi)^2}g(\boldsymbol{K})K^2\,. \tag{36}$$

For the Gaussian random roughness $g(\boldsymbol{K}) = \pi l^2\exp(-l^2K^2/4)$ and Eq. 36 yield $R = 1+2h^2/l^2$.

It should be noted that the roughness factor, R, relevant to the operation of the QCM is not the same as the roughness factor commonly referred to in studies of adsorption and interfacial electrochemistry, because of the difference in corresponding length scales. The QCM roughness factor is mostly determined by the roughness on the scale of the velocity decay length in the liquid, δ, which assumes values of hundreds of nanometers, depending on the frequency of the crystal and the viscosity and density of the liquid. The "interfacial" roughness factor is related to the structure of the molecular adsorbed layer, or the double layer, or to the charge transfer at the interface, and therefore its characteristic scale is about 1 nm.

The first terms in braces in Eqs. 33 and 34 define the shift and the broadening of the resonance at the interface between an ideally smooth crystal and the liquid [13]. The surface roughness leads to an additional decrease of the resonant frequency and a broadening of the half-width of the resonance, expressed by the second terms in this equation.

The particular form of the scaling functions $F(l/\delta)$ and $\Phi(l/\delta)$ is determined by the morphology of the surface. However, the asymptotic behavior of these functions for $l/\delta \gg 1$ and $l/\delta \ll 1$ is universal [82] and has the form:

$$F(l/\delta) = (l/\delta)[\alpha_1 + \alpha_2\delta/l] \quad \text{at} \quad l/\delta \gg 1 \tag{37}$$

$$F(l/\delta) = (l/\delta)[\beta_1 + \beta_2 l/\delta] \quad \text{at} \quad l/\delta \ll 1 \tag{38}$$

$$\Phi(l/\delta) = \gamma_1 \quad \text{at} \quad l/\delta \gg 1 \tag{39}$$

$$\Phi(l/\delta) = (l/\delta)^2\gamma_2 \quad \text{at} \quad l/\delta \ll 1\,. \tag{40}$$

For random Gaussian roughness, the parameters are:

$$\alpha_1 = \pi^{1/2}, \alpha_2 = 2, \beta_1 = 3\pi^{1/2}, \beta_2 = -2 \quad \text{and} \quad \gamma_1 = \gamma_2 = 2\,. \tag{41}$$

It should be noted that for $l/\delta \gg 1$ the roughness-induced frequency shift includes a term that does not depend on the viscosity of the liquid, the first term in Eqs. 37 and 33. It reflects the effect of the non-uniform pressure distribution, which is developed in the liquid under the influence of a rough oscillating surface [80]. The corresponding contribution has the form of the Sauerbrey equation. This effect does not exist for smooth interfaces. The second term in Eq. 37 and Eq. 39 describe a viscous contribution to the QCM response. Their contribution to Δf has the form of the QCM response at a smooth liquid–solid interface, but includes an additional factor R that is a roughness factor of the surface. The latter is a consequence of the fact that for $l/\delta \gg 1$ the liquid "sees" the interface as being locally flat, but with R times its apparent surface area.

Results obtained in [80, 82] show that the influence of slight surface roughness on the frequency shift cannot be explained in terms of the mass of liquid "trapped" by surface cavities, as proposed in [76, 77]. This statement can be illustrated by consideration of the sinusoidal roughness profile. The mass of the liquid "trapped" by sinusoidal grooves does not depend on the slope of the roughness, h/l, and is equal to $S*h$, where S is the area of the crystal. However, Eq. 33 demonstrates that the roughness-induced frequency shift does increases with increasing slope.

Equation 34 and the asymptotic behavior of the scaling functions show that in the regions where $l/\delta \gg 1$ and $l/\delta \ll 1$, the width is proportional to the factors $(\rho\eta)^{1/2}f_0^{3/2}$ and $\rho^{3/2}\eta^{-1/2}f_0^{5/2}$, respectively. In the high viscosity limit, when $\eta > l^2\pi\rho f_0$, the roughness-induced frequency shift approaches a constant value and the roughness-induced width tends to zero.

The results obtained make it possible to estimate the effect of roughness on the response of the QCM, if the surface profiles function $\xi(\boldsymbol{R})$ can be found from independent measurements.

4.1.2 Strong Roughness

Perturbation theory cannot be applied to describe the effect of the strong roughness. An approach based on Brinkman's equation has been used instead to describe the hydrodynamics in the interfacial region [83]. The flow of a liquid through a non-uniform surface layer has been treated as the flow of a liquid through a porous medium [84–86]. The morphology of the interfacial layer of thickness, L, has been characterized by a local permeability, ξ_{H}, that depends on the effective porosity of the layer, ϕ. A number of equations for the permeability have been suggested. For instance, the empirical Kozeny–Carman equation [84] yields a relationship between ξ_{H}^2 and the effective porosity $\xi_{\mathrm{H}}^2 \sim r^2\phi^3/(1-\phi)^2$, where r is the characteristic size of inhomogeneities.

The flow of liquid through the interfacial layer can be described by the following equation [83]:

$$i\omega\rho v(z,\omega) = \eta\frac{\mathrm{d}^2}{\mathrm{d}z^2}v(z,\omega) + \eta\xi_{\mathrm{H}}^{-2}[v_{\mathrm{q0}} - v(z,\omega)]\,, \tag{42}$$

where v_{q0} is the amplitude of the quartz surface velocity and $v(z,t) = v(z,\omega)\exp(i\omega t)$ is the velocity of the liquid in the layer. In this equation the effect of the solid phase on the flow of liquid is given by the resistive force, which has a Darcy-like form, $\eta\xi_{\mathrm{H}}^{-2}[v_{\mathrm{q0}} - v(z,\omega)]$. In the case of high effective porosity, the resistive force is small and Eq. 47 is reduced to the Navier–Stokes equation, describing the motion of the liquid in contact with a smooth quartz surface. For a given viscosity, the resistive force increases with decreasing effective porosity and strongly influences the liquid motion. At very low effective porosity all the liquid located in the layer is trapped by the roughness and moves with a velocity equal to the velocity of the crystal surface itself.

Brinkman's equation represents a variant of the effective medium approximation, which does not describe explicitly the generation of non-laminar liquid motion and conversion of the in-plane surface motion into the normal-to-interface liquid motion. These effects result in additional channels of energy dissipation, which are effectively included in the model by introduction of the Darcy-like resistive force.

The liquid-induced frequency shift and the half-width of the resonance have the following form [83]

$$\Delta f = -\frac{2f_0^2\rho}{(\mu_q\rho_q)^{1/2}} \times \mathrm{Re}\left\{\frac{1}{q_0} + \frac{L}{\xi_H^2 q_1^2} - \frac{1}{W}\frac{1}{\xi_H^2 q_1^2}\left[\frac{2q_0}{q_1}[\cosh(q_1 L) - 1] + \sinh(q_1 L)\right]\right\} \tag{43}$$

$$\Delta\Gamma = -\frac{2f_0^2\rho}{(\mu_q\rho_q)^{1/2}} \times \mathrm{Im}\left\{\frac{1}{q_0} + \frac{L}{\xi_H^2 q_1^2} - \frac{1}{W}\frac{1}{\xi_H^2 q_1^2}\left[\frac{2q_0}{q_1}[\cosh(q_1 L) - 1] + \sinh(q_1 L)\right]\right\} . \tag{44}$$

Here $q_0 = (i2\pi f_0\rho/\eta)^{1/2}$, $q_1^2 = q_0^2 + \xi_H^{-2}$, and $W = q_1\cosh(q_1 L) + q_0\sinh(q_1 L)$. The first terms on the right-hand sides of Eqs. 43 and 44 describe the response of the QCM for the smooth quartz crystal–liquid interface [13]. The additional terms present the shift and the half-width of the QCM response caused by the interaction of the liquid with a non-uniform interfacial layer.

When the permeability length scale is the shortest length of the problem, $\xi_H \ll \delta$ and $\xi_H \ll L$, the layer-induced shift, Δf_L, is proportional to the density of the liquid and does not depend on the viscosity. It has the form of the Sauerbrey equation for mass loading. This effect results from the inertial motion of the liquid trapped by the inhomogeneities in the interfacial layer.

$$\Delta f_L = -\frac{2f_0^2\rho}{(\mu_q\rho_q)^{1/2}}(L - \xi_H) . \tag{45}$$

The effective thickness of the liquid film rigidly attached to the oscillating surface is equal to $L - \xi_H$, and is less than the thickness of the inhomogeneous layer, L. The increase of the permeability ξ_H leads to the enhancement of the velocity gradient in the layer, which results in a decrease of the shift due to mass loading, and an increase of the width caused by the energy dissipation. When the layer thickness is the shortest length of the problem, $L \ll \delta$, $L \ll \xi_H$, and $\xi_H \ll \delta$, the frequency shift is also proportional to the density of the liquid and does not depend on viscosity:

$$\Delta f_L = -\frac{2f_0^2\rho L}{3(\mu_q\rho_q)^{1/2}}(L/\xi_H)^2 . \tag{46}$$

However, in contrast to the previous case, it cannot be related to the mass of trapped liquid. The correction to the width of the resonance depends on the viscosity and is substantially less than the layer-induced shift.

4.2 Experimental Studies

4.2.1 Non-conducting Liquids

Experimentally, correlation between the QCM signal and the surface morphology, as determined by microprofilometry and STM techniques, has already been established in the early experiments with the QCM in liquids [14, 16]. Measurements indicated that the mechanical impedance, Z_L, increases with increasing surface roughness. In contrast to smooth surfaces, interactions of rough oscillating surfaces with liquids do not contribute equally to $\mathrm{Re}(Z_L)$ and $\mathrm{Im}(Z_L)$ [14, 87, 88]. It was also found that the roughness leads to new dependencies of the frequency shift on viscosity, which does not appear for smooth surfaces. For instance, the experimental data obtained in methanol–water mixtures and in alcohols [16] demonstrated that the effect of roughness on the QCM is most pronounced for low viscosities, where the liquid-induced shift of the resonance frequency is small. This conclusion agrees with the theoretical predictions discussed in Sect. 4.1 (see Eqs. 33 and 34). Theory shows that, at low viscosities, the QCM response in liquids is mainly determined by the contribution of the non-uniform pressure distribution, which is developed in the liquid under the influence of a rough oscillating surface [89].

In [27] experiments in liquids having a wide range of viscosity and density were performed, and the response of the QCM was analyzed, using the theoretical models described in Sect. 4.1. Both parameters characterizing the resonator, the shift in fundamental frequency and the width of the resonance, were measured simultaneously. The usual form of presenting the experimental data in liquids is to plot the real and the imaginary components of the response of the QCM as a function of the density of the liquid or of the parameter $\sqrt{\rho\eta}$. However, these parameters are the natural variables only for ideally flat interfaces. Equations 33, 34, 43 and 44 show that for rough surfaces it is more convenient to consider the quantities $\Delta\Gamma/f^2\rho$ and $\Delta f/f^2\rho$, as a function of the velocity decay length in the liquid, δ, as shown in Fig. 4. The dependence of these two parameters on δ is linear for the ideally smooth surface of the quartz crystal resonator loaded on one side, (see line 1 in Fig. 4a,b).

Close points in these figures represent data measured on a relatively smooth surface, (obtained by vacuum sputtering), while open points were taken on a surface with strong roughness, prepared by electroplating. The deviation of the data from the straight line 1 calculated for an ideally smooth surface increases with increasing roughness, as expected.

The experimental dependence of the quantity $\Delta\Gamma/f^2\rho$ on the velocity decay length exhibits a sharp increase at low values of δ, followed by a gentle growth at large values of δ. This effect becomes more pronounced with increasing roughness (open circles).

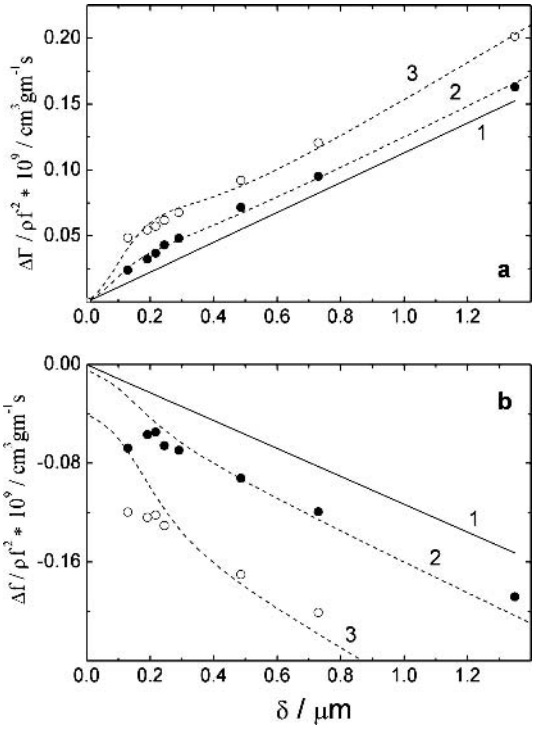

Fig. 4 Dependence **a** of the parameter $\Delta\Gamma/\rho f^2$ and **b** $\Delta f/\rho f^2$ on the velocity decay length in different liquids, for an ideally smooth surface (*lines 1*), and experimental data for two real surfaces: vacuum-sputtered gold (*closed circles*) and electrochemically deposited gold (*open circles*). *Lines 2* and *3* represent results of parameter fitting, see text. (From [27])

In Fig. 5a, the theoretical dependence of the function $\Delta\Gamma/f^2\rho$ on δ is given (lines 2–4) for different values of the local permeability, ξ_H, and a fixed value of the film thickness parameter, L, in the framework of the theory developed for strong roughness (Sect. 4.1.2). At large values of δ, the calculated lines approach line 1 for an ideally smooth surface. This behavior can be understood since it becomes difficult for the liquid to move inside pores in the surface film when δ is much larger than the size of the pores. In the limiting case the liquid moves in-phase with the solid surface, acting only as a mass loading, but adding nothing to the width of the resonance.

Line 5 in Fig. 5 is calculated for a surface having slight roughness, according to Eq. 34 and 39. The hydrodynamic roughness factor R is chosen so that this line connects the origin with the experimental point for the highest value of δ. This yielded a value of $R = 1.3$.

Curves 2–4 in Fig. 5b were calculated for different values of the film thickness, L, and a constant value of the local permeability, ξ_H, according to Eq. 44.

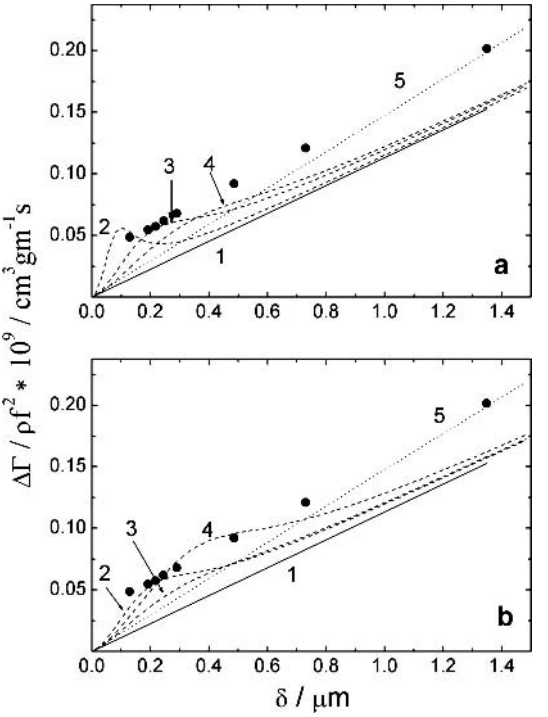

Fig. 5 Dependence of the parameter $\Delta\Gamma/\rho f^2$ on the velocity decay length: *points* experimental data, *line 1* in both plots indicates an ideally smooth surface. **a** Influence of strong roughness according to Eq. 44 for different values of ξ_H: *2* 69, *3* 172, *4* 276 nm) and $L = 506$ nm. **b** The same for different values of L: *2* 460, *3* 506, *4* 690 nm and $\xi_H = 172$ nm. *Line 5* in both plots was calculated for slight roughness (roughness factor $R = 1.3$, Eqs. 34 and 39). (From [27])

Lines 1 and 5 are the same as in Fig. 5a. The width of the resonance is seen to increase with increasing film thickness.

Figure 5 shows that there is no way to fit the experimental data assuming that only one type of roughness is presented on the surface. We are thus forced to conclude that, in these experiments the surface has a multiscale roughness, shown schematically in Fig. 6. The structure of this rough surface is a combination of a slight and a strong roughness shown in Fig. 3a,b. When this is taken into account, it is possible to use Eqs. 33, 34, 43, and 44 to calculate the shift in resonance frequency and shift in the width of the resonance, and fit the experiments to the calculated curves with properly chosen values of the parameters of strong roughness. The result of such a fit is shown in Fig. 4, curves 2 and 3. For details of the fitting procedure, the limitations associated with the use of a simplified model, and the comparison with STM data see [27].

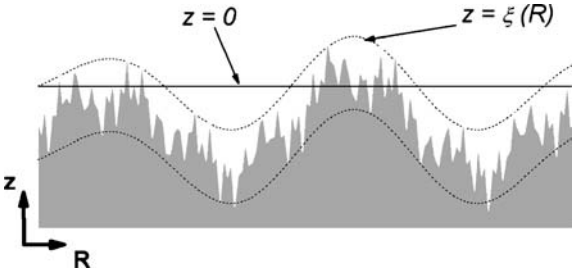

Fig. 6 Schematic representation of multiscale roughness. This structure is a combination of a slight and a strong roughness shown in Fig. 3a,b. (From [27])

Here we should emphasize only one point, of major importance for electrochemical use of the QCM. The velocity decay length of most solvents of interest for electrochemical and analytical purposes happen to be at the lower end of the values of δ shown in Figs. 4 and 5. This is the region where the interplay between the two types of roughness is the strongest, and it is the most difficult to fit the data to either model. This inherent difficulty should be borne in mind whenever an attempt is made to interpret the impedance response of the QCM operating in typical solvents such as water, alcohols, or many of the other non-aqueous solvents employed in electrochemistry.

The importance of measuring the imaginary component of the quartz crystal in order to study metal deposition and dissolution processes has also been noted by the authors of [26, 88]. In particularly, in this way they [26] succeeded in separating contributions of mass loading and roughness to QCM response and to characterize the electrode roughness.

Recently it has been suggested that shear oscillations of rough surfaces can generate acoustic compressional waves in the liquid at the second harmonic frequency if the amplitude of oscillations is large enough [90, 91]. This effect has been detected while electrochemically growing a rough metal surface on the QCM device. It should be noted that mass loading, viscosity, and slippage effect do not contribute to the second harmonic generation, and thus the second harmonic generation would allow for an independent measurement of the surface roughness with the QCM technique. Unfortunately under realistic conditions, the acoustic signal at the second harmonic frequency is too small to obtain quantitative results.

4.2.2 The Electrochemical Case

There are only few publications where the response of the QCM in electrochemical systems has been studied on intentionally roughened surfaces [25,

26, 92–95]. Figure 7 shows how the response of the EQCM changes with the change of surface roughness, induced by extensive cycling into the region of surface oxide formation. When the surface was not roughened, the loops de-

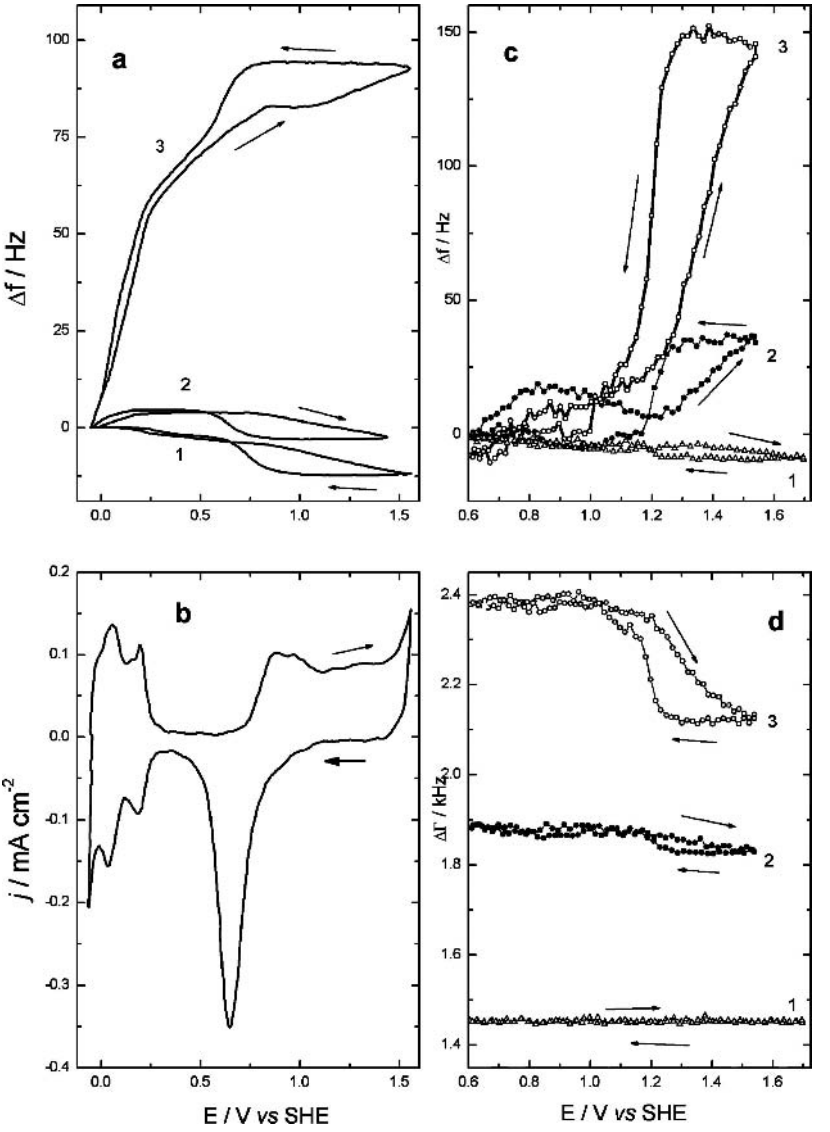

Fig. 7 **a** Influence of the number of oxidation–reduction cycles on the frequency response for platinum in 0.2 M H_2SO_4, at 100 mV/sec (*curve 1* 100, *2* 2000, *3* 10 000 cycles). **b** Stabilized cycling voltammogram for Pt electrode. **c** Frequency shift and **d** width of resonance for gold electrodes in 0.1 M $HClO_4$ at 10 mV/sec (*curve 1* 4, *2* 100, *3* 500 cycles). (**a** and **b** from [93])

scribing the shift in frequency with potential, associated with surface oxide formation, have clockwise directions, (see curves 1 in Fig. 7a,c). On very rough surfaces, (represented by curves 3), the loops are in the opposite direction. The data for platinum electrode (Fig. 7a,b) were taken from [93], in which only the shift of resonance frequency was measured. The data on the gold electrode were obtained in our own laboratory, and both the shift of frequency and the width of the resonance were measured (Fig. 7c,d). The latter shows that when the surface is sufficiently smooth there are no changes in the width of resonance with the potential. The corresponding curves for rough surfaces, when the resonance is wide ($\Delta\Gamma > 1.5$ kHz), show strong potential dependence and remarkable hysteresis. On the one hand the comparison of voltammograms and dependence of the responses of the EQCM on potential clearly shows that the hysteresis is associated with surface oxide formation. On the other hand, the effect cannot be ascribed to mass loading because the frequency shift on rough surfaces is not only larger than that on smooth surfaces – the effect has a reverse sign. Moreover, mass loading alone cannot lead to changes in $\Delta\Gamma$. The loop of frequency shift also changes its sign in the region of hydrogen adsorption on platinum. It should be noted that the surface of Pt is much more resistant to roughening than that of gold. Thus, comparing Figs. 7a,c it would seem that cycling 2000 and 10 000 times on Pt has an effect comparable to that of cycling Au 100 and 500 times, respectively. However, the experiments on Pt and Au shown they were performed under similar, but not identical, conditions.

Comparison of Fig. 7c,d for a highly rough surface (curve 3) shows that a decrease in width is associated with a positive shift in resonance frequency, in the region of surface oxide formation. This is consistent with the notion that both effects result from a weakening of the interactions between the vibrating surface and the liquid under surface oxidation. Similar results have been obtained for gold surfaces having different degrees of roughness.

All the data obtained with rough surfaces and the discussion of these data [25, 28, 92, 93, 95] lead to the following conclusions

1. The roughness of the electrode has a profound influence on the response of the EQCM, see Figs. 7 and 8. This may explain the unusually large discrepancies among data obtained with the EQCM in different laboratories (not necessarily on intentionally roughened surfaces). A good example is the large discrepancy in data reported for the region of surface oxide formation on gold [76, 96–100].
2. The response of the EQCM on rough surfaces cannot be treated in terms of the electrochemically defined roughness factor $\tilde{R}$, which is obtained from adsorption phenomena, e.g., from data such as presented in Fig. 9. This quantity can be considered as representing all adsorption sites on the surface, which is equivalent to the surface roughness on the atomic scale. However, the response of the EQCM depends on roughness on a meso-

scopic scale, which is comparable to the hydrodynamic velocity decay length rather than to the double layer thickness.

3. The width of the resonance is an important characteristic of the surface, as seen in Fig. 8b, and can serve as a semi-quantitative measure of its roughness, on the scale relevant to the response of the EQCM. Unfortunately, only very few publication so far contain this information.

In addition to the conclusions drawn above, one is still left with the need to interpret the dependence of the response of the EQCM on potential on rough surfaces (Figs. 7 and 8). Attempts to provide a qualitative interpretation were made in [95, 101]. The authors ascribed the effects on rough surfaces to "formation of a structured region of solvent which leads to increased viscosity and consequent frequency changes" and agreed that "the exact nature of the changes in the surface ... still has to be established" [95]. Thus, they assumed that the properties of that "structured region of solvent" near the electrode depend on adsorption and on potential.

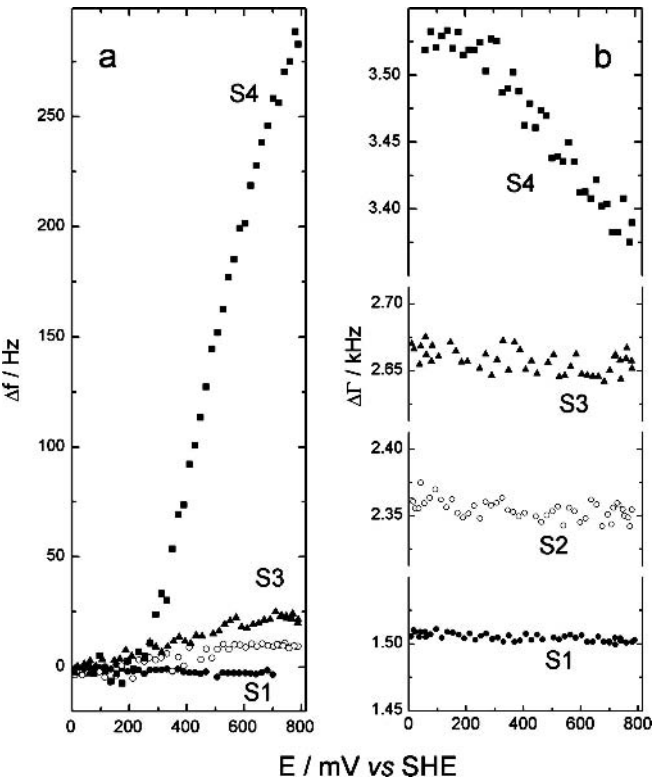

Fig. 8 Dependence of the frequency shift (**a**) and the half-width of the resonance (**b**) of the EQCM on potential, for different gold surfaces, *S1–S4* [28]. (From [28])

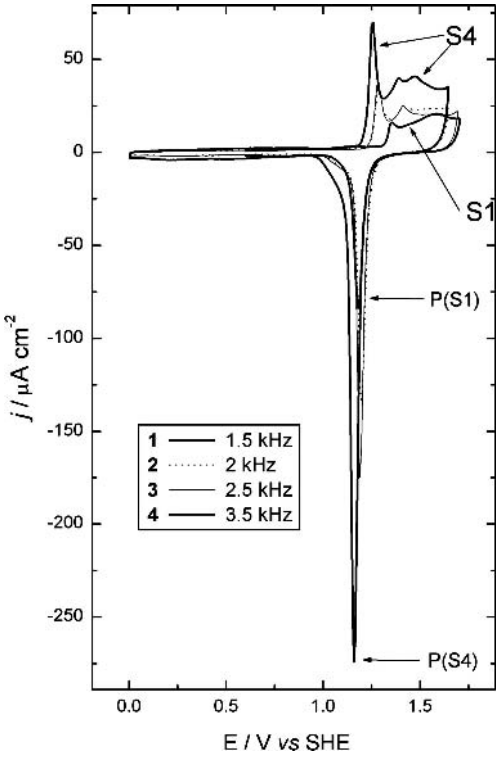

Fig. 9 Cycling voltammetry (5 mV/sec) for gold electrodes of different roughness [28]. *S1* untreated (as received) surface. *S2–S4* surfaces obtained by electrodeposition of gold at currents densities close to the limiting current density. *Inset*: approximate values of the half-width of resonance. *Curves S2* and *S3* lie between *curves S1* and *S4*, in some parts coinciding with them. *Arrows P(S1)* and *P(S4)*, show the peak currents for reduction of the surface oxide, measured for the surfaces *S1* and *S4*, respectively. (From [28])

5
Slippage at Rough Surfaces

Mesoscopic roughness at the solid–liquid interface can greatly modify both interfacial flow and static wetting properties leading to two behaviors, either a decrease [45, 64, 102] or an increase [63, 103] of surface slippage with roughness.

The calculations, which have been made for periodic and random surfaces [6, 104–106], demonstrated that if the liquid fully wets the solid surface, the roughness reduces slip and shifts the position of the effective surface plane (the plane where the liquid and substrate velocities are equal) in the direction of the liquid phase [6, 107]. The authors of [39, 108] suggested intro-

duction of an effective slip length, b_s^{eff}, which takes into account both slippage and roughness, in order to describe an interplay between the slippage and roughness. In this manner, liquid flow at a rough surface has been simulated as a flow at a smooth surface with an effective slip length. Application of this approach to the QCM problem [6] yields the following equation for the effective slip length:

$$b_s^{eff} = b_s \left\{ 1 - \left(\frac{h_0 k_0}{2} \right)^2 \left[\frac{3 + 4 b_s k_0}{1 + 2 b_s k_0} \right] \right\} - \frac{k_0 h_0^2}{2} \left[\frac{2 + 3 b_s k_0}{(1 + b_s k_0)(1 + 2 b_s k_0)} \right] . \tag{47}$$

Equation 47 was derived for a sinusoidal profile of roughness, $z(x) = d + h_0 \sin(k_0 x)$, with an amplitude h_0 and a period of $2\pi/k_0$, assuming that the decay length, δ, is the largest characteristic length of the problem, $\delta/b_s \gg 1$ and $\delta k_0 \gg 1$. Beyond these conditions the effective slip length is a complex function. Equation 47 shows that roughness diminishes the influence of slippage on the QCM response, namely the effective slip length becomes smaller than the corresponding length for the smooth interface. At rough interfaces, the effective slip length decreases with an increase of the amplitude of the surface corrugation and with a decrease of its period.

It should be noted that an effective slip length is not an intrinsic property of the surface. Its value depends also on the experimental configuration, for instance, b_s^{eff} found for the Poiseuille flow between rough surfaces [108] differs from the corresponding value obtained for QCM experiments (Eq. 47).

When the liquid partially wets the solid surface, roughness can lead to the spontaneous dewetting of a surface and the appearance of a superhydrophobic state, resulting in large slip length [103, 109, 110], and possibly in shear-rate-dependent effects [111]. It was also claimed that under these conditions roughness favors the formation of vapor or gas pockets (nanobubbles) trapped at the solid surface, which could be an important factor in slippage phenomena [55, 56]. It was proposed to simulate the effect of nanobubbles on the QCM signal through the introduction of laterally heterogeneous slip [112]. Over the last 5 years many groups have reported experimental observations of nanobubbles against hydrophobic surfaces in water [113–120]. The amount of slip has been observed experimentally to depend on the type and quantity of dissolved gas. However, there is great variation in published results and the observed behaviors are very sensitive to the surface preparation. The formation and stability of nanobubbles, even on hydrophobic surfaces, is not easily explained.

The formation of bubbles at solid surfaces has also been studied with the QCM technique. In [121] a non-linear dependence of $\Delta f/\rho$ on $(\eta\rho)^{0.5}$ was interpreted as the result of the presence of nanobubbles on the surface. However, it should be noted that the observed dependencies could be also explained using the concept of multiscale roughness discussed above (see

Sects. 4.1.2 and 4.2.1). In order to check the hypothesis of bubble formation, the authors of [122] immersed dry surfaces of the QCM of different roughness and hydrophobicity into electrolytes saturated by oxygen (or hydrogen). In all cases removing gases in situ by electrochemical reduction (or oxidation) did not result in changes of either the resonant frequency or the width of resonance. This led to a conclusion that even on freshly formed metal/aqueous solution contacts, the size and coverage of bubbles (if they exist) are so low that they could not influence the QCM response.

The above discussion shows that existing literature contains arguments, both theoretical and experimental, in favor as well as against the presence of nanobubbles at the metal/liquid interface. Many more targeted experiments and theoretical works are required to clarify this issue.

6 Conclusion

The quartz crystal resonator is a useful device for the study of thin-layer and interfacial phenomena. The crystals commonly employed have a fundamental resonance frequency of 5–10 MHz and a resolution of the order of 0.1–0.5 Hz. This high resolution makes the device sensitive to a myriad of physical phenomena, some of which are interrelated and some quite independent of each other. It cannot be overemphasized that the quartz crystal resonator acts as a true microbalance (more appropriately a nanobalance) only if in the course of the process being studied, the nature of the interface (its roughness, slippage, the density and viscosity of the solution adjacent to it, and the structure of the solvent in contact with it) is maintained constant.

In this chapter we have limited our discussion to the effects of interfacial structure on the QCM response in liquids.

Some of the main conclusions are listed below:

- The shift in frequency observed experimentally cannot be interpreted in terms of a change in mass loading alone, unless the conditions have been carefully chosen to ensure that this is the only factor affecting the resonance frequency.
- It seems to be essential to measure the admittance spectrum and determine both the resonant frequency shift and the width of the resonance simultaneously. This yields additional information not available from measurement of the resonant frequency alone, and can hence provides more detailed interpretation of processes occurring at the solid–liquid interface.
- Surface roughness is of paramount importance in the use of the QCM in liquids. The existing theories provide a description of the QCM response for rough surfaces in two limiting cases of slight and strong roughness. How-

ever, much is left to be developed for a quantitative interpretation of data obtained for real surfaces. In order to overcome the gap between existing theory and experiments, measurements on specially prepared surfaces with well-defined roughness should be performed.

- Numerous experimental techniques employed to study solid–liquid interfaces (X-ray and neutron scattering, optical, AFM and STM, adsorption, double layer capacitance, rotating disc electrode and QCM) are sensitive to the roughness of substrate surfaces. It should be noted that each technique probes roughness on the particular characteristic scale only, which is the atomic scale for X-ray and neutron scattering, AFM, STM, adsorption and double-layer capacitance measurements; a wave-length of light for optical measurements; the Nernst diffusion layer for rotating disc electrode experiments; and the hydrodynamic velocity decay length for the QCM. Thus, the impedance of the QCM would be expected to respond to roughness of about 10 nm and above, ignoring most of the so-called atomic scale roughness, but detecting roughness that can usually be ignored in experiments conducted under mass transport limitations.
- The results obtained by the QCM contain information relevant to the understanding of phenomena in the area of nanotribology, where techniques such as SFA and AFM are used. In both cases the results carry information regarding the properties of a nanoscale layer of liquid at the interface.
- An important part of modern experimental surface science and electrochemistry has been performed on single-crystal electrodes. In contrast, the metal deposited on the surface of the quartz resonator always has a rough surface and at best a preferred crystal orientation. Studies with a QCM having a true single crystal surface have not yet been reported. Making a thin (about 1 μm) stable single-crystal metal layer on the surface of quartz seems to be an insurmountable problem.

So far most of the QCM data were analyzed on a qualitative level only. The next step in QCM studies requires a quantitative treatment of the experimental results. The theoretical basis for the solution of this problem already exists, and has been discussed in this chapter. Joint experimental and theoretical efforts to elevate the QCM technique to a new level present a challenge for future investigators.

Finally it would seem that, in spite of some shortcomings, the potential advantages of the QCM far exceed its limitations. There are many challenges to overcome and the QCM will undoubtedly continue to be one of the important tools in studies of metal–solution interfaces in general.

Acknowledgements Financial support for this work by the Israel Science Foundation (grants No. 773/05 and 174/05) and by the Deutsche Forschungsgemeinschaft (HA 1517/26-1) is gratefully acknowledged. We thank Dr. G. Zilberman, and Mrs. G. Katz for their contribution in obtaining the experimental data discussed in this chapter.

References

1. Schumacher R (1990) Angew Chem Int Engl 29:329
2. Buttry DA (1991) Application of the quartz crystal microbalance to electrochemistry. In: Bard AJ (ed) Electroanalytical chemistry. Dekker, NY, p 1
3. Buttry DA (1991) The quartz crystal microbalance as an in situ tool in electrochemistry. In: Abruna HD (ed) Electrochemical interfaces – modern techniques for in situ interface characterization. Wiley, NY, p 531
4. Buttry DA, Ward MD (1992) Chem Rev 92:1355
5. Hepel M (1999) Electrode solution interface studied with electrochemical quartz crystal nanobalance. In: Wieckowski A (ed) Interfacial electrochemistry. Dekkker, NY, p 599
6. Tsionsky V, Daikhin L, Urbakh M, Gileadi E (2003) Looking at the metal/solution interface with the electrochemical quartz crystal microbalance. theory and experiment. In: Bard AJ, Rubinstein I (eds) Electroanalytical chemistry. Dekker, New York, p 1
7. Hillman AR (2003) The electrochemical quartz crystal microbalance. In: Bard AJ (ed) Encyclopedia of electrochemistry. Wiley, Weinheim, p 230
8. Sauerbrey G (1959) Z Phys 155:206
9. Moret H, Louwerix E (1966) Microbalance for ultrahigh-vacuum applications. In: Behrndt KHN (ed) Vacuum microbalance techniques. Plenum, NY, p 59
10. Tsionsky V, Gileadi E (1994) Langmuir 10:2830
11. Nomura T, Iijima M (1981) Anal Chim Acta 131:97
12. Bruckenstein S, Shay M (1985) Electrochim Acta 30:1295
13. Kanazawa KK, Gordon JG (1985) Anal Chim Acta 175:99
14. Martin SJ, Frey G, Ricco A, Senturia S (1993) Anal Chem 65:2910
15. Tsionsky V, Daikhin L, Urbakh M, Gileadi E (1995) Langmuir 11:674
16. Yang M, Thompson M, Duncan-Hewitt WC (1993) Langmuir 9:802
17. Beck R, Pitterman U, Weil KG (1988) Ber Bunsenges Phys Chem 92:1363
18. Frubose C, Doblhofer K, Soares DM (1993) Ber Bunsenges Phys Chem 97:475
19. Noel MAM, Topart PA (1994) Anal Chem 66:484
20. Bandey HL, Gonsalves M, Hillman AR, Glidle A, Bruckenstein S (1996) J Electroanal Chem 410:219
21. Soares DM, Tenan MA, Wasle S (1998) Electrochim Acta 44:263
22. Yamamoto N, Yamane T, Tatsuma T, Oyama N (1998) Bull Chem Soc Jpn 68:1641
23. Bund A, Schwitzgebel G (1998) Anal Chem 70:2584
24. Wunsche M, Meyer H, Schumacher R (1999) Z Phys Chem 208:225
25. Plausinaitis D, Raudonis R, Daujotis V (2000) Polish J Chem 74:559
26. Bund A, Schwitzgebel G (2000) Electrochim Acta 45:3703
27. Daikhin L, Gileadi E, Katz G, Tsionsky V, Urbakh M, Zagidulin D (2002) Anal Chem 74:554
28. Tsionsky V, Katz G, Gileadi E, Daikhin L (2002) J Electroanal Chem 524:110
29. Martin SJ, Frey GC (1991) IEEE Ultrasonics Symp Proc. IEEE, New York, p 393
30. Johannsmann D, Mathauer K, Wegner G, Knoll W (1992) Phys Rev B 46:7808
31. Glidle A, Hillman AR, Bruckenstein S (1991) J Electroanal Chem 318:411
32. Muramatsu H, Kimura K (1992) Anal Chem 64:2502
33. Yang MS, Chung FL, Thompson M (1993) Anal Chem 65:3713
34. Krim J, Solina DH, Chiarello RP (1991) Phys Rev Let 66:181
35. Krim J, Watts ET, Digel J (1990) J Vac Sci Technol A 8:3417

36. Watts ET, Krim J, Widom A (1990) Phys Rev B 41:3466
37. Krim J, Widom A (1988) Phys Rev B 38:12184
38. Krim J, Chiarello RP (1991) J Vac Sci Technol A 9:2566
39. Persson BNJ (2000) Sliding friction: physical priciples and applications. Springer, Berlin, Heidelberg, New York
40. Daly C, Krim J (1996) Phys Rev Lett 76:803
41. Bruschi L, Carlin A, Mistura G (2002) Phys Rev Lett 88:046105
42. Feynman R (1965) Lectures on physics. In: Reading MA (ed) Lectures on physics. Addison-Wesley, Boston
43. Koplik J, Banavar JR (1995) Annu Rev Fluid Mech 27:257
44. Tsionsky V, Daikhin L, Gileadi E (1996) J Electrochem Soc 143:2240
45. Pit R, Hervet H, Leger L (2000) Phys Rev Lett 85:980
46. Churaev NN, Sobolev VD, Somov AN (1984) J Colloid Int Sci 97:574
47. Krim J (1996) Sci Amer 275:74
48. Cottin-Bizonne C, Barrat JL, Bocquet L, Charlaix E (2003) Nature Mater 2:237
49. Cottin-Bizonne C, Cross B, Steinberger A, Charlaix E (2005) Phys Rev Lett 94:056102
50. Vinogradova OI, Yakubov GE (2003) Langmuir 19:1227
51. Zhu YX, Granick S (2001) Phys Rev Lett 87:096105
52. Craig VSJ, Neto C, Williams DRM (2001) Phys Rev Lett 87:054504
53. Thompson PA, Troian SM (1997) Nature 389:360
54. Gupta SA, Cochran HD, Cummings PT (1997) J Chem Phys 107:10316
55. Neto C, Evans DR, Bonaccurso E, Butt HJ, Craig VSJ (2005) Rep Progr Phys 68:2859
56. Lauga E, Brenner MP, Stone HA, Foss J, Tropea C, Yarin A (eds) (2005) Handbook of experimental fluid dynamics. Springer, Berlin Heidelberg New York
57. Ellis JS, Thompson M (2004) Phys Chem Chem Phys 6:4928
58. de Gennes J-P (1979) C R Acad Sci, Paris B 288:219
59. Barrat JL, Bocquet L (1999) Faraday Discuss 112:119
60. Lumma D, Best A, Gansen A, Feuillebois F, Radler JO, Vinogradova OI (2003) Phys Rev E 67:056313
61. Daikhin L, Gileadi E, Tsionsky V, Urbakh M, Zilberman G (2000) Electrochim Acta 45:3615
62. Becker T, Mugele F (2003) Phys Rev Lett 91:166104
63. Bonaccurso E, Butt HJ, Craig VSJ (2003) Phys Rev Lett 90:144501
64. Zhu YX, Granick S (2002) Phys Rev Lett 88:106102
65. Lin ZQ, Granick S (2003) Langmuir 19:7061
66. Andrienko D, Dunweg B, Vinogradova OI (2003) J Chem Phys 119:13106
67. Rodahl M, Kasemo B (1996) Sensor Actuator A-Phys 54:448
68. Barrat JL, Bocquet L (1999) Phys Rev Lett 82:4671
69. Thompson PA, Robbins MO (1990) Phys Rev A 41:6830
70. Pit R, Hervet H, Leger L (1999) Tribol Lett 7:147
71. Tolstoi DM (1952) Dokl Akad Nauk SSSR 85:1329
72. Blake TD (1990) Colloids Surf 47:135
73. Thompson M, Kipling AL, Duncanhewitt WC, Rajakovic LV, Cavicvlasak BA (1991) Analyst 116:881
74. Kipling AL, Thompson M (1990) Anal Chem 62:1514
75. Bruckenstein S, Fensore A, Li Z, Hillman AR (1994) J Electroanal Chem 370:189
76. Schumacher R, Borges G, Kanazawa KK (1985) Surf Sci 163:L621
77. Schumacher R, Gordon JG, Melory OJ (1987) J Electroanal Chem 216:127
78. Yang M, Thompson M (1993) Langmuir 9:1990

79. Beck R, Pitterman U, Weil KG (1992) J Electroanal Chem 139:453
80. Urbakh M, Daikhin L (1994) Phys Rev B 49:4886
81. Bruschi L, Mistura G (1901) Phys Rev B 6323:5411
82. Urbakh M, Daikhin L (1994) Langmuir 10:2836
83. Daikhin L, Urbakh M (1996) Langmuir 12:6354
84. Sahimi M (1993) Rev Mod Phys 65:1393
85. Jones JL, Marques CM, Joanny JF (1995) Macromolecules 28:136
86. Brinkman HC (1947) Appl Sci Res A 1:27
87. Beck R, Pitterman U, Weil KG (1992) J Electrochem Soc 139:453
88. Bund A, Schneider M (2002) J Electrochem Soc 149:E331
89. Urbakh M, Daikhin L (1994) Phys Rev B 49:4866
90. Wehner S, Wondraczek K, Johannsmann D, Bund A (2004) Langmuir 20:2356
91. Wondraczek K, Bund A, Johannsmann D (2004) Langmuir 20:10346
92. Wilde CP, Zhang MJ (1992) J Electroanal Chem 340:241
93. Raudonis R, Plausinaitis D, Daujotis V (1993) J Electroanal Chem 358:351
94. Tsionsky V, Katz G, Gileadi E, Daikhin L (2002) J Electroanal Chem 524:110
95. Wilde CP, De Cliff SV, Hui KC, Brett DJL (2000) Electrochim Acta 45:3649
96. Uchida H, Ikeda N, Watanabe M (1997) J Electroanal Chem 424:5
97. Mao Y, Hwang E, Scherson D (1995) Anal Chem 67:2415
98. Watanabe M, Uchida H, Ikeda N (1995) J Electroanal Chem 380:255
99. Bruckenstein S, Shay M (1985) J Electroanal Chem 188:131
100. Stockel W, Schumacher R (1987) Ber Bunsenges Phys Chem 91:345
101. Daujotis V, Jasaitis D, Raudonis R (1997) Electrochim Acta 42:1337
102. Jabbarzadeh A, Atkinson JD, Tanner RI (2000) Phys Rev E 61:690
103. Cottin-Bizonne C, Jurine S, Baudry J, Crassous J, Restagno F, Charlaix E (2002) Eur Phys J E 9:47
104. Ponomarev IV, Meyerovich AE (2003) Phys Rev E 67:026302
105. Einzel D, Panzer P, Liu M (1990) Phys Rev Lett 64:2269
106. Panzer P, Liu M, Einzel D (1992) Int J Modern Phys B 6:3251
107. McHale G, Newton MI (2004) J App Phys 95:373
108. Einzel D, Panzer P, Liu M (1990) Phys Rev Lett 64:2269
109. de Gennes PG (2002) Langmuir 18:3413
110. Quere D (2002) Nature Mater 1:14
111. Lauga E, Brenner MP (2004) Phys Rev E 70:026311
112. Du BY, Goubaidoulline E, Johannsmann D (2004) Langmuir 20:10617
113. Ishida N, Sakamoto M, Miyahara M, Higashitani K (2000) Langmuir 16:5681
114. Zhang XH, Jun H (2004) Prog Chem 16:673
115. Tyrrell JWG, Attard P (2001) Phys Rev Lett 87:176104
116. Evans DR, Craig VSJ, Senden TJ (2004) Physica A 339:101
117. Mao M, Zhang JH, Yoon RH, Ducker WA (2004) Langmuir 20:1843
118. Attard P (2003) Adv Colloid Interface Sci 104:75
119. Christenson HK, Claesson PM (2001) Adv Colloid Interface Sci 91:391
120. Tretheway DC, Meinhart CD (2004) Phys Fluids 16:1509
121. Theisen LA, Martin SJ, Hillman AR (2004) Analyt Chem 76:796
122. Tsionsky V, Kaverin A, Daikhin L, Katz G, Gileadi E (2005) Phys Chem Chem Phys 7:1830

Springer Ser Chem Sens Biosens (2007) 5: 151–170
DOI 10.1007/5346_026

Published online: 29 July 2006

Studies of Contact Mechanics with the QCM

Diethelm Johannsmann

Institute of Physical Chemistry, Clausthal University of Technology,
Arnold-Sommerfeld-Str. 4, 38678 Clausthal-Zellerfeld, Germany
johannsmann@pc.tu-clausthal.de

Abstract The quartz crystal microbalance can serve as high-frequency probe of the microcontacts formed between the crystal surface and a solid object touching it. On a simplistic level, the load can be approximated by an assembly of point masses, springs, and dashpots. The Sauerbrey model, leading to a decrease in frequency, is recovered if small particles are rigidly attached to the crystal. In another limiting case, the particles are so heavy that inertia holds them in place in the laboratory frame. The spheres exert a restoring force onto the crystal, thereby increasing the stiffness of the composite resonator. The resonance frequency increases in proportion to the lateral spring constant of the sphere–plate contacts. A third limiting case is represented by particles attached to the crystal via a dashpot. Within this model (extensively used in nanotribology) the dashpot increases the bandwidth. The momentum relaxation time τ_S ("slip time") is calculated from the ratio of the increase in bandwidth and the decrease in frequency, $\Delta\Gamma/(-\Delta f)$.

The force–displacement relations in contact mechanics are often nonlinear. A prominent example is the transition from stick to slip. Even for nonlinear interactions, there is a strictly quantitative relationship between the shifts of frequency and bandwidth, Δf and $\Delta\Gamma$, on the one hand, and the force acting on the crystal, $F(t)$, on the other. Δf and $\Delta\Gamma$ are proportional to the in-phase and the out-of-phase component of $F(t)$, respectively. Evidently, $F(t)$ cannot be explicitly derived from Δf and $\Delta\Gamma$. Still, any contact-mechanical model (like the Mindlin model of partial slip) can be tested by comparing the predicted

and the measured values of Δf and $\Delta \Gamma$. Further experimental constraints stem from the measurement of the amplitude dependence of the resonance parameters.

Contacts mechanics in the MHz range is much different from its low-frequency counterpart. For instance, static friction coefficients probed with MHz excitation are often much above 1. Contact mechanics at short time scales should be of substantial practical relevance.

Keywords Contact mechanics · Contact stiffness · Fretting wear · Mindlin model · Nonlinear mechanics · Quartz crystal resonator · Quartz crystal microbalance · Partial slip · Stick-slip

1 Introduction

Contact mechanics is both an old and a modern field. Its classical domains of application are adhesion, friction, and fracture. Clearly, the relevance of the field for technical devices is enormous. Systematic strategies to control friction and adhesion between solid surfaces have been known since the stone age [1]. In modern times, the ground for systematic studies was laid in 1881 by Hertz in his seminal paper on the contact between solid elastic bodies [2]. Hertz considers a sphere–plate contact. Solving the equations of continuum elasticity, he finds that the vertical force, $F_\perp$, is proportional to $\delta^{3/2}$, where δ is the indentation. The sphere–plate contact forms a nonlinear spring with a differential spring constant $\kappa = \mathrm{d}F/\mathrm{d}\delta \propto \delta^{1/2}$. The nonlinearity occurs because there is a concentration of stress at the point of contact. Such stress concentrations – and the ensuing mechanical nonlinearities – are typical of contact mechanics.

Clean, dry single-asperity contacts have intensely been studied both theoretically [3–5] and experimentally [6]. The development of the atomic force microscope (AFM) [7–9] and the surface forces apparatus (SFA) [10–12] have certainly been influential. Both instruments allow for experiments under a control of geometry on the molecular level. Multi-asperity contacts evidently are more difficult to study than clean sphere–plate contacts [13, 14], but are much closer to the real world, as well. Currently, there is quite some activity carrying the knowledge gained on single-asperity contacts to the field of dry and wet granular media [15, 16]. The mechanics of a sand pile (such as its critical angle of sliding, its compactification with time or pressure, or its strengthening upon exposure to water vapor) all depend on the forces (normal and lateral) exerted at the contacts between the individual grains.

Given that nonlinearities are ubiquitous, testing with oscillatory excitation is of less practical importance in contact mechanics than in other fields of material science. For instance, stick-slip motion is most easily studied by steadily pulling the object of interest across the supporting substrate. Oscillatory testing will result in complicated trajectories [17]. Sinusoidal excitation mostly

makes sense in the small-amplitude limit, where force and displacement are linearly (or almost linearly) related. In the linear domain, superposition holds and a system's response is fully specified by its complex, frequency-dependent stiffness. Small nonlinearities can be dealt with in the frame of the two-timing approximation (cf. Sect. 3). Linear behavior, generally speaking, is *always* found in the limit of small stress [5]. This is true for both elastic interactions and sliding. A sliding motion, where the speed is proportional to the force, is termed "creep" in the context of rheology. Linear creep occurs whenever the external force is comparable in magnitude to the random forces related to Brownian motion. The external force then only adds a small bias to the random movement of the sample, and this bias is proportional to the force.

The use of the QCM for contact mechanics has been pioneered by Dybwad [18]. Dybwad placed a sphere onto a quartz resonator and found an *increase* in frequency. He explains this increase by the fact that the sphere rests in place in the laboratory frame due to inertia. It exerts a restoring force onto the crystal, thereby increasing its resonance frequency. He points out that the frequency shift can be exploited to measure the strength of the contact between the sphere and the quartz plate.

Nanotribology has also gained much from the QCM, where the early work has been done by J. Krim [19, 20]. The Krim group studied adsorbed monolayers of noble gas atoms onto the electrode and observed an increase in dissipation. Describing these experiments in the frame of continuum models, where the monolayer would correspond to a film with a viscosity η (Eq. 71 in Chap. 2 of this volume, replace Z_f by $(i\omega\rho\eta)^{1/2}$), cannot explain these findings. The viscosity would have to be orders of magnitude smaller than the viscosity of the corresponding bulk liquid, and it is hard to see why this should be the case. The Krim group models the atoms as discrete objects sliding across the surface. The motion of the atom is coupled to the motion of the surface via a dashpot with a drag coefficient ξ_S. The ratio of mass and drag coefficient has the dimension of a time, called "slip time", τ_S. τ_S is a momentum relaxation time. When the motion of substrate stops abruptly, the speed of the sphere exponentially slows down with a decay time τ_S. There is now experimental evidence that this kind of sliding – at least in certain cases – is not a creep in the sense of biased diffusion. Mistura and coworkers determined the amplitude dependence of the slip time and found a critical minimum amplitude, below which the molecules slick [21]. This finding contradicts liquid-like sliding. In liquid-like sliding, the slip time would be independent of amplitude.

2 Modeling with Discrete Mechanical Elements

In contact mechanics experiments with the QCM, the sample usually does not consist of a planar layer system, but rather of one or more discrete ob-

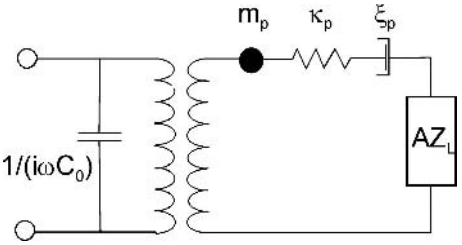

Fig. 1 Equivalent circuit representation of the quartz crystal including a load. Piezoelectric stiffening (described by the element $4Z_k$ in Fig. 13, Chap. 2 in this volume) was neglected. The sample is represented by the load Z_L

jects touching the crystal surface. One can – on a purely heuristic level – describe the sample by an equivalent mechanical model containing elements like a mass, a spring, or a dashpot. The effect, which these elements have on the frequency shift, is readily calculated starting from the small-load approximation (Eq. 51 in Chap. 2 in this volume). We assume that the stress–speed ratio may be replaced by an average stress–speed ratio, where the average stress is just the lateral force divided by the active area of the crystal. Replacing the stress by an average stress certainly is an approximation[1]. It can to some extent be justified by an argument based on the scattering of acoustic waves [22]. Once one has accepted this simple picture, the change of resonance frequency can be easily predicted by means of the Butterworth–van Dyke (BvD) equivalent circuit (Sect. 6 in Chap. 2 in this volume). In the following, we use the version of the BvD circuit, where electrical and mechanical elements are separated as shown in Fig. 1.

2.1 Loading with a Mass

Consider a small sphere rigidly attached to the crystal (Fig. 2). Let the mass of the sphere be m_S. Figure 2a shows a single sphere. Real crystals might be in contact with many such spheres, which is accounted for by including the number density of these spheres, N_S/A, as a prefactor into the equations below. N_S is the number of spheres and A is the active area of the crystal.

If the spheres are small enough, they can be treated like a Sauerbrey film with an areal mass density $m_f = N_S m_S/A$. Let κ_p be the spring constant of the crystal in the BvD sense, m_p the equivalent mass of the crystal in BvD sense (Eq. 116 in Chap. 2 in this volume), and m_q the areal mass density of the

[1] For instance, energy trapping may be affected by a load applied at the center of the disk.

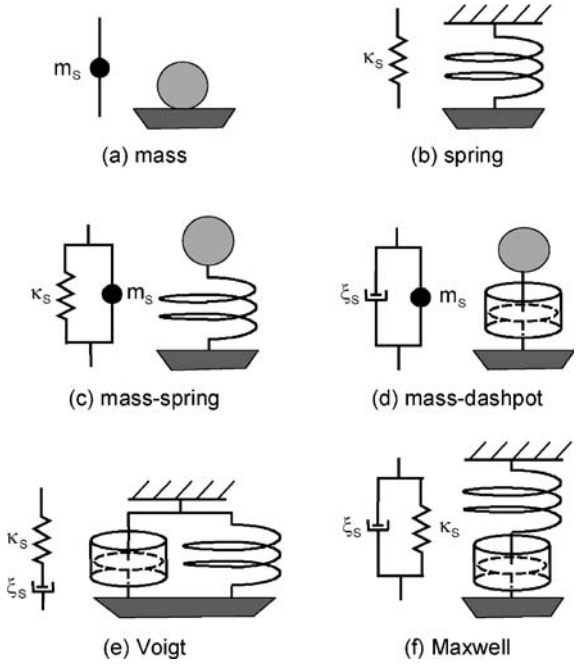

Fig. 2 Different circuits to be inserted for the load in Fig. 1. The conversion from the physical situation (*right*) to the equivalent circuits (*left*) entails a complication because networks are depicted such that the *electrical* Kirchhoff rules apply. Elements which are placed in series, physically, are represented as parallel circuit elements and vice versa (cf. Fig. 5 in Chap. 2 in this volume). For instance, the forces exerted by the spring and the dashpot in *e* are additive. In order to let the corresponding voltages in the electrical circuit also be additive, the circuit elements have to be placed in series. In the literature on polymer rheology, networks of springs and dashpots are drawn according to the physical situation (*right-hand-side* in this figure), which comes down to a different set of Kirchhoff rules

crystal. The frequency shift of the composite resonator then is:

$$\begin{aligned}\Delta f = f_r - f_0 &= \frac{1}{2\pi}\left(\sqrt{\frac{\kappa_p}{m_p + \left(N_S/A\right) m_S}} - \sqrt{\frac{\kappa_p}{m_p}}\right) \\ &= \frac{1}{2\pi}\sqrt{\frac{\kappa_p}{m_p}}\sqrt{\frac{1}{1 + \frac{\left(N_S/A\right) m_S}{m_p}}} - \sqrt{\frac{\kappa_p}{m_p}} \\ &\approx \frac{1}{2\pi}\omega_0\left(1 - \frac{1}{2}\frac{\left(N_S/A\right) m_S}{m_p} - 1\right) = -f_0\frac{m_f}{m_q}, \end{aligned} \tag{1}$$

where f_r is the resonant frequency, f_0 is the resonant frequency of the bare crystal, and $\omega_0 = (\kappa_p/m_p)^{1/2}$ is the radial resonant frequency of the bare crystal. The relation $m_p = Am_q/2$ (Eq. 116 in Chap. 2 in this volume) was used. Equation 1 reproduces the Sauerbrey equation (Eq. 28 in Chap. 2).

The same result is found by use of the small-load approximation (cf. Eq. 51 in Chap. 2) Using the stress $\sigma = -\omega^2(N_S/A)m_S a = -\omega^2 m_f a$ (a is the amplitude of motion) and the speed $\dot{u} = i\omega a \exp(i\omega t)$, one finds:

$$\frac{\Delta f}{f_f} = \frac{i}{\pi Z_q}\frac{\sigma}{\dot{u}} = \frac{i}{\pi Z_q} Z_L = \frac{i}{\pi Z_q}\frac{-\omega^2 m_f a \exp(i\omega t)}{i\omega a \exp(i\omega t)} = \frac{-\omega m_f}{\pi Z_q} = -n\frac{m_f}{m_q}, \qquad (2)$$

where the relation $m_q = Z_q/(2 f_f)$ has been used (Eq. 26 in Chap. 2). $Z_L = \sigma/\dot{u}$ is the load impedance.

2.2 Loading with a Spring

In analogy to Eq. 1, one can add a spring (with a spring constant κ_S) into the BvD circuit, rather than a mass (Fig. 2b). Such a spring would represent the stiffness of a contact between the crystal and an object touching it. The object would have to be so heavy that it does not take part in the movement of the crystal. The analog of Eq. 1 is:

$$\Delta f = f_r - f_0 = \frac{1}{2\pi}\left(\sqrt{\frac{\kappa_p + (N_S/A)\kappa_S}{m_p}} - \sqrt{\frac{\kappa_p}{m_p}}\right)$$
$$\approx f_0\left(1 + \frac{1}{2}\frac{N_S}{A}\frac{\kappa_S}{\kappa_p} - 1\right) = f_f\frac{N_S}{A}\frac{1}{\pi Z_q}\frac{\kappa_S}{\omega}, \qquad (3)$$

where the relation $(\kappa_p m_p)^{1/2} = \kappa_p/\omega_0 \approx \kappa_p/\omega \approx AZ_q n\pi/2$ (Eq. 115 in Chap. 2) has been used. In this context the resonance frequency of the unloaded crystal, ω_0, and the loaded crystal, ω, can be considered to be about equal. The same result is found by application of the small-load approximation if one assumes that the average stress is given by the spring constant multiplied the number density, N_S/A [23]:

$$\frac{\Delta f}{f_f} = \frac{i}{\pi Z_q}\frac{\sigma}{\dot{u}} = \frac{i}{\pi Z_q}\frac{N_S}{A}\frac{\kappa_S u_0}{i\omega u_0} = \frac{i}{\pi Z_q}\frac{N_S}{A}\frac{\kappa_S}{\omega}. \qquad (4)$$

In the following, the small-load approximation is always used to calculate the frequency shift.

The frequency shift in Eq. 4 is *positive*. If the spring constant is independent of frequency, Δf scales as ω^{-1}, that is, as the inverse overtone order, n^{-1}. Damping and frequency dependent interactions can be introduced into Eq. 4

by replacing κ_S with a complex spring constant $\kappa_S(\omega) + i\omega\xi_S(\omega)$, leading to:

$$\frac{\Delta\tilde{f}}{f_f} = \frac{N_S}{\pi Z A_q}\frac{1}{\omega}\left(\kappa_S(\omega) + i\omega\xi_S(\omega)\right) . \tag{5}$$

The parameter $\Delta\tilde{f} = \Delta f + i\Delta\Gamma$ is a complex resonance frequency. Γ is the half-band-half-width (cf. Sect. 2 in Chap. 2 in this volume). The drag coefficient may describe interfacial drag, but also the withdrawal of energy from the crystal via radiation of sound. Equation 5 can be inverted, leading to explicit formulas for $\kappa_S(\omega)$ and $\xi_S(\omega)$:

$$\kappa_S(\omega) = 2\pi^2 Z_q n \frac{A}{N_S}\Delta f(\omega) \tag{6}$$

$$\xi_S(\omega) = \frac{\pi Z_q}{f_f}\frac{A}{N_S}\Delta\Gamma(\omega) . \tag{7}$$

In order to emphasize the generality of the model, the frequency dependence of $\kappa_S(\omega)$ and $\xi_S(\omega)$ was explicitly included in Eqs. 5, 6, and 7. More detailed models (cf. Sects. 2.4 and 2.5) predict the frequency dependence of $\kappa_S(\omega)$ and $\xi_S(\omega)$. For the time being, no such statement is made. The only assumption made here is the absence of inertial effects: Clearly, some of the material close to the contact must move with the crystal. The total mass of this co-moving material was neglected.

2.3 Loading with a Mass in Series with a Spring

In the simple-spring model, the crystal is in contact with an immobile object. The model can be extended to cover situations where the object takes part in the oscillation to some extent. A typical object of this kind would be a small (< 10 μm) sphere [40]. Figure 2c depicts the physical situation and the equivalent circuit representation. Note that the motion occurs into the *lateral* direction even though the spring is drawn vertically. In the following, we assume a spring constant independent of frequency, labeled $\bar{\kappa}_S$. From Fig. 2c, we infer the load to be:

$$\begin{aligned} Z_L &= \frac{N_S}{A}\left(Z_{mass}{}^{-1} + Z_{spring}{}^{-1}\right)^{-1} = \frac{N_S}{A}\left(\frac{1}{i\omega m_S} + \frac{i\omega}{\bar{\kappa}_S}\right)^{-1} \\ &= \frac{N_S}{A}\frac{i\omega m_S\bar{\kappa}_S}{-\omega^2 m_S + \bar{\kappa}_S} = \frac{N_S}{A} i\omega m_S \frac{1}{1 - \frac{\omega^2}{\omega_S^2}} , \end{aligned} \tag{8}$$

where the parameter $\omega_S = (\bar{\kappa}_S/m_S)^{1/2}$ denotes the resonance frequency of the mass-spring system. Using the small-load approximation, we find:

$$\frac{\Delta f}{f_f} = \frac{i}{\pi Z_q} Z_L = -\frac{N_S}{A}\frac{\omega m_S}{\pi Z_q}\frac{1}{1-\frac{\omega^2}{\omega_S^2}}. \tag{9}$$

Since the spring constant is complex due to dissipalion, the denominator never becomes zero. Equation 9 was first proposed by Dybwad [19]. In the limits of $\omega_S^2 \gg \omega$ and $\omega_S^2 \ll \omega$, Eq. 9 reproduces the Sauerbrey equation (Eq. 2) and the simple-spring model (Eq. 4), respectively. Equation 9 can also be derived from Eq. 91 in Chap. 2 in this volume by expanding all tangents to first order. This amounts to a continuum model of the same experimental situation, where the contacts and the spheres correspond to a "soft", first layer and a "hard", second layer, respectively.

2.4 Loading with a Mass in Series with a Dashpot

The connection between the sphere and the crystal can also be made across a dashpot (Fig. 2d). This model is extensively used for the interpretation of nanotribological experiments with the QCM [20]. We consider the drag coefficient of the dashpot, $\bar{\xi}_S$, to be a fixed parameter independent of frequency. Within this model, the sphere slides on the surface in a liquid-like sense (creep). This liquid-like friction is very different from interfacial sliding in the Coulomb sense. For Coulomb sliding, the friction force is proportional to the vertical load with a dimensionless dynamic friction coefficient, μ_D. In particular, the friction force is independent of the sliding speed. Sliding in the Coulomb sense implies a strongly nonlinear force–speed relation. The drag force in creep, on the other hand, depends linearly on sliding speed.

From Fig. 2d one reads:

$$\begin{aligned} Z_L &= \frac{N_S}{A}\left(Z_{\text{mass}}{}^{-1} + Z_{\text{dashpot}}{}^{-1}\right)^{-1} = \frac{N_S}{A}\left(\frac{1}{i\omega m_S} + \frac{1}{\bar{\xi}_S}\right)^{-1} \\ &= \frac{N_S}{A}\frac{i\omega m_S \bar{\xi}_S}{i\omega m_S + \bar{\xi}_S} = \frac{N_S}{A} i\omega m_S \frac{1}{1+i\omega\tau_S} = \frac{N_S}{A} i\omega m_S \frac{1-i\omega\tau_S}{1+i\omega^2\tau_S^2}, \end{aligned} \tag{10}$$

where the slip time $\tau_S = m_S/\bar{\xi}_S$ was used. Using the small-load approximation, we find [19, 24]:

$$\frac{\Delta \tilde{f}}{f_f} = -\frac{N_S}{A\pi Z_q}\omega m_S \frac{1-i\omega\tau_S}{1+\omega^2\tau_S^2}. \tag{11}$$

The tilde denotes a complex frequency shift. We write $\Delta\tilde{f} = \Delta f + i\Delta\Gamma$. The imaginary part, $\Delta\Gamma$, is the shift of the half bandwidth at half maximum. The

slip time is inferred from the ratio of $\Delta\Gamma$ and $(-\Delta f)$ as:

$$\tau_S = \frac{1}{\omega}\frac{\Delta\Gamma}{(-\Delta f)}\,. \tag{12}$$

The mass-dashpot model predicts that the ratio $\Delta\Gamma/(-\Delta f)$ scales as the overtone order (unless the slip time itself depends on frequency).

2.5 Loading with a Spring and a Dashpot

The extension of the previous models to a sphere coupled to the plate via a spring and a dashpot is straightforward. The coupling can be achieved either via a Voigt-type circuit (viscoelastic solid, Fig. 2e) or via a Maxwell-type circuit (viscoelastic liquid, Fig. 2f). Below, we assume that the object is so heavy that it does not take part in the motion. When the mass is infinite, the inertial term drops out of the load impedance. An infinite mass is graphically depicted as a wall. For Voigt-type coupling we find:

$$Z_L = \frac{N_S}{A}\left(Z_{\text{spring}} + Z_{\text{dashpot}}\right) \approx \frac{N_S}{A}\left(\frac{\bar{\kappa}_S}{i\omega} + \bar{\xi}_S\right) \tag{13}$$

leading to a frequency shift of:

$$\frac{\Delta\tilde{f}}{f_f} = \frac{1}{\pi Z_q}\frac{N_S}{A\omega}\left(\bar{\kappa}_S + i\omega\bar{\xi}_S\right). \tag{14}$$

Voigt-type coupling makes sense for multi-asperity contacts. The load-bearing asperities correspond to springs, but there will also be interfacial drag (for instance across capillary bridges) acting in parallel to the elastic contacts. The model predicts a positive frequency shift, which scales as the inversely overtone order, n^{-1}. Both the positive frequency shift and the n^{-1}-scaling are rather characteristic experimental features. Checking for the n^{-1}-scaling, one can easily determine whether or not Voigt-type coupling applies.

Figure 3 shows an example [25]. A monolayer of glass spheres with a diameter of 200 μm was deposited onto the crystal at $t = 0$ (state I). The initial deposition had virtually no effect on the frequency of resonance. Even though the spheres did touch the crystal, the dry contacts only transmitted a minute amount of stress. After about 10 min, the chamber was filled with saturated water vapor, leading to a substantial frequency increase (state II). Capillary forces strengthen the contacts, as known from the sand-castle effect. A further strong increase in frequency was achieved by ramping the humidity back down to a low value (state III). After having been exposed to water vapor, the spheres form a cake. The latter transition is reversible: once the assembly of spheres has been soaked in humid air, one can go back and forth between the states II and III. Comparing the frequency shifts on the different

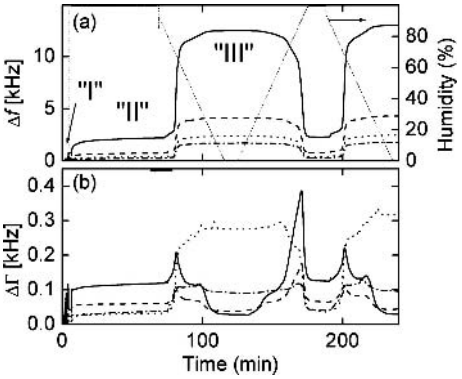

Fig. 3 Shifts of frequency (**a**) and bandwidth (**b**) experienced by a quartz crystal covered with a monolayer of glass spheres (diameter $d = 200\,\mu m$) exposed to humid air. *States I, II*, and *III* correspond to the initial state right after deposition, to humid air, and to a dry state reached after soaking the sample in humid air for a while and then returning to the dry state, respectively. *Full line* 5 MHz, *dashed line* 15 MHz, *dotted line* 25 MHz, *dash-dotted line* 35 MHz (adapted from [28])

overtones, one confirms n^{-1} scaling. This experiment proves the QCM to be a non-destructive monitoring device for capillary aging [26].

For Maxwell-type coupling, the situation is more complicated. From Fig. 2f, one reads:

$$Z_L \approx \frac{N_S}{A}\left(Z_{spring}{}^{-1} + Z_{dashpot}{}^{-1}\right)^{-1} = \frac{N_S}{A}\left(\frac{i\omega}{\bar{\kappa}_S} + \frac{1}{\bar{\xi}_S}\right)^{-1}$$

$$= \frac{N_S}{A}\frac{\bar{\kappa}_S\bar{\xi}_S}{\bar{\kappa}_S + i\omega\bar{\xi}_S} = \frac{N_S}{A}\bar{\xi}_S\frac{1}{1 + i\omega\tau_R} = \frac{N_S}{A}\bar{\xi}_S\frac{1 - i\omega\tau_R}{1 + i\omega^2\tau_R^2}\,. \tag{15}$$

A retardation time $\tau_R = \bar{\xi}_S/\bar{\kappa}_S$ was introduced. For the frequency shift, we find:

$$\frac{\Delta\tilde{f}}{f_f} = \frac{N_S}{A}\frac{i}{\pi Z_q}\bar{\xi}_S\frac{1 - i\omega\tau_R}{1 + i\omega^2\tau_R^2} = \frac{N_S\bar{\xi}_S}{A\pi Z_q}\frac{\omega\tau_R + i}{1 + \omega^2\tau_R^2}\,. \tag{16}$$

The frequency shift is positive. The n-scaling depends on the value of $\omega\tau_R$. In the limit of $\omega\tau_R \gg 1$, n^{-1} scaling is found. In this case, the relaxation time is much longer than the period of oscillation and the Maxwell element behaves elastically. The Maxwell model reduces to the simple-spring model (Sect. 2.2). If, on the other hand, the retardation time is short ($\omega\tau_R \ll 1$), the frequency shift is still positive, but it scales linearly with n. If a positive frequency shift in conjunction with linear n-scaling is found, this in indicative of fast relaxation processes in the contact zone. If this is the case, the damping must also be large.

Two caveats are worth mentioning: Firstly, inertial effects can only be neglected if the contact area is small enough. Otherwise, the co-moving mass needs to be included into the model. The co-moving volume is much smaller than the volume of the entire sphere but it may be nonzero. Secondly, there usually is some increase in bandwidth originating from the radiation of acoustic waves into the sphere. Acoustic radiation can be accounted for by adding a dashpot with a drag coefficient ξ_{ac} as a parallel element into the circuits shown in Fig. 2. The magnitude of the dashpot is of the order of $\xi_{ac} \sim (kr_c)\kappa_S/\omega$, where k is the wave number of sound and r_c is the contact radius [24, 27].

3 Nonlinear Mechanics and Memory Effects

The standard model for analyzing QCM data is based on linear mechanics. All forces and stresses are assumed to be proportional to displacement or speed. Such a linear behavior is a prerequisite for equivalent circuits to apply. Nonlinear behavior, generally speaking, is often found in contact mechanics because of the sharp peaks in the stress distribution.

Importantly, the analysis of QCM data is not limited to situations, where stress and strain at the crystal surface are linearly related. In the presence of nonlinear interactions, the movement of the crystal becomes slightly anharmonic, meaning that it weakly deviates from a pure cosine. It is essential that the deviation from the purely harmonic motion is small. The two-timing approximation used below only holds for weakly nonlinear oscillators. However, since the perturbation of the crystal by the sample is small in any case, the nonlinear term in the dynamical equations governing the crystal's response are always small, as well. They are by far outweighted by the strong, linear stress-strain relation intrinsic to the crystal, even if the interaction between the crystal surface and the sample is strongly nonlinear. Assume that the crystal is in contact with a tip, which undergoes a transition from stick to slip: This would usually be considered a complicated situation. The interaction is so strongly nonlinear that the trajectory of the tip is highly hysteretic. Still: the tip only weakly perturbs the motion of the crystal and the analysis described below therefore holds.

The following section describes the use of the two-timing approximation for the analysis of QCM data. The same formalism is also used in the field of non-contact atomic force microscopy [28, 29]. In the latter context, the tip–sample interaction perturbs the oscillation of the cantilever. As long as the tip–sample force is weak compared to the force needed to bend the cantilever, the interaction potential can be reconstructed from the frequency of the cantilever as a function of amplitude and mean vertical distance.

The behavior of weakly nonlinear oscillators is discussed in the textbooks [30]. For a small external force $F(t)$, the two-timing approximation holds. The motion of the crystal is almost sinusoidal and the consequences of the external force are captured by a slowly varying amplitude $a(t)$ and a slowly varying phase $\Phi(t)$:

$$u(t) = a(t)\cos\left(\omega_0 t + \Phi(t)\right) . \tag{17}$$

$u(t)$ is the lateral displacement of the crystal surface and ω_0 is the resonance frequency of the unperturbed oscillator. The shift in bandwidth, $\Delta\Gamma$, is proportional to the time derivative of the amplitude, whereas the frequency shift, Δf, is proportional to the time derivative of the phase [31, 32]:

$$2\pi\Delta\Gamma = -\frac{1}{a}\frac{\mathrm{d}a}{\mathrm{d}t}$$

$$2\pi\Delta f = \frac{\mathrm{d}\Phi}{\mathrm{d}t} . \tag{18}$$

Here, the time increment $\mathrm{d}t$ is meant to be larger than the period of oscillation. This is the essence of the two-timing approximation. With regard to the details of the two-timing approximation, the reader is referred to [32]. The outcome of the calculation is [31, 32]:

$$\frac{\Delta f}{f_\mathrm{f}} = \frac{2}{a}\frac{1}{\pi A Z_\mathrm{q}}\frac{1}{\omega}\left\langle F(t)\cos(\omega t)\right\rangle \tag{19}$$

and

$$\frac{\Delta\Gamma}{f_\mathrm{f}} = \frac{2}{a}\frac{1}{\pi A Z_\mathrm{q}}\frac{1}{\omega}\left\langle F(t)\sin(\omega t)\right\rangle . \tag{20}$$

The angular brackets denote the average over an entire period of oscillation. The parameter ω is the frequency of the loaded oscillator (as opposed to ω_0). The difference between ω and ω_0 is small.

Note that the quantities in angular brackets are the exact same weighted averages which a lock-in amplifier (referenced to ω) would produce. Although the angular brackets look clumsy at first sight, they represent quantities which are very familiar to the experimentalist. They are the in-phase and the out-of-phase components of the force.

Equation 20 can be made plausible by noting that the term $\langle F(t)\sin(\omega t)\rangle$ is proportional to the energy dissipated per cycle:

$$\left\langle F(t)\sin(\omega t)\right\rangle = \frac{1}{a\omega_a}\frac{1}{T_\mathrm{p}}\int_0^{T_\mathrm{p}} F(t)\frac{\mathrm{d}u(t)}{\mathrm{d}t}\,\mathrm{d}t = \frac{1}{2\pi a}\oint F(u)\,\mathrm{d}u = \frac{1}{2\pi a}\Delta W , \tag{21}$$

where T_p is the period of oscillation and $\oint F(u)\,\mathrm{d}u = \Delta W$ is the area inside the hysteresis loop (see, for example, Fig. 4). The connection to the bandwidth is

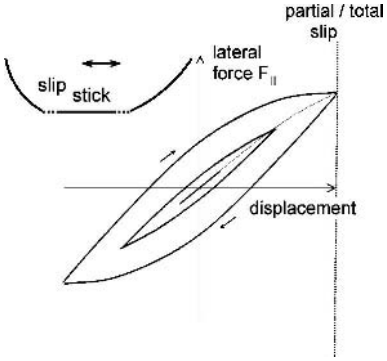

Fig. 4 Force–displacement relation as predicted by the Mindlin model. Since the central area, where the contact sticks, decreases with increasing tangential load, the force increases sub-linearly with displacement. The area under the hysteresis loop is the energy dissipated per cycle, ΔW

made by noting that the Q-factor of a resonance obeys the relation:

$$\Delta(Q^{-1}) = \frac{2\Delta\Gamma}{f} = \frac{\Delta W}{2\pi E_{\mathrm{osc}}} = \frac{\Delta W}{2\pi \frac{1}{2}\kappa_{\mathrm{p}} a^2}\,, \tag{22}$$

where $\Delta(Q^{-1})$ is the shift of the inverse Q-factor and $E_{\mathrm{osc}} = \kappa_{\mathrm{p}} a^2/2$ is the energy contained in the oscillation. Using the relation $(\kappa_{\mathrm{p}} m_{\mathrm{p}})^{1/2} = \kappa_{\mathrm{p}}/\omega = AZ_{\mathrm{q}} n\pi/2$ (Eq. 115 in Chap. 2), we find:

$$\begin{aligned}\frac{\Delta\Gamma}{f_{\mathrm{f}}} &= \frac{1}{f_{\mathrm{f}}}\frac{f}{2}\Delta(Q^{-1}) = n\frac{1}{2\pi\kappa_{\mathrm{p}} a^2}\Delta W \\ &= n\frac{1}{2\pi\kappa_{\mathrm{p}} a^2} 2\pi a\langle F(t)\sin(\omega t)\rangle \\ &= \frac{2}{AZ_{\mathrm{q}}\pi}\frac{1}{a}\frac{1}{\omega}\langle F(t)\sin(\omega t)\rangle\,,\end{aligned} \tag{23}$$

which reproduces Eq. 20. With regard to the frequency shift (Eq. 19), the argument is less intuitive and we leave it with the formal proof as given in [30].

When linear force laws hold, one has $F(t) = \kappa_{\mathrm{S}} u(t) + \xi_{\mathrm{S}}\dot{u}(t)$, which leads to:

$$\begin{aligned}\frac{\Delta f}{f_{\mathrm{f}}} &= \frac{1}{\pi Z_{\mathrm{q}}}\frac{1}{\omega}\frac{2}{A}\langle\kappa_{\mathrm{S}}\cos^2(\omega t)\rangle = \frac{1}{\pi Z_{\mathrm{q}}}\frac{1}{\omega}\frac{1}{A}\kappa_{\mathrm{S}} \\ \frac{\Delta\Gamma}{f_{\mathrm{f}}} &= \frac{1}{\pi Z_{\mathrm{q}}}\frac{1}{\omega}\frac{2}{A}\langle\omega\xi_{\mathrm{S}}\sin^2(\omega t)\rangle = \frac{1}{\pi Z_{\mathrm{q}}}\frac{1}{A}\xi_{\mathrm{S}}\,.\end{aligned} \tag{24}$$

Equations 19 and 20 then reduce to Eqs. 4 and 5. If memory effects are absent, a nonlinear stress–strain relation (quantified by a nonlinear spring constant $\kappa_{\mathrm{S}}(u)$) and a nonlinear stress–speed relation (quantified by a nonlinear drag

coefficient $\xi_S(\dot{u})$) can be explicitly reconstructed from the amplitude dependence of the Δf and $\Delta \Gamma$ [31, 32]. A unique solution is obtained. If, on the other hand, memory and hysteresis may not be neglected, no such explicit inversion of the equations is possible. Still, any assumption on the time-dependent force $F(t)$ can be inserted into Eqs. 19 and 20 in order to predict the frequency shift. The prediction can be compared with the experimentally determined frequency shift and the model can be refined until the prediction matches the experiment. By means of Eqs. 19 and 20, any given hypothesis about the force $F(t)$ (including stick-slip and memory effects) can be checked against the experiment.

4 Continuum Models

The circuits discussed in Sect. 2 contain discrete mechanical elements. They predict the sign, the n-dependence, and the relative magnitude of Δf and $\Delta \Gamma$, but they make no suggestion of how to assign a physical meaning to the model parameters, once they have been determined from experiment. Continuum models evidently are more complicated. On the other hand, they are not only more realistic, they also provide quantitative guidelines for the interpretation of experimentally derived parameters. Two situations have been analyzed, which are the sphere–plate contact and the sheet contact.

4.1 The Mindlin Model

The analysis of the sphere–plate contact under tangential oscillatory load goes back to Mindlin [12]. We refer the reader to [3] with regard to the derivation. Oscillatory tangential load is also discussed in the context for fretting wear [41, 42]. When a Hertzian sphere–plate contact is subjected to a tangential load, there is a stress concentration at the rim of the contact area. Within the continuum treatment, the stress goes to infinity at $r = r_c$, where r_c is the radius of contact. As a consequence, there is a ring-shaped area close to the rim of the contact, inside which the two surfaces slide against each other. The phenomenon is termed “partial slip”. As the stress increases, the sliding part of the contact zone increases in size, until it finally covers the entire contact. At this point, partial slip turns into gross slip.

If roughness plays a role, the Mindlin model does not apply. Still, the Mindlin model is a good example of a broader class of models of partial slip. Bureau et al. have proposed a quantitative extension of the microslip model accounting for multi-contact interfaces [34]. Partial slip also occurs in multi-asperity contacts because the microcontacts located at the rim are expected to rupture first. These contacts experience the largest lateral stress and the low-

est vertical load. While the details will certainly differ when comparing the Hertzian contact and the multi-asperity contact, the generic features should be similar.

Figure 4 shows the force–displacement relation for oscillatory tangential loading. The force–displacement curves bend downward because the part of the contact which sticks becomes smaller and smaller as the lateral force increases. The Hertzian contact is nonlinear under tangential load. (It is nonlinear under vertical load, as well.) The energy dissipated per cycle corresponds to the area inside the loop in Fig. 4. The dissipated energy does not depend on frequency. The Mindlin model describes a quasi-static motion. In particular, the energy dissipation entirely originates from the hysteretic behavior. Energy dissipated during sliding in the outer ring is neglected, which certainly is a shortcoming of the model.

For oscillatory loading, the lateral displacement, $u(t)$, is given by [3]:

$$u(t) = \frac{3\mu_S F_\perp}{8 r_c G_{\text{eff}}} \left[2\left(1 - \frac{F_{||,\max} - F_{||}(t)}{2\mu_S F_\perp}\right)^{\frac{2}{3}} - \left(1 - \frac{F_{\max}}{\mu_S F_\perp}\right)^{\frac{2}{3}} - 1 \right]$$

$$= \frac{3}{2}\lambda_S \left[2\left(1 - \frac{F_{||,\max} - F_{||}(t)}{2\mu_S F_\perp}\right)^{\frac{2}{3}} - \left(1 - \frac{F_{\max}}{\mu_S F_\perp}\right)^{\frac{2}{3}} - 1 \right], \tag{25}$$

where μ_S is the static friction coefficient, r_c is the radius of contact, $F_\perp$ is the vertiacl force, $F_{||}$ is the tangential force, and $F_{||,\max}$ is the maximum tangential force. $G_{\text{eff}} = 2 \times ((2 - \nu_1)/G_1 + (2 - \nu_2)/G_2)^{-1}$ is an effective modulus. G is the shear modulus, ν is Poisson's number, and the indices 1 and 2 label the contacting materials. We will show below that the quantity $4 r_c G_{\text{eff}}$ is the lateral spring constant of the contact in the low amplitude limit, $\kappa_{0,M}$. The characteristic length $\lambda_S = \mu_S F_\perp/(4 r_c G_{\text{eff}}) = \mu_S F_\perp/\kappa_{0,M}$, termed "partial slip length", was introduced for notational convenience. λ_S is defined in analogy to the elastic length $\lambda_e = F_\perp/\kappa$ (κ the lateral spring constant) used by the Paris group to describe multi-asperity contacts [35]. In macroscopic experiments, λ_e is a measure of roughness. λ_S differs from λ_e in that it contains the static friction coefficient μ_S as a prefactor. From the ratio of λ_S and λ_e, one obtains an estimate of the static friction coefficient.

Since the force across the contact only weakly perturbs the motion of the crystal surface, the displacement, $u(t)$, is mainly governed by the dynamics of the quartz crystal. $u(t)$ is sinusoidal with time, and the force $F(t)$ is a function of the displacement and the direction of motion. $F(t)$ can be calculated by inversion of Eq. 25 as:

$$\frac{F_{||}(t)}{\mu_S F_\perp} = \left[\frac{F_{||,\max}}{\mu_S F_\perp} - 2 + \frac{1}{\sqrt{2}} \left(1 + \frac{2u(t)}{3\lambda_S} + \left(1 - \frac{F_{||,\max}}{\mu_S F_\perp}\right)^{\frac{2}{3}} \right)^{\frac{3}{2}} \right]. \tag{26}$$

Inserting Eq. 26 into Eq. 24 and performing the integration leads to a prediction for Δf and $\Delta\Gamma$. In the small amplitude limit ($u(t) \ll \lambda_S$) one finds:

$$\frac{\Delta f}{f_f} \approx \frac{1}{AZ_q\pi}\frac{4r_cG_{eff}}{\omega}\left(1 - 0.20\frac{a}{\lambda_S}\right) = \frac{1}{AZ_q\pi}\frac{\kappa_{0,M}}{\omega}\left(1 - 0.20\frac{a}{\lambda_S}\right) \tag{27}$$

$$\frac{\Delta\Gamma}{f_f} \approx \frac{1}{AZ_q\pi}\frac{\kappa_{0,M}}{\omega}\frac{2}{9\pi}\frac{a}{\lambda_S}. \tag{28}$$

In the case of Eq. 27, the integration was carried out numerically. For the bandwidth (Eq. 28), analytical integration is possible because the integral is proportional to the area inside the hysteresis loop in Fig. 4 [3].

Comparing Eqs. 4 and 27, one sees that the term $4r_cG_{eff}$ can be identified with the spring constant in the small amplitude limit, $\kappa_{0,M}$. The dissipation is small, because the sliding portion of the contact is small. It is proportional to amplitude. This type of interfacial friction may therefore *not* be represented by a dashpot. However, there always is an additional source of dissipation given by radiation of sound into the sphere. This component can be modeled with a dashpot. The acoustic contribution to dissipation may mask interfacial friction at small amplitudes.

Figure 5 shows an example. A quartz crystal was covered with a monolayer of glass spheres (diameter $d = 200\,\mu m$) and exposed to humid air. In this case, the frequency shift and bandwidth were determined by ring-down [31, 32, 36]. The dependence of frequency and bandwidth on amplitude is substantial, indicative of a nonlinear interaction. From the slopes in the plots of Δf and $\Delta\Gamma$ vs a one infers a partial slip length λ_S of the order of

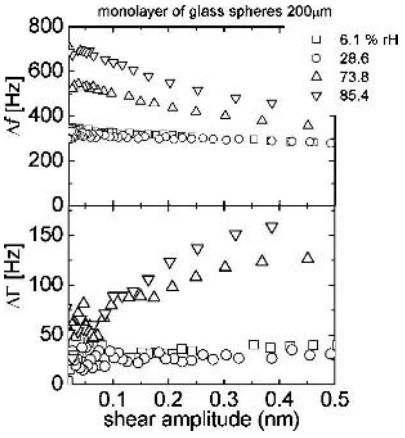

Fig. 5 Shift of frequency **a** and bandwidth **b** as a function of amplitude for a quartz plate covered with a monolayer of glass spheres ($d = 200\,\mu m$) at a various humidities. The data were acquired via ring-down [32]. From the slopes, one infers the partial slip length, λ_S and the coefficient of static friction, μ_s

a nanometer. The slips lengths derived from Δf and $\Delta \Gamma$ differ, indicating that the Mindlin model is not quantitatively applicable.

The sources of discrepancy are sliding friction, capillary interactions, and the fact that we have a multiasperity contact. Rolling (simultaneous release of contacts on one side and formation of new ones at the other) may also be part of the picture.

The elastic length $\lambda_e = F_\perp/\kappa_S$ is explicitly available: The spring constant, κ_S, can be derived from the frequency shift (Eqs. 4 and 27). The vertical force, $F_\perp$, is known from the weight of the spheres[2]. The static friction coefficient $\mu_S = \lambda_S/\lambda_e$ is significantly above one. High coefficients of static friction have also been found with colloidal probe experiments on quartz crystals (Gubaidullin and Johannsmann, in preparation). The reason for the increased static friction is subject to interpretation. Presumably, slip takes time: the MHz oscillation is just too fast for slip to set in [37]. This finding highlights, how much different the contact mechanics at high frequencies is from the corresponding behavior at low frequencies.

4.2 The Sheet-Contact Model

The Mindlin model describes the sphere–plate contact, assuming a contact radius much smaller than the radius of the sphere. The opposing limit, where the contact area is much larger than the wavelength of sound has been treated by the Shull group [38]. Such a geometry is established when a soft object like a hemisphere of a rubbery material touches the crystal. The JKR tester uses this arrangement [39]. The JKR model – underlying the JKR tester – is an extension of the Hertz model, accounting for a finite interfacial energy of the contacting materials. The interfacial interaction must be short-ranged. The model predicts the radius of contact as function of vertical load, stiffness of the material, and surface energy. The radius of contact usually is measured by imaging the contact from a above or below with a microscope. The JKR model and the JKR tester are frequently used in the study of polymer adhesion.

Clearly, combining the JKR tester with the QCM is attractive [38]. The material of interest is molded into the shape of a hemisphere and pushed against the top electrode of the QCM. From the shift in frequency shift and bandwidth one obtains the viscoelastic parameters of the material in the contact zone.

In passing, we note that this approach, in fact, is the only way to determine the viscoelastic parameters of rubbery polymers with the QCM. In principle, one might of course also coat the entire crystal with a thick layer of the respective material. If the thickness of the layer is larger than the penetration depth, the sample is acoustically semi-infinite. The Kanazawa equation

[2] This assumes that the external force is much larger than the force of adhesion.

applies and G' and G'' can be determined from Eq. 62 in Chap. 2 in this volume (using $G = \mathrm{i}\omega\eta$). Unfortunately, the QCM does not work well with semi-infinite media when the viscosity, η, is larger than about 50 cP. The shift of frequency and bandwidth in this case is too large. Most polymers exceed this limit. If, however, the contact area can be confined to a small spot in the center of the crystal, the bandwidth decreases accordingly and, the measurement becomes feasible.

Evidently, the contact established by the JKR-tester is laterally heterogeneous. Experiment shows that the finite contact area can reasonably well be accounted for by modifying the Kanazawa relation as:

$$\frac{\Delta f}{f_\mathrm{f}} = \frac{\mathrm{i}}{\pi Z_\mathrm{q}} K_\mathrm{A} \frac{A_\mathrm{c}}{A} Z_\mathrm{L}\,, \tag{29}$$

where A_c is the contact area and K_A is a "sensitivity factor" [38]. Equation 29 assumes a contact area much larger than the decay length of the shear wave. Also, energy trapping is assumed to be unaffected by the contact (which may be unrealistic in some situations).

The sensitivity factor, K_A, accounts for the non-trivial amplitude distribution over the area of the crystal. For small contact areas, K_A is about constant and equal to two [38]. Since the efficiency of energy trapping depends on overtone order, the parameter K_A depends on overtone order, as well. The K_A-factor can be determined by placing drops of water with known contact radius onto the center of the crystal. Equation 29 has been tested in that way and found to be a good approximation to the data for a large range of experimental conditions [38].

5 Concluding Remarks

The study of contact mechanics is just emerging as an application of the QCM. Clearly, there are limitations: the QCM probes the contacts at a frequency in the megaHertz range[3], it can only provide oscillatory excitation, and the amplitude of excitation is in the namometer range. Comparing the QCM to other devices of mechanical and micromechanical testing, there are following advantages and disadvantages:

- Due to the small amplitude of excitation, the contacts are not usually broken. The QCM is a device for non-destructive testing of interfacial contacts. The evolution of the contact strength with time, temperature, exposure to solvent vapor, or vertical pressure can be monitored without ever breaking a bond.

[3] Analogous studies can be done with torsional resonators in the kHz range. These have a lower sensitivity, but can bridge the frequency gap.

- Because the frequency is so high, inertia comes into play rather strongly. Balancing the force of interest (such as the force transmitted through the sphere–plate contact) against the force of inertia (holding the sphere in place), one gets around the often cumbersome problem of calibrating springs. In low frequency measurements, for example performed with the atomic force microscope, determination of the spring constant is a steady practical challenge. In a way, the situation is reminiscent of astronomy a few hundred years ago, where the force of gravity was analyzed based on a measurement of the orbital frequency of the planets (which admittedly is in a vastly different range).
- It is not true that the QCM is blind to nonlinear interactions. The QCM measures a peculiarly weighted average of the force, but it certainly can access nonlinear phenomena via the amplitude dependence of Δf and $\Delta \Gamma$.
- The QCM probes elastic and dissipative interactions at high frequencies. How relevant these high-frequency interactions are for real world devices, needs to be seen. We know today that things are much different at the MHz scale. We also know that fast processes are important in contact mechanics. Typical phenomena, where high-frequency events are crucial, are the sudden impact of a slider onto a substrate or the advancement of a crack tip in fracture events. At this point, the contact mechanics experiments with the QCM are part of fundamental research, but that may change.

Acknowledgements The author is indebted to Dr. Binyang Du for numerous fruitful discussions and making results available previous to publication.

References

1. Dowsan D (1998) History of tribology. Professional Engineering Publishing
2. Hertz H (1881) J Reine und Angew Mathem 92:156
3. Johnson KL (1989) Contact mechanics. Cambridge, NY
4. Persson BNJ (1998) Sliding friction. Springer, Berlin Heidelberg New York
5. Müser M, Urbakh M, Robbins MO (2003) Adv Chem Phys 126:187
6. Bushan B (ed) (1995) Handbook of Micro/nano tribology, CRC, Boca Raton
7. McClelland GM (1989) In: Grunze M, Kreuzer HJ (eds.) Adhesion and friction. Springer Series in Surface Science 17:1
8. Meyer E, Overney RM, Frommer J (1995) In: Bushan B (ed.) Handbook of micro/nano tribology. CRC, p 223
9. Tshiprut Z, Filippov, AE Urbakh, M (2005) Phys Rev Lett 95:016101
10. Homola AM, Israelachvili JN, Lee ML, McGuiggan PM (1989) J Tribolog 111:675
11. Homola AM, Israelachvili JN, McGuiggan PM, Lee ML (1990) Wear 136:65
12. Kumacheva E (1998) Progr in Surf Sci 58:75
13. Bowden FP, Tabor D (1967) Friction and lubrication. Methuen, London
14. Baumberger T, Heslot F, Perrin B (1994) Nature 367:544
15. Duran J (1999) Sands, powders, and grains. Springer, Berlin Heidelberg New York
16. Herminghaus S (2005) Adv Phys 54:221

17. Scherge M, Schaefer JA (1998) Tribolog Lett 4:37
18. Dybwad GL (1985) J Appl Phys 58:2789
19. Krim J, Solina DH, Chiarello R (1991) Phys Rev Lett 66:181
20. Mak C, Krim J (1998) Phys Rev B 58:5157
21. Bruschi L, Carlin A, Mistura G (2001) Phys Rev Lett 88:46105
22. König AM, Düwel M, Du B, Kunze M, Johannsmann D (2006) Langmuir 22:229
23. Laschitsch A, Johannsmann D (1999) J Appl Phys 85:3759
24. Watts ET, Krim J, Widom A (1990) Phys Rev B 41:3466
25. D'Amour JN, Stålgren JJR, Kanazawa KK, Frank CW, Rodahl M, Johannsmann D (2006) Phys Rev Lett 96:058301
26. Bocquet L, Charlaix E, Ciliberto S, Crassous J (1998) Nature 396:735
27. Berg S, Johannsmann D, Ruths M (2002) J Appl Phys 92:6905
28. Giessibl FJ (2001) Appl Phys Lett 78:123
29. Hölscher H, Schwarz UD, Wiesendanger R (1999) Appl Surf Sci 140:344
30. Strogatz S (1996) Nonlinear dynamics and chaos, chap 7.6. Addison-Wesley
31. Berg S, Prellberg T, Johannsmann D (2003) Rev Sci Instr 74:118
32. Berg S, Johannsmann D (2003) Phys Rev Lett 91:145505
33. Mindlin RD, Deresiewicz H (1953) J Appl Mech 20:327
34. Bureau L, Caroli C, Baumberger T (2003) Proc Royal Soc London A 459:2787
35. Berthoud P, Baumberger T (1998) Proc Royal Soc London A 454:1615
36. Rodahl M, Kasemo B (1996) Rev Sci Instr 67:3238
37. Maier S, Sang Y, Filleter T, Grant M, Bennewitz B, Gnecco E, Meyer E (2005) Phys Rev B 72:245418
38. Flanigan CM, Desai M, Shull KR (2000) Langmuir 16:9825
39. Shull KR (2002) Mat Sci Engin R 36:1
40. Zhang QL, Lec RM, Pourrezaei K (2006) IEEE TRANSACTIONS ON ULTRASONIC FERROELECTRICS AND FREQUENCY CONTROL 53(1):167–174
41. Szolwinski MP, Farris TN (1996) Wear 198:93
42. Varenberg M, Etsion I, Altus E (2005) Tribology Letters 19:263

Part B
Chemical and Biological Applications of the QCM

Springer Ser Chem Sens Biosens (2007) 5: 173–210
DOI 10.1007/5346_027

Published online: 22 July 2006

Imprinted Polymers in Chemical Recognition for Mass-Sensitive Devices

Franz L. Dickert (✉) · Peter A. Lieberzeit

Department of Analytical Chemistry and Food Chemistry, Faculty of Chemistry, Vienna University, Waehringer Strasse 38, 1090 Vienna, Austria
Franz.Dickert@univie.ac.at

Abstract Mass-sensitive devices such as the quartz crystal microbalance (QCM) or the surface acoustic wave device (SAW) are very advantageous for chemical sensing. As their name implies, they react towards mass changes on their respective sensitive areas, which makes them almost universally applicable since every analyte has a mass. Detection limits can be as low as 1 ng for QCM and in the picogram range for SAW. Of course, selectivity also has to be introduced into the sensor system. For this purpose molecular imprinting, where the sensitive layer is generated by polymerising it directly on the respective device surface, is gaining increasing attention. A reason for this is the very straightforward synthetic approach, where the analyte-to-be is used as a template that determines the structure of the interaction sites within the polymer by self-organisation processes. In this chapter, we give an introduction into the electronic background of mass-sensitive devices as well as into molecular imprinting. In the second half, we will introduce selected strategies for actual chemical sensing of analytes covering a size range from molecular to micrometre as well as both pure compounds and mixtures.

Keywords Mass-sensitive transducer · QCM · SAW · Molecular imprinting · Chemical sensor

Abbreviations

AC	Alternating current
AFM	Atomic force microscopy
FBAR	Film bulk acoustic resonator
HRV	Human rhinovirus
MOS	Metal oxide semiconductor device
PAH	Polycyclic aromatic hydrocarbon
PDMS	Polydimethyl siloxane
PVAc	Poylvinylacetate
QCM	Quartz crystal microbalance
SAW	Surface acoustic wave resonator
STW	Shear transverse wave resonator
RBC	Red blood cell
VOC	Volatile organic compound

1 Introduction

Chemical sensing has gained substantial scientific and public interest during the last decade as an effective novel technique in analytical sciences. Modern apparative analytical chemistry has reached extraordinarily low detection limits, high sensitivity and outstanding flexibility, especially with hyphenated techniques. However, the versatility, flexibility and power of these methods comes at the cost of comparably high initial as well as maintenance investment, as the apparatus is usually very elaborate and requires specially trained personnel to reach the peak level of method abilities. Yet there is a range of measurement tasks that do not require this analytical potential. Furthermore, established apparative techniques often lack portability and on-line ability. To address these questions, chemical sensing is gaining increasing acceptance and attention both by the scientific community and industry, but also by the broad public, especially as environmental monitoring is a matter of increasing awareness in the industrialised countries. Generally speaking, a chemical sensor is a small analytical device that is capable of selectively detecting a defined analyte or range of analytes with predetermined sensitivity. Additionally, a sensor system ideally is portable and adequate for on-line measurements and does not require specially trained operators. Figure 1 gives the general scheme of a chemical sensor. In principle, it consists of a chemically sensitive layer that changes one of its physical properties when it selectively interacts with the desired analyte molecule. This change is recorded by the transducer, a device that transforms the chemical information into electronically measur-

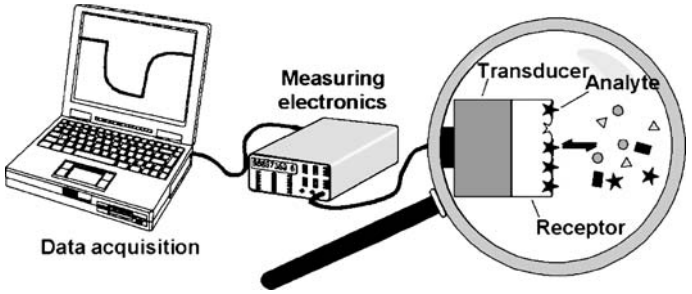

Fig. 1 Scheme of a chemical sensor

able and quantifiable data. Finally, the electronic signal is usually amplified and the measuring data recorded by a signal processing and data evaluation unit.

A wide range of physical parameters are suitable for chemical sensing applications, consequently, there is a very wide variety of different transducers. Some examples of frequent transducing techniques are metal oxide semiconductor devices (MOS diodes and field effect transistors) relying e.g. on changes in electrical fields or opt(r)odes concerning optical phenomena such as absorbance and fluorescence, but also miniaturised capacities [1]. Mass-sensitive, or acoustic, devices constitute another very popular class of transducers. Within this chapter we will focus on this transducing technique and introduce its abilities and properties in combination with selective artificial interaction materials.

2
Mass-Sensitive Devices

2.1
Fundamentals

Any type of acoustic transducer, such as quartz crystal microbalance (QCM) or surface acoustic wave device (SAW), is fundamentally based on the piezoelectric effect. This was first described in 1880 by Jacques and Pierre Curie as a property of crystalline materials that do not have an inversion centre. When such a material is subjected to physical stress, a measurable voltage occurs on the crystal surfaces. Naturally, the opposite effect can also be observed, i.e. applying an electrical charge on a piezoelectric material leads to mechanical distortion, the so-called inverse piezo effect. These phenomena can be used to transfrom an electrical signal to a mechanical one and back, which actually happens in QCM and SAW. Different materials are applied for device fabrication, such as quartz, lithium tantalate, lithium titanate

and lithium niobate. Quartz of course is the most popular, because it is inherently cheap, can be processed to yield single crystals quite easily and can withstand usual chemical, thermal and mechanical stress. The actual type of oscillation induced in the device (i.e. bulk oscillation, surface effect, type of movement) as well as the temperature behaviour depends on the cutting angle of the device substrate with respect to the crystallographic main axis. The AT-cut (35° 15′) shows very low temperature dependence and is therefore very frequently applied for QCMs. For this purpose, two electrodes are deposited on the quartz plate (see also Fig. 2a sketching the cross section). When applying voltage, the device undergoes thickness shear stress, i.e. the two faces are moved against each other in their plane. In case of an AC voltage, the two faces oscillate against each other. Resonance occurs if the AC wavelength exactly matches the plate thickness in a way that $n/2$ wavelengths fit into the device thickness with n being an uneven integer. At this frequency the device oscillation remains almost undamped. Figure 2b depicts the AFM image of a QCM electrode both at 30 V and 0 V applied voltage. When the voltage is switched on, the indentation visible in the centre is

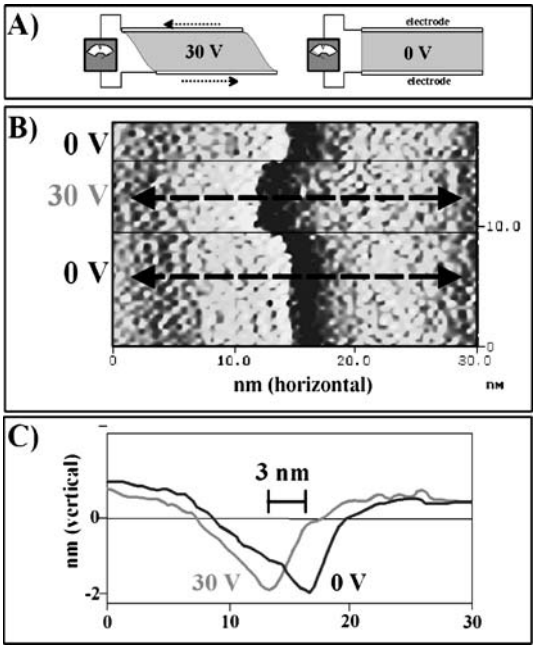

Fig. 2 **A** Schematic cross-section depicting the shear horizontal wave in a QCM device. **B** Contact mode AFM image of a QCM electrode surface at 0 V and 30 V. The horizontal displacement by applying voltage can clearly be seen by the surface scratch. **C** AFM traces recorded on the surface at 30 V and 0 V, respectively. These measurements are optimal for quantifying the displacement, which is 3 nm in the given case

shifted. As the AFM traces show (part c), this leads to a surface displacement of 3 nm.

However, to get further insight into the electronic properties of QCM devices, we have to complement this purely mechanistic view by regarding the damping spectrum of such a device, as shown in Fig. 3b. These two curves covering 95 MHz and 100 kHz frequency ranges, respectively, have been obtained by a network analyser and give the electronic damping of the device as a function of frequency. The base line in the wider frequency range resembles the frequency behaviour of a capacitor, as damping decreases with increasing frequency (see the frequency behaviour of a 10 pF capacitor). This so far is not surprising, as the two gold electrodes with the dielectric insulator quartz in between indeed constitute a capacitor. However, at regular intervals, res-

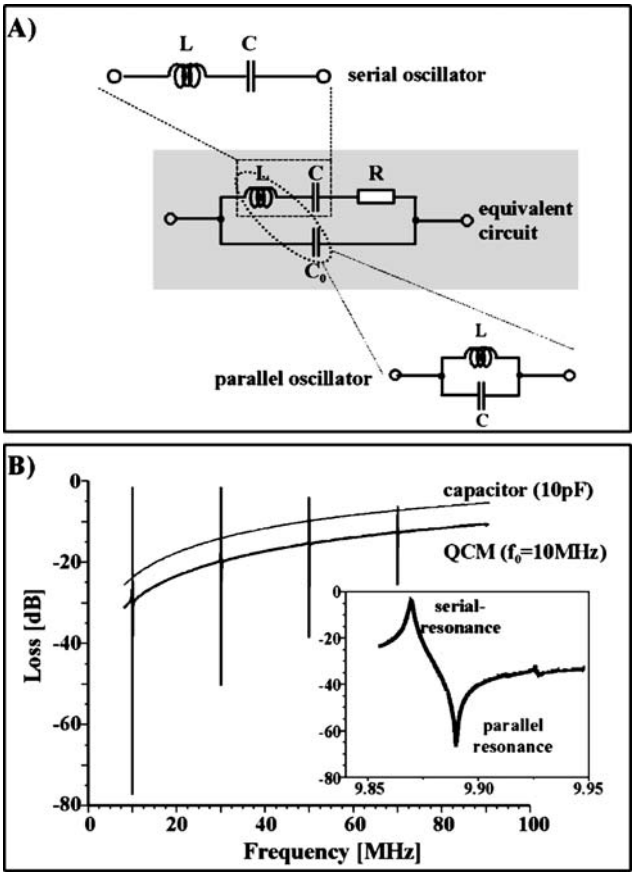

Fig. 3 **A** Electronic equivalent circuit of a QCM resonator. **B** Network analyser damping spectra of a QCM and a 10 pF capacitor recorded with a 95 MHz span. The *inset* shows a QCM spectrum with 100 kHz span around the resonance frequency of 10 MHz

onance spikes towards zero and infinite damping are observable in the QCM spectrum. The insert gives the zoomed frequency range near 10 MHz, where this resonance phenomenon is depicted. Such frequency behaviour can be described by the means of the electronic equivalent circuit also depicted in Fig. 3a: a capacity and an inductance are connected in serial with a further capacity in parallel. In case of a damped device, an Ohmic resistor has to be included into the serial connection. Any combination of a capacity and an inductivity constitutes an oscillator circuit, thus Fig. 3 contains two different oscillators, one of them with the serial frequency and the other with the parallel one. Neglecting R, the impedance of the equivalent circuit is described by Eq. (1):

$$Z_q = \frac{j}{\omega}\left(\frac{\omega^2 LC - 1}{C_0 + C - \omega^2 LCC_0}\right). \tag{1}$$

Evidently, there are two distinct frequencies, where either the numerator or the denominator of the complex impedance becomes zero. However, the case of zero impedance is determined exclusively by the serial capacity, whereas the parallel determines the frequency of infinite impedance. These two frequencies thus correspond to the resonance frequencies of the two "part circuits" mentioned above and are also correctly reproduced in the frequency spectrum of the QCM. Observable side resonances (as shown especially in the insert with lower span) can be traced back to mechanical oscillations that differ from the main one: one is the result of antisymmetric thickness shear oscillation, the other of a twist oscillation. The ratio of intensity between the desired thickness shear wave and the side resonances is mainly defined by the ratio between electrode diameter and quartz substrate thickness. This is illustrated in Fig. 4, where the damping spectra for both a 10 MHz and a 5 MHz device are given. In both cases the electrode diameter here is 8 mm (the spectra in Fig. 3 were recorded with 4 mm electrode diameter). Evidently, the 5 MHz QCM shows the desired response pattern, where the shear resonance by far dominates the electrical behaviour. The 10 MHz QCM, however, shows very pronounced side resonances. The rather large electrode diameter (compared to the thickness) very strongly favours the occurrence of torsional motions within the substrate, thus reasonable amplitudes are generated for this mode.

Commercially, QCMs are usually available with resonance frequencies up to 20 MHz (sometimes 50 MHz). The main reason that no higher frequencies can be reached is mechanical stability: 20 MHz requires quartz plates with a thickness of 84 μm, which already are mechanically sensitive. Two strategies lead to higher frequencies, namely either operating the quartz at a resonance of overtones or by partly etching a QCM, by which methods one can reach 50 MHz or higher [2].

But why are acoustic transducers referred to as mass-sensitive? Evidently, the plate thickness determines the resonance frequency of the quartz, but it

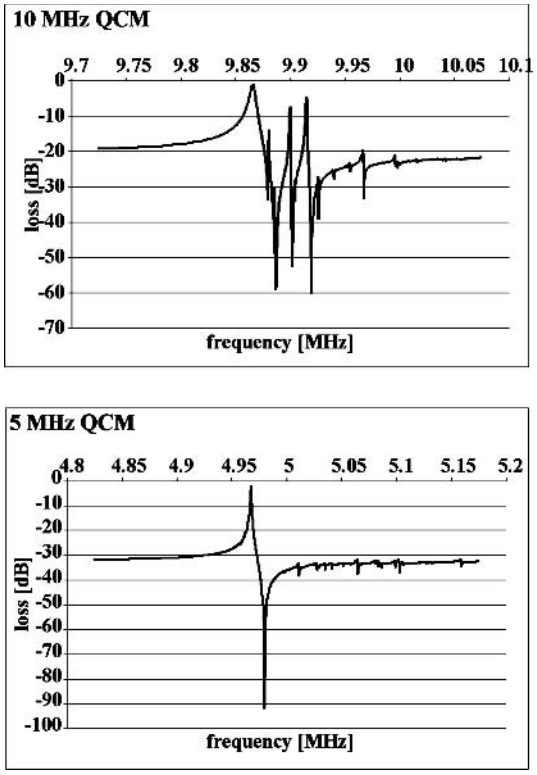

Fig. 4 Damping spectra of two QCMs with 10 and 5 MHz resonance frequency, respectively, and electrode diameters of 8 mm. The different amount of side resonances is a consequence of the ratio between electrode diameter and quartz thickness

is not the only parameter. As Sauerbrey found out in 1959 [3], mass loading on the electrodes is also of fundamental influence on an acoustic device. Equation 2 gives the mathematical expression of his findings:

$$\Delta f = - C_m f_0^2 \Delta m \tag{2}$$

namely that the frequency shifts caused by a mass change on the electrodes depend on the square of the fundamental frequency (which is one of the reasons why higher device frequencies are usually preferred) and linearly from the deposited mass. Therefore, piezoelectric devices can be regarded as highly sensitive scales; e.g. a 10 MHz QCM has a sensitivity of 1 Hz ng^{-1} mass loading. Given the fact that frequencies can be determined with an accuracy of 0.1 Hz this means absolute detection limits of $\sim$ 1 ng in the worst case, sometimes even lower, depending on the standards applied. For chemical sensing the detection of mass is one of the best label-free possibilities, because any analyte has a mass. Compared with other methods, acoustic transducing is

thus inherently very generally applicable and opens up the way for a wide variety of sensors.

2.2 Properties of QCM

Although their mass sensing properties make QCM a very powerful tool in chemical sensing, still some aspects of measuring science have to be taken into account to achieve reliable experiments. As already mentioned, the cutting angle (AT-cut) is chosen to optimise the temperature dependence of the frequency signal. In gas phase, this condition is actually met. Here the piezo effect of the device and the mass load are actually the most prominent reasons for responses of the device. In liquid phase, however, there is a somewhat different picture: strictly speaking the Sauerbrey equation is only valid for ideally rigid masses deposited in an infinitely thin layer on the electrode surface. In gas phase, the deviations of the real system from the ideal one are usually negligible. Liquids, however, are viscous and therefore have to be treated somewhat differently. One reason for this is depicted in Fig. 5, where the frequency signals of a dual-electrode 10 MHz QCM immersed in water are shown for temperature changes of 15–20 °C. Evidently, each temperature step of 1 °C leads to an average frequency shift of 40 Hz. This is much more than would be expected from gas phase measurements. The main effect in this case, of course, is the very high temperature dependence of liquid viscosity: the quartz interacts with the surrounding liquid layers and partly drags them along with itself during oscillation. Therefore, the resonance propagates into the material and the moving quartz surface is also elastically decelerated, as is expected for any moving object in vis-

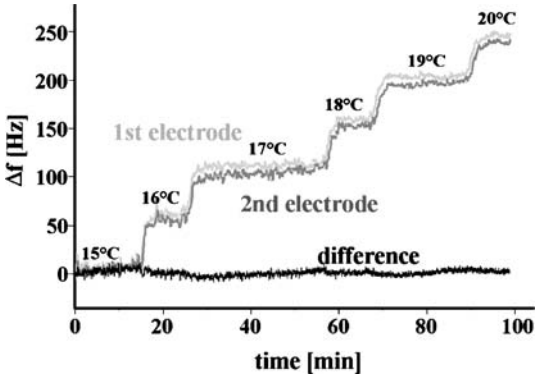

Fig. 5 Temperature response curve between 15 °C and 20 °C of a two-electrode QCM immersed into water with one face. The viscosity effects are perfectly compensated for by the dual-electrode setup

cous media. This results both in a frequency shift and a change in electronic damping: the higher the viscosity, the larger are both the negative frequency shifts and the damping on the quartz. Finally, this is also the reason for the very pronounced temperature dependence of the QCM in liquid phase. One way to overcome this problem, however, is also given in Fig. 5: whereas both channels of the quartz show the effects discussed above, the difference between them remains perfectly constant. This total compensation of physical effects is very favourable for chemical sensing applications, as it makes the measuring technique much easier: one just has to apply dual-electrode devices, coated with a sensitive layer on the first electrode and using the second one as reference.

2.3 Surface Acoustic Wave Devices

Of course, the oscillation type triggered in a piezoelectric material is not restricted to bulk shear waves such as in QCM. As their name already implies, surface acoustic wave devices show oscillation phenomena that are confined to their surface. Figure 6 depicts the basic setup for such a device, which finds widespread application as narrow-bandwidth frequency filters or oscillators, e.g. in TV sets or mobile phones. In principle, they again consist of a piezoelectric substrate (usually ST-cut in the case of quartz), on which interdigitated electrodes are deposited. These electrode patterns resemble comb-like structures that interpenetrate each other. In a "classical" SAW, applying a voltage vertically shifts the two electrode structures against each other, which at the resonance frequency leads to a Rayleigh wave propagating over the surface of the device. This oscillation resembles the waves that can be observed on a tranquil water surface when throwing a stone into a pond. SAW resonance frequencies are determined by the dimensions of the electrode structure, as the distance between the centres of two equally polarised elec-

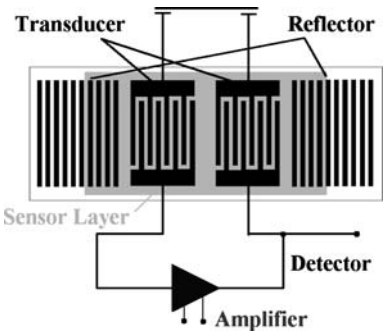

Fig. 6 Scheme of a SAW resonator

trode fingers determines the wavelength. The wave propagates over the free area on the surface that also contains the sensor layer and is re-transformed into an electronic signal by a second interdigital transducer. In principle, two different SAW designs can be found: delay lines and resonators. Both rely on the same transducing mechanism and the above description applies to both of them. The difference, however, is that in a resonator the two sets of transducers on the device surface are surrounded by a large number of electrode fingers that reflect the wave back to the centre and thus ensure resonance of the system. Both types of SAW are usually operated in a ring oscillator setup, where the device determines the frequency of the standing wave in the ring that amplifies the signal, shifts it in phase with the device, and refeeds it to the transducer. Figure 7 shows the resulting damping spectrum of a 434 MHz SAW: the resonance peak is very sharp and more intensive than the side bands by at least a factor of 25 dB. Aside from the resonance peak, the overall band structure is determined by the limited amount of electrode fingers: their number has to be infinity for obtaining only one sharp resonance signal. In reality, of course device dimensions are limited, which in this case means that the surface wave is amplitude-modulated by a rectangular signal that is determined by the lateral dimensions of the transducer. The damping spectrum is given by the Fourier transformation of this time domain. As can bee seen in Fig. 7, the damping of a SAW is very low, which is a consequence of the fact that no bulk material has to oscillate, but the resonance is confined to the surface. Therefore, only a comparably small mass has to be moved thus reducing adverse effects such as friction.

Upper frequency limits of SAW are determined by the resolution of the lithographic process for electrode deposition. Currently, the highest frequencies achieved in electronic engineering reach 2.5 GHz, sensor applications have been reported up to 1 GHz. These frequencies, of course, are much

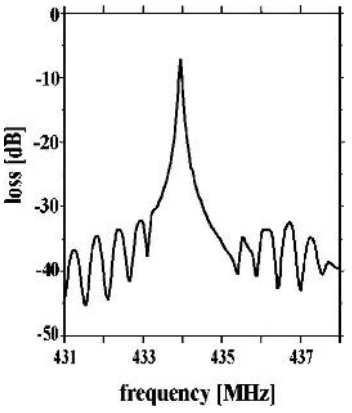

Fig. 7 Damping spectrum of a 434 MHz SAW resonator

higher than those reached with QCM. This gives SAW an excellent sensitivity: with a fundamental frequency of 434 MHz for instance, absolute mass changes as low as one picogram are detectable!

Besides the obvious advantages, there are also some limitations: the most important one is the fact that a customary SAW is very sensitive towards high viscosity and loading. This makes it virtually impossible to operate it in liquid phase, as the surface wave is completely damped by the sample matrix. The second consequence is that sensitive layers for SAW coating usually are thinner than for QCM, however, the highly increased device sensitivity by far overcompensates the lower amount of interaction sites. Additionally, thin layers lead to very favourable sensor response times.

The limitation of a "classical" SAW concerning the operation in liquid phase can be overcome with an alternative design, namely the so-called shear–transverse wave resonator (STW). In contrast to SAW, such devices are made from, e.g., lithium tantalate instead of quartz as transducer material. In this case, applying an alternating voltage causes a surface transverse wave propagating entirely within the substrate surface due to its high dielectric constant. Thus a short circuit in media with high dielectric constants is avoided. Therefore there is no or only negligible viscous interaction with the surrounding medium, thus avoiding the fundamental damping occurring in SAW. Nonetheless, an STW is of course sensitive towards mass loading, making it a highly suitable tool for any application where high sensitivity has to be achieved in liquid phase. Similarly to QCMs, surface acoustic devices usually also measure the difference between the actual sensing channel and a reference to optimally compensate for physical changes in the environment.

3
Generating Selectivity

3.1
Selective Materials – An Introduction

In the chemical sensing process, the transducer provides sensitivity, i.e. it transforms a chemical or physical signal into an electronic quantity for further recording and processing. Thus, it gives us quantitative information, but of course usually no or only minor qualitative insight, as the frequency shifts of an uncoated device depend on the amount of physisorption on the electrodes. Therefore the chemist has to add this missing qualitative information to the sensor system by working on the second crucial aspect in sensing, i.e. selectivity. Let us therefore shift our attention away from electronics and measuring science towards chemical aspects in sensing and recognition. Here, the sensor layer has to interact selectively with the analyte(s) of inter-

est and to change one of its physical properties, which is then detected. In mass-sensitive sensing, the aim is to design a material that forms a host–guest complex with the respective target analyte. The challenge for the chemist is to find the optimal amount of interaction: if binding is too strong, the resulting material will show excellent sensitivity and selectivity; however, it will be reluctant to release the analyte after exposition. A variety of non-covalent interactions meets these premises and is indeed applied both by nature as well as in chemical sensing, such as non-polar, π–π and dipolar interactions (the latter including H-bonds).

In nature all these types of interactions are used, such as for enzyme–substrate binding, immunological recognition or every ligand–receptor binding. Therefore it seems very logical to apply biological materials as recognition layers for chemical sensors. In spite of their unparallelled selectivity (see e.g. [4]), they have some inherent limitations: First, biological compounds usually degrade giving them only limited long-term stability. In a living organism, however, this does not cause defects, because one of the fundamental aspects of life is the ability to regenerate degraded components, a feature that is not (yet) accessible with artificial systems. Second, biomaterials are usually restricted to physiological or nearly physiological conditions, as most enzymes tend to denature and therefore lose their activity when subjected to harsher environmental conditions. So, their use is often limited to aqueous conditions. Third, antibody-antigen bonds are often very strong, leading to reduced reversibility and reusability of the resulting materials.

Therefore, it is of high interest to replace such natural systems with artificial ones, thus overcoming the limitations in chemical, thermal and mechanical stability. A major breakthrough was the concept of "supramolecular chemistry", a term substantially coined by Jean Marie Lehn [5], where the scientific interest in chemistry shifted from molecules and materials more towards inter- and intramolecular non-covalent interactions. Among other impacts, this resulted in artificial recognition systems based on macrocyclic compounds for host–guest interactions with the analyte for chemical sensing. Experiments with different types of compounds have proven to be very successful in terms of selectivity, including calix-[n]-arenes, paracyclophanes and cyclodextrins that all share the excellent sensor performance of the resulting layers [6]. However, synthesising them is often somewhat tedious and time-consuming. Additionally, tuning their sensitivity towards a specific analyte usually requires targeted derivatisation and modification of the macrocyclic core, although computer modelling is a successful tool for alleviating these steps. Finally, such macrocyclic compounds usually have to be chemically cross-linked on the respective sensor surface or have to be embedded into a polymeric matrix to achieve the desired amount of stability.

3.2 Molecular Imprinting

A further step in the design of "artificial antibodies", as they are sometimes termed, for chemical sensing is to generate recognition abilities directly within a polymeric material. This has the following advantages:

- Polmerisations are usually fast and comparably uncomplicated reactions, thus reducing the necessity for tedious synthetic efforts
- The result of the reaction can be either a bulk material or a thin sensor layer, therefore allowing tuning of material properties towards the desired properties
- Polymeric materials can be deposited on most transducers by industrial standard processes such as dip-coating, spin coating or drop-coating and therefore are compatible to current manufacturing processes in the microelectronics industry
- Polymeric matrices usually exhibit very favourable chemical, mechanical and thermal stability

A very elegant and straightforward way to generate such functional matrices is given by molecular imprinting [7]. This technique was established by the groups of Wulff [8] and Mosbach [9] some 25 years ago and has gained very broad scientific interest during the last decade. In principle, imprinting can be compared with casting techniques, e.g. to make copies of a statue on a molecular to micrometre level. Figure 8 shows the principal idea behind it: monomers and a template (usually the analyte-to-be) are mixed and polymerised. The polymer chains are self-organised around the template

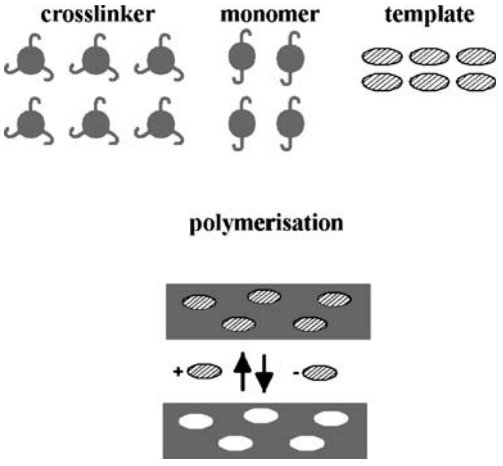

Fig. 8 Principle of molecular imprinting

compound, which is finally removed either by evaporation or by washing. This leaves behind adapted cavities in the material that are capable of reversible re-inclusion and that can be further modified by post-imprinting modification [10, 11], e.g. to enhance selectivity. Of course, the analyte–layer interaction depends on a variety of experimental parameters, including the template–monomer ratio [12] and the polymerisation conditions [13–15]. The system has to fulfil two prerequisites to reach these properties: First, the template compound must not interfere with the polymerisation reaction. Second, the polymer has to be very highly cross-linked to maintain geometrical stability after the analyte has been removed from the matrix. Recently, some evidence has been found that the recognition sites in the material are not only formed by a single template molecule but may rather result from adducts [16].

Usual amounts of cross-linker applied in imprinting are in the range of 40–80%. Just for comparison: polystyrene used for yoghurt cups usually contains 2–3% of cross-linker.

Basically, there are two different imprinting concepts, namely covalent and non-covalent imprinting [17, 18]. In the first case the template compound is covalently linked to a monomer molecule, whereas in the second case it is added separately to the reaction mixture. Of course, both approaches have their inherent advantages and limitations [19, 20]. Comparative chromatographic studies revealed that both chromatographic resolution and peak asymmetry are more favourable for the covalently imprinted materials [21, 22]. Non-covalent imprinting on the other hand offers the advantage of an extremely straightforward approach, because in this case no further synthetic steps are necessary to introduce the template into the polymeric matrix. Consequently, removing the template is usually also very fast and elegant, as no bond-breaking is necessary.

This brings us to another great advantage of imprinting techniques: as the features of the interaction centres are directly determined by the template, the method is by no means restricted regarding the nature and the size of the analyte. This, of course, is only true under the premises already mentioned, namely that the template compound must not interfere with the polymerisation reaction. However, these inherent advantages make MIPs the ideal platform technology for the design of sensor layers, as they combine high selectivity with compatibility to established industrial techniques and an extremely straightforward synthetic approach. Actually generating selectivity with MIPs, however, still remains a more empirical approach based on trial and error. Therefore, several attempts have been made to streamline these processes by chemometric [23] or combinatorial [24–26] approaches. It turns out as well that the polymerisation technique applied also has substantial influence on rebinding. When, e.g. producing MIP particles, the rebinding ability is different for polymers produced by bulk, suspension, precipitation, two-step swelling or emulsion core–shell polymerisation [27], although the order of rebinding ability depends strongly on the solvent system in which

the particles are applied. Schmidt et al. [28, 29] very recently published a fundamental study on substantially improving the sensitivity of bulk-imprinted materials towards propranolol by adding a sacrificial polymer – in this case polyvinylacetate (PVAc) – to the process. PVAc is removed from the material together with the template and leaves behind a nanoporous structure that can be assessed, e.g. by AFM, and that substantially increases the availability of the molecular interaction sites resulting from the propranolol.

Finally, imprints can also be distinguished by another criterion, which is the distribution of the interaction sites in the final sensor layer. Either the recognition events take place in the entire bulk of the polymer or exclusively at the surface. Whereas in chemical sensing the former approach is usually preferred for detecting small molecules (below 500 g mol^{-1}), the latter is most promising in the case of larger analytes such as (bio-)polymers or even entire microorganisms/cells. The reason for this is to be found in the nature of the analyte: an individual small molecule will usually not lead to a detectable sensor response because, e.g. in the case of mass-sensitive devices, the mass change of one individual recognition event is simply too small. An average 10 MHz QCM usually has a mass sensitivity of 1 Hz ng^{-1} loading (e.g. an entire monolayer of octanethiol deposited on the surface leads to 60 Hz frequency shift). SAW even detects masses that are lower by a factor of 1000 or more, nonetheless this is by far not enough for detecting a single small molecule. Therefore in this case it is crucial to generate as many interaction sites as possible within the sensitive layer to make optimal use of the sensing properties of the thin film. By this strategy even sensor responses in the kHz range can be achieved with QCM, where a monolayer of an average solvent molecule leads to a 80 Hz effect. However, in the case of particle MIPs surface approaches can also be found [30], where the template is usually immobilised on the surface of a nanoporous particle, which is dissolved after polymerisation.

With bioanalytes, different aspects have to be taken into account: in this case even an analyte monolayer covering of the transducer surface leads to highly appreciable sensor effects. But on the other hand it is absolutely useless to design a sensor layer with interaction centres distributed throughout the bulk of the material, for two reasons: First, the sensor layers would become very bulky, which can lead to problems with mass-sensitive transducers. Second, such layers would require very long diffusion pathways, thus making real sensor detection in a reasonable time impossible.

A completely different imprinting approach, however, has been proposed by the group of Tepper [31]: they polymerised 2,5-distyrylpirazine and diethyl-*p*-phenylenediacrylate on SAW in the presence of alkane vapours. Upon deposition, the two monomers form nanoparticles on the surface that polymerise in solid phase instead of in solution. During polymer formation, the material takes up vapours from their environment leading to imprint sites that readily reincorporate the template compound.

4
Exemplary Sensor Applications

4.1
Organic Species in Gases and Liquids

Regardless of the exact nature of the respective analyte, the main interest in sensor design is to achieve ideal sensitivity and selectivity. Increasing either the device frequency or the amount of recognition sites in the material are two ways in which sensitivity can be improved. The second possibility, i.e. recognition abilities towards an increased number of analyte molecules, is the fundamental way to detect small molecules by means of mass-sensitive devices. This increased number is of course achieved by applying bulk imprinting procedures, where – as the name already implies – recognition takes place in the entire bulk of the polymer film, thus overcoming the limitations of pure surface sensitivity. In this case the templates usually fulfil a double role: on the one hand they naturally determine the sterical and chemical properties of the interaction centres within the materials, but on the other hand they also very frequently determine the diffusion pathways within the material and therefore make the interaction sites accessible to the analyte compounds. For detecting small molecular compounds, this is an ideal behaviour: due to their small size and mass they only lead to a frequency shift if a reasonable amount is incorporated into the respective sensor layers. Imprinting techniques are often criticised with the argument that it is not possible to generate recognition sites for compounds that are smaller than the monomer used. In fact this is fortunately not true, as one of the smallest molecule that has been detected selectively is acetaldehyde [32], by suitable methacrylates. Compared with acetone, these MIPs incorporate up to 11 times more acetaldehyde when exposed to the same gas concentrations.

As previously mentioned, selectivity is the second key issue. Imprinted polymers lead to astonishing results, which usually are even better for rigid analyte compounds [33] and can be fundamentally improved by suitable functional monomers, such as vinylpyridine for detecting caffeine [34]. Less pronounced functionalities can also be seen, e.g. by the example of aromatic solvents with different substitution patterns (i.e. benzene, toluene and xylene). As templates for synthesising, e.g. polystyrene MIPs [35, 36], they lead to the interaction properties that can be seen in Fig. 9. The figure shows the QCM responses obtained with toluene-imprinted polystyrene against benzene, toluene and *o*-xylene, respectively. Evidently, the MIP most favourably incorporates toluene (the template component) and only shows smaller responses to the other analytes. The very low sensitivity towards the *o*-xylene can be explained straightforwardly by geometrical considerations: the second methyl group on the xylene molecule causes steric hindrance and thus makes it much more complicated for the xylene to enter the interaction sites within

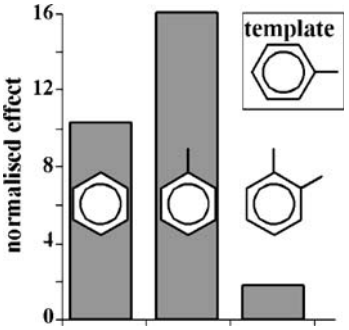

Fig. 9 Normalised QCM sensor effects of a toluene-imprinted polystyrene towards 200 ppm of three different aromatic solvents (benzene, toluene, xylene); all signals were referenced by the molar mass of the analyte

the toluene imprint. The lower response to benzene reveals the high selectivity of the material, in spite of the fact that it should geometrically fit into the imprinted cavities. Therefore, obviously chemical considerations have to be taken into account. Although the most prominent functional group in all analyte compounds is the benzene ring that is capable of undergoing π–π interactions, still the aliphatic van der Waals interactions due to a methyl group are important. The layer thus incorporates a lower amount of the "lean" analyte molecule than expected, because the overall interaction cross-section, including both the aromatic and the aliphatic hydrocarbons, is smaller. This combination of chemical and sterical aspects leading to the selective reactions is further underpinned by the interaction behaviour of different xylene imprints. The xylenes have exactly the same molar masses and their vapour pressures differ only slightly. Nonetheless, a MIP gives highly selective results in this case, as can be seen in Fig. 10, where the response characteristics of the three xylene isomer imprints are shown. Evidently, each imprinted polymer

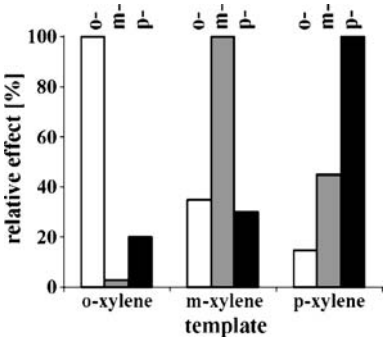

Fig. 10 QCM selectivity pattern obtained with xylene MIPs (all isomers)

preferably incorporates their respective "own" analyte and gives substantially lower responses for the other two isomers, thus exhibiting selectivity factors that lie between 3 in the worst and 100 in the optimal case. Both results impressively show the ability of the imprinting technique, as selectivity is generated by the presence or position of a single methyl group. This can even be observed for much larger compounds such as steroids [37]. The authors linked nandrolone (used for illegal doping in sports) covalently to vinyl phenol as carbonate ester and incorporated this adduct into a methacrylate polymer. The resulting materials did not show any cross-sensitivity at all towards testosterone and episterone, which is highly remarkable because nandrolone and testosterone only differ by one methyl group, whereas the conformations at all stereogenic centres are absolutely the same.

All these selectivities are even more remarkable if one takes into account that the chemical composition of each layer is exactly the same. Functionality is indeed introduced into the material by the templating process that forces the growing chains to adopt conformations determined by the template compound itself.

Of course, hydrogen bonding between a layer and an analyte is not necessary for sensor effects. Polycyclic aromatic hydrocarbons (PAH) e.g. usually do not bear hydrogen bonding functionalities. Despite this fact they have been very successfully used as templates for mass sensitive as well as for fluorescence sensing. Initial work showed that the cavities generated by a defined PAH are usually somewhat larger than the template component and consequently prefer to incorporate an analyte that is slightly larger, with excellent selectivity and sensitivity. In terms of imprinting technique, however, PAH show very interesting behaviour that on the first sight even contradicts the premises of the templating process: when applying a template mixture consisting of two components instead of only one, both selectivity and sensitivity of the resulting materials are substantially higher [38]. A result for this can be seen in Fig. 11, where the QCM sensor characteristic of a double-imprinted material is given towards pyrene.

Compared with single imprints, the signals are increased by a factor of five. Additionally, a very favourable linear range can be observed, which ends in a plateau above 60 $\mu g\,L^{-1}$ pyrene, where obviously all available interaction sites are occupied. The increase in sensitivity compared with "single" imprints can be correlated to an improved accessibility of the interaction sites, which is a consequence of the increased amount of diffusion pathways within the material. These are obviously generated by fast evaporation of the smaller analyte and kept accessible by the slower removal of the larger compound. Response times of the resulting layers remain in the range of some seconds to some minutes and primarily depend on layer thickness.

Not only organic, but also inorganic matrices are highly suitable for imprinting approaches. Titanate sol-gel materials imprinted with different carbonic acids based on PAH [39], such as 2-anthracene carbonic acid and

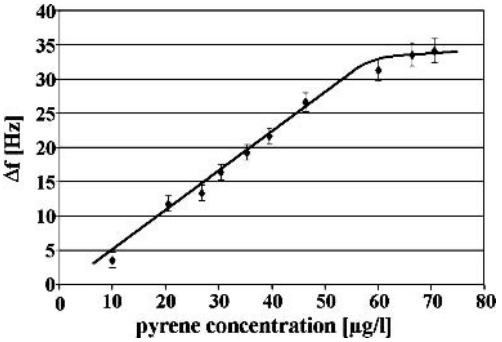

Fig. 11 10 MHz QCM sensor characteristic of a polyurethane MIP templated with acenaphtene/pyrene towards pyrene

9-anthracene carbonic acid, lead to excellent isomeric selectivity. In the case of chiral analytes, the different optical isomers are also clearly distinguishable from each other. The authors in this case use film thicknesses of some 10 nm, which leads to very fast sensor responses, about 30 s, and still very favourably detectable mass signals.

In some cases MIPs can reach stereoselectivity factors of more than four, e.g. in the case of detecting serine by QCM sensors [40] coated with molecularly imprinted methacrylates. One main reason for the outstanding selectivity in this case can be found in the comparably high amount of functional groups within the polymeric material, which is capable of undergoing H-bonds with all three functional groups of the analyte. Such three-point interactions are known to be absolutely necessary for chiral recognition. Compared with separation techniques based on MIPs (as e.g. very successfully demonstrated for dichlorobenzoyl amino acids [41]), chemical sensing requires higher selectivity factors as a consequence of the fact that a chemosensor offers only one theoretical plate for separation. Naturally, not only H-bonds lead to such high selectivity but also coordinative bonds, as presented by sensing glucose via complexing it with copper ions bound to methacrylamidohistidine [42].

4.2 Complex Mixtures

Chemical sensing is not restricted to selectively detecting a single analyte within a matrix, but can also be applied for characterising more complex phenomena. In principle, one can distinguish between two different tasks: first, the parallel monitoring of several selected compounds (i.e. markers) in a more complex matrix; and second, the overall characterisation of changes in such a multicomponent matrix by a single sensor that therefore translates a wide variety of changes into a single detectable signal. With its straight-

forward and flexible approach, molecular imprinting adds to the success of both approaches. Within the following paragraphs we will introduce some successful examples for such sensors.

4.2.1 Multiselective Arrays

By nature, animals and humans possess two chemically sensitive organs, namely the nose and the tongue. Both of them are able to detect selectively a vast variety of compounds in gas and liquid phase and thus are multiselective systems. So-called electronic noses (gas phase) [43] and tongues (liquid phase) [44] try to mimic these organs to assess multicomponent mixtures. For this purpose, usually sensor arrays consisting of up to a dozen different sensors or more are assembled. In this case the selectivity of each individual sensor layer need not necessarily be very pronounced, as any analyte mixture leads to a sensor response pattern, which then is evaluated with chemometric methods such as partial least squares or neural networks. Consequently, a sensor array usually consists of more sensors than the number of analytes, because this "over-definition" ensures optimal calculation results due to redundancies in the system. As the final selectivity is achieved by mathematical methods, many groups prefer to coat their respective sensor arrays with affinity materials known from gas chromatography.

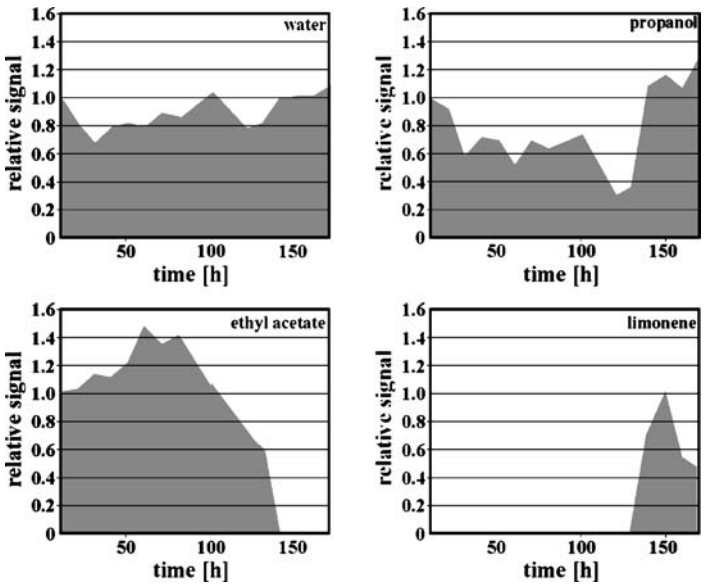

Fig. 12 Trend lines for composting. The composting lead analytes were water, propanol, ethyl acetate and limonene obtained by on-line sensing with a 6–10 MHz QCM sensor array

Nonetheless, sensor arrays consisting of highly selective individual sensors have been proposed in the literature. One example for this is to monitor composting procedures on-line via the organic solvent pattern in the headspace gas [45]. An array consisting of six QCM sensors has been coated with five different imprinted materials for detecting low aliphatic alcohols, ethyl acetate and limonene, plus an affinity material for humidity. The ratios between these analytes characterise the composting stage: at the beginning of the process alcohols play a prominent role as degradation products of sugars and carbohydrates. Within the thermophilic phase that is characterised by composter core temperatures of up to 80 °C the alcohol levels decrease and make way for elevated amounts of acetic esters. Finally, in the advanced stages of degradation, the amount of terpenes increases as a consequence of degrading cell walls in wood materials and the digestion of plant fats and waxes. As can be seen in Fig. 12, the sensors reproduce these trends very well. Additionally, GC-MS data (demonstrated with the example of limonene) confirms the sensor data, thus indicating the ability of the imprinted material. The main difference between sensor and GC-MS data of course is the fact that all sensor data is obtained directly on-line, whereas chromatography requires sampling and off-line analysis.

4.2.2 Degradation Processes

Molecular imprinting opens up the way to sensors for processes that are sometimes not even entirely known in all details, such as analytics in degrading engine oil and also in edible oils. Both imprinted organic [46] and inorganic [47] polymers have been reported for this purpose. Sensors based on organic polymers – mostly polyurethanes – have been prepared with the entire oil matrix, both with fresh oil and waste oil. In contrast to this, inorganic polymeric sol-gel materials based, e.g., on Si or Ti are imprinted with a mid-chain carbonic acid as model compound for oxidised oil components. Such sol-gels outperform organic materials mainly in terms of chemical, thermal and mechanical stability. Deposited on a QCM, both layer types yield pronounced mass effects combined with frequency shifts originating from changing oil viscosity during degradation. Therefore, the frequency shift of the fresh oil imprint is lower than for an uncoated device, whereas it is higher for the waste oil imprint. Of course, the reason for this is that each MIP preferably incorporates the respective template. By this strategy a way has indeed been opened up that allows us to transform oxidative processes within a chemically very complex matrix into a single frequency signal. This can also be seen in Fig. 13 that gives the sensor responses for such a change from fresh oil to waste oil and back. Evidently, the MIP material leads to higher frequency responses due to incorporating oxidised waste oil components.

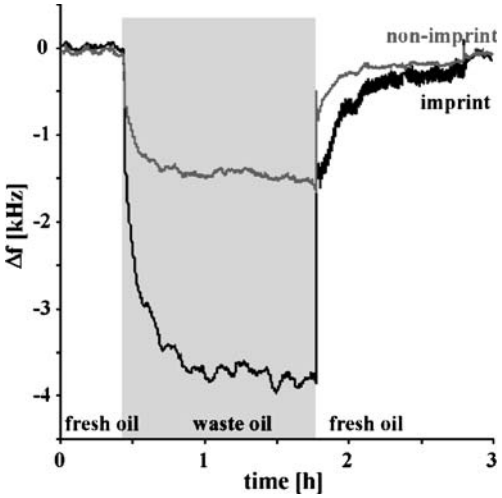

Fig. 13 10 MHz QCM sensor responses of a carbonic acid imprinted Ti-sol-gel material and the reference channel when changing from fresh to waste oil and back

Viscosity effects can be additionally minimised by applying a shear transverse wave (STW) resonator, because in these devices the oscillation takes place exclusively within the piezoelectric substrate. Therefore, they are almost uninfluenced by viscosity and additionally lead to highly increased sensitivities as a consequence of the higher fundamental frequency.

4.3 Cells and Microorganisms

There is no reason why MIPs should be restricted to molecular analytes. During the last one or two decades, life science and its application have boosted scientific interest in various fields. Modern biotechnology also requires adapted analytical techniques to cope with the new challenges. Let us also recapitulate that the dimensions of microorganisms make bulk imprinting strategies impossible, because both removing the analyte and reincorporating it is substantially hindered. One of the first successful imprints of a biological species was published by the group of Vulfson in 1996 [48] in a short communication, followed by the full report one year later [49]. The key to their technique is the observation that bacteria tend to assemble on oil/water interfaces. Therefore, they introduced a highly non-polar monomer mixture (e.g. leading to polyamides or fluoropolymers) into an aqueous suspension of bacteria and initiated emulsion polymerisation. This process results in polymer microbeads that contain bacteria on their outer shell. After removing the microorganisms, surface imprints remain that are

defined in size and morphology by the initial templating bacteria. A similar approach can also lead to imprinted surfaces, if a homogeneous oligomer–bacteria mixture is deposited on a suitable surface, such as mica. In this case, the polymer also grows around the templating bacteria and leads to the respective nanostructured surfaces. Albeit excellent work in terms of material science and characterisation, the authors have not yet reported any sensor applications of their materials.

A slightly different approach is given by the surface imprinting process via stamping that has been introduced in our group. Yeast cells were the first biological species for which this approach has been reported including both organic polymers [50] and sol-gel materials [51]. For generating the sensitive materials (see also Fig. 14), first a suitable stamp has to be prepared, often by self-assembly. In the case of yeast cells, this process is comparably simple and straightforward, as yeast deposited on a glass or quartz plate is pressed against a flat, inert Teflon surface, leading to an optimally flat surface of most densely packed cells. In parallel, a suitable polymer system has to be generated and prereacted to an oligomeric state that allows spin coating of thin layers. After depositing this material onto a suitable transducer, the above-mentioned stamp is pressed into the forming oligomer and the system hardened. During polymerisation, the chains thus grow around the cells and arrange themselves by forming e.g. H-bonds with protein or carbohydrate components of the outer cell membrane. Finally, after washing away the template species, the respective imprints remain behind in the polymer surface. An example of this can be seen in Fig. 15, where not only the pits generated

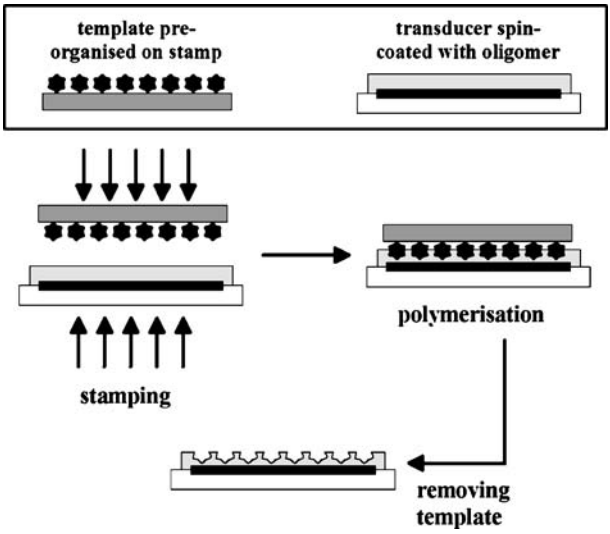

Fig. 14 Principle of surface imprinting by the stamping technique

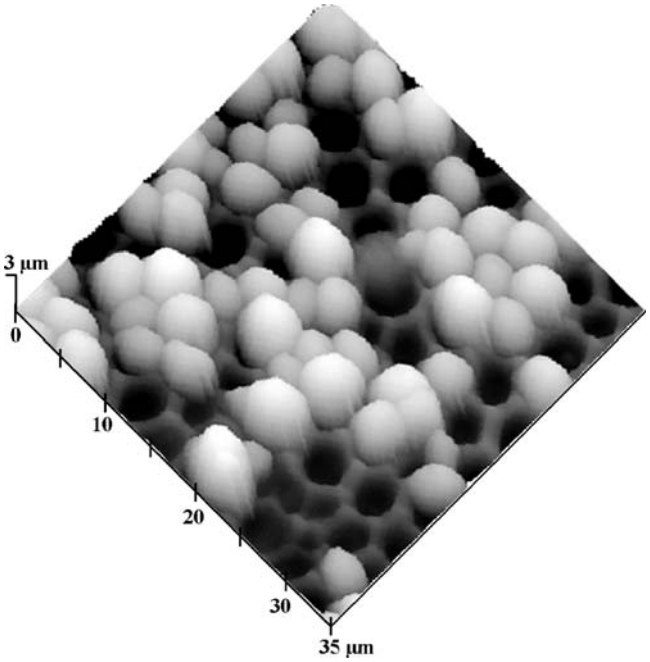

Fig. 15 AFM image of a partly occupied yeast imprint

by the individual cells are evident, but also some of these cavities are occupied by yeast cells that have been reincorporated into the material. Compared with imprinting by molecular templates, this approach is slightly different: as the dimensions of the imprinted cavities by far exceed the size of a single molecule, the amount of cross-linker in the polymer formulation plays a less predominant role, because no collapse of the structure is expected after removing the template. Second, the interaction centres in this case are of course not distributed within the entire bulk of the polymer layer, but are only concentrated on the surface. This evidently ensures that the analyte species can enter the interaction sites without being hindered by diffusion. The apparent loss in sensitivity is not important because the interaction with one individual analyte may already lead to a detectable frequency shift due to its high mass. Preliminary tests with polystyrene microbeads have been carried out with 433 MHz SAW devices. Depositing a single microbead with 5 µm diameter on the device surface, which can be followed by light microscopy, leads to a frequency shift of 273 Hz. Geometric considerations lead to the conclusion that adherence of a single yeast cell thus results in a frequency shift of about 60 Hz, which is easily detectable.

Evidently, the cavities resulting from surface imprinting correctly reproduce the geometrical features of a yeast cell on the micrometre scale. How-

ever, two levels of structuring are to be seen in this system. When comparing the frequency shifts of a QCM coated with a *Saccharomyces bayanus*-imprinted polyurethane towards different species, one can clearly see that the template species leads to the largest frequency shifts. Other yeast strands show smaller effects and bacteria give no response at all, although they definitely fit into the yeast cavities as they are much smaller in size. These findings indicate that in the layers not only a microstructure is present, but that additionally in each cavity a nanostructure must exist that gives the polymer almost antibody-like selectivity and therefore optimised interaction properties. The best proof for this hypothesis is to generate imprints of a cell species with exactly the same geometrical dimensions but different surface chemistry. Very prominent examples for such a species are erythrocytes or red blood cells (RBC). They are disc-shaped (see also the AFM image in Fig. 16a) with a disc diameter of roughly 7 μm.

Due to their shape with the pit in the centre, red blood cells nonetheless are very flexible and thus fit even through the tiniest veins. From the point of view of imprinting the interesting fact is that erythrocytes are not only responsible for oxygen transport, but they also carry the blood group information. The four principal blood groups within the ABO system (i.e. A, B, AB and O) are encoded by glycolipids present on the respective cell surface. All these glycolipids consist of a chain of at least five sugars (BG O), at which in the case of A, B and AB a sixth molecule is bound that is N-acetyl-D-galactosamine in the case of BG A and D-galactoside in the case of BG B. When imprinting polymers with RBC, the expected imprint pattern can be observed in the material, so the geometrical features of the individual cells are indeed depicted in the matrix. Using such a material as sensitive layer on a QCM additionally yields selectivity, i.e. imprints with BG A prefer BG A erythrocytes and vice versa for BG B (see Fig. 16b). Obviously, not only the geometric features of the ana-

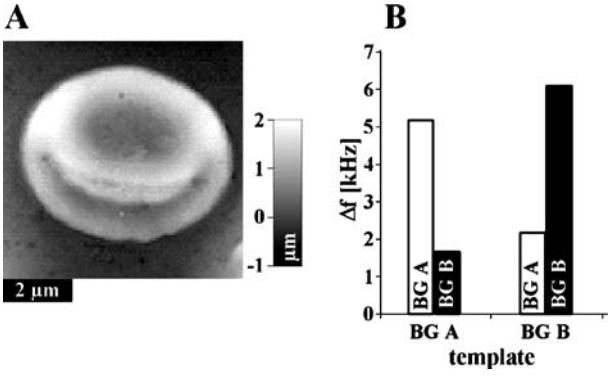

Fig. 16 **A** AFM image of a single human erythrocyte, **B** Blood group selectivity of surface imprinted sensor layers on a 10 MHz QCM

lyte on the micrometre scale are depicted in the material, but there must also be some self-organisation at the molecular level that leads to antibody-like interaction properties.

4.4 Viruses

4.4.1 Direct Imprinting

For chemical sensing applications, viruses represent a type of species that is of special interest because their size normally is in the range between 10 and some 100 nm. Therefore, they are too small to be visualised by optical microscopy, which means that currently there are no fast, easy-to-use techniques for their detection. Additionally, as viruses may be a substantial threat to humans, livestock or plants, a direct on-line method for their determination would be highly desirable. The imprinting approach promises to solve these problems, because, as already mentioned, it is inherently applicable to a very wide variety of analytes and not restricted to a certain size or to defined chemical properties of the material or the template.

Among the wide variety of different viruses, the Tobacco Mosaic Virus (TMV) seems to be a highly suitable template as test system for imprinting techniques. Figure 17 shows an AFM image of some TMV on a flat mica surface: the species has a rod-like shape with a length of 300 nm and a cylinder diameter of 18 nm, although at higher concentrations the individual viruses tend to form hexameric aggregates (as also suggested by the vertical dimension in the AFM image). The detailed structure of TMV is well-known: it consists of a central, helically wound RNA strand that is covered by a protein shell. The latter consists of one protein type and every virus shell consists

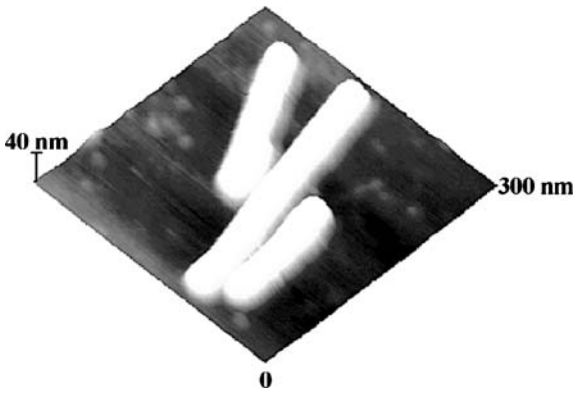

Fig. 17 TMV assembled on an atomically flat mica surface

of about 2000 individual protein molecules. Therefore the apparent rods are rather cylinders with an inner cavity of 4 nm diameter. Due to their comparably simple structure and the resulting low complexity, TMV are astonishingly robust for a biological species: they can withstand temperatures up to 90 °C and pH values between 3.5 and 9. This inherent robustness combined with the comparably low pathogenicity for humans and animals make it an ideal model organism for imprinting studies. Additionally, a sensor for TMV is also of economic interest because the virus can do large amounts of damage to tobacco or cucumber plantations.

Currently, only very few papers exist that deal with viruses as templates in general, and even less that report sensing applications. The group of Bittner published reports where they used TMV as structure-directing templates for inorganic matrices [52]. This work aims at two different targets: on the one hand the authors achieved nanostructured materials defined by the TMV, on the other hand they were interested in contrast enhancement for transmission electron microscopy characterisation of the virus. For all these strategies, the starting point is the high amount of hydroxyl and carbohydroxy groups on the virus surface. Uranyl acetate can be readily adsorbed both on the inner cavity walls and the outer surface of a virus species. Due to their very high molar mass, the uranium atoms strongly absorb in TEM leading to a highly enhanced contrast for this method. On the same sites, other metal ions also adsorb (e.g. platinum and palladium ions), which then are the starting point for electroless deposition of pure metal coatings on the virus. By this strategy the authors succeeded in designing nanostructured Ni and Co particles, whose shape was determined by the templating TMV.

Thus, such approaches have led both to successful materials structuring and novel analytical tools for characterising the TMV, however, no sensor applications have been reported. Sensors, however, have been successfully implemented with an imprinting strategy similar to the technique used for the yeast-imprinted materials introduced earlier [53, 54]. In this case, the TMV are again self-assembled on a flat surface to form a stamp that is then pressed into a forming polymer film. In Fig. 18 both a stamp and a TMV imprint layer are depicted. On the stamp surface one can clearly see the aligned virus species that partly arrange themselves along their cylinder axes. The linear shape is also retained within the imprinted cavities, whose dimensions additionally are in excellent correlation with the size of the individual TMV species. Again, the imprinting approach proves to be a rapid and highly practical tool for actually casting the shape of a complex template species into a material and generating functionality in this way. As in the case with other templates, the imprint layer indeed incorporates the template species and acts as an artificial antibody. Compared with the state of the art in virus analytics this is a major improvement because for the first time it allows detection of these species directly on-line and reversibly with a fast and robust method. Naturally, not only the detection as such is important, but also selectivity is

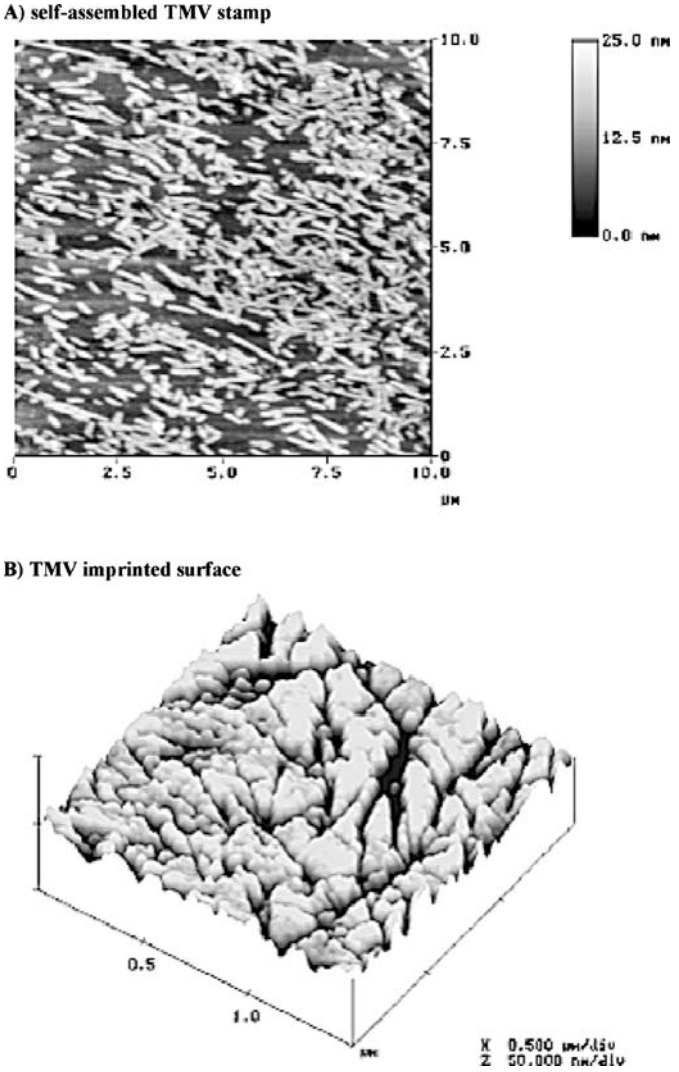

Fig. 18 AFM images of **A** a TMV stamp and **B** corresponding imprinted polymer surface

obtained, a key parameter of a sensor measurement or, more generally, of analysis. We have carried out two different measurement series for this purpose: one series included experiments for directly detecting TMV in crude plant saps of infected leaves rather than in standardised virus suspensions, which gives information about possible cross-reactivities towards plant components. The second was to test the selectivity of the layer for different virus types, which we assessed by control measurements with both the TMV and the human rhinovirus (HRV).

Measurements checking the first case have been successful [55]: a QCM coated with a TMV-imprinted layer can also clearly recognise the template species, even in a filtrate of shock-frozen and ground tobacco leaves and therefore represents a highly useful analytical tool.

Figure 19 summarises the results of the selectivity measurements with both the TMV and the HRV imprints and therefore illustrates the second of the above-mentioned. Each of the two sensors clearly prefers the respective template component, as 8 ng mL^{-1} TMV in water lead to a frequency response of 70 Hz on the TMV MIP, whereas the more than thousand-fold concentration of HRV only yields about 10 Hz. The HRV imprint on the other hand shows exactly the opposite effect, as in this case about 1 μg mL^{-1} HRV results in 1.4 kHz effect and the fivefold concentration of TMV does not give any detectable frequency shift at all. Evidently, excellent selectivity factors can be achieved by the virus imprints. In this case, however, one can perfectly understand them from geometrical considerations. As already mentioned, the TMV is a rod-shaped species with a cylinder diameter of 18 nm and a length of 300 nm, whereas the HRV has icosahedral shape (and can be very accurately approximated by a sphere) with a diameter of 30 nm. Therefore, it can be understood that the two species show only a minor cross-selectivity between each other; however, it is astonishing that no unspecific adsorption occurs on the sensor layers. Besides this somewhat obvious geometrical selectivity, it is of course of fundamental interest whether also "chemical" selectivity can be observed for virus MIPs in the same way as for the cell imprints, i.e. blood group selectivity for erythrocyte MIPs.

The above-mentioned Human rhinovirus (the cause of common colds) represents an ideal model system for this purpose because it exists in a large variety of different so-called serotypes. All of them have the same "microscopic" shape, i.e. they are almost spherical with 30 nm diameter, but they differ in the chemical structure of the proteins constituting the respective re-

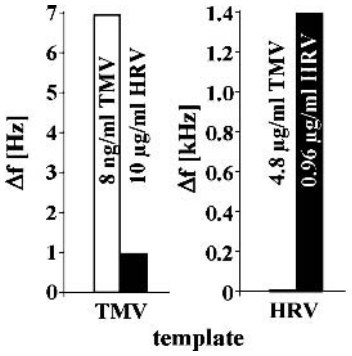

Fig. 19 Selectivity pattern of both TMV- and HRV2-templated surface MIPs towards TMV and HRV2, respectively. All data is based on QCM measurements

ceptor sites for docking onto cells. Figure 20 shows the results of such an imprinting process with HRV-2 and HRV-14, where once again the template species is very preferably incorporated by the sensitive layer. Therefore once again there must be a preformed non-covalent interaction network (presumably mainly based on hydrogen bonds) present that ensures the recognition abilities. Thus, the main message we receive from imprinting is that selectivity is always generated on a molecular level during imprinting, irrespective of the template size. This unique feature of imprinting therefore makes the strategy highly interesting for the design of artificial antibodies, i.e. for generating functionality in completely man-made materials that combine biological recognition abilities with the stability, ruggedness and manageability of man-made systems.

Another aspect of imprinting is that by carefully choosing the experimental parameters, sensor layers for very sensitive templates can also be generated very straightforwardly, as has been shown with the example of the parapox ovis virus (PPOV) [56]. This species is a member of the large group

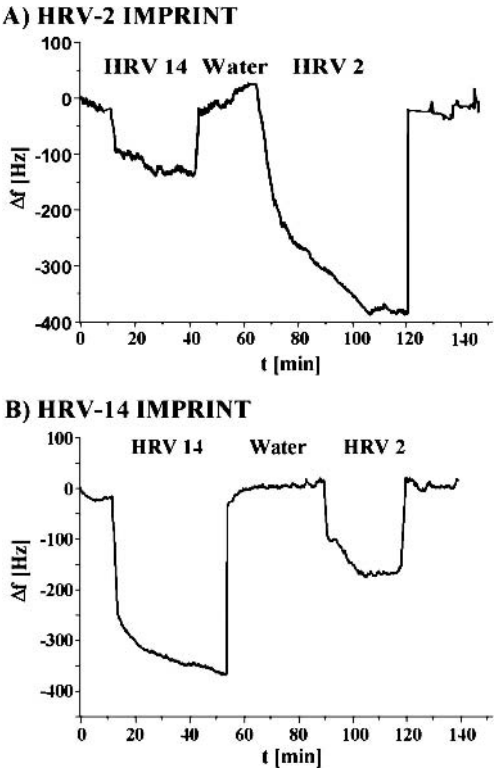

Fig. 20 Selective QCM sensor responses for **A** HRV2 and **B** HRV14 imprints when exposed to both species

of poxviruses, which cause disease in sheep and cattle but are not threat to humans, as is e.g. the smallpox virus. PPOV have a very delicate morphology (see also Fig. 21): they consist of the virus core containing the genetic information, which is surrounded by a so-called core envelope and a palisade layer leading to a biconcave disc. The two concave "cavities" hold the two liquid-filled lateral bodies. Finally, an outer envelope covers the entire aggregate, leading to an ellipsoid shape. The entire assembly is both mechanically and thermally very sensitive, mainly as a consequence of the lateral bodies. The stamping approach with hard stamping surfaces therefore can not be used in this case, because during hardening the viruses would burst. The solution for this problem is to utilise a flexible, elastic stamping material. Such approaches are also well-known from soft lithography techniques, where mainly polydimethyl-siloxane (PDMS) is used. In the case of PPOV this leads to successful imprints, as can be seen in Fig. 21, where the respective mass effect can be seen. The sensor curve shown already represents the differential measurement between the imprint and the non-imprint channel.

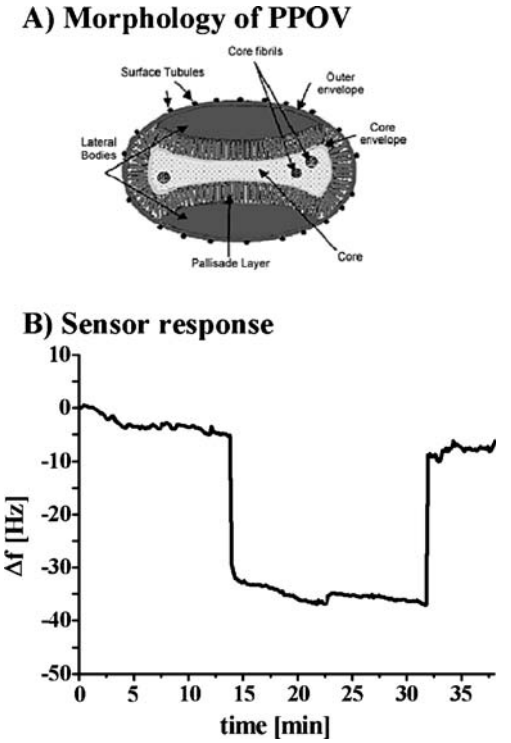

Fig. 21 **A** Morphology of PPOV, and **B** 10 MHz QCM response of a PPOV MIP showing selective incorporation. The data represented gives the difference between imprint and non-imprint material

4.4.2
Epitope Approaches

Imprinting approaches with microorganisms are somewhat rare in the literature; however, apart from using the whole species as a template, so-called epitope approaches can also be found. In this case a characteristic (protein) sequence is used as template, and the entire microorganism is then detected. This principle is directly derived from nature, e.g. natural antibodies usually only interact with a very small part of an outer cell membrane, the so-called antigen, and usually do not contain the entire information about the species leading to the immunoreaction. One successful example for such a strategy is the detection of Dengue virus proteins [57]. It is well known that the Dengue virus is responsible for hemorrhagic fevers that are frequently fatal and thus represent a real threat to humans, especially in tropical zones of Africa. As already previously described, surface imprinting techniques are most suitable for (mass-sensitive) bioanalyte detection with molecularly imprinted polymers, which is also demonstrated by the approach the authors use here. Instead of templating with the entire analyte species, they chose a pentadecapeptide as being typical for the so-called Dengue virus NS-1 (non-structural protein 1) and prepared surface imprints in polyacrylic acid by directly casting the template–polymer mixture on a QCM and made mass-sensitive test measurements. These led to very appreciable sensor effects, which the authors also describe as being the result of the epitope approach. As the template is much smaller than the final analyte, it produces many more interaction sites on the surface than could possibly be covered. Therefore, geometrically "wrongly" oriented imprinted cavities play a smaller role because plenty of "correct" sites still remain in the material. A somewhat similar approach for virus detection, in this case based on electrochemical detection, has also been reported for the Bovine Leucaemia Virus glycoproteins [58].

4.5
Biomacromolecules

In previous chapters, we have already discussed the mass-sensitive detection of both small molecules and microorganisms and thus have covered the analyte size range below 1 nm and above 10 nm. The gap in between is bridged by macromolecules and some colloidal particles. Special analytical interest is devoted to biomacromolecules, such as proteins and enzymes and nucleic acids, which are also of clinical interest. For these classes of compounds, a wide variety of rapid testing techniques exist, which can also be seen by the number of excellent and recent reviews both on protein [59] and DNA [60–62] detection. Due to the broad range of techniques already available in chemistry and clinical science, MIP sensor applications for these analytes are still somewhat rare. For entire DNA strands, no imprinting strategy related to

chemical sensing has yet been published. One reason for this may be the fact that DNA itself is a system that shows a perfect non-covalent interaction network offering highly selective recognition abilities. One paper for the detection of biomacromolecules, however, has been published by the group of Willner, who imprinted phenylboronic-acid-derivatised acrylamides both with sugars and nucleotides [63]. The authors achieved very favourable imprinting effects both for the sugars glucose, galactose and fructose, and for the four possible nucleotides (i.e. nucleobase monophosphates) with a bulk imprinting approach. From the point of imprinting, one aspect is of especially pronounced interest: the boronic acid residues within the polymeric material form strong hydrogen bonds with OH groups of the respective templates that are all multifunctional. The final polymer thus shows a swelling/deswelling behaviour when switching between the occupied and the unoccupied cavities. In the "loaded" state the polymer itself is swollen, nonetheless selective recognition properties are achieved due to the preformed non-covalent interaction network that most optimally fits the analyte of interest. So, in contrast to the other materials introduced up to now, this is a case, where a man-made material shows almost nature-like adaptive behaviour, which means another step of science towards optimally mimicking natural interaction behaviours. Phenylboronic acid with its strong ability to undergo non-covalent interactions by double hydrogen bonds therefore is a highly suitable compound for generating selectivity in materials, as shown for detection of the strong antibiotic ampicillin [64]. There are also other approaches for creating multidentate interactions between a polymer and a multifunctional compound, sometimes even with adaptive behaviour. Friggeri et al. [65] anchored a monolayer of poly-L-lysine on a gold surface in the presence of glucose, which led to highly glucose-selective, ultrathin adaptive polymer films.

The only class of biomacromolecules that some imprinting sensor work has been published on are proteins and enzymes, although only very few papers deal with sensor applications. A comparably early work on the way to protein MIPs was published by Kempe and Mosbach [66] in 1995 on chromatographic protein and peptide separation by the means of MIP stationary phases. These consisted of bulk-imprinted polyacrylates and methacrylates templated with a variety of di- to tetrapeptides. The materials then were used as stationary phases in HPLC after grinding and sieving and led to selectivity to baseline-separated chiral selectivity. At the very end of their paper the authors also propose an imprinting approach for detecting entire proteins by the means of grafted silica surfaces, where they immobilised imidodiacetic acid derivatives and generated interactions with the protein via joint complexation of protein and surface graft by calcium ions. But generally speaking, protein MIPs were initially mainly designed for chromatographic purposes [67, 68].

Such surface grafting approaches via non-covalent, directed interactions between the protein and the MIP – which in fact often is formed by a surface

monolayer – have proven to be very successful also in terms of sensor application. For example, MIP sensor layers towards microperoxidase, horseradish peroxidase, hemoglobin and lactoperoxidase have been designed by such an approach [69]. The polymeric basis in this case was 3-aminophenylboronic acid that can be radically polymerised and deposited on a polymer surface. As already mentioned, the boronic acid moiety undergoes strong hydrogen bonds with vicinal and geminal OH groups within the protein. For this polymer system, calorimetric binding studies have also been performed that suggest a strong enthalpic term during recognition and formation of the non-covalent polymer–protein bond network [70]. Similar approaches have also been published for selectively detecting hemoglobin with silica surfaces [71], albumin with methacrylates [72], smaller peptides (oxytocin, vasopressin) with polyacrylamides [73] or sialic acid with methacrylates [74].

A further possibility for generating protein-selective surfaces is the stamping technique, which has also proven to be successful in the case of microorganism imprinting [75] and yielded very appreciable sensor responses with a QCM. In this case lysozyme was first self-assembled on a glass surface and then again pressed into a forming oligomer methacrylate/divinylbenzene film. The resulting polymers readily reincorporate the lysozyme, as can be seen in Fig. 22.

For analyte removal, the sensor surface is flushed with an SDS solution, which is an anionic surfactant. Additionally, imprinted layers proved catalytic for protein crystallisation. One could also regard MIP materials as model system of biomineralisation processes: D'Souza et al. [76] showed an application where crystal-imprinted materials indeed fundamentally increase calcite growth on the surface and therefore work as seeds.

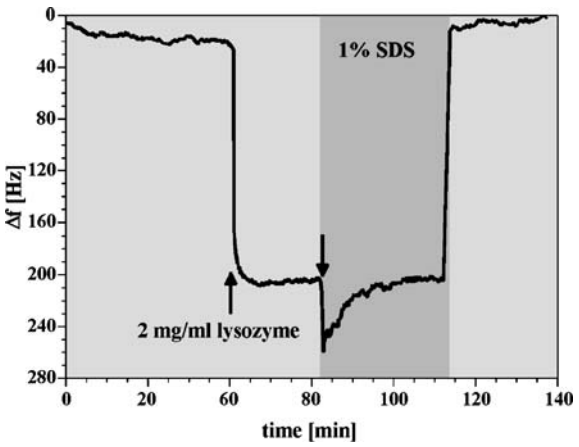

Fig. 22 Lysozyme surface imprint incorporating lysozyme from solution and analyte removal by SDS

A somewhat unconventional, yet very successful way to generate protein imprints in a surface comes from the group of Ratner [77], who imprinted proteins into glow-charge plasma-deposited polymer films made of fluoropolymers. The authors first deposited the protein on an atomically flat mica surface, which then underwent the plasma process. To avoid heat-denaturing of the proteins, they coated the template surface with a protective saccharide layer prior to film deposition. In contrast to the virus imprints, where similar protective layers prevent covalent bonds between the virus and the forming polymer, the saccharide in this case is mainly a thermal insulator for protecting the protein. These materials also showed a pronounced uptake of the respective template, such as albumin or immunoglobulin.

With hemoglobin as analyte, one approach has proven to be successful, which in principle does not meet all the premises of molecular imprinting because it uses acrylamide hydrogels for selective hemoglobin detection [78] and contains a cross-linking ratio of only about 10%. As a consequence, the material obviously remains more flexible than other MIPs, which also makes the bulk of the polymer hydrogel accessible to such large species as hemoglobin. Once again there must be self-organisation between the growing polymer chains and the template molecules, because otherwise no selectivity would be observed. This is not the case; when exposing the materials to the competing proteins cytochrome c and myoglobin, the authors find selectivity factors of up to ten.

5
Future Outlook and Perspective

Template-directed generation of nanostructures in polymers thus indeed leads to antibody-like interaction abilities and thus highly appreciable selectivities. Sensitivity is added to the systems mainly by the transducer device, where the mass-sensitive strategy offers the big advantage of detecting a property that is inherent for any analyte. On a laboratory scale, sensor systems for a variety of analytes ranging from small molecules (volatile organic compounds) up to entire cells have been proposed.

The future outlook of the technique covers both the transducer and the layer side:

On the transducer side, there have been more recent developments like the Lamb oscillator or the so-called film bulk acoustic resonators (FBAR). Lamb wave devices are related to SAW in terms of using interdigitated structures for transduction. The difference, however, is that in a Lamb wave resonator not only the surface, but the entire bulk of the device oscillates. This makes it much less sensitive against viscous damping. FBAR on the other hand consist of a metal/aluminium nitride/metal sandwich, where bulk waves (thickness oscillations) are induced in the AlN material. Both these devices have in com-

mon that their sensitivity is up to a factor of 1000 higher than for quartz, therefore requiring much lower operational frequencies. This is not only an advantage in terms of less sophisticated electronics, but will also open up the way for detection of a single analyte/layer interaction step for smaller analytes (such an approach has already been successful with SAW for yeast cell detection).

In molecular imprinting, the main task will be to further increase the interaction abilities of the layers generated. Several approaches show future perspectives.

One is to generate virtual libraries of different monomers that are then tested "in silico", i.e. in modelling approaches to streamline MIP design. A further aim is to introduce rationally designed non-covalent interaction networks within the polymeric matrices formed by pre-organising functional monomers with the respective template compound. This also includes introducing further types of interactions, such as coordinative binding. One of the main differences between current biological recognition materials (mainly enzymes) and artificial systems on the basis of polymers is the ability of the biomaterials to adapt themselves to the respective analyte or substrate component (induced-fit behaviour). In the future, we expect the implementation of such strategies into the artificial layers. Finally, the polymer properties of imprinting will be more rationally designed in terms of porosity and interaction site accessibility. At the moment, many groups are working on elucidating the actual mechanism leading to selective interaction between the polymeric layer and the target analyte, as the knowledge in that field is still somewhat empirical.

The overall goal, however, will be to implement nature's ability for recognition within an artificial system and thus overcome nature's main limitations in stability, long-term effectiveness and operational environment.

Acknowledgements Part of our own work was supported by the FWF, the Austrian Science Fund, project number P15512.

References

1. Dickert FL, Lieberzeit P (2000) Solid state sensors for field measurements of gases and vapours. In: Meyers RA (ed) Encyclopaedia of analytical chemistry. Wiley, Chichester, p 3831
2. Buettgenbach S, Rabe J, Zimmermann B, Hauptmann PR (2001) Proc SPIE 4205:207
3. Sauerbrey G (1959) Z Phys 155:206
4. Katz E, Willner I (2004) Immunosensors and DNA sensors based on impedance spectroscopy. In: Springer series on chemical sensors and biosensors 2 (ultrathin electrochemical chemo- and biosensor). Springer, Berlin Heidelberg New York, p 67
5. Lehn JM (1993) Science 260:1762
6. Dickert FL, Lieberzeit P (2004) Chemical recognition and sensing by self-organization. In: Atwood JL, Steed JW (eds) Encyclopaedia of supramolecular chemistry. Dekker, New York, p 1

7. Sellergren B (ed) (2001) Molecularly imprinted polymers – techniques and instrumentation in analytical chemistry 23, 1st Edn. Elsevier, Amsterdam
8. Wulff G (1995) Angew Chem Intl Ed Engl 34:1812
9. Mosbach K, Haupt K (1998) J Mol Recog 11:62
10. Kirsch N, Alexander C, Lübke M, Whitcombe MJ, Vulfson EN (2000) Polymer 41: 5583
11. Piletska EV, Romero-Guerra M, Guerreiro AR, Karim K, Turner APF, Piletsky SA (2005) Anal Chim Acta 542:47
12. Andersson HS, Karlsson JG, Piletsky SA, Koch-Schmidt AC, Mosbach K, Nicholls IA (1999) J Chromatogr A 848:39
13. Piletsky SA, Piletska EV, Karim K, Freebairn, Legge CH, Turner APF (2002) Macromolecules 35:7499
14. Piletsky SA, Mijangos I, Guerreiro A, Piletska EV, Chianella I, Karim K, Turner APF (2005) Macromolecules 38:1410
15. Piletsky SA, Guerreiro A, Piletska EV, Chianella I, Karim K, Turner APF (2004) Macromolecules 37:5018
16. Baggiani C, Giraudi G, Giovannoli C, Tozzi C, Anfossi L (2004) Anal Chim Acta 504:43
17. Wulff G, Biffis A (2001) Techn Instrum Anal Chem 23:71
18. Sellergren B (2001) Techn Instrum Anal Chem 23:113
19. Piletsky SA, Piletskaya EV, Panasyuk TL, El'skaya AV, Levi R, Karube I, Wulff G (1998) Macromolecules 31:2137
20. Spivak DA, Simon R, Campbell J (2004) Anal Chim Acta 504:23
21. Khasawneh MA, Vallano PT, Remcho VT (2001) J Chromatogr A 922:87
22. Hwang CC, Lee WC (2002) J Chromatogr A 962:69
23. Davies MP, De Biasi V, Perrett D (2004) Anal Chim Acta 504:7
24. Lanza F, Dirion B, Sellergren B (2005) Molecularly imprinted materials. Dekker, New York, p 225
25. Batra D, Shea KJ (2003) Curr Opin Chem Biol 7:434
26. Chianella I, Lotierzo M, Piletsky SA, Tothill IE, Chen B, Karim K, Turner APF (2002) Anal Chem 74:1288
27. Pérez-Moral N, Mayes AG (2004) Anal Chim Acta 504:15
28. Schmidt RH, Haupt K (2005) Chem Mater 17:1007
29. Schmidt RH, Belmont AS, Haupt K (2005) Anal Chim Acta 504:118
30. Yilmaz E, Haupt K, Mosbach K (2000) Adv Mater 39:2115
31. Pestov D, Levit N, Maniscalco V, Deveney B, Tepper G (2004) Anal Chim Acta 504:31
32. Hirayama K, Sakai Y, Kameoka K, Noda K, Naganawa R (2002) Sensor Actuator B 86:20
33. Fu Y, Finklea HO (2003) Anal Chem 75:5387
34. Kobayashi T, Murakawi Y, Reddy SP, Abe M, Fujii N (2001) Anal Chim Acta 435:141
35. Lieberzeit PA, Gazda-Miarecka S, Halikias K, Schirk C, Kauling J, Dickert FL (2005) Sensor Actuator B 111–112:259
36. Dickert FL, Lieberzeit P, Gazda-Miarecka S, Mann KJ, Hayden O, Palfinger C, Biosens Bioelectron 20:1040
37. Percival CJ, Stanley S, Braithwaite A, Newton MI, McHale G (2002) Analyst 127:1024
38. Dickert FL, Achatz P, Halikias K (2001) Fresenius J Anal Chem 371:11
39. Lee SW, Yang DH, Kunitake T (2005) Sensor Actuator B 104:35
40. Stanley S, Percival CJ, Morel T, Braithwaite A, Newton MI, McHale G, Haynes W (2003) Sensor Actuator B 89:103
41. Gavioli E, Maier NM, Haupt K, Mosbach K, Lindner W (2005) Anal Chem 77:5009
42. Ersöz A, Denizli A, Özcan A, Say R (2005) Biosens Bioelectron 20:2197

43. James D, Scott SM, Ali Z, O'Hare WT (2005) Mikrochim Acta 149:1
44. Legin A, Rudnitskaya A, Vlasov Y (2003) Electronic tongues: new analytical perspective for chemical sensors. In: Salvador A (ed) Comprehensive analytical chemistry 39. Elsevier, Amsterdam, p 437
45. Dickert FL, Lieberzeit PA, Achatz P, Palfinger C, Fassnauer M, Schmid E, Werther W, Horner G (2004) Analyst 129:432
46. Dickert FL, Forth P, Lieberzeit PA, Voigt G (2000) Fresenius J Anal Chem 366:802
47. Dickert FL, Greibl W, Rohrer A, Voigt G (2001) Adv Mater 13:1327
48. Aherne A, Alexander C, Payne MJ, Perez N, Vulfson EN (1996) J Am Chem Soc 118:8771
49. Alexander C, Vulfson EN, (1997) Adv Mater 9:751
50. Dickert FL, Hayden O (2002) Anal Chem 74:1302
51. Hayden O, Dickert FL (2001) Adv Mater 13:1480
52. Knez M, Sumser M, Bittner AM, Wege C, Jeske H, Martin TP, Kern K (2004) Adv Funct Mater 14:116
53. Dickert FL, Hayden O, Lieberzeit P, Haderspoeck C, Bindeus R, Palfinger C, Wirl B (2003) Synth Methods 138:65
54. Hayden O, Bindeus R, Haderspöck C, Mann KJ, Wirl B, Dickert FL (2003) Sensor Actuator B 91:316
55. Dickert FL, Hayden O, Bindeus R, Mann KJ, Blaas D, Waigmann E (2004) Anal Bioanal Chem 378:1929
56. Lieberzeit PA, Gazda-Miarecka S, Halikias K, Schirk C, Kauling J, Dickert FL (2005) Sensor Actuator B 111–112:259
57. Tai DF, Lin CY, Wu TZ, Chen LK (2005) Anal Chem 77:5140
58. Ramanaviciene A, Ramanavicius A (2004) Biosens Bioelectron 20:1076
59. Leca-Bouvier B, Blum LJ (2005) Anal Lett 38:1491
60. Kuswandi B, Tombelli S, Marazza G, Mascini M (2005) Chimia 59:236
61. Logrieco A, Arrigan DWM, Brengel-Pesce K, Siciliano P, Tothill I (2005) Food Addit Contam 22:335
62. Ferrari M, Stenirri S, Bonini P, Cremonesi L (2003) Clin Chem Lab Med 41:462
63. Sallacan N, Zayats M, Bourenko T, Kharitonov BK, Willner I (2002) Anal Chem 72:702
64. Sreenivasan K (2005) Macromol Biosci 5:187
65. Friggeri A, Kobayashi H, Shinkai S, Reinhoudt DN (2001) Angew Chem Intl Ed Engl 40:4279
66. Kempe M, Mosbach K (1995) J Chromat A 691:317
67. Liao JL, Wang Y, Hjertén S (1996) Chromatographia 42:259
68. Hjertén S, Lioa JL, Nakazato K, Wang Y, Zamaratskaja G, Zhang HX (1997) Chromatographia 44:227
69. Bossi A, Piletsky SA, Piletska EV, Righetti PG, Turnern AFP (2001) Anal Chem 73:5281
70. Rick J, Chou TC (2005) Biosens Bioelectron 20:1878
71. Shiomi T, Matsui M, Mizukami F, Sakaguchi K (2005) Biomaterials 26:5564
72. Lin TY, Hu CH, Chou TC (2004) Biosens Bioelectron 20:75
73. Lin CY, Tai DF, Wu TZ (2003) Chem Eur J 9:5107
74. Kugiyama A, Yoneyama H, Takeuchi T (2000) Electroanalysis 12:1322
75. Dickert FL, Hayden O, Lieberzeit P, Haderspoeack C, Bindeus R, Palfinger C, Wirl B (2003) Synth Methods 138:65
76. D'Souza SM, Alexander C, Carr SW, Wallers AM, Whitcombe MJ, Vulfson EN (1999) Nature 398:312
77. Shi H, Tsai WB, Garrison MD, Ferrari S, Ratner BD (1999) Nature 398:593
78. Hawkins DM, Stevenson D, Reddy SM (2005) Anal Chim Acta 542:61

Springer Ser Chem Sens Biosens (2007) 5: 211–235
DOI 10.1007/5346_028

Published online: 22 July 2006

Analytical Applications of QCM-based Nucleic Acid Biosensors

Maria Minunni · Marco Mascini (✉) · Sara Tombelli

Dipartimento di Chimica, Università degli Studi di Firenze, Via della Lastruccia 3, 50019 Sesto Fiorentino, Italy
mascini@unifi.it

Abstract Recent advances in nucleic acid-based detection coupled to piezoelectric transduction will be reported here. The main aspects involved in the development of nucleic acid sensors are considered: the immobilization of the probe, the sample pretreatments (DNA extraction, amplification, denaturation of the amplified material), the sensitivity and specificity, etc.

These systems have been applied to different fields from environmental analysis to clinical diagnostics. Examples taken from different analytical problems will be reported.

Another nucleic acid sensor, also based on the affinity between the analyte and the receptor immobilized on the surface, is reported as an example of the most recent trend in the field. This receptor, called aptamer, acts as capturing receptor for a molecule in solution, such as a protein. An aptasensor developed for a specific protein will be reported.

Keywords Biosensor · QCM · Nucleic Acids · Hybridization · Aptamers

1 Introduction

The first report on the direct detection of nucleic acid interactions based on the use of acoustic wave devices was provided by Fawcett et al. in 1988 [1].

They described a quartz crystal microbalance (QCM)-based biosensor for DNA detection by immobilizing single-stranded DNA onto quartz crystals and detecting the mass changes after hybridization.

Since this early work, a number of articles have appeared employing similar procedures, resulting in microgravimetric measurements based on nucleic acids [2–5].

In general, when dealing with biosensing for this kind of application a few considerations are mandatory. First, the system should be specific and sensitive enough for the required application and should provide reproducible results. The system should have short analysis time and easy formats. Moreover, the sample pretreatment should be as little as possible, ideally absent.

In this chapter, the main aspects related to piezoelectric sensing based on nucleic acids are considered and examples taken from different fields of application, from environmental analysis to clinical diagnostics, will be considered.

A nucleic acid-based sensor consists of a nucleic acid immobilized on the transduction surface, which interacts with the analyte free in solution. Depending on the immobilized nucleic acid sequence and the relative interaction that drives the binding, different sensors can be distinguished. One based on the detection of the hybridization reaction can be developed by immobilizing a nucleic acid probe on the surface of the sensor to recognize the complementary sequence present in the sample solution. The hybridization reaction between the probe and the target sequence drives the biospecific interaction, which results in the formation of a double helix complex on the sensing surface with the detection of the specific sequence of interest. The interaction is based on the specific recognition between the two single-stranded DNA filaments leading to the formation of the DNA helix. The hydrogen bonds stabilize selectively the couples adenine–thymine (AT) and guanine–cytosine (GC).

In QCM-based sensing, the recognition is displaced as a measurable shift in the resonant frequency. Ideally, the frequency shift is maximum with the fully complementary sequence and it is absent with non-complementary DNA.

A typical profile of a QCM-based DNA sensor signal is reported in Fig. 1, where the addition of complementary sequences leads to the formation of the double helix and causes an increase in the mass loading at the sensor surface, recorded as a decrease in the frequency shift of the crystal.

With QCM-based sensing it is then possible to detect, in real time and without the use of any label, specific target sequences characteristic of the DNA of interest as well as point mutations. This kind of QCM DNA sensor has been applied by this research group to the analysis of many different target sequences like genetically modified organisms (GMOs) [2] and bacteria detection [6, 7] in the field of food and environmental analysis, respectively. In clinical diagnostics application, the sensor has been used for the detection of point mutations such as the mutation occurring in the p53 oncogene, related to cancer research, diagnosis and prognosis [8].

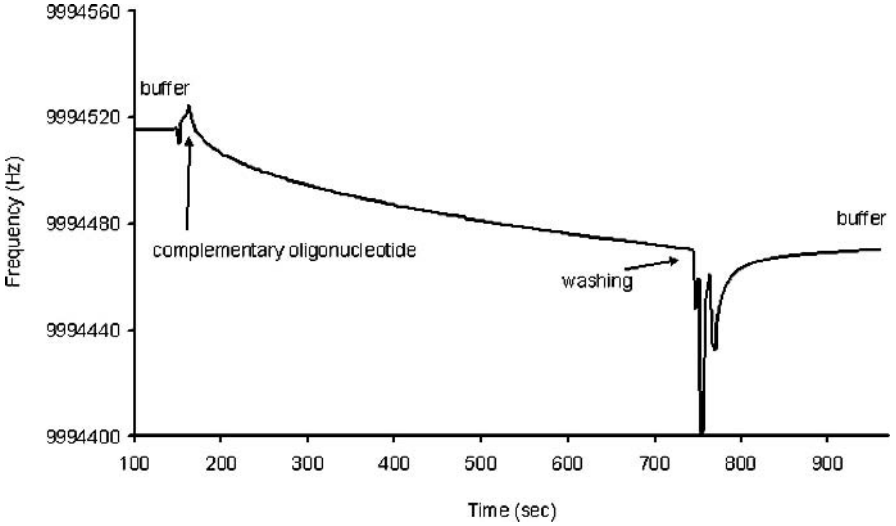

Fig. 1 Typical sensorgram recorded with a 10 MHz AT-cut quartz crystal coated with gold electrodes, during a hybridization cycle between the immobilized probe and the target oligonucleotide in solution. The frequency spikes are due to the replacement of the different solutions by pipetting

A different nucleic acid sensor, not based on the hybridization reaction, can be developed by immobilizing a nucleic acid sequence which acts as capturing receptor for a molecule in solution (i.e., a protein). The probe shows an affinity for the target analyte and binds it, when present in solution. This system can be applied for studying DNA–protein interaction [9], or to show the ability of different chemical compounds (intercalators) to bind DNA [10]. The binding is driven by the affinity of the nucleic acid sequence for the target molecule.

An example will be reported here, based on nucleic acid receptors called aptamers, selected in vitro, which can be produced for a wide range of molecules [11] and represent now one of the frontiers of nucleic acid-based sensing.

2
DNA-Based QCM Sensors Based on the Hybridization Reaction

2.1
Availability of DNA Material

Some important aspects should be considered when dealing with nucleic acid sensors based on the hybridization reaction. Direct detection in complex ma-

trices is not possible because DNA should be extracted from the cell. In prokaryotic organisms (i.e., bacteria) the DNA is located in the cytoplasm, while in eukaryotic it is confined to the nucleus.

Another important step to be considered in the case of nucleic acid detection, absent in the case of other analyte detection (protein, small molecules, etc.), is the amplification of the extracted DNA. This latter can be imagined as a sample enrichment in the target analyte sequence. From a single starting molecule of DNA, many copies of the target analyte (2^n with n equal to the number of amplification cycles) can be obtained by running, for example, the polymerase chain reaction (PCR). Protocols for DNA extraction and amplification are available from molecular biology and directly applied to DNA-based sensing, although optimization of the PCR reaction is needed whenever a new target sequence is analyzed.

Once the PCR-amplified material is available, an additional sample pretreatment is required. Denaturation of the amplified sample is done to allow hybridization of the target sequence with the immobilized probe. It consists of a denaturation step, in which the double strand of the DNA is dissociated to facilitate the hybridization between the target sequence in solution and the probe immobilized on the sensor surface.

These aspects should be considered whenever developing a new DNA-based analytical method. DNA extraction is a critical step. In fact, since the extracted DNA is used as template in the PCR reaction, the integrity of the DNA molecule is a prerequisite for the success of the reaction. Moreover, the presence of any potential interfering molecule should be avoided to prevent false negative or positive results. DNA extracted from processed food can be, for example, undetectable by PCR due to DNA fragmentation. The degradation can be caused, for example, by heating treatments or by exposure to pH changes during the sample processing.

The degradation of genomic DNA, following a heating treatment is well described by Ahmed [12], who reported that the degree of DNA degradation increases with the increasing time of heat treatment. In particular, it is found that there is a direct proportional relationship between the time exposure and the fragment size in which the DNA is degraded. The longer the time of exposure, the shorter are the fragments resulting from the DNA degradation. Exposure to acid pH also influences the efficiency of PCR amplification [13].

There is another important factor that could affect the amplification step that should be taken into consideration in the analysis and leads also to false negative results This is the presence of different inhibitors of the enzyme Taq polymerase, used in the PCR reaction, such as proteins, fats, polysaccharides, polyphenols and other compounds that may be present in DNA extracted from many different food matrices [14–16] In order to avoid false negative results and to evaluate the possibility to amplify the extracted DNA, it is necessary to first amplify a reference gene present in the genome of the analyzed species [17].

2.2 Immobilization of the Nucleic Acid Probe

In a piezoelectric device, as a mass device, any contribution to the signal, which is identified as a shift in the resonant frequency due to surface interactions different from the specific binding, is considered an interference. Interferences, ideally, should be absent if the sensor is specific. Moreover, the immobilized molecule should maintain the biological activity after the immobilization. To assure a specific and reliable response it is necessary to properly chemically modify the sensor surface. For this reason, an appropriate chemical modification of the sensing surface should be applied for the immobilization of the biological molecule, in this case a nucleic acid. Two different approaches, involving in one case a multilayer immobilization method using biotinylated probes, to be coupled via streptavidin–biotin coupling and, in the other case, a thiolated probe to be directly coupled onto gold electrodes, have been proven to be suitable for the development of nucleic acid-based sensors. The first immobilization procedure is very suitable for DNA sensing and for this reason has been often applied and used as reference method [18, 19]. The direct immobilization of the thiolated probe can be used with the aim of significantly reducing the time required to chemically modify the sensor. The comparison between the two immobilization procedures is reported in Fig. 2a,b. The detailed procedures are described in Mannelli et al. [2].

Both procedures are suitable for nucleic acid sensing application. The thiol-dextran has a higher surface capacity compared to the thiol direct coupling. When comparing the hybridization signal obtained with the target sequence at the same concentration (0.5 ppm) with the two immobilization protocols, a double signal with the thiol-dextran method is obtained as compared to the thiol direct coupling (Table 1). However, the direct probe coupling is a much faster immobilization procedure, which reduces the sensor surface chemistry from 5 days down to 4 h (Fig. 2).

When a suitable immobilization protocol is identified for the application of interest, the sensor is studied and optimized in its analytical performances. The specificity is tested by using a negative control, which is a non-complementary sequence and does not hybridize the probe and, if the immobilization is properly performed, no recordable signal should be found. The reproducibility, expressed as coefficient of variation (CV, equal to (standard deviation)/Δf_{av}), is another important parameter to be considered.

The values of CV% obtained by testing the same concentration of synthetic oligonucleotides on the same crystal (CV% within crystal) and also on different crystals (CV% among crystals) when the gold surfaces were modified with the two different procedures are shown in Table 1.

The response time for nucleic acid detection in PCR amplified samples is 30 min per sample, considering 20 min of interaction, the regeneration of the

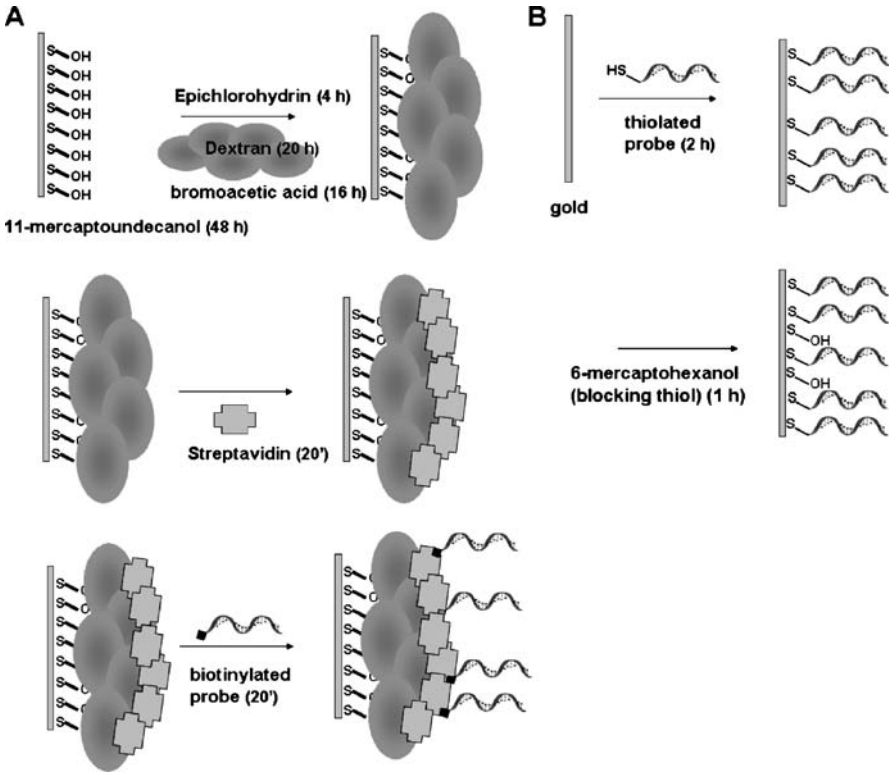

Fig. 2 **a** Immobilization procedure based on the streptavidin/biotin interaction. The probe to be immobilized is biotinylated and interacts with streptavidin covalently fixed onto the crystal. **b** Immobilization procedure based on the direct coupling of a thiolated probe onto the crystal

Table 1 Reproducibility of the detection of the hybridization between the target oligonucleotide (0.5 ppm) and the immobilized biotinylated (A) or thiolated (B) probe

Probe	Within crystal ($n = 3$)			Among crystals ($N = 4$, $n = 3$)		
	Δf (Hz)	SD (Hz)	CV (%)	Δf (Hz)	SD (Hz)	CV (%)
A	– 29	3	10	– 20	8	40
B	– 13	2	15	– 14	3	21

probe, and the sample pretreatment. In amplified samples, in fact, a dissociation step should be considered. Some denaturation approaches are discussed in the next section.

2.3
Sample Pretreatment for Target DNA Detection

The double stranded amplicons resulting from the PCR step should be dissociated into single-stranded DNA (ssDNA) to allow hybridization of the target sequence with the immobilized probe. The nucleic acid helix is very often dissociated by treatment with heat (thermal denaturation), which is the easiest way to obtain single strands. Depending on the working conditions, this method may not be sufficient to generate a recordable analytical signal. For this reason other denaturation approaches can be applied when only thermal treatment is not suitable (Fig. 3a–d). For example, thermal treatment, consisting of 5 min at 95 °C and 1 min cooling in ice, is not applicable when the measurement occurs in a flow system instead of the batch mode [20, 21]. This is due to the fact that re-annealing of the complementary strands occurs preventing the target sequence from reaching and binding the immobilized probe. For this reason it is important to avoid this re-annealing by prolonging the lifetime of the ssDNA. This can be achieved by different strategies. The use of physical separation by magnetic particles of one strand of the PCR amplicon, not containing the target sequence and having a biotinylated end, as well

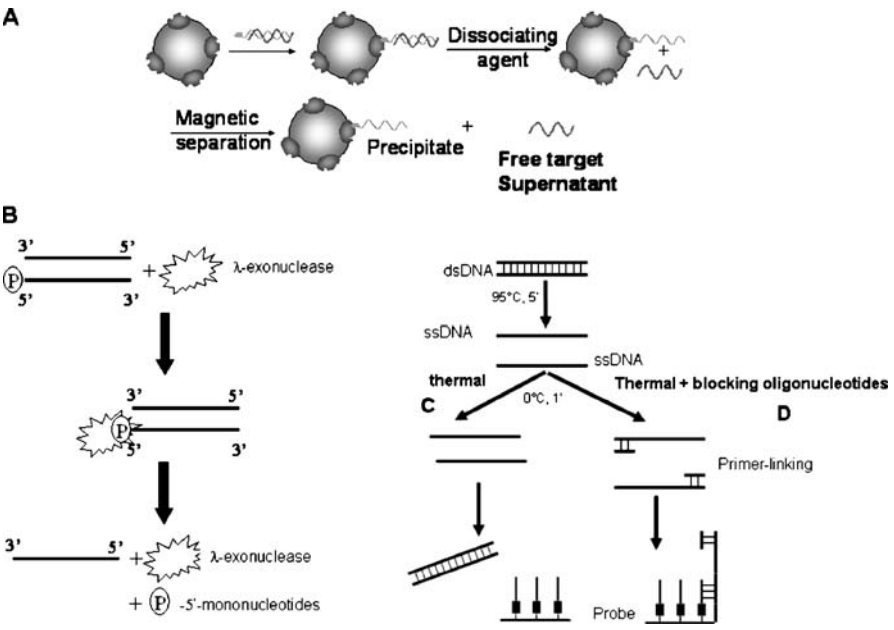

Fig. 3 Denaturation procedures. **a** Magnetic particles coated with streptavidin; **b** enzymatic digestion with λ-strendase; **c** thermal denaturation; **d** thermal denaturation with blocking oligonucleotides

as the enzymatic digestion with λ-strendase, which recognizes the phosphorylated end on one strand, have been successfully applied to QCM DNA-based sensing [2].

Finally, we have reported a new denaturation approach, allowing direct genomic detection of target DNA as well as PCR amplicons in flow mode [22–24].

This denaturation method, called thermal plus blocking oligonucleotides, was found to be a simple and useful way to obtain DNA available for hybridization after PCR amplification. The principle of this method relies on the use of small (10–30 bases) oligonucleotides (which can correspond to the PCR reaction primers), added to the denaturation mixture. These oligonucleotides are complementary to some sequences on the strand, which hybridizes the immobilized probe, but are positioned laterally and do not overlap the portion forming the complex with the probe. By the interaction between the thermally separated DNA strands and these oligonucleotides, re-association between DNA strands of PCR amplicons is prevented, and surface hybridization can occur. The whole denaturation procedure consisted of 5 min incubation at 95 °C and 1 min at a specific temperature, which is the suitable temperature for primer annealing used in the PCR procedure. These oligonucleotides are chosen on the basis of the particular sequence of the PCR fragment to be analyzed [22].

3
Application of QCM Sensors Based on the Hybridization Reaction

Some examples of nucleic acid-based sensing are reported to show which are the application fields and the potentials of this device. Most of the examples are based on the hybridization detection mode: target sequences, chosen as markers, are detected in different samples, consisting both in PCR and directly in non-amplified genomic DNA. The examples deal with the detection of GMOs in food samples, identification of pathogenic bacteria (*Staphylococcus aureus)* and analysis of highly repeated sequence in genomic bovine DNA.

The last example is based on the interaction between a new receptor (aptamer) able to interact with a specific protein and represents an example of nucleic acid–protein interaction. The aptamers can represent an alternative to an antibody-based sensor and are an interesting challenge in biosensing research.

3.1
Detection of Genetically Modified Organisms

With the advent of biotechnology, new "products" have appeared such as genetically modified organisms (GMOs). The introduction of new genes into

a host, which would never naturally exchange the DNA with the donor, leads to the "synthesis" of mixed genomes by the use of molecular biology techniques that allow one to insert a bacterial or viral DNA into a eukaryotic genome. The products of these approaches are called genetically modified organisms (GMOs), defined as living organisms, whose genome has been altered in a way that does not occur naturally by mating or natural recombination. The modification involves the introduction of an exogenous sequence in the host genome, either capable of expressing an additional protein that confers new characteristics or able to hybridize specifically to target m-RNA and inactivating it. The foreign DNA is "usually" inserted in a gene cassette consisting of an expression promoter (P), a structural gene ("encoding region") and an expression terminator (T) (Fig. 4). The gene cassette is built up by assembling some DNA sequences, with a known function, coming from different species. Such a cassette can be made by assembling bacterial or viral DNA (generally for the promoter and terminator region) together with an eukaryotic DNA, coding for the inserted gene conferring the desired characteristics. In the patented GMOs, so far, approximately the same promoters and terminators have been used. The promoter of the subunit 35S of ribosomal RNA of the cauliflower mosaic virus (P35S) and the terminator NOS from *Agrobacterium tumefaciens* are widely used for the production of many transgenic vegetables, such as soy Roundup Ready™, maize MaisGard and the tomato Flavr Savr. In consequence of the introduction on the market of GMOs to be used in food production, an intense debate has occurred on the risk occurring from the introduction of GMOs in agriculture, in their use in the human diet, and the dispersion of modified DNA into the environment with unknown consequences.

There are some analytical procedures already available for GMO detection, involving two approaches based on the detection of exogenous DNA and proteins, respectively [13, 17, 25–30]. One method for the detection of transgenic material at DNA level has been already validated; it refers to the detection of P35S and TNOs in flour samples [31]. This method associates the amplification by PCR with gel electrophoresis, which does not give any sequence information and employs toxic reagents. More recently, quantitative methods for transgenic DNA detection have been studied; some results have been reported [32] using the "real-time" PCR approach.

DNA sensors based on optical, electrochemical, and piezoelectric transduction have been reported for the detection of P35S target sequence [2, 20–22, 33, 34].

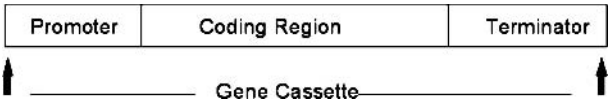

Fig. 4 Scheme of a gene cassette generally inserted in genetically modified organisms

Probes specific for P35S were immobilized on 10 MHz quartz crystals coated with gold, employing both the mentioned immobilization procedures: streptavidin/dextran-modified surfaces using a biotinylated probe and direct thiol coupling with 5′ thiolated probes.

The systems are initially optimized in terms of the main analytical parameters including specificity, sensitivity, reproducibility, and analysis time, using synthetic oligonucleotides. The optimized system is then applied to the analysis of samples consisting of DNA from GMOs, extracted and amplified by PCR.

For thiol/dextran-modified surfaces, P35S synthetic oligonucleotides were tested in a concentration range of 0–0.4 μM. An experimental detection limit of 0.025 μM was found with a saturation of the signal at 0.1 μM. The reproducibility of the measurements has been estimated by considering the analytical signals obtained using the same concentration in different cycles. The average frequency shift obtained with 0.5 μM complementary oligonucleotide solutions was − 52 Hz with SD = 6 Hz and CV% = 11% calculated for eight measurements performed over 2 days. It should be noted that the reproducibility of the sensor is particularly good since it should be taken into account that it has been calculated over eight samples but during a set of 20 measurements, where complementary oligonucleotide solutions at different concentrations, PCR DNA amplified from real samples and non-complementary oligonucleotide solutions were also used.

The reproducibility of the sensor has also been calculated using a 0.2 μM solution of target oligonucleotide over 3 days of continuous use with only synthetic oligonucleotides. The calculated CV% for these measurements was 10–15%. Using only synthetic oligonucleotides it was possible to perform up to 25 measurements on the same crystal.

The specificity of the interaction was tested using 1 μM solutions of 25-mer non-complementary oligonucleotides and no recordable signal was observed. The PCR samples tested were amplified from plasmidic and genomic DNA obtained from the pBI121 plasmid, DNA extracted from commercially available soybean powder (CRM) and from real samples consisting of dietetic products of various origin; they were amplified following the procedure reported by Pietsch et al. [31]. From the PCR, amplification fragments of 195 base pairs (bp) were obtained. The control solution (blank) contained all the PCR reagents except the DNA template.

When testing DNA amplified samples, the amplicons were denatured to “dissociate” the dsDNA into ssDNA, using the approaches reported in Sect. 2.3 of this chapter. In Fig. 5 the response obtained with the different denaturation procedures using the biotinylated probe and streptavidin-modified surfaces is shown. A good reproducibility was found with PCR-amplified material (CV% 6 ($n = 3$)).

In Fig. 6 the responses obtained using the thiolated probe are reported. The sensor showed a CV% of 15%.

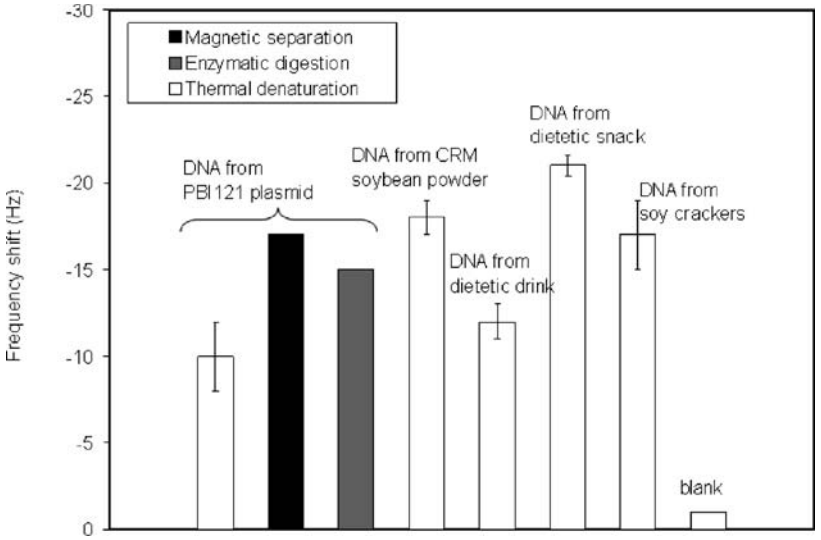

Fig. 5 Results obtained with the sensor modified with the biotinylated probe. The samples analyzed were PCR amplicons from plasmid PBI121, CRM soybean powder, and different commercially available food samples

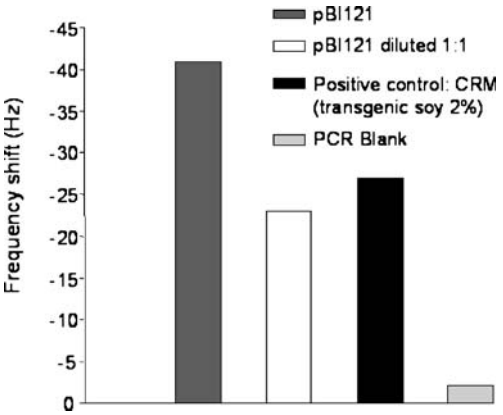

Fig. 6 Results obtained with the sensor modified with the thiolated probe. The samples analyzed were PCR amplicons from plasmid PBI121 and CRM soybean powder

3.2 Detection of Pathogenic Bacteria

The development of a DNA piezoelectric biosensor for the detection of the mecA gene, present in methicillin resistant *Staphylococcus aureus* (MRSA) strain, was described [6]. Methicillin resistant *Staphylococcus aureus* is the

causative agent of a wide variety of infections and toxin-mediated diseases [35–37] and it is a major cause of hospital- and community-acquired infections worldwide. One of the characteristics of this strain is its possible resistance to β-lactamic antibiotics, such as penicillin and methicillin. These compounds are substrate analogs of penicillin-binding proteins (PBPs) [38] and methicillin resistance in MRSA strains is due to acquisition of the mecA gene [39], which encodes for PBP2a, a new protein with a low affinity for the β-lactamic antibiotics [40].

Historically, isolates were distinguished by phenotypic methods, including antibiotic susceptibility testing and bacteriophage typing. Both methods have limitations, as genetically unrelated isolates commonly have the same antibiogram, and many *S. aureus* isolates are non-typeable by phage typing [41]. With the advent of molecular biology, strain typing focused on DNA-based methods, included Southern blot hybridization using gene-specific probes, polymerase chain reaction (PCR), and pulsed-field gel electrophoresis (PFGE) [42, 43].

The developed biosensor employed a probe specific for a fragment of the mecA gene and was used for the detection of methicillin-resistant bacteria. The specific probe was immobilized onto the gold electrode of 10 MHz quartz crystals, following two procedures based on its modification with biotin or with an SH group. The analytical parameters of the sensor were studied using synthetic oligonucleotides complementary to the immobilized probe. Moreover, the developed sensor was applied to the analysis of DNA samples amplified by PCR, extracted from bacterial DNA. The DNA was from MRSA and *Staphylococcus lugdunensis*, sensitive to methicillin, used as negative control.

Genomic DNA from the methicillin resistant strain *Staphylococcus aureus* subsp. *aureus* Rosenbach (ATCC 700699) was used as specific sample, whereas DNA from *Staphylococcus lugdunensis* (ATCC 43809D) was used as negative control since this strain is known to be methicillin sensible.

The immobilized probe was designed to recognize a region of the mecA gene and its sequence is included in the fragment amplified by PCR. The gold electrode of the quartz crystal was modified as reported in Tombelli et al. [19] for the immobilization of streptavidin. The biotinylated probe was then bound to the streptavidin layer. For the immobilization of the thiolated probe, the clean crystal surface was treated with 200 μL of a 1 μM solution of thiolated probe in immobilization solution (KH_2PO_4 1 M, pH 3.8) for 2 h. After washing, 200 μL of a solution of 1 mM of mercaptohexanol (MCH) as blocking thiol were added to the cell and the reaction was allowed to proceed for 1 h.

For sensor optimization, experiments were performed with different concentrations of the target oligonucleotide in the range 0.06–0.75 μM and the results for the two different immobilization procedures were compared. The two sensors showed a similar behavior with a saturation of the signal for concentrations higher than 0.5 μM. A 35% higher response was obtained

with the crystal modified by using the biotinylated probe for all the tested concentrations.

The specificity of the interaction was tested by using a 25-mer non-complementary oligonucleotide at 1 μM concentration. The signal resulting from this interaction when using the biotinylated or the thiolated probe was negligible, evidencing the specificity of the system in both cases.

The reproducibility of the measurements has been also estimated for the results obtained on the same crystal (reproducibility intracrystal) and on different crystals (reproducibility intercrystals). Both the sensors showed a good reproducibility (CV% $\leq$ 11%) but the one with the biotinylated probe evidenced a lower variation both for the intra- (CV% 4%, $n = 3$) and intercrystal signals (CV% 7%, $n = 13$).

For the analysis of more complex samples, bacterial DNA was amplified by PCR following an adapted protocol from the one reported by Jenison et al. [44]. The amplified DNA fragment, internal to the mecA gene, was 617 bp in length and contained the complementary sequence to the immobilized probe. In order to obtain a hybridization signal from the sensor, the amplified samples were denatured to dissociate the dsDNA into ssDNA, ready for the binding with the probe. Thermal denaturation has been compared with the denaturation protocol involving blocking oligonucleotides explained in Sect. 2.3 of this chapter. The latter denaturation procedure has been further optimized by using different couples of blocking oligonucleotides in order to verify the effect of their position in the fragment on the sensor performance.

With the biotinylated probe, PCR blanks, negative controls and the mecA amplified product (0.03 μM) were initially tested after a thermal treatment consisting of 5′ at 95 °C followed by 1′ in ice and a measurable signal of -27 ± 5 Hz could be observed only for the specific sample.

The other denaturation procedure involving blocking oligonucleotides was further used on these samples at the same concentration of 0.03 μM: different couples of blocking oligonucleotides were tested, differing in their position inside the amplified fragment and with respect to the probe (Fig. 7). The first two oligonucleotides, called P1 and P2, were both positioned at the ends of the fragment and "far" from the probe, which is positioned near the center of the sequence. The other two, P3 and P4, were instead inside the fragment and near the probe; P3 was directly attached to the probe. Other two combinations of these oligonucleotides have been also tested: P2 + P3 and P2 + P4.

All the combinations of oligonucleotides allowed a successful hybridization of the sample with the immobilized probe. Moreover, the signals obtained with the second denaturation approach are higher than the one recorded when only thermal denaturation is applied. In particular, the lowest signal (-27 ± 4 Hz) was observed for oligonucleotides P3–P4 mapping very close to the target sequence recognized by the probe. This could be due to a steric hindrance of the two oligonucleotides P3 and P4 in the target-probe binding.

The best results, in terms of signal and reproducibility, were found for the couples P1–P2 (– 38 ± 3 Hz, CV% 5%) and P2–P3 (– 38 ± 2 Hz, CV% 8%). The specificity of the sensor was evidenced by the very low signals (– 1 Hz) obtained with PCR blanks and negative controls for all the tested denaturation procedures.

Further experiments were conducted with the PCR-specific samples at different concentrations (0.015, 0.03, and 0.06 μM) (Fig. 8).

taatagttgtagttgtcgggtttgGTATATATTTTTATGCTTCAAAAGATAAA
GAAATTAATAATACTATTGATGCAATTGAAGATAAAAATTTCAAAC
AAGTTTATAAAGATAGCAGTTATATTTCTAAAAGCGATAATGGTG
AAGTAGAAATGACTGAACGTCCGATAAAAATATATAATAGTTTAG
GCGTTAAAGAATAAACATTCAGGATCGTAAAATAAAAAAAGTATC
TAAAAATAAAAAACGAGTAGATGCTCAATATAAAATTAAAACAAA
CTACGGTAACATTGATCGCAACGTTAAATTTAATTTTGTTAAAGA
AGATGGTATGTGGAA*gttagattgggatcatagcgtcatt*A<u>TTCCAGGAATGC</u>
<u>AGAAAGACCAAAGCA</u>TACATATTGAAAATTTAAAATCAGAACGTG
GTAA*aattttagaccgaaacaatgtggaatt*GGCCAATACAGGAACACATATG
AGATTAGGCATCGTTCCAAAGAATGTATCTAAAAAAGATTTAAAG
CAATCGCTAAAGAACTAAGTATTTCTGAAGACTATATCAACAACA
AATGGATCAAAATGGGTACAAGATG**atacctttcgttccactttaaaacc**

Fig. 7 Amplified fragment of the mecA gene. *Bold*: primers for the amplification and denaturation (P1 and P2); *italics*: blocking oligonucleotides P3 and P4; *underlined*: immobilized probe

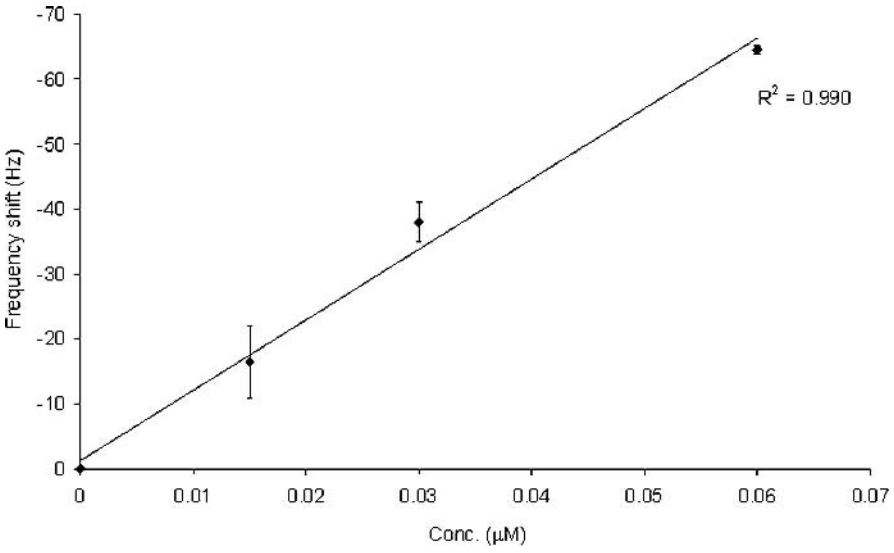

Fig. 8 Calibration plot obtained with different concentrations of the amplified fragment of the mecA gene. The biotinylated specific probe was immobilized on the sensor

PCR blanks and the negative controls at the same concentrations were also tested using the thermal + oligonucleotides treatment. The signal obtained with the specific sample increased with the concentration up to a value of -64 ± 1 Hz for the concentration 0.06 μM. This dependence of the signal on the concentration was not found for the negative control nor for PCR blanks since the measurable signals obtained (– 7 Hz for the negative control and – 10 Hz for the blank) were probably due to non-specific adsorption of some component of the PCR mixture on the sensor surface.

The same experiments were conducted using the two denaturation procedures, with the crystal modified with the thiolated probe. All the samples were tested at a concentration of 0.03 μM. Also with this probe immobilization, a slightly higher signal was obtained for the thermal with oligonucleotides denaturation protocol (-27 ± 5 Hz and -22 ± 2 Hz, respectively). When PCR blanks and negative controls were tested very low signals were obtained; this behavior was found when both the denaturation methods were applied to the samples (-2 ± 1 Hz and -4 ± 2 Hz, respectively). The absence of significant frequency shifts evidences the specificity of the sensor.

3.3
Direct Detection of Target Sequences in Non-amplified DNA

An important improvement in DNA sensing, in terms of analysis time and costs, would come from the direct analysis of extracted DNA without any amplification step. The possibility of analyzing non-amplified DNA (genomic DNA) is very attractive and, so far, only few works operating directly with genomic DNA have been reported in literature. These papers deal with different detection principles (optical, electrochemical, and piezoelectric) that have been applied to bacterial, viral, or human DNA analysis [45–51].

To approach the problem of direct sequence detection in non-amplified genomic DNA, the example reported here focused on target sequences highly repeated in genomes, which are species-specific and, in some cases, could represent a significant part of the genome [23].

In particular, the development of a biosensor for the detection of the highly repeated sequence called satellite 13, present in *Bos taurus* genome, is reported. In the bovine genome eight highly repetitive and several minor repetitive sequences have been detected comprising a total of 27% of the DNA. The target sequence chosen in this case is situated in highly repeated DNA and is therefore present in the genome in a high number of copies, increasing the amount of target sequence available for hybridization with the probe immobilized on the sensing element.

The developed sensor (with 10 MHz quartz crystals) based on the detection of highly repetitive and species-specific DNA sequence present in bovine (*Bos Taurus*) genomic (non-amplified) DNA extracted from meat samples, has been applied to the identification of animal species in meat samples.

However, prior to the genomic DNA analysis a sample pretreatment should be applied. The DNA should be first extracted and then fragmented into smaller fragments, to allow dissociation of the dsDNA and subsequent hybridization with the probe. The fragmentation of non-amplified DNA is achieved by a treatment with restriction enzymes.

Samples consisting of genomic DNA are commercially available (Novagen, Germany): bovine DNA (*Bos Taurus*) containing the target sequence, and pig DNA from *Sus scrofa domesticus*, not containing the target sequence are used as negative control. An additional bovine DNA was extracted from muscle (Istituto Zooprofilattico, Teramo, Italy).

The genomic DNA was digested using the restriction enzyme EcoRI, to obtain DNA fragments of around 400 ± 500 bp, containing the target sequence. Using the WebCutter 2.0 software (web available), it was verified that the consensus sequence recognized by the enzyme was not present inside the *Bos Taurus* satellite 13 (247 bp). This is important to ensure that the fragmentation does not affect the ability of the target sequence to hybridize to the immobilized probe. The detailed procedure is reported in Minunni et al. [23]. The digested fragment containing the target sequence was 247 bp long. Thermal and thermal plus blocking oligonucleotides denaturation methods were applied to the samples.

In the case of thermal denaturation, although it was possible to distinguish the bovine (-80 Hz for 10 ppm and -55 Hz for 25 ppm) from the porcine DNA (-25 Hz), a non-specific adsorption effect could be observed, which generated a significant signal (-25 Hz) from the non-complementary sequence. The frequency shifts in Fig. 9 were obtained after the interaction between the probe and non-amplified genomic DNA samples previously digested and thermally denatured with blocking oligonucleotides. The evaluated sample concentration of target fragment was 3 nM.

Different samples were treated with this denaturation procedure: bovine genomic DNA and porcine genomic DNA, both at concentrations of 5, 10, and 20 ppm. Different blank solutions containing all the reagents for digestion except for the genomic DNA were also tested to exclude any non-specific effect due to the digestion matrix. A detectable frequency shift was obtained with all the tested concentrations of bovine genomic DNA ($\Delta f = 8 \pm 2$ Hz for 5 ppm; $\Delta f = 17 \pm 5$ ppm for 10 ppm; $\Delta f = 26 \pm 5$ Hz for 20 ppm). Moreover, the frequency shift increased with the increase of the DNA concentration.

Negligible signals were obtained when testing porcine DNA or blank solutions. These results demonstrated the high selectivity of the sensor also when testing DNA samples of high complexity such as digested genomic DNA. The sensor was actually able to distinguish between complementary and non-complementary sequences both in synthetic oligonucleotides and in digested non-amplified genomic DNA.

The same results were found when DNA extracted from muscle was tested (Fig. 10).

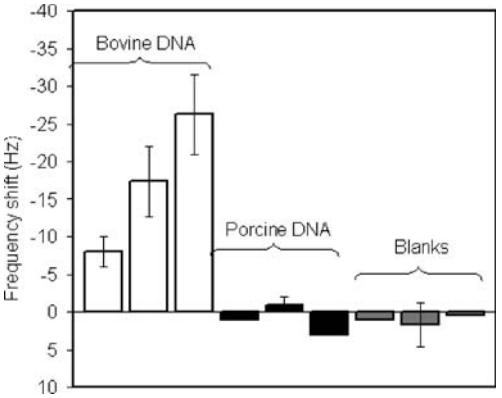

Fig. 9 Detection of highly repeated DNA sequences (satellite 13) in non-amplified genomic DNA, treated by thermal denaturation with blocking oligonucleotides. 1 Bovine genomic DNA 5 ppm ($n = 4$); 2 Bovine genomic DNA 10 ppm ($n = 6$); 3 Bovine genomic DNA 20 ppm ($n = 4$); 4 Porcine genomic DNA 5 ppm ($n = 1$); 5 Porcine genomic DNA 10 ppm ($n = 3$); 6 Porcine genomic DNA 20 ppm ($n = 1$); 7 Blank solution for 5 ppm ($n = 2$); 8 Blank solution for 10 ppm ($n = 3$); 9 Blank solution for 20 ppm ($n = 2$)

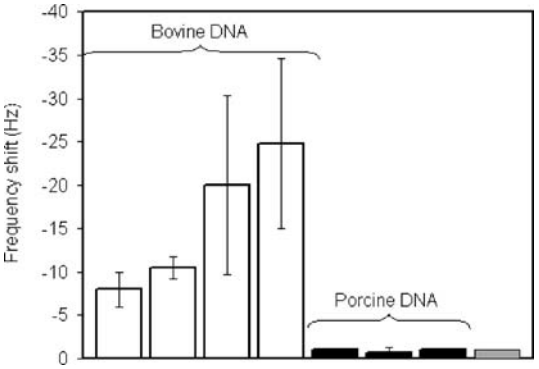

Fig. 10 Bovine DNA extracted from muscle, treated by thermal denaturation with blocking oligonucleotides. 1 Commercial bovine genomic DNA 5 ppm ($n = 4$); 2 Real sample (bovine genomic DNA) 5 ppm ($n = 4$); 3 Real sample (bovine genomic DNA) 10 ppm ($n = 5$); 4 Real sample (bovine genomic DNA) 20 ppm ($n = 5$); 5 Porcine genomic DNA 5 ppm; 6 Porcine genomic DNA 10 ppm ; 7 Porcine genomic DNA 20 ppm; 8 Blank solution

The successful application of this transduction principle to the PCR-free detection of highly repeated sequences was a starting point for the eventual detection of target DNA present as a single copy per genome [24].

Genomic DNA was extracted from the plant *Nicotiana glauca*, used as a model system. The target sequence was a portion of the promoter region (P35S), a part of the gene cassette introduced as foreign DNA into the genetically modified plant, as described in Sect. 3.1. The extracted DNA was

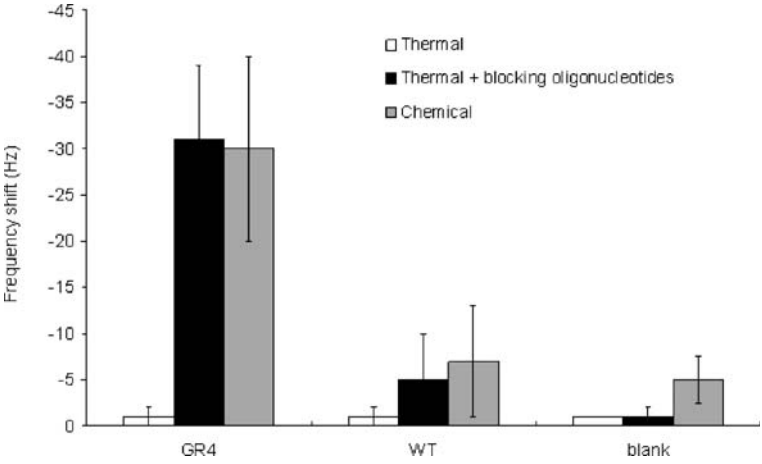

Fig. 11 Results obtained with genomic DNA samples, specific (GR4), and non-specific (WT) for the immobilized probe, by using different denaturation procedures

processed with restriction enzymes for fragmentation, as in the case of highly repeated DNA detection, reported in the previous section.

The fragmented DNA was denatured with the different approaches reported so far and the hybridization with the immobilized probe was investigated (Fig. 11).

A significant signal was obtained by samples treated with thermal + blocking oligonucleotides and chemical denaturation. The thermal treatment alone did not result in a measurable signal. A better reproducibility was achieved with the thermal + oligonucleotide procedure than with the chemical one. It should be noted that the lifetime of the sensor was dependent on the sample denaturation treatment. With chemical denaturation the surface could be regenerated just five times, while with the thermal + blocking oligonucleotides procedure the sensor surface could be regenerated up to 13 times before losing sensitivity and specificity. The system was able to distinguish the positive sample (GR4) from the negative control (WT) except when the thermal treatment alone was applied.

This work demonstrated that it is possible to detect the target sequence directly in non-amplified genomic DNA, even considering the low concentration of the target in the sample, 4×10^5 copies in 10 ppm of sample.

4
New Frontiers in Nucleic Acid-Based Piezoelectric Biosensors: Aptasensors

So far, several bioanalytical methods, including biosensors, have used nucleic acid probes to detect specific sequences in RNA or DNA targets through

hybridization. More recently, specific nucleic acids, aptamers, selected from random sequence pools, have been shown to bind non-nucleic acid targets, such as small molecules or proteins. Aptamers are DNA or RNA oligonucleotides that can bind with high affinity and specificity to a wide range of target molecules, such as drugs, proteins, or other organic or inorganic molecules [11, 52–54]. They are generated by an in vitro selection process called SELEX (systematic evolution of ligands by exponential enrichment) which was first reported in 1990 [55, 56]. In comparison to antibodies, aptamer receptors have a number of advantages that make them very promising in analytical and diagnostic applications. The main advantage is the overcoming of the use of animals for their production. Most antibody production starts in biological systems by inducing an immune response to the target analyte, but the immune response can fail when the target molecule, i.e., protein, has a structure similar to endogenous proteins and when the antigen consists of toxic compounds. In contrast, aptamers are isolated by in vitro methods that are independent of animals; an in vitro combinatorial library can be generated against any target.

Moreover, the application of aptamers as biocomponents in biosensors offers a multitude of advantages over classical affinity sensing methods, mainly based on antibodies. These include the possibility of easily regenerating the function of immobilized aptamers, their homogeneous preparation, and the possibility of using different detection methods due to easy labeling [11, 52, 54, 57]. Besides antibodies, the selection process itself, with the amplification step, gives some advantages to aptamers as compared to other "non-natural" receptors, such as oligopeptides, which cannot be amplified during their selection procedure.

The advantages of aptamers as recognition element for biosensing have been presented in conjunction with colorimetric [58], acoustic waves [9, 59–61], and surface plasmon resonance (SPR) [62, 63] transduction. Among these, in exploring the potential of RNA aptamers as small-molecule discriminating tools, the SPR technology has been applied to study the selection of new aptamers against specific targets, to be used as therapeutic agents [64]. Some more papers have appeared in the literature very recently, in which SPR is used for studying the interaction between the selected aptamers and their relative targets [63, 65–67].

With the piezoelectric transduction, an RNA aptamer has been used as biorecognition element to develop an aptasensor for the detection of Tat (trans-activator of transcription) protein [9].

Tat is a protein of 86 to 101 amino acids controlling the early phase of the human immunodeficiency virus type 1 (HIV-1) replication cycle [68, 69]. Yamamoto et al. [70, 71] were the first to develop an aptamer that yielded an efficient binding specificity against Tat, but not for other cellular factors. This novel aptamer RNA^{Tat} demonstrated a 133 times higher binding affinity than the natural RNA fragment binding to Tat (trans-activation response element

(TAR) RNA, 59-mer). The aptamer has a TAR-like motif in its randomized region, having two bulge units adjacent to one another in opposite orientations. The core element for binding to Tat is a four central base pair helix flanked by two residues on each side.

This aptamer is a very promising biorecognition element for the detection of Tat, since it combines unique characteristics such as high affinity for Tat and possibility of altering its design to enhance sensitivity and stabilization against nucleases, allowing monitoring of viral protein levels in vivo.

The biotinylated RNA aptamer has been immobilized on the gold electrode of 10 MHz piezoelectric quartz crystals and the interaction with Tat protein in solution has been studied following the changes in the oscillation frequency of the crystal.

Ten crystals were modified and the frequency shifts due to the aptamer immobilization were recorded. Only on six crystals was a measurable signal for aptamer immobilization obtained with an average value of 26 ± 20 Hz, indicating a very low reproducibility for the aptamer immobilization step.

On these six crystals, the interaction between the aptamer and Tat protein in a concentration range of 0–5 ppm was studied. The reproducibility in terms of average coefficient variation (CV %), for all the concentrations tested in triplicate, was 14%. The CV% among different crystals ($n = 6$) was 21%. This low reproducibility found for the affinity interaction between Tat and the aptamer can be probably related to the irreproducibility of the immobilization step.

In order to improve the reproducibility both for the immobilization of the receptor and for the interaction between the aptamer and Tat protein, the aptamer has been thermally treated before the immobilization. This treatment can unfold the aptamer RNA strand making the biotin label at the 5′ end available for the interaction with streptavidin on the crystal surface. Before the immobilization, the biotinylated aptamer was heated at 90 °C for 1 min to unfold the RNA strand and then cooled in ice for 10 min in order to block the RNA in its unfolded structure [72]. Six different crystals were modified with this treated aptamer and the frequency shift due to the immobilization step was recorded. An average value ($n = 6$) of 63 ± 10 Hz was obtained, confirming the efficacy of the thermal treatment on the aptamer in significantly improving the reproducibility of this step (CV% = 16).

The interaction between the aptamer, immobilized after the thermal treatment, and Tat has been studied and the calibration signals are reported in Fig. 12 in comparison with the ones related to a crystal modified with the untreated aptamer. A better reproducibility (CV% = 6) for the interaction between the treated aptamer and Tat was obtained (each concentration tested in triplicate) on one crystal. The reproducibility was also improved (CV% = 8) among different crystals ($n = 6$).

The selectivity of the sensor was further studied testing Rev protein (regulator of expression of viral proteins), which can be considered to be the

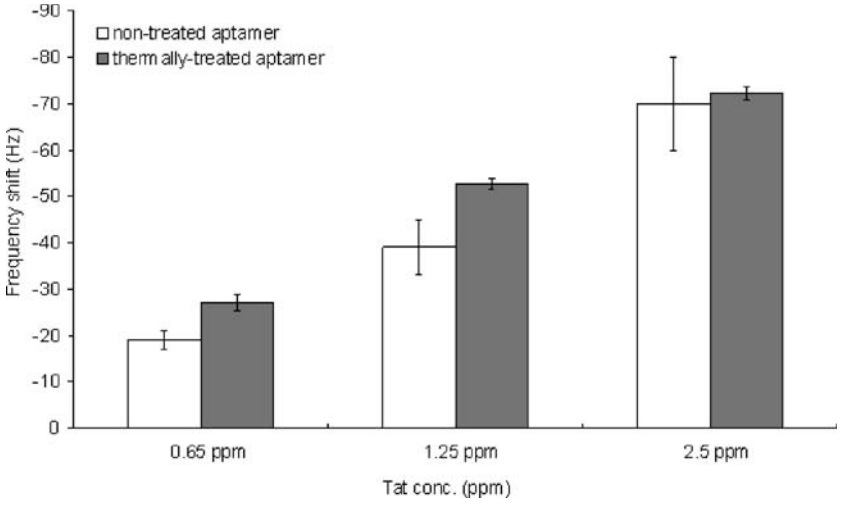

Fig. 12 Frequency shifts recorded after the interaction of Tat at different concentrations and the aptamer immobilized after the thermal treatment (*grey*) or without it (*white*)

major interfering protein for the system, and human IgG, which has a higher molecular weight than Tat. Two different concentrations of Rev protein, 0.65 and 2.5 ppm, were tested. The signals recorded were 5 ± 1 and 12 ± 1 Hz, respectively. On the same crystal, measurements were performed with hIgG 0.65 ppm and 1.25 ppm, obtaining signals of 5 ± 1 and 6 ± 1 Hz. These experiments confirmed the selectivity of the aptamer versus Tat protein.

The immunosensor for Tat protein was realized with the specific monoclonal antibody anti-Tat, immobilized on the sensor following the same procedure used for the aptamer. The same concentrations of Tat used for the aptasensor were tested.

The two receptors, aptamer and antibody, have been compared considering the response to different concentration of Tat; the results are reported in Fig. 13.

Both receptors detected Tat protein at a minimum concentration of 0.25 ppm, and the frequency shifts at this concentration were 13 ± 1 and 8 ± 1 Hz for the aptamer and the antibody, respectively. The reproducibility of the two sensors is comparable (CV% 6%). Injections of several negative controls at different concentrations generated no signal in either case.

Comparison of the developed aptasensor with other Tat detection methods is very difficult since most of the published papers on this subject deal with Tat-derived peptides and not with the full length protein. Anyway, the results demonstrated that the use of a biosensor with a specific aptamer as biorecognition element could be an interesting approach in the detection of proteins, which has been examined here considering a model system.

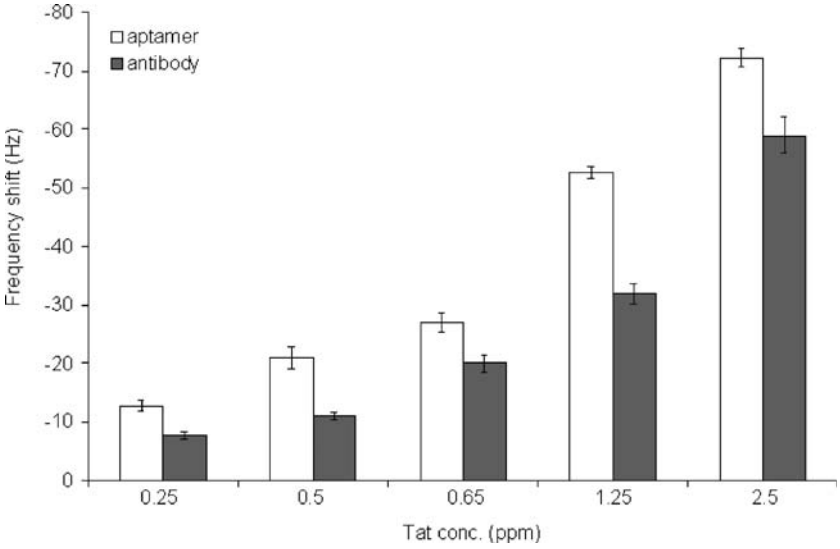

Fig. 13 Comparison between the interaction of Tat at different concentrations with the immobilized aptamer or antibody

5 Conclusions

Piezoelectric sensing can be successfully applied for nucleic acid sequence detection using the hybridization reaction. The range of applications is wide, and the given examples show how it is possible to detect a sequence in different kind of samples. The basis of the analytical application of the system is the integrity of the target molecule, which is very important in the amplification step. If the nucleic acid is degraded, there is a serious possibility of having false negative results. For this, also in the case of piezoelectric sensing based on nucleic acids, the considerations for other bioanalytical approaches making use of DNA analysis (PCR coupled to electrophoretical detection, real-time PCR, etc.) are valid.

Sample pretreatment is a very critical step, on which depends the success of the analysis. In this chapter, by the use of different examples, it was shown how this step should be carefully considered when dealing with sensing based on the hybridization reaction. The possibility of detection of so many different target sequences in many complex matrices (such as bacterial, plant, and animal DNA) with good reproducibility, high sensitivity, and short analysis time shows the robustness of piezoelectric sensing. Moreover, the possibility of detecting target sequences directly in non-amplified genomic DNA represents a significant improvement in the potential of this system. More work is

in progress to extend this detection to different biological systems with target genes present in single copies in genomic DNA.

The advent of new receptors based on nucleic acids, called aptamers, is a new challenge in piezoelectric sensing, not based on the hybridization reaction. The development of aptasensors has analogies to the introduction of immunosensing almost two decades ago: the direct detection of analytes in complex matrices by immobilizing an optimized receptor on the sensing surface.

An example for the HIV protein was reported together with the relative immunosensor. The advantage, in this case, is that the receptor is selected in vitro, avoiding the use of animals, and in short times.

The expectations are great for aptasensing and are supported by the constant increase of new aptamers, with a wide specificity spectrum, appearing in literature.

References

1. Fawcett NC, Evans JA, Chien LC, Flowers N (1988) Anal Lett 21:1099
2. Mannelli I, Minunni M, Tombelli S, Mascini M (2003) Biosens Bioelectron 18:129
3. Skládal P, dos Santos Riccardi C, Yamanaka H, da Costa PI (2004) J Virol Methods 117:145
4. Mo X, Zhou Y, Lei H, Deng L (2002) Enzyme Microb Technol 30:583
5. Zhou X, Liu L, Hu M, Wang L, Hu J (2002) J Pharmaceu Biomed Anal 27:341
6. Tombelli S, Minunni M, Santucci A, Spiriti MM, Mascini M (2006) Talanta 68:806
7. Tombelli S, Mascini M, Sacco C, Turner APF (2000) Anal Chim Acta 418:1
8. Tombelli S, Minunni M, Mascini M (2005) Method 37:48
9. Minunni M, Tombelli S, Gullotto A, Luzi E, Mascini M (2004) Biosens Bioelectron 20:1149
10. Minunni M, Tombelli S, Mascini M, Bilia AR, Bergonzi MC, Vincieri FF (2005) Talanta 65:578
11. Luzi E, Minunni M, Tombelli S, Mascini M (2003) Trends Anal Chem 22:810
12. Ahmed F (ed) (2004) Testing of genetically modified organisms in food. Haworth, Binghampon New York
13. Lipp M, Bluth A, Eyquem F, Kruse L, Schimmel H, Van den Eede G, Anklam E (2001) Eur Food Res Technol 212:497
14. Miraglia M, Berdal KG, Brera C, Corbisier P, Holst-Jensen A, Kok EJ, Marvin HJP, Schimmel H, Rentsch J, van Rie JPPF, Zagon J (1994) Food Chem Toxicol 42:1157
15. Van Hoef AM, Kok EJ, Bouw E, Kuiper HA, Keijer J (1999) Food Addit Contam 15:767
16. Studer E, Dahinden I, Luthy J, Hubner P (1997) Mitt Gebiete Lebensm Hyg 88:515
17. Meyer R (1999) Food Control 10:391
18. Lofas S, Johnsson B, Edstrom A, Hansson A, Lindquist G, Hillgren R-MM, Stigh L (1995) Biosens Bioelectron 10:813
19. Tombelli S, Mascini M, Turner APF (2002) Biosens Bioelectron 17:929
20. Mariotti E, Minunni M, Mascini M (2002) Anal Chim Acta 453:165
21. Giakoumaki E, Minunni M, Tombelli S, Tothill IE, Mascini M, Bogani P, Buiatti M (2003) Biosens Bioelectron 19:337

22. Wang R, Minunni M, Tombelli S, Mascini M (2004) Biosens Bioelectron 20:598
23. Minunni M, Mannelli I, Spiriti MM, Tombelli S, Mascini M (2004) Anal Chim Acta 526:19
24. Minunni M, Tombelli S, Fonti J, Spiriti MM, Mascini M, Bogani P, Buiatti M (2005) J Am Chem Soc 127:7966
25. Anklam E (1999) Anal Chim Acta 393:177
26. Gachet E, Martin GG, Vigneau F, Meyer G (1999) Trends Food Sci Technol 9:380
27. Van Duijn J, Van Biert R, Bleeker-Marcelis H, Peppelman H, Hensing M (1999) Food Control 10:375
28. Vollenhofer S, Burg K, Schmidt J, Kroath H (1999) J Agric Food Chem 47:5038
29. Erickson BE (2000) Anal Chem 472:454A
30. Berdal KG, Holst-Jensen A (2001) Eur Food Res Technol 213:432
31. Pietsch K, Waiblinger HU, Brodmann P, Wurz A (1997) Deutsche Lebensmittel-Rundschau 93:35
32. Studer E, Rhyner C, Luetry J, Hubner P (1998) Lebensm Z Unters Forsch A 207:207
33. Feriotto G, Borgatti M, Mischiati C, Bianchi N, Gambari R (2002) J Agric Food Chem 50:955
34. Lucarelli F, Marrazza G, Mascini M (2005) Biosens Bioelectron 20:2001
35. Martineau F, Picard FJ, Roy PH, Ouellette M, Bergeron MG (1998) J Clin Microbiol 36:618
36. Fidalgo S, Vasquez F, Mendoza MC, Perez F, Mendez FJ (1990) Rev Infect Dis 12:520
37. Roberts FJ, Geere IW, Coldman A (1991) Rev Infect Dis 13:34
38. Ghuysen J-M (1977) Int J Antimicrob Agents 8:45
39. Lim D, Strynadka NCJ (2002) Nat Struct Biol 9:870
40. Niemeyer DM, Pucci MJ, Thanassi JA, Sharma VK, Archer GL (1996) J Bacteriol 178:5464
41. Maslow JN, Mulligan ME, Arbeit RD (1993) Clin Infect Dis 17:153
42. Tenover FC, Arbeit RD, Goering RV (1997) Infect Control Hosp Epidemiol 18:426
43. Kreiswirth B, Kornblum J, Arbeit RD, Eisner W, Maslow JN, McGeer A (1993) Science 259:227
44. Jenison R, Haeberli A, Yang S, Polisky B, Ostroff R (2000) Clin Chem 46:1501
45. Fukuba T, Yamamoto T, Naganuma T, Fujii T (2004) Chem Eng J 101:151
46. Obeid PJ, Christopoulos TK, Crabtree HJ, Backhouse CJ (2003) Anal Chem 75:288
47. Wang J (2000) Nucleic Acids Res 28:3011
48. Almadidy A, Watterson J, Piunno PAE, Raha S, Foulds IV, Horgen PA, Castle A, Krull U (2002) Anal Chim Acta 461:37
49. Goodrich TT, Lee HJ, Corn RM (2004) J Am Chem Soc 126:4086
50. Patolsky F, Lichtenstein A, Kotler M, Willner I (2001) Angew Chem Int 40:2261
51. Towery RB, Fawcett NC, Zhang P, Evans JA (2001) Biosens Bioelectron 16:1
52. Jayasena S (1999) Clin Chem 45:1628
53. Clark SL, Remcho VT (2002) Electrophoresis 23:1335
54. You KM, Lee SH, Im A, Lee SB (2003) Biotechnol Bioprocess Eng 8:64
55. Ellington AD, Szostak JW (1992) Nature 355:850
56. Tuerk C, Gold L (1990) Science 249:505
57. O'Sullivan CK (2002) Anal Bioanal Chem 372:44
58. Stojanovic MN, Landry DW (2002) J Am Chem Soc 124:9678
59. Liss M, Petersen B, Wolf H, Prohaska E (2002) Anal Chem 74:4488
60. Groneowld TMA, Glass S, Quandt E, Famulok M (2005) Biosens Bioelectron 20:2044
61. Schlensog MD, Gronewold TMA, Tewes M, Famulok M, Quandt E (2004) Sensor Actuator B 101:308

62. Tombelli S, Minunni M, Luzi E, Mascini M (2005) Bioelectrochemistry 67:135
63. Kawakami J, Hirofumi I, Yukie Y, Sugimoto N (2000) J Inorg Biochem 82:197
64. Gebhardt K, Shokraei A, Babaie E, Lindqvist BH (2000) Biochemistry 39:7255
65. Fukusaki E, Hasanuma T, Kijiyama S, Okazawa A, Itoh TJ, Kobayashi A (2001) Bioorg Med Chem Lett 11:2927
66. Rhodes A, Smithers N, Chapman T, Parsons S, Rees S (2001) FEBS Lett 506:85
67. Lisdat F, Utepbergenov D, Haseloff RF, Blasig IE, Stocklein W, Scheller FW, Brigelius-Flohe R (2001) Anal Chem 73:957
68. Chang HC, Samaniego F, Nair BC, Buonaguro L, Ensoli B (1997) AIDS 11:1421
69. Mucha P, Szyk A, Rekowski P, Barciszewski J (2002) J Chromatogr A 968:211
70. Yamamoto R, Katahira M, Nishikawa S, Baba T, Taira K, Kumar PKR (2000) Genes Cells 5:371
71. Yamamoto R, Baba T, Kumar PK (2000) Genes Cells 5:389
72. Ducongè, Di Primo C, Toulmè JJ (2000) J Biol Chem 275:21287

Springer Ser Chem Sens Biosens (2007) 5: 237–280
DOI 10.1007/5346_029

Published online: 16 September 2006

Piezoelectric Immunosensors

Robert D. Vaughan · George G. Guilbault (✉)

Laboratory of Sensor Development, Department of Chemistry,
National University of Ireland, Cork, Ireland
g.guilbault@ucc.ie

Abstract This chapter reviews the basic theory and applications of piezoelectric immunosensors. The immunosensor assay formats most often used are introduced as well as a brief explanation of the typical methods of measurement. Immobilisation is discussed, the importance of each characteristic, the basic techniques employed and a comparison of their performance as investigated by many researchers. The main historical developments of piezoelectric sensors and how these have led to early piezoelectric immunosensors are reviewed. Immunosensor applications and a comparison of sensor performance, for various analytes are summarised. The potential future of this field is also discussed.

Keywords Piezoelectric · Immunosensors · Immobilisation

1
General Introduction

1.1
Piezoelectric Immunosensors

Immunosensors are a class of biosensors that exploit the antibody–antigen interaction. They are generally more specific and sensitive than other biosensors because of the highly specific molecular recognition and affinity between an antibody and its antigen. Affinity constants are usually of the order of $10^8\ M^{-1}$ and can be as high as $10^{15}\ M^{-1}$, this being significantly higher than for other biomolecules such as enzymes, which have typical affinity constants of $10^6\ M^{-1}$. The specificity of this immuno-interaction combined with the very sensitive nature of piezoelectric (Pz) transducers makes a very powerful basis for sensor development.

Since a Pz transducer is basically a mass balance, it can be used to directly detect an immunoreaction by mass alone. This eliminates the need for labelling or the use of a secondary antibody to generate a response, as required by most other immunosensor formats.

Bulk acoustic wave (BAW) or surface acoustic wave (SAW) Pz devices are incorporated for immunosensor development. SAW devices consist of two interdigitated electrodes placed a few millimetres apart on the surface of a Pz slab. When an alternating current is passed a standing surface wave is set up on the Pz material. Addition of mass to the surface causes a change in the wave velocity and thus can be monitored by the frequency change. The quartz crystals generally incorporated are ST-cut (– 49°00′) operating between 30 and 200 MHz. Theoretically SAW devices are more sensitive than BAW devices since they oscillate at much higher frequencies. But, in comparison, they are rarely employed in immunosensor development, since they suffer from a lot of practical operational problems. BAW devices generally consist of an AT-cut (+ 35°15′) piezoelectric crystal disks, with a gold or silver electrode on each side, that typically vibrate fundamental frequencies of 5–20 MHz. This frequency will change if the surface mass of the crystal is altered. A reduction in frequency will occur if the mass is increased. For immunosensor development, crystals with a fundamental frequency of 10 MHz are most often used. Higher frequency crystals are more sensitive but can have robustness issues in solution, particularly when heavily loaded, whereas lower frequency crystals are less sensitive but less effected by liquid damping or heavy mass loading. The choice of crystal depends on its exact application and is often a compromise between sensitivity, robustness and availability.

1.2 Assay Formats

1.2.1 Capture

Direct capture assays are the most common format used in piezoelectric immunosensors. Primarily, because its simplistic format exploits the label-free advantages of piezoelectric transducers.

This format involves modification of the gold surface with an appropriate immobilisation layer followed by attachment of the specific antibody. This antibody-coated crystal can be exposed to a solution containing the analyte, which will bind specifically to the surface and cause a frequency change. In most cases, the frequency change is proportional to the mass added and thus the concentration of the analyte. A diagrammatic representation of a capture is seen in Fig. 1.

Indirect captures can also be used, but generally as a method to detect the specific antibody concentration. In this case the antigen is immobilised and used to capture the specific antibody from the solution.

Pre-coated crystals can be placed in a solution and give a direct result of the concentration of the specific analyte in a matter of minutes without any need for extra assay steps or washings. This approach is particularly useful for those developing portable sensors with a view to field analysis. Pre-prepared coated crystals can be used with a portable instrument for direct analysis in minutes without the need for a skilled operator.

The only downfall of this format is the fact that the sensitivity of the assay is heavily dependent on the mass of the analyte. Thus the analysis of light analytes such as drugs, hormones and toxins may require a different approach.

1.2.2 Displacement

The displacement assay format is often used if the analyte does not have adequate mass to cause significant frequency changes, by exploiting the large mass of the antibody. The crystal is modified with an appropriate immobilisation layer followed by attachment of the antigen. The antibody is then added, which specifically binds to the immobilised antigen. The prepared crystal is exposed to a solution containing the antigen. The immobilised antibody will have a higher affinity for the free antigen in solution and will be displaced from the immobilised antigen, thus causing a frequency increase as the mass of the crystal is reduced due to loss of the immobilised antibody. The overall change in mass will be proportional to the concentration of the free analyte in solution. Since the antibody, which has significant mass, causes the

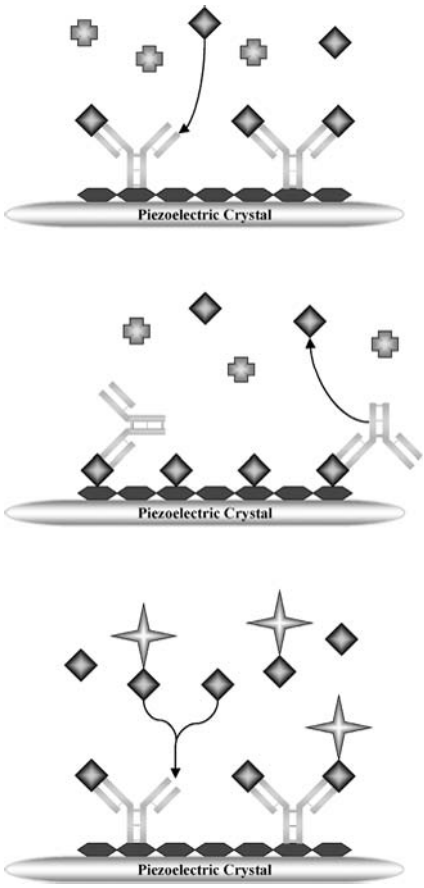

Fig. 1 A typical direct capture (*above*). The immobilised antibody captures the specific analyte from the solution, which results in a decrease in frequency. A typical displacement (*centre*). The immobilised antibody is displaced from the surface and specifically binds to the free antigen in solution resulting in a frequency increase. A typical direct competition (*below*). Free antigen and labelled antigen in solution compete for the available binding sites on the immobilised antibodies: immobilisation layer, non-specific antigen, antibody, antigen, labelled antigen

frequency change, a good sensitivity is often achieved even for very low molecular weight analytes. This assay format generally has fewer problems due to non-specific binding effects since removal from the surface is what is being measured. Thus, applications to real samples are less hindered by matrix effects.

As with the capture, prepared crystals can be applied to a real sample and give results in a few moments without the need for extra assay steps or washings. A diagrammatic representation of a displacement is seen in Fig. 1.

1.2.3 Competition

Another assay format used for the detection of low molecular weight analytes is the competition. A disadvantage of this method is the fact that there is often a need for the use of labels, the lack of which is one of the major advantages of Pz detection. But since the analyte being tested is light, conjugates would have been already prepared in the production of antibodies to make it immunogenic. Thus a ready supply is generally available. Also since the type of conjugate label used is irrelevant as long as it has sufficient mass, they can be easily prepared.

In a competitive assay the crystal is prepared as it would for a direct capture. The antibody-coated crystal is exposed to a solution containing the analyte and a fixed concentration of conjugated analyte. The conjugated analyte has sufficient mass to produce a significant frequency change upon specific binding to the immobilised antibodies. As the concentration of the free analyte is increased it will compete more with the conjugated analyte for the specific binding sites of the immobilised antibodies, thus a lower frequency change will be observed. The overall mass binding to the surface will be less. Since the conjugate label used is irrelevant, heavier ones can be incorporated to enhance the sensitivity of the assay. The major disadvantage for real sample analysis lies in the fact that a mixing step (the antigen and labelled antigen) has to be incorporated. Thus the assay will take longer to perform and potentially involves exposure to harmful analytes.

Competition assays can also be performed by immobilisation of the analyte to the crystal surface. A fixed concentration of the specific antibody is pre-incubated with the free analyte in a test solution, and this solution added to the crystal. Any free antibody will specifically bind to the immobilised analyte on the crystal surface. The lower the concentration of analyte in the test solution the more antibody will bind to the surface and thus a larger frequency change will be observed. This format eliminates the need for a label (but the immobilised analyte is often a conjugate) but involves an extra incubation step. A diagrammatic representation of a capture is seen in Fig. 1.

1.3 Measurement

Pz immunosensor analysis is mainly carried out in liquid phase. Measurements can be taken in two different ways, dip and dry or directly in solution.

Dip and dry involves reading the crystal's frequency while dry in the air. It is exposed to a sample or modified in some way. After sufficient time, in which binding or immobilisation of a species is complete, the crystal is washed and dried. The frequency is recorded again in a dry state in the air. The change in frequency, from before and after modification, is propor-

tional to the mass of the species immobilised on the surface. The dip and dry method can be very useful since both sides of the crystal can be used, with increased mass change and thus increased sensitivity. Also, solution effects due to viscosity etc. are eliminated. It is also very attractive to field analysis as the crystal can literally be dipped into the sample for a period of time, after a quick rinsing and drying step instant results can be obtained. The sensitivity of the method is part of its downfall, since it can be plagued by interferences form environmental effects, especially humidity changes. Repeatability and reproducibility are often the biggest validation obstacles to the development of dip and dry type sensors. The use of a reference crystal is often used to counteract these environmental effects.

Measurements taken directly in solution are less affected by changing environmental conditions and much more reproducible and repeatable results are generally obtained. Damping effects due to the liquid, however, can reduce the sensitivity of the sensor. Also the behaviour of a crystal in solution may not be due directly to the effect of mass on the surface. The frequency response of a layered crystal in solution is dependent on many factors, such as the viscosity and temperature of the liquid, and the thickness and rigidity of the immobilised layers.

Analysis is generally carried out in specifically designed flow cells (Fig. 2) and frequency changes can be recorded in real time yielding kinetic informa-

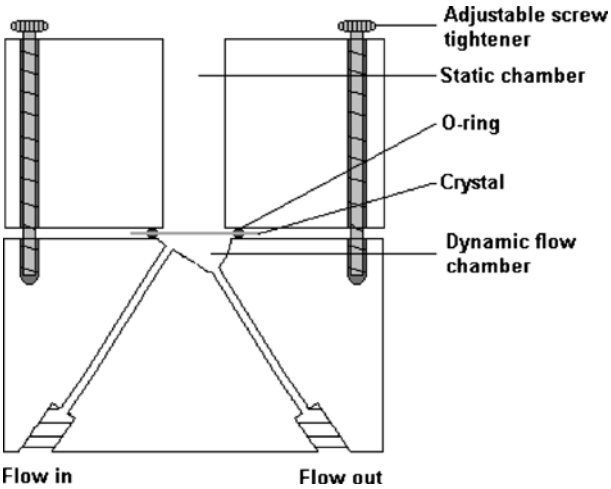

Fig. 2 Diagram of a typical flow cell used for solution analysis. The cell allows exposure of one side of the crystal to a static solution and allows exposure of the other side to a dynamic solution. The dynamic side of the flow cell typically has a specially designed chamber to help eliminate bubbles. Low pressure peristaltic pumps are generally incorporated. The flowing solution can greatly increase sensitivity since large volumes of dilute solutions can be passed over the crystal surface

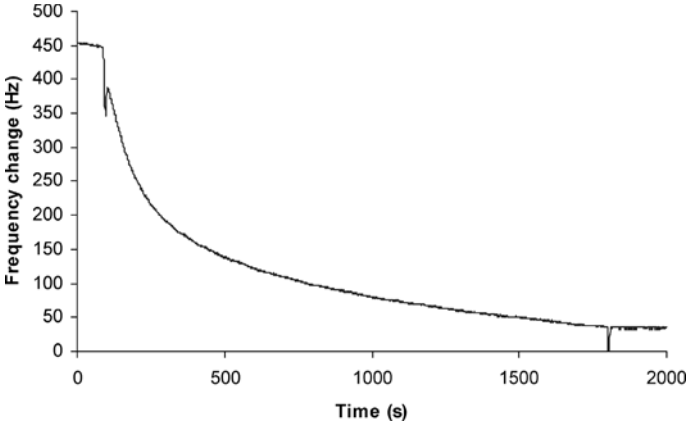

Fig. 3 Real-time Pz response of a direct capture. The antibody-coated crystal is in solution. After 100 s the specific antigen is added. A sharp decrease is initially recorded as the antigen binds to the immobilised specific antibodies on the crystal surface due to the mass increase. The frequency change eventually levels off as equilibrium at the surface is reached. The total frequency change is proportional to the concentration of the analyte added

tion if required. The flow cells allow exposure of gold surface on one side of the crystal to the solution and the other to the air. Analysis can be performed in a static or dynamic solution. Figure 3 shows the typical real time response of an antigen specifically binding to an antibody-coated crystal in solution.

Using a flowing solution can greatly increase the sensitivity of a sensor since very large sample volumes can be flowed over the crystal surface, greatly increasing the potential surface loading and thus the sensitivity of the sensor.

1.4 Immobilisation

1.4.1 Introduction to Immobilisation

Immobilisation of the antibody to the crystal surface is of critical importance to the overall performance of the sensor. Stability, orientation and reproducibility of the immobilised layer will affect the sensitivity, lifetime, reusability and potential applications of the sensor.

The type of immobilisation dictates the ability to regenerate the sensor surface, or the antibody surface, for reuse as well as the stability and storage conditions needed to extend the lifetime of the sensor. The importance of immobilisation is reflected in the fact that a significant percentage of Pz immunosensor publications deal with the development of novel or the improvement of existing immobilisation methods.

Biomolecular immobilisation remains the primary challenge to commercialisation of immunosensors. Many successful sensors have been produced for numerous analytes, incorporating many different immobilisation methods, but most never make it past a laboratory, with very few ever making it to manufacturing prototypes. The transfer of a laboratory-based sensor to a mass-produced product while still retaining stability, reliability and sensitivity requires simple and reproducible procedures. Complex multistep immobilisation procedures that require a trained operator to perform in a laboratory will not be easy to transfer to a manufacturing situation and would probably result in a poor quality product when compared to its laboratory-based prototype.

Stability. A stable coated surface with a long lifetime is essential. The immobilised protein layer must also have a reasonable lifetime. The surface should be chemically and mechanically stable and allow washings and exposure to different conditions without any detrimental effect on the protein layer. If commercialisation is desired then very robust layers are required and must be reasonably stable under simple storage conditions for at least one year.

Orientation. The orientation of the immobilised antibody is also very important to the sensitivity of the sensor. A large concentration of immobilised antibodies does not guarantee good sensitivity. If the immobilised antibodies are randomly orientated then a significant percentage of them may be unavailable for binding. If they are regularly immobilised, but through one or both of their Fab sites then they will be partially or completely deactivated. The most desirable immobilisation methods are those that bind to the antibodies Fc sites, thus orientating their binding sites towards the analyte in solution. This has been observed by many researchers while comparing different immobilisation procedures. Protein A treated surfaces, which bind antibodies through their Fc sites, may immobilise a significantly smaller amount of antibodies but show a much greater sensitivity towards the analyte. Coupling the antibody to the immobilisation layer should occur in such a manner so as not to cause conformational changes and affect its biological activity.

Reproducibility and capacity. An important requirement is to reproducibly produce an immobilisation layer on different crystals. Even if similar crystals can be produced in a batch, this batch production must be reproducible. Obviously, if each immobilisation layer is slightly different then each crystal will have a slightly different sensitivity and lead to errors. Generally the most simplistic methods that require minimal amount of human interference are the easiest to reproduce. The homogeneity or distribution of the coating on the surface is also very important due to the greater sensitivity of the centre of the gold electrode. The most sensitive crystals will be one that can bind most to its centre. A crystal that binds the same amount to the edges of its electrodes will be less sensitive and show a lower frequency change. Thus the distribution of the coating must also be reproducible, not just the amount.

The amount of immobilised antibody is also a very important factor that can affect the sensitivity of the sensor. It must have the potential to bind a sufficient amount of the antibody. Although this is usually not a problem, since it is often found that excess immobilised antibody can lead to a reduction in sensitivity due to steric hindrance.

Simplicity. If commercialisation is to be realised then the method must be mass producible and very simplistic. Multistep immobilisation procedures that may be easy to perform reproducibly in a laboratory-based situation may be very difficult to perform in a manufacturing situation. Generally, one step procedures that can be reproducibly carried out under ambient conditions by untrained workers are desirable. A method such as adsorption that may lead to reduced sensitivity may still be more viable when compared to a very complex method that leads to a more sensitive product. Reduced production costs will generally win out over performance if the performance difference is not too significant.

Importance of each characteristic. Overall, the importance of each characteristic depends on the application and specific situation. For research purposes generally the best sensitivity is required, often regardless of the complexity of the technique, but if the sensitivity is far superior to that required for a specific application then less complex procedures are often employed at the loss of performance. For commercialisation purposes stability and simplicity are the main objectives. An ultra-sensitive device that needs a highly trained operator and only lasts a number of days has very little, if any, commercial application.

1.4.2 Summary of Immobilisation Techniques

Non-covalent methods. The easiest method of antibody immobilisation is physical adsorption. It involves the simple addition of the antibody solution to the surface and allowing it to adsorb. The antibodies bind to the surface via van der Waals, hydrogen bonding and hydrophobic interactions. Thiol–gold interactions from sulfur residues on the antibodies also play a major role. This method has no effect on the conformation of the protein but some activity is lost due to random orientation. Loss of protein from the surface is also a problem and its rate can depend greatly on changes in pH and temperature. Thus chaotroping and reuse of the antibody surface is not possible, since it is difficult to reproducibly generate the antibody surface. However, reuse of the sensor surface is possible since all the protein layers can be easily removed.

Adsorption onto polymer-coated surfaces has also been attempted [1]. Polystyrene was used, presumably to mimic the binding capabilities of enzyme linked immunosorbant assay (ELISA). While the method showed good binding of the antibodies the sensor had a low sensitivity to cells. This was

due to random orientation of the immobilised antibodies, leading to deactivation of a high percentage of them due to binding via their Fab sites. The main advantages of polystyrene are the fact that it is inert, very cheap and widely available, but problems due to its hydrophobic nature can also yield poor results. When used in the production of ELISA plates the well surfaces are often pre-treated to produce hydrophobic and hydrophilic areas to enhance the adsorption of proteins. But this pre-treatment is not feasible for the production of individually coated Pz crystals. Sakti et al. [2] used crystals spin coated with polystyrene with a view to developing commercial Pz immunosensors. Various parameters were optimised and the authors showed that pre-prepared coated crystals as a basis for disposable immunosensors were commercially feasible. Insulin detection was used as an example to demonstrate an application of the system. Mass production of these types of crystals is possible with good reproducibility, but the loss in activity due to the random orientation of adsorbed antibodies is a major disadvantage.

Immobilisation of the antibody via adsorbed protein coatings is also widely used. Protein A and G are generally used. They are proteins isolated from the cell walls of certain pathogenic bacteria and show high affinities, in excess of 10^6 M^{-1}, for the Fc portions IgG molecules [3]. Their tertiary structures are very similar but there is significant difference in their amino acid composition and both have a mass of about 40 000 kDa. The specificity of the binding helps to reduce non-specific effects and binding through the Fc terminal ensures orientated immobilisation with no loss of antibody activity. It has been reported that each protein molecule can bind two IgG molecules [4]; however, others have suggested that they are pentavalent towards IgG binding [5]. Much lower values have been reported in Pz immunosensor work. Ratios of protein molecules to bound IgG molecules of around 1 : 2 [6] and 2 : 1 [7] have been reported. These lower values are probably due to steric hindrance and saturation of the crystal surface with protein molecules. Also a loss in activity is expected because of immobilisation and the formation of multi-layers that will inhibit some of the molecules.

The ease of use of these proteins is another advantage. They are simply adsorbed onto the gold surface of crystals and after a simple washing step are ready for use. The gold–protein bond has an association constant of 10^8 M^{-1} and is believed to be van der Waals in nature [6]. The gold–protein complex has been shown to be stable at pH 2–8 [7]. Enhanced binding of protein A has also been reported near its isoelectric point (pH 5.5) [8], but it is unclear from the author's work if this was just due to longer incubation times.

Regeneration and lifetime of antibody-coated crystals formed using these proteins varies considerably, but reports of 25 regenerations without loss in activity and lifetimes of 7 weeks have appeared [9]. Most authors have reported significant removal of the protein layers after a few regenerations of the antibody surface, however.

Their ease of use and the high sensitivity usually obtained means that these are the most common immobilisation method used in Pz immunosensor work, with protein A most often used.

Incorporation of other biological components such as biotin–avidin coupling has also been used. The system has an affinity constant of 10^{-15} M and is resistant to extreme pH, vigorous washings and chaotroping conditions. Generally they are used in conjunction with other immobilisation methods.

Covalent methods. Covalent attachment offers many advantages over adsorption but has longer and more complex immobilisation procedures. Better stability and extended lifetimes of the antibody surface are often observed. There is minimal or no loss of the antibody surface, even in solutions of high ionic strength. This allows easier chaotroping of the antibody/antigen complex and reproducible regeneration of the antibody surface, since generally none of the antibody is lost.

With commercialisation in mind, immobilisation methods need to be easily mass produced, cost effective and be able to form a stable biomolecule surface. Most covalent methods satisfy these requirements but their main downfall is the sometimes complex procedure. But despite this they are much more useful than the simple adsorption methods and it is ultimately the stability of the antibody-coated surface that will dictate the commercial potential of any sensor. A lifetime of several months is the absolute minimal requirement and such a stable sensor would have greater commercial appeal than a more sensitive reliable version with a short shelf life.

Generally, immobilisation is attempted through functional groups so as not to affect the activity of the antibodies. Functionalisation of the gold surface is easily achieved through the self-assembly of thiols or sulfides, the formation of organic polymer layers or the formation of thin inorganic layers. The covalent binding generally involves carbonyl-type reactions with nucleophilic groups (– SH, – NH, and – OH) on the protein to the functionalised surface layer.

The first Pz immunosensor to be used directly in solution incorporated an inorganic silane layer for immobilisation [10]. Incorporating results from chromatographic studies, which at the time had recently shown the high reactivity of silane-modified surfaces for proteins, the authors coated their ST-cut crystals with trimethoxyorganosilane.

Silanisation has many advantages over the use of organic polymers due to its high mechanical strength, resistant to solvents, stability, ease of handling and the fact that the structure is more or less constant at varying pH and temperature.

The most commonly used silane-coupling agent is 3-aminopropyltriethoxysilane (APTES). Treatment of the gold surface with chromic acid or HCl generates a hydroxylated surface. Water catalyses the polymer formation since it hydrolyses APTES ethoxy groups, creating a siloxane bond between APTES and the hydroxyl groups on the surface. Mild curing of the surface is

generally performed to ensure bonding of the first few layers of APTES and subsequent washings remove the other weakly bound layers. This curing has been shown to enhance the stability of the silane surface [11]. Coupling of the antibody to this silanised surface is generally performed using glutaraldehyde, which covalently cross-links the protein to the silanised gold surface. Increased sensitivity from the use of other aldehydes has been noted [12]. This was attributed to the fact that glutaraldehyde deteriorates very quickly to unsuitable polymeric products [13]. The method is based on the formation of a Schiffs base linkage between carbonyl groups and free amino groups on the silanised surface and protein.

An excellent study by Raman Suri et al. investigated various parameters and developed an optimised method for the use of APTES as an immobilisation method for Pz immunosensor development [12]. In terms of surface density, binding capacity and stability vapour deposited layers were most useful. Under optimised conditions the protein layers were reusable eight times, were very stable, withstood vigorous washing steps and have a lifetime of over 12 weeks. The system was also shown to be very reproducible, but problems in procedures such as the need for dry solvents and the pre-treatment of glassware were noted. APTES reacts strongly with glass, so laborious pretreatment of any glass to be used was required. The presence of water hydrolyses the APTES ethoxy groups and leads to catalysed polymerisation. This then electrostatically adsorbs to the surface instead of covalently binding, leading to a less stable layer that leaches with time.

There has been wide use of silane as Pz immobilisation layers, mainly because of their stability and the ability to produce reproducible surfaces. But because of the fact that the antibody is bound via a primary amine, deactivation from binding through Fab sites can be a problem. But for use in assays where the analyte is an antibody with an affinity for the immobilised species or when used to first immobilise protein A/G [12] they are acceptable, since deactivation of the primary antibody is not a problem.

Covalent immobilisation to organic polymer layers is also widely practised. The most commonly used polymer is polyethylenemine (PEI), but many others including polystyrene, polyacrylamide and various methacrylates have been incorporated. The main advantage of polymers is their versatility. They are easy to prepare, have a very large potential application and can be tailored for any use. Co-polymers, usually methacrylates, can be activated and modified easily to suite individual needs.

As with silane, immobilisation of the antibody is usually performed using glutaraldehyde and deactivation of the antibody is often a problem as a result, but the versatility of polymers means that various functionalised surfaces can be produced allowing antibody binding through other groups besides amines.

Practically, the production of polymer layers is very simple. Usually the polymer of choice is just dissolved in an appropriate solvent and evaporated onto the gold surface. Spin coating is also often used to increase the unifor-

mity and to improve the reproducibility of the formed layer. Stability of the layer is another advantage since most of the polymers used are relatively inert and can be stored for long periods without changes in the crystal surface coating occurring.

Reproducibility problems in the production of polymer layers as described above can sometimes occur. Since washing steps and drying procedures are often incorporated to remove loosely bound material, and changes in intensity or duration of these steps can result in different layers. Thus the amount of the immobilised protein will be different and reduce the reproducibility of the sensors response. The use of thick organic films produced by this method can also lead to frequency instability and loss of sensitivity. It is also difficult to control film thickness and homogeneity, which also effect the reproducibility of the surface produced. Weak adhesion between the polymer and the substrate can also be a problem. Methods, such as plasma polymerisation and electropolymerisation, have been developed to overcome these problems and to gain more control over the layer parameters.

The use of plasma polymerised layers for Pz immunosensor development was first described by Nakanishi et al. [14]. The method retained the many advantages of polymers but eliminated the need for washings. The procedure was automated so human error was eliminated and very reproducible flawless surfaces were made. The process produced very thin ($< 1\,\mu m$), highly branched and cross-linked structures that were mechanically and chemically stable. The plasma glow discharge treatment only took a minute to complete and numerous crystals could be prepared at a time. Then the crystals were ready for use. The direct cross-linking of antibodies to this surface showed good binding but poor sensitivity was observed, primarily due to deactivation of most of the immobilised antibodies. Cross-linking protein A initially to the surface followed by the antibodies ensured orientated immobilisation, and despite the lower amount that bound a much improved sensitivity of the sensor was observed. The authors also cross-linked the antibody to protein A using dimethyl pimelimidate dihydrochloride to avoid disassociation during the regeneration steps. While this was the first use of this technique in Pz immunosensor work, it had been previously used for Pz gas sensor development [15].

Monomers such as ethylenediamine are usually chosen since they lead to hydrophilic surfaces with plenty of amine groups. It has longer polymerisation rates when compared to many other possible monomers, but this allows easier control over the film thickness and increases reproducibility.

Problems of reproducibility between batches of polymerised films have been reported [16]. To avoid this, the authors developed a method of adsorbing their antibodies to the surface so that easy regeneration of the original plasma film was possible. But this led to many other potential problems in that the antibodies were randomly adsorbed and the antibody layer was not very stable. While a new surface was easily regenerated the usefulness is ques-

tionable. Generally the ability to regenerate the antibody surface is a much more desirable characteristic.

Electropolymerisation of layers again offers control over the growth and thickness of the film. Production of the layer is also quite simplistic. The gold surface is placed in a solution containing the polymer, which is electropolymerised onto the surface at the appropriate potential for the desired time. After this a very stable highly branched structure is formed on the surface that can be further modified to immobilise the antibodies. As with plasma polymerised methods many crystals can be easily prepared at a time.

Kurosawa et al. incorporated a method that eliminates the need for surface pre-treatment or immobilisation of any sort [17]. It was based on polymer agglutination of latex. A cleaned crystal was placed in a solution containing latex particles pre-labelled with antibodies. Addition of the specific analyte caused cross-linking of these particles as the antibodies bound to the analyte. This agglutination caused a change in viscosity of the solution, which in turn caused a change in the frequency of the oscillating crystal. The fact that polymer agglutination is used in many commercial test kits means that many antibody labelled latex particles for different analytes are commercially available. Also stability and lifetime of immobilised species is not a problem. The authors later incorporated initial rates analysis that allowed the detection of their analyte in 2–3 min and allowed the use of sample volumes as low as 20 μL [18]. It was shown that the latex particles in solution prevented adsorption of proteins to the crystal, thus eliminating non-specific effects. This approach to immunosensor development offers many advantages over the conventional methods of analysis and commercially is as viable as any method of pre-coated crystals.

Self-assembly. Self-assembled monolayers (SAMs) offer a method of orientated, covalent attachment of antibodies to the gold surface to form densely packed monolayers, which should lead to tightly bound, regular layers of proteins. This potentially has the advantage that exposure to a high or low pH, often used in regeneration, should lead to desorption of the electrostatically bound analyte. The covalently bound antibody should be unaffected, leading to the ideal reusable system [19]. They have the added advantage over other covalent methods, such as PEI and APTES, in that there is a high affinity between the gold and sulfur so loss of the layer over time is unlikely.

Various techniques have been used to study the kinetics and structures of SAMs [20]. Thiols and sulfides are of particular interest especially in the area of electrochemistry, mainly because of their spontaneous chemisorption, regular organisation and high thermal, mechanical and chemical stability on gold surfaces [21]. An additional advantage is the inertness of gold towards the chemisorption of most polar organic functionalities; thiols and sulfides bind very strongly via chemisorption bonds [22], thus offering a good method of functionalising gold surfaces. Monolayers of thiols on gold appear to be indefinitely stable at room temperature, but desorption at elevated

temperatures is evident [23]. Long chain thiols have been shown to be more thermally stable [23] and the adsorption to the surface has been shown to proceed by two methods [24], ionic dissociation and more favourably by radical formation.

The monolayers spontaneously and reproducibly form when the gold is placed in the thiol or sulfide solution. Lack of reproducibility may occur due to differences in the gold surface from crystal to crystal but this generally is not significant.

Due to the stability, orientation and ability to functionalise the terminal groups on the molecules they can offer a very versatile method for immobilisation of biomolecules to gold electrode surfaces for biosensor development [25, 26].

The functionality of the layer depends on the terminal functional groups on the molecule used. Generally compounds with carboxylic acid or amine functional groups are used and this allows covalent attachment of the antibody using a carbodiimide or glutaraldehyde, respectively. This results in a highly ordered layer with orientated covalent attachment of antibodies to the surface, without altering their biological activities [27]. While the immobilisation may not change the conformation the orientation of its binding may lead to deactivation of the antibody. The thin layers (monolayer) used ensure no loss of sensitivity or frequency instability, often observed when using thick organic polymer layers. The strength of the sulfur–gold bond and the covalent attachment of the antibody ensure reproducible regeneration of the antibody surface. Even exposure to harsh conditions should not affect the layer. Regeneration of the antibody surfaces using most methods of immobilisation is generally only possible a few times before a loss in activity is observed. Even if the antibody is covalently bound, weak adhesion between the layer and the substrate will lead to its loss from the surface.

Duan et al. used a monolayer of thioctic acid to covalently immobilise monoclonal antibodies to a gold electrode while performing amperometric analysis [28]. Frey et al. demonstrated potential biosensor application of this immobilisation method by binding polylysine to gold surface plasmon resonance (SPR) electrodes via a SAM of 11-mercaptoundecanoic acid [29].

The functionalisation of antibodies for the immobilisation onto Pz crystals has been performed by Caruso et al. [30] and Neuman et al. [31]. Both authors used similar procedures to those initially described by Leggett et al. [32]. The method introduced functionality to the protein, which had high affinity for the chosen substrate, gold scanning tunnelling microscopy (STM) electrodes in Leggetts' case and gold Pz crystals in Caruso and Neumans' case. The procedure involved the thiolisation of the antibodies using Trauts reagent (2-iminothiolane). The methods were based on the original work performed by Traut and coworkers [33–35]. They discovered that unlike most imidates, 2-aminothiolane was very stable in acidic or neutral solutions and did not cause any protein cross-linking, and thus was a very useful compound for

the thiolisation of proteins. The fact that the thiolisation occurs at an amine group means that deactivation of the antibody may occur if the Fab amino groups were thiolated. Also if all amino groups were thiolated then random orientation of the immobilised antibodies could potentially occur, although after self-assembly a regular surface is likely to have occurred. Caruso et al. also observed strange results while using the thiolated antibody solution after several days. This was attributed to the fact that the antibodies may have oxidised and formed disulfide bonds. If this was the case then polymerisation of the antibodies was a possibility and thus this method of immobilisation is only useful for antibodies that are used immediately.

Park et al. also described a method for the thiolisation of antibodies and self-assembled these onto gold electrodes [36].

Protein engineering to tag protein A molecules with cysteine residues and to self-assemble these onto gold surfaces has been performed [37]. This method would incorporate the simplicity, reproducibility and covalent advantages of self-assembly with the orientational advantages of protein immobilisation and potentially lead to the most useful immobilisation method. Cleaving of antibodies to break the disulfide bridges and self-assembling these portions onto electrodes has also been attempted by many authors.

As with most immobilisation methods that rely on antibody binding through amine groups, deactivation can be a problem. But Spangler and Tyler have described a method of covalent antibody attachment to a SAM without any loss of antibody activity [38]. It is based on the oxidation of the antibody prior to use and then binding of this to an activated monolayer on the gold surface. This type of approach was first suggested by Taylor [39]. This method was based on the oxidation of sugar residue in the Fc portion of the antibody. The oxidised antibodies could then be immobilised onto an activated transducer surface, resulting in orientated attachment without any loss in activity. This method had not been applied to any immunosensor when suggested by Taylor.

Other monolayer-forming techniques such as the use of Langmuir–Blodgett films to immobilise antibodies have been reported [40]. The method of formation of the layers is very simplistic but their practical applications are limited.

1.4.3
Comparison of Immobilisation Methods

All immobilisation methods have different advantages and disadvantages over others. Many authors have compared different methods with varying results.

Plomer et al. compared protein A, APTES and PEI as immobilisation layers while detecting *E. coli* [41]. Best results were obtained using protein A immobilisation but regeneration of the antibody surface was not possible. Atilla and

Seuluman observed similar results while detecting cortisol [42]. Better sensitivity was found using protein A-coated crystals but regeneration of the antibody surface was not possible. König and Grätzel also found crystals coated with protein A more stable, sensitive and reproducible than those coated with PEI or APTES for the detection of enterobacteria [9] and viruses [43, 44], and were able to regenerate the antibody surface 18 [43] and 10 [9] times without detectable loss in activity. Others have also found protein A most sensitive and were able to regenerate the surface numerous times without detectable loss in activity [45]. From these results the orientated immobilisation of protein A could explain the greater sensitivity of these sensors, but this cannot be generalised since many others have found different methods of immobilisation better than protein A. Carter et al. found better sensitivity from adsorption of antibodies [46]. One explanation for this could be the differences in procedures between different researchers but this is not the case. König and Grätzel have also found PEI a better choice than protein A on other occasions [47–49]. The authors found very similar results for PEI, APTES and protein A while detecting human granulocytes [47], but PEI showed better stability. They observed poor sensitivity and very large non-specific binding with protein A while detecting lymphocytes [48, 49]. Again PEI was the immobilisation method of choice.

Caruso et al. investigated the orientational aspects of different immobilisation procedures and its effect on immunological activity [30]. They compared four antibody immobilisation methods, physical adsorption, binding to a layer of protein A, covalent attachment using thiolated antibodies (Trauts reagent) and covalent attachment to a thiol monolayer. A 30% increase in binding of the initial antibody layer was observed for the physical adsorption when compared to the other methods, but due to the random orientation enhanced binding of the second layer was not observed. Increased amounts of second layer binding were observed with the protein A layer compared to the covalent methods, due to the orientation of the protein A binding. It was not possible to separate the contributions from improved antibody alignment and non-specific binding from investigations using site-specific secondary antibodies, however.

From these reports and many other investigations it seems the choice of immobilisation methods is dependent on the specific situation and cannot be predicted. The orientation of protein A-immobilised antibodies is far superior to most other methods and an improvement in sensitivity is often evident, but the formation of reproducible stable layers and the inability to regenerate the antibody surface is a problem. Despite the results reported, the protein layers are only adsorbed to the surface and will eventually leach from the surface.

The stability of the layers produced by other methods such as SAMs often makes them more useful. In this author's experience PEI and APTES generally have the best antibody binding capacity, but the loss in activity and difficulty

with reproducibility often leads to poorer detection characteristics than other methods. Of the covalent methods of immobilisation, SAMs are the easiest to form and are more reproducible than most, if not all, methods of immobilisation. They covalently attach the antibody to the surface and combined with the strong sulfur–gold bond lead to the formation of a very stable surface. In terms of simplicity, stability and reproducibility SAMs are the best choice of immobilisation, but the loss in activity of immobilised antibodies due to binding through their Fab sites can be a problem. In cases where the analyte is an antibody and the particular orientation of the primary layer is not important, then they are the obvious choice.

Combining immobilisation methods seems to be the best option, such as incorporating the stability and reproducibility of covalent methods such as SAMs with the orientated binding of protein A/G. The first example of this was in 1987 by Muramatsu et al. [4]. The authors cross-linked protein A to a layer of APTES, although it is unlikely that it was done to combine the advantages of both immobilisation methods since this was one of the earliest Pz immunosensors and more basic fundamental problems were being overcome at this stage.

The advantages of such an approach were highlighted by Nakanishi et al. [14]. Cross-linking of antibodies to an electropolymerised surface using glutaraldehyde caused a large frequency reduction, indicating immobilisation of the antibody. However, it showed little or no response when exposed to the antigen solution due to deactivation, presumably from binding through amine groups that inhibited the Fab sites. Cross-linking protein A to the layer first resulted in less antibody binding but showed a much better sensitivity to the antigen due to the orientated binding of the antibody by protein A. The authors also cross-linked the antibody to protein A to ensure further stability. This helped prevent loss of antibody during regeneration and washing steps.

These types of immobilisations combine the stability and reproducibility of covalent immobilisation with the orientational advantages of protein A/G coupling. Together they offer many advantages over each method individually, but they have longer and more complex procedures, and in some cases this may not be justified by the increase in sensitivity. Realistically the production of a SAM, activation and immobilisation of protein A/G followed by antibody immobilisation is not too difficult, and in a laboratory-based test the potential increase in sensitivity makes the procedure worthwhile. But for commercialisation and mass production the increase in sensitivity must be significant before the increase in preparation time and cost can be justified.

2
Piezoelectric Immunosensors

2.1
Historical Developments

2.1.1
First Piezoelectric Sensor

The first analytical use of Pz crystals with view to sensor or detector development was presented by King in 1963 [50], the basis of his commercialised moisture detector. In 1964 he published details of his sorption detector [51], although earlier Oberg and Ligensjo had used Pz crystals for the monitoring of film thickness [52].

Kings sorption detector could detect moisture to 0.1 ppm and hydrocarbons such as xylene to 1 ppm. The sensors consisted of Pz crystals coated with different coatings (of varying selectivities), and their interaction with different analytes were monitored. The coatings used were based on gas chromatography (GC) stationary phases. An uncoated crystal was also incorporated as a reference.

Being the first to realise the potential of this sensor type he predicted that many more similar sensors would be developed in the future. It is also quite probable that King was the first to investigate the use of Pz crystals as detectors in solution, since he mentions the impaired ability of crystals to vibrate when a solution was placed on the surface. He states the possible reason for this is the dissipation of energy from the vibrating crystal to the liquid.

In the following years many similar sensors were developed [53–57]. During this period many fundamental problems were solved and developments in instrumentation were made, many of which are still incorporated in today's Pz immunosensor design.

2.1.2
Piezoelectric Biosensors

The use of biological coatings, such as enzymes and antibodies, was a natural progression from the initial Pz sensor development.

The first reported gas phase biosensor was in fact an enzyme-based Pz sensor [58]. Crystals coated with formaldehyde dehydrogenase were used to linearly detect formaldehyde in air from 10 ppb to 100 ppm. A portable version of the sensor was also developed. The battery-operated instrument contained a digital readout and miniature sampling pump. Weighing just 3 lbs it was used in field for on site analysis.

2.1.3 Piezoelectric Immunosensors

The first Pz immunosensor was developed by Shons et al. in 1972 [59]. They incorporated a layer of Neybar C to immobilise bovine serum albumin (BSA) to the surface of a 9 MHz Pz crystal. They used this to detect BSA antibodies in a liquid sample. Their results in terms of sensitivity were comparable to the conventional antibody assay technique of passive agglutination. This method requires hours for an assay to be completed, but the Pz sensor only required minutes.

In 1980 Olivera and Silver disclosed details of a competitive microgravimetric-based Pz immunoassay that could be used for the determination of many analytes, even low molecular weight compounds [60]. They firstly immobilised the analyte on the surface of the crystal and measured the frequency. These crystals were then exposed to a solution containing the analyte and the antibody against the particular analyte. Any free antibody in solution would bind to the immobilised antigen on the crystal surface. Thus a reduction in frequency was observed, the magnitude of which was proportional to the concentration of free antibody in solution. When the amount of antibody was fixed, the amount of free antibody in solution was proportional to the amount of analyte in solution. Thus the overall frequency change was inversely proportional to the concentration of the analyte in solution. The system was applied for the detection of many analytes, including drugs, immunoglobulins, nucleic acids and polysaccharides.

In the same year, Rice also patented another Pz-based immunoassay [61]. The sandwich-based assay was used to determine the type of antibody subclass and the concentration of the antibody present. Crystals coated with the antigen were exposed to the antibody solution. A secondary antibody against the primary antibody was then added. The frequency change observed here is indicative of the amount and type of the primary antibody present. Later, Rice described a similar assay that was used to determine the amount of a particular class or species of antibody and also the amount of total immunocomplex present in the antibody layer [62]. The assay was also based on a sandwich format and proved useful for low molecular weight antigens.

Konash and Bastiaans were the first to demonstrate the use of a Pz sensor in liquid phase [63]. They used a coated crystal as a liquid chromatography detector, vibrating in a flowing solution. The authors incorporated a reference crystal to eliminate the effect of viscosity changes in the solution. The sensitivity of the detector was relatively poor but for the first time showed that a crystal could be vibrated with a stable oscillation while submerged in a liquid.

The first Pz immunosensor to be used directly in solution was developed by Roederer and Bastiaans in 1983 [10]. This novel method, termed microgravimetric immunoassay, was based on a SAW device. Incorporating results

from chromatographic studies, which at the time had recently shown the high reactivity of silane-modified surfaces for proteins, the authors coated their ST-cut crystals with trimethoxyorganosilane. This coupling agent was used to immobilise goat anti-human IgG to the crystal surface. In their detector cell it was noted that the shift in frequency was dependent on the sample volume, but that this dependence diminished as the sample volume was increased. The sensor could measure human IgG from 0.0225 to 2.25 $mg\,mL^{-1}$ with a limit of detection of 13 μg. Regeneration of the antibody surface was also demonstrated after measurement by exposing the surface to a salt solution of high ionic strength. The primary reason for the poor sensitivity and limit of detection was due to non-specific adsorption occurring both at the reference and measuring crystal. The authors also stated, when discussing the limitations of immunosensing, that Pz devices could only be applied to analytes of high molecular weight. This statement was later shown to be untrue by many groups.

Thompson et al. were the first group to study Pz immunochemistry using a flowing solution [64]. They incorporated 5 and 2.5 MHz crystals. Crystals of lower fundamental frequency will have a lower sensitivity but will have a higher *Q* factor. These would be more stable in solution since less acoustic energy is lost to the solution than crystals of higher frequencies. Different immobilisation procedures were tested and the system was applied to the detection of IgG. This work was mainly a study of interfacial interactions and a study to show that it is feasible to oscillate Pz crystals in solution with a high degree of reproducibility.

The first Pz immunosensor for microbial pathogens was developed by Muramatsu et al. in 1986 [65]. Their Pz crystals were coated with antibodies against *Candida albicans*. The antigen was detected from 1×10^6 to 5×10^8 cells mL^{-1}. The sensor proved to be specific with no detectable response observed with the other species tested.

Muramatsu et al. later described a sensor for the detection of immunoglobulins [4]. Protein A was immobilised to the surface of crystals by cross-linking to a layer of silane via glutaraldehyde. This protein layer was then used to immobilise the immunoglobulin molecules. The authors immersed the whole crystal in the solution. Apart from when in highly conducting solutions, in which the frequency would cease due to a short circuit across the crystal, a very stable oscillation was observed. This was due to the fact that no mechanical stress was applied to the crystal, as is the case when they are in a flow cell with only one side exposed to the solution. Human IgG was determined from 10^{-4} to 10^{-2} $mg\,mL^{-1}$ in a flowing solution. The authors also used the protein-coated crystal to determine different IgG subclasses in a step gradient buffer solution. The resonance frequency was also studied in different solutions and at different temperatures.

Ebersole and Ward described their amplified immunosorbent assay (AMISA), which was used for the detection of APS reductase and human

chronic gonadotropin (hCG) [66]. After the direct capture of the antigen, a secondary enzyme-labelled antibody was added. Subsequent exposure of the surface to 5-bromo-4-chloro-3-indolyl phosphate (BCIP) resulted in a blue precipitate, which caused a large frequency change. The precipitate was due to the enzymatic dimerisation of BCIP by the immobilised alkaline phosphatase. The use of this enhancement step led to limits of detection of 5 ng mL^{-1} (10^{-14} M) of APS reductase. The hCG assay was based on the enzymatic oxidation of I^- to I_2/I_3^-. While AMISA incorporates extra steps when compared to the usual direct Pz capture it demonstrated that amplification routes via enzymatic catalysis can significantly lower detection limits. The main advantage of AMISA is the fact that the measured mass change is independent of the mass of the analyte. Thus detection of low molecular weight analytes, such as drugs and hormones, would be possible.

Davis and Leary in 1989 performed probably the first thorough investigation of Pz immunosensors in solution [8]. Using a human IgG system they continually monitored the crystals resonance in solution. They used a plexiglass reaction cell, which exposed one surface of the crystal to air and the other gold surface to the solution. Protein A was used as the immobilisation method, with different incubation times and pH buffers investigated. It was noted that immobilisation times longer than 45 min in buffers of pH 5.5 (near the iso-electric point of the protein) produced more complete coverage. This was shown by the lack of significant non-specific protein binding to the crystal. The importance of diffusion was also demonstrated. Mixing of the solution over the crystal during binding caused a sharp increase in the rate of frequency change. This was expected since the liquid depth over the crystal was 50 mm. Regeneration of the protein surface was also demonstrated by the addition of a low pH buffer. The increased frequency shifts observed clearly showed dissociation of the IgG from the protein A surface. The authors mentioned further experiments to see if any irreversible effect was caused to the protein A surface upon repeated exposure to low pH buffers. The authors obtained a frequency change of 1 Hz ng^{-1} of protein immobilised, ten times less than the value predicted by the Sauerbrey equation. They suggested that the reason was due to incomplete binding of their protein and also binding to the "non-resonating" parts of the system. The non-resonating parts referred to by the authors probably mean the areas of the crystal of lower sensitivity, away from the centre of the electrode as explained by Sauerbrey's sensitivity curve [67]. Overall, they demonstrated that continuous real-time monitoring and regeneration of a Pz immunosensor in solution was easily achieved and that countless applications could be found.

Muramatsu et al. described a Pz immunosensor for the detection of *E. coli* [68]. The specific antibody was cross-linked using glutaraldehyde to a layer of silane. Under optimised reaction times the cells could be measured from 10^6 to 10^8 cells mL^{-1}. Enhancement of the response was performed by addition of polystyrene beads coated in the specific antibody. The addition of

this third layer caused a further reduction in frequency and reduced the limit of detection to 10^5 cells mL^{-1}. Different size beads were tested and 1 μm gave best results.

Later Ebersole et al. described a novel method for the immobilisation of biological species [69] based on the spontaneous formation of avidin and streptavidin monolayers onto gold. The monolayers formed irreversibly from aqueous solutions onto freshly formed gold surfaces of Pz crystals; monolayers formed on aged gold surfaces showed lower activity. They demonstrated the use of this method using a DNA hybridisation assay and incorporated their AMISA technique to enhance the measured frequency change.

At the same time Prusak-Sochaczewski et al. also described a Pz immunosensor for the detection of *Salmonella typhimurium* [70]. They also incorporated avidin/biotin chemistry, but immobilised the avidin to a layer of polyethyleneimine, not formed as Ebersole et al. [69]. While not being the first Pz immunosensor to be published for the detection of microbial pathogens, it marked the first systematic attempt to produce a practical Pz immunosensor. The authors compared various immobilisation procedures for the attachment of their monoclonal antibodies to the surface of the crystal. Immobilisation via glutaraldehyde to a thin layer of polyethyleneimine gave best results. Bacterial cells could be detected from 10^5 to 10^9 cells mL^{-1}, although extensive incubation times were needed to measure the lower concentrations. The antibody-coated crystals displayed minimal non-specific binding when exposed to *E. coli* cells. The antibody-coated crystals displayed no detectable loss in activity for up to 4 days when stored at 4 °C, and could be reused for six to eight consecutive assays. This publication marked the way for future sensor developments. All previous Pz immunosensor publications were generally investigating fundamental parameters and performed to show that a certain assay or format could be achieved. This was the first attempt to produce a practical useful sensor. Their systematic approach, i.e. optimising parameters, investigating lifetime, reusability and regeneration would be the approach incorporated by most investigators to follow.

Prusak-Sochaczewski and Luong also published details of a reusable Pz immunosensor for the detection of human albumin [71]. Of the immobilisation methods tested, protein A proved best for the attachment of anti-human albumin to the surface of a Pz crystal. The antigen could be detected from 10^{-4} to 10^{-1} mg mL^{-1}. Regeneration was achieved by saturation of the surface with the antigen followed by subsequent immobilisation of the antibody. This new antibody layer could then be reused for the detection of the antigen. This could be repeated for five assays without loss of sensitivity, after which time sensitivity decreased. This was probably due to distance from the surface, which decays exponentially and damping of the crystals oscillation due to excess mass deposited. IgG could also be removed from the protein A layer by immersion of the crystal in a low pH buffer. But the removal was incomplete, 40% at best, so this method was not a viable method for regeneration

of the surface. Earlier work using protein A layers observed complete removal of the IgG layers under similar conditions [8], the only difference was that the earlier publications used a flowing glycine solution, which obviously helped removal.

The first gas phase immunosensor was also a Pz-based device, developed in 1986 [72]. Crystals coated with anti-parathion antibodies could detect the antigen linearly from 2 to 35 ppb under optimised conditions in real time. The system was reversible and coated crystals could be used for a week without detectable loss in activity. Interferences from similar compounds were only observed when they were present in very large concentrations. To ensure the responses observed were not non-specific adsorption of the antigen to protein molecules, the authors also tested crystals coated with IgG and BSA. Only small irreversible frequency changes of a few Hertz were observed ensuring that the responses observed were specific immunoreactions. Despite this it was noted that the antibodies appeared to be relatively much less selective in this sensor than when compared to their activity in solution. Assuming that this observation was not due to non-specific binding to the crystal, it demonstrated that the activity of antibodies in solution and gas phase was very different. Despite the promising results, the authors discussed the many unknown parameters that needed to be investigated before correct understanding of the sensor response can be achieved. The activity and nature of the immunoreaction in the gas phase is not known or well understood.

A gas phase immunosensor for the detection of cocaine has also been reported [73]. The antibody-coated crystals were used to detect cocaine in air to 0.5 ppb. Responses were observed in 30 s and full recovery was observed in 30 s, indicating a full analysis time of less than 2 min, allowing for base line stabilisation between measurements. Negligible effects were seen from the interferents tested. Coated crystals lasted 3 days without detectable loss in activity.

Preliminary results for a vapour phase tuberculosis Pz sensor have also been published [74]. Polyclonal antibodies against the antigen were immobilised onto the gold of piezoelectric crystals by two methods. Oxidised antibodies were attached to a silane layer and thiolated antibodies, were self-assembled onto the surface, using Trauts reagent. The sensor was used to detect the antigen in nebulised droplets of $\cong$ 10 μm, approximately the size of respiratory droplets. It is envisaged that this sensor could also be used for the direct detection of the analyte in expired breath. The fact that the antigen is only present in the breath of infected patients and completely absent in healthy patients means that quantitative determination is not very important. The sensor could be used for a fast positive/negative response, which is required in a clinical situation.

Obvious advantages over solution-based immunosensors are the fact that real-time analysis is possible while exposing both sides of the crystal to the

sample; in solution only one side can be exposed to the sample. Damping effects due to solution are eliminated, so larger frequency shifts can be expected as well as a behaviour closer to that predicted by the Sauerbrey equation [68], depending on the coating.

Despite the previous examples very little fundamental understanding exists about the nature of biological interactions in the gas phase. More thorough investigations are needed to determine binding affinities, association and dissociation constants, and rates of the antigen/antibody interaction. These then need to be compared to the parameters in the aqueous phase. The activity of the enzyme or antibody could be affected by many factors such as accessibility and reactivity. Orientation of the bio-component, which is affected by its immobilisation method, will probably differ significantly when in gas and liquid phase.

The possibility if gas phase biosensing could even occur has been questioned and caused an amount of controversy [75]. Rajakovic et al. [76] demonstrated the adsorption of pesticides and organics to antibody-coated Pz crystals. The responses observed were completely reversible and were shown to be due to non-specific chemisorption and not selective immunochemical binding. They coated a crystal with parathion antibodies and tested its response to a number of gaseous compounds including parathion. Similar frequency responses were observed for all compounds. Also crystals coated with anti-parathion antibodies, BSA, IgG and anti-valporic acid antibodies showed similar frequency responses to parathion. Crystals coated with anti-valporic acid were equally responsive to valporic acid and parathion. These results indicated that any frequency responses observed were directly due to adsorption of the compounds to the immobilised proteins on the crystal surfaces and not due to selective immunochemical binding by the immobilised antibody. This was not evident in the parathion immunosensor developed by Ngeh-Ngwainbi et al. [72]; where the authors showed that no non-specific binding occurred to crystals coated with non-specific proteins. Despite the views of these authors [76] it is very likely that immunosensors and biosensors in gaseous phase do work. A review on gas phase biosensors has been published [77], which describes numerous examples.

It is likely that in gas phase biosensor's water of hydration is retained in the immobilised structure, since none of authors used forceful drying procedures. It is possible that this water is sufficient to allow the bio-component to act to some extent as if it were in solution. Thus the sensors respond in an expected manner as they would in solution, but with an obvious difference in magnitude of response and activity. Even dry air contains 5 ppm or more of water, which is considered sufficient for the activity of the antibody or enzyme [78]. Partial humidification of the carrier stream has also been suggested so as to retain the behaviour of the biologically active coatings [79]. This area has been specifically reviewed elsewhere [80, 81] and also discussed in general Pz biosensor reviews [82–84].

This initial work paved the way for the development of limitless numbers of Pz immunosensors. The later developments mainly focused on the improvement and optimisation of previous methods to develop sensitive, selective and robust sensors for various analytes. Others concentrated on the development of new immobilisation procedures or assay techniques in order to improve on previous methods.

2.2 Piezoelectric Immunosensor Applications

2.2.1 Bacterial Detection

Conventional bacterial detection methods generally require laborious procedures and many hours or even days for complete analysis. The relatively large mass of bacterial cells, combined with the availability of antibodies to most species means that Pz immunosensor detection offers a very attractive alternative to microbiological methods. Generally giving results in minutes, with adequate sensitivity and selectivity. The earliest Pz immunosensors for bacterial detection have already been discussed [65, 68, 70].

Plomer et al. described a sensor for the detection of enterobacteria [85]. Of the immobilisation procedures tested, protein A was found to be most useful for the immobilisation of the antibodies. Under optimised conditions *E. coli* K12 could be measured from 10^6 to 10^9 cells mL^{-1}. The antibodies used were raised against enterobacterial common antigen (ECA), chosen so as to develop a family-specific Pz immunosensor for the detection of all enterobacteria. But the sensor's response towards other members of the family tested {*Enterobacter*, *Citrobacter*, *Proteus* and *E. coli* (wild strain)} was small. The weak response was due to the smooth surface of these strains, which masked the ECA, a glycophospholipid of the outer bacterial membrane shared by all enterobacteria. Heat treatment allowed release of this ECA, and detection to different degrees of the other strains was possible. It was also discovered that drying the antibody to the surface of the crystal had no detrimental effect on its activity. Regeneration of the antibody surface was not possible since addition of low pH buffers not only removed the antigen but partially removed the antibody layer also. Cleaning of the crystal using NaOH allowed regeneration of the gold surface, which could be reused for more than 50 assays.

König and Grätzel published results of a Pz immunosensor for the detection of various diarrhoea-causing enterobacteria [9]. Common detection methods take 2 days and in about 40% of the cases the causative pathogen cannot be determined. Unlike the sensor developed by Plomer et al. [85], the authors used specific antibodies for each strain since in clinical applications the exact pathogen is often important. Protein A was chosen as the method of

antibody immobilisation since it displayed superior sensitivity, reproducibility and was most stable when compared to other methods. The bacteria tested, including *Camylobacter* and *Shigella*, could be measured from 10^6 to 10^8 cells/crystal. The sensor was also applied to real stool samples. A 5% increase in response was observed and believed to be due to non-specific binding from other bacteria present in the stool sample. The antibody-coated crystals could be stored for 6 weeks and regenerated 25 times without detectable loss in activity.

Su and Li [86] used a SAM of an alkanethiol to immobilise antibodies for the detection of *E. coli* 0157 : H7. A detection limit of 10^3 CFU (colony forming units) mL^{-1} was obtained using dip and dry detection. Poorer performance in solution, dynamic and static, was observed.

A Pz immunosensor for the detection of *Listeria monocytogenes* was published by Jacobs et al. [87]. The bacteria could be measured to 10^5 cells mL^{-1} using dip and dry methods of detection. Analysis carried out directly in solution allowed detection to 5×10^5 cells mL^{-1}. Antibody coated crystals were stored for 17 days without detectable loss in activity. Protein A was used as the immobilisation method but not compared to others. Later the group published details of a displacement assay for the detection of this species [88]. This assay could detect the antigen from 2.5×10^5 to 2.5×10^7 cells/crystal directly in solution monitoring the response in real time. The assay was also performed in milk. Assays in milk were also shown to be specific for *L. monocytogenes*. A later study incorporated SAMs to immobilise antibodies to detect, in real time, this species in solution [89]. The sensor was specific and reusable at least ten times without detectable loss in activity. The sensitivity, however, was poor with a limit of detection of 10^{-7} cells mL^{-1}. Of note, however, was the fact that an increase in frequency was observed upon exposure of the antibody-coated crystal to the specific cells, an observation also seen by Thompson et al. [64].

A displacement assay was also used for the detection of *Pseudomonas aeruginosa* by Bovenizer et al. [90]. However, a poor detection limit of 1.5×10^7 cells mL^{-1} was found and high cross reactivity with other *Pseudomanas* species was observed. The fact that the antibodies showed high selectivity in ELISA indicated that the displacement observed was possibly due to removal of species during the washing steps and not due to any immunological reaction. Kim et al. [91] used thiolated antibodies to detect this species directly in a flowing solution. This sensor had comparable sensitivity to the previous sensor [90] and was used seven times with a relative sensitivity loss of less than 10%. Issues with selectivity were attributed to the specific antibody used.

Adsorption of antibodies was used to develop a sensor for the detection of *Vibrio cholerae* 0139 [92]. A fast detection method was required to measure and differentiate this strain with the Ogawa serotype of the bacteria. The sensor could measure the bacteria to 10^5 cells mL^{-1} against a background of the

Ogawa strain. No cross-reactivity to other bacteria such as *E. coli*, *L. monicytogenes* and *S. marcescens* was observed.

Le et al. described a sensor for the detection of *Staphyococcus aureus* [93]. They used a layer of YWG-$C_{18}H_{37}$ cross-linked with glutaraldehyde to immobilise the specific antibodies to the crystal surface. YWG-$C_{18}H_{37}$ is normally used as a protein purification ligand in chromatography and has a high affinity for antibodies. Under optimised conditions the analyte could be detected from 5×10^5 to 1×10^8 cells mL^{-1} in solution. Antibody-coated crystals could be reused 15 times and stored for 1 month without detectable loss in activity. Negligible response to *P. aeruginosa*, *S. epidermidis* and *E. coli* was observed.

Si et al. used electropolymerised films as functional coatings for antibody immobilisation for the detection of *Staphyococcus aureus* [94]. Antibodies were linked to the film using glutaraldehyde. The antigen was detected from 10^5 to 10^9 cells mL^{-1}. The antibody-coated crystal could be regenerated ten times with minimal loss in activity and was stable for up to 5 weeks, after which time only an 8% loss in activity was observed. It was also found that the sensor performed best at pH 7–8.

A SAM based immobilisation procedure was incorporated by Ben-Dov et al. for the detection of *Chlamydia trachomatis* [95]. A monolayer of cysteamine was formed on the gold surface. Using a suitable cross-linker anti-IgG was immobilised to this monolayer. Anti-*C. trachomatis* was then added to form the active sensing layer. The sensing layer was subsequently exposed to the antigen. Responses were recorded in real time directly in solution. Amplification of the response was shown by the addition of a secondary antibody. The bacteria could be detected from 260 ng mL^{-1} to 7.8 μg mL^{-1}. Analysis of the analyte was also performed directly in urine and the assay was more sensitive than current ELISA tests. The fragmented $F(ab')_2$ antibody-coated crystals were stable for up to 90 days.

Salmonella species have been the most studied bacteria in Pz immunoanalysis because of their importance to the medical field and food industries. The detection of various strains has already been described [9, 69, 71] and further sensors are summarised in Table 1.

An enzymatically amplified sandwich assay was used for the detection of *Helicobacter pylori* infection by Su et al. [103]. Elevated concentrations of the antibody against the bacteria in serum were a sign of infection. Recombinant *H. pylori* protein was immobilised to the crystal by means of an activated thioctic acid monolayer. The surface was then exposed to serum or a solution containing the specific antibody. An enzyme-labelled secondary antibody was then added, followed by an appropriate substrate. As with Ebersole and Ward's AMISA [66], an enzymatically generated product precipitated on the surface of the crystal, thus enhancing and amplifying the frequency change. The assay significantly reduced interferences from non-specific antibodies or other serum components. It was used for the analysis of positive and negative serum, using both dip and dry and real-time monitoring.

Table 1 Detection of Salmonella species using piezoelectric immunosensors. The sensor's linear range and, where available, the limit of detection have been listed

Strain	Detection	Immobilisation	Refs.
S. paratyphi	10^5–10^9 cells mL^{-1}	Electropolymerised films	[96]
S. enteritidis	3×10^5–5×10^8 cells mL^{-1}	Electropolymerised films	[97]
All strains	9.9×10^5–1.8×10^8 cells mL^{-1} 10^5 cells mL^{-1}	Thiolated antibodies	[98, 99]
S. typhimurium	3.2×10^6–4.8×10^8 CFU mL^{-1}	Thiolated antibodies	[36]
S. typhimurium	5.3×10^5–1.2×10^9 CFU mL^{-1} 10^5 CFU mL^{-1}	PEI	[100]
S. typhimurium	10^2–10^7 cells mL^{-1} 350 cells mL^{-1}	Langmuir–Blodgett films	[101]
S. paratyphi	6×10^4 cells mL^{-1}	PEI	[102]
S. typhimurium	8×10^4 cells mL^{-1}		
S. enteritidis	6×10^4 cells mL^{-1}		

Wu et al. also used the elevated antibody levels in serum as an indication of pathogen infection [104, 105]. The concentration of specific antibodies against the parasite *Schistosoma japonicum* was measured. Initially the authors used polymer agglutination to determine the antibody concentration in rabbit serum [104]. It was noted after scanning electron microscopy (SEM) analysis of the crystal surface that adsorption to the crystal surface was a dominant factor in the frequency response. Various parameters were investigated and the antibody was measured linearly from 3.6 to 42.0 μg mL^{-1}. In the later publication the authors immobilised *S. japonicum* antigen to the crystal surface using a copolymer of methacrylate [105]. This was then exposed to a solution containing the specific antibody, whose concentration was proportional to the frequency change upon binding to the immobilised antigen. The antibody was linearly measured from 7.2 to 90.0 μg mL^{-1}. The gold surface could be regenerated and reused 20 times without any detrimental effect on its frequency stability. The sensor was used to measure the degree of infection in rabbit serum. The valent value of binding of the antigen and affinity constant were also estimated.

Other non-immunosensor-based Pz sensors for the detection of bacteria have been produced. He et al. described a separated electrode Pz sensor for *E. coli* [106]. Ebersole et al. used Pz detection to monitor the growth and metabolic rates of *E. coli* cells [107]. Bao et al. developed a sensor for the detection of *Staphylococcus epidermidis* [108]. A Pz-based assay for *Saccharomyces cerevisiae*, *Bacillus subtilis* and *Klebsiella* spp. have also been described [109].

Reviews dealing to some extent with the detection of bacteria using Pz immunosensors have appeared [110, 111].

Pz immunosensors for the detection of other micro-organisms such as plankton have also appeared. The plankton *Chattonella marina*, which causes red tide, was detected directly in sea water from 10^2 to 10^4 cells mL^{-1} by Nakanishi et al. [112]. Immobilisation of the antibodies using protein A and polystyrene gave better results than when using silane or polyethyleneimine. Protein A was the method of choice since a relatively low sensitivity to the cells was observed with the polystyrene-immobilised antibodies. This was due to the fact that fewer antibodies bound to the polystyrene surface and also to random orientation of the immobilised antibodies, leading to deactivation of a high percentage of them due to binding via their Fab sites. No interferences were observed from another plankton that causes red tide, *Alexandrium catenella*. They later described a sensor for the detection of *Alexandrium affine*, another red tide causing plankton [113]. A novel method of antibody immobilisation was incorporated, the use of plasma polymerised films, the theory of which was excellently described earlier by the authors [114]. While this was the first use of this technique in Pz immunosensor work, it had been previously used for Pz gas sensor development [115]. Plasma polymerised coated crystals performed better than polyethyleneimine and silane in terms of sensitivity and reproducibility. The importance of orientated immobilisation was discussed [114]. IgM antibodies were cross-linked via glutaraldehyde to the plasma polymerised coated crystals and were used to detect the plankton directly in seawater. The cells were measured from 10^2 to 10^5 cells mL^{-1} and the sensor showed no response to *A. catenella*.

2.2.2 Viral Detection

The first Pz immunosensor developed for the detection of viruses was reported in 1992 by Kößlinger et al. [116]. They used synthetic human immunodefficiency virus (HIV) peptides adsorbed on a Pz crystal for the detection of anti-HIV antibodies, an indication of HIV infection. The authors used very sensitive 20 MHz crystals to monitor the binding of monoclonal antibodies to the immobilised peptide layer in solution. The high relative standard deviation observed in the measurements was due to insufficiently reproducible experimental conditions. Non-specific binding of other proteins was also observed. Surprisingly, the authors observed that the Sauerbrey formula gave sufficiently accurate values for the frequency observed due to adsorption and binding of proteins.

In a later publication the group incorporated their sensor in a flow system [117]. Detection of the HIV antibodies was also carried out in serum samples. Dilution of the serum in buffer ensured the suppression of non-specific effects and that negligible viscosity effects were observed. As long as the antibody concentration in the serum was not too high and didn't saturate the receptor layer on the crystal surface, several assays could be performed on

each crystal. The sensor's performance was comparable to that of a commercial ELISA HIV kit. Similar results also appeared elsewhere [118].

The group later published details of a sensor for the detection of African swine fever virus and antibodies against the virus [119, 120]. Analysis was carried out in both serum and buffer incorporating a flow injection analysis (FIA) system, using 10 MHz crystals in serum and 20 MHz crystals in buffer. In terms of cost, experimental expenditure, response, regeneration and lifetime, immobilisation of the antibody using dimethyl sulfoxide was best when compared to other methods. Detection of the virus protein was performed in buffer and pig serum; limits of detection were $0.31\,\mu g\,mL^{-1}$ and $1\,\mu g\,mL^{-1}$, respectively. Immobilisation of the virus protein for the detection of the antibodies was best using adsorption for 4 days. Detection limits in serum and buffer, were $0.2\,\mu g\,mL^{-1}$ and $0.1\,\mu g\,mL^{-1}$, respectively. The use of different blocking solutions and the addition of substances to counteract viscosity effects were also investigated.

König and Grätzel published details of a sensor for the detection of diarrhoea-causing bacteria and viruses [9]. Immunosensors were described for the detection of rotavirus and adenovirus. Both viruses were measured linearly from $10^6$to 10^{10} virions. As explained earlier, protein A was shown to be the most favourable immobilisation method but immobilisation using silane and polyethyleneimine showed a 40% increase in response when detecting rotavirus in stool samples.

They also developed a sensor for the detection of herpes viruses [43]. The sensor was used to specifically detect five human herpes viruses, herpes simplex type 1 and 2, viracella-zoster virus, cytomegalovirus and Epstein-barr virus. Of the immobilisation procedures tested, protein A was best in terms of reusability, sensitivity and stability. Each virus was measured linearly from 54 to 1×10^9 virions/crystal. The sensor was reusable 18 times and stable for 8 weeks without detectable loss in activity. When applied to complex human specimen no non-specific effects were observed and the sensor performed identically for each virus as it did in buffer.

The authors later published details of a sensor for the detection of human hepatitis viruses type A and B [44]. Immobilisation using protein A gave best results. Both types of virus could be detected linearly from 10^5 to 10^{10} virions mL^{-1} in solution. The sensor was stable for 4 weeks and could be reused ten times without detectable loss in activity. Results were comparable to those of a commercial ELISA kit.

Susmel et al. describes a competitive immunoassay for the detection of human cytomegalovirus [121]. Direct capture of the virus from solution, using a number of immobilisation procedures, yielded unsatisfactory results, contrary to what was observed before [43]. A competitive assay performed using a monolayer of poly-L-lysine (covalently attached to a monolayer of thiosalicylic acid) yielded a preliminary linear range of $2.5–5\,\mu g\,mL^{-1}$ of gB epitope and a limit of detection of $1\,\mu g\,mL^{-1}$.

Su et al. adsorbed recombinant porcine reproductive and respiratory syndrome virus (PRRSV) protein to the surface of a Pz crystal to detect infection in pigs by the presence of PRRSV antibodies [122]. As seen in earlier work [119, 120], immobilisation of the protein via self-assembly led to deactivation, thus no significant binding of the antibody was observed. Analysis in pig serum was carried out, using both dip and dry and real time analysis. A one in ten dilution in serum was used as a compromise between loss of sensitivity and suppression of non-specific effects. Screening of positive and negative sera displayed similar results to that of a commercial ELISA kit. Regeneration of the protein-coated crystal was possible four times, after which 92% of its activity was still retained. Using harsher conditions the gold surface could be easily regenerated for reuse.

Rickert et al. described a sensor for the detection of antibodies against the foot and mouth disease virus [123–125]. Synthetic peptides constituting an epitope of the virus were immobilised using activated self-assembled thiols. The antibodies were detected in a flowing solution in real time. Regeneration of the surface was also performed.

Lee and Chang [126] used a cystamine SAM to immobilise antibodies to develop a sensor for the detection of bovine ephemeral fever virus. The unoptimised sensor was used in a flowing solution and detected the antigen in real time to 5 $\mu g\,mL^{-1}$. Positive results were observed in bovine sera samples.

2.2.3 Clinical Analysis

The detection of some of the above bacteria and viruses are of major clinical importance. The development of sensors for various analytes of clinical importance, especially human blood products has been intensely investigated.

König and Grätzel first reported the Pz detection of human erythrocytes [127, 128]. The later was an improved version of the sensor. Polyethyleneimine was used to immobilise the antibody to the crystal, which was stable for 10 weeks, if stored dry at room temperature or 4 °C, without detectable loss in activity. Regeneration of the surface was improved from eight to 12 times without detectable loss in activity. This was done by the addition of a synthetic peptide, which competed for the bound antigen and allowed regeneration of the antibody surface without the use of harsh chemicals. Analysis in blood was carried out.

A sensor for the detection of human granulocytes was also reported by the authors [47]. Immobilisation was carried out using silane, protein A and polyethyleneimine. Similar results were observed for each method but the later showed better stability. The antigen was measured linearly in blood from 2×10^3 to 3×10^5 cells. The antibody-coated surface was stable for 8 weeks without detectable loss in activity. Regeneration was not possible since removal of all the bound cells even under harsh conditions did not occur.

The authors again used polyethyleneimine to immobilise antibodies for the detection of T-lymphocytes [48] and B-lymphocytes [49]. T-lymphocytes were measured linearly from 5×10^3 to 4.5×10^5 cells. The antibody-coated crystals were stable for 10 weeks without detectable loss in activity. Regeneration was not tested. A 10% increase in response was observed when tested in whole blood, due to non-specific binding. B-lyphocytes could be measured linearly from 5×10^3 to 5.6×10^5 cells, in blood and buffer. The antibody-coated crystal was stable for 6 weeks and could be regenerated eight times without detectable loss in activity.

Many authors have developed Pz sensors capable of detecting IgGs, but generally these are used as test analytes in fundamental investigations or the development of new techniques and immobilisation methods.

Raman Suri et al. described a sensor for the detection of IgM [129]. They removed the central 5 mm of the gold electrode surface to expose more Pz surface for chemical modification. This causes an increase in the resonance frequency and a reduction of the *Q* factor, but the crystal still vibrates. This surface was then refluxed in acid to produce stable hydroxyl groups. Modification with tresyl chloride gave more surface coverage than silane and showed better sensitivity when protamine was immobilised. IgM could be measured linearly from 10^{-5} to 10^{-2} mg mL^{-1}, with a limit of detection of 10 ng mL^{-1}. Tresyl chloride treated crystals were stable for 5 days without significant loss in activity whereas silane treated crystals were only stable for 3 days. Negligible interferences were observed from IgG.

Chu et al. also described a sensor capable of detecting IgM in solution [130]. The authors used an array of 5 Pz crystals coated with different ratios of antibodies against two analytes, IgM and C-reactive protein. The array was then used for the simultaneous analysis of the dual analytes in solution. Of the linear regression models tested, least terminated squares gave best results for the estimation of analyte concentrations in mixed unknown samples. The authors also carried out kinetic studies on the immunoreaction of IgM [131]. An activated methacrylate copolymer was used to immobilise the antibodies against IgM. Various immunoreaction kinetic parameters were determined under varying conditions by continuous monitoring of the reaction using the QCM.

IgA was measured in real time, directly in saliva by Tajima et al. [132]. Immobilisation of the antibody using cysteamine gave superior results to that of adsorption. The antibody-coated crystal was reusable for 15 times without detectable loss in activity. The concentration of IgA measured in saliva using the Pz sensor was confirmed using ELISA.

Su et al. incorporated SAMs in the development of a Pz sensor for IgE [133]. Thioctic acid and cysteamine, coupled with EDC and glutaraldehyde respectively, were tested. IgE was measured linearly from 5 to 300 IU mL^{-1} and the antibody-coated crystal could be regenerated five times without detectable loss in activity. The SAM coated crystals showed three

to five times less non-specific binding than crystals prepared with other methods (polyethyleneimine, silane and protein A). The sensor's performance was comparable to that of two commercially available IgE test kits.

The detection of complement proteins has also received much attention. Pei and coworkers described a Pz immunosensor for the detection of complement C4 [134, 135]. The authors first used adsorption to immobilise the specific antibody, showing better results than for the use of polyethylenieimine [134]. They measured the protein linearly from 0.1 to 10 $\mu g\,mL^{-1}$. The sensor showed no response to any materials present in serum and the gold surface could be regenerated 15 times for repeated use. Later they self-assembled the antibodies onto a layer of protein A, a method which gave superior results to the previously tested immobilisation procedures [135]. This setup gave a better linear range of 5×10^{-4}–1×10^{-2} $\mu g\,mL^{-1}$, but the crystal was only reusable about ten times.

The group later published a similar sensor for the detection of complement C6 [136]. Immobilisation of the antibody via polyethyleneimine showed superior results to physical adsorption. Under optimised conditions the protein could be determined linearly from 10^{-4} to 10^{-2} $\mu g\,mL^{-1}$. The gold surface could be regenerated 12 times for repeated use before loss of sensitivity due to damage of the gold was observed.

Chu et al. used polymer agglutination to determine the concentration of complement C3 in serum [137]. Determination of the protein concentration under optimised conditions using initial rates and end-point methods produced linear ranges of 22.0–49.1 $\mu g\,mL^{-1}$ and 22.0–43.2 $\mu g\,mL^{-1}$, respectively. Analysis of clinical samples showed that the Pz method was comparable to turbimitry analysis.

Deng et al. [138] used a novel immobilisation procedure based on a nafion membrane to detect compliment C4. The well optimised sensor was easily prepared and allowed regeneration of the nafion surface. It could detect C4 from 0.08 to 1.6 $\mu g\,mL^{-1}$.

Lepesheva et al. incorporated the use of Langmuir–Blodgett IgG films, on Pz crystals for immunosensing [139]. Ferritin was used as a model and could be detected from 10^{-10} to 10^{-7} M.

Chu et al. used an activated copolymer of methacrylate for antibody immobilisation to develop a Pz immunosensor for the detection of α-fetoprotein in serum [140]. The analyte was measured linearly from 100 to 800 $ng\,mL^{-1}$ and no interferences from other serum components were observed. Valent values and affinity constants of the immunoreaction were also determined. Comparable results to RIA were obtained.

Pei et al. used protein A immobilisation in the development of a sensor for fibrin in serum [141]. The immobilisation gave better results than those obtained with polyethyleneimine and adsorption of BSA, glutaraldehyde was used to cross-link the antibodies to the adsorbed BSA layer. Under optimised conditions the analyte could be measured from 10^{-4} to 10^{-2} $g\,L^{-1}$. The

antibody-coated surface could be stored for 6 weeks without detectable loss in activity. No interferences from other serum components were observed and the gold surface could be regenerated ten times before loss in sensitivity was observed.

Shao et al. used polyethyleneimine-coated crystals to measure haemoglobin (bovine) directly in solution from 0.001 to 0.1 mg mL^{-1} [142]. No interference was observed from BSA and the effect of different liquid depths over the crystal was also investigated.

Muratsugu et al. described a sensor for the detection of human serum albumin (HSA) [143]. Adsorption of the antibody was the immobilisation method used. The antigen binding was monitored in real time directly in a flowing solution. The system could specifically detect HSA in the presence of BSA. The antigen could be measured from 0.1 to 100 μg mL^{-1}. The frequency change observed by the authors was larger than that predicted by the Sauerbrey equation; also the binding of the HSA was larger than that of the adsorbed antibody. This was related to the hydrophobicity and hydrophilicity of proteins.

Sakai et al. also described a sensor for the detection of HSA in a flowing solution [144]. After initial capture of HSA by the immobilised monoclonal antibodies, a solution of secondary polyclonal antibodies was added, thus performing a sandwich assay. This sandwich method was effective in significantly increasing the sensitivity of the assay due to the larger mass of the polyclonal antibodies compared to HSA. The sensor showed a linear response to the antigen from 0 to 20 ppm. The antibody-coated crystal could be reused for 30 assays over 4 days without significant loss in activity.

Xia et al. also described a Pz immunosensor for the detection of HSA based on polymer agglutination [145]. The analysis was carried out in serum but had a much lower sensitivity than the previous sensors, linearly detecting the antigen from 112 to 878 μg mL^{-1}. Rubbing the crystal and washing allowed regeneration of the surface and reuse of the crystal. The authors used a carboxymethyl cellulose polymer.

Polymer agglutination has also been applied to other analytes of clinical importance. The technique was pioneered by Kurosawa and coworkers in 1990 [17]. They used it for the analysis of C-reactive protein (CRP). In a recent publication further details of its use for the detection of CRP have appeared [146]. It was successfully used in serum for the diagnosis of disease. The technique termed latex piezoelectric immunoassay (LPEIA) was also applied for the detection of antistreptolysin O antibodies in serum [18]. The technique was very rapid, requiring an assay time of only 2–3 min, incorporating the initial rates method. Only 20 μL of serum was needed to perform an assay. The antigen could be measured up to 1040 IU mL^{-1}. It was shown that the latex particles in solution prevented adsorption of proteins to the crystal, thus eliminating non-specific effects. Clinical samples were tested and LPEIA results were confirmed using turbidimetry.

Ghourchian et al. later applied LPEIA to the detection of rheumatoid factor [147]. Stable oscillation of crystals in PBS solutions generally required sealing of one side of the crystal. This was often time consuming and altered the sensitivity of each crystal, resulting in irreproducibility from crystal to crystal. The authors improved on this by designing a cell which exposed only one side of the crystal to the solution, still allowing stirring thermostatic control of the solution over the other surface. A novel surface regeneration method was also employed and allowed 38 assays to be carried out using one crystal without detectable loss in activity. Under optimised conditions the antigen could be measured from less than 5–5.5 IU mL^{-1}. The effect of HSA and BSA were also investigated.

In combined publications both groups describe the application of LPEIA in the clinical analysis of CRP, antistreptolysine O antibody and rheumatoid factor [148, 149].

Zhang et al. [150] used a novel micro-array of crystals to develop a sensor for human chronic gonadotropin. The SAM-based system retained 70% of its activity after five regenerations and had a range of 2.5–500 mIU mL^{-1}. Its performance in real urine and serum samples was comparable to radioimmunoassay.

The application of a novel immobilisation procedure, based on cystamine SAMs and chitosan/alginate multilayers, has been demonstrated in the detection of factor B [151]. A positively charged chitosan layer was immobilised via glutaraldehyde to a cystamine SAM on the crystal surface. A layer of alginate, with covalently bound antibodies, was then electrostatically bound to the charged chitosan layer. This technique allowed a fast and reproducible regeneration of the chitosan layer, with no detectable loss in activity after eight attempts. The use of this chitosan/alginate layer demonstrated increased sensitivity when compared to direct antibody immobilisation to the cystamine SAM. Analysis in serum samples was also carried out.

Michalzik et al. [152] developed an immunosensor for the detection of bone morphogenic protein-2. 20 MHz crystals were incorporated to increase the potential sensitivity of the sensor, which had a limit of detection of 0.5 $\mu g\, mL^{-1}$. Immobilisation was performed via protein A covalently bound to a SAM of cystamine and the sensor was reused six times without detectable loss in activity. More important, however, was the fact that this publication demonstrated a practical application of this group's excellent miniaturised flow system [153]. The crystals incorporated consisted of 2 mm gold electrodes and were only 3 mm diameter in total. The flow cell was just 5.5 mm in width. The possibility of applying this technology to microfluidic transducer arrays was mentioned.

2.2.4 Low Molecular Weight Analytes

The detection of low molecular weight analytes of importance including steroids, herbicides, pesticides and toxins have also appeared. Generally, because of their low molecular weight, assay formats other than direct captures are performed or their presence is measured indirectly. The direct capture of such analytes can often lead to a sensor with low sensitivity due to minor frequency changes. Table 2 summarises some of the Pz immunosensors developed for the detection of low molecular weight analytes.

Masson et al. described a bioaffinity Pz sensor for biotin [174]. The sensor was based on the displacement of avidin from the crystal surface, which caused a large frequency increases when biotin was added to the solution. The surface was easily regenerated by addition of more avidin after analysis.

Table 2 Detection of low molecular weight analytes using piezoelectric immunosensors. Capture assays were used unless otherwise stated

Analyte	Detection	Immobilisation	Assay	Refs.
Insulin	10^{-6}–10^{-1} mg mL^{-1}	Protein A	Capture	[154]
Insulin		Spin coated	Capture polystyrene	[2]
Cortisol	36–3628 ppb	Protein A	Capture	[42]
Cocaine	10–300 ppb	Protein B	Capture	[155]
Cocaine	100 pmol L^{-1}	SAM	Competitive	[156]
Metamphetimine	0.02–100 ppm	Adsorption	Competitive	[157]
2-Phenyloxazolone	10^{-5}–10^{-8} M	Adsorption	Competitive	[158, 159]
Ricin	0.5 μg	Adsorption	Capture	[160]
Staphyllococcal enterotoxin B	0.1–10 μg mL^{-1}	Adsorption	Competitive	[161]
Staphyllococcal enterotoxin C_2		Protein A	Capture	[162, 163]
Staphyllococcal enterotoxin			Capture	[164]
Atrazine	0.03–100 μg mL^{-1}	Protein A	Capture	[165, 166]
Atrazine	0.1–100 ppb	Silane	Competition	[167]
Atrazine	0.01–1 ng mL^{-1} 0.001 ng mL^{-1}	Polystyrene	Competition	[168]
Atrazine	0.1 μg L^{-1}	Silane	Competition	[169]
2,4-Dichlorophenoxyacetic acid	0.001–100 ppb	Silane	Competitive	[170, 171]
Polycyclic aromatic hydrocarbons	1–4 nM	SAM	Displacement	[172]
Polychlorinated biphenyls			Capture Competition	[173]

The assay was very versatile and would be especially useful in the detection of low molecular weight analytes. The authors demonstrated its use using a FIA system.

Horacet and Sckladal used direct competitive assays of two test analytes, 2,4-D and 4,4′-dichlorobiphenyl, to investigate the effect of organic solvents on immunoassays [175]. The effect of different concentrations of methanol on the immunoreaction was investigated. It was demonstrated that hydrophobicity of the solvent was the important factor when determining the effect of the solvent; the less soluble the solvent was in water the lower the influence it had on the immunointeraction. The authors also performed a real-time competitive assay in toluene. The first time an immunoaffinity interaction in pure solvent has been shown. The effect on affinity and kinetics were discussed.

An enzyme-based Pz biosensor for the detection of organophosphorous and carbamate pesticides has also appeared [176]. The assay was based in the inhibitory effect of the pesticides on immobilised acetylcholinesterase. After exposure of the enzyme to the pesticides, the substrate 3-indoyl acetate was added. This was enzymatically converted to an insoluble product, the concentration of which was determined by the resulting frequency change. The rate and amount of conversion was due to the concentration of the active immobilised enzyme, which was dependent on the amount of pesticide present. The system was very similar to that used by Ebersole and Ward in their AMISA [66]. The authors measured paroxon to 5×10^{-8} M and carbaryl to 1×10^{-7} M.

2.3 Future Trends

The main disadvantage of Pz immunosensors with a view to commercialisation seems to be their stability. As can be seen from the many previous examples they generally have a working lifetime of only a few days. Even unused sensors only last a number of weeks. This lack of stability is unacceptable if commercial success is to be realised.

The Pz sensor is sensitive enough on its own to theoretically measure what is required. The antibodies are quite robust and stable when stored correctly, retaining their activity for long periods. The problems arise when the two are combined. Separately, each of the components easily has the required sensitivity and specificity for the specific detection. But a lot of this is lost when they are coupled. Even with all the advances in immobilisation techniques no significant improvement in overall sensor performance has been found, rendering most Pz immunosensors useless outside the laboratory environment. Further research is needed to try and find a method of extending the lifetime of antibody-coated crystals. Only then can their advantages be fully exploited. Another solution could be to find an alternative to the antibodies, something that retains their main advantages of biologically optimised specificity and

affinity, but is more versatile and robust. The use of synthetic peptides have already been incorporated into Pz immunosensors [116–118, 123–125]. As chemical synthesis improves, the production of molecularly imprinted polymers with the selectivity of antibodies is also a real possibility. Combinatorial techniques, which are widely used in drug production, have already been applied to the development of antibody mimics. While the initial production costs would be large, mass production would generally be very cheap, once a suitable molecule has been produced. These synthetic mimics can have the desired specificity, are cheap to produce and are generally very stable.

These synthetic alternatives are much more versatile than antibodies and can be functionalised or easily tailored for individual needs without affecting their specificity. At the moment specificity is their major drawback but with developing techniques this is improving and getting closer to that of antibodies. With these technologies the production of cheap and robust, specifically coated crystals with good stability should be possible. Then the successful commercialisation of Pz sensors would be a real possibility.

The use of sensor arrays should also play an important role in the future. They could be used to simultaneously give an accurate account of many different analytes and an overall result at once. For example, an array of Pz sensors coated with specific antibodies against different freshwater cyanobacterial toxins could be used to give an overall toxicity indication and also a specific result on the concentration and type of each toxin present. Incorporation of miniaturised flow cells and crystals, such as the excellent system developed by Michalzik et al. [152, 153], could allow real-time monitoring directly in solution.

Sakti et al. have shown how a simple modification of the crystal surface can greatly improve its performance and increase the lifetime of the silver electrodes [2]. At the same time this provides a good matrix for immobilisation. This sort of modification can help improve the commercial potential of a sensor.

Theoretically Pz immunosensors are still very promising. In the short few years since the first immunosensor huge developments have been made. As more fundamental research paves the way for a better understanding of the exact mechanistics, the benefits should be conveyed in improved sensors. To overcome the stability problem a completely new approach may be required, rather than just trying to improve on already existing techniques.

References

1. Nakanishi K, Karube I, Hiroshi S, Uchida A, Ishida Y (1996) Anal Chim Acta 325:73
2. Sakti SP, Rosler S, Lucklum R, Hauptmann P, Buhling F, Ansorge S (1999) Sensor Actuator A 76:98
3. Richman DD, Cleveland PH, Oxman MN, Johnson KM (1982) J Immunol 128:2300

4. Muramatsu H, Dicks JM, Tamiya E, Karube I (1987) Anal Chem 59:2760
5. Moks T, Abrahmsen L, Nilsson B, Hellman U, Sjqöuist J, Uhlen M (1986) Eur J Biochem 156:637
6. Horisberger M, Clerk MF (1985) Histochemistry 82:219
7. Prusak-Sochaczewski E, Luong JHT (1990) Anal Lett 23:401
8. Davis KA, Leary TR (1989) Anal Chem 61:1227
9. König B, Grätzel M (1993) Anal Lett 26:1567
10. Roederer JE, Bastiaans GJ (1983) Anal Chem 55:2333
11. Weethall HH, Curley MF (1996) Sensor Actuator B 36:527
12. Raman Suri C, Mishra GC (1996) Biosens Bioelectron 11:1199
13. Barnes C, D'Silva C, Jones JP, Lewis TJ (1991) Sensor Actuator B 3:295
14. Nakanishi K, Muguruma H, Karube I (1996) Anal Chem 68:1695
15. Kurosawa S, Kamo N, Matsui D, Kobatake Y (1990) Anal Chem 62:353
16. Wu Z, Yan Y, Shen G, Yu R (2000) Anal Chim Acta 412:29
17. Kurosawa S, Tawara E, Kamo N, Ohta F, Hosokawa T (1990) Chem Pharm Bull (Tokyo) 38:1117
18. Muratsugu M, Kurosawa S, Kamo N (1992) Anal Chem 64:2483
19. Frey BL, Corn RM (1996) Anal Chem 68:3187
20. Nuzzo RG, Fusco FA, Allara DL (1987) J Am Chem Soc 109:2358
21. Ohtani M, Sunagawa T, Kuwabata S, Yoneyama H (1995) J Electroanal Chem 396:97
22. Nuzzo RG, Zegarski BR, Dubios LH (1987) J Am Chem Soc 109:733
23. Bain CD, Troughton EB, Tao YT, Evall J, Whitesides GM, Nuzzo RG (1989) J Am Chem Soc 111:321
24. Schessler HM, Karpovich DS, Blanchard GJ (1996) J Am Chem Soc 118:9645
25. Dong S, Ling J (1997) Bioelectrochem Bioenerget 42:7
26. Wink T, Zuilen SJ, Bult A, van Bennekom D (1997) Analyst 122:43R
27. Su X, Chew FT, Li SFY (1999) Anal Biochem 273:66
28. Duan C, Mayerhoff ME (1994) Anal Chem 66:1369
29. Frey BL, Jordan CE, Kornguth S, Corn RM (1995) Anal Chem 67:4452
30. Caruso F, Rodda E, Furlong N (1996) J Coll Intr Sci 178:104
31. Neuman MR, Perlaky SC, Mickalski JP, Bass JB, McCombs CC (1995) EMBC 95, paper 7.1.3.8
32. Legget GJ, Roberts CJ, Williams PM, Davies MC, Jackson DE, Tendler SJB (1993) Langmuir 9:2356
33. Jue R, Lambert JM, Pierce LR, Traut RR (1978) Biochemistry 17:5399
34. Lambert JM, Jue R, Traut RR (1978) Biochemistry 17:5406
35. Kenny JW, Fanning TG, Lambert JM, Traut RR (1979) J Mol Biol 151
36. Park IS, Kim WY, Kim N (2000) Biosens Bioelectron 15:167
37. Aizawa M, Yun K, Haruyama T, Yanagida Y, Kobatake E (1998) Supramol Sci 5:761
38. Spangler BD, Tyler BJ (1999) Anal Chim Acta 399:51
39. Taylor RF (ed) (1991) Protein immobilisation, fundamentals and applications. Dekker, New York, p 278
40. Lepesheva GI, Turko IV, Ges IA, Chashchin VL (1994) Biochem (Moscow) 59:701
41. Plomer M, Guilbault GG, Hock B (1992) Enzyme Microb Technol 14:230
42. Atilli BS, Suleman AA (1995) Anal Lett 28:2149
43. König B, Grätzel M (1994) Anal Chem 66:341
44. König B, Grätzel M (1995) Anal Chim Acta 309:19
45. Raman Suri C, Jain PK, Mishra GC (1995) J Biotechnol 39:27
46. Carter RM, Jacobs MB, Lubrano GJ, Guilbault GG (1995) Anal Lett 28:1379
47. König B, Grätzel M (1993) Anal Lett 26:2313

48. König B, Grätzel M (1993) Anal Chim Acta 281:13
49. König B, Grätzel M (1994) Bioorg Med Chem Lett 20:2429
50. King WH Jr (1963) International symposium on humidity and moisture, paper C15.11
51. King WH Jr (1964) Anal Chem 36:1735
52. Oberg P, Ligensjo J (1959) Rev Sci Instrumen 30:1053
53. Hlavay J, Guilbault GG (1977) Anal Chem 49:1890
54. Guilbault GG (1980) Ion-Selec Electrode Rev 2:3–16
55. Guilbault GG (1981) Intern J Environ Anal Chem 10:89
56. Alder JF, McCallum JJ (1983) Analyst 108:1169
57. Guilbault GG, Jordan JM (1988) Crit Rev Anal Chem 19:1
58. Guilbault GG (1983) Anal Chem 55:1682
59. Shons A, Dorman F, Najarian N (1972) L Biomed Mat Res 6:565
60. Olivera JR, Silver SP (1980) US Patent No. 4242096
61. Rice TK (1980) US Patent No. 4236893
62. Rice TK (1982) US Patent No. 4314821
63. Konash PL, Bastiaans GJ (1980) Anal Chem 52:1929
64. Thompson M, Arthur CL, Dhaliwal GK (1986) Anal Chem 58:1206
65. Muramatsu H, Kijiwara K, Tamiya E, Karube I (1986) Anal Chim Acta 188:257
66. Ebersole RC, Ward MD (1988) J Am Chem Soc 110:8623
67. Sauerbrey G (1959) Z Phys 155:206
68. Muramatsu H, Watanabe Y, Hikuma M, Ataka T, Kubo I, Tamiya E, Karube I (1989) Anal Lett 299:2155
69. Ebersole RC, Miller JA, Moran JR, Ward MD (1990) J Am Chem Soc 112:3239
70. Prusak-Sochaczewski E, Luong JHT, Guilbault GG (1990) Enzyme Microb Technol 12:173
71. Prusak-Sochaczewski E, Luong JHT (1990) Anal Lett 23:401
72. Ngeh-Ngwainbi J, Foley PH, Kuan SS, Guilbault GG (1986) J Am Chem Soc 108:5444
73. Hahn EC (1988) PhD Thesis, University of New Orleans, New Orleans LA
74. Neuman MR, Perlaky SC, Mickalski JP, Bass JB, McCombs CC (1995) EMBC, paper 7.1.3.8
75. Borman S (1987) Anal Chem 59:1161A
76. Rajakovic J, Ghaemmaghami V, Thompson M (1989) Anal Chim Acta 217:111
77. Barzana E (1995) Adv Biochem Eng Biotechnol 53:1
78. Guilbault GG, Schmid RD (1991) Electrochemical, piezoelectric and fibre optic biosensors. In: Turner APF (ed) Advances in biosensors, vol 1. JAI-Elsevier, Amsterdam, P 264
79. Luong JHT, Guilbault GG (1991) Analytical applications of piezoelectric crystal biosensors. In: Blum LJ, Coulet PR (eds) Biosensors, principles and applications. Dekker, New York
80. Guilbault GG, Luong JHT (1988) J Biotech 9:1
81. Guilbault GG (1988) 5th Symposium on ion-selective electrodes, Matrafured
82. Bunde RL, Jarvi EJ, Rosentreter JJ (1998) Talanta 46:1223
83. Ngeh-Ngwainbi J, Suleiman AA, Guilbault GG (1990) Biosens Bioelectron 5:13
84. Walton PW, Butler ME, O'Flaherty MR (1991) Biochem Soc Trans 19:44
85. Plomer M, Guilbault GG, Hock B (1992) Enzyme Microb Technol 14:230
86. Su XL, Li Y (2004) Biosens Bioelectron 19:563
87. Jacobs MB, Carter RM, Lubrano GJ, Guilbault GG (1995) Am Lab 26
88. Minunni M, Mascini N, Carter RM, Jacobs MB, Lubrano GJ, Guilbault GG (1996) Anal Chim Acta 325:169

89. Vaughan RD, O'Sullivan CK, Guilbault GG (2001) Enz Microb Technol 29:635
90. Bovenizer JS, Jacobs MB, O'Sullivan CK, Guilbault GG (1998) Anal Lett 31:1287
91. Kim N, Park IS, Kim DK (2004) Sensor Actuator B 100:432
92. Carter RM, Mekalanos JJ, Jacobs MB, Lubrano GJ, Guilbault GG (1995) J Immunol Methods 187:121
93. Le D, He FJ, Jiang TJ, Nie L, Yao S (1995) J Microbio Meth 23:229
94. Si SH, Chen JH, He FJ, Nie LH, Yao SZ (1996) Chinese J Chem 14:222
95. Ben-Dov I, Willner I, Zisman E (1997) Anal Chem 69:3506
96. Si S, Ren F, Cheng W, Yau S (1997) Fresenius J Anal Chem 357:1101
97. Fung YS, Si SH, Zhu DR (200) Talanta 51:151
98. Park IS, Kim N (1998) Biosens Bioelectron 13:1091
99. Park IS, Kim N (1998) Biosensors '98, Berlin, 3–5 June
100. Ye JM, Letcher SV, Rand AG (1997) J Food Sci 62:1067
101. Pathirana ST, Barbaree J, Chin BA, Hartell MG, Neely WC, Vodyanoy V (2000) Biosens Bioelectron 15:135
102. Wong YY, Ng SP, NG MH, Si SH, Yao SZ, Fung YS (2002) Biosens Bioelectron 17:676
103. Su X, Li SFY (2001) Anal Chim Acta 429:27
104. Wu ZY, Shen GL, Yu RQ, Wang SP, Zeng XF (1997) Chem J Chinese U 18:1774
105. Wu ZY, Shen GL, Li ZQ, Wang SP, Yu RQ (1999) Anal Chim Acta 398:57
106. He F, Geng Q, Zhu W, Nie L, Yao S, Meifeng C (1994) Anal Chim Acta 289:313
107. Ebersole RC, Foss RP, Ward MD (1991) Bio Technol 9:450
108. Bao L, Deng L, Nie L, Yao S, Wei W (1996) Anal Chim Acta 319:97
109. Ishimori Y, Karube I, Suzuki S (1981) Appl Environ Microb 42:632
110. Ivnitski D, Abdel-Hamid I, Atanasov P, Wilkins E (1999) Biosens Bioelectron 14:599
111. Guilbault GG, Luong JHT (1995) Piezoelectroc immunosensors and their applications in food analysis. In: Guilbault GG, Wagner G (eds) Food biosensor analysis. Dekker, New York
112. Nakanishi K, Karube I, Hiroshi S, Uchida A, Ishida Y (1996) Anal Chim Acta 325:73
113. Nakanishi K, Masoe A, Sako Y, Ishida Y, Muguruma H, Karube I (1996) Anal Lett 29:1247
114. Nakanishi K, Muguruma H, Karube I (1996) Anal Chem 68:1695
115. Kurosawa S, Kamo N, Matsui D, Kobatake Y (1990) Anal Chem 62:353
116. Kößlinger C, Drost S, Aberl F, Wolf H, Koch S, Woias P (1992) Biosens Bioelectron 7:397
117. Kößlinger C, Drost S, Aberl F, Wolf H (1994) Fresenius J Anal Chem 349:349
118. Aberl F, Wolf H, Kößlinger C, Drost S, Woias P, Koch S (1994) Sensor Actuator B 18–19:271
119. Uttenhaler E, Kößlinger C, Drost S (1998) Anal Chim Acta 362:91
120. Uttenhaler E, Kößlinger, Drost S (1998) Biosens Bioelectron 13:1279
121. Susmel S, O'Sullivan CK, Guilbault GG (2000) Enzyme Microb Technol 27:639
122. Su XD, Li SFY, Liu W, Kwang J (2000) Analyst 125:725
123. Rickert J, Weiss T, Kraas, Jung G, Gopel W (1996) Biosens Bioelectron 11:591
124. Rickert J, Weiss T, Gopel W (1996) Sensor Actuator B 31:45
125. Rickert J, Brecht A, Gopel W (1997) Biosens Bioelectron 12:567
126. Lee YG, Chang KS (2005) Talanta 65:1335
127. König B, Grätzel M (1992) Anal Chim Acta 276:329
128. König B, Grätzel M (1993) Anal Chim Acta 280:37
129. Raman Suri C, Raje M, Mishra GC (1994) Biosens Bioelectron 9:535
130. Chu X, Jiang JH, Shen GL, Yu RQ (1996) Anal Chim Acta 336:185
131. Chu X, Lin ZH, Shen GL, Yu RQ (1996) Chem J Chinese U 17:1025

132. Tajima I, Asami O, Sugiura E (1998) Anal Chim Acat 365:147
133. Su X, Chew FT, Li SFY (1999) Anal Biochem 273:66
134. Hu JM, Pei RJ, Hu Y, Zeng YE (1998) Chinese J Chem 16:219
135. Pei RJ, Hu JM, Hu Y, Zeng Y (1998) J Chem Technol Biotech 73:59
136. Hu J, Liu L, Danielsson B, Zhou X, Wang L (2000) Anal Chim Acta 423:215
137. Chu X, Shen GL, Yu RQ (1996) Analyst 121:1689
138. Deng T, Li JS, Wang H, Shen GL, Yu RQ (2004) J Immunol Methods 299:1
139. Lepesheva GI, Turko IV, Ges IA, Chashchin VL (1994) Biochem (Moscow) 59:701
140. Chu X, Lin ZH, Shen GL, Yu RQ (1996) Chem J Chinese U 17:870
141. Pei RJ, Hu JM, Hu Y, Zeng YE (1998) Chem J Chinese U 19:363
142. Shao B, Hu Q, Hu J, Zhou X, Zhang W, Wang X, Fan X (1993) Fresenius J Anal Chem 346:1022
143. Muratsugu M, Ohta F, Miya Y, Hosokawa T, Kurosawa S, Kamo N, Ikeda H (1993) Anal Chem 65:2933
144. Sakai G, Saiki T, Uda T, Miura N, Yamazoe N (1995) Sensor Actuator B 24:134
145. Xia C, Guoli S, Feiye X, Ruqin Y (1997) Anal Lett 30:1783
146. Kurosawa S, Aizawa H, Yoshimioto M (2000) IEEE T Ultrason Ferr 47:1256
147. Ghourchian HO, Kamo N, Hosokawa T, Akiyawa T (1994) Talanta 41:401
148. Kurosawa S, Muratsugu M, Ghourchian HO, Kamo N (1990) ACS Symp Ser 657:185
149. Muratsugu M, Kurosawa S, Ghourchian HO, Kamo N (1997) Bunseki Kagaku 46:917
150. Zhang B, Mao Q, Zhang X, Jiang T, Chen M, Yu F, Fu W (2004) Biosens Bioelectron 19:71
151. Deng T, Wang H, Li JS, Hu SQ, Shen GL, Yu RQ (2004) Sensor Actuator B 99:123
152. Michalzik M, Wendler J, Rabe J, Buttgenbach S, Bilitewski U (2005) Sensor Actuator B 105:508
153. Michalzik M, Wilke R, Buttgenbach S (2005) Sensor Actuator B 111–112:410
154. Raman Suri C, Jain PK, Mishra GC (1995) J Biotechnol 39:27
155. Atilli BS, Suleman AA (1996) Microchem J 54:174
156. Halamek J, Makower A, Skladal P, Scheller FW (2005) Biosens Bioelectron 17:1045
157. Miura N, Higobashi H, Sakai G, Takeyasu A, Uda T, Yamazoe N (1993) Sensor Actuator B 13:188
158. Yun K, Kobatake E, Haruyama T, Laukkanen ML, Keinanen K, Aizawa M (1998) Anal Chem 70:260
159. Kobatake E, Yun K, Yanagida Y, Haruyama T, Keinanen K, Aizawa M (2000) Sensor Actuator B 65:42
160. Carter RM, Jacobs MB, Lubrano GJ, Guilbault GG (1995) Anal Lett 28:1379
161. Harteveld JLN, Nieuwenhuizen MS, Wils ER (1997) Biosens Bioelectron 12:661
162. Gao Z, Chao F, Chao Z, Li G (2000) Sensor Actuator B 66:193
163. Gao Z, Tao G, Li G (1998) J Hyg Res 2:122
164. Bizet K, Gabrielli C, Perrot H, Therasse J (1998) Biosensors '98, Berlin, 3–5 June
165. Guilbault GG, Hock B, Schmid R (1992) Biosens Bioelectron 7:411
166. Kindervater R, Gebbert A, Kramer P, Schmid R (1990) DECAMA Biotechnology Conference, vol 4. VCH, Weinheim, p 19–27
167. Minunni M, Skladal P, Mascini M (1994) Life Chem Rep 11:391
168. Yokoyama K, Ibekuburo K, Tamiya E, Karube I, Ichiki N, Arikawa Y (1995) Anal Chim Acta 304:139
169. Steegborn C, Skladal P (1997) Biosens Bioelectron 12:19
170. Minnuni M, Skladal P, Mascini M (1994) Anal Lett 27:1475
171. Horacek J, Skladal P (1997) Anal Chim Acta 347:43
172. Liu M, Li QX, Rechnitz GA (1999) Anal Chim Acta 387:29

173. Pribyl J, Hepal M, Skládal P (2006) Sensor Actuator B 113:900
174. Masson M, Yun K, Haruyama T, Kobatake E, Aizawa M (1995) Anal Chem 67:2212
175. Horacet J, Skladal P (2000) Anal Chim Acta 412:37
176. Abad JM, Pariente F, Hernandez L, Abruna HD, Lorenzo E (1998) Anal Chem 70:2848

Springer Ser Chem Sens Biosens (2007) 5: 281–302
DOI 10.1007/5346_030

Published online: 11 August 2006

Specific Adsorption of Annexin A1 on Solid Supported Membranes: A Model Study

Claudia Steinem[1] · Andreas Janshoff[2] (✉)

[1]Institute of Organic and Biomolecular Chemistry, Georg August-University, Tammannstr. 2, 37077 Göttingen, Germany

[2]Institute of Physical Chemistry, University of Mainz, Welder Weg 11, 55128 Mainz, Germany
janshoff@mail.uni-mainz.de

Abstract The quartz crystal microbalance (QCM) is an invaluable tool to monitor protein–membrane and membrane–membrane interactions mediated by proteins without labeling one of the components. In this chapter we show that the formation process of solid supported membranes by spreading and fusion of lipid vesicles can be readily followed by the QCM technique, and that Monte Carlo simulations allow for a detailed modeling of the process. We further demonstrate that only membranes attached to a solid support make it possible to separate the two binding modes of annexin A1 to membranes, hence allowing a quantitative analysis of the two processes. By monitoring the changes in the resonance frequency of 5-MHz quartz plates combined with Monte Carlo simulations, the kinetics of the annexin A1–membrane interaction can be followed in detail, which contributes to the biological understanding of annexin A1 function in the cell. The simultaneous readout of the change in resonance frequency and dissipation allows one to follow the binding of lipid vesicles, the second membrane binding process, to membrane-bound annexin A1, which gives information on the impact of different parameters, such as the *N*-terminus of annexin A1 and the protein surface coverage.

Keywords Solid supported membranes · Annexin A1 · Vesicle adsorption · Monte Carlo simulations · Kinetic analysis

Abbreviations

BSA	Bovine serum albumin
DOPE	1,2-Dioleoyl-*sn*-glycero-3-phosphoethanolamine
DPPC	1,2-Dipalmitoyl-*sn*-glycero-3-phosphocholine
DPPS	1,2-Dipalmitoyl-*sn*-glycero-3-phosphoserine
LB	Langmuir–Blodgett
MC	Monte Carlo
POPC	1-Palmitoyl-2-oleoyl-*sn*-glycero-3-phosphocholine
POPS	1-Palmitoyl-2-oleoyl-*sn*-glycero-3-phosphoserine
QCM	Quartz crystal microbalance
RSA	Random sequential adsorption
SSM	Solid supported membrane

1 Solid Supported Membranes

1.1 Introduction

Biological membranes are the common basis for all living organisms. A thin lipid bilayer with extraordinary mechanical and electrical properties not only forms the essential permeability barrier to the outer world but also hosts most of the functional components necessary, for example, to create chemical energy, and provides nanoscopic compartments effectively separating different biochemical pathways within living cells. Composed mainly of phospholipids, which form the basis of its fluid crystalline nature, a number of particular lipids, steroids, and membrane-associated proteins are required to add function to this unique structure. Interaction of biological membranes with the outer world is mainly governed by a large variety of proteins specifically interacting with particular receptor lipids and proteins presented by the biomolecular layer.

As a consequence, researchers from different disciplines of the life sciences ask for efficient and sensitive techniques to characterize protein binding to and release from natural and artificial membranes. Native biological membranes are often substituted by artificial lipid bilayers bearing only a limited number of components and rendering the experiment more simple, which permits the extraction of real quantitative information from binding experiments. Adsorption and desorption are characterized by rate constants that reflect the interaction potential between the protein and the membrane interface. Rate constants of adsorption and desorption can be quantified by means of sensitive optical techniques such as surface plasmon resonance spectroscopy (SPR), ellipsometry (ELL), reflection interference spectroscopy (RIfS), and total internal reflection fluorescence microscopy (TIRF), as well as acoustic/mechanical devices such as the quartz crystal microbalance (QCM)

and, more recently, cantilever arrays. A typical binding experiment using these techniques is performed as follows. The sensor surface, which is generally made of gold, glass, or a polymer coating, is functionalized with membrane-embedded molecules that serve as the binding sites for the proteins in solution. A solution containing the protein ligand is then applied to the sensing surface, and adsorption is monitored by recording the change of a quantity as a measure of the surface coverage such as the optical thickness or the decrease in frequency as a function of time [1].

1.2 Monitoring the Formation of SSMs by QCM

A prerequisite for adsorption studies of proteins on membranes is the formation of solid supported lipid membranes (SSMs) with sufficient lateral lipid mobility on the quartz resonator. Planar lipid bilayers on solid substrates can be prepared by a variety of methods depending on the chosen lipids and supports. Successful preparations on mica, glass, semiconductors, for instance indium tin oxide (ITO) or silicon, and various metal surfaces such as gold or platinum have been described [2]. Surface attachment can be achieved by employing the Langmuir–Blodgett (LB) method or self-assembly techniques or even a combination of both [3]. While LB films offer control over the composition and lateral pressure of both leaflets, self-assembly techniques are more versatile and the bilayers are easier to prepare. Depending on the surface properties, different strategies are required to form bilayers. While anchoring of lipids via covalent or quasi-covalent linkage appears to be an attractive solution to the problem of membrane immobilization, the maintenance of lateral mobility and a sufficient distance between solid support and the surface-facing membrane leaflet is desirable, if not essential, for the functioning of the lipid bilayer as a matrix for hosting proteins [4].

Among the different available preparation techniques, direct formation of planar lipid bilayers from unilamellar vesicles is the most widespread method for obtaining solvent-free model membranes providing the required platform to study adsorption of proteins.

The QCM has added valuable information about the mechanism of vesicle fusion on a surface. For instance, Kasemo and coworkers have unraveled the formation of planar lipid bilayers on SiO_2 and glassy surfaces by means of the QCM with dissipation (QCM-D) technique in conjunction with SPR, atomic force microscopy (AFM), and computer simulations [5–12]. They found that the process of bilayer formation occurs in three successive steps: (1) in the first stage, vesicles attach to the surface via intermolecular interactions; (2) at a critical surface coverage, the vesicles start to rupture, fuse on the surface, and thus form bilayer islands coexisting with vesicles and uncovered substrate; (3) eventually, a coherent bilayer is formed covering the entire surface.

A critical coverage is not always necessary, as was shown by AFM analysis of single vesicle rupturing as a function of interaction forces. Decher, Brisson, as well as Kasemo and coworkers scrutinized the impact of vesicle size, temperature activation, pH, osmotic pressure, and surface chemistry on the kinetics of bilayer formation employing mainly the QCM-D technique [9, 13–15]. Reimhult et al. [8] recently managed to separate coverage of adsorbed vesicles from planar bilayers by means of SPR in combination with QCM-D making use of the fact that the dissipation signal originates solely from attached vesicles. The results were corroborated by AFM images of the process. The critical vesicle surface coverage to initiate rupture and fusion was determined to be around 33% at 22 °C for monodisperse 1-palmitoyl-2-oleoyl-*sn*-glycero-3-phosphocholine (POPC) vesicles on SiO_2.

Faiss et al. [16] and Pignataro et al. [17] modified the interaction force by tuning the number of receptor ligand bonds and surface charge density between appropriately functionalized vesicles and gold surfaces to study the influence of adhesion energy on the bilayer formation kinetics [18, 19]. We found that 30–50% of receptor-bearing lipids is required to provide a reasonably fast kinetics to create lipid bilayers on the surface. Figure 1 schematically depicts the bilayer formation process of biotin-bearing vesicles spreading on a protein cushion composed of a monolayer of biotinylated bovine serum albumin (BSA) and a second monolayer of streptavidin [17, 19].

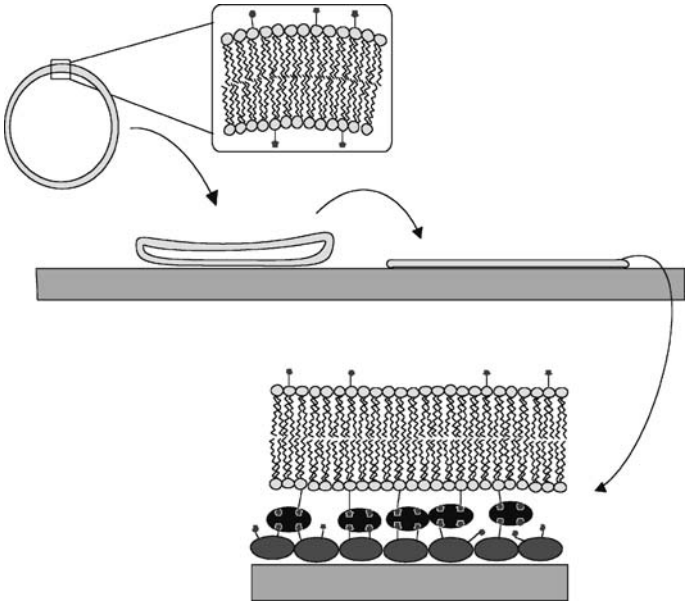

Fig. 1 Schematic view of the SSM formation process of biotinylated vesicles on a protein cushion of streptavidin and biotinylated bovine serum albumin attached to mica

Depending on the biotin content, we observed mainly intact vesicles on the surface exhibiting a height that decreases with increasing amount of biotinylated lipids, then the coexistence of vesicles and bilayers, and at very high biotin content above 30 mol % solely bilayer patches. In fact, we found that no critical vesicle coverage is necessary, in this case supported by the observation that individual liposomes rupture on the functionalized surface. Figure 2 shows in situ AFM images of vesicles adsorbed on streptavidin containing only 2 mol % of biotinylated lipids, as well as bilayer patches originating from ruptured liposomes functionalized with 30 mol % of biotinylated lipids.

A simple model as proposed by Lüthgens [20] and Janke [21] is depicted in Fig. 3a capturing the two relevant processes, adsorption and rupture, following the pioneering work of Kasemo and coworkers [5]. The master equation has been solved numerically by means of Monte Carlo (MC) simulations, typically resulting in a surface coverage as depicted in Fig. 3b depending on the rate constants involved. Intact vesicles are white circles, bilayers are gray patches, and the uncovered surface is black. The impact of variation in k_{rup} on the response of a shear-mode resonator is illustrated in Fig. 3c. Due to the fact that vesicles are viscoelastic bodies causing a considerably larger frequency decrease than a bilayer, an overshoot is sometimes displayed (solid

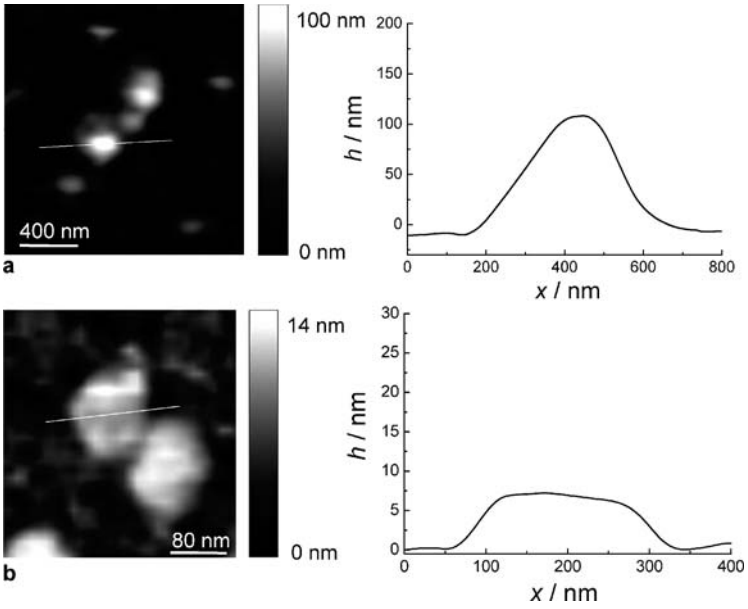

Fig. 2 In situ AFM images (*left*) and line scans (*right*) of biotinylated vesicles with a nominal diameter of 100 nm attached to a streptavidin monolayer. **a** A low biotin content (2 mol %) results in the adsorption of intact liposomes within the timescale of observation (about 1 h); **b** a high biotin content (30 mol %) yields planar lipid bilayers exhibiting a typical height of 5–6 nm

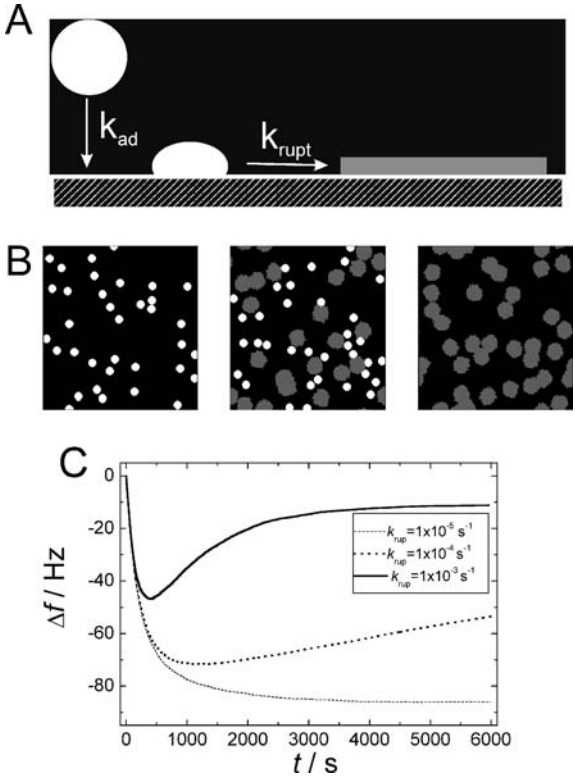

Fig. 3 **a** Model of vesicle rupture induced by adhesion involving two rate constants; k_{ad} represents the adsorption rate determined by the interaction potential and k_{rup}, the constant of vesicle rupture. **b** Surface coverage after different time periods during the Monte Carlo simulation. **c** Impact of increasing k_{rup} on the frequency shift of the QCM covered with biotinylated vesicles

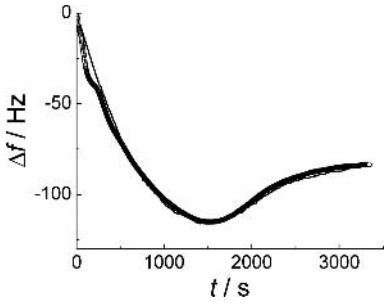

Fig. 4 Results of fitting k_{rup} and k_{ad} to find best accordance between the dynamic Monte Carlo simulations and experiments. In this particular case, POPC vesicles were doped with 5 mol % of biotinyl Cap DOPE and the frequency change of a 5-MHz quartz plate functionalized with avidin was read out. The *solid line* is the result of the Monte Carlo simulation

line) depending on the rate constants. Janke managed to extract the relevant rate constants involved in the rupture process from fitting MC simulations to the experimental data (Fig. 4) [21].

In this way, it was possible to assign the two rate constants of vesicle adsorption k_{ad} and rupture k_{rup} to a number of ligand–receptor pairs represented by the biotin content of the liposomes. The procedure is shown in Fig. 5a–d. The solid lines denote the simulation while the gray dots are results from QCM measurements. The insets show the surface coverage at the

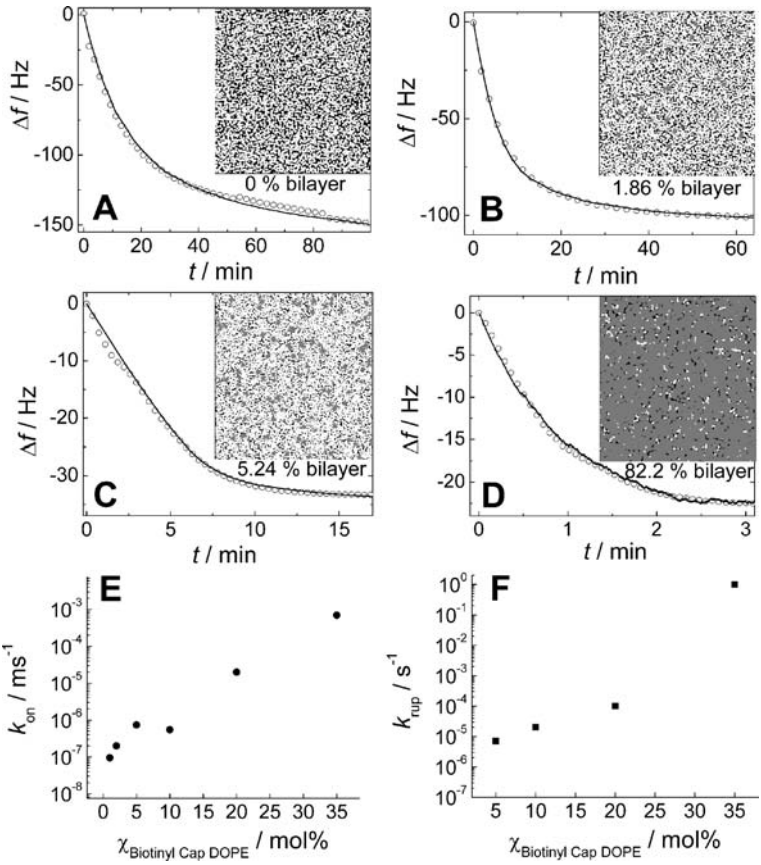

Fig. 5 Frequency response (*dots*) of a 5-MHz quartz resonator after addition of DPPC/biotinyl Cap DOPE vesicles with varying amounts of biotinylated lipid. The *solid black line* is the result of the dynamic MC simulation. The *images in the insets* are snapshots of the MC simulation taken at the end of the simulation given by the experiment. The final bilayer coverage is also depicted. **a** $\chi_{biotin} = 0.02$, $k_{on} = 2.4 \times 10^{-7}$ ms^{-1}. **b** $\chi_{biotin} = 0.1, k_{on} = 1.3 \times 10^{-6}$ ms^{-1}, $k_{rup} = 2 \times 10^{-6}$ s^{-1}. **c** $\chi_{biotin} = 0.2, k_{on} = 6.0 \times 10^{-5}$ ms^{-1}, $k_{rup} = 2 \times 10^{-5}$ s^{-1}. **d** $\chi_{biotin} = 0.35$, $k_{on} = 4.2 \times 10^{-4}$ ms^{-1}, $k_{rup} = 2.5 \times 10^{-2}$ s^{-1}. **e** k_{on} as a function of biotin content in the liposomes. **f** k_{rup} as a function of biotin content

end of the corresponding dynamic MC simulation. Figure 5e summarizes the outcome of the fitting procedures. Naturally, both rate constants increase tremendously with increasing biotin content in the vesicles (note that the *y* scale is logarithmic). In conclusion, a simple model involving merely two rate constants satisfactorily explains the dynamics of vesicle rupture based on increased adhesion to the surface.

2
Interaction of Annexin A1 with Membranes

2.1
Adsorption of Annexin A1 on SSMs

2.1.1
Introduction

Annexin A1 belongs to a protein family that is identified by its common property of binding cellular membranes in a Ca^{2+}-dependent manner (for a review, see [22]). Hundreds of annexin genes are expressed in vertebrates ("A" annexins), invertebrates ("B" annexins), plants ("D" annexins), and other eukaryotes [23]. Twelve different annexin genes were found in mammals, at least some of which are expressed simultaneously in each cell type. This complex and overlapping expression pattern of a structurally conserved protein family renders the elucidation of their individual cellular functions very cumbersome. It is common for all annexins that the highly conserved protein core domain bears the Ca^{2+}- and phospholipid-binding sites, which are all located at the convex side of the slightly curved disk-shaped protein (Fig. 6a). Preceding this core is an *N*-terminal domain, which is unique, varies in length and amino acid composition, and harbors phosphorylation and binding sites for other proteins (Fig. 6b) [24, 25]. Based on this individuality it is proposed that the *N*-terminal domain might mediate specialized functions of each annexin, explaining the need for a large variety of different annexin gene products. For example, annexin A1 has been found primarily at the plasma membrane and at early as well as late endosomes [26, 27], and it is thus proposed to be involved in endocytosis.

To elucidate the particular binding characteristics of each annexin as a function of the calcium ion concentration, membrane model systems have been employed [28–31]. The most common ones are vesicle copelletation assays to elucidate the Ca^{2+} sensitivity of the different annexins [32]. One major problem of vesicle copelletation assays is that membrane binding of annexin might be superimposed by vesicle aggregation, and that the reversibility of binding at a certain Ca^{2+} concentration cannot be accessed, which hampers quantitative analysis of annexin adsorption to membranes.

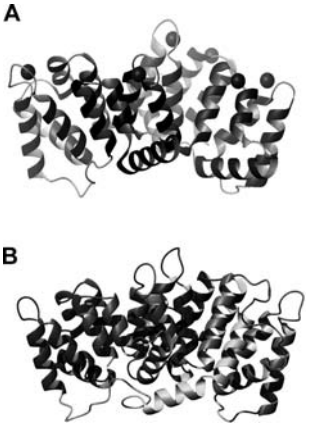

Fig. 6 **a** Crystal structure of annexin A1. The *N*-terminus is not displayed. The balls show bound Ca^{2+} ions (PDB-number: 1HM6). **b** Crystal structure of full length annexin A1 including the *N*-terminus in the absence of Ca^{2+} ions (PDB-number: 1MCX) [49]

To overcome the problem of aggregation, planar artificial membranes have been used such as phospholipid monolayers at the air–water interface [33–35] and SSMs [36–39]. By means of SSMs, the primary binding of annexin can be readily separated from membrane aggregation, which involves two membrane interfaces.

2.1.2 Monitoring Adsorption of Annexin A1 on SSMs by QCM

In order to exclusively investigate annexin binding to one membrane interface we used lipid bilayers attached to a gold support [40]. Our goal was to elucidate to what extent the amount of reversibly bound protein, the kinetic parameters, and the lateral organization on the membrane are influenced by the Ca^{2+} concentration. The QCM technique turned out to be an excellent tool to unravel the mechanism of annexin A1 adsorption to phospholipid membranes as a function of the calcium content in solution. SSMs composed of POPC/POPS (4 : 1) on top of a self-assembled monolayer of octanethiol immobilized on the gold electrode of a quartz plate were used for these investigations [37]. Protein binding to the membrane was initiated by adding 0.4 μM annexin A1 in the presence of different Ca^{2+} concentrations. Annexin A1 binding to the SSM was manifested by a substantial decrease in resonance frequency, with maximum frequency shifts (compiled in Table 1) that are a function of the Ca^{2+} concentration in solution (Fig. 7) [40].

Control experiments with no observable frequency shifts, in which annexin A1 was either added to POPC/POPS membranes in the absence of Ca^{2+} ions or added to POPC membranes in the presence of 1 mM $CaCl_2$,

Table 1 Frequency shifts after adsorption Δf_{ads} and desorption Δf_{des} of annexin A1 on and from POPC/POPS (4 : 1) membranes in the presence of different Ca^{2+} concentrations $c_{Ca^{2+}}$

$c_{Ca^{2+}}$ (mM)	Δf_{ads} (Hz)	Δf_{des} (Hz)
0.01	6 ± 1	4 ± 1
0.05	11 ± 2	8 ± 2
0.50	20 ± 2	15 ± 3
1.00	23 ± 3	18 ± 3

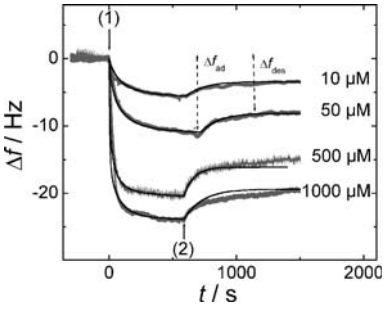

Fig. 7 Response of 5-MHz quartz plates functionalized with solid supported POPC/POPS (4 : 1) membranes upon addition (1) and removal (2) of annexin A1 (0.4 µM) at different Ca^{2+} concentrations. The *black solid lines* are the result of computer simulations by the RSA model [40]

confirm that the observed frequency shifts can solely be attributed to a specific and Ca^{2+}-dependent binding of annexin A1 to acidic phospholipids. Desorption of annexin from the POPC/POPS membranes was initiated by rinsing the system with pure buffer solution containing the corresponding $CaCl_2$ concentration 10 min after protein addition (Fig. 7). Independent of the Ca^{2+} concentration, removal of annexin A1 from solution led to a small increase in resonance frequency indicating annexin A1 desorption from the membrane. From this finding we inferred that the majority of the protein is irreversibly bound on the membrane, while only a minor part is reversibly bound at a given Ca^{2+} concentration. One way to understand these results is to assume a heterogeneous lipid bilayer, in which two differently bound protein populations coexist. In fact, AFM images of POPC/POPS bilayers revealed that such a membrane is partly phase separated in the presence of Ca^{2+} ions [41]. Slightly higher areas (around 0.5–1.0 nm) were observable in the topography images with irregular shapes and mean dimensions of about 20–100 nm, which can be assigned to a POPS-enriched phase that

is rigidified by Ca^{2+}. From the observable size one can roughly estimate that approximately 1000–10 000 POPS molecules participate in one individual POPS-enriched domain.

These phase separated POPC/POPS membranes display two different binding sites for annexin A1. The POPS-enriched phase, to which annexin A1 binds in an irreversible manner, and the POPC-enriched phase, which is composed of single POPS molecules embedded in a POPC matrix, to which annexin A1 adsorbs reversibly. From the area occupied by an individual annexin A1 molecule [42] we estimate that 30–35 lipids are covered by a single protein.

2.1.3 Monte Carlo Simulation of Partly Reversible Adsorption of Annexin A1 on a Heterogeneous Surface

On the basis of the model of a heterogeneous membrane, it is possible to create a simulation scheme based on dynamic Monte Carlo computer simulations of the adsorption and desorption process on heterogeneous surfaces to extract the involved rate constants as a function of the calcium ion concentration. A simple simulation based on a modified, partly reversible, random sequential adsorption (RSA) algorithm provides very good accordance between experiment and measurement. Figure 8 schematically depicts the assumed model.

The surface is divided into areas of irreversible binding sites (POPS-enriched) and reversible binding sites (POPC-enriched). Protein adsorption takes place on both areas, however, at different rates. Protein desorption is allowed only from the reversible binding sites. Mass transport of the proteins to the surface is considered by using a mean field ansatz of a stagnation point flow in accordance with the experimental setup. The kinetics of reversible

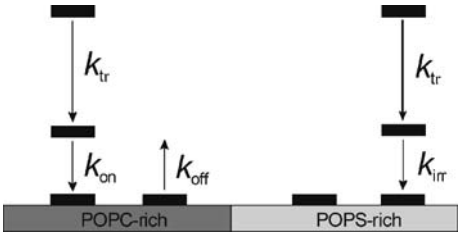

Fig. 8 Illustration of the RSA computer simulations based on the model of heterogeneous surfaces. Annexin A1 binds irreversibly with k_{irr} to circular POPS-rich domains in the membrane, while the adsorption of the protein to POPC-enriched regions is reversible and described by the two rate constants k_{on} and k_{off}. The mass transport to the surface is taken into account by the rate constant k_{tr}

adsorption on a homogeneous surface is governed by the rate equation [43]:

$$\frac{\mathrm{d}\Theta}{\mathrm{d}t} = k_{\mathrm{on}} A \rho(\delta) \Phi(\Theta) - k_{\mathrm{off}} \Theta \tag{1}$$

$$\frac{\mathrm{d}\Theta}{\mathrm{d}t} = k^{*}_{\mathrm{on}} N_{\mathrm{a}}^{-1} \rho(\delta) \Phi(\Theta) - k_{\mathrm{off}} \Theta \,, \tag{2}$$

where Θ denotes the surface coverage, k_{on} and k_{off} are the rate constants of protein adsorption and desorption, A is the area occupied by an adsorbed protein, $\rho(\delta)$ is the number density of protein at the position of the interface, and $\Phi(\Theta)$ is the available surface function. $\rho(\delta)$ depends on the mass transport of proteins to the surface. $k^{*}_{\mathrm{on}} = k_{\mathrm{on}} A N_{\mathrm{a}}$ denotes the rate constant of adsorption in units of $\mathrm{M}^{-1}\mathrm{s}^{-1}$. In the present setup, we used a QCM cell with stagnation point flow geometry so that the flux j to the surface can be approximated by:

$$j = k_{\mathrm{tr}} \left(\rho(\infty) - \rho(\delta) \right) \,, \tag{3}$$

with the transport rate constant k_{tr} and the number density of protein in bulk solution $\rho(\infty)$ [38]. Equation 1 then becomes:

$$\frac{\mathrm{d}\Theta}{\mathrm{d}t} = \frac{k_{\mathrm{on}} A \rho(\infty) \Phi(\Theta) - k_{\mathrm{off}} \Theta}{1 + \frac{k_{\mathrm{on}}}{k_{\mathrm{tr}}} \Phi(\Theta)} \,. \tag{4}$$

Since adsorption of annexin A1 takes place on a heterogeneous surface with different rate constants of adsorption and desorption, Eq. 4 is no longer valid. The Monte Carlo simulation numerically solves the corresponding master equation for off-lattice adsorption on a heterogeneous surface.

$$\frac{\partial P(\alpha, t)}{\partial t} = \sum_{\beta} \left[k_{\beta\alpha} P(\beta, t) - k_{\alpha\beta} P(\alpha, t) \right] , \tag{5}$$

Here, $k_{\alpha\beta}$ and $k_{\beta\alpha}$ denote the transition rates to change from state α to β and vice versa, while $P(\alpha, t)$ and $P(\beta, t)$ are the probabilities that the system is either in state α or β. In accordance with our model, we assume that adsorption on POPS-rich domains is irreversible, while proteins adsorb on the POPC-enriched phase in a fully reversible fashion [44].

By variation of the rate constants k_{on}, k_{off}, and k_{irr}, the course of the simulated frequency shifts can be fitted to the QCM results for a given number and area of domains. The reversible adsorption rate constant (k_{on}) governs the frequency difference before and after rinsing with protein-free buffer, whereas the desorption rate constant (k_{off}) is solely responsible for the time course after rinsing. k_{off} can be approximated independently from the QCM data by fitting a monoexponential function to the time course after the wash. The final frequency shift after buffer rinsing is exclusively determined by irreversible protein adsorption on the POPS-enriched domains (k_{irr}).

Figure 9 shows the surface coverage of a typical dynamic MC simulation before and after rinsing the protein-covered surface with calcium-containing buffer. The small white circles represent annexin A1 molecules, the light gray area the POPS domains, and the black phase is the POPC-enriched membrane phase.

The experimental findings indicate that the membrane domain structure is directly influenced by the Ca^{2+} concentration. Lowering the Ca^{2+} concentration leads to a smaller overall domain area, thus the amount of irreversibly bound protein is reduced. The different Ca^{2+} concentrations could be modeled by altering the area covered by domains. Supported by earlier

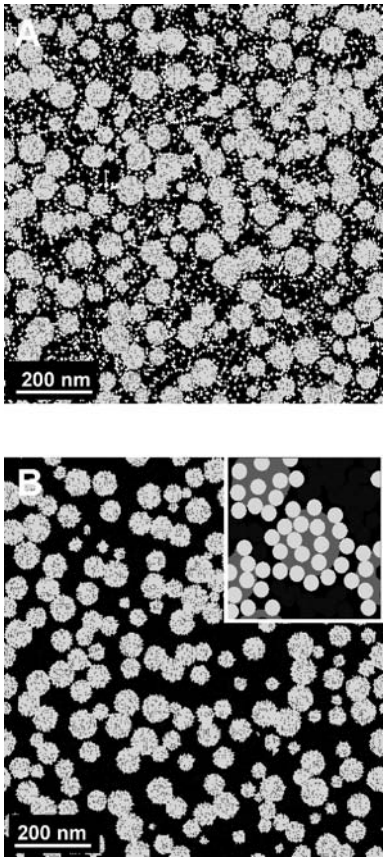

Fig. 9 Surface coverage as obtained by dynamic Monte Carlo simulations **a** before and **b** after rinsing the surface with buffer. Proteins with a diameter of 5 nm (*white circles*) are irreversibly adsorbed on the circular domains (*gray*) that are distributed randomly over the simulation area of $1 \times 1\ \mu m^2$. After the buffer rinse no particles are adsorbed on the POPC-rich area (*black*). The *inset* in **b** shows a magnification to point out the edge effect when particles adsorb irreversibly on the domains [40]

AFM measurements of the domain structure of DPPC/DPPS (4 : 1) monolayers [39, 45], we set the domain area for 1 mM Ca^{2+} to 35% (see Fig. 10c). The POPS-enriched domain area is assumed to be larger than 20%, since PC molecules might also be present in the PS-enriched domains as demonstrated previously [45].

In Fig. 7, the simulated frequency courses for different Ca^{2+} concentrations are shown together with the QCM measurements. The rate constants k_{on}, k_{off}, and k_{irr} were stepwise adapted to achieve the best accordance between QCM data and simulation. The most important parameters as a function of Ca^{2+} concentration are illustrated in Fig. 10.

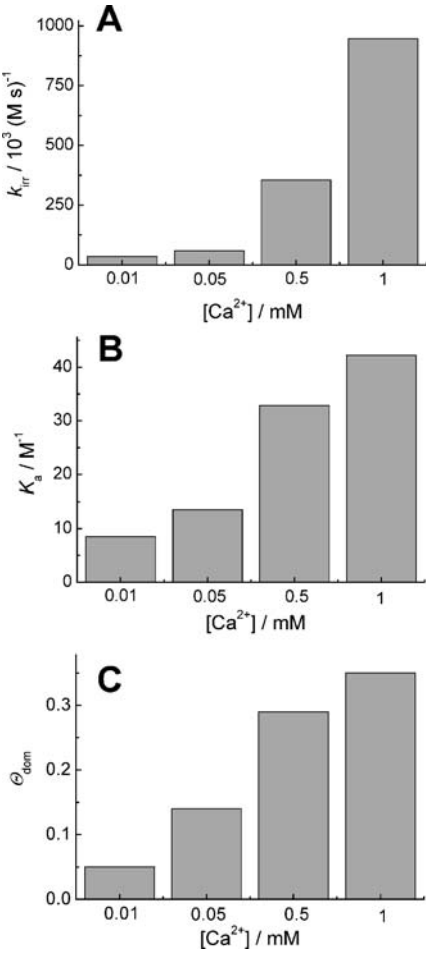

Fig. 10 Parameters obtained from the Monte Carlo simulations shown in Fig. 7 as a function of Ca^{2+} concentration in solution. **a** rate constant of the irreversible binding process, **b** association constant, and **c** surface domain coverage

It turned out that an increase in Ca^{2+} concentration leads to a significant increase of the overall domain area Θ_{dom}, on which irreversible adsorption takes place. k_{off} is constant for all Ca^{2+} concentrations. An increase in Ca^{2+} results in a slight increase of the binding constant indicative of stronger protein binding. k_{irr} exhibits the same behavior; it increases from 35.5×10^3 $(M\,s)^{-1}$ at 10 μM Ca^{2+} to 946×10^3 $(M\,s)^{-1}$ at 1 mM Ca^{2+}.

The fact that annexin A1 binds in part irreversibly to POPC/POPS membranes shows that a simple Langmuir model as assumed in a previous work is not appropriate to model the data [37]. Instead, by simulating the adsorption kinetics using a simple dynamic MC algorithm that essentially numerically integrates the master equation of the adsorption process, we were able to extract kinetic and thermodynamic parameters of the binding process including the heterogeneity of the membrane surface. Although lateral movement of the lipids and proteins was excluded, we were able to establish a good correlation between experiment and simulation.

The results demonstrate that adsorption and desorption of annexin A1 on and from a lipid membrane are rather modular processes and that the combination of SSMs on quartz resonators, and the time-resolved monitoring of the adsorption process in conjunction with Monte Carlo simulations, allow detailed conclusions to be drawn concerning the adsorption process. In particular, a given Ca^{2+} concentration defines the amount of bound annexin at the membrane, in which the majority of the protein is irreversibly bound as long as Ca^{2+} ions are present. In fact, the amount of reversibly bound protein decreases with increasing Ca^{2+} concentration. The rate constant of the irreversible adsorption process on the POPS-enriched domains is considerably increased by the Ca^{2+} concentration. In the context of a biological implication of these observations, it can be envisioned that a Ca^{2+} trigger in the cell leads to the formation of PS-enriched domains on which annexin A1 is irreversibly bound and laterally confined, thus acting as a static platform as long as the Ca^{2+} trigger is on, which might then interact with a variety of other reaction partners.

2.2 Membrane–Membrane Interaction Mediated by Annexin A1

2.2.1 The Binding Assay: Experiment and Simulation

One of the functions of annexin A1 is to connect the plasma membrane with another membrane located in the cell as a function of the calcium ion concentration in the cytosol [28, 32, 36]. In order to prove that annexin A1 is capable of interconnecting two membranes, aggregation assays on 5-MHz quartz resonators were performed as schematically depicted in Fig. 11.

While the convex side harboring the Ca^{2+} binding sites of annexin A1 interacts with the primary membrane, the *N*-terminal domain is thought

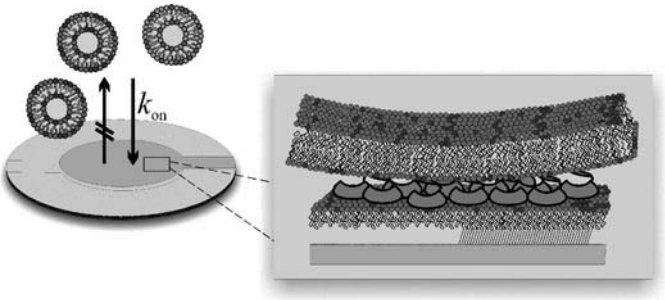

Fig. 11 Schematic drawing of a SSM immobilized on a quartz resonator with membrane-bound annexin A1. Clusters of annexin A1 exposing the *N*-terminus to the aqueous phase appear to be responsible for the binding of lipid vesicles. Vesicles bind irreversibly to the annexin A1 protein platform and do not rupture to planar bilayers upon adsorption

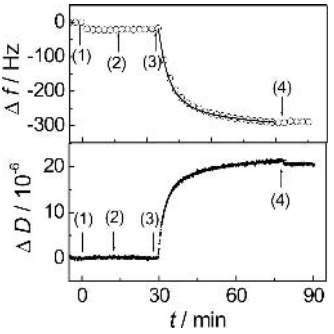

Fig. 12 Change of the resonance frequency and dissipation of a 5-MHz quartz plate upon adsorption of vesicles to membrane-bound annexin A1. After annexin A1 had been bound to the membrane in the presence of 1 mM $CaCl_2$ (1) and the removal of nonbound protein (2), POPC/POPS (4 : 1) vesicles (3) were added. After final values of Δf and ΔD were reached, the system was rinsed with a 1 mM $CaCl_2$ buffer (4). The *solid line* is a result of a RSA simulation [38]

to interact with the second membrane linking the two together [29, 42, 46]. To investigate annexin A1 mediated membrane–membrane interactions, the protein was first adsorbed on a lipid membrane composed of POPC/POPS (4 : 1) at 1 mM $CaCl_2$. A typical time course obtained by means of the QCM technique is shown in Fig. 12.

A frequency shift of $\Delta f = -(21 \pm 2)$ Hz was obtained, which only increased by (2 ± 1) Hz after rinsing with buffer, consistent with the result that a large Ca^{2+} concentration of 1 mM mostly prevents the desorption of membrane-bound annexin A1. The dissipation D did not alter during protein adsorption and the subsequent buffer rinse, demonstrating that the bound protein behaves as a thin rigid mass.

Lipid vesicles with a mean diameter of 120 nm composed of POPC/POPS (4 : 1) (0.1 mg ml^{-1}) were added to membrane-bound annexin A1 and the changes in resonance frequency and dissipation were monitored (Fig. 12). After 45 min, a maximum frequency shift of $\Delta f = -(270 \pm 10)$ Hz and a dissipation shift of $\Delta D = (21 \pm 2) \times 10^{-6}$ were obtained. Notably, the QCM technique is very susceptible to changes in the vesicles' shape on the surface since the liposomes behave as viscoelastic bodies on the resonator's surface. From the observed time course of Δf and ΔD during the vesicle adsorption process, we conclude that the vesicles attach to the SSM via annexin molecules, but remain intact and do not rupture. Since rinsing with buffer does not result in vesicle desorption from the surface, this process can be described as essentially irreversible, at least on the observed timescale. The consequence of an irreversible adsorption process is that the maximum surface coverage is only a function of available binding sites. Assuming that the protein molecules are rather tightly packed, around a hundred annexins at least would be involved in the binding of one individual vesicle. Even if each single binding event was reversible, the overall binding process including multiple binding events would be irreversible. Thus, the maximum coverage is a fixed value only depending on the shape of the vesicles, and not a matter of binding affinity. Binding affinity is solely represented by the rate constant of adsorption. The binding behavior of vesicles to membrane-bound annexin A1 was modeled by Monte Carlo simulations employing a simple, irreversible RSA approach treating the vesicles as hard spheres that adsorb on the surface extended with a mean field ansatz to account for mass transport as described above [5, 47]. The parameter k_{on} was varied in the simulation to provide best agreement between experimental ($\Delta f(t)$) and simulated data, while the starting value of the transport rate k_{tr} was estimated from the geometry of the stagnation point flow cell and then adapted to the data. The result of such a procedure is given in Fig. 12 as a solid line, showing that the simulation is in very good agreement with the experimental data.

2.2.2
Impact of Protein Coverage on Membrane–Membrane Interaction

One advantage of SSMs is the fact that certain parameters such as protein coverage can be individually adjusted. Theoretically, if one annexin A1 bound one vesicle a protein surface coverage of 0.2% would be sufficient to obtain maximum vesicle coverage. However, it turned out that at a protein surface coverage of 8% the maximum change in frequency and dissipation is only about one half of that obtained at maximum annexin surface coverage, indicating that fewer vesicles have been bound. The protein surface coverage was calculated assuming a linear relation between frequency shift and surface coverage, and assuming that the maximum frequency shift of 21 Hz corresponds to a surface coverage of 54% according to the RSA model.

This can easily be explained in terms of lateral two-dimensional aggregates of membrane-bound annexin A1 that bind one vesicle and are in agreement with the observed irreversibility of vesicle binding. It is conceivable that a critical amount of lateral aggregated annexins is needed to represent a binding site. However, the rate of adsorption might be gradually increased with the increased number of annexins (Fig. 13a) contributing to the binding site, as supported by the simulations shown in Fig. 13b.

The dynamic MC simulations depicted in Fig. 13b (curves b and c) were performed leading to k_{on} values of 10 and 24 $(M\,s)^{-1}$, respectively. The difference in maximum surface coverage of the vesicles due to the different number of binding sites (variation in annexin A1 coverage) on the surface was taken into account for the simulations. In summary, a decrease in annexin surface

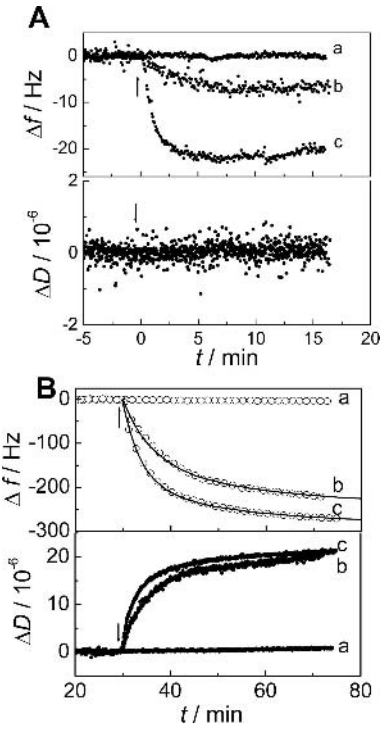

Fig. 13 Time courses of the frequency and dissipation shifts upon addition of POPC/POPS (4 : 1) vesicles to SSMs covered with different amounts of annexin A1. **a** Annexin A1 was added in different concentrations to SSMs composed of POPC/POPS (4 : 1): *a* 0 μM, *b* 0.045 μM, and *c* 0.3 μM. Nonbound annexin A1 was removed by rinsing with buffer. Different surface coverages were obtained as expressed in terms of frequency shifts: *a* 0 Hz, *b* – (6 ± 2)Hz, and *c* – (21 ± 2)Hz. **b** POPC/POPS (4 : 1) vesicles were added to annexin A1 covered membranes. The *solid lines* are the results of simulations using the RSA model

coverage resulted in a decrease in the rate of adsorption by roughly a factor of 2. In similar experiments using a chimeric protein consisting of the *N*-terminus of annexin A1 and the core of annexin A5, Andrée et al. [30] found a linear dependence of vesicle adsorption on protein surface coverage. They also suggested that two-dimensional clustering of the chimeric protein on the SSM is involved in the interaction with phospholipid vesicles.

2.2.3 The Significance of the *N*-terminus for the Membrane–Membrane Interaction

The first membrane binding is mediated via multiple calcium binding sites located at the convex side of the disk-shaped annexin core. The *N*-terminus of the protein that is presumed to harbor the second membrane binding site is buried in the core domain in the absence of Ca^{2+}, and is supposed to get exposed to the aqueous phase if annexin A1 binds to a membrane in the presence of calcium ions (see Fig. 6) [42]. To verify this hypothesis, again SSMs are well suited, since they allow separation of the first and second membrane binding events. *N*-terminal truncated annexin A1 (Δ^{1-29} annexin A1) was prepared by tryptic digestion resulting in a 33-kDa protein fragment as supported by SDS-gel electrophoresis [26]. Adding a 0.3 μM solution of *N*-terminally truncated Δ^{1-29} annexin A1 to POPC/POPS (4 : 1) membranes in the presence of 1 mM $CaCl_2$ results in a similar frequency shift of $-(19 \pm 3)$ Hz upon addition of the protein, compared with that observed for full-length annexin A1 $-(21 \pm 2)$ Hz, which shows that the *N*-terminal truncated protein retains its full membrane binding activity (Fig. 14a).

However, we observed a significantly reduced shift in frequency and dissipation upon vesicle adsorption (POPC/POPS (4 : 1)) to *N*-terminally truncated membrane-bound annexin A1, although the same protein coverage was obtained, which agrees with the idea that a second membrane binding site is located in the *N*-terminal region (Fig. 14b). As the reduced Δf and ΔD values show that fewer vesicles have been bound to the surface, we conclude that the *N*-terminal truncated annexin A1 does not form as many binding sites as full-length annexin. However, it is not yet clear whether the decreasing number of binding sites is caused by a reduced clustering of the *N*-terminal truncated annexin A1 on the surface or, compared to full-length annexin A1 binding sites, larger *N*-terminal truncated protein clusters are necessary to bind one vesicle, as in the latter case the adsorption can only be mediated by part of the protein core. Bitto et al. [36] suggested that some amino acids in the *N*-terminal domain including lysine-26 and -29 as well as the core domain are directly involved in the second membrane interaction of annexin A1. Wang et al. [48] found that truncation of *N*-terminal residues of annexin A1 changes the Ca^{2+} sensitivity for aggregation of chromaffin granules. A further indication for the *N*-terminal domain to participate in the second membrane binding event is given by Andrée et al. [30], who found that a chimeric an-

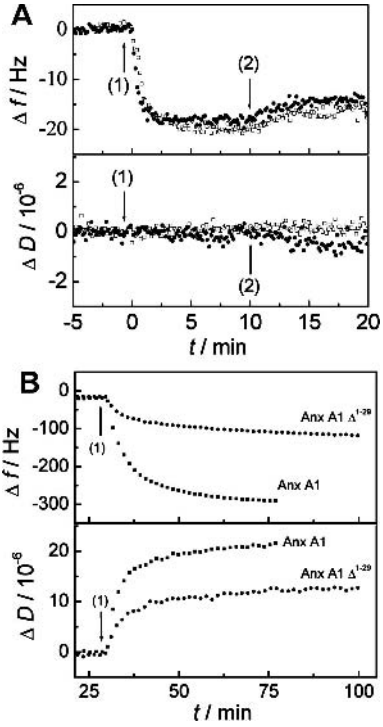

Fig. 14 **a** Frequency and dissipation response of a 5-MHz quartz plate upon (1) addition of annexin A1 (●) and 0.3 μM Δ^{1-29} annexin A1 (□). Nonbound protein was removed by rinsing with buffer (2). **b** Time courses of adsorption of POPC/POPS (4 : 1) added at (1) to membrane-bound annexin A1 (□) or Δ^{1-29} annexin A1 (◯)

nexin $A5_{core}$–annexin $A1_{N\text{-terminus}}$ protein bound to a SSM is able to aggregate vesicles, while annexin A5 is not. Yoon et al. [46] specified the interaction of an *N*-terminal peptide (2–26) of annexin A1 with phospholipids as partially calcium-dependent.

3 Conclusions

Solid supported membranes immobilized on quartz resonators allow for the detection and quantification of protein–membrane and membrane–membrane interactions mediated by proteins. The advantage of the QCM technique is not only that a label-free monitoring of proteins is possible, but also that the good time resolution allows for a detailed quantitative analysis of kinetics, as demonstrated in this chapter by means of Monte Carlo simulations. Moreover, since the quartz oscillation is not only sensitive to

changes in mass but also sensitive to changes of the viscoelasticity of the attached bodies, it is a well-suited technique to monitor vesicle adsorption processes. The technique enables one to elucidate the attachment, deformation, and spreading of vesicles, which gave us new insights into the vesicle spreading process on a surface and the function of annexin A1 in connecting membranes.

Acknowledgements We would like to thank all those people who have contributed experimental data to this work, namely Dr. K. Kastl, Dr. E. Lüthgens, S. Faiß, and M. Janke.

References

1. Janshoff A, Galla H-J, Steinem C (2000) Angew Chem Int Ed 39:4004
2. Janshoff A, Steinem C (2006) Anal Bioanal Chem 385:433
3. Steinem C, Janshoff A (1996) Biochim Biophys Acta 1279:169
4. Janshoff A, Galla H-J, Steinem C (2003) Membr Sci Technol Ser 7:991
5. Zhdanov VP, Keller CA, Glasmästar K, Kasemo B (2000) J Chem Phys 112:900
6. Zhdanov VP, Kasemo B (2001) Langmuir 17:3518
7. Zhdanov VP, Kasemo B (2006) Langmuir 22:3477
8. Reimhult E, Zach M, Höök F, Kasemo B (2006) Langmuir 22:3313
9. Reimhult E, Höök F, Kasemo B (2003) Langmuir 19:1681
10. Keller CA, Glasmästar K, Zhdanov VP, Kasemo B (2000) Phys Rev Lett 84:5443
11. Reimhult E, Höök F, Kasemo B (2002) Phys Rev E 66:051905
12. Dimitrievski K, Reimhult E, Kasemo B, Zhdanov VP (2004) Colloids Surf B 39:77
13. Seantier B, Breffa C, Felix O, Decher G (2005) J Phys Chem 109:21755
14. Richter R, Brisson A (2005) Biophys J 88:3422
15. Richter R, Mukhopadhyay A, Brisson A (2003) Biophys J 85:3035
16. Faiss S, Lüthgens E, Janshoff A (2004) Eur Biophys J 33:555
17. Pignataro B, Steinem C, Galla H-J, Fuchs H, Janshoff A (2000) Biophys J 78:487
18. Lüthgens E, Herrig A, Kastl K, Steinem C, Reiss B, Wegener J, Pignataro B, Janshoff A (2003) Meas Sci Technol 14:1865
19. Reiss B, Janshoff A, Steinem C, Seebach J, Wegener J (2003) Langmuir 19:1816
20. Lüthgens E (2005) Modellierung der Oberflächenreaktionen von Vesikeln und Proteinen mit Hilfe dynamischer Monte Carlo Simulationen. University of Mainz, Mainz
21. Janke M (2004) Molekulare Kontrolle der Adsorption, Adhäsion und Deformation von Liposomen auf funktionalisierten Oberflächen. Eine Quarzmikrowaage Studie. University of Mainz, Mainz
22. Gerke V, Moss SE (2002) Physiol Rev 82:331
23. Moss SE, Morgan RO (2004) Genome Biol 5:219.1
24. Gerke V, Moss SE (1997) Biochim Biophys Acta 1357:129
25. Donato R, Russo-Marie F (1999) Cell Calcium 26:85
26. Seemann J, Weber K, Osborn M, Parton RG, Gerke V (1996) Mol Biol Cell 7:1359
27. Seemann J, Weber K, Gerke V (1997) FEBS Lett 413:185
28. Meers P, Mealy T, Pavlotsky N, Tauber AI (1992) Biochemistry 31:6372
29. de la Fuente M, Parra AV (1995) Biochemistry 34:10393
30. Andree HAM, Willems GM, Hauptmann R, Maurer-Fogy I, Stuart MCA, Hermens WT, Frederik PM, Reutelingsperger CPM (1993) Biochemistry 32:4634

31. Blackwood RA, Ernst JD (1990) Biochem J 266:195
32. Raynal P, Pollard HB (1994) Biochim Biophys Acta 1197:63
33. Rosengarth A, Wintergalen A, Galla H-J, Hinz H-J, Gerke V (1998) FEBS Lett 438:279
34. Koppenol S, Tsao FHC, Yu H, Zografi G (1998) Biochim Biophys Acta 1369:221
35. Freites JA, Ali S, Rosengarth A, Luecke H, Dennin MB (2004) Langmuir 20:11674
36. Bitto E, Tikhonov AM, Schlossmann ML, Cho W (2000) Biochemistry 39:13469
37. Kastl K, Ross M, Gerke V, Steinem C (2002) Biochemistry 41:10087
38. Kastl K, Herrig A, Luthgens E, Janshoff A, Steinem C (2004) Langmuir 20:7246
39. Janshoff A, Ross M, Gerke V, Steinem C (2001) ChemBioChem 7/8:587
40. Kastl K, Menke M, Lüthgens E, Faiß S, Gerke V, Janshoff A, Steinem C (2006) ChemBioChem 7:106
41. Menke M, Gerke V, Steinem C (2005) Biochemistry 44:15296
42. Rosengarth A, Gerke V, Luecke H (2001) J Mol Biol 306:489
43. Adamczyk Z, Weronski P (1999) Adv Colloid Interface Sci 83:137
44. Lüthgens E, Janshoff A (2005) ChemPhysChem 6:444
45. Ross M, Steinem C, Galla H-J, Janshoff A (2001) Langmuir 17:2437
46. Yoon MK, Park SH, Won HS, Na DS, Lee BJ (2000) FEBS Lett 484:241
47. Zhdanov VP, Kasemo B (2000) Langmuir 16:4416
48. Wang J (1994) Int J Mod Phys 5:707
49. Rosengarth A, Luecke H (2003) J Mol Biol 326:1317

Springer Ser Chem Sens Biosens (2007) 5: 303–338
DOI 10.1007/5346_031

Published online: 29 July 2006

The Quartz Crystal Microbalance in Cell Biology: Basics and Applications

Vanessa Heitmann · Björn Reiß · Joachim Wegener (✉)

Institute for Biochemistry, Westfälische Wilhelms-University, Wilhelm-Klemm Str. 2, 48149 Münster, Germany
wegenej@uni-muenster.de

Abstract This chapter describes recent studies in which the quartz crystal microbalance (QCM) technology has been applied as a monitoring tool for animal cells in vitro. With shear wave resonators used as growth substrates it is possible to follow the de novo formation or the modulation of established cell–substrate contacts from readings of the resonance frequency with a time resolution in the order of seconds. From cell adhesion studies it became clear that different cell types induce an individual shift of the resonance frequency but it has been a matter of debate, which subcellular structures determine the individual impact of a given cell type on the QCM response. This question has been addressed by our group in recent years and a summary of our current understanding of this problem will be given here. Different approaches have been applied to challenge the cells in a well-defined way and to monitor the associated changes of the QCM readout. Taken together, these studies have led us to the following conclusions: (i) The cellular bodies primarily lead to an increased energy dissipation that does not correspond to a simple

viscous behavior. (ii) The adhesive proteins underneath the cells provide a measurable contribution to the overall QCM response of adherent cells. (iii) The average distance between lower cell membrane and substrate surface does not have a significant impact on the acoustic load situation. (iv) The QCM is sensitive to cell stiffness and reports in a similar way on changes in cell stiffness, as accessible from scanning force microscopy measurements. (v) The cortical actin cytoskeleton is a dominant contributor to the cells' acoustic response.

Keywords QCM · Cell–substrate interactions · Cell adhesion · Cell spreading · Extracellular matrix · Cellular micromechanics · Cytoskeleton · Cell elasticity · Liposomes · Impedance analysis

Abbreviations

QCM	Quartz crystal microbalance
ECIS	Electric cell–substrate impedance sensing
RICM	Reflection interference contrast microscopy
FLIC	Fluorescence interference contrast microscopy
HC	Hydrocortisone
SFM	Scanning force microscopy

1 QCM as an Emerging Tool in Cell Biology

The quartz crystal microbalance (QCM) was already well-known and established as an analytical tool for studying adsorption phenomena at the solid–liquid interface [1–4] when its potential for studying cell–substrate adhesion was recognized. As reviewed in preceding chapters of this book, the QCM approach is based on thin disks made from α-quartz that are sandwiched between two metal electrodes. Due to the piezoelectric nature of α-quartz, an oscillating electrical potential difference between the two surface electrodes induces a mechanical oscillation of the crystal and vice versa. For QCM purposes, only AT-cut resonators are used that perform shear oscillations parallel to the surface with the maximum amplitude at the crystal faces [5]. The resonance frequency of the mechanical oscillation responds very sensitively to the adsorption of any material upon the resonator surface. In 1959 a linear relationship between the observed shift in resonance frequency and the amount of mass deposited on the surface was established by Sauerbrey [6]. The so-called Sauerbrey equation is, however, only valid for rigid and homogeneous mass films that move synchronously with the resonator surface. If these conditions are met, the device is sensitive enough to report on mass depositions in the submicrogram regime. In a typical bioanalytical application, a receptor molecule (e.g., cell surface receptor, antibody) is immobilized on the quartz surface and the ligand is offered from solution, or the other way round [7, 8].

As soon as molecular recognition and binding occurs, a shift in the resonance frequency of the crystal is induced. The frequency shift can be easily measured and – as long as the Sauerbrey conditions are fulfilled – interpreted in terms of mass increase. It is the strength of the technique to provide label-free, mass-sensitive detection of the binding reaction at the crystal surface in real time.

It was then recognized that the adhesion of cells to the quartz surface also induced a shift in resonance frequency that was shown to be linearly correlated with the fractional surface coverage [9, 10]. Time-resolved measurements of the resonance frequency were then used to follow the attachment and spreading of cells to the quartz surface, with extraordinary time resolution. Comparison with established cytological techniques has proven that the QCM readout reports reliably on the number of cells on the surface and the time course of adhesion [9, 11, 12]. But the technique is more versatile. A few studies have been published in which the QCM is used as a transducer in cell-based drug testing assays [13–15]. Here the change in resonance frequency of already established cell layers serves as a very sensitive measure for changes in cell vitality, which are often mirrored in an perturbed substrate adhesion. Clearly, the technique is still in its infancy with respect to in vitro drug and toxicity testing. But, an enormous number of fundamental or applied scientific problems in cell biology may take advantage of the QCM approach in the future, in particular since the quartz resonators are easily integrated into any cell culture vessel and multi-well devices will be available soon.

However, in order to explore the full potential of the QCM device for cell biological applications it is imperative to understand the individual contributions of subcellular components to the overall signal in detail. A pool of experimental observations exists indicating that the QCM is primarily sensitive to mechanical phenomena associated with the ventral (i.e., the lower, substrate-facing) membrane and the molecular architecture of cell–substrate adhesion sites [16]. To the best of our knowledge, there is only one study in the literature that reports on resonance frequency shifts in response to cellular activities at the apical (upper) membrane. Here, Cans et al. [17] described measurements in which butting and retrieval of exocytotic vesicles was monitored, which only occurs at the site of the cell that is not facing the substrate. In all other reports the observed changes of the QCM parameters could be attributed to the cell–substrate adhesion zone plus the ventral, substrate-facing membrane. It is, however, unclear how parameters like the density of cell–substrate contact sites, the topography of the cell–substrate adhesion zone, or the mechanical properties of the cytoskeleton exert an individual impact on the QCM signal. When all subcellular contributions have been identified, the number of QCM applications in cell biology will increase and the full potential of the technique will be visible. Thus, the present chapter will focus on these questions and provide a few answers as they are known today.

2
Lessons from Cell Adhesion

Although cell adhesion studies based on QCM readings have been successfully performed for many years and are widely known, they will be addressed here in more detail in order to emphasize certain insights extracted from these simple-to-perform experiments. Figure 1 shows a schematic of the experimental setup that was used in our laboratory to measure the shift in resonance frequency during attachment and spreading [12].

The quartz resonator with a fundamental resonance frequency of 5 MHz forms the bottom plate of a measuring chamber that holds approximately 0.5 mL of cell suspension. The oscillation at minimum impedance is stabilized by a feedback-control oscillator circuit[1] that is placed close to the crystal inside a temperature-controlled Faraday cage (37 °C). The oscillator circuit is driven by a 5 V power supply and the resonance frequency is determined by a commercially available frequency counter.

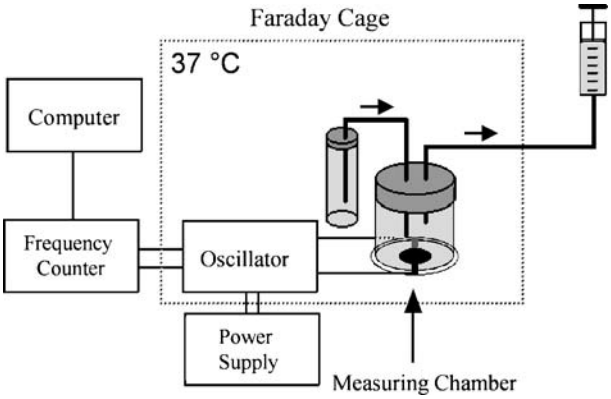

Fig. 1 Experimental setup to monitor the time course of cell attachment and detachment by reading the resonance frequency of the quartz resonator that forms the bottom plate of a cell culture vessel. The measuring chamber is housed in a 37 °C incubator. When an exchange of culture fluid is needed, for instance to expose the cells to some trigger compound, a corresponding reservoir is also placed inside the incubator with a simple transfer mechanism as indicated

2.1
Time Course of Attachment and Spreading

Cells were seeded into the measuring chamber in a sterile flow hood. Immediately afterwards attachment and spreading of the cells was followed with time. Figure 2a compares the time-dependent shift in resonance frequency when

[1] The oscillator circuit based on a Texas Instruments TTL chip was developed by A. Janshoff.

increasing amounts of epithelial MDCK II cells are seeded into the chamber at time zero.

From the upper to the lower part of Fig. 2a the cell density in the measuring chamber was continuously increased from a cell-free control to a maximum of 1.5×10^6 cells cm^{-2}. In the very early phase of all curves there is a moderate increase of the resonance frequency by 50 to 100 Hz, which is exclusively due to warming of the medium inside the chamber to 37 °C. After a transient maximum the resonance frequency continuously decreases and thereby mirrors the formation of cell–substrate adhesion sites and continuous progress in cell attachment and spreading. The time resolution of such measurements can be reduced well below one second so that even very subtle details of the cell adhesion kinetics are available using QCM measurements. The more cells are seeded, the bigger is the resulting shift in resonance frequency upon attachment and spreading.

When the maximum frequency shift Δf_{max} for an individual experiment, as shown in Fig. 2a, is plotted against the number of cells seeded into the measuring chamber at time zero, we obtained a saturation type relationship that is presented in Fig. 2b. We have interpreted this result as follows: as long

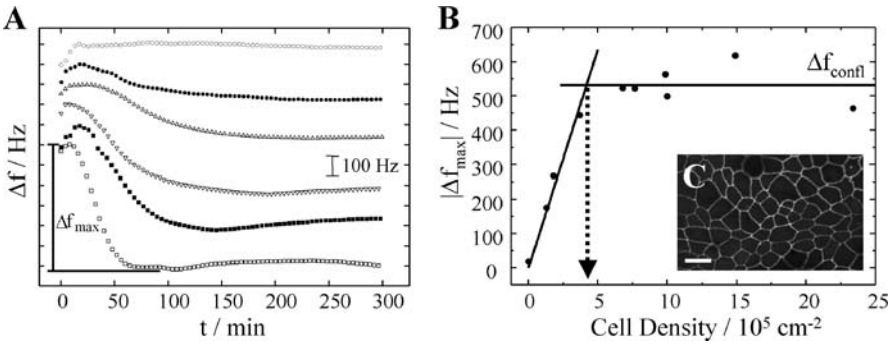

Fig. 2 **a** Shift of the resonance frequency during attachment and spreading of initially suspended MDCK II cells. Each curve represents a different number of cells that were seeded at time zero. From the *upper* to the *lower curve* seeding densities were as follows (in cm^{-2}): *open circles* 0; *filled circles* 1.3×10^5; *up triangle* 1.8×10^5; *down triangle* 3.7×10^5; *filled squares* 7.7×10^5; *open squares* 1.5×10^6. Δf_{max} indicates the maximum frequency shift observed for a given seeding density. Please note that an offset was used to present all experiments together in one figure. **b** Maximum frequency shift Δf_{max} as a function of cell density seeded into the measuring chamber at time zero in the experiments shown in **a**. The data is analyzed by a two-case approach: (i) For low cell densities the *ascending line* indicates the linear correlation between surface coverage and frequency shift. (ii) For high seeding densities a *horizontal regression line* is applied that represents the frequency shift associated with a confluent cell layer. The intersection of lines (i) and (ii) corresponds to the number of cells on the surface (per unit area). **c** Fluorescence micrograph of a confluent MDCK II cell layer after staining for a junctional protein exclusively localized at the cell border. *Scale bar* represents 20 μm

as the density of seeded cells is small enough that all cells reaching the surface can find an adhesion site, an increase in the maximum resonance frequency shift $|\Delta f_{max}|$ is observed with increasing seeding density. This frequency shift is proportional to the fractional surface coverage. However, when the number of seeded cells is further increased, all adhesion sites are occupied and consistently we do not find any further increase in $|\Delta f_{max}|$. This observation already implies that the QCM device is primarily sensitive to phenomena that occur at the quartz surface but does not report on cells that are beyond the first cell monolayer. Based on this data it is hard to imagine that biological activities that occur at the apical surface of an established cell layer can be observed by QCM.

If this interpretation is valid, we should be able to determine the number of cells that actually adhered onto the quartz surface from measurements like those shown in Fig. 2b. To do so, we have chosen a two-case approach: (i) for low seeding densities the relationship is approximated by a straight line with positive slope that indicates the linear correlation between frequency shift and surface coverage; (ii) beyond a certain cell density the experimental adhesion curve is modeled by a horizontal line indicating that any surplus of cells, which do not find an adhesion site on the substrate, does not contribute to the measured QCM response. Accordingly, the interception between the two straight lines should mark the actual cell density on the surface. For the MDCK cells (strain II) that were used in these experiments, we found the interception to be located at a seeding density of $4.3 \pm 0.5 \times 10^5$ cells cm^{-2} (arrow in Fig. 2b). In order to validate this result we have also determined microscopically the cell density in an entirely confluent monolayer after the cell borders had been stained by immunocytochemistry. Figure 2c shows a typical fluorescence micrograph that was used to determine the cell density. Images recorded by fluorescence microscopy revealed a cell density of $5.5 \pm 0.3 \times 10^5$ cells cm^{-2} on the surface, which is slightly above the value extracted from QCM readings. However, microscopic experiments were conducted on cell monolayers that were allowed to grow to confluence for several days while QCM experiments were limited to attachment and spreading within 5 h. Since the cells tend to multiply to some degree even in a confluent monolayer, it is not surprising to find somewhat higher cell densities in our microscopic control experiments. Repeating these kind of experiments with other cell types confirmed our conclusions. We found consistently that the basic interpretation of the data is valid and that the number of cells on the surface is determined correctly from QCM readings.

Table 1 compares the QCM-based cell density on the surface for MDCK cells strain I (MDCK I), MDCK cells strain II (MDCK II) and 3T3 fibroblasts with the outcome of cell density estimates derived from microscopic images [12]. The final shifts in resonance frequency that we observed when the resonator was completely covered by a continuous cell monolayer of either kind (Δf_{confl}) are also summarized in Table 1. Interestingly, different cell

Table 1 Shifts of the resonance frequency Δf_{confl} induced by attachment and spreading of different cell types. In all cases the resonator was completely covered with cells at the end of the experiment. The number of cells per unit area on the surface is determined from QCM experiments N_{QCM} and compared to a microscopic determination N_{Mic}

Cell type	Δf_{confl} (Hz)	N_{QCM} ($10^5 \times \text{cm}^{-2}$)	N_{Mic} ($10^5 \times \text{cm}^{-2}$)
MDCK II	530 ± 25	4.3 ± 0.5	5.5 ± 0.3
MDCK I	320 ± 20	3.1 ± 0.4	3.7 ± 0.2
3T3	240 ± 15	1.9 ± 0.5	1.3 ± 0.1
BAEC	40 ± 5	n.d.	n.d.

types create individual shifts in resonance frequency when they adhere to the quartz surface. It is important to stress that these differences are not due to incomplete coverage of the quartz resonator but mirror individual differences in the contact mechanics. Indeed, the key question is: *what are the factors that give rise to this individual frequency response and what cellular property is mirrored therein*?

2.2 Specific or Non-Specific Surface Interactions

Before addressing this topic it might be helpful to mention for readers unfamiliar with the subject, that cells do not interact directly with an in vitro surface but only with proteins or polysaccharides that are adsorbed to it. The cells express certain cell-surface receptors that are specialized to recognize and *specifically* bind to these adhesion-promoting proteins on the surface. The major class of these cell-surface receptors specialized on binding to extracellular adhesive proteins are the so-called *integrins*. Since both, the cell surface and the growth substrate are decorated with ionic or polar groups, there are also many *non-specific* electrostatic or electrodynamic interactions involved in cell adhesion. It has been a matter of long scientific debate and discussion whether specific or non-specific interactions are predominantly responsible for anchorage of cells to a given surface [18–20]. Nowadays it is widely accepted that both specific and non-specific interactions contribute, but there is compelling evidence that specific ligand–receptor interactions are more important for the final strength and the dynamic properties of the adhesion sites [18]. Thus, the question arises whether the QCM response requires specific, receptor-mediated adhesion of the cells to the surface or whether the sole presence of the cell body close to the resonator surface is sufficient to induce the observed QCM response.

To answer this question we tried to block the specific interactions between cell-surface receptors and adhesive proteins on the substrate by adding

short peptides to the culture fluid that correspond to the amino acid sequence within the primary structure of adhesive proteins that integrins bind to. When these soluble peptides are added to the cell suspension, they compete for the receptor binding site and delay or omit specific interactions with substrate-immobilized proteins.

In our experiments we used serum containing medium as culture fluid. Serum naturally contains the adhesive proteins vitronectin (VN) and fibronectin (FN). Since these proteins adsorb instantaneously from solution to the surface, there is no need to precoat the resonators with any other adhesive protein before. Both proteins, VN and FN, are recognized by cell surface receptors via the same amino acid sequence, namely Arg-Gly-Asp-Ser or RGDS in one letter code. Accordingly, we studied the impact of soluble peptides with this amino acid sequence on the time course of cell attachment and spreading as revealed by measurements of the resonance frequency. Figure 3 shows the outcome of four experiments in which either the penta-peptides Gly-Arg-Gly-Asp-Ser (GRGDS) and Ser-Asp-Gly-Arg-Gly (SDGRG), the tetra-peptide Arg-Gly-Asp-Ser (RGDS) or the tri-peptide Arg-Gly-Asp (RGD) are added to the cell suspension in a concentration of 1 mM each.

The two penta-peptides GRGDS and SDGRG contain exactly the same amino acids but in reverse order. Thereby, the two molecules carry the same charge density and would provide the same perturbation to non-specific interactions – if at all. However, due to the reversal of the amino acid sequence only GRGDS has the correct sequence to interact specifically with the integrins whereas SDGRG does not. The time course of the resonance frequency as presented in Fig. 3 clearly demonstrates that in the presence of 1 mM

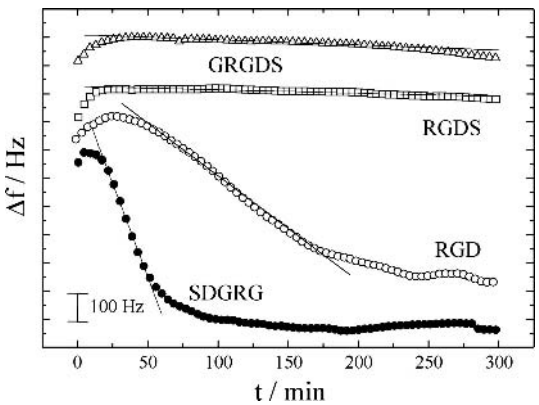

Fig. 3 Time course of attachment and spreading when equal amounts of MDCK II cells were seeded into the quartz dish in presence of the soluble peptides Arg-Gly-Asp (RGD), Arg-Gly-Asp-Ser (RGDS), Gly-Arg-Gly-Asp-Ser (GRGDS), and Ser-Asp-Gly-Arg-Gly (SDGRG). The concentration of each peptide was 1 mM, the cell densitiy was adjusted to 8×10^5 cm^{-2}

GRGDS the resonance frequency does not indicate any cell adhesion to the resonator surface. In contrast, when SDGRG is added to the culture fluid, there is no difference compared to experiments in which no peptide is present at all (compare Fig. 2a). Thus, when specific interactions between cell-surface receptors and substrate-immobilized proteins are not allowed to form, we do not observe any measurable impact on QCM readings. Apparently, loose attachment of the cell bodies to the substratum does not produce any significant acoustic load [12, 16].

When the amino acid sequence of the soluble peptides is gradually shortened by removing first the initial G from GRGDS giving RGDS (GRGDS → RGDS), followed by removal of the final S from RGDS yielding RGD (RGDS → RGD), the peptides eventually lose their potency to inhibit cell adhesion. While RGDS is still capable of blocking cell adhesion completely when applied in 1 mM concentrations, the same concentration of RGD is not (Fig. 3). These observations indicate that the final Ser is crucial in order to compete successfully for integrin binding sites. As shown in Fig. 3, the QCM readout provides the necessary sensitivity and time resolution to perform these kind of studies automatically.

For a correct interpretation of this data it is imperative to learn more about the situation at the crystal surface when specific interactions are blocked by RGDS-containing peptides. One technique that allows visualization of the "footprints" of cells on a surface is reflection interference contrast microscopy or short RICM. Practically, RICM is limited to transparent growth substrates so that we conducted a correlation experiment on ordinary coverslips instead of quartz resonators. In these experiments we seeded cells in serum-containing medium that was either supplemented with 1 mM RGDS or not. In both cases, the cells were allowed to attach and spread on the glass surface for 200 min before we recorded RICM images of each sample. Figure 4 provides a comparison of the recorded RICM images for both situations.

In Fig. 4a the cells form typical cell-surface junctions with the protein decorated growth substrate. The footprints indicate a spread morphology under these conditions. When RGDS is present in the medium the situation is rather different. As shown in Fig. 4b the cells are hardly visible in the RICM image although they have settled to the surface in this particular field of view. Bright field images taken from the very same spot (not shown) clearly prove that this is not a cell-free area of the substrate. In the center of the image (arrow) a typical fringe pattern reveals a small projection of a cell reaching to the surface. Based on the principles of RICM image formation and some technical parameters of the microscope, one can estimate that the lower cell membrane must be farther away from the substrate surface than 100 nm, probably significantly more. Apparently the presence of the cell bodies within this distance from the substrate surface and with only a very limited contact area – like a hard sphere on a flat surface – does not provide any significant acoustic load for the quartz resonator.

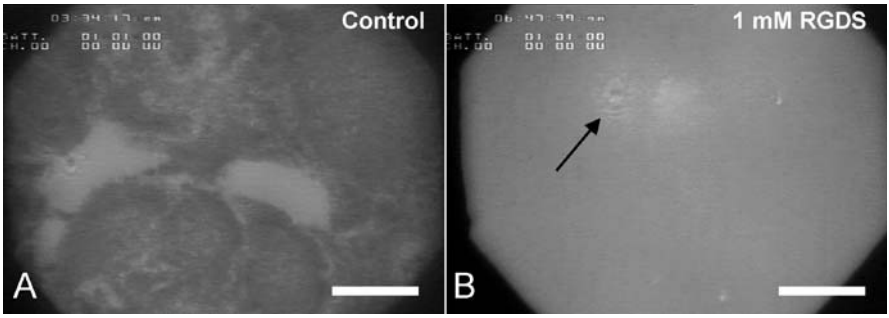

Fig. 4 RICM micrographs of MDCK II cells 200 min after seeding. The cells in **a** were suspended in serum-containing medium with no inhibitory peptides included, while the cells in **b** were exposed to 1 mM RGDS in the bathing fluid. The *black arrow* indicates the presence of a cell body that does not make close contact with the surface. *Scale bar* represents 10 μm

Thus, two main conclusions can be drawn from these experiments: (i) The QCM does only report on cells that are specifically anchored to the resonator surface. The method is blind to cells that just settle to the surface and attach only loosely. (ii) When specific cell–substrate interactions are omitted, the cells stay away from the surface by more than 100 nm, according to our RICM data. Theoretical considerations have previously indicated that cells may approach the surface as closely as 5–10 nm just by non-specific attraction [21]. This is, however, not confirmed by our optical measurements.

Looking more deeply at QCM principles, further support arises for the fact that the cells do not approach the surface as closely as 5–10 nm when specific interactions are blocked. According to Eq. 1 the penetration depth of the shear wave in an aqueous environment δ is approximately 250 nm at room temperature:

$$\delta = \sqrt{\frac{\eta_{\mathrm{fl}}}{\pi \cdot f \cdot \rho_{\mathrm{fl}}}}\,. \tag{1}$$

However, since the loosely attached cell bodies do not create any significant acoustic load on the resonator, they seem to be far enough from the quartz surface that the shear wave does not hit them with considerable amplitude. In one of the following chapters we will get back to these experiments and put them in context with further studies on confluent cell monolayers.

2.3 Titrating Cell–Substrate Contacts

Similar experiments as the ones shown in Fig. 3 have also been performed with different concentrations of RGDS-peptides. It was the objective of these

studies to *titrate* the cell–substrate adhesion sites and use the QCM response as an experimental indicator. We found that increasing concentrations of RGDS do not alter the final frequency response that is characteristically found for a given cell type, but the time course of the frequency shift is altered dramatically. Above a certain threshold concentration of RGDS the process of attachment and spreading was considerably delayed but in the long run we always observed a very similar final response, as in control experiments without any interfering peptides. Apparently the cell has certain mechanisms to overcome integrin blockade by RGDS with time. Several mechanisms could account for this observation: (i) When the integrin receptors are occupied by the peptide, they become internalized and fresh receptors are recruited to the cell surface. (ii) The cells synthesize and secrete their own extracellular matrix proteins at the site of cell adhesion so that the protein concentration and, thus, the number of binding sites on the surface continuously increases until RGDS blockade becomes ineffective. The observed behavior may also be a combination of both effects.

Even though RGDS blockade was not permanent it is possible to use QCM measurements to quantify the inhibitory effect of a given RGDS concentration from the slope of the curve during the first 5 h after inoculation. Figure 5 presents the results of such a series of measurements. The slope derived from the time course of the frequency shift is plotted as a function of RGDS concentration on a semilogarithmic scale. As anticipated, the curve is sigmoidal in nature and it is possible to derive the concentration of half maximum efficiency (EC_{50}) to $6 \pm 1\,\mu$M.

Following cell adhesion and spreading in the presence of soluble peptides that mimic the recognition sequence of adhesive proteins was historically the

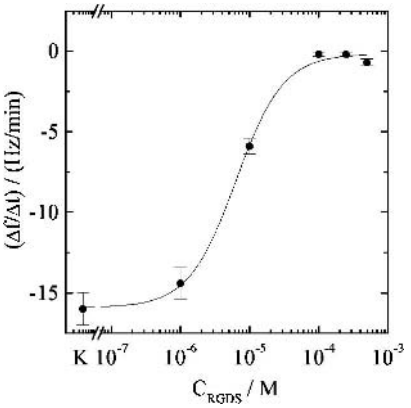

Fig. 5 Slope of the attachment curve of MDCK II cells as a function of RGDS concentration present in the bathing fluid. The concentration of half-maximum efficiency EC_{50} was determined to $6 \pm 1\,\mu$M RGDS

most direct experiment for learning about these binding sites and to identify them [22, 23]. At the time, the readout was based on time-lapse microscopy or colorimetric assays. In the future the QCM may serve as an alternative monitoring device in these kind of studies with outstanding sensitivity and the opportunity to automate the experiment for higher compound throughput in industrial screening.

Titration of cell adhesion sites may also be performed in the opposite direction when cell detachment is used as an experimental indicator. Then cells are first grown to confluence on the shear wave resonators and the competing peptides are then added to the bathing fluid. Once these peptides reach the site of cell–substrate adhesion they may displace the adhesive proteins from the receptor binding site and thereby loosen cell–substrate contacts. Figure 6 shows two examples for such experiments in which confluent Swiss 3T3 fibroblasts were exposed to 1 mM SDGRG or GRGDS (see above). Besides very minor changes, which are due to fluid handling, SDGRG does not induce any significant changes of the resonance frequency (Fig. 6a). Thus, the cell–substrate adhesion is not affected, consistent with the inverse amino acid sequence of this peptide. However, when GRGDS is added to the established 3T3 cell layers, an immediate rise of the resonance frequency is observed that stabilizes after 200 min. The frequency shift amounts to more than 150 Hz, which indicates that the cell layer is entirely removed.

Similar results were obtained when the cells were detached from the surface by means of EDTA, which chelates all divalent cations, that are necessary for stable cell adhesion (not shown).

What can be learnt from these kind of experiments with respect to the superordinate question, *what determines the QCM response of a given cell type*?

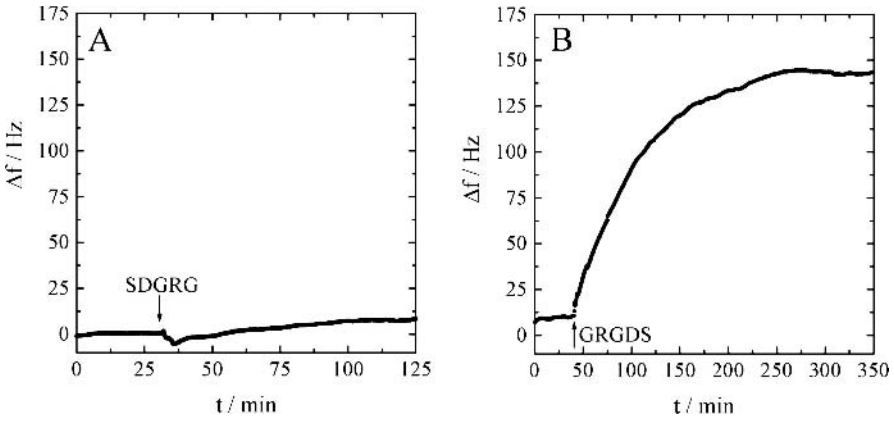

Fig. 6 Time course of the resonance frequency when preestablished, confluent monolayers of 3T3 fibroblasts were exposed to the penta-peptides SDGRG (**a**) or GRGDS (**b**) in 1 mM concentration, respectively. Addition of the peptides is indicated by *black arrows*

Unfortunately the answer is, *not very much*. These studies do indeed show that the QCM approach is a very sensitive tool for studying any perturbation of cell–substrate interactions in real time and with a highly quantitative readout. But the system itself is too complicated and holds too many variables to draw significant conclusions on the number of binding sites between cell and surface just from measurements of attachment and spreading in the presence of specific inhibitors. The enormous complexity arises from phenomena like: (i) When one integrin–protein interaction is blocked, another one of a different kind may take over the dominant role and mediate cell adhesion. This is easily possible since many integrins are promiscuous with respect to the proteins they bind to. (ii) Different cell types may express individual mixtures of integrins with graded affinities to the ECM proteins. Thus, a comparative study among different cell types is difficult to interpret. It seems that the only way to learn more about the underlying principles of the QCM response to adherent cells is using well-defined model systems with a significantly reduced complexity.

2.4 Cell Adhesion Versus Liposome Adsorption

In order to understand the laws that determine the QCM response towards the anchorage of living cells, it seemed helpful to use chemically well-defined model systems [24–26] that allow more systematic studies. By using liposomes with varying amounts of biotinylated lipids we tried to mimic the cell body (liposome) and its cell surface receptors (biotin moieties). The adhesive proteins on the surface were modeled by a layer of predeposited avidin that provides binding sites for the biotin residues in the lipid shell. Thus, receptor density and protein concentration on the surface have been under experimental control and can be adapted according to the experimental needs. In our initial studies we used large unilamellar vesicles made from dipalmitoylphosphatidylcholine (DPPC) doped with increasing molar ratios of dipalmitoylphosphatidylethanolamine (DPPE) that carried a biotin residue. The biotin was covalently attached to the lipid headgroup via a C_6 spacer.

In these experiments we used a technical setup that was originally described by Rodahl and coworkers [27] and is referred to as QCM-D. This device not only records the change in resonance frequency Δf but also changes of the so-called dissipation factor D, which is the inverse of the quality factor Q of the oscillation:

$$D = \frac{1}{Q} = \frac{Dissipated\ energy\ per\ cycle}{Stored\ energy\ per\ cycle} \tag{2}$$

According to Eq. 2 the shift ΔD mirrors changes in energy dissipation of the shear oscillation. Measuring the change in energy dissipation becomes im-

portant whenever systems are studied that do not behave like a rigid mass. Only for homogeneous mass films can an experimentally observed frequency shift be attributed unequivocally to mass deposition to the resonator surface according to the Sauerbrey relationship [6]. When the microviscosity or elasticity close to the quartz surface changes, the Sauerbrey equation no longer holds since these effects change the resonance frequency as well and are indistinguishable from simple mass deposition. Thus, viscous energy losses can make QCM measurements ambiguous and hard to interpret, if at all [28]. The device developed by Rodahl and coworkers overcomes this problem by recording both the shift in resonance frequency and the energy dissipation at a time which makes data interpretation more robust and provides twice the information of the system under study.

When living cells are studied within this setup we typically found frequency shifts Δf between 50 and 500 Hz, dependent on the cell type. The cell-type specific change in dissipation factor ΔD ranged between 1 and 4×10^{-4}. When we used undoped DPPC liposomes of 100 nm diameter that were allowed to settle on an avidin-coated resonator, we recorded frequency shifts in the order of 400–500 Hz, thus very similar to the readout for living cells. However, with respect to energy dissipation the liposomes behaved completely different. For the undoped DPPC liposomes we only observed an increase in energy dissipation in the order of 3×10^{-5}, which is roughly an order of magnitude less than that recorded for the substrate-anchored cells. Adding biotin-labeled lipids into the liposome shell, in order to allow for molecular recognition between liposome and surface bound protein, led to a gradual reduction of both Δf and ΔD. As demonstrated in Fig. 7 there is a gradual drop in both parameters with increasing concentrations of biotin residues in the liposome shell. In other words, the more ligand–receptor pairs were available the more the QCM response was reduced [24].

The reason for this unexpected behavior was revealed by scanning force microscopy [29]. With increasing biotin loaded into the liposome shell, the liposomes spread out on the surface. Eventually, they rupture when the adhesion forces provided by the ligand–receptor interactions dominate over the intermolecular forces between individual lipids in the liposome shell. The ruptured liposomes eventually form a lipid double-layer on the surface with the water-filled interior of the original liposome being emptied into the bulk phase. These lipid bilayers on the surface behave essentially like a rigid mass deposited on the surface so that the shifts in resonance frequency and dissipation decline.

So in a sense, these experiments suggest that liposomes, as they were used here, are not a suitable model system for systematic studies on cell-surface interactions by QCM, mostly due to the unavoidable rupture of the liposome when surface attraction becomes too strong. Nevertheless, for intermediate biotin concentrations these experiments did provide important information since they indicate that an aqueous compartment surrounded

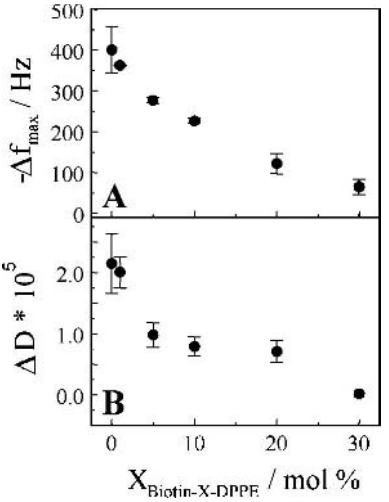

Fig. 7 Summary of liposome adhesion studies as performed with a QCM-D setup described in the text. *Panel A* shows the frequency shift Δf when the concentration of biotinylated lipids in the liposome shell is gradually increased. *Panel B* summarizes shifts of the dissipation factor ΔD from the same experiments. Data points are averages of at least two independent experiments

by a lipid double-layer is not sufficient to explain the acoustic load that is exerted on the resonator by a confluent cell layer. There is more to it than just a membrane-confined fluid compartment close to the surface. And this result is not dependent on the size of the liposome. The data in Fig. 7 was recorded for large unilamellar liposomes with an average diameter of 100 nm, but giant liposomes with diameters in the micrometer range show a similar behavior. Even for these vesicles, which have roughly the size of a typical animal cell, we could not observe an energy dissipation similar to that observed for adherent cells[2]. In a later paragraph we will address this issue again and demonstrate experimentally that the cortical cytoskeleton underlying the plasma membrane of living cells is very important for understanding their acoustic behavior in QCM experiments.

3 Analyzing Confluent Cell Layers

In the preceding sections we have studied the time course of cell attachment and spreading upon the resonator surface, dependent on the cell number and the presence of anti-adhesive peptides. The following paragraphs will

[2] Information provided by A. Janshoff.

describe experiments that were performed with confluent cell monolayers that had been preestablished on the resonator surface prior to the QCM experiment. A variety of cell types was included in these experiments in order to find cell-type specific differences that can lead to a better understanding of the system. Instead of reading the resonance frequency of the free oscillation we applied impedance analysis in a frequency range close to the fundamental resonance of 5 MHz.

3.1 Impedance Analysis of the Shear Oscillation

The experimental setup to perform impedance analysis of the loaded resonator is shown in Fig. 8a.

The quartz disk is used as the bottom plate of a cell culture vessel and is mounted in a temperature controlled crystal holder (37 °C). The surface electrodes on either side of the quartz are connected to an impedance analyzer (Solatron Instruments, SI-1260) operating in continuous wave mode. The frequency-dependent complex impedance $Z(f)$ returned by the impedance analyzer is expressed as magnitude of impedance $|Z|(f)$ and phase shift between voltage and current $\Phi(f)$. The raw data is analyzed by the well-known Butterworth–Van Dyke (BVD) equivalent circuit with the lumped impedance elements C_0, R_q, L_q, C_q and Z_L. R_q, L_q and C_q represent the piezoelectric properties of the unperturbed resonator itself, whereas C_0 summarizes its dielectric properties and all parasitic contributions arising from contacts and wiring. The load material in contact with the resonator surface is represented by the complex impedance Z_L. As long as the resonator is not loaded too

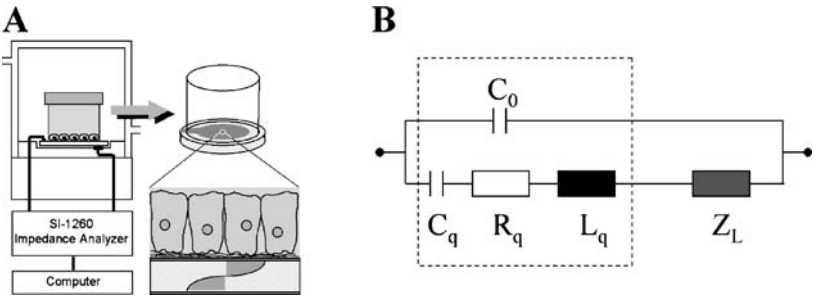

Fig. 8 **a** Experimental setup to perform impedance analysis of the shear oscillation. Quartz resonators are used as the bottom plate of a measuring chamber that is mounted in a temperature-controlled Faraday cage. Impedance data is recorded with a gain/phase analyzer in the vicinity of the fundamental resonance of 5 MHz (typically from 4.97 MHz to 5.04 MHz). **b** Butterworth–Van Dyke equivalent circuit to analyze the impedance raw data of the loaded resonator. All parameters except Z_L are assigned to the unperturbed resonator whereas Z_L denotes the impedance of the load material (cell layer) on the resonator surface

heavily, the BVD circuit is a good approximation for the more complex and comprehensive Mason model [30] that is well suited to describe any load situation [31]. For low-load conditions, for which the BVD approximation is valid, the electrical impedance of the material in contact to the resonator Z_L is directly proportional to its acoustic impedance $Z_{m,L}$ as given in Eq. 3:

$$Z_L = \frac{\pi}{4K^2\omega_0 C_0}\frac{Z_{m,L}}{Z_{m,q}}, \tag{3}$$

with the acoustic impedance of quartz $Z_{m,q}$, the electrochemical coupling constant K^2, and the angular resonance frequency ω_0. For the cellular systems studied here it is difficult, if not impossible, to confirm the validity of the low-load condition ($Z_{m,L} \ll Z_{m,q}$). However, recent studies have shown that even for heavy mass ($\leq 5\ \mathrm{mg\,cm^{-2}}$) or viscous loading ($\eta\rho \leq 1000\ \mathrm{g^2\,cm^{-4}\,s^{-1}}$), the lumped equivalent circuit is still in very good agreement with the distributed Mason model (deviations $\leq 1\%$) [32]. For simple and laterally homogeneous material films some of their mechanical properties can be deduced from the acoustic impedance, like for instance, their density or elasticity modulus G. For complex systems like layers of living cells, this is not possible yet. However, it is the objective of the experiments described in this chapter to increase our understanding of these systems and to pave the way for a more quantitative acoustic analysis.

Figure 9 compares the frequency spectra of the impedance modulus $|Z|$ and phase shift Φ for resonators with or without a confluent layer of cells on the surface. In either case, the measuring chamber is filled with cell culture medium so that the resonator is always at least under liquid loading.

The presence of the cells (compared to medium only) gives rise to a strong impact on both quantities, $Z(f)$ and $\Phi(f)$, and is most obviously expressed in a significant damping of the shear oscillation, or in other words an increase in energy dissipation. Anchorage of the cells to the resonator induces only a minor shift of the impedance and phase spectra towards lower frequencies which would otherwise indicate an increase in energy storage. Since the cell-free but medium-loaded resonator (open symbols in Fig. 9) was always the beginning or end of any QCM experiment, we have chosen this as the basis relative to which the change in load impedance ΔZ_L due to the presence of different cell types on the resonator is expressed. The QCM response to culture medium was always very stable and highly reproducible. Thus, it was not necessary to run additional impedance experiments of the cleaned and dried resonator as a reference.

Quantitative analysis of the impedance data recorded with and without cells provides the change in the complex load impedance ΔZ_L that is due to the presence of cells on the resonator surface relative to medium loading. Table 2 compares the magnitude of the load impedance $\Delta|Z_L|$ for seven different cell types that had been grown to confluence prior to the QCM experiment. The change in load impedance varies considerably for the var-

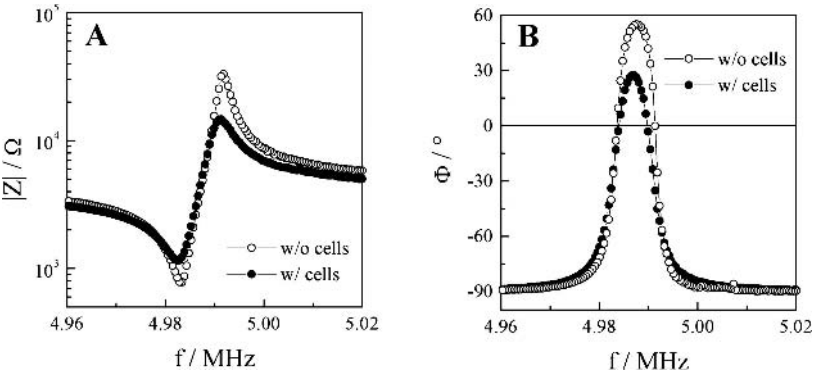

Fig. 9 Experimental raw data of the shear oscillation as recorded by impedance spectroscopy. **a** Impedance magnitude of a cell-covered and a cell-free resonator as a function of frequency. **b** Phase spectra of a cell-covered (*filled circles*) and a cell-free (*open circles*) resonator in comparison

Table 2 Change in the load impedance of quartz resonators covered with confluent layers of different cell types relative to resonators in contact with culture medium only. The complex load impedance ΔZ_L is expressed by its magnitude $\Delta|Z_L|$ as well as in its real and imaginary components

Cell type	$\Delta\|Z_{load}\|$ (Ω)	$\Delta\text{Real}(Z_{load})$ (Ω)	$\Delta\text{Imag}(Z_{load})$ (Ω)
NRK	720 ± 60	700 ± 60	170 ± 15
MDCK I	550 ± 35	550 ± 35	80 ± 22
MDCK II	425 ± 26	425 ± 26	19 ± 10
HUVEC	435 ± 65	405 ± 70	157 ± 16
PBCEC	380 ± 23	370 ± 25	79 ± 22
3T3	247 ± 40	245 ± 40	– 30 ± 30
BAEC	160 ± 13	99 ± 13	126 ± 14

ious cell types, very similar to the individual shifts in resonance frequency that were reported in the preceding sections (Table 1). The values range from 160 Ω for bovine aortic endothelial cells (BAEC) to a maximum of 725 Ω for epithelial-like normal rat kidney cells (NRK). Thus, the observed changes in load impedance $\Delta|Z_L|$ relative to a medium-loaded resonator differ by as much as a factor of five, dependent on the cell type. This reflects significantly different acoustic properties of the different cell types and probably also their individual anchorage to the resonator. Assigning these differences to a structural correlate is the problem to solve.

It is instructive to decompose the complex load impedance into its real (load resistance) and imaginary (load reactance) components. These two

quantities mirror the energy that is dissipated in the system – Real(Z_L) – or the energy that is elastically stored in the system – Imag(Z_L). Except for bovine aortic endothelial cells we have found that the dissipated energy is always many times larger than the stored energy. This was already apparent from the change in the spectra as discussed above. In this respect MDCK II cells represent the extreme, when the dissipated energy overcomes the stored energy by more than a factor of 20. For most other cell types this ratio is between two and ten. We only found for bovine aortic endothelial cells (BAEC) that the stored energy (imaginary) is bigger than the dissipated energy (real). However, these cells in general had only very little impact on the shear displacement so that it is somewhat questionable whether this deviation from the general trend observed for all other cells is real.

Taken together, these studies revealed that confluent cell layers in contact to the resonator lead to a significant increase of energy dissipation from the shear oscillation [33] as we had learned already from the QCM-D experiments presented in Sect. 2.4. The impact of the cells on energy dissipation is individual and dependent on the cell type. It is important to mention in this context that different batches of a certain cell line may also cause a different QCM response within certain limits. This is not surprising for cell biologists since cells of the same kind but taken from different batches may show a certain variance in their behavior and it underlines that the QCM is capable of picking up these subtle differences.

When we compare the acoustic behavior of the cells with simple and well-defined systems, the cells do not behave like a rigid and homogeneous mass layer. This is obvious from the occurrence of significant energy dissipation that cannot be found for rigid mass films. On the other hand, the cells also do not behave like a simple viscous (Newtonian) fluid such as water or water/glycerol mixtures. It has been shown many times in the past that Newtonian fluids increase the real and the imaginary part of the load impedance to the same degree, and the increase of both quantities scales linearly with the square-root of the density–viscosity product of the liquid [33, 34]. The reason for the increase of energy storage (reactance of the load impedance) observed for viscous fluids is assigned to (i) the synchronous movement of the first liquid layer that tightly adsorbs to the resonator surface (no slip behavior) and (ii) the entrainment of liquid in nano- or mesoscopic cavities on the surface due to surface roughness. These mechanisms do not apply to adherent cells, as can be concluded from the imaginary part of the load impedance that lags behind the real part [16].

This latter finding is indeed not surprising since the microscopic structure at the interface between an adherent cell and its growth substrate is very different from the wetting of viscous fluids upon the resonator surface. Figure 10 sketches the contact area between lower cell membrane and substrate surface, including the major structural components that contribute to cell adhesion. Most importantly, the cell membrane is not in direct contact with the

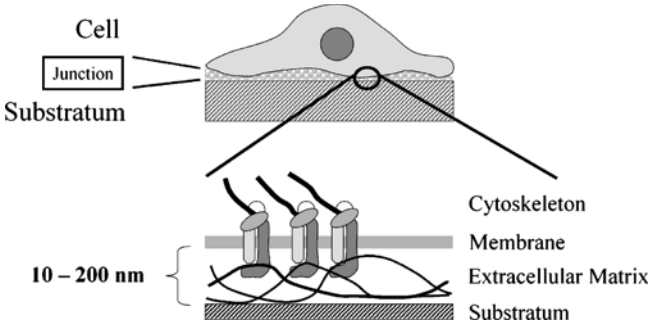

Fig. 10 Schematic of the interface between an adherent animal cell and a technical substratum. The blow-up provides a rough overview of the structural arrangement within the contact area in which cell membrane receptors bind to proteins immobilized on the substrate surface. It is important to note that there is a thin cleft between the lower cell membrane and the substratum that is approximately 10–200 nm in width

resonator surface but is hovering an average distance between 10 and 200 nm above, as mentioned in Sect. 2.2 already.

The thin cleft between substrate surface and plasma membrane is filled with an aqueous electrolyte solution that contains proteins, carbohydrates, and low molecular weight components. Anchorage to the surface is provided by cell-surface receptors that bind to adhesive proteins immobilized on the growth substrate. The most prominent cell surface receptors – the *integrins* – stick out of the membrane by approximately 20 nm and thereby bridge the gap between cell membrane and substratum. Very often these integrins are not evenly distributed in the plasma membrane but they tend to cluster to so-called *focal adhesions* or *focal contacts*. Focal contacts are adhesion sites in which the cells are believed to have the closest distance to the substrate. Thus, the interface between cell and substrate is not at all isotropic but is filled with filamentous polymers (proteins, sugars) and may have a gel-like constitution due to the water-storage capacities of the carbohydrates. Furthermore, the cell membrane may approach the surface closely in focal contacts (< 20 nm) but may be farther away in other areas underneath the same cell. So not only the molecular composition but also the width of the contact area is laterally heterogeneous.

3.2 No Correlation between Cell–Substrate Separation Distance and QCM Response

As mentioned in Sect. 2.2 the decay length of the shear wave into a viscous medium in contact wiht the resonator can be estimated from Eq. 1. If a 5 MHz resonator, as used in our studies, is loaded with pure water at room temperature, the characteristic axial decay length of the shear displacement amounts

to approximately 250 nm. When the fluid within the thin cleft underneath the cells is assumed to behave like water in a first approximation, then the decay length of the shear wave is in the same range as the average width of the cleft between cell membrane and growth substrate. Thus, the hypothesis arose that the individual QCM responses for different cell types may be due to the individual separation distances between cell body and resonator surface. As a consequence, the cells may have been exposed to different amplitudes of the propagating acoustic wave, which may in turn lead to an individual sensitivity of the QCM for these different cells.

In order to measure the average distance between lower cell membrane and growth substrate accurately, we made use of fluorescence interference contrast microscopy or FLIC, which has been recently developed by Lambacher, Braun, and Fromherz [35–37]. Readers interested in this novel technique and its theoretical background are referred to the above references as only a brief introduction will be given here. In FLIC, the cells are grown on silicon substrates that have regular steps of 5 μm $\times$ 5 μm made from silicon oxide on their surface. The step heights are well-defined and range between 20 and 200 nm and are, thus, only a fraction of the wavelength of visible light. After the cells have attached and cultured on these micropatterned FLIC substrates, their membranes are stained by a lipid-soluble fluorescent dye that integrates into the plasma membrane. When the cell-covered FLIC substrate is then placed in the incident light beam of a fluorescence microscope, the silicon/silicon oxide interface acts as a mirror and standing waves of the incident light are formed with a node at the silicon surface. Thus, the intensity of fluorochrome excitation is dependent on the distance between dye (membrane) and mirror (silicon). The same mechanism applies to the fluorescent light emitted by the fluorophore upon excitation so that the intensity of the fluorescent light is also modulated by the distance between dye (membrane) and mirror (silicon). Taken together, the intensity of the fluorescence light is a function of the cell–substrate separation distance and introduces a strong dependency of pixel brightness on distance between membrane and mirror. However, tracing fluorescence intensity versus distance between membrane and silicon substratum provides a (damped) periodic function so that any distance determination from a single fluorescence intensity reading is not unique. Introduction of terraces of silicon oxide of at least four different heights provides well-known spacers between cell membrane and reflecting interface such that four different fluorescent intensities are measured and analyzed. These four point measurement makes the intensity–distance relationship unique. Lambacher, Braun, and Fromherz developed an optical theory for this system with the distance between membrane and oxide surface as the only adjustable parameter [35, 37]. Fitting of this theory to the experimental data provides the cell-substrate separation distance. The accuracy of the FLIC approach has been estimated to be better than 1 nm.

We have performed FLIC microscopy for all cell types that have been listed in Table 2 in order to quantify their individual distance to the growth substrate. It is an inherent problem of this approach that the cells had to be grown on micropatterned silicon for FLIC measurements and not on a quartz resonator as used in QCM. But the uncertainty whether the cells behave differently on either substrate cannot be bypassed in principle. Figure 11 shows the change in load impedance $\Delta|Z_L|$ for the different cell types studied here as a function of their individual cell–substrate separation distance extracted from FLIC measurements. If the hypothesis applies that cells provide a more sustained QCM response the closer they are to the surface, one would have to expect a decrease of $\Delta|Z_L|$ with increasing distance d. The graph in Fig. 11, however, shows no obvious correlation between the acoustic load of the resonator and the distance between lower cell membrane and its surface. Please note that, for instance, BAEC and NRK cells show very similar distances from the surface of approximately 75 nm but the change in load impedance $\Delta|Z_L|$ differs by more than a factor of four.

Another very obvious deviation from the working hypothesis is given by the porcine brain capillary endothelial cells (PBCEC) that have been studied in the presence and absence of the steroid hormone hydrocortisone (±HC). As demonstrated in Fig. 11 the steroid does not change the distance between membrane and substrate surface significantly (101 ± 6 nm without HC versus 94 ± 3 nm with HC) but it does change the acoustic load of the resonator from $\Delta|Z_L| = 380\ \Omega$ (without HC) to $\Delta|Z_L| = 890\ \Omega$ (with HC) indicating that there is no direct correlation between both quantities.

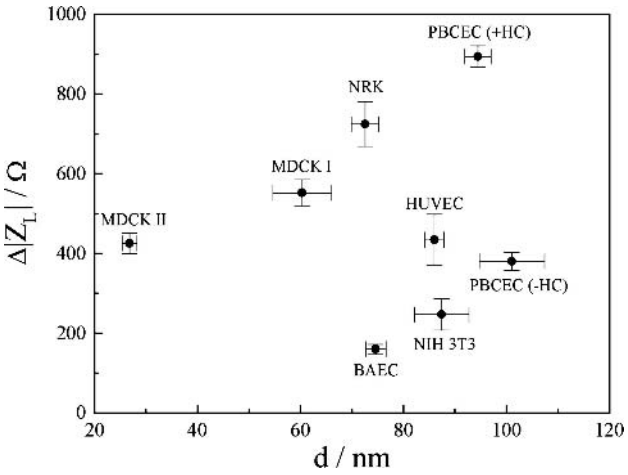

Fig. 11 Magnitude of the load impedance $\Delta|Z_L|$ for different cell types as a function of the individual distance d between their lower membrane and the substrate surface. The data does not show any correlation between both quantities, indicating that the distance between resonator and cell body is not dominating the QCM readout

Taken together, these studies show that cell–substrate separation distance is not the most significant parameter when explaining the acoustic load of shear wave resonators covered by confluent cell layers. It may still have a minor impact but the QCM response is apparently dominated by other mechanisms.

3.3
Adhesive Proteins Underneath the Cells Contribute to the QCM Readout

As sketched in Fig. 10 and mentioned before, the cells anchor to adhesive proteins that are immobilized on the surface. When cells are cultured for a certain time, they even produce their own adhesive proteins and secrete it into the space between membrane and substratum. Thus, we tried to address whether or not these adhesive proteins underneath the cell body may contribute to the total QCM readout of a confluent cell layer. Instead of limiting the analysis to preadsorbed layers of one or two purified proteins, we tried to study the complex extracellular material underneath the cells (extracellular matrix or ECM) by removing the cell bodies but leaving the macromolecular network of proteins and sugars behind on the substrate. The protocol required a combination of hypotonic stress and detergent extraction [16]. Microscopic inspection of reference substrates revealed that this procedure lifted the cell bodies effectively off the substrate. The surface was, however, still decorated with proteins as revealed by immunocytochemical staining.

Impedance analysis of the shear oscillation was performed for resonators covered with a confluent layer of cells and after the cell bodies had been removed by hypotonic lysis. The changes in load impedance ΔZ_L are again expressed relative to the identical quartz resonator that was loaded with protein-free medium only. Consistent with our expectation, we observed in these experiments that the magnitude of the load impedance $\Delta|Z_L|$ was significantly reduced when the cell bodies were removed from the resonator with only their ECM being left behind. In particular, the real component of ΔZ_L was barely detectable after cell removal and ranged in the order of 20–30 Ω for resonators that MDCK and 3T3 cells had been removed from. Please compare Table 2 for the corresponding values of the confluent cell layers, which ranged between 250 Ω for 3T3 and even 550 Ω for MDCK I. Accordingly, either the cell bodies themselves with their membranes and cytoskeleton or the liquid confined in the thin cleft underneath the cells must be the site of energy dissipation. As a matter of fact the complex protein and carbohydrate layer that remained on the surface does not show the considerable dissipating properties as one would expect. In a more recent study these results have been confirmed by Marx and coworkers [38].

It was, however, interesting to recognize that the load reactance, that mirrors the kinetically stored energy, was only reduced by 10 or 20% upon removal of the cell bodies with the ECM remaining on the surface. In some

rare cases we found a reduction of the load reactance by 50%, but never more than that. Although the acoustic properties of the extracellular matrix on the one hand and the cell bodies on the other are not strictly additive, it is reasonable to assume that a significant fraction of the load reactance observed for confluent cell monolayers, relative to a medium-loaded quartz, resides in the extracellular matrix that is adsorbed on the quartz surface [16]. This finding has to be recognized whenever the QCM response to an adherent cell monolayer is analyzed, interpreted, and modeled.

In general, all QCM measurements that were done with resonators initially coated with a confluent cell monolayer, which was later removed by hypotonic lysis, characteristically showed a load resistance at the limit of detection but a considerable load reactance. As discussed in the preceding section, this is a typical behavior of rigid mass films that adsorb to the resonator surface. Apparently the ECM remaining on the surface behaves like an adsorbed mass layer that does not provide any significant energy dissipation. The remaining load reactance disappeared when the surface was exposed to the protease *trypsin* indicating that the remaining material on the resonator was primarily made from protein.

A very similar result was found when we coated the resonator with a layer of collagen. In a typical experiment we measured an increase for $\Delta|Z_L|$ of $236 \pm 18\ \Omega$ relative to a medium-loaded resonator. Decomposing the complex load impedance in real and imaginary components revealed a load resistance of $43 \pm 15\ \Omega$ compared to a load reactance of $232 \pm 18\ \Omega$. Thus, the layer of purified collagen shows similar acoustic properties as the remaining ECM on the surface [16].

3.4
Cortical Actin–Cytoskeleton is a Major Contributor

The mechanical properties of living cells are significantly determined by the cytoskeleton. There are three major classes of protein filaments that belong to the cytoskeleton and have individual functions: microfilaments, intermediate filaments, and microtubules [39]. Whereas microfilaments and microtubules are highly dynamic structures that can form rapidly by polymerization of actin or tubulin monomers, respectively, the intermediate filaments are stationary structures that are important for the basal mechanical stability of the cell but not for dynamic changes. Since the microfilaments are composed of filamentous actin they are also referred to as actin filaments [39]. Both expressions can be used synonymous.

With respect to the mechanical properties of the plasma membrane the microfilament system is considered the most important since a network of these filaments underlies the plasma membrane and stabilizes it. This membrane supporting network of actin filaments is often called the *cortical actin*. In order to test whether the mechanical properties of the membrane (de-

termined to a large degree by the cortical cytoskeleton) contributes to the acoustic load on the resonator surface we applied different strategies to modulate the actin cytoskeleton. By adding a membrane-permeable drug that interferes with actin polymerization we were able to decompose actin filaments in the corresponding monomers. On the other hand, we cross-linked and stiffened all cellular protein by chemical fixatives and studied the associated QCM response.

3.4.1 Disintegration of Actin Filaments

Actin filaments are continuously assembled and disassembled in living cells by concomitant polymerization and depolymerization. Since the elongation and shortening of the filaments occur at opposing ends of the filaments, it is possible to distinguish between filament poles. The growing end is termed the *plus end* whereas the site of depolymerization is called the *minus end* [39]. The fungal toxin Cytochalasin D (CD) is a membrane-permeable compound of low molecular weight that specifically inhibits the polymerization of actin monomers into growing filaments but leaves depolymerization unaffected. Thus, when cells are exposed to this drug the actin filaments shorten and finally disappear [40]. Figure 12a and 12b provide microscopic images of

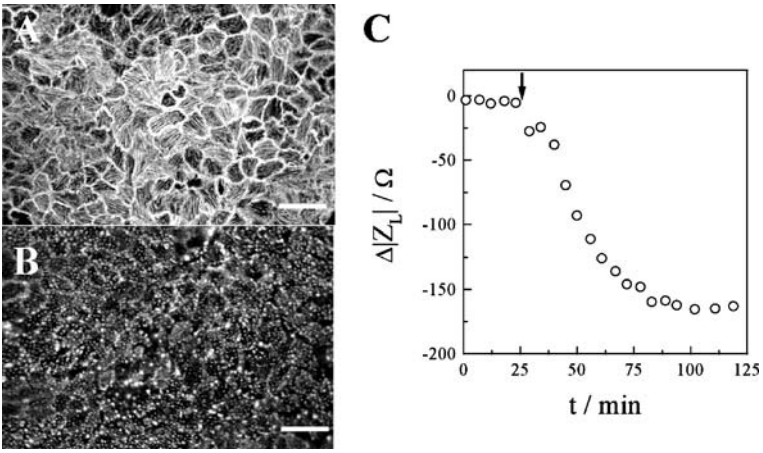

Fig. 12 Fluorescence micrographs of confluent MDCK II cell monolayers after the actin cytoskeleton has been stained by fluorescence-labeled phalloidin. **a** Control cells were not exposed to Cytochalasin D. **b** Cells were exposed to 5 μM Cytochalasin D for 100 min. The staining confirms that actin filaments have been degraded to small actin aggregates. The *scale bar* represents 25 μm. **c** Magnitude of the load impedance $\Delta|Z_L|$ as a function of time when confluent MDCK II cell monolayers were exposed to 5 μM Cytochalasin D at the time indicated by the *arrow*. The value of $|Z_L|$ at the beginning of the experiment was set to zero

confluent MDCK cells that have been stained for their actin cytoskeleton by fluorescence-labeled phalloidin, a compound that specifically binds to filamentous but not monomeric actin. The cells shown in Fig. 12a served as a control, whereas those in Fig. 12b were challenged with 5 μM CD for 100 min prior to fixation and staining.

In the control cells one can easily spot two very prominent actin structures: (i) *stress fibers* that run along the lower, substrate-facing membrane interconnecting two sites of cell–substrate adhesion and (ii) the *junctional actin ring* that follows the cell periphery and stabilizes cell-to-cell junctions. After exposure to CD both actin structures change dramatically. Instead of stress fibers and an actin belt around the cells, there are only actin aggregates that look like clumped monomeric actin without any filamentous structure. Thus, within 100 min of exposure time the actin filaments are disassembled. However, the cells remain spread and anchored to the growth substrate, so that after CD treatment there is still a confluent cell monolayer on the surface.

The same experiment was performed with MDCK cells that had been grown to confluence on quartz resonators. We then recorded impedance spectra under basal conditions, applied 5 μM CD and followed the acoustic load by continuously recording impedance data of the shear oscillation. In Fig. 12c the change in load impedance $\Delta|Z_L|$ is traced as a function of time in a typical experiment. Addition of CD is indicated by an arrow. Upon CD exposure the acoustic properties of the cell layer change considerably. Relative to the confluent MDCK II monolayer the magnitude of the load impedance $\Delta|Z_L|$ decreases by approximately 170 Ω, which is more than 40% of $\Delta|Z_L|$ for the intact cell layer. The time course in Fig. 12c correlates favorably with the time course of actin disassembly as monitored by microscopic studies similar to the ones shown in Fig. 12a,b. Decomposing Z_L into real and imaginary components reveals that both load resistance and load reactance contribute almost equally to the observed changes. In other words, we do see very similar changes in load resistance and load reactance under the influence of CD.

Treating cells with CD to disassemble their actin cytoskeleton has been described many times in the literature. When cells were studied by scanning force microscopy (SFM) after CD exposure, a significant reduction of membrane stiffness was reported for various cell types [41, 42]. Since the acoustic impedance also decreases, it seems reasonable to propose that the QCM may serve as a micromechanical probe to study membrane stiffness. Further experiments will be presented below that support this point of view.

In more general terms, the experiments described in this paragraph provide two major conclusions: (i) The actin cytoskeleton has a strong impact on the acoustic properties of the cell layer and (ii) the QCM is capable of monitoring functional changes in the cytoskeleton quantitatively and under physiological conditions. The second point should be emphasized since the

QCM provides this kind of readout without the necessity to open the incubator door. As the cells are anchored directly onto the surface of the mechanical transducer, the device can be easily integrated into biotechnological reactors or other experimental setups. Alternative techniques like scanning force microscopy or scanning acoustic microscopy [43] are more powerful in the sense that they may provide a laterally resolved elasticity mapping; however, due to the technical requirements of these devices, the cell cultures have to be manipulated and removed from their cell culture environment.

3.4.2 Cross-Linking all Cellular Protein by Chemical Fixatives

Motivated by the experimental findings that the QCM may serve as a micromechanical probe for monitoring membrane stiffness, we studied the QCM response when the cells on the resonator surface were treated with chemical fixatives that are known to cross-link all cellular proteins. Scanning force microscopy (elasticity mapping) has revealed that cross-linking of cell protein by aldehydes like glutaraldehyde (GA) or paraformaldehyde (PFA) stiffens the plasma membrane and increases the Young's modulus (a quantitative measure of mechanical stiffness) of the cells considerably [44, 45]. Thus, we monitored the acoustic response when confluent MDCK cell monolayers were exposed to either GA or PFA in concentrations that are typically used to prepare cytological samples. Upon exposure to 2.5% (v/v) glutaraldehyde for 30 min the load impedance relative to a medium-loaded resonator $\Delta|Z_L|$ increased from $472 \pm 72\,\Omega$ for the native MDCK II monolayer to $2340 \pm 245\,\Omega$ after fixation. Accordingly, protein cross-linking increased the load impedance more than fivefold. In a different set of experiments in which we applied 4% (w/v) paraformaldehyde instead of glutaraldehyde for 30 min we observed a change in load impedance $\Delta|Z_L|$ from $529 \pm 18\,\Omega$ for the native MDCK II cell layer to $1004 \pm 49\,\Omega$ after fixation. Here the relative increase of $\Delta|Z_L|$ is still twofold but less pronounced than in the case of GA.

The time course of protein cross-linking and the associated cell stiffening is rather fast with respect to the time resolution of the measurements. Figure 13 compares the time course of $\Delta|Z_L|$ for confluent MDCK II cells exposed to GA with a corresponding control that did not receive any fixative. For a meaningful, time-resolved monitoring of the cross-linking reaction by QCM measurements we had to dilute the GA solution tenfold to 0.25% (v/v) and still found that the system was stationary again after less than 10 min. The final increase of $\Delta|Z_L|$ was, however, the same as with the higher concentrations of GA. According to this data, the incubation time of 30 min, as chosen in the experiments described above, was more than sufficient to reach a steady state in the protein cross-linking reaction.

In order to correlate the acoustic response upon cell fixation with the change in Young's modulus of the same cells under identical conditions as in

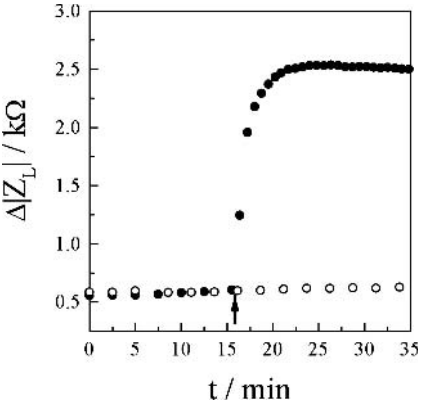

Fig. 13 Magnitude of the load impedance $\Delta|Z_L|$ relative to a medium-loaded resonator as a function of time when confluent MDCK II cell monolayers on the resonator surface are either treated with a 0.25% (v/v) solution of glutaraldehyde (*filled symbols*) or by a corresponding buffer control (*open symbols*). Addition of glutaraldehyde and buffer exchange are indicated by the *arrow*

QCM measurements, we also recorded elasticity maps of MDCK cells before and after fixation with PFA and GA by scanning force microscopy (SFM). Applying the commonly used Hertz model to the recorded raw data, we obtained a median Young's modulus of 2.5 ± 0.3 kPa for native MDCK cells that was increased to 3.7 ± 0.9 kPa after PFA fixation. The highest median values of 25 ± 3 kPa were found after a 30 min fixation with GA. Thus, the well-established SFM measurements indicate that there is a graded and individual stiffening of the cells when different fixatives are used. Consistent with the QCM experiments, PFA was found to be less efficient in cell stiffening than GA. In SFM studies the cortical actin cytoskeleton is considered to be the dominant contributor to the mechanical properties of the cell membrane [46]. Since the QCM readout correlates with SFM measurements, the conclusion may apply that the cortical actin cytoskeleton is also predominantly responsible for the acoustic load of the resonator.

We consider these studies to be strong evidence that the protein content of the cell, and in particular the cytoskeleton, is a prominent if not the predominant contributor to the acoustic load that is created on shear wave resonators by adherent cells. The reduction of $\Delta|Z_L|$ after disassembly of the actin cytoskeleton supports this hypothesis. Please note that all the experiments described in this paragraph have been performed with MDCK II cells. In order to exclude that the observed increase in acoustic load after fixation is a cell-type-specific phenomenon of MDCK II cells, analog experiments were performed with other cell types and returned the same answer. Only the numerical value of the increase in $\Delta|Z_L|$ varied to some extend.

3.4.3
Monitoring Steroid-Induced Changes in Cell Stiffness

In the preceding Sects. 3.4.1 and 3.4.2 we have described the QCM response to a disintegration of the actin cytoskeleton on the one hand and to cross-linking of all cellular protein by chemical fixatives on the other. The data implied that cell stiffness brought about by the cytoskeleton determines the acoustic response. However, the experimental means to arrive at this conclusion were rather drastic, in particular when chemical fixatives were applied. With respect to future applications of the QCM in cell biology it seems important to understand whether the technique is sensitive enough to monitor physiological alterations in cell stiffness. We therefore tested the QCM approach on an established phenomenon that has been published recently.

When endothelial cells isolated from porcine brain capillaries are grown in vitro, they respond in a very distinct way to the glucocorticoid hydrocortisone (HC) [47]. Upon exposure to this steroid in physiological concentrations, the cells have been shown to stiffen and improve their differentiation. The stiffening of the cells has been quantified by scanning force microscopy similar to the data presented above. The Young's modulus for these cells increases within 24 h from 5.1 ± 1.9 kPa to 8.3 ± 2.6 kPa when the medium is supplemented by 550 nM HC [48]. Apparently the stiffness of the cells increases due to the biochemical alterations induced by HC. The authors assign the observed stiffening of the cells to changes in the cortical actin network, since (i) the cortical actin is generally considered to be the decisive structure that determines cell stiffness and (ii) many studies have shown in various cell types that glucocorticoids like hydrocortisone may have an impact on cytoskeletal structures by regulating the expression of actin linker or actin bundling proteins [49].

When these cerebral endothelial cells are grown to confluence on quartz resonators under identical conditions as applied in the SFM studies, we observed an increase of the load impedance $\Delta|Z_L|$ from $380 \pm 23\,\Omega$ without HC to $890 \pm 27\,\Omega$ when the cells were treated with 550 nM hydrocortisone. Accordingly, the load impedance more than doubles in response to HC. Thus, QCM readings provide a similar answer to SFM with respect to the micromechanical changes that are induced in the cells by incubation with the hormone hydrocortisone. The QCM approach is obviously sensitive enough to monitor even physiological alterations within the cytoskeleton, which paves the way for many applications as a transducer for micromechanical changes in adherent cells.

Comparing QCM with the most established technique to study micromechanical changes in the plasma membrane of living cells, scanning force microscopy, there are advantages and limitations. Clearly, the QCM does not provide a laterally resolved image of the micromechanics within an adherent cell layer or even within different regions of a single cell. And at this point,

QCM readings cannot be translated into mechanical parameters that allow direct mechanical interpretation and modeling. On the other hand shear wave resonators provide (i) a much better time resolution than SFM, (ii) a readout that is averaged over many thousands of cells, and (iii) an entirely non-invasive measurement that can be easily automated and integrated into any cell culture vessel. Thus, the QCM may become an alternative or an additional means to study mechanical changes in adherent cells. It is important to recognize that SFM provides primarily the mechanical properties of the upper (apical) cell membrane whereas the QCM response is more sensitive to changes occurring in the lower (basal) cell membrane, so that SFM and QCM may complement each other.

4 Electrochemical QCM: New Options and New Insights

When the QCM is used as a mass-sensitive device in electrochemical experiments, it is often important to control the electrical potential of the electrode that is facing the liquid. Thus, an additional (reference) electrode is introduced into the QCM chamber in order to provide well-defined electrochemical conditions and to allow for various kinds of electrochemical reactions at the crystal surface. A well-known example is the electrodeposition of metals on the electrode surface that is often used to calibrate the device and calculate its mass sensitivity. When these kind of electrochemical studies are combined with QCM readings, the acronym EQCM is used, abbreviating electrochemical quartz crystal microbalance.

In order to extend the analytical options of the QCM measurement in cell biology we have introduced an additional low-impedance dipping electrode into the QCM chamber (compare Fig. 14) that serves as a counter electrode to perform electrochemical impedance analysis of the cells grown on the upper gold electrode of the quartz resonator.

Impedance analysis of cell-covered gold film electrodes in the frequency range between 1 Hz and 1 MHz was established more than 20 years ago as a non-invasive means to follow morphological changes in adherent cells [50–53]. The technique is referred to as electric cell–substrate impedance sensing or ECIS. The principle of ECIS relies on the fact that the cell bodies behave similarly to insulating particles at most frequencies that force the current to flow around the cell bodies. Accordingly, the overall impedance of the system increases when cells attach and spread on the electrode surface since the current has to pass through the narrow cleft between lower cell membrane and electrode surface before it can escape through the intercellular shunt between adjacent cells into the bathing fluid. Thus, the observed impedance increase originates from the cell–substrate adhesion zone as well as from the intercellular cleft that is often narrowed by cell-to-cell junctions [54]. Thus, ECIS

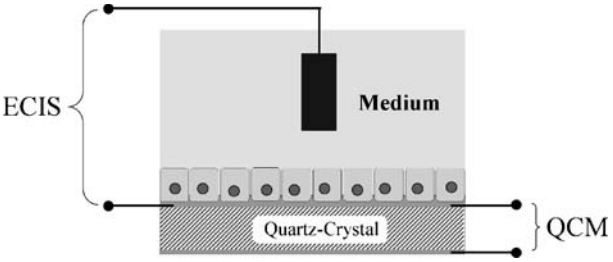

Fig. 14 Schematic of the combined QCM-ECIS setup. In order to perform electrochemical impedance analysis of the adherent cell layer on the substrate electrode, an additional low impedance platinum dipping electrode is introduced into the measurement chamber. Impedance analysis of the cell layer (ECIS mode) is performed in the frequency range between 1 Hz and 1 MHz, whereas the shear oscillation is analyzed close to its fundamental resonance between 4.97 MHz and 5.04 MHz. A computer-controlled relay allows switching between both modes automatically

readings can be used to follow both changes in cell–cell contacts as well as changes in the contact area to the conducting electrode surface. By selecting the AC sampling frequency properly, it is possible to make cell–cell or cell–substrate contacts dominate the overall impedance readout and thereby tune in on a certain portion of the cell bodies.

We have used this combined QCM-ECIS setup to study barrier-forming endothelial or epithelial cell layers that express tight intercellular contacts to occlude the paracellular shunt between adjacent cells. In vivo these cells serve as an interfacial cell layer that separates two fluid compartments and strictly regulates the exchange of solutes between both spaces. Examples are the lining of the blood vessels or the urinary bladder. In our experiments we used the epithelial cell line MDCK that originates from the lining of the kidney tubules and is a widespread model for a barrier forming cell layer. The QCM chamber was inoculated with a sufficiently high number of suspended MDCK II cells so that the growth substrate is completely covered after attachment and spreading without any need for further cell division. We then followed the establishment of a cell monolayer by continuously recording impedance data of the shear oscillation (*QCM mode*) on the one hand, and impedance data of the cells on the surface (*ECIS mode*) on the other hand. Switching between both modes was performed by a computer-controlled relay. Figure 15 compares the time course of the load impedance $\Delta|Z_L|$ as recorded in QCM mode as well as the time course of the electrode impedance (ECIS mode) at a sampling frequency of 400 Hz. The former reports on attachment and spreading of the cells whereas the latter indicates the formation of barrier-forming cell–cell contacts.

The time course of $\Delta|Z_L|$ is characterized by an immediate rise shortly after seeding the cells. After roughly 300 min the values stabilize before they

increase again to their maximum roughly 500 min after cell inoculation. The first part of the curve ($t < 300$ min) mirrors the kinetics of attachment and spreading of the cells in good accordance with microscopic studies and the resonance frequency measurements reported in Sect. 2.1. The second rise of $\Delta|Z_L|$ starting at $\sim 600\,\Omega$ till $\sim 800\,\Omega$ can, however, not be explained by a change in surface coverage. The additional load impedance must arise from acoustic changes within the cell bodies anchored to the quartz surface.

Triggered by our understanding of the contribution of the actin cytoskeleton, we stained for filamentous actin 3 and 10 h after cell inoculation. Microscopic images representative for the entire cell population are shown in Fig. 15. Approximately 3 h after seeding (Eq. 1) the cells are attached and fully spread but the actin cytoskeleton is not yet fully established. Diffuse actin is present but neither the very prominent actin belt around the cell periphery at cell–cell contact sites nor any stress fibers running along the lower cell membrane can be seen. The situation is different after 10 h of observation (Eq. 2). Staining of the actin filaments now reveals a continuous actin belt around the cells and stress fibers interconnecting individual focal adhesion sites. It seems plausible that shaping up of the actin cytoskeleton, as indicated by visible structural changes, induces the observed increase in load impedance and is thus detectable by QCM readings. Together with the experiments presented in Sect. 3.4 we take this observation as another experimental finding that supports our understanding that the actin cytoskeleton is an important contributor to the acoustic load of the resonator.

Figure 15 also shows the time course of the electrochemical impedance at a sampling frequency of 400 Hz (ECIS-mode). It is important to note that this dataset was recorded in exactly the same experiment and from the identical cell population that was used to collect the QCM data. Since both time traces originate from the same sample it is fair to compare the time course of both quantities in detail. The expression of barrier-forming cell–cell contacts cannot start before the cells have completely attached and spread on the electrode surface ($t > 300$ min). After 300 min the impedance starts to rise and is stationary again 700 min after cell inoculation, indicating full establishment of cell–cell contacts. The half-maximum barrier formation mirrored in the time course of the impedance at 400 Hz (ECIS) and the maximum of the load impedance $\Delta|Z_L|$ (QCM), which has been associated with the formation of a mature and polarized actin cytoskeleton, coincide at approximately 500 min. This finding strongly supports our understanding of the biphasic time course of the load impedance since it is well known from molecular cell biology that two adjacent cells have to form mechanically stable *adherens junctions* before they can establish barrier-forming *tight junctions* that occlude the intercellular shunt [54]. Adherens junctions are characterized by the thick actin belt that follows the cell periphery close to the apical pole. This actin belt can be easily spotted in Fig. 15 10 h after seeding but not 3 h after seeding.

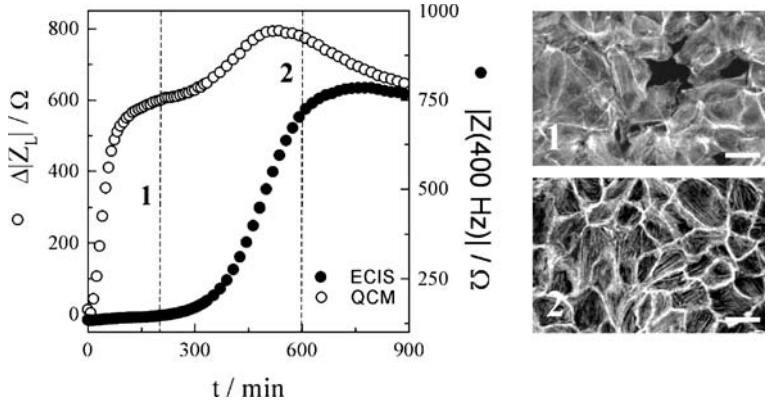

Fig. 15 Attachment, spreading, and differentiation of MDCK II cells followed by the combined QCM-ECIS approach. The change in load impedance $\Delta|Z_L|$ (*open circles*) reports on attachment, spreading, and reorganization of the actin cytoskeleton. The electrical impedance at 400 Hz (*filled symbols*) mirrors the establishment of barrier-forming cell-cell contacts and, thus, differentiation. The fluorescence micrographs in the *right panel* visualize the status of the actin cytoskeleton 3 h and 10 h after cell seeding. These time points are indicated in the graph by the *dashed lines* marked as *1* and *2*

Taken together, the combined QCM-ECIS approach provides the experimental options to follow attachment, spreading, cytoskeletal reorientation and cellular differentiation for barrier-forming cell types in a single experimental setup. Since the data is recorded from one and the same cell monolayer, the individual time courses of either parameter provide additional clues for a correct interpretation of the data. The electrochemical ECIS approach provides a lot more experimental options that have not been addressed in this article. These will help to broaden our understanding of QCM readings for adherent animal cells and guide us in the development of additional cell-based assays in which the QCM is used as a transducer to monitor cell behavior.

5
Outlook on QCM Applications in Cell Biology

The most obvious application of the QCM technology in biomedical research with living cells is the online observation of cell–substrate contacts, either when they form de novo as in attachment and spreading, or when established cell–substrate contacts reorganize under the influence of biological, chemical, or physical stimuli. It is a unique advantage of the QCM technique that these kinds of measurements are still possible when the quartz resonator is first coated with a thin layer of any technical material of interest like, for instance,

a metal or polymer film. Thus, the device may become an extremely useful tool for evaluating the cytocompatibility of technical surfaces, as required for the development of implants and other devices that need to be in contact with living tissue. The only limitation with respect to the pre-adsorbed material film on the resonator surface is that it is rigid in nature, of limited thickness and does not produce significant acoustic losses.

Even in more fundamental biomedical research the QCM is very versatile and broadly applicable. Proteins derived from native extracellular matrices may be deposited on the surface in order to study the interaction of cells with these protein coatings. A recent study by Li and coworkers [11] has shown that the QCM provides similar readouts as the traditionally applied cytological techniques. Due to its enormous time resolution even subtle differences in the kinetics of attachment and spreading become accessible.

Another striking new direction of the QCM in the field of cell biology are motility measurements based on noise analysis of the resonance frequency. When the cells move and crawl on the surface of the quartz plate the resonance frequency fluctuates as a direct consequence of the continuous assembly and disassembly of cell–substrate contacts during cell movement. Pax and coworkers have recently shown that the contraction of heart muscle cells can be easily recorded from the associated alterations of the resonance parameters [55]. We recently found that even in stationary cell layers without any open spaces that would allow for lateral migration, metabolically driven micromotion can be recorded [56].

All these different QCM modes can be used to develop whole-cell biosensors in which the cells serve as the sensory elements and the QCM device is used as a transducer. Of course the presence of living cells on the resonator surface provides certain practical limitations since the rather stringent experimental conditions required by living cells have to be met at all times. On the other hand, living cells allow monitoring the biological activity of the test compound rather than just the binding or blocking of some receptor binding site. Furthermore the assay may take advantage of intracellular amplification cascades, for instance second messenger cascades that provide a significantly improved sensitivity of the device.

Finally, the QCM can not only be used in a sensory mode but also as an actuator. It has been recently shown by Dultsev and coworkers [57] that virus particles deposited on the resonator surface may be displaced by increasing the shear amplitude of the resonator. Thus, it seems plausible that the resistance of cell–substrate interactions to lateral shear forces may be inferred from QCM measurements when the shear amplitude is increased to invasive magnitudes. The ease of the measurement, which can be automated and multiplexed, the rather simple experimental design, as well as the unique experimental access to the interface between living cells and technical substrates is very likely to create growing interest within the cell culture community for these new experimental options.

Acknowledgements The authors would like to express their gratitude to the Kurt-Eberhard-Bode Stiftung (Germany) for financial funding. VH is supported by the international Graduate School of Chemistry Muenster (GSC-MS, Germany). The expert help of Sandra Grunewald in preparing and maintaining the cell cultures is gratefully acknowledged.

References

1. Martin SJ, Granstaff VE, Frye GC (1991) Anal Chem 63:2272
2. Martin SJ, Frye GC, Ricco AJ (1993) Anal Chem 65:2910
3. Buttry D, Ward MD (1992) Chem Rev 92:1355
4. Bottom VE (1982) van Nostrand Reinhold Company, New York
5. Martin A, Hager HE (1989) J Appl Phys 65:2630
6. Sauerbrey G (1959) Z Phys 155:206
7. Janshoff A, Steinem C, Sieber M, el Baya A, Schmidt MA, Galla HJ (1997) Eur Biophys J 26:261
8. Janshoff A, Steinem C, Sieber M, Galla H-J (1996) Eur Biophys J 25:93
9. Gryte DM, Ward MD, Hu WS (1993) Biotechnol Prog 9:105
10. Redepenning J, Schlesinger TK, Mechalke EJ, Puleo DA, Bizios R (1993) Anal Chem 65:3378
11. Li J, Thielemann C, Reuning U, Johannsmann D (2005) Biosens Bioelectron 20:1333
12. Wegener J, Janshoff A, Galla HJ (1999) Eur Biophys J 28:26
13. Zhou T, Marx KA, Warren M, Schulze H, Braunhut SJ (2000) Biotechnol Prog 16:268
14. Marx KA, Zhou T, Montrone A, Schulze H, Braunhut SJ (2001) Biosens Bioelectron 16:773
15. Hug TS (2003) Assay Drug Dev Technol 1:479
16. Wegener J, Seebach J, Janshoff A, Galla HJ (2000) Biophys J 78:2821
17. Cans AS, Hook F, Shupliakov O, Ewing AG, Eriksson PS, Brodin L, Orwar O (2001) Anal Chem 73:5805
18. Bongrand P (1998) J Dispersion Sci Technol 19:963
19. Bell GI, Dembo M, Bongrand P (1984) Biophys J 45:1051
20. Pierres A, Benoliel AM, Bongrand P (2002) Eur Cells Mat 3:31
21. Vogler EA, Bussian (1987) J Biomed Mat Res 21:1197
22. Pierschbacher MD, Ruoslahti E (1987) J Biol Chem 262:17294
23. Pierschbacher MD, Ruoslahti E (1984) Nature 309:30
24. Reiss B, Janshoff A, Steinem C, Seebach J, Wegener J (2003) Langmuir 19:1816
25. Pignataro B, Steinem C, Galla HJ, Fuchs H, Janshoff A (2000) Biophys J 78:487
26. Luthgens E, Herrig A, Kastl K, Steinem C, Reiss B, Wegener J, Pignataro B, Janshoff A (2003) Meas Sci Technol 14:1865
27. Rodahl M, Höök F, Krozer A, Brzezinski P, Kasemo B (1995) Rev Sci Instrum 66:3924
28. Voinova MV, Jonson M, Kasemo B (2002) Biosens Bioelectron 17:835
29. Pignataro B, Steinem C, Galla HJ, Fuchs H, Janshoff A (2000) Biophys J 78:487
30. Rosenbaum JF (1988) Acoustic wave theory and devices. Artech House, Boston
31. Bandey HL, Martin SJ, Cernosek RW, Hillman AR (1999) Anal Chem 71:2205
32. Bandey HL, Hillman AR, Brown MJ, Martin SJ (1997) Faraday Discuss 107:105
33. Janshoff A, Wegener J, Sieber M, Galla HJ (1996) Eur Biophys J 25:93
34. Kanazawa KK, Gordon JG (1985) Anal Chem 57:1770
35. Lambacher A, Fromherz P (1996) Appl Phys A 63:207
36. Braun D, Fromherz P (1998) Phys Rev Lett 81:5241

37. Braun D, Fromherz P (1997) Appl Phys A 65:341
38. Marx KA, Zhou T, Montrone A, McIntosh D, Braunhut SJ (2005) Anal Biochem 343:23
39. Insall R, Machesky L (2001) Encyclopedia of life sciences. Wiley, Chichester
40. Brenner SL, Korn ED (1979) J Biol Chem 254:9982
41. Rotsch C, Braet F, Wisse E, Radmacher M (1997) Cell Biol Int 21:685
42. Hofmann UG, Rotsch C, Parak WJ, Radmacher M (1997) J Struct Biol 119:84
43. Bereiter-Hahn J, Karl I, Luers H, Voth M (1995) Biochem Cell Biol 73: 337
44. Shroff SG, Saner DR, Lal R (1995) Am J Physiol 269:C286
45. Hutter JL, Chen J, Wan WK, Uniyal S, Leabu M, Chan BM (2005) J Microsc 219:61
46. Rotsch C, Jacobson K, Radmacher M (1999) Proc Natl Acad Sci USA 96:921
47. Hoheisel D, Nitz T, Franke H, Wegener J, Hakvoort A, Tilling T, Galla HJ (1998) Biochem Biophys Res Commun 244:312
48. Schrot S, Weidenfeller C, Schaffer TE, Robenek H, Galla HJ (2005) Biophys J 89:3904
49. Castellino F, Heuser J, Marchetti S, Bruno B, Luini A (1992) Proc Natl Acad Sci USA 89:3775
50. Giaever I, Keese CR (1993) Nature 366:591
51. Giaever I, Keese CR (1991) Proc Natl Acad Sci USA 88:7896
52. Wegener J, Hakvoort A, Galla HJ (2000) Brain Res 853:115
53. Wegener J, Keese C, Giaever I (2002) Biotechniques 33:348
54. Wegener J (2003) Encyclopedia of life sciences. Wiley, Chichester
55. Pax M, Rieger J, Eibl RH, Thielemann C, Johannsmann D (2005) Analyst 130:1474
56. Sapper A, Wegener J, Janshoff A (2006) Anal Chem 78:5184
57. Dultsev FN, Ostanin VP, Klenerman D (2000) Langmuir 16:5036

Part C
Applications Based on Advanced QCM-Techniques

Springer Ser Chem Sens Biosens (2007) 5: 341–369
DOI 10.1007/5346_032

Published online: 29 July 2006

Enzyme Reactions on a 27 MHz Quartz Crystal Microbalance

Yoshio Okahata (✉) · Toshiaki Mori · Hiroyuki Furusawa · Takanori Nihira

Frontier Collaborative Research Center, Department of Biomolecular Engineering, Tokyo Institute of Technology, 4259 Nagatsuda, Midori-ku, 226-8501 Yokohama, Japan
yokahata@bio.titech.ac.jp

Abstract A quartz crystal microbalance (QCM) is known as a useful tool to detect gravimetric molecular interactions. We have developed a 27-MHz QCM (Affinix Q^4) to detect various biomolecular interactions such as DNA–DNA hybridization, DNA–protein interactions, glycolipid–protein interactions, and protein–protein interactions. In this chapter, we show that the 27-MHz QCM is also useful to detect the kinetics of enzyme reactions, because all the steps of enzyme reactions, such as the enzyme binding process to substrates, the enzyme catalytic reaction, and the release of enzyme from the product, accompany mass changes. We introduce here kinetic analyses of enzyme reactions on DNA (DNA polymerization, DNA ligation, and DNA cleavage) and enzyme reactions on glycans (glycosylation, phosphorylation, and mutation of enzymes) by using the substrate-immobilized 27-MHz QCM in solution.

Keywords QCM · Enzyme reaction · DNA polymerase · DNA hydrolysis · DNA ligation · DNA cleavage · Glycosylation · Phosphorylation · Mutation of enzyme

1 Introduction

A quartz crystal microbalance (QCM) is known to provide very sensitive mass measuring devices in gas phase [1–9] and in aqueous solution [10–18]. Its resonance frequency decreases linearly upon the increase of mass on a QCM

electrode at the nanogram level. We have recently developed a 27-MHz QCM instrument (Affinix Q4) to detect molecular recognitions in aqueous solution. An *Affinix* Q^4 (Initium, Tokyo, http://www.initium 2000.com) having four 500 μL cells equipped with a 27 MHz QCM plate (8 mm diameter of a quartz plate and an area of 4.9 mm^2 of Au electrode) at the bottom of the cell and a stirring bar with the temperature controlling system (see Fig. 1).

The Sauerbrey equation [19] was obtained for the AT-cut shear mode QCM:

$$\Delta f = -\frac{2f_0^2}{A\sqrt{\rho_q \mu_q}}\Delta m\,, \tag{1}$$

where Δf is the measured frequency change (Hz), f_0 the fundamental frequency of the quartz crystal prior to a mass change (27×10^6 Hz), Δm the mass change (g), A the electrode area (0.049 cm^2), ρ_q the density of quartz (2.65 g cm^{-3}), and μ_q the shear modulus of quartz (2.95×10^{11} dyn cm^{-2}). Calibration of the 27 MHz QCM was performed such that a frequency decrease of 1 Hz corresponded to a mass increase of 0.62 ± 0.1 ng cm^{-2} on the QCM electrode [17–42, 50–52, 58, 59, 64, 66, 72]. The noise level of the 27 MHz QCM was ±1 Hz in buffer solutions at 25 °C, and the standard deviation of the frequency was ±2 Hz for 2 h in buffer solutions at 25 °C. We have applied Affinix Q4 to detect various biomolecule interactions such as DNA–DNA hybridization [20–24], DNA–RNA interactions [25], in vitro selection of RNA and/or DNA [26, 27], DNA-protein interactions [28–32], RNA–peptide interactions [33, 34], sugar–protein interactions [35–40], and protein–protein interactions [41, 42] in aqueous solution.

Recently, we have applied this QCM system to detect enzyme reactions [50–52, 58, 59, 64, 72, 88]. Enzyme reactions have been kinetically

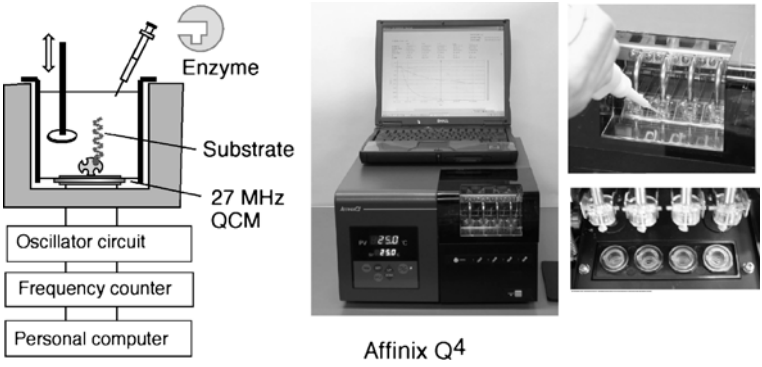

Fig. 1 Schematic illustration of Affinix Q4 having four 500 μL cells equipped with a 27 MHz QCM plate (8 mm diameter of a quartz plate and an area of 4.9 mm^2 of Au electrode) at the bottom of the cell and a stirring bar with the temperature controlling system

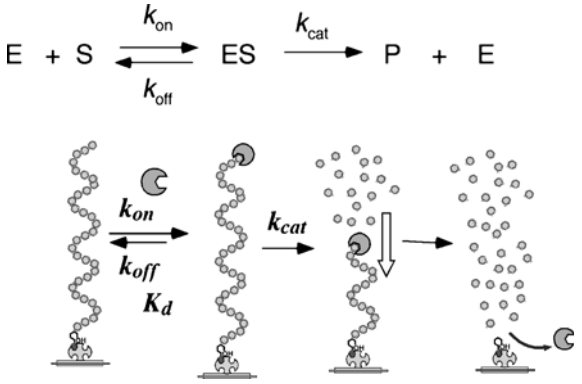

Fig. 2 Enzyme reactions on a substrate-immobilized QCM

studied by using a Michaelis–Menten equation (steady-state kinetics), in which the concentration of the enzyme–substrate (ES) complex is hypothesized to be nearly constant during the reaction, because it is difficult to detect the concentration of the ES complex. The reaction rate was simply obtained from the initial rate of the product increase. If the formation and decay of the ES complex could be followed during the reaction, more precise or quantitative enzyme kinetics could be expected. By using the substrate-immobilized QCM and injecting the enzyme in the solution, all reaction processes (the enzyme binding to the substrate (k_{on} and k_{off}), the catalytic reaction (k_{cat}), and the enzyme release from the product) could be followed as mass changes. We introduce here kinetic analyses of enzyme reactions on DNA (DNA polymerization, DNA ligation, and DNA cleavage) and enzyme reactions on glycans (glycosylation, phosphorylation, and mutation of enzymes) by using the substrate-immobilized 27-MHz QCM in solution.

2 Enzyme Reactions on DNA

Replication is one of the key reactions in the cellular processes. In this process, many kinds of proteins including enzymes interact with nucleic acids and express various functions [43]. Enzyme reactions on DNA strands such as DNA polymerization reactions, DNA ligations, and DNA cleaving reactions include the mass changes such as the mass increase due to the enzyme binding to DNA, the DNA elongation, the DNA ligation, and the mass decrease due to the DNA cleaving and the enzyme release from the product. In this chapter, we describe how some kinds of enzyme reactions on DNA can be precisely followed by using a DNA-immobilized QCM in aqueous solution.

2.1 DNA Polymerase Reactions

DNA polymerase is one of the enzymes responsible for replication and repair of DNA along the sequence of a template strand [43]. The reaction mechanism of polymerases has been mainly studied by Benkovic et al. by measuring the accumulation of radio isotope (RI)-labeled products as a function of time, which has been achieved by the combination of gel electrophoresis with a stopped flow/quenched flow technique, and by measuring time-resolved fluorescent spectroscopy [44–49]. Despite several improvements, these techniques have still some difficulties such as the requirement of isotope-labeling of probes and of special techniques. We show that the template/primer-immobilized 27 MHz QCM is a useful tool to detect directly and quantitatively each step of polymerase reactions in aqueous solution (Fig. 3) [50, 51]. Three steps of (1) binding of polymerase to the primer of the immobilized DNA on the QCM (mass increase), (2) elongation of complementary nucleotides along the template (mass increase), and (3) release of the enzyme from the polymerized DNA (mass decrease), could be observed continuously from time dependencies of frequency changes of the QCM.

Oligonucleotides having both a primer (25-mer) and a template (template I $(TTTTC)_3$ or template II $(TTTTC)_{10}$) were immobilized on a cleaned Au electrode of the QCM using a biotin–avidin method. The immobilized amount of the biotinylated template I or II was estimated to be 120 ± 10 and

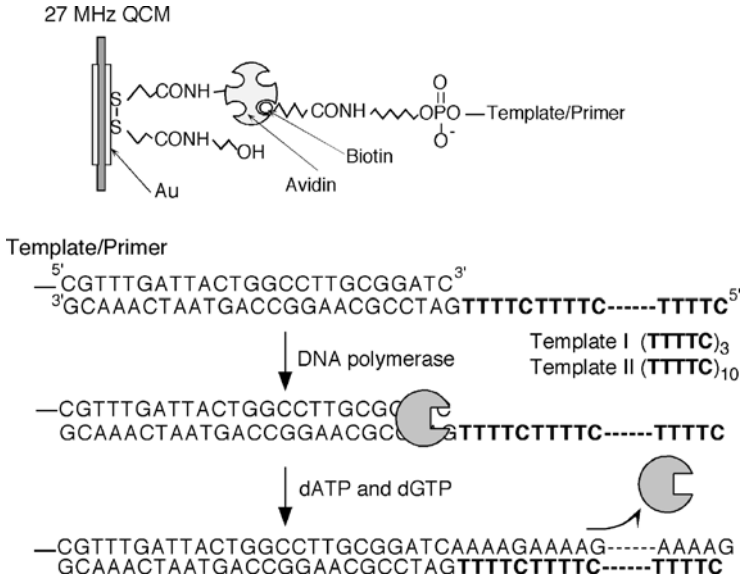

Fig. 3 DNA polymerase reactions on a template/primer-immobilized 27-MHz QCM

180 ± 10 ng cm^{-2} (ca. 6.0 ± 0.5 pmol cm^{-2}), respectively. The amount corresponds to ca. 15% coverage of the surface and this small coverage would give enough space for binding of a large enzyme molecule. Klenow fragment of DNA polymerase I from *E. coli* was chosen as a polymerase because it is expected to show only polymerase activity from 5′ to 3′ along the template in this experiment [43].

Figure 4 shows typical frequency changes as a function of time of the template I $(TTTTC)_3$-immobilized QCM, responding to the addition of Klenow fragment (Mw. 68 000, TaKaRa, Shiga, Japan) as a polymerase and/or dATP and dGTP as complementary monomers in aqueous solution. In curve A, when polymerase was injected at the arrow (7.0 pmol per 8 mL of a cell), the frequency decreased (mass increased) gradually for ca. 15 min due to the slow binding of polymerase on the primer (step 1). The binding amount at equilibrium was 140 ± 10 ng (2.0 pmol) cm^{-2}, which indicates one polymerase binds per ca. three template/primer chains, since 6.0 pmol (120 ± 10 ng cm^{-2}) of DNA was immobilized on the QCM. When monomers were added excessively at the second injection of the curve A (520 nmol per 8 mL), the mass rapidly increased within 1 min (step 2, $\Delta m = 40 \pm 5$ ng cm^{-2}) and then rapidly decreased to a constant value (step 3, Δm from the starting point is 40 ± 5 ng cm^{-2}). The elongated mass of 40 ng cm^{-2} (6.0 pmol) corresponds to the immobilized amount (6.0 pmol) of the single strand of the template $(TTTTC)_3$. The mass decrease at step 3 (140 ± 10 ng cm^{-2}) corresponds well to the mass increase due to the polymerase binding of the step 1 ($140 \pm$

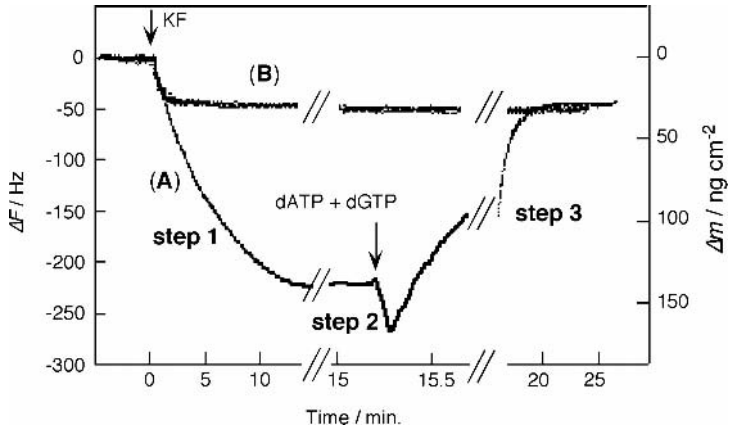

Fig. 4 Typical time courses of frequency changes of template I $(TTTTC)_3$-immobilized QCM, responding to the addition of polymerase (Klenow fragment) and monomers (dATP and dGTP). *A*: Polymerase was added at first and then excess monomers were added after the enzyme bound. *B*: Polymerase was added in the presence of excess monomers. 30 °C, pH 7.8, 20 mM Tris buffer, 10 mM $MgCl_2$, 40 mM KCl, [Klenow fragment] = 7.0 pmol per 8 mL, [dATP] = [dGTP] = 520 nmol per 8 mL

10 ng cm^{-2}). When a nonsense solution of dCTP and dTTP was injected instead of complementary monomers as a second injection, no changes in the frequency were observed. Thus, the mass increase at step 2 indicates elongation along the template, and the mass decrease at step 3 means the release of the enzyme from the completely polymerized DNA. After the release of the bound enzyme, the resulting mass increase was consistent with the mass increase at step 2 (40 ng cm^{-2} (6.0 pmol)).

When monomers of dATP and dGTP were present in advance and then polymerase was injected at the arrow, the mass simply increased as shown in curve B and reached the same mass increase as curve A (Fig. 4). Thus, the frequency change apparently reflects the mass increase due to the elongation on the QCM. This slow frequency change may reflect the slow binding of polymerase to the template, since the elongation process and the release of enzymes may proceed very fast in the presence of excess monomers.

When the long template II $(TTTTC)_{10}$ was employed at the same condition of curve A, both the binding amount (step 1) and the release amount (step 3) of polymerase were similar to those for template I (Table 1). In contrast, the mass increase due to the elongation (step 2 and the final mass increase) became ca. three times larger, corresponding to the 3.3 times longer length of the template.

Each step of these polymerase reactions observed in curve A was studied kinetically with changes in polymerase and NTP monomer concentrations.

The enzyme binding process: The KF binding process to the template/primer (step 1 of curve A in Fig. 4) is described by Eq. 2). The amount of the DNA/KF complex formed at time t after injection is given

Table 1 Kinetic parameters for ligase binding on bottom DNA having various terminal ends[a]

	k_{on} (10^{-4} M^{-1}s^{-1})	k_{off} (10^{-3} s^{-1})	K_a (10^{8} M^{-1})
	90	20	0.5
	20	8	0.3
	80	8	1
	80	1	8

[a] 20 °C, pH 7.5, 5 mM Tris-HCL, [ATP] = 1 mM, 40 mM NaCl, 6.6 mM $MgCl_2$, and 10 mM DTT

by: Eqs. 3–5:

$$\mathrm{DNA} + \mathrm{KF} \underset{k_{\mathrm{off}}}{\overset{k_{\mathrm{on}}}{\rightleftharpoons}} \mathrm{DNA/KF} \tag{2}$$

$$[\mathrm{DNA/KF}]_t = [\mathrm{DNA/KF}]_\infty \left[1 - \exp(-t/\tau)\right] \tag{3}$$

$$\Delta m_{\mathrm{t}} = \Delta m_\infty \left[1 - \exp(-t/\tau)\right] \tag{4}$$

$$\tau^{-1} = k_{\mathrm{on}}\,[\mathrm{KF}] + k_{\mathrm{off}}\,. \tag{5}$$

The relaxation time (τ) of KF binding is calculated from curve fitting the QCM frequency changes at various KF concentrations. KF binding and dissociation rate constants (k_{on} and k_{off}) could be obtained from the slope and intercept of the plot of τ^{-1} against KF concentration. The binding constants (K_{a}) could be also obtained from the ratio of k_{on} to k_{off}. The results are summarized in Fig. 5.

The DNA elongation process: Elongation reactions along the DNA template (step 2 of curve A in Fig. 4) were initiated by addition of complementary monomers (dNTP) after formation of the DNA/KF complex on the QCM. The elongation process is expressed simply by the Michaelis–Menten reaction between the DNA/KF complex and added monomers (Eqs. 6–8):

$$\mathrm{DNA/KF} \underset{}{\overset{k_{\mathrm{cat}}}{\rightleftharpoons}} \mathrm{DNA/KF/dNTP} \xrightarrow{k_{\mathrm{cat}}} \mathrm{DNA'/KF} \tag{6}$$

$$v_{\mathrm{o}} = \frac{k_{\mathrm{cat}}[\mathrm{DNA/KF}]_0[\mathrm{dNTP}]_0}{K_{\mathrm{m}} + [\mathrm{dNTP}]_0} \tag{7}$$

$$\frac{1}{v_0} = \frac{K_{\mathrm{m}}}{k_{\mathrm{cat}}[\mathrm{DNA/KF}]_0}\frac{1}{[\mathrm{dNTP}]_0} + \frac{1}{k_{\mathrm{cat}}[\mathrm{DNA/KF}]_0}\,, \tag{8}$$

where DNA′ indicates elongated DNA.

The initial elongation rate (v_0) increased with the addition of monomers, and the plot of v_{o} against NTP concentrations shows saturation behavior. From the reciprocal plots, the dissociation constants of dNTP monomers

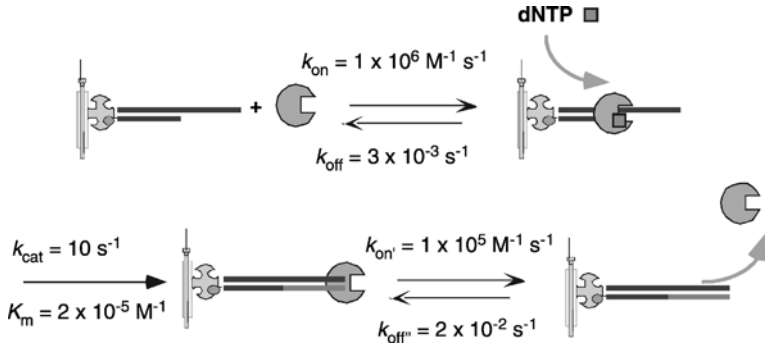

Fig. 5 Kinetic parameters of enzymatic reactions of DNA polymerase

(K_m) and the elongation catalytic rate constants (k_{cat}) were obtained from the slope and intercept (Eq. 8). Michaelis–Menten parameters for the template/primer **1** are summarized in Fig. 5.

The KF dissociation process: KF dissociation processes from the elongated DNA duplexes (step 3 of curve A in Fig. 4) were observed as frequency increases (mass decreases) on the QCM following the elongation process. The dissociation process is described by Eq. 9). The amount of DNA/KF complex remained at time t is given by Eqs. 10–12:

$$\mathrm{DNA/KF} \underset{k'_{on}}{\overset{k'_{off}}{\rightleftharpoons}} \mathrm{DNA} + \mathrm{KF} \tag{9}$$

$$-[\mathrm{DNA/KF}]_t = -[\mathrm{DNA/KF}]_\infty \left\{1 - \exp\left(\frac{-t}{\tau'}\right)\right\} \tag{10}$$

$$-\Delta m_t = -\Delta m_\infty \left\{1 - \exp\left(\frac{-t}{\tau'}\right)\right\} \tag{11}$$

$$\frac{1}{\tau'} = k'_{on} + k'_{off}\,. \tag{12}$$

The dissociation and rebinding rate constants (k'_{off} and k'_{on}) and binding constants (K'_a) for the dissociation process could be obtained similarly to that for step 1. These values were obtained by changing the template/primer sequences, and the results are summarized in Fig. 5.

We have determined all kinetic parameters for a three-step DNA polymerization by a Klenow fragment using a template/primer-immobilized QCM: KF binding of the template/primer with $K_a = 10^8\ M^{-1}$ ($k_{on} = 10^5\ M^{-1}s^{-1}$ and $k_{off} = 10^{-3}\ s^{-1}$ in step 1); Michaelis–Menten parameters of KF in the elongation process ($K_m = 10^{-5}$ M for monomers, $k_{cat} = 10\ s^{-1}$; and $K_m = 10^6\ M^{-1}s^{-1}$)(step 2), and $K'_a = 10^6\ M^{-1}$ ($k'_{on} = 10^4\ M^{-1}s^{-1}$ and $k'_{off} = 10^{-2}\ s^{-1}$) (step 3).

Thus, the binding constant of KF to the template was 100 times larger than that to the produced flat end. This is the first example of investigating both kinetically and quantitatively the binding, catalysis, and release processes of DNA polymerase reactions in situ on the same device.

2.2 DNA Ligation Reactions

DNA ligase has been used as a tool for in vitro DNA manipulation and cloning techniques. The reaction mechanism of DNA ligation has been mainly studied by measuring the combination of RI-labeled substrates and gel electrophoresis. Despite several improvements, these techniques have still some difficulties such as the requirement of isotope-labeling of probes and of special techniques.

In this section, we show the DNA ligation catalyzed by T4 phage ligase on the DNA-immobilized 27-MHz QCM in aqueous solution (Fig. 6) [52]. Oligonucleotides having various terminal ends were immobilized on one side of the Au electrode of the 27 MHz QCM through avidin–biotin linkages. The coverage of DNA strands on the QCM was estimated to be 17% of the electrode area to avoid steric hindrance for enzyme bindings.

Figure 7 shows typical time courses of frequency decreases (mass increases) of the bottom DNA-immobilized QCM, responding to the injection of T4 phage DNA ligase into the solution. Apparently, ligase bound largely to the bottom DNA having a TTCC-$P^{5'}$-phosphorylated terminal end, rather than to those having the short terminal end. Ligase hardly bound to the single strand DNA, nor even to the dsDNA in the absence of ATP. These results are consistent with findings that ligase is activated by transfer of the adenosyl group of AMP with ATP before bindings [53].

When the concentrations of injected ligase were increased in the range of 0.47–11.3 nM, binding amount showed a typical saturation curve. Binding and dissociation rate constants (k_{on} and k_{off}) and the association constant (K_a) could be obtained from time courses of Fig. 7. Results are summarized in Table 1. When the length of the terminal end increases or the terminal phos-

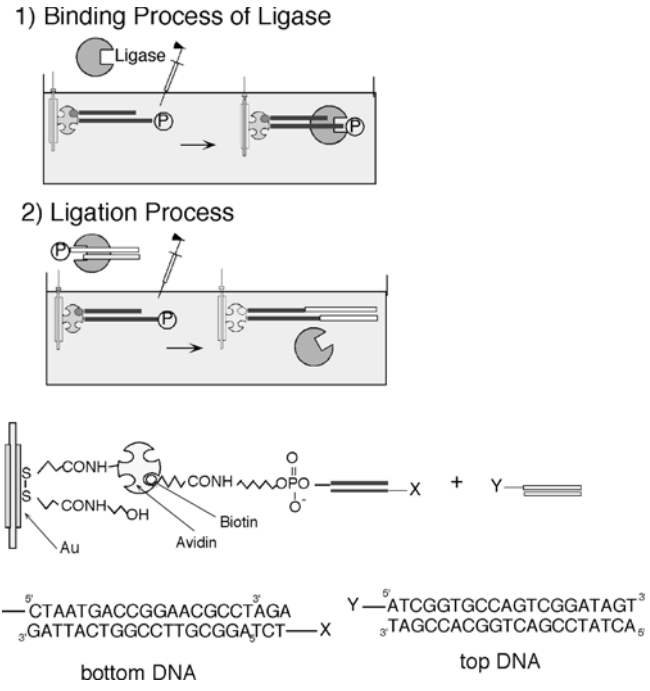

Fig. 6 Schematic illustration of ligase reactions detected on a 27-MHz QCM

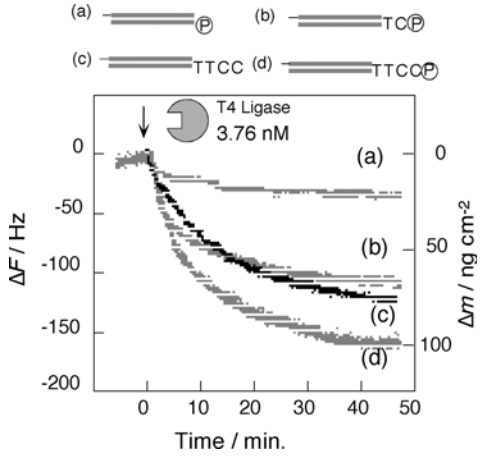

Fig. 7 Binding behavior of T4 phage DNA ligase onto various bottom DNAs on the QCM (20 °C, pH 7.5, 5 mM Tris-HCl, [ATP] = 1 mM, 40 mM NaCl, 6.6 mM $MgCl_2$, and 10 mM DTT)

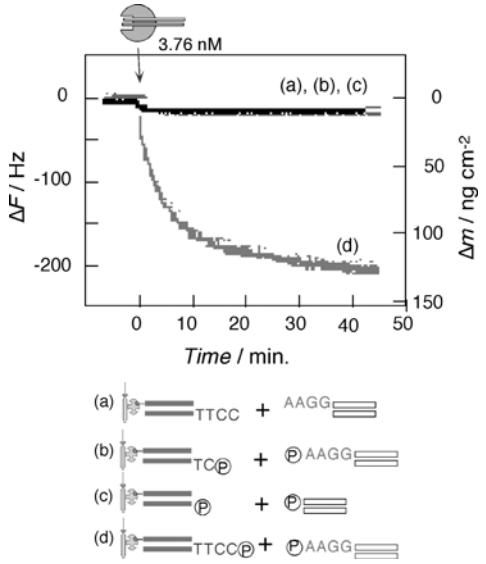

Fig. 8 Time course of ligation reactions responding to the addition of the complex of ligase and top DNA (5 mM Tris-HCl, pH 7.5, 40 mM NaCl, 6.6 mM $MgCl_2$, 10 mM DTT, 20 °C)

phate exists, K_a increases due to the decrease of k_{off}, and k_{on} is independent of the terminal structures.

When the complex of ligase and top DNA was injected to the bottom DNA-immobilized QCM, the mass increase due to the ligation reaction was observed only for the combination between the top and bottom DNA having

the terminal end and phosphate group (Fig. 8). Ligation was confirmed from mass changes of binding of complementary top DNA after washing with 0.1 M NaOH (dehybridization).

In conclusion, the QCM is useful to detect kinetically and quantitatively both the enzyme binding and ligation processes on the same device.

2.3 DNA Cleavage Reactions

ATP-dependent deoxyribonucleases (DNase) are enzymes that hydrolyze the phosphodiester linkage between deoxyribonucleosides in the presence of ATP. These enzymes are thought to be involved in the processes of genetic recombination and repair of radiation damages. The ATP-dependent DNase from *Micrococcus luteus* (Mw 160 kDa) shows the activity for single or double stranded linear DNA via an end-attachment $3' \rightarrow 5'$ exonucleolytic processive mechanism, and shows no activity for circular DNA [54–56]. It has been used as a tool for DNA manipulation to prepare circular DNA in vitro [57]. The reaction mechanism of DNA hydrolysis by this enzyme has been studied mainly in solution by measuring the accumulation of the acid-soluble hydrolysis products from radioisotope-labeled substrates as a function of time [54–56]. Despite several improvements, this technique still has some difficulties, such as the requirement of radioisotope labeling of probes and of special techniques.

In this section, we describe the DNA cleavage reactions catalyzed by ATP-dependent DNase on the DNA-immobilized 27 MHz-QCM [58, 59]. A schematic illustration of the experimental setup and chemical structures of oligonucleotides are shown in Fig. 9. Various oligodeoxyribonucleotides with different chemical structures were used: the 3′-biotinylated dsDNA (51 bp) having a blunt end (**1**) and a 5′–15 base overhanging (**2**), and the 3′-biotinylated or 5′-biotinylated single strand DNA (**3** or **4**, respectively). These oligodeoxyribonucleotides were immobilized on a cleaned Au electrode of the QCM using a biotin–avidin linkage and a tetraethyleneglycol spacer. The immobilized amount of the dsDNA (**1**) was estimated to be 60 ± 2 ng cm^{-2} (ca. 1.9 ± 0.1 pmol cm^{-2}). The amount corresponds to approximately 4% coverage of the Au surface, and this small coverage would give enough space for binding of a large enzyme molecule. The immobilized amount of other DNAs was also estimated to be 4% coverage.

Figure 10 shows typical frequency changes of the dsDNA (**1**)-immobilized QCM as a function of time, responding to the addition of the ATP-dependent DNase and ATP in the solution. In curve a, when 138 nM of DNase was injected at the first arrow, the frequency decreased (mass increased) gradually for 30 min due to the slow binding of DNase to the dsDNA (step 1). When an ATP solution (0.5 mM) was added excessively at the second injection of curve a, the frequency rapidly increased (mass decreased) to a constant value (30 ± 3 ng cm^{-2} over the starting point) within a few minutes (step 2). This

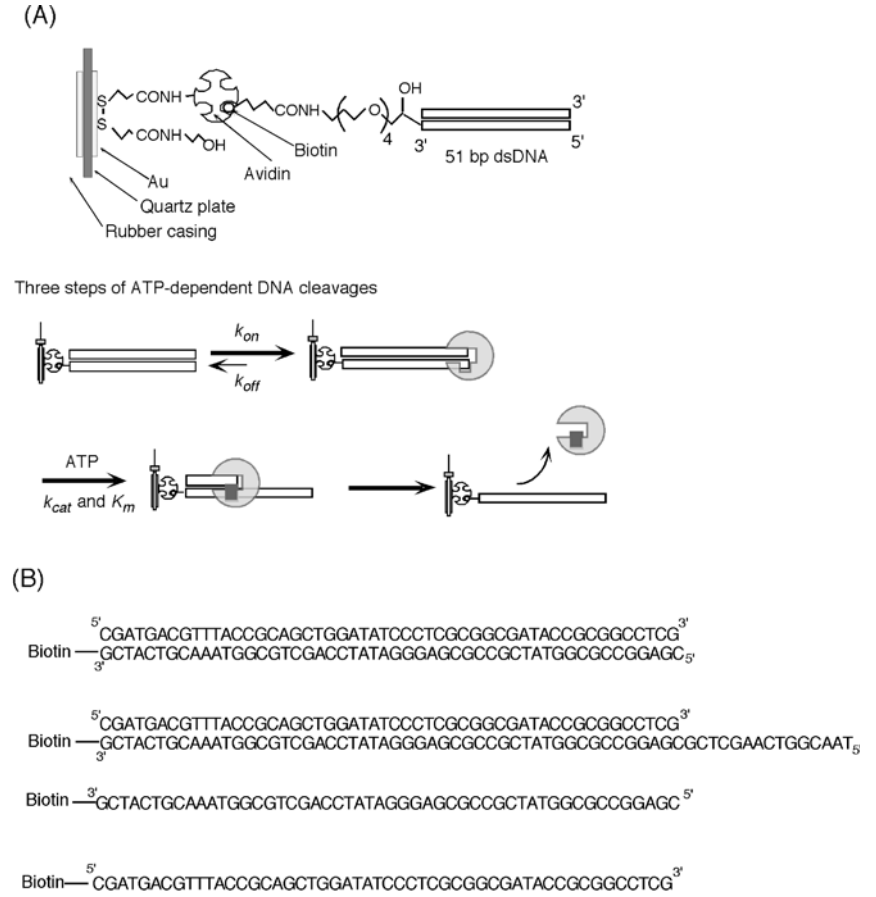

Fig. 9 **a** Experimental setup of enzymatic DNA cleavage reactions on a DNA-immobilized 27-MHz QCM in buffer solution. **b** DNA structures immobilized on the QCM

indicates that ATP-dependent DNase can hydrolyze dsDNA using the hydrolysis energy of ATP. When ATP had existed in advance and then the enzyme was injected, the frequency simply increased (mass decreased) as shown in curve (b) and reached the same mass decrease as shown in curve (a). The decreased mass from the starting point was 30 ± 3 ng cm^{-2}, corresponding to 50 ± 5% of the immobilized dsDNA (**1**); the one strand is completely hydrolyzed. Since the ATP-dependent DNase is reported to hydrolyze dsDNA from the 3′-end [54–56], the 3′ → 5′ hydrolysis occurs only the upper strand of dsDNA because the 3′-end of the lower strand is blocked by a biotin–avidin linkage. Thus, the mass decrease in step 2 of curve a reflects two processes: the complete 3′ → 5′ hydrolysis of the upper strand of immobilized dsDNA and the release of enzyme from the QCM after the hydrolysis. The frequency change in curve b also reflects the mass decrease due to the hydrolysis on the

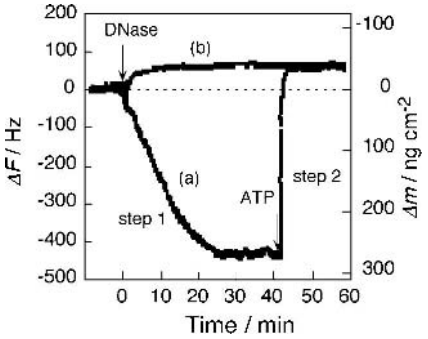

Fig. 10 Typical time course of frequency changes of the dsDNA **1**-immobilized QCM, responding to the addition of ATP-dependent DNase and ATP at *arrows*. *Curve a* DNase was added at first, and then ATP was excessively added after the enzyme bound. *Curve b* DNase was added in the presence of excess ATP. Conditions: 66.7 mM Glycine-NaOH buffer, pH 9.4, 30 mM $MgCl_2$, 8.4 mM 2-mercaptoethanol, 0.1% Nonidet P-40 (ethylphenyl polyethyleneglycol), 30 °C, [DNase] = 138 nM, [ATP] = 0.5 mM

QCM. This slow frequency change may reflect the slow binding of enzyme to the dsDNA, since the hydrolysis process and the release of enzymes may proceed faster in the presence of excess ATP in the solution.

When the concentrations of the injected DNase were changed in the range of 14–56 nM in the absence of ATP, the binding amount of the enzyme showed a typical saturation curve. Binding and dissociation rate constants (k_{on} and k_{off}) and association constant (K_a, the ratio of k_{on} to k_{off}) of the enzyme for various DNA strands could be obtained from time courses of step 1 of curve a. Results are summarized in Table 2. In comparison, the kinetic parameters of the dsDNA having the blunt end (**1**) with those of the dsDNA having the 5′-overhanging (**2**), the K_a value of (**2**) was twice as large as that of (**1**) due to

Table 2 Kinetic parameters of ATP-dependent DNase for various DNA strands[a]

DNA	Binding process			Hydrolysis process		
	k_{on}/ (10^3 $M^{-1}s^{-1}$)	k_{off}/ (10^{-3} s^{-1})	K_a/ (10^6 M^{-1})	k_{cat}/ (10^3 s^{-1})	K_m/ (10^{-6} M)	k_{cat}/K_m/ (10^6 $M^{-1}s^{-1}$)
1	8.0 ± 0.3	0.29 ± 0.01	28 ± 2	4.0 ± 0.1	15 ± 1	270 ± 5
2	7.9 ± 0.1	0.14 ± 0.01	56 ± 6	–	–	–
3	nd	nd	nd	nd	nd	nd
4	97 ± 7	4.9 ± 0.5	19 ± 5	0.7 ± 0.1	11 ± 1	64 ± 3

[a] pH 9.4, 66.7 mM glycine-NaOH buffer, 30 mM $MgCl_2$, 8.4 mM 2-mercaptethanol, 0.1% Nonidet P-40 (ethylphenylpolyethyleneglycol), 30 °C
nd not detected

the decrease of the k_{off} value by half. Since the overhanging structure of (**2**) corresponds to the hydrolyzing process by the enzyme, the higher affinity of the enzyme for the overhanging structure than for the blunt end is reasonable for the progressive and efficient hydrolysis due to the low dissociation rate constant (k_{off}). For the 5′-free ssDNA (**3**) structure that corresponds to the completely hydrolyzed dsDNA (**1**), the binding of the enzyme could not be observed in the same range of enzyme concentration. These results clearly reflect that the DNase can bind to the blunt end of dsDNA (**1**) and the K_a value increased twofold during the $3' \rightarrow 5'$ hydrolysis process, and then the DNase is easily released from the completely hydrolyzed form of ssDNA (**3**). The DNase can bind to the 3′-free ssDNA (**4**) with the similar K_a value to that for the blunt end dsDNA (**1**), in which both k_{on} and k_{off} values for (**4**) are ten times larger than those for (**1**). This indicates that the DNase can bind to the 3′-end whether the single or double strand. However, the dsDNA structure is favorable for the stable enzyme–DNA complex due to the very slow binding and dissociation rate constants.

Hydrolysis by the enzyme for dsDNA (**1**) and 3′-free ssDNA (**5**) was also investigated. When ATP concentrations injected in step 2 were changed in the range of 2.5–200 μM, the initial rates of step 2 showed the saturation behavior of Michaelis–Menten kinetics. The catalytic hydrolysis rate constant (k_{cat}), K_m for ATP, and apparent second-order rate (k_{cat}/K_m) are also summarized in Table 2. The k_{cat}/K_m value for (**1**) was fourfold larger than that for (**4**) due to the large k_{cat} and the constant K_m values for (**1**). Thus, the binding ability of ATP to the enzyme–DNA complex was independent of the DNA structure, and the DNase can efficiently hydrolyze the dsDNA compared with the ssDNA.

In summary, the QCM is useful for detecting kinetically and quantitatively, as the mass changes on the same device, each step of DNA cleavage reactions, such as the enzyme binding, the hydrolysis process along DNA strands in the presence of ATP, and then the release of the enzyme from the completely hydrolyzed ssDNA.

3 Enzyme Reactions on Glycans

In the case of enzyme reactions on DNA, several conventional methods for following the reactions have been developed, such as gel electrophoresis using a radio-isotope reagent and fluorescent analysis introducing a fluorescent probe in the DNA molecules. However, in the case of glycans, it is difficult to employ gel electrophoresis and to introduce a functional reagent into the sugar molecules. Therefore, even now, the conventional colorimetric method (Somogyi–Nelson method) is one of the most popular techniques used for following the glycosidase reactions [60, 61]. If the glycan-immobilized QCM is employed, we can follow the ES complex formation and kinetic parameters

for the enzyme binding process to the substrate, the catalytic process, and the release of the enzyme from the product.

3.1
Hydrolysis of Amylopectin by Glucoamylase

Glucoamylase (from *Aspergillus niger*, EC 3.2.1.3, Mw 63 kDa) is known to catalyze the release of β-D-glucose from the non-reducing ends of a soluble starch such as amylopectin (α-1,4 glucan with α-1,6 linkages at branch points) and of pullulan (glucan of α-1,6 linked maltotriosyl units) [62, 63]. The total steps of (1) the binding of glucoamylase to the glucan substrate (mass increase) and (2) the hydrolysis of substrate (mass decrease) could be observed continuously from the time dependence of frequency changes of the QCM [64]. The biotinylated amylopectin (average Mw 100 ± 50 kDa) or pullulan (Mw 400 kDa), in which the reducing ends were reacted with biotinamidocaproyl hydrazide, was anchored on a streptavidin-immobilized QCM (Fig. 11). The immobilized amounts of the biotinylated amylopectin or pullulan were estimated to be 150 ± 10 ng cm^{-2} or 140 ± 10 ng cm^{-2}, respectively, which correspond to ca. 20% coverage of the surface. This small coverage would give enough space for binding of a large enzyme molecule.

Figure 12a shows typical frequency changes as a function of time of the amylopectin- or pullulan-immobilized QCM, responding to the addition of different concentrations (16–54 nM and 540 nM, respectively) of glucoamylase in the aqueous solution. By the addition of enzyme to the glucan-immobilized QCM, the frequency decreased (mass increased) at first due to the binding of glucoamylase to the non-reducing ends of glucans. Then, the frequency gradually increased (mass decreased) due to the hydrolysis of substrates on the QCM, and then it reached the constant value (-150 ± 10 ng cm^{-2} over the starting point) independent of the added enzyme con-

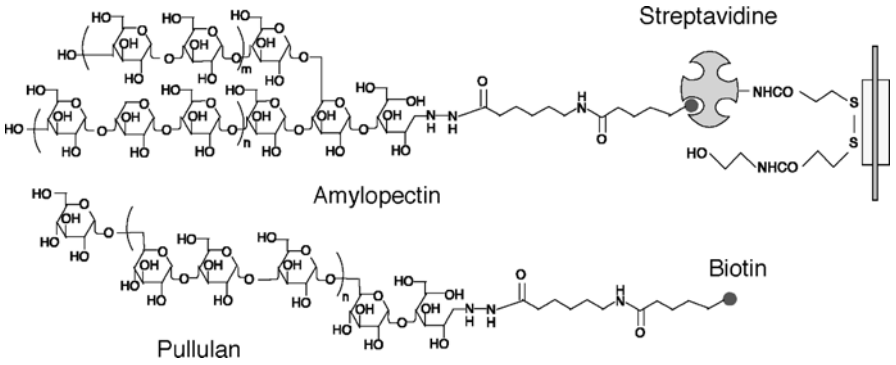

Fig. 11 Chemical structures of amylopectin- and pullulan-immobilized 27-MHz QCM (reaction schemes and experimental setup are the same as in Fig. 2)

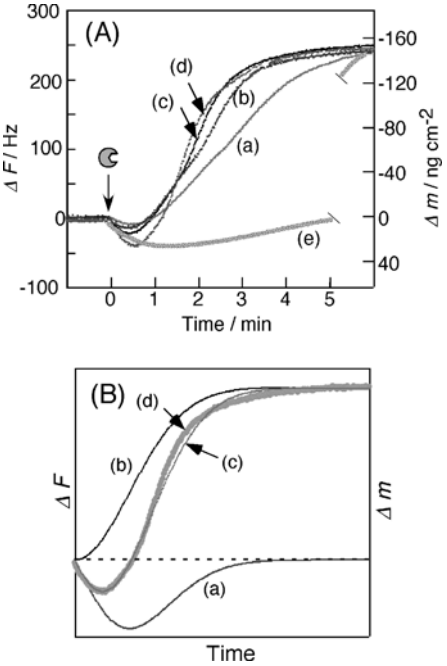

Fig. 12 **a** Time course of frequency changes of the amylopectin-immobilized QCM, responding to the addition of glucoamylase at *curve a* 16 nM, *curve b* 27 nM, *curve c* 38 nM, and *curve d* 54 nM. The *curve e* shows the hydrolysis of the pullulan-immobilized QCM at 540 nM glucoamylase (25 °C, 20 mM acetate buffer, pH 4.8, 0.1 M NaCl). **b** *Curve a* theoretical time dependence of [ES] as shown in Eq. 13, *curve b*) theoretical time dependence of [P] as shown in Eq. 14, *curve c* the fitted curve obtained from simultaneous equations of Eqs. 13 and 14, and *curve d* the experimental curve at $[E]_0 = 54$ nM and $[S]_0 = 140\ \mathrm{ng\,cm^{-2}}$ on a QCM

centrations (curves a–d). Since amylopectin or pullulan was immobilized in the amount of $150 \pm 10\ \mathrm{ng\,cm^{-2}}$ or $140 \pm 10\ \mathrm{ng\,cm^{-2}}$ on the QCM plate, this clearly indicates that all of amylopectin or pullulan were hydrolyzed by the enzyme and the enzyme was released from the QCM plate. In the case of the pullulan-immobilized QCM (curve e), the hydrolysis reaction looks very slow even with the high concentration of glucoamylase (540 nM).

In the sigmoidal curves of Fig. 12a, the time dependence of Δm values reflect both the formation of the ES complex (Eq. 13) and the hydrolysis of substrate (the product formation (Eq. 14)):

$$[\mathrm{ES}] = [\mathrm{ES}]_{\max}\left(1 - e^{-\frac{t}{\tau}}\right) - [\mathrm{P}]\left(1 - e^{-\frac{t}{\tau}}\right) \tag{13}$$

$$[\mathrm{P}] = \frac{k_{\mathrm{cat}}}{D_{\mathrm{p}}} \int [\mathrm{ES}]\,\mathrm{d}t \tag{14}$$

$$\tau^{-1} = k_{\mathrm{on}}[\mathrm{E}]_0 + k_{\mathrm{off}}\,, \tag{15}$$

where, ES, P, and D_p are the enzyme–substrate complex, product, and the degree of polymerization of substrate, respectively. The curves a and b in Fig. 12b were calculated from Eqs. 13 and 14, respectively. Curve c is the fitted curve obtained from the simultaneous equations both of Eqs. 13 and 14, and curve d is the experimental curve at $[E]_0 = 54$ nM and $[S]_0 = 140$ ng cm^{-2} on the QCM. The plot of the reciprocal relaxation time versus enzyme concentrations was linear; the slope and y-intercept of the plot yielded values for k_{on} and k_{off}, respectively (Eq. 15). The dissociation constant (K_d) of enzyme to the substrate was obtained from k_{off}/k_{on}. These kinetic parameters are summarized in Table 3.

The dissociation constant K_d for pullulan was larger than that for amylopectin due to the slow binding (k_{on}) and the fast release (k_{off}) of the enzyme (Table 3). The hydrolysis rate constant in the ES complex (k_{cat}) of pullulan was ca. 30 times slower than that of amylopectin. This reflects the slow reaction of pullulan compared with amylopectin (curve e of Fig. 10a), due to the slow hydrolysis of α-1,6 linkages compared with α-1,4 linkages catalyzed by glucoamylase [62, 63].

When the QCM technique was employed for the starch hydrolysis, all kinetic parameters both of the enzyme binding process (k_{on}, k_{off} and K_d) and the hydrolysis process (k_{cat}) could be obtained simultaneously on the same device, as shown in Table 3. In the conventional enzyme reactions in the bulk solution, Michaelis–Menten kinetics have been applied to obtain both the Michaelis constant (K_m) and the hydrolysis rate constant (k_{cat}) according to Eq. 16. If $k_{off} \gg k_{cat}$, the K_m value is thought to be the apparent dissociation constant ($K_d = k_{off}/k_{on}$):

$$K_m = \frac{k_{off} + k_{cat}}{k_{on}} . \tag{16}$$

In the Michaelis–Menten kinetics of glucoamylase for amylopectin, $K_m = 5.9 \times 10^{-5}$ M and $k_{cat} = 40$ s^{-1} had been obtained (Table 3) [65]. The k_{cat} values

Table 3 Kinetic parameters of α-glucanhydrolysis catalyzed by glucoamylase

Method	Substrate	k_{on} (10^3 M^{-1}s^{-1})	k_{off} (10^{-3} s^{-1})	K_d (10^{-6} M)	K_m (10^{-6} M)	k_{cat} (s^{-1})
QCM [a]	Amylopectin	23	0.093	0.0040	–	93
	Pullulan	1.8	0.36	0.20	–	2.8
Michaelis–Menten [b]	Amylopectin	–	–	–	59	40

[a] Substrate was immobilized on a QCM plate (this work); 25 °C, 20 mM acetate buffer, pH 4.8, 0.1 M NaCl

[b] Glucose oxidase method monitored into microtiter plates; initial rates were analyzed by Michaelis–Menten equation; 45 °C, 50 mM acetate buffer, pH 4.5, from [65]

obtained from the QCM and the Michaelis–Menten kinetics were relatively consistent with each other, however, the dissociation constants K_d is a factor of 10^4 smaller than the Michaelis–Menten constant K_m. In the Michaelis–Menten equation, K_m value is the dissociation constant only when $k_{off} \gg k_{cat}$ (Eq. 16). However, the value of $k_{off} = 9.3 \times 10^{-5}\ s^{-1}$ was obtained as a very small value compared with $k_{cat} = 93\ s^{-1}$ from the QCM experiment. Thus, in the case of the α-1,4 glucan hydrolysis such as amylopectin by glucoamylase, K_m value does not reflect the dissociation constant (K_d), and the K_d value obtained from k_{off}/k_{on} by the QCM method reflects the real dissociation constant. Therefore, it is important to grasp all kinetic parameters such as k_{on}, k_{off}, K_d, and k_{cat} on one device in the enzyme reactions.

3.2
Phosphorolysis of Amylopectin by Phosphorylase b

Glycogen phosphorylase (EC 2.4.1.1) catalyzes the phosphorolysis of α-1,4 glucosidic linkages from the non-reducing ends of glycogen to produce a glucose-1-phosphate (G-1P) [66]. Phosphorylase b (from rabbit muscle) is a typical glycogen phosphorylase for amylopectin in the presence of excess phosphate anions, and generally exists as an inactive T-state conformation in the liver. It is changed to the active R-state conformation by AMP (adenosine monophosphate) binding [67–71]. Thus, the activity of phosphorylase b can be regulated by the addition of AMP. The cleavage of α-1,4 glucosidic linkages has been studied using radioisotope-labeled phosphoric acid to follow the production of glucose-1-phosphate in solution. If the formation and decomposition of the ES complex can be followed directly during the reaction, more accurate kinetic constants might be obtained.

All kinetic processes of phosphorylase b for the amylopectin substrate, such as enzyme binding (mass increase), the activation of enzyme by AMP binding, and a phosphorolysis of substrates (mass decrease), were analyzed by following the frequency (mass) changes of the amylopectin-immobilized 27 MHz-QCM (Fig. 13) [72]. In the binding process of phosphorylase b to the non-reducing ends of amylopectin, the binding (k_{on}) and dissociation (k_{off}) rate constants, and dissociation constant (K_d) of the enzyme–substrate complex could be obtained. In the following activation step by AMP, the Michaelis constant for AMP (K_{AMP}) to the enzyme could be obtained. In the phosphorolysis step, the catalytic rate constant (k_{cat}) was obtained from the initial rate of phosphorolysis.

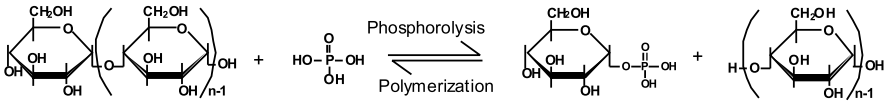

Equation 17

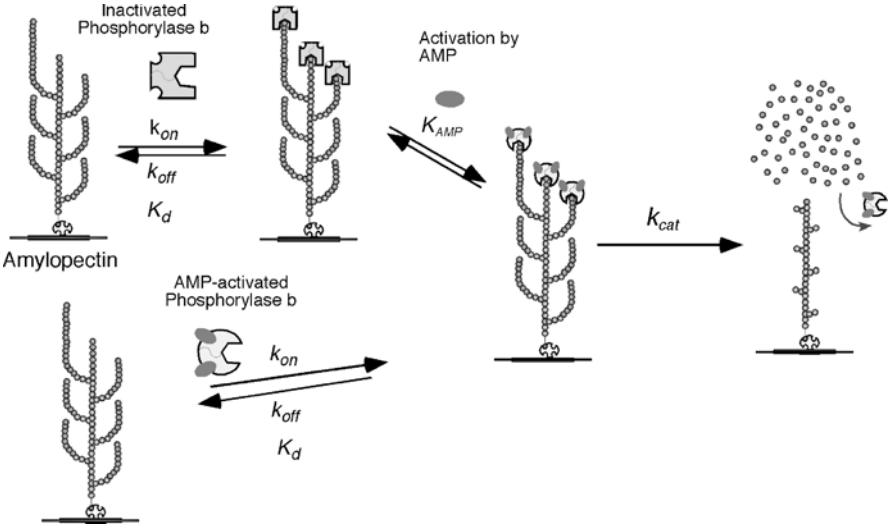

Fig. 13 Reaction schemes of phosphorolysis reactions on an amylopectin-immobilized 27-MHz QCM in phosphate buffer solution (chemical structure of amylopectin is shown in Fig. 11)

Figure 14 shows typical frequency changes of the amylopectin-immobilized QCM as a function of time, responding to the addition of phosphorylase b and/or AMP in the buffer solution containing excess amount of phosphate ions (50 mM). In method A, the inactivated phosphorylase b was injected (13.4 nM) and this corresponded to a gradual frequency decease for 15 min due to the slow binding of the enzyme to amylopectin (step 1). After the frequency change reached equilibrium, excess AMP (2 mM) was injected to the solution. The frequency rapidly increased (mass decreased) to a constant value (-180 ± 20 ng cm^{-2} over the starting zero point) within a few minutes (step 2). This indicates that phosphorylase b could bind to amylopectin even as the inactivated form and the activated enzyme by AMP could phosphorolyze amylopectin on the QCM. In method B, when the AMP-activated enzyme was injected in the presence of excess AMP, the frequency decreased (mass increased) slightly at first and then spontaneously increased (mass decreased) and reached the same mass decrease obtained by method A. This continuous frequency change shows that the binding of AMP-activated enzyme to the substrate (mass increase) was followed by phosphorolysis (mass decrease).

The mass decrease from the starting zero point was -180 ± 20 ng cm^{-2}, which corresponds to 30% of the immobilized amylopectin (620 ng cm^{-2}, ca. 6.2 pmol cm^{-2}). The amylopectin is a branched α-1,4 glucan with α-1,6 glucosidic linkages at branched points as shown in Fig. 13. It is known that AMP-activated phosphorylase b can phosphorolyze amylopectin from the

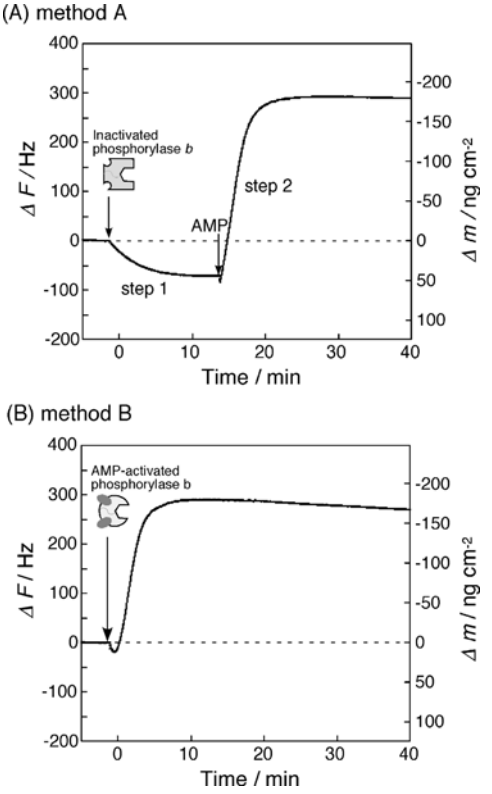

Fig. 14 Typical time course of frequency changes of the amylopectin-immobilized 27-MHz QCM, responding to the addition of **a** the inactivated phosphorylase b and then AMP, and **b** the AMP-activated phosphorylase b in the presence of excess AMP. Immobilized amount of amylopectin = 620 ± 20 ng cm^{-2} (6.2 pmol cm^{-2}) on a QCM plate (4.9 mm^2 Au electrode), [phosphorylase b] = 13.4 nM, [AMP] = 2 mM; 50 mM phosphate buffer, pH 6.8, 200 mM NaCl, 25 °C

non-reducing ends of α-1,4 glucosidic linkages, but cannot phosphorolyze the α-1,6 branched points of amylopectin. Thus, the mass decrease of 180 ± 10 ng cm^{-2} after phosphorolysis in both methods A and B indicates that the enzyme phosphorolyzed the branched α-1,4 glucosidic linkages of amylopectin and released these fragments.

Curve-fittings of step 1 of method A enabled us to obtain:

1. The binding and dissociation rate constants (k_{on} and k_{off}, respectively) and dissociation constant ($K_d = k_{off}/k_{on}$) of inactivated phosphorylase b to substrate
2. From step 2 of method A, we obtained the catalytic phosphorolysis rate constant (k_{cat}) and Michaelis constant for AMP (K_{AMP}) of the AMP-activated enzyme

3. From method B, we determined the binding and phosphorolysis rate constants (k_{on}, k_{off}, K_d, and k_{cat}) of AMP-activated enzyme

All kinetic parameters obtained are summarized in Table 4.

Dissociation constant (K_d) of AMP-activated enzyme from amylopectin was ca. ten times smaller than that of the inactivated enzyme (1.4 nM and 12 nM, respectively). This is mainly because AMP-activated phosphorylase b has a ca. 40 times lower dissociation rate constant ($k_{off} = 5.0 \times 10^{-5}$ s^{-1}) than that of the inactivated enzyme ($k_{off} = 1.9 \times 10^{-3}$ s^{-1}). Thus, AMP activation of phosphorylase b is more effective at decreasing the dissociation rate constant (k_{off}) than increasing the binding rate constant (k_{on}) to amylopectin.

The phosphorolysis reaction is started by activated phosphorylase b. In method A, the ES complex is first formed and then phosphorolysis is triggered by the addition of AMP. The k_{cat} value (21 s^{-1}) of the inactivate phosphorylase was similar to $k_{cat} = 18$ s^{-1} of the AMP-activated enzyme. In addition, the k_{cat} value of AMP-activated enzyme also gave a similar k_{cat} value (18 s^{-1}). This result indicates that the inactivated enzyme could be activated by the addition of AMP and shows the same activity as the AMP-activated enzyme. The dissociation constant for AMP (K_{AMP}) was found to be 1.0×10^{-4} M, and this is a reasonable value as the dissociation constant for small substrates. The K_{AMP} obtained from the QCM method was consistent with a previous determination using a radio-isotope method in the bulk solution ($K_{AMP} = 1.2 \times 10^{-4}$ M) [73].

In the Michaelis–Menten kinetics of phosphorylase b for amylopectin, $K_m = 2.0 \times 10^{-6}$ M and $k_{cat} = 24$ s^{-1} was previously obtained in bulk solution (Table 4) [74–77]. Catalytic rate constants ($k_{cat} = 21$ s^{-1}) obtained from the QCM method were relatively consistent with $k_{cat} = 24$ s^{-1} obtained from Michaelis–Menten kinetics in the bulk solution. The dissociation constants, however, were 10^3 times different from each other ($K_d = 1.4 \times 10^{-9}$ M from

Table 4 Comparison of kinetic parameters of phosphorolytic reactions catalyzed by phosphorylase b from rabbit muscle [a]

Phosphorylase b	k_{on} (10^3 $M^{-1}s^{-1}$)	k_{off} (10^{-3} s^{-1})	K_d (10^{-9} M)	K_m (10^{-6} M)	k_{cat} (s^{-1})	K_{AMP} (10^{-4} M)
Inactivated enzyme (method A)	160	1.9	12	–	21	1.0
AMP-activated enzyme (method B)	36	0.05	1.4	–	18	
In bulk solution	–	–	–	2.0	24	1.2

[a] [Immobilized amount of amyl opectin] = 620 ± 20 ng cm^{-2} (6.2 pmol cm^{-2}), [Phosphorylase b] = 9.4–27 nM, pH 6.8, 50 mM phosphate buffer, 200 mM NaCl, at 25 °C

the QCM method and $K_m = 2.0 \times 10^{-6}$ M from the Michaelis–Menten kinetics method). This is for the same reason as mentioned in the case of the hydrolysis of amylopectin by glucoamylase (Sect. 3.1). Thus, in the case of the amylopectin phosphorolysis by phosphorylase b, the K_m value may reflect the k_{cat}/k_{on} value, but not the dissociation constant (K_d). The K_d value obtained from k_{off}/k_{on} by the QCM method reflects the real dissociation constant. In these enzyme reactions, enzymes slowly bind to substrate and proceed to phosphorolysis or hydrolysis without releasing from the substrate ($k_{cat} \gg k_{off}$). Therefore, it is important to grasp all kinetic parameters such as k_{on}, k_{off}, K_d, and k_{cat} on one device in the enzyme reactions.

In conclusion, phosphorylase b can bind strongly to the amylopectin substrate even as the inactivated form, and the enzyme is activated promptly by the addition of AMP leading to phosphorolysis of α-1,4 linkages of amylopectin. This is the first example of simultaneous detection of the binding and catalysis of phosphorylase b reactions in situ on the same device.

3.3
Mutation Studies of Isomalto-dextranase for Dextran Hydrolysis

For analyses of the active center of enzymes, site-directed mutagenesis has been widely studied and the kinetic effect of mutations has been again studied by using a Michaelis–Menten method of product analysis. However, when the site-directed mutagenesis nearly diminishes the enzyme activity and the product is hardly produced, it is difficult to distinguish whether mutations affect the substrate binding or the catalytic process since only the product is followed. If the formation and decay of the ES complex could be followed directly during the reaction, more precise and quantitative discussions on the site-directed mutagenesis can be expected.

Isomalto-dextranase (1,6-α-D-glucan isomaltohydrolase, EC 3.2.1.94) is an *exo*-type enzyme that is capable of hydrolyzing dextran and releasing α-isomaltose units successively from the non-reducing ends of dextran-chains via a retaining reaction mechanism [78, 79]. It is produced extracellularly by *Arthrobacter globiformis* T6 and *Actinomadura* sp. R-10 [78, 80], and the cloning of the *imd* gene encoding this enzyme has been reported [81]. It was classified as a member of a family comprising mainly eukaryotic α-galactosidases [82] and α-*N*-acetylgalactosaminidases [83], which is designated as a glycoside hydrolase (GH) family 27 [84, 85]. The crystallization and preliminary X-ray diffraction analysis of isomalto-dextranase from *A. globiformis* T6 has been reported [86]; however, the three-dimensional structure and reaction mechanisms of this enzyme are as yet unknown. Multiple sequence alignments of a GH family 27 such as *A. globiformis* T6 isomalto-dextranase (IMD) [81], chicken α-*N*-acetylgalactosaminidase (NAG) [83], rice α-galactosidase (GALA) [82], and human α-galactosidase (GALH) [87] are shown in Fig. 15. The letters with black background have

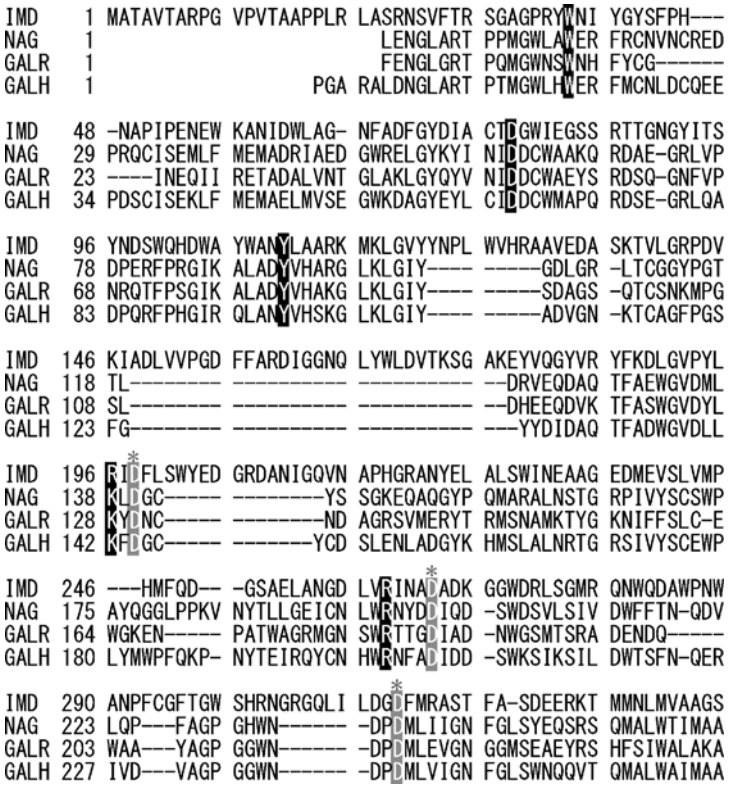

Fig. 15 Multiple sequence alignments of *A. globiformis* T6 isomalto-dextranase (IMD), chicken α-*N*-acetylgalactosaminidase (NAG), rice α-galactosidase (GALA), and human α-galactosidase (GALH). The *letters with black background* have been reported as identical active site residues, and three aspartic acids *marked with grey background and asterisks* are thought to be critical residues of the enzyme activities

been reported as identical active site residues, and three aspartic acids marked with grey backgrounds and asterisks are thought to be critical residues of the enzyme activities. From the molecular modeling and the prediction of isomalto-dextranase structure from comparison of primary, secondary, and crystal structures of a GH family 27, we predict that the three aspartic acids of Asp198, Asp266, and Asp313 (marked with grey backgrounds and asterisks) are critical residues of the enzyme activity. Therefore, three kinds of site-directed mutants (D198N, D266N, and D313N) of isomalto-dextranase, by substituting aspartic acids to asparagines, are interesting for looking at whether these aspartic residues act as the binding site in addition to the catalytic site.

In this section, we describe how a dextran-immobilized 27-MHz quartz crystal microbalance (QCM) is applied to detect whether the site-directed

mutagenesis for isomalto-dextranase is effective to the substrate binding or the catalytic process (Fig. 16) [88]. We prepared three kinds of mutant enzymes such as D198N, D266N, and D313N of isomalto-dextranase as well as a wildtype. They were found to have a markedly reduced level of the hydrolyzing activity for dextran, less than 0.01% of the wild type obtained by the conventional product analyses of Somogyi–Nelson method [60, 61] in the bulk solution (see Table 5). Therefore, it is difficult to discuss further enzyme activity by the conventional method of following the product.

Figure 17 shows frequency changes of the dextran-immobilized QCM, responding to additions of site-directed mutant enzymes (D198N, D266N, and D313N) as well as the wild type. When the wild type was employed, the hydrolysis (the mass decrease) was observed. When mutant enzymes were employed, however, the frequency simply decreased (the mass increased), indicating that only the enzyme binding to the substrate is observed, but the catalytic hydrolysis process was hardly observed. The binding ability seems to be in order of D266N $\gg$ D198N > D313N. The hydrolysis properties of these mutants were confirmed to be less than 0.01% of the wild type from the conventional Somogyi–Nelson method in the bulk solution. Kinetic parameters for the wild type and mutant enzymes were obtained from the time-courses of Fig. 17, and summarized in Table 5.

The retaining enzymes, as GH family 27 members, act via a double-displacement mechanism, wherein one of the catalytic carboxylate group

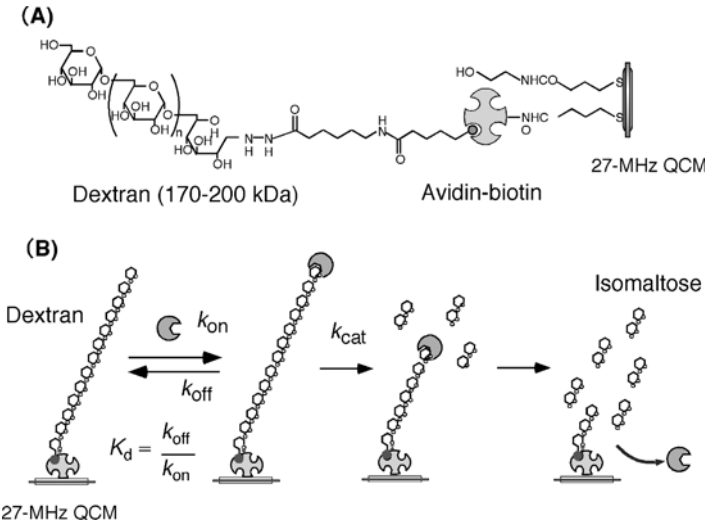

Fig. 16 **a** Chemical structures of dextran immobilized on a QCM plate through an avidin–biotin linkage, and **b** hydrolysis schemes of the dextran on the QCM plate catalyzed by isomalto-dextranase (wild type, D198N, D266N, and D313N) and kinetic parameters obtained in this work

Table 5 Kinetic parameters of the wild type and mutants of isomalto-dextranase for the hydrolysis of the dextran immobilized on the 27-MHz QCM[a], and relative enzyme activity in the bulk solution[b]

	k_{on}^{a} (10^3 $M^{-1}s^{-1}$)	k_{off}^{a} (10^{-3} s^{-1})	K_d^{a} (10^{-9} M)	k_{cat}^{a} (s^{-1})	Relative enzyme activity[b] (%)
Wild type	–	–	5.0	1.1(2.5) [b]	100
D266N	78	0.4	5.1	~ 0	0.011
D198N	167	39	234	~ 0	0.003
D313N	29	15	518	~ 0	0.002

[a] Obtained from the QCM method in 20 mM acetate buffer, pH 5.2, 150 mM NaCl, 25 °C
[b] Obtained from Somogyi–Nelson method in the bulk solution at 20 mM acetate buffer, pH 5.2, 150 mM NaCl, 30 °C

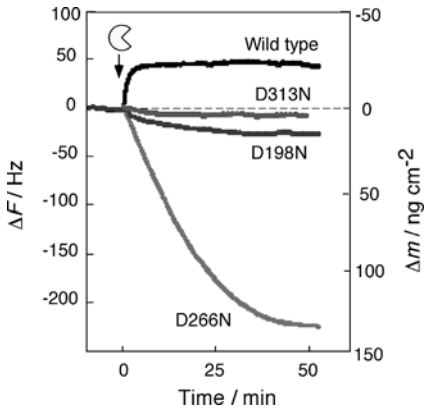

Fig. 17 Time course of frequency changes of the dextran-immobilized QCM, responding to the addition of the wild type and mutants of D198N, D266N, and D313N. The immobilized amount of dextran (170–200 kDa)was 150 ± 10 ng cm^{-2}; 20 mM acetate buffer, pH 5.2, 150 mM NaCl, 25 °C

operates as a nucleophile to generate a glycosyl–enzyme intermediate. The second carboxylate group acts, in turn, as a general acid and general base catalyst to promote the formation and breakdown of the intermediate, respectively [89]. Thus, in isomalto-dextranase, Asp198 exists as a catalytic nucleophile and Asp266 exists as a catalytic general acid and general base. The role of Asp313, however, is not clear, although it is predicted to exist in the active site.

The substitution of the COOH to the $CONH_2$ group of D266N diminished the cleavage activity but not the binding activity (see Table 5). This means that the COOH residue acts as a general acid to cleave the glucosidic linkage

but does not interact with the substrate (see Fig. 18b). Since the D198N mutant diminished the cleavage activity and increased the K_d value by more than 40 times due to the large increase of k_{off} with the small increase of k_{on} values. This indicates that the carboxylate anion of Asp198 may interact with the $^{\delta+}C_1$ atom of the substrate as a nucleophile to generate an isomaltosyl-enzyme intermediate. The D313N mutant drastically increased the K_d value by more than 100 times due to both the decrease of k_{on} and the increase of k_{off}, in addition to diminishing the cleavage activity. This indicates that Asp313 may strongly interact with the substrate binding, probably through a hydrogen bond with the C_3 – OH group to give a twisted and deformed conformation of the glucose ring at position – 1 [89].

From our kinetic results of mutants as well as the wild type by using the QCM system, we propose the following catalytic mechanism of isomalto-dextranase, as shown in Fig. 18. (a) Before the binding of the substrate, the un-ionized Asp266 in the hydrophobic environment, is interacting with Asp313 through a hydrogen bond. (b) The binding of the substrate to the enzyme disconnects this hydrogen bond, and Asp313 binds to the C_3 – OH of the substrate and works to give a twisted and a deformed conformation of the glucose ring at position – 1. In the glycosylation step, Asp266 provides general acid-catalyzed leaving group departure simultaneously with a nucleophilic

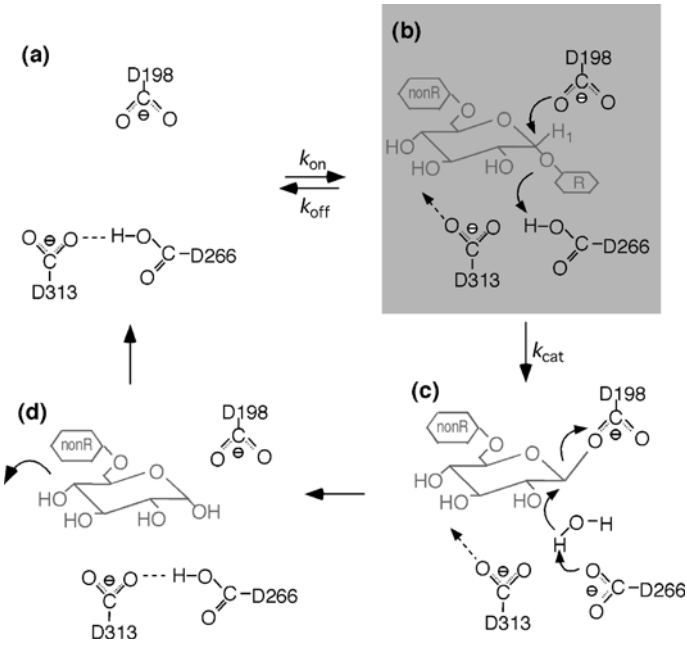

Fig. 18 Catalytic model of retaining isomalto-dextranase based on both the predicted enzyme structure from GH family 27 enzymes and our QCM kinetic results

attack by the carboxylate anion of Asp198 to form a isomaltosyl–enzyme intermediate. (c) In the deglycosylation step, Asp266 functions as a general base to activate the incoming nucleophile that hydrolyses the isomaltosyl–enzyme intermediate. (d) Finally, the product (α-isomaltose) is released from the active site to revert to the starting point.

4 Conclusions

The 27-MHz quartz crystal microbalance (QCM) is a very sensitive mass measuring device and can detect the selective binding of guest molecules onto host molecules that are immobilized on the QCM substrate at the nanogram level. In addition to the simple and static molecular recognition, the QCM is also useful for following reactions such as enzyme-catalyzed reactions. In general, enzyme reactions have been kinetically studied by using a Michaelis–Menten equation (steady-state kinetics), in which the concentration of the enzyme–substrate (ES) complex is hypothesized to be nearly constant during the reaction, because it is relatively difficult to detect the concentration of the ES complex. The reaction rate is simply obtained from the initial rate of the product increase by various methods such as colorimetric and stopped-flow fluorescent methods. By using a substrate-immobilized QCM, we can follow the ES complex formation as a mass change and all kinetic parameters, such as the binding and dissociation rate constant and the catalytic rate constant of enzymes. We describe the enzyme reactions on DNA and polysaccharides in this chapter. The QCM method is also applicable for other enzyme reactions such as protease when enough mass change can be expected through the reaction.

References

1. Guilbault GG (1983) Anal Chem 55:1682
2. Schierbaum KD, Weis T, von Velzen EUT, Engbersen JFJ, Reinhoudt D, Göpel W (1994) Science 265:1413
3. Yang HC, Dermody DL, Xu C, Ricco AJ, Crooks RM (1996) Langmuir 12:726
4. Grate JW, Patrash SJ, Abraham MH, Du CM (1996) Anal Chem 68:913
5. Okahata Y, Kimura K, Ariga K (1989) J Am Chem Soc 111:9190
6. Okahata Y, Ebato H (1991) J Chem Soc Perkin Trans 2:457
7. Okahata Y, Ebato H (1991) Anal Chem 63:203
8. Okahata Y, Matsuura K, Ito K, Ebara Y (1996) Langmuir 12:1023
9. Matsuura K, Ebara Y, Okahata Y (1997) Langmuir 13:814
10. Thompson M, Arthur CL, Haliwal GK (1986) Anal Chem 58:1206
11. Muramatsu H, Dicks JM, Tamiya E, Karube I (1987) Anal Chem 59:2760
12. Ebersole RC, Ward MD (1988) J Am Chem Soc 110:8623

13. Tamiya E, Suzuki M, Karube I (1989) Anal Chim Acta 217:321
14. Ebersole RC, Miller JA, Moran JR, Ward MD (1990) J Am Chem Soc 112:3239
15. Yamaguchi T, Shimomura T, Tatsuma S, Oyama N (1993) Anal Chem 65:1925
16. Lin Z, Yip CH, Joseph IS, Ward MD (1993) Anal Chem 65:1546
17. Ebato H, Gentry CA, Herron JN, Mueller W, Okahata Y, Ringsdorf H, Suci PA (1994) Anal Chem 66:1683
18. Wakamatsu K, Hosoda K, Mitomo H, Ooya M, Okahata Y, Yasunaga K (1995) Anal Chem 67:3336
19. Sauerbrey GZ (1959) Z Phyzik 155:206
20. Okahata Y, Matsunobu Y, Ijiro K, Mukai M, Murakami A, Makino K (1992) J Am Chem Soc 114:8299
21. Piscevic D, Lawall R, Veith M, Liley M, Okahata Y, Knoll W (1995) Appl Surf Sci 90:425
22. Caruso F, Rodda E, Furlong DN, Niikura K, Okahata Y (1997) Anal Chem 69:2043
23. Okahata Y, Matsuno H, Niikura K (1998) Nucleic Acids Symposium Ser 39:209
24. Okahata Y, Kawase M, Niikura K, Ohtake F, Furusawa H, Ebara Y (1998) Anal Chem 70:1288
25. Ozeki T, Furusawa H, Okahata Y (2006) Chem Lett 35:46
26. Furusawa H, Ebara Y, Okahata Y (1999) Chem Lett 28:823
27. Furusawa H, Morii T, Okahata Y (2000) Nucleic Acids Symp 44:245
28. Niikura K, Nagata K, Okahata Y (1996) Chem Lett 10:863
29. Okahata Y, Niikura K, Sugiura Y, Sawada M, Morii T (1998) Biochemistry 37:5666
30. Matsuno H, Niikura K, Okahata Y (2001) Biochemistry 40:3615
31. Furusawa H, Kitamura Y, Hagiwara N, Tsurimoto T, Okahata (2002) ChemPhysChem 446
32. Niikura K, Matsuno H, Okahata Y (1999) Chem Eur J 5:1609
33. Fukusho S, Furusawa H, Okahata Y (2002) Chem Commun, p 88
34. Furusawa H, Murakawa A, Fukusho S, Okahata Y (2003) ChemBioChem 217
35. Ebara Y, Okahata Y (1993) Langmuir 9:574
36. Ebara Y, Okahata Y (1994) J Am Chem Soc 116:11209
37. Ebara Y, Itakura K, Okahata Y (1996) Langmuir 12:5165
38. Ebara Y, Mizutani K, Okahata Y (2000) Langmuir 16:2416
39. Kawasaki T, Asaoka K, Mihara K, Okahata Y (2006) J Colloid Inter Sci 294:295
40. Mori T, Sekine Y, Yamamoto K, Okahata Y (2004) Chem Commun, p 2692
41. Matsuno H, Furusawa H, Okahata Y (2004) Chem Eur J 10:6172
42. Eguchi A, Furusawa H, Yamamoto A, Akuta T, Hasegawa M, Okahata Y, Nakanishi M (2005) J Contr Release 104:507
43. Kornberg A, Baker T (1992) DNA replication, 2nd edn. Freeman, New York
44. Benkovic SJ, Cameron CE (1995) Methods Enzymol 262:257
45. Bryant FR, Johnson KA, Benkovic SJ (1983) Biochemistry 22:3537
46. Kuchta RD, Mizrahi V, Benkovic PA, Johnson KA, Benkovic SJ (1987) Biochemistry 26:8410
47. Allen DJ, Benkovic SJ (1989) Biochemistry 28:9586
48. Cowart M, Gibson KJ, Allen DJ, Benkovic SJ (1989) Biochemistry 28:1975
49. Guest CR, Hochstraser RA, Dupuy CG, Allen DJ, Benkovic SJ, Miller DP (1991) Biochemistry 30:8759
50. Matsuno H, Niikura K, Okahata Y (2001) Chem Eur J 7:3305
51. Niikura K, Matsuno H, Okahata Y (1998) J Am Chem Soc 120:8537
52. Okahata Y, Masunaga Y, Matsuno H, Furusawa H (1999) Nucleic Acids Symp Ser 42:147

53. Raae AJ, Kleppe RK, Kleppe K (1975) Eur J Biochem 60:443
54. Cerio-Ventura G, Fossato M, Vellante A, Palitti F, Fasella PM, Whitehead EP (1981) Biochim Biophys Acta 652:283
55. Dorp BV, Ceulen MTE, Heijneker HL, Pouwels PH (1973) Biochim Biophys Acta 299:65
56. Dorp BV, Caulen MTE, Pouwels PH (1974) Biochim Biophys Acta 340:166
57. Palitti F, Vellante A, Cerio-Ventura G, Fasella P, Salerno C, Whitehead E (1979) Eur J Biochem 97:147
58. Matsuno H, Okahata Y (2002) Chem Commun, p 470
59. Matsuno H, Furusawa H, Okahata Y (2005) Biochemistry 44:2262
60. Somogyi M (1952) J Biol Chem 195:375
61. Nelson N (1944) J Biol Chem 153:375
62. Hiromi K, Hamauzu ZI, Takahashi K, Ono SJ (1996) Biochem (Tokyo) 59:411
63. Hiromi K, Takahashi K, Hamauzu ZI, Ono SJ (1996) Biochem (Tokyo) 59:469
64. Nishino H, Nihira T, Mori T, Okahata Y (2004) J Am Chem Soc 126:2264
65. Abe J, Nagano H, Hizukuri SJ (1985) Appl Biochem 7:235
66. Madsen NB (1991) In: Kuby SA (ed) A study of enzymes, vol II. CRC, Boca Raton, p 139
67. Martin JL, Johnson LN, Withers SG (1990) Biochemistry 29:10745
68. Browner MF, Fletterick RJ (1992) Trends Biochem Sci 17:66
69. McLaughlin PJ, Stuart DI, Klein HW, Oikonomakos NG, Johnson LN (1984) Biochemistry 23:5862
70. Barford D, Schwabe JWR, Oikonomakos NG, Acharya KR, Hajdu J, Papageorgiou AC, Martin JL, Knott JCA, Vasella A, Johnson LN (1988) Biochemistry 27:6733
71. Palm D, Klein HW, Schinzel RS, Bucher M, Helmreich EJM (1990) Biochemistry 29:1099
72. Nishino H, Murakawa A, Mori T, Okahata Y (2004) J Am Chem Soc 126:14752
73. Vandenbunder B, Dreyfus M, Buc H (1978) Biochemistry 17:4153
74. Segel H (1975) Enzyme kinetics. Wiley, Weinheim
75. Kuby SA (ed) (1991) A study of enzymes, vol I. CRC, Boca Raton
76. Fukui T, Shimomura S, Nakano K (1982) Mol Cell Biochem 42:129
77. Drueckers P, Boeck B, Palm D, Schingel S (1996) Biochemistry 35:6727
78. Sawai T, Toriyama K, Yano K (1974) J Biochem 75:105
79. Okada G, Takayanagi T, Miyahara S, Sawai T (1988) Biol Chem 52:829
80. Sawai T, Ohara S, Ichimi Y, Okaji S, Hisada K, Fukaya N (1981) Carbohydr Res 89:289
81. Iwai A, Ito H, Mizuno T, Mori H, Matsui H, Honma M, Okada G, Chiba S (1994) J Bacteriol 176:7730
82. Fujimoto Z, Kaneko S, Momma M, Kobayashi H, Mizuno H (2003) J Biol Chem 278:20313
83. Garman SC, Hannick L, Zhu A, Garboczi DN (2002) Structure 10:425
84. Henrissat B (1991) Biochem J 280:309
85. Henrissat B, Romeu A (1995) Biochem J 311:350
86. Akita M, Mizuno M, Tonozuka T, Sakano Y, Matsui H, Hidaka Y, Ito S, Horikoshi K (2004) Acta Cryst D60:572
87. Garman SC, Garboczi DN (2004) J Mol Biol 19:319
88. Hart DO, He S, Chany II CJ, Withers G, Sims PFG, Sinnott ML, Brumer H III (2000) Biochemistry 39:9826
89. Hasegawa K, Kubota M, Matsuura Y (1999) Protein Engineering 12:819

Springer Ser Chem Sens Biosens (2007) 5: 371–424
DOI 10.1007/5346_033

Published online: 15 July 2006

The Quartz Crystal Microbalance and the Electrochemical QCM: Applications to Studies of Thin Polymer Films, Electron Transfer Systems, Biological Macromolecules, Biosensors, and Cells

Kenneth A. Marx

Center for Intelligent Biomaterials, Department of Chemistry,
University of Massachusetts, Lowell, MA 01854, USA
Kenneth_Marx@uml.edu

Abstract In this chapter we focus on the application of the piezoelectric-based quartz crystal microbalance (QCM) technique to create and study thin polymeric films. The electrochemical variant of the quartz crystal microbalance technique (EQCM) allows one to study changes in the interfacial mass and physical properties associated with electron transfer processes occurring at the electrode surface, such as those accompanying

electropolymerization of thin films. We have applied EQCM to study and compare the formation and properties of polymeric thin films formed from amphiphilic and non-amphiphilic phenolic and tyrosine monomers and comonomer systems. Also, we show the applicability of using EQCM to study polymeric films formed as a result of enzymatic polymerization processes, to create enzyme-entrapped polymer electrodes, and to create biosensors. Lastly, we briefly discuss QCM application to studies of cell properties such as adhesion and to create cell QCM biosensors that have interesting applications in the area of drug discovery.

Keywords Biosensor · Cells · Electrochemistry · Electron transfer · Films · Polymer · Quartz crystal microbalance

1 Introduction to Piezoelectric Techniques and the Quartz Crystal Microbalance

Piezoelectric Materials. Although other materials have been used for a broad range of piezoelectric applications such as in the measurement of pressure, force and acceleration, quartz is still a superior material for most uses for the following reasons. It possesses a high materials stress limit, a high temperature resistance, has high rigidity and high linearity with negligible hysteresis, and the most widely used AT-cut form of quartz crystals has a low temperature-dependent frequency variation around room temperature. As a consequence, in high quality quartz crystal resonators used in various electrical instruments for frequency control, over the short term, frequency is controlled to one part in 10^{10} and long term frequency stability, over weeks duration, exceeds 1 ppb [1] (see Chap. 1 in this volume).

Piezoelectric sensor approaches also occur using materials and geometries other than traditional AT-cut quartz crystals. We illustrate a few of these with just two examples, since this broader subject lies outside the scope of the present chapter, which is focused upon quartz based QCM systems. In the first example, in certain applications such as large area ultrasonics where large crystals of quartz are unavailable, specialty piezoelectric materials such as the polymer PVDF, poly(vinylidene difluoride), have been developed and used for decades [2]. In the second example, following the development of microcantilever technology used in the atomic force microscope, mass-produced microcantilever arrays have been applied to the creation of multiplexed sensors to study various physical, biological, and chemical systems. While laser-based cantilever deflection methodology was used originally to determine cantilever deflection, new methodologies involving piezoelectric microcantilevers have been developed for both AFM [3] and sensor applications [4, 5]. Some efficient piezoelectric microcantilevers require power levels as low as nanowatts to determine the resonance deflection and/or resonance frequency response [6, 7]. Responses are determined by variations in the external en-

vironment that can be sensed by bringing about measureable changes in the microcantilever's mass loading, adsorption-dependent surface stress, and damping.

QCM Advantages. As a potential sensor technology platform for solution applications, the QCM possessed a number of features that investigators have long recognized as advantageous. First was the absence of any need for a labeling step to measure the mass of bound analyte being sensed, as long as some specific recognition mechanism was employed for the analyte/mass binding and the interfering level of non-specific mass binding was low. A second advantage was that the piezoelectric signal transduction mechanism operated well in very complex optically opaque media, where optical approaches could not be effective. Third, was the unique ability of the QCM device to not only measure mass binding but also to qualitatively assay the energy dissipation properties of the system being studied at the surface–solution interface. Fourth, a major advantage was the ability of the upper electrode in the QCM device to function as the working electrode in an electrochemical cell. Thus, mass and energy dissipation changes associated with electron transfer processes could be sensitively quantitated by this electrochemical quartz crystal microbalance (EQCM) variant of the standard technique. These electron transfer processes include creating polymer films in situ on the electrode of the QCM crystal via electropolymerization of suitable electroactive monomers. This is a research area we have actively pursued in the Center for Intelligent Biomaterials. Lastly, a fifth advantage might be added to this list. This is that the QCM technique is relatively easy to implement and the equipment is inexpensive.

The QCM Device. The standard QCM device involves electrodes on either side of an AT-cut quartz crystal, driven to oscillate in the thickness shear mode by an applied AC voltage. This widely used crystal geometry produces a very stable oscillation that is invariant to temperature fluctuations around room temperature. Crystals typically operate in the 5–20 MHz range, with 5–10 MHz being the most common frequency range encountered for commercially available systems. Measurements using systems with higher oscillating frequencies have been reported with considerable non-linear improvements in mass sensitivity [8, 9]. In the latter reference, an $f^{2.8}$ fold improvement in mass sensitivity was reported for increasing quartz crystal frequencies up to 110 MHz. However, the thinner and consequently more fragile crystals required for these higher frequencies make them problematic for routine experimental use. Therefore, in the typical operating range of 5–10 MHz, QCM device mass sensitivities are comparable to the surface plasmon resonance technique, a general optical-based technique not requiring specific chromophore labels [10]. An advantage of the piezoelectric-based QCM sensing approach over the surface plasmon resonance technique is that QCM only detects mass actually physically coupled or bound to the surface [11]. By contrast, the surface plasmon approach detects all mass occur-

ring within the evanescent wave distance of a few hundred nanometers from the surface. This can be a combination of specifically bound "signal" mass as well as solution phase mass, "noise", that would lead to sensor artifacts. On the other hand, QCM cannot routinely achieve the sensitivities of optical techniques that require prior labeling with optically sensitive chromophores chosen for their optimal properties in a given system and device configuration. The higher sensitivities of such optical chromophore approaches must be balanced against the distinct disadvantage of implementing them on a case by case basis for different systems. For broad applicability and ease of use, the general mass sensing by the QCM methodology can provide superior performance [12]. Attempts have been made to enhance the sensitivity of the QCM device by modifying the crystal surface. For example, this has yielded improvements of > 2.5-fold for micromachined crystals [13] and ~threefold for electrodeposited gold surfaces that increase the working surface area due to increased porosity [14].

Quartz crystals, oscillating in the thickness shear mode, produce lateral displacement amplitudes around 1–2 nm, with the solution penetration depth of the lateral shear wave extending out in solution to around 0.25 μm before being attenuated [15, 16]. Therefore, other than from changes in surface mass loading, other alterations in the systems occurring within this penetration depth region may be capable of being sensed if they effect energy dissipation changes. These can include changes in density or viscosity of the solution and viscoelastic properties of surface-bound or surface proximal materials such as polymer films.

The EQCM. In electron transfer systems under study, the upper electrode on the quartz crystal surface in contact with the solution can be made to be the working electrode in an electrochemical cell. This arrangement, termed EQCM, allows electrochemical processes to be carried out in a controlled fashion at an applied potential, while mass and energy dissipation changes at this electrode surface are simultaneously recorded. In Fig. 1 we describe this experimental setup schematically. A standard QCM device is shown in cross-section contained within a covered water-containing reservoir in order to maintain a vapor-saturated environment. The quartz crystal within the frequency range described above is labeled QCM. It has gold upper and lower electrodes (black bars) deposited on it and the quartz crystal is sealed within the device holder with the O-rings shown. The oscillator produces the resonant frequency of the quartz crystal, in the 5–20 MHz range, through an AC voltage applied at the two electrodes. The computer-controlled frequency and admittance (inverse of motional resistance, R) acquisition setup is also indicated schematically. This portion represents a complete standard QCM setup in typical use. In the case of EQCM, the upper electrode has also been made the working electrode in an electrochemical cell where the solution under study is contained in the upper cylindrical reservoir sealed by the O-ring. Here, we show schematically that the upper electrode is the working electrode

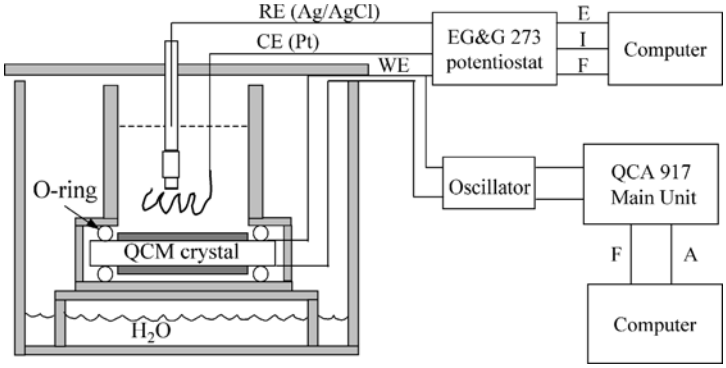

Fig. 1 Electrochemical quartz crystal microbalance schematic of the three-electrode setup used for carrying out the electropolymerization/adsorption studies presented later in this chapter. This figure was reprinted with permission from [71]

(WE) connected to a computer-controlled potentiostat. A controlled DC voltage, E, can be applied to the WE electronically separate from the high applied AC voltage. A counter electrode (CE) and reference electrode (RE) placed in the solution under study and connected to the potentiostat complete the electrochemical cell. This setup allows the collection of QCM parameters such as f and R at the same time that electrochemical parameters such as the current (I), associated with an electron transfer process, are being collected at an applied voltage E.

Recent review articles have appeared that describe the research application areas of QCM ranging from analytical electrochemistry [17] to drug discovery [18], thin film formation [19], biosensors, and the characterization of living cells [11, 12, 20–24]. Although the bulk of these applications have been in the study of continuous resonance devices, discontinuous resonance, embodied largely in the QCM-D technique, is gaining in importance [25] and is the subject of Chap. 12 in this volume. Equivalent circuit model impedance analyses can result in greater insights into the viscoelastic properties of complex materials. These are based upon models such as the Butterworth–Van-Dyke model to yield capacitance, resistance, and inductance data in addition to series and parallel frequencies for the model elements [26]. Such studies have been carried out on a number of systems including polymer films [27], organic thin films [28], films formed by blood clotting [29], and biological macromolecule containing systems [22–24, 30–32].

In this chapter, we focus on the use of the continuous resonance QCM and EQCM devices to study enzymatic polymerization reactions, biochemical and biomimetic processes and to create thin polymer films electrochemically on the QCM electrode surface. We describe some QCM applications of thin polymer films in enzyme electrode and other biosensors and briefly describe specific cell binding systems to create whole cell biosensors.

2 Studying Thin Film Systems with the QCM

The creation and study of thin films tailored to meet specific applications is an important area of research that has broad implications for a wide variety of technology areas. These include improving industrial and biotechnology processes and developing new integrated circuit and sensor technology, to name just a few. One promising area of thin films research involves polymer films. These films offer a number of distinct advantages. They include convenient synthetic methodologies for polymer formation and modification, allowing them to be tailored for specific applications, as well as ease of processing to form films. The QCM technique has the advantage that it can be used to study the process of polymer film formation on the crystal surface as well as to characterize properties of the final structures formed. Because the piezoelectric mechanism is a label-free technique, all steps in the process of forming multilayered structures, or further additions or modifications to a polymer film, can be monitored using the QCM or EQCM. Moreover, polymer films often possess characteristics that are distinct from the solutions in which they are soluble, such as increased viscosity, altered density, and potentially viscoelastic behavior. These properties can significantly change the quartz surface interfacial properties and solution properties immediately above the quartz crystal, allowing the study of polymer film formation in situ on the QCM surface. As we illustrate below via measurement of QCM parameters, one can obtain unique information on film formation, modification, and energy dissipation properties on surfaces.

Studying Elastic Mass vs Energy Dissipating Systems. For any purely elastic mass deposited on an oscillating quartz crystal, the well-known Sauerbrey equation linearly relates the elastic mass deposited to the decrease in frequency output by the oscillating quartz crystal [33]. However, before this relationship can be used as an accurate mass measuring tool for liquid phase systems, the mass deposited must be demonstrated to exhibit elastic behavior and be free of entrapped solvent mass. In many cases in the literature involving interesting polymer films, biochemical systems and living cells, the surface-bound molecular assemblies do not exhibit elastic behavior but dissipate energy [12]. Whether the mass of a system undergoing change is acting elastically or inelastically can be determined by measuring the motional resistance, ΔR, of the oscillating crystal. If there is no change in energy dissipation, then $\Delta R = 0$; whereas, if energy dissipation is increasing or decreasing during a system change, ΔR will be a positive or negative quantity. One simple approach taken by investigators to accurately determine elastic mass deposited, without including entrapped solvent contributing to the frequency decrease, is to determine the mass in the dried state on the crystal surface compared to

the bare crystal frequency value. More detailed and elegant approaches to characterizing energy dissipation in systems are presented in Chap. 2 in this volume.

The QCM-D technique was designed for the characterization of energy dissipation (D) in systems on the quartz surface ([25]; Chap. 12 in this volume). Briefly, in this technique, the fundamental frequency and a series of overtone frequencies are studied and the energy dissipation quantity (D) is determined by periodically switching off the AC voltage and the crystal oscillation and then measuring the decay signal. Variations in this damped signal for different surfaces leads to the calculation of the dissipation level D from the decay time constant and reflects their different viscoelastic properties and their surface roughness [34]. The viscosity, elasticity, and thickness of a film can be estimated from the measurements. The QCM-D technique has been growing in popularity recently and has been used to study a number of systems comprised of polymers [35–37] and biological macromolecule containing films [38–44].

Non-Ideal Factors Affecting QCM Measurements. Use of QCM f and R measurements to characterize films relies upon a number of other factors being controlled. Not only will viscoelastic effects produce non-mass changes in frequency, but high mass loadings (> 2% of crystal mass), interfacial slippage, surface roughness, surface stress, non-uniform mass distribution and ambient temperature changes may also produce similar effects [25, 45, 46]. Large slippage events at the electrode surface on the quartz would be expected to result in discontinuities in measured properties. Large variations in surface roughness, where surface cavities are hydrophilic, could lead to entrapped liquids contributing to the mass increases sensed by the QCM [47, 48]. On the other hand, surface cavities that are hydrophobic could avoid being wetted and lead to entrapment of air, causing underestimation of the film mass. These effects resulting from surface roughness variations have motivated the creation of a model for surface roughness [49], that describes the QCM behavior for different levels of surface hydrophobicity and incomplete surface wetting. Such considerations are important for understanding local variations of real surfaces that might lead to altered mass binding and could produce heterogeneous local chemical environments and altered local surface electrochemistry at the working electrode in EQCM experiments. Some qualitative effects of varying surface energies have been noted in non-uniform distributions observed for cells on surfaces [50]. And in a recent report using QCM in the impedance mode, surface roughness effects were proposed to account for results observed for cells binding to extracellular matrix proteins [51]. In practice, since there are no easy ways to determine whether these non-ideal surface factors are operating or effectively being controlled in given systems under study, they are generally not assumed to be playing a dominant confounding role in QCM measurements. This practical assumption allows investigators to make unambiguous interpretations of their

data. Some of the non-mass related surface factors affecting frequency have been incorporated within advanced models of piezoelectric systems [52, 53]. Chap. 3 in this volume provides a detailed view of these non-ideal surface effects.

2.1 Combining Techniques with QCM to Characterize Thin Films

Most often, the QCM or EQCM techniques are not applied in isolation to study thin film systems. Complementary surface characterization techniques are routinely utilized by investigators in order to make unambiguous interpretations of their QCM results. These surface techniques are comprised of two basic types: ones that measure large area averaged properties, and those that image details of the surface at some level of lateral surface resolution. Examples of the area averaged techniques are ones as simple as contact angle measurements or UV-Vis spectroscopy. These have been used to reveal the relative hydrophilicity of the surfaces of thin films as a function of changes in solution conditions or chemical treatment of films on QCM surfaces [50]. More informative surface techniques for film characterization, such as ellipsometry and surface plasmon resonance, are also used to measure film thicknesses. Moreover, by combining QCM with these techniques, characteristics such as the water content of films have been estimated [12, 39, 54–56]. Another important complementary surface technique to QCM, X-ray photoelectron spectroscopy (XPS), measures the characteristic energies of X-ray photoelectrons emitted from atoms in the film sample and the underlying substrate. This quantitative technique can reveal both atomic identity and its % composition in the film [57] as well as details of the orientation of atoms of unique atomic number in the film via angle resolved XPS. Furthermore, the technique can also provide estimates of average film thickness. These estimates derive from the thickness-dependent magnitude of the film's attenuation of high kinetic energy photoelectrons ejected from an underlying atomic layer, such as the typical gold (e.g., – 4f electrons, 1170 eV) QCM electrode surface, upon which films are often formed [58].

The second type of surface characterization technique complementary to QCM are the various microscopies. They are often combined with QCM measurements of films to image surface detail at varying levels of lateral resolution. This imaging view of films provides valuable complementary information since QCM parameters represent film properties averaged over the most sensitive central portion of the quartz crystal surface. Probably the most widely used imaging techniques have been the traditional electron microscopies, SEM and TEM. Gaining rapidly in importance in recent years as a high resolution imaging technique for films is AFM [59–61]. Variants of the scanning probe microscopies, such as scanning electrochemical microscopy [62], differential electrochemical mass spectrometry [63], or the scanning Kelvin

microprobe [64], provide laterally resolved images or maps of different local physicochemical properties on a film's surface.

As we described in Sect. 1, the application of electrochemical methods as a complementary technique to QCM is called EQCM. We discuss example applications of EQCM to film characterization in Sect. 3.

2.2 The QCM as a Sensor of Films Formed by Enzymatic Polymerization and Degradation Processes

Although the QCM has been used to quantitate the mechanisms of enzymatic reactions in some instances, more often it has been used to determine the overall rates and characteristics of products formed in these reactions. For example, multistep processes have been studied that are involved in the enzymatic degradation of polymeric films formed from poly(L-lactide) [61] and poly(3-hydroxybutyrate) [60]. In QCM studies at a high resonance frequency, 27 MHz, DNA polymerase was studied using immobilized DNA to obtain rate constants for three individual steps in the mechanism of this enzymatic reaction ([65]; Chap. 10 in this volume).

QCM Studies of pH-Dependent Self-Assembling Chiral Amphiphilic Tyrosine Derivatives. Enzyme-catalyzed polymer formation can be followed via QCM parameters that are sensitive to and reflect physicochemical changes occurring in solution as products form. Using the QCM, we have studied a system comprised of two amphiphilic chiral derivatives of tyrosine, the decyl esters of D- and L-tyrosine (DEDT and DELT respectively) shown in Fig. 2a [57, 59, 66–71]. In Fig. 2b we present a schematic of the solution equilibrium self-assembly system of these monomers and their polymerization by the enzyme horseradish peroxidase (HRP). These monomers possess concentration-dependent self-assembly properties whose onset is characterized by a critical micelle concentration (cmc). The cmc is a pH-dependent quantity, depending critically upon the titrable charge present on the monomers. For example, with increasing pH deprotonation of the amino group (pK_a of 6.5 [57]) occurs, bringing about enhanced self-assembly of the monomers and a corresponding drop in the cmc. We determined the cmc values for these monomers using Raman scattering [68]. In Fig. 2c and Fig. 2d we present Raman scattering intensities for the DEDT and DELT isomers in pH 6.0 phosphate buffer. These results demonstrated that both isomers possess identical cmc values of 0.17 mM, as would be expected for two chemically identical isomers. However, at pH 5.5 a greater fraction of protonated amine groups exist on the monomers than at pH 6.0. This makes them less able energetically to self-assemble and the cmc has correspondingly increased to 0.23 mM. When the DEDT and DELT monomers self-assemble above their cmc values they form tubule-shaped structures in solution. After their formation, these aggregates can be enzymatically polymerized in situ in aque-

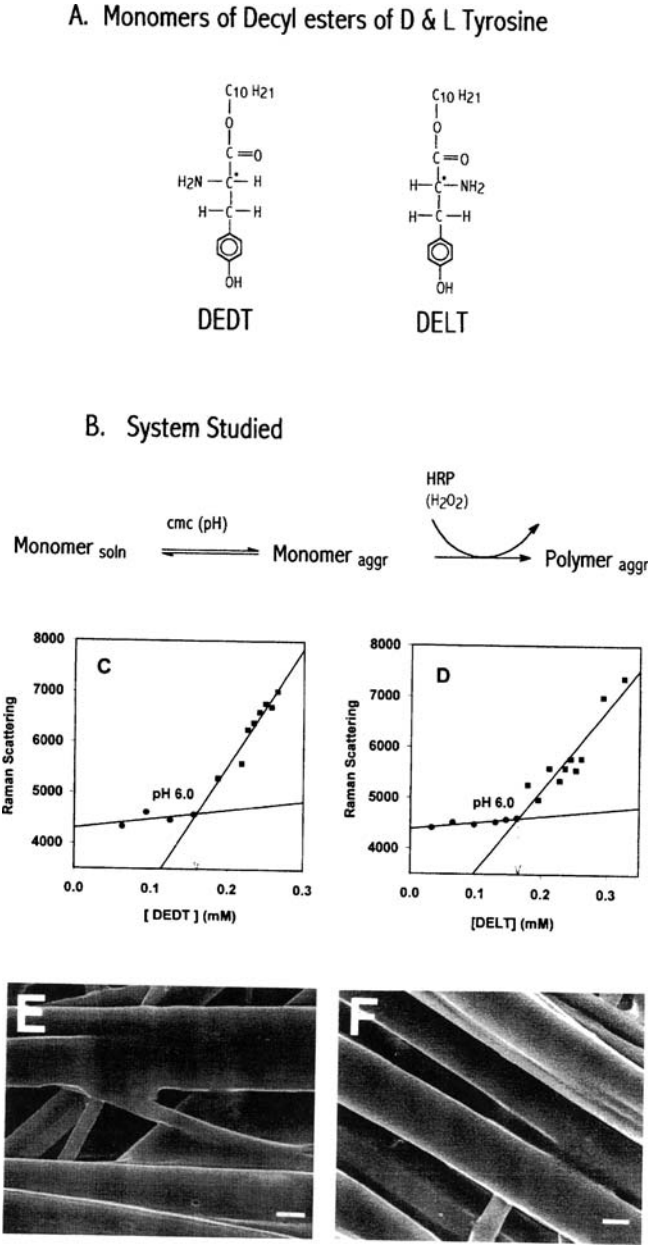

Fig. 2 Schematic diagram of: **a** monomer isomers studied; **b** monomer self-assembly equilibria and fibrous aggregate polymerization scheme with horseradish peroxidase. Raman scattering intensities as a function of unpolymerized monomer concentration are presented for: **c** DEDT at pH 6.0, and **d** DELT at pH 6.0. SEM images are presented for the enzymatically polymerized: **e** DEDT at pH 6.0 (*Scale bar* = 2 μm), and **f** DELT at pH 6.0 (*Scale bar* = 2 μm). This figure was reprinted with permission from [68]

ous phosphate buffer with HRP and hydrogen peroxide. Figure 2e,f presents SEM images of the self-assembled monomers following polymerization. The structures have not changed their macroscopic appearance or diameter dimensions as a result of polymerization, maintaining a diameter averaging around 2.5 ± 1.0 μm [68]. The only discernible change in the self-assembled polymerized structures is an overall greater length stability and everywhere a smoother appearance to their surfaces compared to the unpolymerized aggregates.

Using the QCM to study this system allowed us to conveniently characterize the pH-dependent self-assembly properties of the monomers as well as their polymerization by HRP [67]. In Fig. 3 we present results where we examined as a function of varying pH the self-assembly of the DEDT monomer at 0.31 mM, above its cmc, and its binding to the gold electrode surface of a 9 MHz oscillating quartz crystal. It is clear that at equivalent self-assembly times there is a pronounced f decrease exhibited by the crystal for reactions carried out at increasing pH values. At pH 3, no net frequency decrease was observed. This behavior is consistent with a complete lack of self-assembly and binding at this low pH, since the fully protonated amine group is present on all DEDT monomers. Confirming this interpretation, no aggregates were observed by SEM at this pH. Given the monomer amine $pK_a = 6.5$, at higher pH values the increasingly uncharged DEDT is known from its measured cmc values to undergo self-assembly. This behavior is clearly being expressed in the QCM measurements where progressively larger f decreases were observed at increasing pH values of 5.55 ($\sim$ 400 Hz) and 5.99 ($\sim$ 1000 Hz). The self-assembled polymerized tubule structures shown in Fig. 2e,f correspond to the solution condition of the pH 5.99 QCM trace result. At the pH 6.99 value, where amine deprotonation would be largely complete and self-assembly maximized, the f has decreased by over 2300 Hz. Since the measured R at the

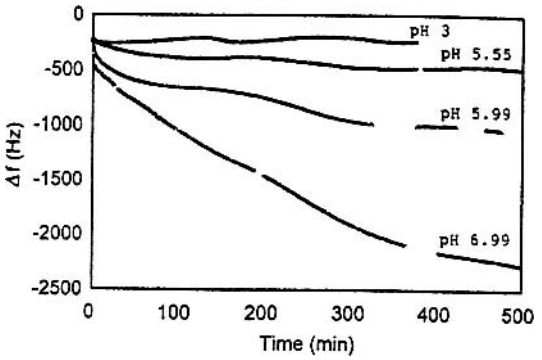

Fig. 3 Kinetics of Δf shifts induced by DEDT monomer aggregates binding to the QCM surface at a series of increasing pH values. This figure was reprinted with permission from [67]

crystal–solution interface was shown not to change with decreasing f (elastic behavior) at every pH value except for the highest we studied, we were able to utilize this fact to estimate the bound masses at each pH from the f decrease using the Sauerbray equation [33]. A plot of the relative mass bound vs pH allowed us to estimate the pK_{app} to be 8.3 for the complex two state equilibrium going from the monomer cationic DEDT state to the deprotonated and uncharged DEDT in its aggregated state, as shown below in Eq. 1:

$$DEDT^{+}_{[m]} \rightleftharpoons DEDT_{[aggr]} + H^{+} \quad (1)$$

similar to that shown in Fig. 2b. When we examined the system at a pH of 7.01 for long times, we obtained the short and long time f and R shift data shown in Fig. 4a and Fig. 4b. For times up to 1 h, a significant f decrease occurred ($\sim$ 700 Hz). This was accompanied by no R increase, indicating a lack of energy dissipation change and elastic mass behavior at the crystal surface. However, after 1 h R did begin to rise nearly linearly as f continues to decrease. This unique aspect of the self-assembling monomer system could only be described using piezoelectric methods. At longer times, as shown in Fig. 4b, the R increase and f decrease both continued until around 20 h before they leveled off as the system reached equilibrium, then remained nearly constant with time.

QCM Detection of Enzymatic Polymerization. It was at the 50 h quasi-equilibrium point in the QCM experiment that we initiated the QCM study of horseradish peroxidase (HRP) polymerization of the self-assembled monomers. Part of our motivation for trying this QCM-based approach was that under these conditions (at 0.31 mM monomer > cmc) the system is optically opaque due to significant light scattering and therefore polymerization could not be accurately described by traditional spectroscopic methods. At the position labeled 1, the HRP enzyme was added and no changes in f and R were observed. Only when H_2O_2 was added (at points labeled 2–4) to initiate the reaction were the f and R parameters observed to change. This is because H_2O_2 is the oxidizing agent stoichiometrically required for monomer polymerization. That HRP-based polymerization was occurring under these conditions was confirmed qualitatively by observed increases in visible absorbance from 300–500 nm, above the monomer absorbance band which ends at 300 nm. This emerging broad absorption band is due to the presence of increased levels of electron delocalization that exist between adjacent covalently bonded phenol rings in the partially planar HRP reaction products. To corroborate these QCM results, where this self-assembling system is binding to the upper gold electrode, we have shown via X-ray photoelectron spectroscopy measurements that complete saturation coverage of gold surfaces (similar to the QCM surface) was achieved by their immersion in solutions of either HRP polymerized DEDT or DELT [57].

Enzymatic Polymerization Products Possess Increased Energy Dissipation Properties. Interestingly, starting at point 2 in Fig. 4b, the f and R values

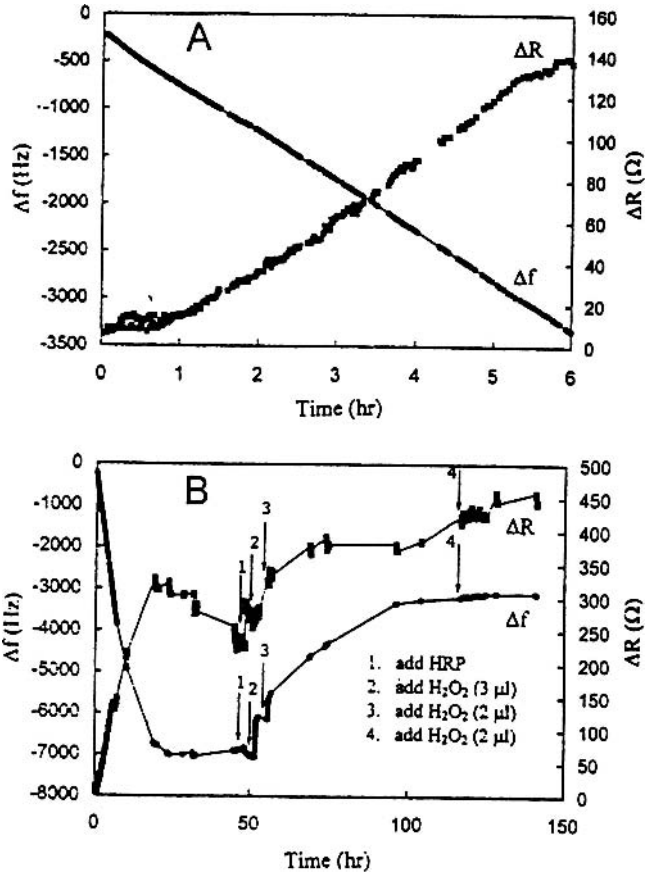

Fig. 4 Kinetics of Δf and ΔR shifts induced by DEDT monomer aggregates at pH 7.01. **a** Early linear region of sedimentation and binding to the gold QCM surface; **b** longer time region including equilibrium Δf and ΔR values and how they are affected by HRP polymerization of monomer aggregates at *arrows 2–4*, where hydrogen peroxide is added. This figure was reprinted with permission from [67]

of the oscillating quartz crystal began changing in the *same direction*, both increasing. This was unlike the previous 46 h of f and R changes for the system, which always moved in the *opposite direction* from each other. What this new parameter direction change indicated was that the fundamental physical properties of the self-assembled aggregates were changing as a result of HRP polymerization. When presented as a $\Delta f - \Delta R$ plot in Fig. 5, the series of successive time data points indicated by the arrows are presented originating at the right hand origin of the plot. During the first 1 h the points follow a horizontal line that is the response of a pure elastic mass bound to the QCM surface, where successive mass binding dissipates no additional en-

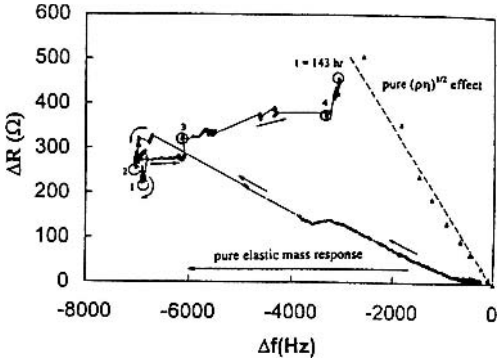

Fig. 5 The $\Delta f - \Delta R$ diagram of the time course of DEDT monomer aggregates binding to the QCM surface is shown, starting at $\Delta f = 0$ and following *arrows*. At *point 1*, horseradish peroxidase was added and at *points 2* through *4*, successive hydrogen peroxide aliquots were added to carry out polymerization. After a total of 143 h of polymerization, the final point was reached. The pure elastic mass (*solid line*) and pure density–viscosity $(\rho\eta)^{0.5}$ (*dashed line*) effect lines are shown. The *triangles* represent the experimental values determined for solutions of increasing sucrose concentrations. This figure was reprinted with permission from [67]

ergy. After 1 h and continuing until around 46 h the points move progressively to the left with increasing energy dissipation (ΔR increase). At the point labeled 2, where enzymatic polymerization begins, successive points in this plot change direction, indicative of very different physicochemical behavior by the self-assembled system as a result of being polymerized. The final position at 143 h is at significantly increased R, from $\sim$ 260 ohms to $\sim$ 450 ohms. Thus, the polymerized system is dissipating significantly more energy than it did prior to polymerization. The final state of the polymerized self-assembled system is near that of the experimental and theoretical calibration line produced by a pure liquid density–viscosity response of Newtonian liquids of different $(\rho\eta)^{0.5}$ values. These relationships for f [72]:

$$\Delta f = -f^{3/2}\left(\frac{\rho_L \eta}{\pi \mu \rho_q}\right)^{1/2} \tag{2}$$

and for R [30]:

$$\Delta R = \left(2\pi f \rho_L \eta\right)^{1/2} \frac{A}{k^2} \tag{3}$$

were first predicted and demonstrated to be valid for pure liquids. The closeness of the final polymerized self-assembled state to the pure liquid $(\rho\eta)^{0.5}$ response line represented by Eqs. 2 and 3, suggests that the alteration in physical properties as a result of HRP polymerization has produced effective solution properties at the quartz surface that mimic the energy dissipation of a pure liquid of higher $(\rho\eta)$ product than that of the pure solution in which

the aggregates occur. This interpretation is reasonable given that the polymerization reaction will certainly increase η as a result of increased polymer chain length within the self-assembly, which increases the aggregate's stiffness and therefore its energy dissipation. As a general method, the Fig. 5 type of QCM data display is useful for interpretation since the plot places these data in relation to both the elastic mass response and pure liquid $(\rho\eta)^{0.5}$ response lines.

In addition to studying single monomers in enzymatic polymerization reactions, comonomer reaction schemes are of interest because they have the potential to produce copolymer films possessing more interesting and varied properties. To illustrate this possibility, in Fig. 6 we show how the mixing of the amphiphilic DELT monomer with the same chirality but nonamphiphilic L-tyrosine monomer has been studied in a comonomer system [59]. We present an equilibrium coupled to the HRP-catalyzed reaction for this comonomer system that has the same character as the steps we pre-

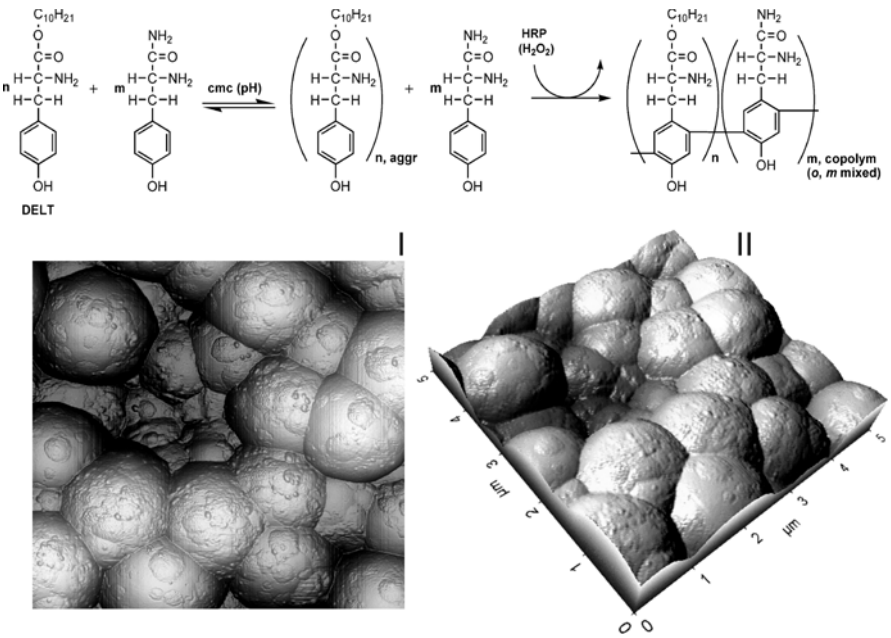

Fig. 6 *Above*: Schematic view of steps involved in the self-assembly process in the comonomer mixture (DELT and L-tyrosine) and its enzymatic copolymerization. States I and II represents the species we visualized in this study, where $n = m$ (a 1 : 1 ratio of comonomers). State II is an hypothetical structure of the final copolymer formed. *Below*: NC-AFM visualization (vertical and 3-D views) of samples following the 1 : 1 ratio comonomers (DELT and L-tyrosine) copolymerized over a 24 h reaction and equilibrium period, followed by immersion of the gold coated mica: **a** 20 µm × 20 µm area and **b** 5 µm × 5 µm area. This figure was reprinted with permission from [59]

sented for the single amphiphilic monomer in Fig. 2b. In the equilibrium step, a pH-dependent cmc exists for the amphiphilic DELT monomer that is self-assembling to form aggregates. This equilibrium will largely be unaffected by the non-amphiphilic L-tyrosine species. In the second HRP-catalyzed reaction step, both comonomer species react, potentially forming block copolymer species as we suggest diagrammatically. We show in the AFM images, the appearance of the HRP polymerized 1 : 1 comonomer mixture above the DELT cmc. These structures are very different from the polymerized DELT tubule-shaped structures that were presented previously in Fig. 2f. For the comonomer structures, uniform hemispherical shapes were observed having average diameters of $1.51 \pm 0.24\,\mu$m. They possess nanoscale surface structure detail, in contrast to the amorphous structures of varied dimension and shape we observed for the comonomer mixtures prior to polymerization (data not shown). Clearly, the addition of the second non-amphiphilic L-tyrosine monomer species has created a copolymer with obviously different and possibly enhanced flexibility, allowing it to form the spherical aggregates rather than the tubules observed for polymers formed from just DELT monomers.

3 Electron Transfer Studies of Chemical and Polymer Systems with the EQCM

The EQCM technique is particularly useful in helping elucidate the mechanisms of various physicochemical processes that involve electron transfer steps. As a result, EQCM has become widely used in a number of basic research disciplines involving studies of electron transfer processes in chemical systems. These include electrochemistry and electroanalytical chemistry, with specific applications to studies of topics as diverse as corrosion [73, 74], conducting salts [75], batteries [76], electroplating [77], electrosorption [78, 79], and double layer studies [80]. Different materials studied with the EQCM have involved the following focus areas: metal deposition [81], semiconductors [82], membrane research [83], layered nanostructures [84], and self-assembling monolayers [85, 86]. EQCM studies of electropolymerization reactions, in particular the formation of electroactive polymer film modified electrodes, have been widespread [87–91]. These studies have described a range of system behaviors that include such things as temperature effects, viscoelastic properties, film non-uniformity and surface changes during early portions of the film formation phase. A significant focus of many EQCM investigations, and where this technique can provide unique information, has been on solvent and ion transport associated with electrochemical processes or electropolymerization during film formation and with the properties of the films once formed. It is on this area of polymer film formation and characterization with the EQCM that we focus in the sections that follow.

3.1 EQCM Characterization of Polymer Films

Polymer films of various types have been studied with the EQCM technique, both from the standpoint of film creation as well as the final film properties like redox behavior, ion and solvent transport, and energy dissipation level. Some of the classes of polymer films studied include: micellar–polymer films, molecular imprinted polymer films used as chemical sensors of small molecules, layer-by-layer nanoarchitectured polymer films and electropolymerized films, some containing electroactive functional groups. In this section, we briefly discuss some of the EQCM approaches taken with representative examples from each of these polymer film classes.

Self-Assembling Amphiphilic Polymer Film Systems. A number of self-assembling polymer systems have been studied using the EQCM. These include: amphiphilic molecules that self-assemble to form rodlike multilayer structures [57, 59, 66–71], micellar interactions with polymer films [92–94], self-assembled monolayers such as those formed from the widely studied alkylthiols on metallized electrode surfaces on the quartz crystal [32, 85, 95–99], and LB monolayers formed from monomers or polymers that can be picked up on electrode surfaces on the quartz crystal [100]. Self-assembling systems are all characterized by a cmc value. This phase transition critical concentration is a feature that the QCM is able to detect via increased mass deposition above the cmc as well as changes in the solution properties at the crystal surface–solution interface at and above the cmc. Thermal phase transitions are also a commonly studied property of self-assembling film systems and the QCM can detect great detail during these phase changes. As an example, in studies of multilayers of LB monolayer films formed from the $C_{18}OH$ fatty acid (1,3-dioctadecyl-rac-glycer-2-ol), thermal phase transition behaviors could be dissected in detail [100]. When the QCM f and R changes as a function of temperature were compared to the heating and cooling differential scanning calorimetry traces, multilayer number-dependent details were observed in the QCM parameters for the different films even at temperatures below the phase transition. In particular, changes in the film elasticity and viscosity were interpreted to be occurring concomitant with changes in noncovalent fatty acid interactions during the phase transition. Where EQCM can play a significant and unique role is in redox studies. As an example of the utility of the EQCM, in a study of films formed from self-assembled electroactive quaternary amine alkylferrocene monomers adsorbed to the gold electrode surface above a quartz crystal, oxidation and reduction of the ferrocene moiety allowed direct comparisons between the adsorption ΔG of both species [96, 100].

Molecularly Imprinted Polymer Film Systems. Molecularly imprinted polymer films have been developed to provide recognition networks for small and large molecules (Chap. 5 in this volume). These films are formed in situ

on surfaces by polymerization of monomers around the recognition analyte. The great advantage of this approach is that the recognition site is formed via monomer self-assembly with the analyte molecule during polymer synthesis, resulting in a methodology that eliminates the requirement for the synthetic chemist to design and then create a binding site by traditional rational synthesis. With molecularly imprinted films formed upon the QCM, small molecules have been detected by these chemical sensors from both gas phase and solution phase environments. Examples of sensors include detection of water [101], terpenes [102], caffeine [103], sialic acid [104], as well as large molecules such as the enzyme lysozyme [105] and the protein microsystin-LR [106]. Chiral recognition is particularly easy to build into the molecularly imprinted polymer synthesis approach. For example, chiral discrimination between D- and L-glutamic acid has been demonstrated [107]. Chiral recognition by molecularly imprinted films may have important applications in clinical diagnostics and drug discovery.

Nanoarchitectured Polymer Film Systems. Nanoarchitectured films can be created by many approaches. A layer-by-layer methodology can create nanoscale ordered films with specific desired properties when care is given to how successive layers of the polymer films interact. Because of its general mass-sensing capability, the QCM is aptly suited to measure this layer-by-layer deposition of polymer films. Examples of studies of the layer-by-layer approaches include their use in creating stable biocompatible surfaces for medical devices [108, 109]. Also, layer-by-layer films have been shown to be stable environments for incorporating large biological macromolecules such as DNA and proteins [110, 111]. For example, in one EQCM study hemoglobin (Hb) protein layers alternating with polycationic poly(diallyldimethylammonium)-formed multilayer films where the native Hb protein was demonstrated to be present via its visible Soret absorption band and an amide band in the IR. Then the Fe(III)/Fe(II) redox couple of the immobilized Hb was studied electrochemically interacting with a variety of oxidizing and reducing agents [112]. Also, a number of redox enzymes have been immobilized within layer-by-layer films and studied with the EQCM. Since these represent a class of biosensors, we discuss them in detail in Sect. 4.3.

Electropolymerization-Based Film Studies. A wide range of different monomer types have been examined in different electropolymerization film studies. Examples of these include monomers as diverse as pyrrole and substituted pyrroles, a large 32-unit ferrocenyl-dendrimer, reversible C_{60} derivatives, phenols, and biomimetic tyrosine derivatives. In the case of electropositive conducting polypyrrole films formed on the EQCM surface, the flux of counterions, some as large as the mainly immobile 30-base DNA polyanion, have been observed [113]. For electroactive polyvinylferrocene films, reversible mass changes measured during EQCM redox cycling of the ferrocene groups were determined to be due to flux of the PF_6^- counterion

through the polymer film [114]. Reversible redox behavior of the C_{60}^{3-} ion was studied with the EQCM and successive single electron oxidations to the C_{60} species were shown to deposit mass in the form of films on the electrode surface [115]. By correlating the charge passed at the electrode with the f change interpreted entirely as a mass change, the investigators concluded that the film was comprised entirely of neutral C_{60}, not solvent or ions. Reduction of the film steadily reversed the f change, concomitant with total film dissolution, as the soluble C_{60}^{3-} ion was completely regenerated. For tyrosine and phenol derivatives electropolymerized to form non-conducting and self-limiting films, in Sect. 3.2, we discuss in detail some studies of film formation and the film properties that we have measured over a number of years [57, 59, 66–72].

3.2 Electropolymerization and Properties of Films Formed from Phenolic and Tyrosine Monomers

Our aim in this section is to present details of a case study where we have used the EQCM technique to study the self-assembly, electropolymerization-based film formation process and film stability properties, for films created from phenolic and tyrosine monomers of the class shown in Fig. 7 [69, 71]. This figure depicts a schematic representation of the self-assembly and electropolymerization behavior of a family of monomers that are all derivatives of phenol, where the amino acid tyrosine has phenol as the major portion of its pendant side chain residue. In the discussion below we illustrate the use of the DEDT and DELT monomers, decyl ester derivatives of tyrosine, participating in the self-assembly equilibrium shown below and above their cmc. The EQCM technique can be used to monitor the extent of monomer electropolymerization, labeled E in Fig. 7, where polymer is formed by coupling of two free radical species generated at the electrode to form a growing chain, the adsorbed $m + 1$ species. As well, the EQCM technique can determine whether the self-assembled species in the absence of electropolymerization, labeled A, is adsorbing to the metal electrode surface. To distinguish between these two possibilities is an important capability of the technique, since both processes can contribute to the bound mass, labeled the $m + 1$ species, during an electropolymerization experiment of an amphiphilic monomer. Assuming the $m + 1$ species is insoluble and binds the Pt electrode surface, it's mass will be detected and can be compared to the electrochemical charge passed at the Pt electrode during the electropolymerization experiment. For simplicity of the representation, we show in Fig. 7 the possibility of product occurring either as *ortho*- or *meta*-coupling of phenol rings, since a distribution of the two is likely to occur in these experiments [71]. We do not show the potential for ether linkage formation between adjacent phenol rings involving the phenolic oxygen. This product species is likely to be

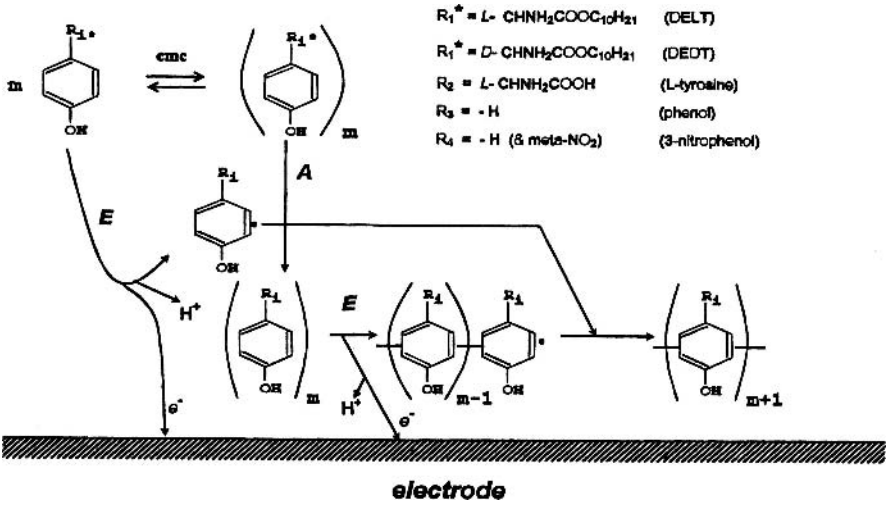

Fig. 7 Schematic of the tyrosine and phenolic monomers studied, DELT and DEDT self-assembly, and the adsorption vs electropolymerization processes occurring at the Pt electrode surface. For simplicity, we have not attempted to indicate the – O-ether linkage products that may also represent a minor fraction of the linkages found in the electropolymerized phenolic film products. This figure was reprinted with permission from [71]

selected against under the mildly acidic conditions under which we carried out these experiments [116].

Cyclic Voltage Sweep Experiments and Self-Limiting Film Behavior. For these monomers, the "electroxidation" process, labeled E in Fig. 7, results in the monomer donating an electron to the electrode surface. Therefore, determination of the total charge, *Q*, passed during an electrochemical experiment may be used to calculate the corresponding mass electroxidized and polymerized via the Faraday equation. This electroxidized mass can then be compared to the total frequency-based mass change on the QCM surface in order to assess the relative contributions to film formation of electropolymerization vs adsorption in any given experiment. Alternately, the frequency vs *Q* can be compared directly as we show in the examples presented below. These concepts and EQCM measurements were implemented in a study of film formation comparing electropolymerization vs adsorption for the amphiphilic DEDT and DELT monomers vs non-amphiphilic L-tyrosine monomers [71]. In Fig. 8a,b we present the cyclic voltammograms of 0.11 mM DEDT and 3.0 mM tyrosine. For both monomers there is an oxidation peak clearly visible during the first half of the first cyclic voltage sweep. In the case of L-tyrosine, the peak is quite broad due to the high concentration utilized in this experiment. In the case of both monomers, the oxidations are not reversible. No reduction peaks are evident in the second half of the

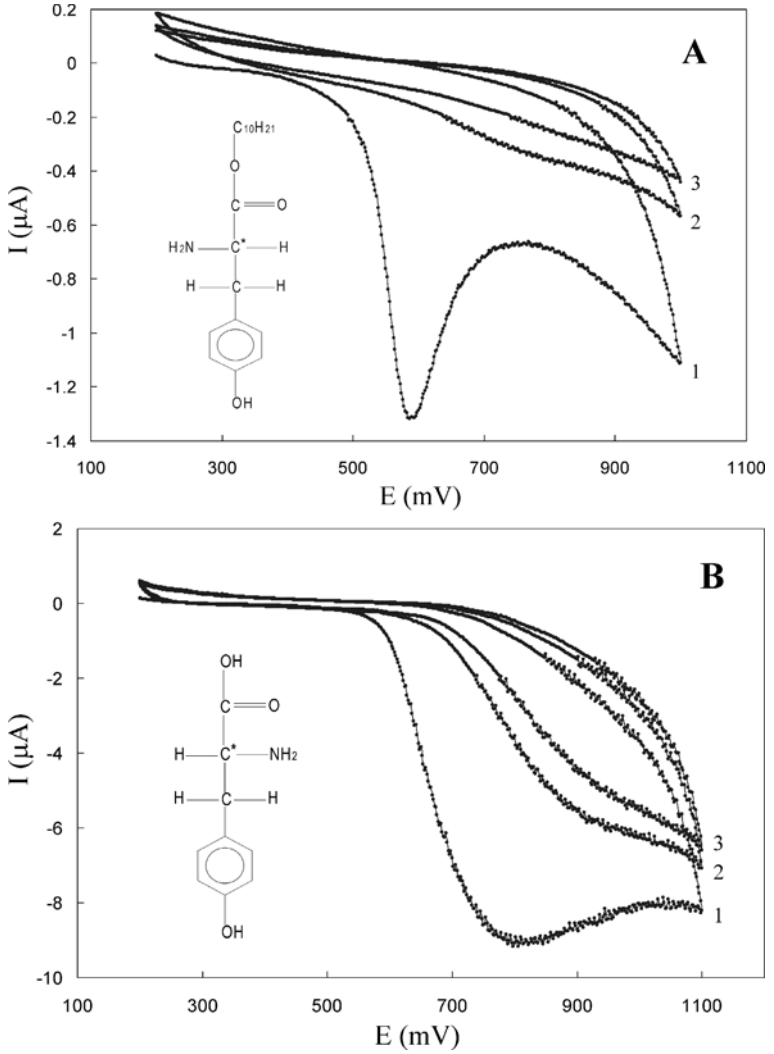

Fig. 8 Cyclic voltammograms (the first three cycles) at 20 mV s^{-1} of unstirred solutions of **a** 0.11 mM DEDT in pH 6.5 buffer, and **b** 3.0 mM tyrosine in pH 6.5 buffer. *Insets* show the unprotonated amine chemical structures. This figure was reprinted with permission from [70]

first cyclic voltage sweep because no oxidized monomers remain to undergo reduction; they have all polymerized. This behavior is consistent with the oxidized monomer from the first half of the cycle reacting via free radical coupling to the growing polymer chain. As early as the second and third cyclic voltage sweeps, the DEDT oxidation peak has virtually disappeared. This is due to film formation on the electrode preventing access of the dif-

fusing monomer to the Pt surface, a film electropolymerization phenomenon called self-limiting behavior. An intermediate behavior is exhibited by the L-tyrosine. The second and third voltage sweep peak magnitudes are similar, but about half that of the first sweep peak. This different behavior is due to the fact that free radical coupling of these monomers is not forming a significant film rapidly on the Pt surface, thereby allowing continued monomer access for electroxidation. This behavior for L-tyrosine is likely due to the partial solubility of the relatively hydrophilic polymer products resulting from free radical coupling of these electroxidized monomers. We present evidence for this in subsequent EQCM experiments.

Electrode Adsorption Behavior of Monomers. In order to understand the pure adsorption behavior of the monomers at the Pt electrode, we carried out the EQCM experiments presented in Figs. 9 and 10. In Fig. 9, monomers in the absence of an applied potential and at pH 6.5 were allowed to interact with the Pt electrode surface on the quartz crystal [70]. The results clearly indicated that even at the high concentration of 3 mM, little, if any, L-tyrosine adsorbs to the Pt surface. On the other hand, DEDT at the low concentration of 0.032 mM, well below the cmc, adsorbs to the Pt surface readily from solution. These results are in agreement with the Fig. 8 cyclic voltage sweep results where the electropolymerized DEDT rapidly formed a film that almost completely prevented monomer oxidation. In contrast, L-tyrosine had less restricted access to the electrode, since a significant level of monomer

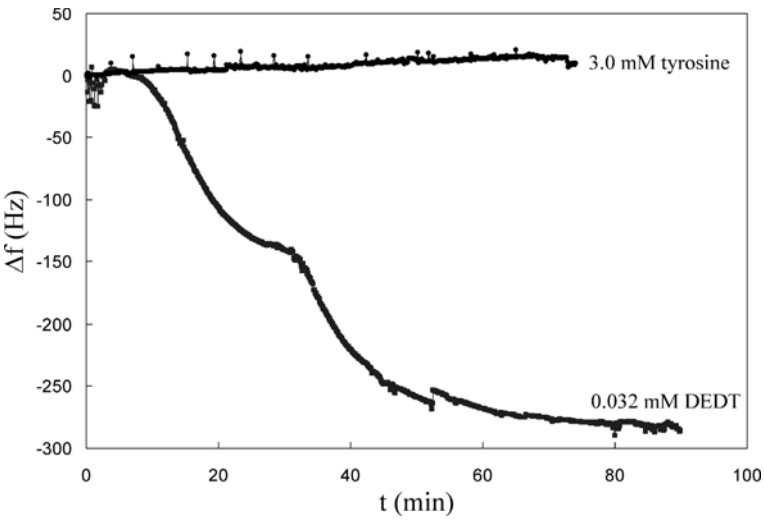

Fig. 9 QCM Δf shifts measured as a function of time in the presence of either 0.032 mM DEDT or 3.0 mM tyrosine in pH 6.5 buffer in the absence of an applied potential. This figure was reprinted with permission from [70]

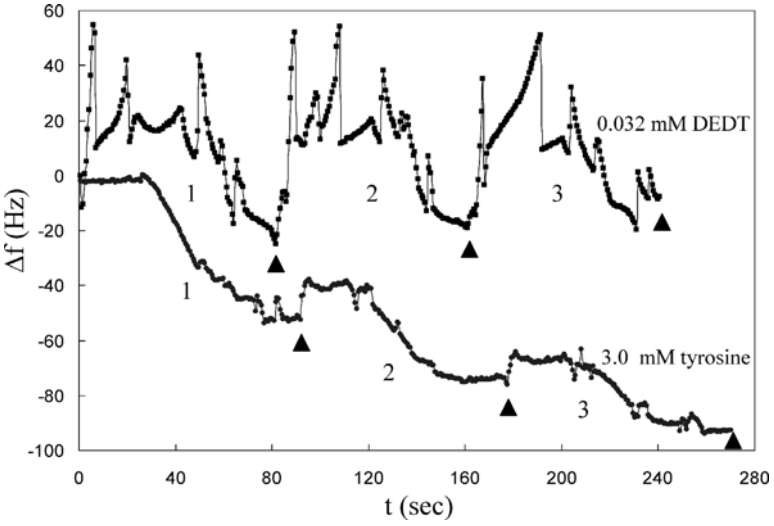

Fig. 10 Potential-dependent EQCM Δf shifts measured on Pt during cyclic voltammetry following a pre-adsorption phase with DEDT and tyrosine monomers. The *arrowheads* indicate the approximate beginning and end times of three adjacent c.v. cycles (between 200 and 1000 mV; Ag/AgCl ref.) in the two monomer polymerization experiments. This figure was reprinted with permission from [70]

oxidation continued in subsequent voltage sweep cycles. This result was expected, given our previous studies of the adsorption of DEDT in Figs. 3 and 4 and the formation of the completely covered gold surface by DELT copolymers in the Fig. 6 AFM images. This view was also supported by our previously discussed X-ray photoelectron spectroscopy results showing complete coverage of a gold surface by HRP polymerized DEDT after incubation for 24 h [57].

In Fig. 10, we continued to characterize these two monomer systems by measuring Δf as we carried out cyclic voltage sweeps after first allowing a 10 min pre-adsorption of each monomer to the Pt electrode in the absence of an applied potential, as in Fig. 9 [70]. Here, the first three complete voltage sweep cycles for each monomer are presented in the time domain and they are numbered. What is immediately clear is that there is no net Δf change for the DEDT monomer. This suggests that little or no electropolymerization is occurring. On the other hand, for L-tyrosine Δf decreases with each successive cycle, indicating a significant level of electropolymerization. These results are also consistent with the DEDT having formed a film by a self-assembly process during the pre-adsorption step. The film does not allow continued diffusion of DEDT monomer to the Pt surface for electroxidation. On the other hand, the L-tyrosine monomer does not adsorb to the Pt surface. As a consequence, this monomer is able to continue accessing the Pt

electrode for electropolymerization during the three voltage sweep cycles, thereby forming a growing film on the Pt surface.

Evidence for Potential-Dependent Ion Mobility in the Films. Another indication that a film has formed in the DEDT experiment during the adsorption phase prior to applying potential is the presence of the interesting Δf spikes that occur reproducibly at specific E values within each of the three voltage sweep cycles. These behaviors are due to reversible effects most likely resulting from soluble ion flows in and out of the film. In sodium phosphate buffer at pH 6.5, the $H_2PO_4^-$ and HPO_4^{2-} anionic species predominate and Na^+ is the cation. Therefore, these would be expected to be the predominant soluble counterions available for electrophoresis during the applied potential phase. Most likely, these ions account for the complex pattern of reversible potential-dependent Δf spikes present in each voltage sweep cycle. Of course, the α-NH^{3+} present on monomers within the adsorbed/electropolymerized mass of DEDT film may also be responsible for some of the characteristic spikes, although they are likely to possess a lower mobility within the film. For L-tyrosine the overall relative f change increasing then decreasing within each cycle is similar to the DEDT pattern, but the Δf spike behavior is almost entirely absent. This behavior is consistent with the observed lack of any significant mass of pre-adsorbed film in that system that would give rise to a significant mass of bound ions capable of potential-dependent mobility behavior. This ability of the EQCM to observe complex potential-dependent ion mobility is another example that illustrates its unique capability not only to monitor the process of forming films, but equally to characterize interesting physicochemical behavior in those films once formed [113, 114].

Electropolymerization of Monomers. To further investigate the film formation properties of these monomers we compared the electropolymerization kinetics of the DEDT, DELT and L-tyrosine monomers at the Pt electrode. We carried out these experiments at constant + 0.75 V, close to the peak potential for the monomers under the 0.44 mM phosphate buffer pH 6.5 conditions we used, and higher than the 0.12 mM phosphate used in Figs. 8, Fig. 9, and 10. In a series of experiments not shown here, we measured the Δf and ΔR as a function of time at different monomer concentrations. For all the EQCM experiments with DEDT and DELT, these monomers exhibited decreasing Δf, with a gradual lessening of the decrease to nearly a constant Δf by around 3 h at + 0.75 V. For all of these film formation experiments, there was no change in ΔR, indicating that the energy dissipation remained constant during the entire process of film formation. This agreed with our previous demonstration that no significant energy dissipation at this pH occurred for DEDT films formed from monomers spontaneously self-assembling on gold in the absence of an applied potential in Figs. 3 and 4. For L-tyrosine at 3 mM, Δf decreased by $\sim$ 500 Hz at 3 h and ΔR was unchanged, indicating no change in energy dissipation for the film being formed. As a summary

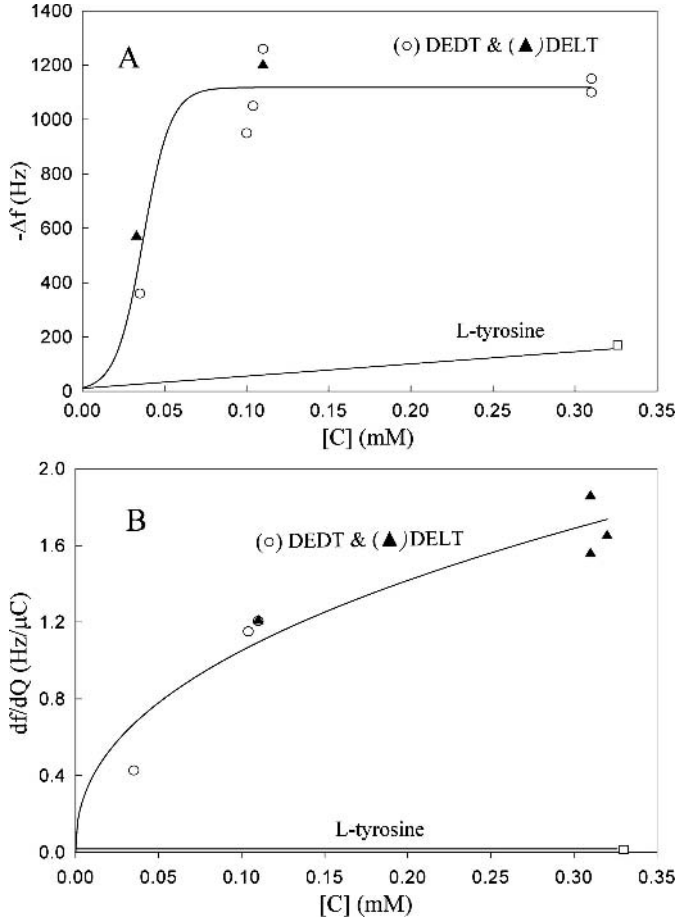

Fig. 11 **a** Dependence of the films' final measured Δf shifts on the monomer concentration during + 0.75 V electropolymerizations for DEDT, DELT, and L-tyrosine films. The *fit lines* are linear for the L-tyrosine and *sigmoid curves* for the DEDT and DELT data. The *fit lines* are included to simply indicate the data trends. **b** Dependence of df/dQ calculated from individual electropolymerization experiments on the monomer concentration during film synthesis for DEDT, DELT, and L-tyrosine films. A *linear fit* was used for the L-tyrosine point and a *hyperbolic curve* was fit to the DEDT and DELT data to indicate the data trends. This figure was reprinted with permission from [71]

of all these film electropolymerization experiments, we present in Fig. 11a a plot of the maximum Δf decrease at the 3 h condition of the electropolymerization experiments vs the monomer concentration present in each of the experiments [71]. The total Δf decrease during L-tyrosine electropolymerization was quite small compared to that of both DEDT and DELT isomers, which exhibited essentially identical behavior. Also, the shape of the plot for

DEDT and DELT is very different from that of the L-tyrosine. The Δf decrease indicative of film formation for DEDT and DELT is initially very steep at low concentration followed by a leveling off or saturation of the decrease. The 0.05–0.10 mM range, where saturation behavior roughly occurs under these conditions, is close to the cmc. This saturation behavior makes sense, since above cmc, the free monomer concentration available for oxidation at the electrode, remains constant.

Electropolymerization vs Adsorption Contributions to Film Formation. In order to use the EQCM to gain further insight into the relative contributions to film formation from adsorption vs electropolymerization, we have plotted in Fig. 11b the quantity df/dQ vs monomer concentration during film formation. Plots were made of the Δf vs charge Q passed at the electrode during each of the electropolymerization time-course experiments (not shown) and from the linear portions of each plot the slopes, df/dQ, were calculated (all plots had $R^2 > 0.97$). In using df/dQ from these plots the assumption was made that there was a constant steady state charging current set up soon after electropolymerization started, which could therefore be ignored. For each monomer, the df/dQ values reflect the relative amounts of total mass deposited per unit of total charge transfer. Therefore, the total charge reflects the extent of electropolymerization. Clearly, both DEDT and DELT have increasingly greater df/dQ values with increasing monomer concentration compared to a small value for L-tyrosine. In fact, at 0.33 mM the df/dQ values are 1.50 for DEDT and DELT compared to 0.0144 for L-tyrosine. This indicates that there is a 104-fold greater mass deposition for DEDT and DELT/electron transferred at the Pt electrode than for L-tyrosine/electron transferred [71].

We believe that this striking df/dQ difference is due primarily to two factors. The first is the significant level of adsorption of DEDT and DELT monomers to the Pt electrode in the absence of electropolymerization, as we saw in Figs. 9 and 11a. This contributes to the major fraction of the mass increase and f decrease, irrespective of any electron transfer occurring. The second factor is poor film formation properties by the L-tyrosine electropolymerization products. This contributes to an artificially low df/dQ for L-tyrosine. The difference between the monomer df/dQ values cannot be explained on the basis of Faraday's law and the ratio of the masses of the two monomers. This ratio is 1.7 (1.7 = 307/182; since for DEDT & DELT = 307 g mol^{-1} and L-tyrosine = 182 g mol^{-1}) assuming all electropolymerization products bound to the electrode. In fact, when Faraday's law was used to calculate the monomer masses in each experiment, we obtained values well below the real values. For most of the DEDT and DELT experiments, calculated masses of 100–130 g mol^{-1} were obtained, below the 307 g mol^{-1} value of these monomers. For L-tyrosine the discrepancy was even greater. The calculated monomer mass was 1.53 g mol^{-1} compared to the actual monomer value of 182 g mol^{-1}. Thus, the DEDT and DELT films appear to possess less mass

than expected based upon Q, and the L-tyrosine film even less so, indicating that little of the electropolymerization product winds up contributing to film mass on the Pt electrode surface. Self-assembly and electropolymerization contribute to surface adsorption for DEDT and DELT films. However, no self-assembly and Pt adsorption occurs for L-tyrosine monomer. Only upon electropolymerization do some of the product species adsorb to the Pt electrode. These factors account for a large part of the 104-fold difference seen between these two monomer types. In fact, L-tyrosine films were studied in at least one previous report and were found to be poor at forming films under conditions related to, but not identical to, ours [117]. Certain of the L-tyrosine reaction products, perhaps those of low molecular weight, may be far more water soluble than the amphiphilic DEDT or DELT reaction products. Only

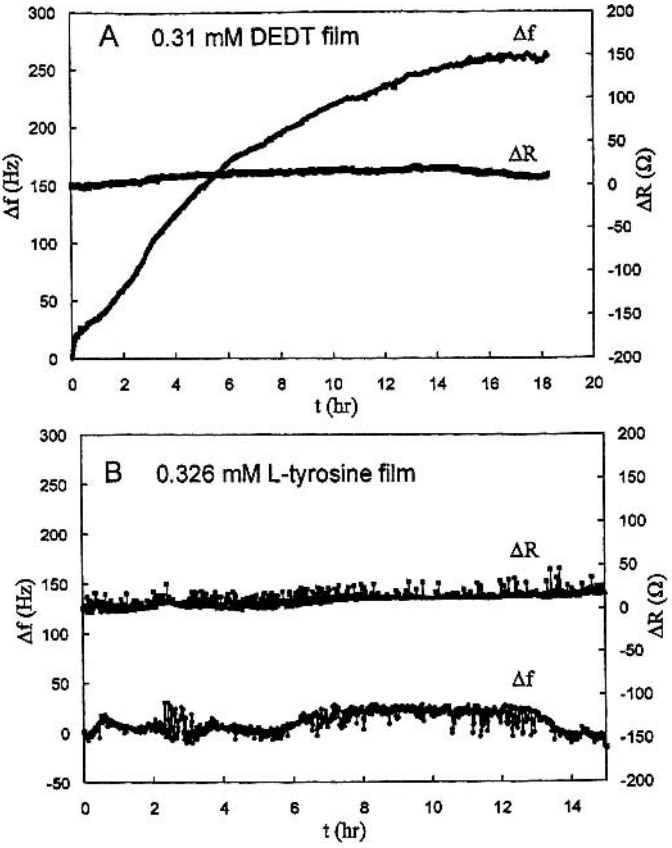

Fig. 12 Film stability kinetics for: **a** 0.31 mM DEDT film, and **b** 0.326 mM L-tyrosine film. Following a 3 h film synthesis period and removal of all unreacted monomer, the time-dependent Δf and ΔR values for the films were measured during a 15–18 h period to gauge film stability. This figure was reprinted with permission from [71]

less soluble higher molecular weight products of L-tyrosine electroxidation begin to form films on a Pt electrode. This line of reasoning can account for the very low L-tyrosine monomer mass (1.53 g/mol) determined from experiments using Faraday's law. On the other hand, for DEDT and DELT monomers the increasing df/dQ values with increasing monomer concentrations gradually levels off. This must be because as monomer concentration increases, there is a progressively smaller fraction of film mass added to the Pt surface due to electropolymerization compared to adsorption, since adsorption of progressively larger aggregates will occur as monomer concentration increases above the cmc.

Film Stability. The monomer mass range we determined for DEDT and DELT from Faraday's law (100–130 g mol^{-1}) is below the actual mass (307 g mol^{-1}). This can result from the fact that only some fraction of the electropolymerization products formed at the Pt electrode are in fact adsorbed to the Pt at the end of the experiment. This question concerning the interpretation of df/dQ for these monomers led us to carry out the following film stability experiment. For a DEDT film formed by the electropolymerization process after 3 h at 0.32 mM ($\sim$ 1180 Hz decrease) and an L-tyrosine film formed similarly at 0.326 mM ($\sim$ 170 Hz decrease), we examined the Δf and ΔR shifts as a function of time in the same buffer but in the absence of monomer. Figure 12 shows the results of these long term film stability experiments [71]. Over 18 h, the DEDT film has lost $\sim$ 250 Hz of the $\sim$ 1180 Hz mass deposited during synthesis, while the ΔR is unchanged indicating that no film alteration has occurred to change energy dissipation properties. Thus, the DEDT film is slowly lost from the Pt electrode while the L-tyrosine film is stable. From all of these EQCM results taken together, we conclude that for films from both monomers, not all electropolymerized products are adsorbed onto the Pt electrode. However, there is a greater overall mass of film formed and retained for DEDT and DELT films than for the L-tyrosine film. The dynamic film stability seems to be greater for the thinner L-tyrosine films once they have formed, with DEDT and DELT films being slowly lost from the surface. The DEDT and DELT film mass slowly lost from the surface is likely to result from the purely adsorbed component, comprised of monomer species that did not undergo electropolymerization.

4 EQCM Use in Studying Biochemical Processes, Biomimetic Systems and in Creating Biosensors

The versatility of the QCM and EQCM techniques for studying mass deposition in the absence of any prior chemical labeling in the system of interest, have permitted them to be used to study a wide variety of biologically related processes and systems. These include: biomimetic systems, fundamental

biochemical processes and assemblies involving DNA, proteins and other molecules, and the creation of biosensor systems where biological recognition and reporter components have been integrated into a piezoelectric-based signal transduction strategy. A number of review articles describe the applications of QCM in these areas [12, 18, 20–24]. We discuss briefly in the next section some selected examples of these different application types.

4.1 Studying Biochemical Processes and Biomimetic Systems

In general, as individual biological macromolecules are nearly two orders of magnitude larger in mass than small molecules, processes involving them are easier to detect at low molarities via the mass sensing capabilities of the QCM. Therefore, DNA, proteins, antibodies, glycoproteins, and lipid membrane assemblies have all been studied in various ways at the quartz crystal surface, using a variety of immobilization strategies and often in complexes with other non-biological polymers. The QCM and EQCM have been applied to studies of certain types of biomimetic systems. Examples of the range and properties of biomimetic systems studied include: characterizing film properties such as energy dissipation, phase behavior, adhesion and water content for protein monolayers and multilayers following their formation on surfaces [42, 118, 119], ion channeling phenomena in model membranes studied with the EQCM [120], lipopolysaccharide phase behavior influenced by an antibiotic [121], small molecule disinfectant activity correlated with its adsorption by a synthetic multibilayer membrane [122], the reversible adsorption of Annexin A1 protein onto lipid bilayers [123] (Chap. 8 in this volume), the attachment to the QCM surface and behavior of vesicles and liposomes [124], studies of a bioadhesion model for the glycocalix, the biological lipid–protein bilayer complexed with cytoskeleton [125], and the creation of gold nanoparticles by electroreduction of $AuCl_4^-$ ions bound to periodic lipid arrays on the EQCM surface [126].

Nucleic Acid Systems. The QCM has been used to study a number of fundamental biological processes. For example, DNA hybridization has been examined where an immobilized probe strand and its complementary strand in solution were observed to possess values for a second order association rate constant and a first order dissociation rate constant that corresponded to their free solution values [18, 127] (Chap. 6 in this volume). Changing physicochemical properties of DNA occurring during hybridization were measured [128, 129], as were the DNA-PNA hybrids formed [130]. Formation and properties of DNA–drug complexes have been determined for the covalent *cis*-platin complex [131, 132] and non-covalent intercalating drugs nogalomycin [133] and Hoechst 33258 [134]. DNA- and RNA-protein complexes have also been studied [133, 135, 136]. The EQCM has been used to first monitor the electrostatic binding of DNA to fatty acid amine films, then

to carry out the electroreduction of DNA-bound gold cations to form gold nanoparticles [137]. This represents a method to both create nanoparticles and a potential mass amplification strategy for sensing.

Protein and Enzymatic Systems. Proteins have been studied with the QCM and EQCM in a variety of contexts that are relevant to their complex physiological environments and biological properties. For example, the process of blood clotting has been examined on the oscillating quartz surface [41, 138]. The mass sensing as well as energy dissipation measurement capabilities of the QCM make it unique in its ability to measure blood clotting kinetics. Not only the mass of clotted protein, but the changing viscoelastic properties of the clot were followed in these studies. The biocompatibility of new materials surfaces have been studied with the QCM-D device [139, 140]. Examples of protein–protein interactions have been studied with the QCM and include systems as diverse as antibody–antigen protein interactions [141–145] and glycoprotein–protein interactions [122, 146, 147]. An affinity ligand method was developed to selectively bind and purify enzymes such as lysozyme using an aminoglycoside antibiotic (kanamycin) immobilized on a QCM surface [148, 149].

As described previously in Sect. 2.2, enzyme catalysis has been measured from the standpoint of following polymer product forming activity [67]. This study demonstrated the advantage that the QCM provides through its ability to measure both mass and energy dissipation behavior under conditions of optical opacity in the system. In another example, the synthetic activity of a vanadium-dependent bromoperoxidase was studied with the QCM in terms of its ability to crosslink and form the phenolic cell wall polymer found in the marine alga *Fucus serratus* [150]. The degradative activity of certain enzymes has also been measured. For example, the enzymatic degradation rates of poly(L-lactide) and poly(3-hydroxybutyrate) films have been studied [66, 67], as well as aspects of the enzymatic mechanisms and resulting film morphology changes. In another QCM study, the kinetics of DNA polymerase activity upon immobilized DNA was measured using very mass sensitive 27 MHz quartz crystals [65, 151]. With this unusually sensitive QCM setup (described in Chap. 10 in this volume) these investigators found that they could measure the rate constants for the three separate phases of the DNA polymerase reaction that are known to exist from other studies.

4.2 Creating QCM-Based Biosensors

Biosensors are a class of sensors designed from the combination of three basic components. The first is a biological component, possessing the specificity and efficiency resulting from its evolutionary history. It represents the molecular recognition or sensing element and may be enzyme or protein, nucleic acid, or living cell. The second component is some molecular method

of immobilizing the biological component, typically to a surface. The surface upon which the biological component senses the analyte of interest is often part of a sensitive signal transduction platform, which represents the third component. The biosensor is designed so that the platform transduces the physicochemical signal produced as a result of analyte binding to the biological recognition component. Finally, the platform creates an analog signal whose output represents the concentration of the analyte of interest.

A number of signal transduction mechanisms are commonly employed in different biosensor platforms [12, 152], with the piezoelectric mechanism of the QCM platform being the major focus of this chapter section. As a platform, the EQCM technique has the advantage that it contributes to two of these biosensor components. First, it provides the sensitive piezoelectric mechanism for detecting mass and energy dissipation behavior of the bound mass. Second, it provides both an electrochemical means for quantitating electron transfer processes in a sensing format as well as for electropolymerizing polymeric surface films that can be used for immobilization of biological components.

Protein- and Antibody-Based Biosensors. QCM biosensors have been created using a wide range of biological components. Many involve the powerful recognition properties of proteins in the form of antibodies (immunosensors) and the catalytic properties of enzymes (enzyme biosensors). Immunosensors have been created to detect analytes ranging in size from small molecules [144, 149, 153] to whole viruses [9, 154–156]. In the case of small molecules, lower sensitivity limits are typically a few $\mu g\,mL^{-1}$ of analyte. A new QCM multicrystal FIA-analysis system (Akubio) has been described as being capable of sensitively measuring k_{on} and k_{off} rate constants for analyte binding to immobilized antibodies and proteins [11] (Chap. 13 in this volume). As few as 20 HSV-1 virions, a large analyte, were detected using a novel variant of the QCM technique termed rupture event scanning [154, 155]. Here the acoustic energy associated with rupturing the bond between an immobilized antibody and a bound virus particle was measured, allowing a signal amplitude range over nearly six orders of magnitude change in virus particle number.

A number of mass amplification strategies have been developed for QCM- and EQCM-based biosensors to create more sensitive devices. In particular, the catalytic properties of enzymes have been targeted for this strategy. Typically, the analyte of interest is designed to be the substrate for an enzyme that catalyzes formation of an insoluble reaction product on the QCM surface, leading to a mass amplification of the analyte reactant signal [157, 158]. An impressive 0.1 pM detection sensitivity for cholera toxin was achieved using an enzymatic amplification approach and electrochemical-based signal detection with an EQCM device [159].

Nucleic Acid-Based Biosensors. Nucleic acid biosensors have been created most commonly based upon detecting the extent of hybridization of an

immobilized probe strand by an analyte nucleic acid sequence from an unknown sample. Sensitivities down to a few nanograms of analyte DNA have been reported [134, 160, 161]. For example, nanogram levels of mRNA were detected in an adsorption QCM biosensor of gene expression [162]. However, mass amplification can lead to more sensitive detection. A 0.1 pM detection level of an analyte nucleic acid sequence in solution was achieved using the mass amplification resulting from a biosensor incorporating large liposome particles during a multistep hybridization protocol [163]. Applications for nucleic acid hybridization biosensors range from analysis of clinical samples, to basic research studies. For example, EQCM impedance analysis has been used to characterize DNA damage brought about by a Quercetin-Cu(II) complex [164] and DNA point mutations were sensitively detected via the binding behavior of MutS, a DNA mismatch binding protein [165]. While we have concentrated on biosensors formed from some major biological component types, many other biosensor applications have been created that are too numerous to mention in this chapter.

4.3 Using Electropolymerized Films to Form Enzyme Electrode Biosensors

The EQCM technique not only provides a sensitive piezoelectric platform for mass and energy dissipation detection, but also an electrochemical means for quantitating electron transfer processes and for creating polymeric surface films. Such films are valuable for creating biosensors since they can be designed for the immobilization of biological components. As we illustrated in Sect. 3, the EQCM provides a valuable tool to monitor the formation and properties of polymer films formed via electropolymerization strategies.

Enzyme Electrode Biosensors. Here we demonstrate an application for electropolymerized polymer films in the creation of enzyme electrode biosensors. In these biosensors the unique advantage of the EQCM technique is utilized; that is its ability to directly measure electrochemically the redox activity of small molecules, or redox enzymes sensing small molecules such as H_2O_2. In these experiments we utilized the same phenolic and tyrosine-based monomers described in the previous section to create electropolymerized films on Pt electrodes. Here we have added the enzyme HRP to solution during electropolymerization. As a result, HRP was physically entrapped by the growing film during synthesis. Systems such as this one have been termed enzyme electrodes and they represent a class of biosensors [166]. Probably the best known and most commercialized example of an enzyme electrode is the glucose oxidase biosensor, sold as a glucose monitoring device for personal use [167]. In our system, for those HRP molecules sufficiently coupled electronically to the Pt surface, the biosensor current at a specific potential indicates the rate of HRP reactivity for the H_2O_2 substrate and therefore its solution concentration. We demonstrate this in the

experiments presented below. The H_2O_2 reduction reaction, shown below in Eq. 4:

$$H_2O_2 + 2H^+ + 2e^- \overset{HRP}{\rightleftharpoons} 2H_2O \tag{4}$$

is catalyzed by the HRP enzyme, providing two electrons to H_2O_2. HRP, being oxidized in the process, must then be reduced. It can transfer its oxidation state to appropriate solution monomers, in the type of enzymatic polymerization reaction we described earlier in the HRP experiments in Figs. 2–5. Alternately, HRP's original native oxidation state can be regenerated electrochemically via direct mediator-less electron transfer from the Pt electrode. This direct HRP regeneration can be accomplished at relatively low potentials, from – 0.05 to – 0.2 V with respect to the Ag/AgCl electrode [69]. At a different potential, + 0.85 V, $[H_2O_2]$ can be directly detected at the Pt electrode by being oxidized to O_2. Given the fixed molar reaction stoichiometry for H_2O_2 reduction by two electrons required from HRP (1 : 2), the current measured for this biosensor system is proportional to the rate of HRP activity and to $[H_2O_2]$. In Fig. 13 we present typical current measurements for an HRP enzyme electrode formed by physical entrapment of the HRP during a DEDT monomer electropolymerization at a Pt electrode. In the inset, the cyclic voltammogram represents the first potential sweeps that readily form the DEDT polymer film via electron transfer as well as adsorption, as we have already described in Sect. 3.2. In these biosensor experiments, there is no electron mediator present and the HRP enzyme electrode can be maintained

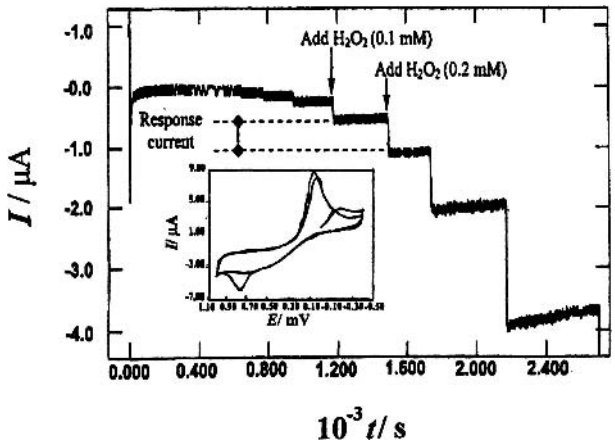

Fig. 13 Typical amperometric response of a poly-DEDT film modified sensor to successive additions of hydrogen peroxide. The sensor was operated at + 0.85 V vs Ag/AgCl in 0.1 M phosphate buffer, pH 6.5. The *inset* is the cyclic voltammogram of a bare Pt electrode sensor in the presence of 1 mM hydrogen peroxide in buffer. This figure was reprinted with permission from [69]

at – 0.05 V for HRP regeneration detection or at + 0.85 V for direct $[H_2O_2]$ detection. In Fig. 13, we show an example of data for the biosensor current levels measured at + 0.85 V at different times in a sequence of additions of progressively greater $[H_2O_2]$. At each $[H_2O_2]$ the current was allowed to equilibrate to steady state values.

Data of the type presented in Fig. 13 was then used to construct biosensor calibration curves for increasing $[H_2O_2]$ values. In Fig. 14a we present a number of examples of $[H_2O_2]$ calibration curves created using a DEDT film-HRP enzyme electrode as well as HRP enzyme electrodes created with DELT and L-tyrosine films. However, these biosensor data were all collected at the – 0.05 V condition, representing $[H_2O_2]$ detection by direct HRP regeneration at the electrode. For all the different electropolymerized film HRP enzyme electrode biosensors we studied, the measured current values exhib-

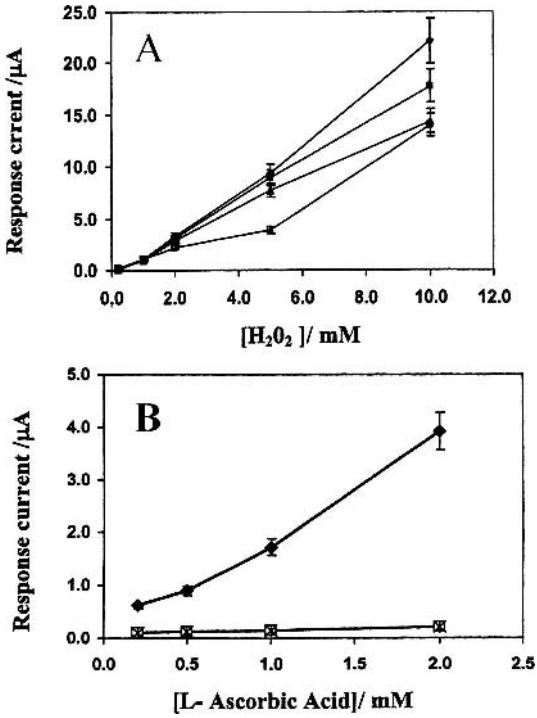

Fig. 14 **a** Current response of thin film modified Pt electrodes incorporating horseradish peroxide at – 0.05 V to various hydrogen peroxide concentrations, where *filled diamonds* are HRP-poly-DEDT films, *filled squares* are HRP-poly-tyrosine films, *open squares* are bare Pt electrode, and *open triangles* are poly DEDT films; **b** Current responses to interfering L-ascorbic acid concentrations at + 0.85 V, where *filled diamonds* are bare Pt electrode, *unfilled squares* are poly-DEDT films, and *asterisks* are poly-phenol films. This figure was reprinted with permission from [69]

ited linear increases with $[H_2O_2]$ down into the sub-mM range, without major differences in sensitivity. Over the entire concentration range studied, down to the lowest detectable concentration of 20 μM, the slopes of linear fits of $\log I$ vs $\log[c]$ plots, $d\log I / d\log[c]$, were obtained for HRP enzyme electrode films formed from all of the monomers presented in Fig. 7 (data not shown). These slopes represent the different biosensor film enzyme electrode sensitivities to $[H_2O_2]$ detection. The poly-DEDT (0.710) and poly-DELT (0.709) films had the lowest slopes/sensitivities, close to poly-tyrosine (0.715) and poly-3-nitrophenol (0.712) films, while poly-phenol (0.803) films had by far the highest slopes/sensitivities to $[H_2O_2]$. This may be due to the fact that H_2O_2 is an uncharged hydrophilic small molecule. The DEDT, DELT, and L-tyrosine films all possess partial charges at the pH of these experiments and the first two films also possess hydrophobic moieties making for slower diffusion of H_2O_2 in their matrices, compared to the uncharged hydrophilic poly-phenol matrix.

Interferents at the Biosensor Electrode. One of the problems with these enzyme electrode biosensors is illustrated by the result for the bare Pt electrode. At this low potential, Pt exhibits evidence for direct $[H_2O_2]$ reduction occurring at its surface [168]. Furthermore, dissolved O_2 has been shown to be a problem, interfering with H_2O_2 measurement at these potentials. However, in spite of these factors reducing the HRP enzyme electrode sensitivities at – 0.05 V, this potential condition still produces a better biosensor sensitivity for $[H_2O_2]$ than does the + 0.85 V direct H_2O_2 detection condition [69].

A different type of problem that H_2O_2 sensors possess when real biological samples are tested for $[H_2O_2]$, is the presence of small molecules that interfere with accurate analyte determination. Direct $[H_2O_2]$ electrochemical determination in clinical samples by a sensor at + 0.85 V, faces the problem of interfering electroactive species active at that potential such as ascorbate, acetaminophen, and dopamine [169]. In order to understand how a potential clinical contaminant might affect our electropolymerized HRP enzyme electrodes, we studied L-ascorbate as a clinically important interfering species. In Fig. 14b we present the measured currents for two different monomers electropolymerized on Pt electrodes and the bare Pt electrode in the presence of increasing [L-ascorbate]. The bare Pt electrode has a significant [L-ascorbate] response current in the millimolar concentration range. Possessing nearly the same current/mM response level as $[H_2O_2]$, L-ascorbate would be a major interferent to accurate $[H_2O_2]$ determination in clinical samples. However, as we see next, the use of electropolymerized polymer films to cover the Pt surface allows this problem to be overcome. The other two current response profiles are for a poly-DEDT film created on the Pt electrode and a poly-phenol film created on the Pt electrode. Both these film-covered electrodes showed negligible responses to L-ascorbate at all concentrations, under conditions where the smaller H_2O_2 molecule was able to reach the Pt electrode and be detected. This is due to this class of phenolic and tyrosine monomer

based films possessing self-limiting behavior, a property that we discussed in Sect. 3.2. This is where the polymer chains comprising the film are so tightly packed that they effectively exclude monomers and other small molecules from reaching the electrode surface, thereby preventing any electron transfer activity. This self-limiting behavior has been especially well documented for polyphenol films [170] but we have also shown this to be true for films electropolymerized from these other Fig. 7 monomers, such as DEDT [69]. Since these two phenol-based films possess very different hydrophobicity and charge properties, these results suggest that the films' selectivity allowing H_2O_2 diffusion and disallowing the L-ascorbate ion to reach the Pt electrode is predominantly due to a size exclusion effect.

Enhancing Enzyme Electrode Biosensor Performance by Enzyme Evolution and Direct Coupling of the Enzyme to the Electrode. Performance enhancements can be achieved in enzyme electrode biosensor systems in a number of ways. We briefly discuss two approaches that have been used to this end. In the first, rational methods have been developed to modify protein and enzyme structures through primary sequence alterations in order to overcome stability, specificity, and other functional limitations. Directed evolution is a recent methodology that seeks to modify these molecules by a repeated process of sequence evolution coupled to a criterion-based selection protocol applied to each cycle of the evolving sequences [171, 172]. As an example of these sequence modification approaches, we discuss the widely used enzyme HRP. This peroxidase possesses a broad substrate specificity, a property that is atypical of most enzymes [173]. Yet the substrate specificity was further expanded through a genetic engineering approach to include increased enantioselectivity for oxidation of alkyl aryl sulfides, a substrate that is not catalyzed by the native enzyme [174].

A second approach to enhancing enzyme electrode biosensor performance has been the development of enzyme "wiring" to the electrode surface. Applied potential selectivity of an electron transfer process at an electrode is an advantage of the EQCM approach that we have already discussed. However, the advantage is operative only when there is efficient electronic coupling of the electron transfer species to the electrode surface. The efficiency of electron transfer is described by Marcus theory where a uniform exponential decrease in the effective electron transfer coupling results from increasing distance between the two transfer species [175]. Only recently has evidence emerged that ordered water molecules around enzyme active sites can facilitate electron transfer from the site to produce distance independent electron transfer rates, but only at intermediate distances for these biological systems [176]. This report notwithstanding, at a relative short distance from the electrode surface, electron transfer efficiency drops significantly and nearly exponentially for most species, including enzymes. For an immobilized electron transfer enzyme this can be a problem if the enzyme is not sufficiently close to the electrode surface to efficiently couple electronically. Some inves-

tigators have used soluble electron transfer mediators to span the distance and effect coupling, but this 3-D diffusion approach is not nearly as efficient as the "wiring" approach. Here, the enzyme is immobilized onto an electrode surface or entrapped near the surface and the "linear" electron transfer coupling is effected by a redox polymer that directly connects the enzyme to the electrode. An example of a redox polymer is poly(diallylamine), covalently modified with osmium $(pyridine)_2$ redox complexes arrayed periodically along its length to ensure efficient electron transfer. Poly(diallylamine) has been used to "wire" immobilized glucose oxidase, lactate oxidase, and soybean peroxidase to an electrode surface [177]. Use of this polymer allowed efficient electron transfer from the enzyme to be carried out essentially via a 1-D transfer scenario along the polymer directly to the electrode surface. The authors showed that the efficiency of the enzyme coupling electronically to the surface via this Os redox polymer varied significantly depending on the method used to carry out the "wiring" process. This undoubtedly resulted from the fact that some methods yielded much closer contact between the osmium $(pyridine)_2$ redox groups and the active sites of the immobilized enzymes.

4.4
Thin Polymer Film–Peptide Conjugates Created by EQCM for Cell Binding Studies

Electropolymerized thin films have many potential applications. They can be both electropolymerized on conducting surfaces and then studied in different applications using the EQCM. One of their interesting uses is to selectively promote the binding of living cells via specific ligands located in the films. Cells on their exterior contain many potential binding sites for specific small molecule ligands. One important broad class of ligand binding sites are the membrane-bound protein receptors on the exterior surface of cells that nature has evolved for cell attachment and for cell–cell signaling purposes. In response to the binding of specific signaling molecules, these receptors can act as switches effecting changes in the regulation of specific gene transcription states. Membrane-bound receptors represent a vast topic area in cell and molecular biology that is beyond the scope of this chapter section. In this short discussion we present one important specific cellular membrane receptor complex necessary for cell attachment, which acts to bind a short minimum peptide recognition sequence, RGD, contained within the protein molecule laminin. Laminin is a major protein component of the extracellular matrix, ECM, that all normal endothelial cells synthesize, secrete underneath themselves, and then bind too [178]. Endothelial cells express integrins, integral membrane receptors that possess a binding site for RGD on their extracellular face. Formation of a complex enables these cells to create a stable attachment to their ECM. The stable attachment state is a requirement for the existence of normal cells in vivo and in tissue culture environments. The RGD

in laminin binds to the integrin membrane receptors on the surface of normal cells allowing these cells to spread and maintain a normal attachment phenotype. Our aim was to first demonstrate covalent linkage of the Arg-Gly-Asp, RGD, peptide to our poly-phenol derivative films via electropolymerization in the EQCM, so that the peptides would be available in a subsequent step to bind to integrins on the surface of cells added to the film under growth media. The demonstration of binding specificity could lead to a "cassette" type system whereby any cell-specific recognition peptide could be covalently linked to the film by electropolymerization. This would lead to specific attachment of a cell type with receptors that bound the electropolymerized peptide, but not other cell types lacking the receptor.

Our synthetic approach to creating this film was to carry out the electropolymerization of two comonomers, both containing tyrosine derivative oxidizable groups as we have already indicated schematically in Fig. 7. This example will be illustrated with the first monomer being L-tyrosineamide, the amide derivative of the amino acid L-tyrosine, shown in the Fig. 6 schematic. The other monomer was the tetrapeptide Arg-Gly-Asp-Tyr, RGDY, where the terminal amino acid L-tyrosine (Y) will undergo electropolymerization with L-tyrosineamide. We used the EQCM to carry out these comonomer electropolymerizations for a number of different monomers mixed with the RGDY tetrapeptides at different monomer ratios. All monomers formed films, with better films being formed at comonomer ratios that limited the RGDY monomer ratio in the mixture. Due to space limitations in this chapter, the comparative EQCM data for these different comonomer ratio films are not shown. We believe that this RGDY monomer ratio limit effect is due to the hydrophilic nature of the short tetrapeptide, so that RGDY-rich product peptides are reasonably soluble "protein-like" complexes that did not bind particularly well to the metal electrode surface.

As an assay for films electropolymerized at three of the comonomer ratio conditions, we present in Fig. 15 the light microscopy results following addition, attachment, and growth of bovine capillary endothelial cells on the different films [179].

For the pure L-tyrosineamide monomer film in Fig. 15a, few cells are found attached to the film formed on the gold surface. What cells are evident do not have a normal appearance, but exhibit a spindly neuronal-like spreading behavior on the surface. Since this film lacks any RGD recognition peptide, it would appear that the underlying polymer properties do not encourage a significant level or normal type of cell attachment. In the Fig. 15b, cells have attached and spread on a good portion of the film electropolymerized from a 1 : 20 molar mixture of RGDY : L-tyrosineamide monomers. Importantly, there is evidence of good cell–cell contact and the cell monolayer has the normal "cobblestone" visual appearance exhibited by this cell type. Therefore, the RGDY covalently incorporated into this film has produced a significant positive enhancement of the cell attachment and spreading. In Fig. 15c, cells

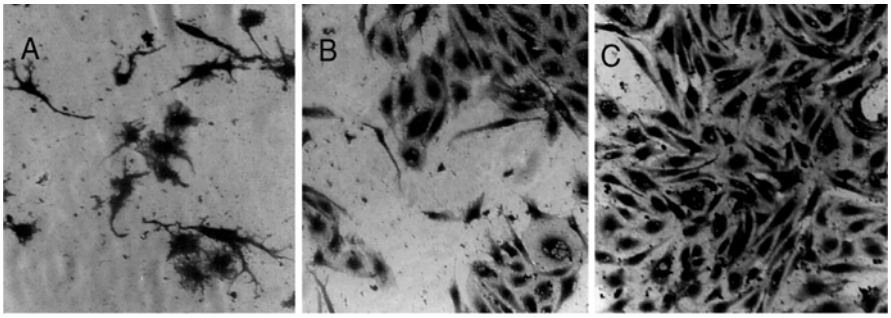

Fig. 15 Coomassie blue stained ECs grown on three different electropolymerized films in three different wells of the ECIS device: **a** tyrosineamide film; **b** RGDY : tyrosineamide (1 : 20 molar ratio) film; **c** RGDY : tyrosineamide (1 : 3 molar ratio) film. This figure was reprinted with permission from [179]

have attached and spread everywhere on the film electropolymerized from a 1 : 3 molar mixture of RGDY : L-tyrosineamide monomers. Here, the significant enrichment of RGDY has produced a uniform normal appearing cell monolayer. Electropolymerization of pure RGDY produced more soluble fully peptide-like products and a poorly adhering film, as judged by the frequency behavior of the EQCM experiment. As a result, cell attachment was not promoted under these film conditions (data not shown). These data suggest that electropolymerization of comonomer mixtures that include cell recognition peptides can be used in a modular or cassette-like fashion to produce polymer films adhering to electrode surfaces of various devices, including the EQCM. By varying the cell-recognition peptide, the films can be used to select and bind specific cell types for different biosensor applications such as cell QCM and EQCM drug biosensors [11, 12, 18, 152], helping design tissue engineering architectures [12, 152, 180], and creating new clinical tissue diagnostic systems [12, 152].

5
Applications of QCM to Studies of Cell Behavior

Normal cells adhere to surfaces as a requirement for their continued existence. Cell detachment typically results within hours in the onset of apoptosis or programmed cell death. Adhesion of cells to a surface is a complex process and its detailed description is beyond the scope of this discussion. However, in this short section we wish to briefly discuss both the use of the QCM to measure interesting aspects of the cell attachment process as well as to characterize the behavior of fully attached cells in response to changes in their environment. We believe that piezoelectric techniques have a unique role to play in the understanding and utilization of these complex cellular

phenomena. A small number of groups worldwide have examined the use of QCM, QCM-D and associated impedance techniques to study various aspects of the cell attachment process to metal-coated quartz crystals [50, 51, 181–194]. These include straightforward demonstrations of cell attachment as well as more detailed examinations of the time- and environment-dependent attachment behavior of normal cells and transformed or cancer cells. More recent detailed studies have begun to establish important aspects of how the QCM in the impedance mode and using various overtone frequencies can better be used to monitor attaching human ovarian cancer cells to underlying extracellular matrix proteins [51]. Also, investigations using QCM are providing more insight into some fundamental biological processes undergone by attached cells, such as the dynamics of exocytosis and dense core vesicle retrieval [189], and shear-induced senescence [195]. In the sections that follow we focus discussion on our use of the QCM to describe two different cell systems. The first is a study of experiments exploring the time- and cell number-dependent attachment process of normal endothelial cells that suggests the operation of cell–cell cooperativity behavior in the initial few hours of the attachment process [50]. The second is a study of attaching normal cells to form a cell QCM drug biosensor and then using the biosensor to detect microtubule-binding drugs [192].

5.1 QCM Studies of Energy Dissipation Changes During the Cell Adhesion Process

In a series of investigations, we have studied the initial process of endothelial cell (EC) adhesion and the subsequent achievement of their steady state properties on the gold electrode surface of a QCM device [50, 181]. These experiments have been carried out where the solution covering the upper gold electrode is comprised of cellular growth media and serum and where the QCM device has been placed in the controlled CO_2 environment of a cell culture incubator at 37 °C. In a study of varying cell numbers added to the gold surface, we demonstrated that consistent calibration curves of Δf or ΔR vs numbers of firmly bound cells could be determined [181]. The procedure involved carefully removing media and serum at the conclusion of an experiment followed by careful washing of the electrode surface with PBS to remove dead or poorly adherent cells. Then a series of trypsin digestions was carried out to remove firmly adhering cells by disrupting their integrin receptor–ECM protein complexes. Electronic counting of all the wash and digestion steps accurately determined the number of firmly attached cells.

Increasing Energy Dissipation Characterizes the Cell Attachment Process. The process of cell attachment as monitored by the QCM is rather lengthy, involving many hours of change before steady state invariant behavior is observed. We have followed this process for normal ECs as well as for other transformed cell types, but our most detailed studies have been performed

with ECs. In general, the qualitative features of Δf or ΔR shift change with time observed for ECs are found in all cell types [181]. In Fig. 16 we present a representative Δf vs ΔR plot of the time course of cell attachment to the gold QCM electrode surface. Starting at the arrowhead labeled $t = 0$, where the cells were added to the device and where Δf or ΔR shifts are 0, the ECs sediment within a few minutes to the gold surface. Since each point represents a successive 1 min interval in the experiment, this time for the ECs to reach the surface is characterized by a small region of points arrayed horizontally along the pure liquid $(\rho\eta)^{0.5}$ effect response line. We know from another study that when the ECs have been added to the solution, there is a lag time of at least 10 min before they reach the surface and exhibit any attachment via small changes in Δf or ΔR [50]. At these times the points are moving along the pure liquid $(\rho\eta)^{0.5}$ effect response line. This is the behavior that might be expected from ECs that have arrived at the crystal surface but have not yet established significant surface attachments. That they follow this liquid-like behavior is reasonable since the internal structures of these cells would be expected to make the solution near the solution–gold electrode interface mimic solutions of increasing $(\rho\eta)^{0.5}$ magnitude as the number of ECs accumulates at the surface. However, gradually with time there is an observed decrease in Δf and increase in ΔR, represented by the progression of arrows in Fig. 16. During the time period of this rapid change in shift parameters,

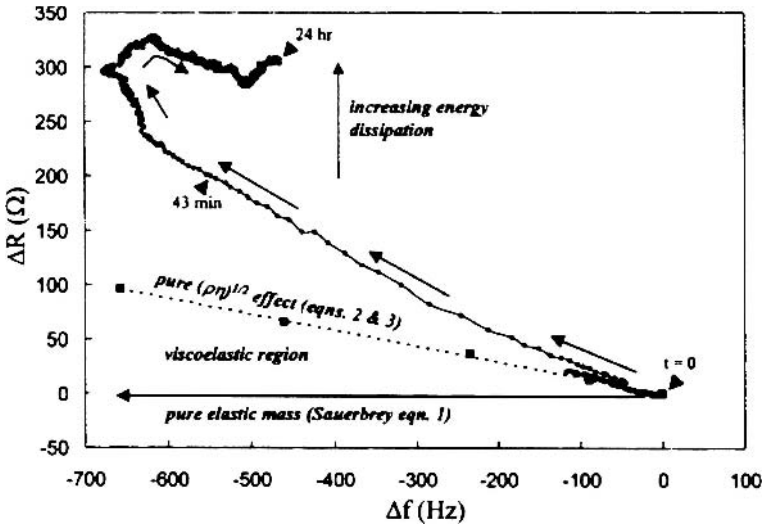

Fig. 16 Δf – ΔR diagram representing the time course (*arrows*) of 30 000 cells added to the QCM at $t = 0$. The pure $(\rho\eta)^{0.5}$ effect line is indicated with the *dashed line* and some experimental data points (*solid squares*) for different % sucrose solutions. The *horizontal solid line* indicates behavior for elastic mass binding to the surface. This figure was reprinted with permission from [181]

the ECs begin the process of establishing their firm attachment to the surface. Not only are there rapid changes in shift parameters, but with time the negative slope slowly increases in magnitude. This signifies an increasing rate of energy dissipation with time by the ECs. Beyond the region around 45 min, the ECs begin to exhibit even greater levels of energy dissipation until they reach an upper limit to their ΔR shift before eventually reversing the Δf shift back to around – 500 Hz at 24 h. The magnitude of these parameters represents steady state attachment behavior for the normal ECs. During this latter phase of maximum ΔR shift, the ECs have assembled and put in place much of their internal cytoskeleton and are spread to their final extent upon their extracellular matrix, ECM [50, 181].

Extracellular Matrix Exhibits Elastic Behavior. The energy dissipation expressed by the ECs at their steady state may be due to contributions from the cells as well as the extracellular matrix, ECM, upon which the cells are attached via integrin–ECM linkages. Therefore, we asked whether the ECM contributed any significant level of energy dissipation to the overall system. To answer this question we removed steady state ECs from their underlying ECM by a chemically gentle process involving three separate EGTA treatments. EGTA is a chelator molecule that removes Ca^{2+}, a necessary inorganic cofactor that stabilizes the integrin–ECM bond. All ECs have detached from their intact ECM surface at the end of the EGTA treatments. We demonstrated that intact ECM remained on the upper gold electrode surface using total protein staining and immunohistochemical staining of laminin, a major ECM structural protein [180]. The Δf vs ΔR shifts, exhibited by the resulting ECM films from a series of these experiments, were arrayed along a zero slope line close to $\Delta R = 0$. This is behavior indicative of an elastic mass type of response on the QCM surface. Nothing like the type of energy dissipation exhibited by the cells in Fig. 16 was observed for the isolated intact ECM films. This type of elastic behavior may be exactly what one expects for such a biological film in vivo. Rather than dissipate energy that could lead to the ECM transducing mechanical energy into structural and/or chemical damage accumulating over time, the elastic ECM behavior would make this impossible. This elastic property may be advantageous to the organism, because its constituent cells would not be required to constantly repair damage to their underlying elastic ECM.

Cell–Cell Cooperativity Behavior Exhibited During Initial Attachment at Low Cell Density. We have also studied the dependence of Δf and ΔR upon EC number added to the gold QCM surface. We observed a difference in the early (1 h) vs steady state (24 h) response of the parameters to varying cell number in the QCM [50]. At 1 h, both Δf and ΔR exhibited sigmoid curve shaped dependencies upon EC number, while at 24 h there was a hyperbolic curve shaped dependence to the data. Sigmoid behavior is indicative of cooperative phenomena in physicochemical systems. For the ECs this suggests that not at the steady state, but only early in the cell attachment process, does suc-

cess in attachment with the concomitant expression of Δf or ΔR shift values rely non-linearly upon sufficient numbers of ECs being present upon the surface. We verified this supposition by using light microscopy to demonstrate that at equivalent times 1–3 h following seeding of ECs, the firmly bound cells at low density remained rounded, indicating poor progress in the attachment process [50]. By contrast, at equivalent times those at higher densities demonstrated more spread shapes with protruding cellular processes that indicated they were farther along in the attachment process. We believe that the cells express this cell–cell number cooperativity in their attachment behavior via long processes that they use to sense the number of neighboring ECs in their vicinity. That this cooperativity phenomenon should exist makes sense since these normal ECs, both in vitro and in vivo, establish native monolayer structures in which the cells maintain close cell–cell contact as part of their normal phenotype, as is shown in Fig. 15c.

5.2 Cellular QCM Drug Biosensors

Among the many potential uses for the QCM, its ability to directly detect small molecules or the effects of small molecules binding to molecular recognition elements on the crystal surface, make the technique well suited for a variety of biosensor applications in the area of drug discovery. A number of recent reviews describe such applications [11–13, 18]. At their simplest, these drug discovery approaches involve the specific detection of individual small analyte molecules of pharmaceutical interest. In drug characterization and drug target-based assays involving target systems such as important cell surface protein receptors, the testing of small drug candidates' binding to the isolated and immobilized targets is carried out. A more complex and information-rich drug QCM biosensor utilizes immobilized living cells containing the drug target to monitor drug effects (a cell biosensor). We have created a cell QCM biosensor in order to illuminate how the complex biological drug effects that occur within living cells may be measured and thus exploited in useful ways. Drug effects in vivo can involve biological responses from multiple interacting cellular subsystems or proteins within cells. The biological complexity of these coupled systems is not necessarily captured by studying the response of single isolated biological targets – even where the correct primary biological target for that drug in the cell is being studied. Therefore, there is real value in the use of living cells to create information-rich cell biosensors. We next briefly discuss our use of the QCM to create a cell QCM drug biosensor system that detected the complex cellular response of normal endothelial cells attached to the QCM surface to added drugs that bound to and affected the intracellular microtubule system.

Our efforts to create a cell QCM biosensor focused initially on characterizing the early attachment behavior of normal endothelial cells as well as

their steady state adhesion properties and the relationship between the measured QCM parameters (Δf and ΔR shifts) and the number of cells actually bound to the surface [50, 181]. These studies were summarized in the previous section of this chapter. Having characterized the steady state behavior of endothelial cells, we next investigated whether cells bound to the QCM surface under these conditions could function as the biological recognition elements in a biosensor. To carry this out, we decided to study small and large molecules whose effects on these cells were known. The small molecules we studied were nocodazole and paclitaxel [192]. Both molecules bind to tubulin sites on the intracellular microtubule structures, but have very different effects. Nocodazole dissociates the microtubules to the monomer form, while paclitaxel hyperstabilizes the microtubule structures. Also, using the cell QCM biosensor we studied the biological activity of a large protein, the cytokine FGF that binds a cell surface receptor on ECs with subsequent initiation of growth [181].

In a study of nocodazole effects, the cell QCM biosensor revealed a significant Δf shift magnitude decrease, nearly 100% that of the initial steady state signal [192]. This biosensor response resulted from complete disruption of the intracellular microtubules. This disruption of intact microtubules produced a loss of the well-spread state of the cells, leading to a more rounded smaller shape. It was accompanied by a concomitant loss of viscoelastic behavior at the QCM surface and a greater effective coupling of cellular mass to the QCM surface. A typical sigmoid shaped drug dose response curve was observed for nocodazole with a midpoint at around 900 nM of the drug. We also observed in this study, via fluorescence light microscopy of stained intracellular actin, that the nocodazole concentration producing the maximum Δf decrease effect on the surface attached cells had a dramatic effect on the appearance of the cells. The cells lost their normal monolayer morphology of closely contacting, well-spread cells. The cells appeared smaller, more rounded, had lost most of their cell–cell contacts and had their normal actin microfilaments rearranged to form peripheral actin stress fibres [192]. This visual appearance of the cells is consistent with the loss of intracellular microtubules that are critical to stabilizing the spread morphology of the cells. Even at as little as 330 nM nocodazole, the cells' shape and cytoskeleton were observed to be altered.

In a related study focused on the dynamics of the nocodazole response of the cell QCM biosensor, we observed that the Δf shift alteration kinetics could be fit by a single first-order exponential relationship [193]. In all cases, the response to nocodazole was complete by around 5.5 h and the $t_{0.5}$ of the fit equation averaged 0.83 h, irrespective of the nocodazole concentration we studied. These results strongly suggest that a single dynamic system within the cells, the disruption of the microtubules, was responsible for the biosensor response we observed. All these results suggest that the cell QCM biosensor is revealing important information regarding the complex response of cells to drugs that affect components of the cell's cytoskeleton.

Paclitaxel and docetaxel are both members of a class of taxane molecules that have been developed for the chemotherapeutic treatment of many human cancers [196]. Currently, there is no assay to reliably predict tumor responses to taxanes prior to chemotherapy. We adapted the QCM to study responses of human mammary epithelial cells to the taxane molecules paclitaxel and docetaxol [197]. When these two microtubule hyperstabilizing drugs were studied with the cell QCM biosensor, we observed, not surprisingly, little change in Δf, even in the physiologically active dose range. There were small Δf decreases and ΔR increases until around 6 h after drug addition, whereupon distinct reversals of Δf and ΔR shift occurred. These Δf and ΔR shift reversals accurately predicted the onset of apoptosis, a fact that was confirmed by comparison with the drugs administered to the same cells in parallel conventional assays. Our cell QCM biosensor analysis also accurately predicted that docetaxel was more effective than paclitaxel and that MCF-7 cells were more resistant to these molecules than MDA-MB-231 cells. These studies suggest important cell biosensor applications like the following: The cell QCM biosensor could be used to produce signature patterns for taxane responsitivity of particular cell types, including diagnosed tissue biopsies. These signatures could then be compared to those of cells from new patient biopsy samples used to construct the biosensor, in order to predict a patient's therapeutic outcome prior to drug treatment. In this way, the biosensor could be used by an oncologist as a diagnostic tool for helping decide between different chemotherapy options in the clinic.

The effects of large biologically active molecules can also be detected with the cell QCM biosensor. For example, we studied the response of normal endothelial cells at their steady state on the biosensor surface to the administration of 3 ng mL^{-1} fibroblast growth factor (FGF), a known growth stimulating protein for these cells [181]. The effect of FGF upon the steady state endothelial cells was to produce a steady decrease in the measured Δf expressed by the cells, going from – 300 Hz to – 800 Hz over a period of 48 h after FGF addition. The magnitude of this steady Δf decrease exactly mirrored the increase in cell number due to cell growth and division that was measured independently by electronic cell counting in a parallel experiment using the same initial cell density and FGF concentration.

We believe that the QCM as a signal transduction platform offers real advantages over other platforms for studying drug effects in living cells. For example, a drug's effect on whole cells can have consequences for entire cellular subsystems that then contribute to the biosensor signal. This can effectively represent a signal amplification by the cell, since it involves the intact integrated metabolically driven biological machinery responding to the drug. This cell response can be contrasted with just the localized drug response effecting specific attached labels, as is the case in optical based biosensors for example. We believe that cell QCM biosensors offer particular advantages for studying drug effects targeted to the major components of the cellular cytoskeleton.

6 Future Prospects

A number of technology developments can be identified that promise to advance the applications of QCM and related piezoelectric resonance techniques. These involve modifications in the QCM device, the crystal, as well as in the systems under study and their methods of analysis. Some of these approaches have already begun to be studied and implemented. The specific areas of these improvements include: increasing mass sensitivity, hybrid devices and novel resonance techniques, enabling determination of the kinetics of processes, use of cells as information-rich sensing elements, and applying data mining techniques to provide accurate analyses and outputs from complex sensor inputs in future devices. We briefly discuss each of these below.

Increasing Mass Sensitivity. A few reports have described the use of higher oscillating frequencies to achieve more mass-sensitive QCM platforms [8, 9]. Especially in the latter reference, a significant improvement in mass sensitivity by a factor of $f^{2.8}$ was demonstrated over the frequency range studied. However, as noted by these investigators, the thinner crystals required to achieve the higher frequencies make them problematic for routine use. Therefore, 27 MHz seems to represent a practical upper limit at the present time. Higher frequencies may be less problematic in other oscillating sensor devices such as microcantilever arrays [3–7].

Besides frequency increases, another way that some investigators have increased the mass sensitivity of standard QCM crystals is by modifying the metal surface of the crystal. Improvements in mass sensitivity of > 2.5-fold have been measured using micromachined surfaces [13] and for electrodeposited gold surfaces that increase the surface area due to increased porosity [14]. For a process where the effective surface area is the limiting factor in mass sensitivity, the latter type of approach is of particular importance for future applications. It remains to be determined whether a systematic examination of creating microscale or nanoscale surface features on the upper electrode of the QCM crystal can reveal as yet unobserved increases in mass sensitivity.

Mass amplification is another strategy to increase the mass sensitivity of a standard QCM device and crystal. Such approaches commonly involve enzymatic catalysis to greatly increase either the rates of electron transfer processes in EQCM applications or to increase rates of insoluble mass deposition as the product of an enzymatic reaction [157–159]. However, mass amplification can also involve the use of larger mass objects binding to the QCM crystal, such as gold particles. We expect that future studies will continue to adapt these general mass amplification strategies to specific systems.

Lastly, an increase in mass sensitivity can be achieved through measurement modification. For example, by examining the higher harmonics of the

crystal, an increased mass sensitivity for cells binding to the quartz crystal surface was recently demonstrated [51].

Hybrid Devices and Novel Resonance Techniques. Combinations of the QCM with other techniques and novel variations of the standard QCM resonance technique have recently provided interesting advances in the study of different systems. One such approach is the relatively new QCM-D technique, a discontinuous resonance decay approach for obtaining energy dissipation behavior of film surfaces [198]. We believe that this convenient device for measuring the viscosity, elasticity, and thickness of films will continue to expand in popularity for film characterization.

A hybrid QCM/calorimetry device, Masscal, has been developed recently [199]. This technique combines the mass measurement change upon gas adsorption with the accompanying isothermal heat flow that allows a molar binding enthalpy to be determined. Various thin film chemical and biochemical systems have been studied, such as the hydration isotherms and associated hydration enthalpies determined for the immobilized enzyme lysozyme [200].

The unique and sensitive resonance scanning technique, rupture event scanning, has been recently reported [155] and is the subject of Chap. 13 in this volume. For relatively large mass analytes like viruses, bound to an antibody on the QCM surface, this bond "rupture" technique has allowed the detection of varying numbers of viral particles over a range of more than five orders of magnitude in concentration, down to a demonstrated single virus particle detection level.

By combining complementary analysis techniques with QCM, novel insights into the contact mechanics properties of films can be obtained. It has been shown that a change in the resonant frequency could be linearly related to the change in contact area between a hemispherical cap shaped gel and the crystal surface [201]. Utilizing this contact mechanics approach, elastic polymeric materials can be studied, as well as the effects of changes in solvent and energy dissipation properties of the materials [202]. Also, a novel combination of the QCM with the surface force apparatus has allowed the contact mechanics scenario to be augmented with measurements of the interfacial friction of systems driven by the lateral oscillations of the quartz crystal [203, 204].

Observing the QCM mass determination of polymer films of known hydration properties within a humidity chamber has allowed investigators to create an accurate microosmotic pressure device for determining the hydration level of biological tissue samples undergoing swelling [205]. The superiority of this device resulted from its use of quite small tissue samples (< 1 mg), its rapid equilibration time, and its ability to measure variable hydration levels and osmotic pressure behavior in different local regions of inhomogeneous tissue samples. Lastly, it is worth mentioning that a plug-in PC version of the QCM device makes the use of QCM, especially for field applications, even easier

since the operating power for the QCM device comes directly from the USB port of the PC acquiring the data [206].

Enabling Kinetic Determinations. Up to the present, with a few notable exceptions [65, 207], there has been little reporting of absolute reaction rates and rate constants for processes studied via QCM. This capability is now available in the RAPid device (Akubio), a multi-well QCM system utilizing flow-through cells for rapid changes of reagents. It is described in Chap. 13 in this volume. The device software allows for quantitative kinetic descriptions (k_1, k_{-1} and K), enabling mechanistic insights into all aspects of complex formation between immobilized and solution species [20]. The QCM-D device also has the software capability to obtain rate data for processes under study.

Living Cells as Information-Rich Sensing Elements. Living cells possess a complete set of evolved intelligent properties that make them ideal candidates for information-rich sensing components in biosensors [152]. It is for this reason that we have studied the adhesion and steady state properties of cells in the QCM device [50, 180, 181] and have demonstrated that the cell QCM biosensor can function as a novel biosensor for drug discovery applications [191–193]. We believe that the integrated systems level behavior of the macromolecular components present in living cells, representing targets for potential drugs, can function in biosensors to provide unique information. This information may not be available from tests carried out with the isolated macromolecular target in standard assays of the type routinely used in drug testing. Also, using the cell QCM biosensor we have described the unique temporal ability of cells to describe different phases of cancer cells' responses to the cancer chemotherapeutic drugs taxol and docetaxel [197]. These results suggest the potential of the QCM technique for use in examining the behavior of populations of individual cells released from cellular biopsies to aid the oncologist in a patient's diagnosis, as well as to aid the oncologist in prescribing chemotherapy regimens for treatment of a patient's tumor.

Applying Data Mining Techniques to Provide Accurate Analyses and Outputs from Complex Sensor Inputs. Data mining techniques include a variety of machine learning clustering and classification algorithms. When these are combined with high dimensional data visualization techniques, they allow the analyses of huge multidimensional datasets to discover trends and nonlinear relationships that humans unaided are unable to perceive. These data mining techniques have become necessary for the analysis of large biological, biomedical, and drug discovery related datasets. We have used data mining integrated with high-dimensional visualization techniques to carry out analyses of large datasets such as the nucleic acid microarray analyses of gene transcripts in cells [208] and the analysis of the cancer cell response effects of the large National Cancer Institute cancer compound library [209]. We and others [210] have demonstrated that important discoveries in such datasets can only occur through the use of data mining techniques.

We believe that data mining techniques will find utility in the future in determining accurate outputs from complex piezoelectric sensors yet to be developed. In the future, ever more complex biosensors and chemical sensors will be created on piezoelectric platforms. The accurate analyses of complex multidimensional inputs from such sensors may critically depend upon the use of machine learning algorithms. Such algorithms will "learn" to identify characteristic non-linear features of the inputs and associate them accurately with particular outputs (classification activity), such as an analyte concentration, that are then reported to the end-user.

Acknowledgements The author would like to acknowledge Prof. Susan Braunhut and Dr. T. Zhou for stimulating and productive collaborations, some published results of which were described in this review chapter. The author gratefully acknowledges funding support from a number of federal agencies including NIH Grant GM58583 and a DARPA Grant for a portion of the research described in this chapter. Funding is also acknowledged from the UML Chancellor's Fund and Research Foundation Seed grants, NSF NSEC Grant EEC-0425826. We acknowledge financial support from Aventis Pharmaceuticals for one project described herein.

References

1. Salt D (1978) Hy-Q handbook of quartz crystal devices. Van Nostrand Reinolds, UK
2. Kawai H (1969) Jpn J Appl Phys 8:975
3. Meyer G, Amer NM (1988) Appl Phys Lett 53:1045
4. Porter T, Eastman M, Pace D, Bradley M (2001) Sensor Actuator A 88:47
5. Datskos P, Oden P, Thundat T, Wachter E, Warmack R, Hunter S (1996) Appl Phys Lett 69:2968
6. Lange D, Hagleitner C, Herzog C, Brand O, Baltes H (2003) Sensor Actuator A 103:150
7. Adams JD, Parrott G, Bauer C, Sant T, Manning L, Jones M, Rogers B, McCorkle D, Ferrell TL (2003) Appl Phys Lett 83:3428
8. Okahata Y, Nikura K, Furusawa H, Matsuno H (2000) Anal Sci 16:1113
9. Uttenthaler E, Schraml M, Mandel J, Drost S (2001) Biosens Bioelectron 16:735
10. Kosslinger C, Uttenthaler S, Drost F, Aberl H, Wolf G, Brink A, Stanglmaier E, Sackmann E (1995) Sens Actuators B 107:24
11. Cooper MA, Whalen C (2005) Drug Disc Today: Technol 2:241
12. Marx KA (2003) Biomacromolecules 4:1099
13. Ghafouri S, Thompson M (2001) Analyst 126:2159
14. Van Noort D, Rani R, Mandenius C-F (2001) Mikrochim Acta 136:49
15. Steinem C, Janshoff A, Wegener J, Ulrich WP, Willenbrink W, Sieber M, Galla HJ (1997) Biosens Bioelectron 12:787
16. Wegener J, Janshoff A, Galla HJ (1998) Eur J Biophys 78:2821
17. Ward MD (1995) In: Rubenstein I (ed) Physical electrochemistry: principles, methods and applications. Dekker, New York, p 293
18. Pavey KD (2002) Expert Rev Mol Diag 2:173
19. Buck RP, Lindner E, Kutner W, Inzelt G (2004) Pure Appl Chem 76:1139
20. Godber B, Thompson KSJ, Rehak M, Uludag Y, Kelling S, Sleptsov A, Frogley M, Wiehler K, Whalen C, Cooper MA (2005) Clinical Chem 51:10

21. O'Sullivan CK, Guilbault GG (1999) Biosens Bioelectron 14, 663
22. Janshoff A, Galla HJ, Steinem C (2000) Angew Chem Int Ed 39:4004
23. Wegener J, Janshoff A, Steinem C (2001) Cell Biochem Biophys 34:121
24. Cavic BA, Hayward GI, Thompson M (1999) Analyst 124:1405
25. Rodahl M, Hook F, Krozer A, Brzenzinski P, Kasemo B (1995) Rev Sci Instrum 66:3924
26. Van Dyke KS (1925) Phys Rev 25:895
27. Reddy SM, Jones JP, Lewis TJ (1997) Faraday Disc 107:177
28. Johannsmann D (1999) Macromol Phys Chem 200:501
29. Si S, Zhou T, Liu D, Nie L,Yao S (1994) Anal Lett 27:2027
30. Muramatsu H, Tamiya E, Karube I (1988) Anal Chem 60:2142
31. Schroder J, Borngraber R, Lucklum R, Hauptmann P (2001) Rev Sci Instrum 72:2750
32. Rickert J, Weiss T, Krass W, Jung G, Gopel W (1996) Biosens Bioelectron 11:591
33. Sauerbrey GZ (1959) Z Phys 155:206
34. Rodahl M, Kasemo B (1996) Sensor Actuator B 37:111
35. Irwin EF, Ho JE, Kane SR, Healy KE (2005) Langmuir 21:5529
36. Munro JC, Frank CW (2004) Macromolecules 37:925
37. Voinova MV, Rodahl M, Jonson M, Kasemo B (1999) Physica Scripta 59:391
38. Keller CA, Glasmastar K, Zhdanov VP, Kasemo B (2000) Phys Rev Letters 84:5443
39. Rickert J, Weiss T, Gopel W (1996) Sensor Actuator B 31:45
40. Otto K, Elwing H, Hermannson M (1999) J Bacteriol 181:5210
41. Vikinge TP, Hansson KM, Sandstraon P, Liedberg B, Lindahl TL, Lundstrom I, Tengvall P, Hook F (2000) Biosens Bioelectron 15:605
42. Hook F, Kasemo B, Nylander T, Fant C, Sott K, Elwing H (2001) Anal Chem 73:5796
43. Reimhult E, Larsson C, Kasemo B, Hook F (2004) Anal Chem 67:7211
44. Plunkett MA, Wang ZH, Rutland MW, Johannsmann D (2003) Langmuir 19:6837
45. Lu C, Czanderna AW (1984) Applications of quartz crystal microbalances. Elsevier, Amsterdam
46. Buttry DA, Ward MD (1992) Chem Rev 92:1355
47. Schumacher R (1990) Angew Chem Int Ed Engl 29:329
48. Daikhin L, Gileadi E, Katz V, Tsionsky M, Urbakh D, Zagidulin D (2002) Anal Chem 74:554
49. Theisen LA, Martin SJ, Hillman AR (2004) Anal Chem 76:796
50. Marx KA, Zhou T, Warren M, Braunhut SJ (2003) Biotech Prog 19:987
51. Li J, Thielemann C, Reuning U, Johannsmann D (2005) Biosensor Bioelectron 20:1333
52. Hayward G (1992) Anal Chim Acta 264:23
53. Soares DM, Tenan MA, Wasle S (1998) Electrochim Acta 44:263
54. Muratsugu M, Ohta F, Miya Y, Hosokawa T, Kurosawa S, Kamo N, Ikeda H (1993) Anal Chem 65:2933
55. Caruso F, Furlong DN, Kingshott P (1997) J Colloid Interface Sci 186:129
56. Fawcett NC, Craven RD, Zhang P, Evans JA (1998) Anal Chem 70:2876
57. Angelopoulos AP, Marx KA, Oh KS (2002) Proceedings materials research society: polymer interfaces and thin films. Karim A, Russell TP, Frank CW, Nealey PF (eds) MRS, Pittsburgh 710:207
58. Hernandez JE, Ahn H, Whitten J (2001) Phys Chem B 105:8339
59. Marx KA, Lee JS, Sung C (2004) Biomacromolecules 5:1869
60. Kikkawa Y, Yamashita K, Hiraishi T, Kanesato M, Doi Y (2005) Biomacromolecules 6:2084
61. Yamashita K, Kikkawa Y, Kurokawa K, Doi Y (2005) Biomacromolecules 6:850

62. Gollas B, Bartlett PN, Denuault G (2000) Anal Chem 72:349
63. Jusys Z, Massong H, Baltruschat D (1999) J Electrochem Soc 146:1093
64. Cheran LE, McGovern ME, Thompson M (2000) Faraday Disc 16:23
65. Matsuno H, Niikura K, Okahata Y (2001) Eur J Chem 75:3305
66. Sarma R, Alva KS, Marx KA, Tripathy SK, Akkara JA, Kaplan DL (1996) Mater Sci Eng C 4:189
67. Marx KA, Zhou T, Sarma R (1999) Biotech Prog 15:522
68. Marx KA, Alva KS, Sarma R (2000) Mater Sci Eng C 11:155
69. Long DD, Marx KA, Zhou T (2001) J Electroanal Chem 501:107
70. Marx KA, Zhou T (2002) J Electroanal Chem 521:53
71. Marx KA, Zhou T, Long DD (2005) Biomacromolecules 6:1698
72. Kanazawa KK, Gordon G (1985) Anal Chim Acta 175:99
73. Smyrl WA, Butler MA (1993) Interface(ECS) 2:35
74. Jardy A, Lasalle-Molin AL, Keddam M, Takenouti H (1992) Electrochim Acta 37:2195
75. Freund MS, Brajter-Toth A, Ward MD (1990) J Electroanal Chem 289:127
76. Desilvestro J, Scheifele W, Hass O (1992) J Electrochem Soc 139:2727
77. Gileadi E, Tsionsky V (2000) J Electrochem Soc 147:567
78. Wilde CP, Zhang M (1993) J Chem Soc, Faraday Trans 89:385
79. Nomura T, Kanazawa T (1991) Anal Chim Acta 245:71
80. Kautek W, Sahre M, Soares M (1995) Ber Bunsenges Phys Chem 99:667
81. Niece BK, Gewirth AA (1997) Langmuir 13:6302
82. Wei C, Bose CSC, Rajeshwar K (1992) J Electroanal Chem 327:331
83. Kutner W (1992) Electrochim Acta 37:1109
84. Bohannan EW, Huang LY, Miller HF, Schumsky G, Switzer JA (1999) Langmuir 15:813
85. Nordyke LL, Buttry DA (1991) Langmuir 7:380
86. Wang J, Frostman LM, Ward MD (1992) J Phys Chem 96:5224
87. Borjas R, Buttry DA (1990) J Electroanal Chem 280:73
88. Pater E, Bruckenstein S, Hillman AR (1996) J Chem Soc, Faraday Trans 92:4087
89. Brukenstein S, Brzezinska K, Hillman AR (2000) Phys Chem 2:1221
90. Barbero C, Miras MC, Kotz R, Haas O (1993) Synth Methods 55–57:1539
91. Martinusz K, Czirok E, Inzelt G (1994) J Electroanal Chem 379:437
92. Stalgren JJR, Claesson PM, Warnheim T (2001) Adv Colloid Interface Sci 89–90:383
93. Njue CK, Rusling JF (2000) J Am Chem Soc 122:6459
94. Johnsson M, Bergstrand N, Edwards K, Stalgren JJR (2001) Langmuir 17:3902
95. Donohue JJ, Buttry DA (1989) Langmuir 5:671
96. DeLong HC Donohue JJ, Buttry DA (1991) Langmuir 7:2196
97. Shen D, Huang M, Chow LM, Yang M (2001) Sensor Actuator B 77:664
98. Satjapipat M, Sanedrin R, Zhou F (2001) Langmuir 17:7637
99. Tsuchida A, Matsuura K, Kobayshi K (2000) Macromol Chem Phys 201:2245
100. Muramatsu H, Kimura K (1992) Anal Chem 64:2502
101. Sharp JS, Forrest JA, Jones RAL (2001) Macromolecules 34:8752
102. Percival CJ, Stanley S, Galle M, Braithwaite A, Newton MI, McHale G, Hayes W (2001) Anal Chem 73:4225
103. Kobayashi T, Murawaki Y, Reddy PS, Abe M, Fujii N (2001) Anal Chim Acta 435:141
104. Kugiyama A, Yoneyama H, Takeuchi T (2000) Electroanalysis 12:1322
105. Hirayami K, Sakai Y, Kameoka K (2001) J Appl Polymer Sci 81:3378
106. Chianella I, Piletsky SA, Tothill IE, Chen B, Turner APF (2003) Biosens Bioelectron 18:119
107. Deore B, Chen Z, Nagaoka T (2000) Anal Chem 72:3989

108. Hasegawa T, Kazunori M, Katsuhiko A, Kazukiyo K (2000) Macromolecules 33:2772
109. Picart C, Lavalle P, Cuisinier FJ, Decher G, Schaaf P, Voegel JC (2001) Langmuir 17:7414
110. Wang Y, Wallace E, Walton A, Bathia G, Park M, Advincula R (2000) Polym Prep 41:1026
111. Baba A, Kaneko F, Advincula R (2000) Colloids Surf 173:39
112. Pingli H, Hu N, Zhou G (2002) Biomacromolecules 3:139
113. Wang J, Jiang M (2000) Langmuir 16:2269
114. Varineau PT, Buttry DA (1987) J Phys Chem 91:1292
115. Koh W, DuBois D, Kutner W, Jones MT, Kadish KM (1992) J Phys Chem 96:4163
116. Lapeunte R, Cases F, Garces P, Morallon E, Vazquesz JL (1998) J Electroanal Chem 451:163
117. Malfoy B, Reynaud JA (1980) J Electroanal Chem 114:213
118. Nakata S, Kido N, Hayashi M, Hara M, Sasabe H, Sugawara T, Matsuda T (1996) Biophys Chem 52:63
119. Sadik O, Cheung M (2001) Talanta 55:929
120. Hepel M (2001) J Electroanal Chem 509:90
121. Fukuoka S, Karube I (1994) Appl Biochem Biotech 49:1
122. Chang HC, Yang CC, Yeh TM (1997) Anal Chim Acta 340:49
123. Kastl K, Herrig A, Luthgens E, Janshoff A, Steinem C (2004) Langmuir 20:7246
124. Reimhult E, Hook F, Kasemo B (2003) Langmuir 19:1681
125. Liebau M, Hildebrand A, Neubert RHH (2001) Eur J Biophys 30:42
126. Mandal S, Sankar SK, Sastry M (2001) Nanotechnology 12:358
127. Tower RB, Fawcett NC, Zhang P, Evans JA (2001) Biosens Bioelectron 16:1
128. Furtado M, Thompson M (1998) Analyst 123:1937
129. Su H, Chong S, Thompson M (1996) Langmuir 12:2247
130. Hook F, Ray A, Norden B, Kasemo B (2001) Langmuir 17:8305
131. Su H, Williams P, Thompson M (1995) Anal Chem 67:1010
132. Wang Y, Farrell N, Burgess J (2001) J Am Chem Soc 123:1576
133. Pope L, Allen S, Davies M, Roberts C, Tendler S, Williams P (2001) Langmuir 17:8300
134. Ito K, Hashimoto K, Ishimori Y (1996) Anal Chim Acta 327:29
135. Furtado M, Su H, Thompson M, Mack DP, Hayward GL (1999) Anal Chem 71:1167
136. Matsuno H, Niikura K, Okahata Y (2001) Biochemistry 40:3615
137. Kumar A, Ramakrishnan V, Gonnade R, Ganesh KN, Sastry M (2002) Nanotechnology 13:597
138. Si SH, Zhou T, Liu D, Nie L, Yao S (1994) Anal Lett 27:2027
139. Andersson M, Sellborn A, Fant C, Gretzer C, Elwing H (2002) J Biomat Sci Polym Ed 13:907
140. Sellborn A, Andersson M, Fant C, Gretzer C, Elwing H (2002) Colloids Surf B Biointerfaces 27:295
141. Thompson M, Arthur GL, Dhaliwal GK (1986) Anal Chem 58:1206
142. Ghouechian HO, Kamo N, Hosokawa T (1994) Talanta 41:401
143. Vaughn RD, O'Sullivan CK, Giulbault GG (2001) Enzyme Microbial Tech 29:636
144. Sakti K, Hauptmann P, Zimmerman B, Buhling F, Ansorge S (2001) Sensor Actuator B 78:257
145. Aizawa H, Krosawa S, Tanak M, Wakeda S, Talib Z, Park JW, Yoshimoto M, Muratsugu M, Hillborn J, Mayake J, Tanaka H (2001) Mater Sci Eng C 17:127
146. Ebara Y, Okahata Y (1994) J Am Chem Soc 116:11209
147. Uzawa H, Kimiya S, Minoura N, Dohi H, Nishida Y, Taguchi K, Yokoyama S, Mori H, Shimizu T, Kobayashi K (2002) Biomacromolecules 3:411

148. Liu Y, Zhang W, Yu X, Zhang HW, Zhao R, Shangguan DH, Li Y, Shen BF, Liu GQ (2004) Sensor Actuators B 99:416
149. Liu Y, Yu X, Zhang HW, Zhao R, Shangguan DH, Bo ZY, Liu GQ (2003) Biosens Bioelectron 19:9
150. Berglin M, Delage L, Potin P, Vilter H, Elwing H (2005) Biomacromolecules 5:2376
151. Yan F, Sadik O (2001) Anal Chem 73:5272
152. Marx KA (2006) In: Knopf and Bassi (eds) Smart biosensor technology. Dekker, New York (in press)
153. Imai S, Mizuno H, Suzuki M, Takeuchi T, Tamiya E, Mashige F, Ohkubo A, Karube I (1994) Anal Chim Acta 292:65
154. Dultsev FN, Speight RE, Fiorini MT, Blackburn JM, Abell C, Ostanin VP, Klenerman D (2001) Anal Chem 73:3935
155. Cooper MA, Dultsev FN, Minson T, Ostanin VP, Abell C, Klenerman D (2001) Nature Biotechnol 19:833
156. Wang H, Zeng H, Liu ZM, Yang YH, Deng T, Shen GL, Yu RQ (2004) Anal Chem 76:2203
157. Reddy SM, Jones JP, Lewis TJ, Vadgama PM (1998) Anal Chim Acta 363:203
158. Patolsky F, Zayats M, Katz E, Willner I (1999) Anal Chem 71:3171
159. Alfonta L, Willner I, Throckmorton DJ, Singh AK (2001) Anal Chem 73:5287
160. Su H, Yang M, Kallury KMR, Thompson M (1993) Analyst 118:309
161. Lasalles N, Mailley P, Vieel E, Livache T, Roget A, Corriea JP, Abrantes LM (2001) J Electroanal Chem 509:48
162. Xie H, Yu Y, Xie F, Lao YZ, Gao Z (2004) Anal Chem 76:4023
163. Patolsky F, Lichtenstein A, Willner I (2000) J Am Chem Soc 122:418
164. Liu Y, Deng K, Liu S, Yao S (2004) Biophys Chem 112:60
165. Su XD, Robelek R, Wu YG, Wang GY, Knoll W (2004) Anal Chem 76:489
166. Magner E (1998) Analyst 123:1967
167. Kuhn LS (1998) The Electrochemical Society Interface Winter:26
168. Gamburzev S, Atanasov P, Ghindilis AL, Wilkins E, Kaisheva A, Iliev I (1997) Sensor Actuator B 43:70
169. Eddy S, Warriner K, Christie I, Ashworth D, Purkiss C, Vadgama P (1995) Biosens Bioelectron 10:831
170. Bartlett PN, Cooper JM (1992) J Electroanal Chem 362:1
171. Arnold FH (1998) Acct Chem Res 31:125
172. Waldo GS (2003) Curr Opinion Chem Biol 7:33
173. Colonna S, Gaggero N, Richelmi C, Pasta P (1999) TIBTECH 17:163
174. Ozaki S, Ortiz de Montellano PR (1995) J Am Chem Soc 117:7056
175. Marcus RA (1996) Electron transfer reactions in chemistry theory and experiment. In: Bendall DS (ed) Protein electron transfer. BOIS Scientific, Oxford UK, Chap. 10
176. Lin J, Balabin JA, Beratan DN (2005) Science 310:1311
177. Calvo EJ, Etcheniqu R, Pietrasanta L, Danilowicz C, Wolociuk A (2001) Anal Chem 73:1161
178. Rosso F, Giordano A, Barbarisi M, Barbarisi A (2004) J Cell Physiol 199:174
179. Marx KA, Zhou T, McIntosh D, Braunhut SJ (2004) In: Proceedings MRS: architecture and applications of biomaterials and biomolecular materials. vol EXS-1 Materials Research Society Pittsburgh PA, p 169
180. Marx KA, Zhou T, Montrone A, McIntosh D, Braunhut SJ (2005) Anal Biochem 343:23
181. Zhou T, Marx KA, Warren M, Schulz H, Braunhut SJ (2000) Biotech Prog 16:268
182. Fredriksson C, Kihlman S, Rodahl M, Kasemo B (1998) Langmuir 14:248

183. Redepenning J, Schlesinger TK, Mechalke EJ, Puleo DA, Bizios R (1993) Anal Chem 65:3378
184. Gryte DM, Ward MD, Hu WS (1993) Biotech Progress 9:105
185. Nivens DE, Chambers JQ, Anderson TR, White DC (1993) Anal Chem 65:65
186. Muratsugu M, Romanschin AD, Thompson M (1997) Anal Chim Acta 342:23
187. Wegener J, Janshoff A, Galla HJ (1998) Eur Biophys J 28:26
188. Fredriksson C, Kihlman S, Rodahl M, Kasemo B (1998) J Mater Sci Materials Medicine 9:785
189. Cans AS, Hook F, Shupliakov O, Ewing AG, Eriksson PS, Brodin L, Orwar O (2002) Anal Chem 73:5805
190. Wegener J, Seebach J, Janshoff A, Galla HJ (2000) Biophysical J 78:2821
191. Zhou T, Braunhut SJ, Medeiros D, Marx KA (1999) In: Mater Res Soc Symp: biomedical materials: drug delivery, implants and tissue engineering. Materials Research Society Pittsburgh PA 550:177
192. Marx KA, Zhou T, Schulze H, Montrone A, Braunhut SJ (2001) Biosens Bioelectron 16:773
193. Marx KA, Zhou T, Montrone A, Braunhut SJ (2002) In: Moss SC (ed) Materials research society symposium: advanced biomaterials-characterization, tissue engineering and complexity. Materials Research Society Pittsburgh PA 711:125
194. Marxer CG, Coen MC, Greber T, Greber UF, Schlapbach L (2003) Anal Bioanal Chem 377:578
195. Jenkins MS Wong KCY, Chhit O, Bertram J, Young R, Subaschandar N (2004) Biotech Bioeng 88:392
196. Drukman S, Kavallaris M (2002) Int J Oncol 21:621
197. Braunhut SJ, McIntosh D, Vorotnikova E, Zhou T, Marx KA (2005) Assay Drug Devel 3:77
198. www.q-sense.com
199. www.masscal.com
200. Smith AL, Shirazi HM, Mulligan SP (2002) Biochim Biophys Acta 1594:150
201. Flanigan CM, Desai M, Shull KR (2000) Langmuir 16:9825
202. Nunalee FN, Shull KR (2004) Langmuir 20:7083
203. Berg S, Johannsmann D, Ruths M (2002) J Appl Phys 92:6905
204. Berg S, Ruths M, Johannsmann D (2002) Phys Rev E 65:026119
205. Horkay F, Horkayne-Szakaly I, Basser PJ (2005) Biomacromolecules 6:988
206. www.bioage-srl.com
207. Luthgens E, Janshoff A (2005) Chem Phys Chem 6:444
208. McCarthy JF, Marx KA, Hoffman PE, Gee AG, O'Neil P, Ujwal ML, Hotchkiss J (2004) In: Umar A, Kapetanovic I, Khan J (eds) The application of bioinformatics in cancer detection. Ann NY Acad Sci 1020:239
209. Marx KA, O'Neil P, Hoffman P, Ujwal ML (2003) J Chem Inform Comput Sci 43:1652
210. Petricoin EF, Liotta LA (2004) Curr Opin Biotechnol 15:24

Springer Ser Chem Sens Biosens (2007) 5: 425–447
DOI 10.1007/5346_034

Published online: 22 July 2006

The QCM-D Technique for Probing Biomacromolecular Recognition Reactions

Fredrik Höök[1] (✉) · Bengt Kasemo[2]

[1]Div. of Solid State Physics, Lund University, 22100 Lund, Sweden
fredrik.hook@ftf.lth.se

[2]Dept. of Applied Physics, Chalmers University of Technology, 41296 Göteborg, Sweden

Abstract In recent years there has been an exponential growth in scientific reports in which the quartz crystal microbalance (QCM) technique plays a key role in elucidating various aspects of biomacromolecular recognition reactions. In this short overview, the key steps in the development of a special variant of the QCM technique, generally named quartz crystal microbalance with dissipation monitoring (QCM-D), are summarized. The key feature of the QCM-D technique, in comparison with the traditional variant, is that, in addition to changes in resonance frequency, f, it also provides simultaneous measurements of changes in energy dissipation, D, induced upon interfacial reactions. Although these two parameters can be measured in various ways, focus is herein put on a means to obtain temporal variations in f and D by probing the decay of the crystal's oscillation after a rapid excitation close to the resonance frequency. By highlighting studies focusing on (i) DNA immobilization and subsequent hybridization, (ii) supported cell membrane mimics, and (iii) more complex situations, such as systems displaying film resonance behavior, we highlight both technical and theoretical aspects that have been essential for the increasing popularity of the QCM-D technique. Hence, far from all existing literature will be covered, and this contribution should therefore be read as a brief overview, rather than a comprehensive review, focusing on key components responsible for the high potential of the QCM-D technique to contribute to biointerface science in general, and the fields of research devoted to primarily biomacromolecular interactions in particular.

Keywords Biorecognition · Biosensor · Energy dissipation · QCM · Viscoelasticity

1 A Brief QCM History

In 1959, Prof. Günter Sauerbrey at Physikalisch-Technische Bundesanstalt, Berlin, Germany [1] demonstrated that upon adding mass to a QCM sensor surface there is a frequency decrease, which is proportional to the added mass, provided that the mass is (i) small compared to the weight of the crystal, (ii) rigidly adsorbed, and (iii) evenly distributed over the active area of the crystal. The linear relation between changes in frequency, Δf, and adsorbed mass, Δm, is therefore often refereed to as the Sauerbrey relation:

$$\Delta m = \frac{C}{n}\Delta f\,, \tag{1}$$

where $C = t_q \rho_q / f_0$ ($\approx -17.7\,\mathrm{ng\,Hz^{-1}\,cm^{-2}}$ for a 5 MHz crystal) and n (= 1, 3, ...) is the overtone number. Of note, the sensitivity factor C varies as the square of the frequency ($t_q \propto 1/f_0$); a 10 MHz crystal has a sensitivity of ($\approx -4.5\,\mathrm{ng\,Hz^{-1}\,cm^{-2}}$). This sensing principle, schematically summarized in Fig. 1, was originally utilized almost exclusively for gas-phase and vacuum applications, the most common use being as a film thickness monitor during film depositions in vacuum systems. Other recent applications were for measuring dry etching rates, oxidation rates of metals, and various gas adsorption and sorption phenomena (see e.g. [2] and references therein). These applications are all built on the fact that the technique has much below monolayer sensitivity for gas adsorption and desorption phenomena, when temperature and other perturbations such as mechanical vibrations, stress, or temperature gradients etc. are controlled. The vacuum environment is ideal from that perspective.

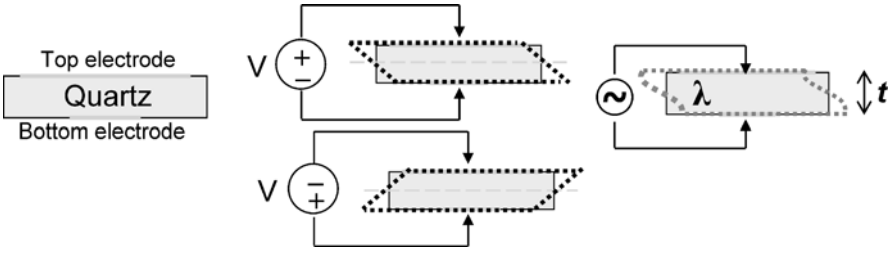

Fig. 1 The QCM principle. An applied voltage over an (AT-cut) quartz crystal induces a shear strain in the quartz. The direction of the strain depends on the polarity of the applied field, which means that a mechanical resonance can be excited if the frequency of the applied voltage generates a standing wave with antinodes at the crystal's interfaces

The work in 1980 by Nomura and coworkers at Shinshu University, Nagano, Japan, demonstrating that the QCM could also be used for liquid-phase applications [3], paved the way for numerous new applications in the liquid phase and especially in electrochemistry and biotechnology; in the latter case primarily for various biosensor applications, as recently reviewed by Janshoff et al. [4]. It was soon realized, however, that in many of these studies, the adsorbed/deposited films do not fulfill the assumptions underlying the Sauerbrey relation. In particular, the combined effect of hydration water and/or water trapped between adsorbed species, and the non-rigid character of many polymers/biomolecules, induces frictional (viscous) losses in the deposited sample film, and thus a damping of the crystal's oscillation. When the damping in the deposited film becomes sufficiently large, the simple linear relation between Δf and Δm is no longer valid. This leads to two new requirements to maintain the technique as a useful sensor technique, namely (i) technical solutions that provide information not only about changes in resonance frequency, but also changes in energy dissipation, D, of the oscillating system, and (ii) suitable theories to make full use of this new information.

1.1 Utilization of the Full Potential of the QCM Technique

Information about changes in D can be obtained via either impedance spectroscopy [4], or alternatively, as done in previous work by our group, by recording the oscillation decay of the freely oscillating crystal after rapid excitation at resonance [5]. In the former case, the damping of the crystal, which is the inverse of the Q-factor, is obtained by measuring the width of the resonance peak; the larger the damping the broader is the resonance peak. The alternative way, described below, is to measure the decay of the oscillation amplitude for the freely oscillating sensor crystal. In this case, the decay time constant is instead inversely proportional to the resonance width and thus the damping of the crystal. However, these two parameters (f and D) alone are not sufficient to translate the measured response into a physical representation of the probed systems, such as thickness, density, viscosity, and elasticity. A pioneering step in that direction was taken in the mid-1990s by Johansmann (now at Clausthal University of Technology) demonstrating a theoretical description capable of representing the QCM-D response for viscoelastic films probed in either air or liquids (see Chap. 2 in this volume and [6]). In parallel work, we [7] and others [8] utilized the multiparameter information contained in f and D measurements with analogous viscoelastic representations, capable of providing information about not only coupled mass, but also about changes in the viscoelastic components of adsorbed films (Sect. 2 for illustrative examples).

1.1.1 Technical Solution for Combined *f* and *D* Measurements

In this section, we describe briefly our solution for obtaining simultaneous measurements of f and D at multiple harmonics, and with good time resolution, as schematically illustrated in Fig. 2.

The principle of the measurement is to periodically switch on and off the driving power to the sensor and to record the output voltage from the freely decaying oscillator. To a very good approximation, the amplitude of oscillation decays exponentially in time, while the driver circuit is disconnected. The decay of the QCM oscillation is recorded on a digitizing oscilloscope using a low- or high-resistance probe, which ensures that the crystal decays close to its series or parallel mode, respectively [9]. The decaying voltage output from the crystal, which has a frequency given by the resonance frequency (f_0) of the crystal (in our system most often ~ 5 MHz), is mixed prior to reading with a constant reference frequency (f_r) (which is about 100 kHz lower than f_0) and filtered in a low-pass filter with a cut off frequency of ~ 500 kHz. The output signal is thus the difference frequency, f, between f_r and the QCM oscillator (sensor) frequency, f_0, i.e., in the order of 100 kHz. The recorded signal, $A(t)$, is then transferred to a computer, where a numerical fit to an exponentially damped sinusoidal is performed:

$$A(t) = A_0 \, e^{t/\tau} \sin(2\pi f t + \alpha) \,, \tag{2}$$

where $f (= f_0 - f_r)$ is obtained directly and D via the relation:

$$D = \frac{1}{\pi f \tau} \,. \tag{3}$$

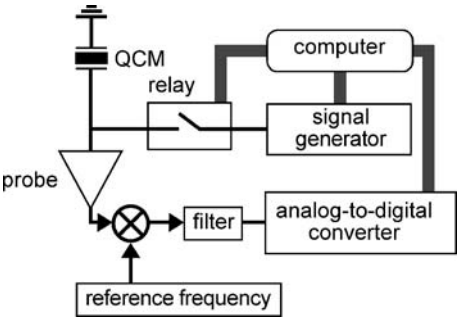

Fig. 2 QCM-D measurements. The key components are (i) the sensor crystal (*QCM*) mounted in a measurement chamber with facilities for batch or flow mode measurements in liquid or gas, (ii) the drive electronics (relay and signal generator) and (iii) the recording electronics (probe, reference frequency, filter) including data-handling and software (analog-to-digital converter and computer)

The energy dissipation is a dimensionless quantity defined as:

$$D = \frac{1}{Q} = \frac{E_{\text{dissipated}}}{2\pi E_{\text{stored}}}, \tag{4}$$

where Q is the quality factor, E_{stored} is the energy stored in the oscillating system and $E_{\text{dissipated}}$ is the energy dissipated during one period of oscillation. A graphic representation of combined f and D measurements is shown in Fig. 3.

In this way simultaneous measurements of both f and D are performed with a repetition rate of typically 1 Hz. Alternatively, the measurements can be alternated between different harmonics of the crystal (n = 1, 3, ...), thus allowing measurements of the frequency dependence of the QCM response. These are valuable in order to compare the experimental observations with theoretical representations (Sect. 1.1.3). The resolution in f and D (as defined above) in liquid environment is typically $< \pm 0.1$ Hz and $< 1 \times 10^{-7}$, respectively, while in vacuum or air it is at least a factor of ~ 10 better. As a comparison, the shifts in f and D, for a typical protein, vesicle or cell adsorption measurement is 10–100 Hz and $0.5–10 \times 10^{-6}$, respectively, and generally one order of magnitude larger for thick (> 100 nm) and soft polymer films (Sect. 2). Consequently, sensitivity has not been the limiting factor in most applications so far, although this does not mean that sensitivity might not be an issue in future applications aiming at, for example, drug-receptor interactions, when one of the interacting components is orders of magnitude smaller than the other.

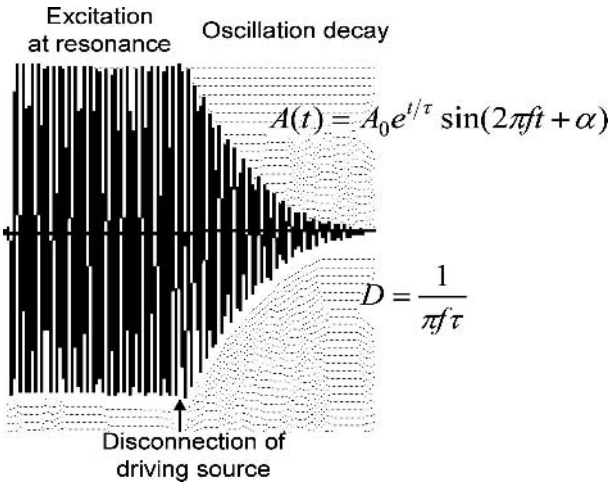

Fig. 3 Rapid excitation of a QCM near resonance, followed by an exponentially damped sinusodial wave after rapid disconnection of the excitation frequency

Furthermore, the measurement chambers for liquid phase measurements must be constructed with special attention primarily to temperature stability and mechanical stress induced on the crystal when mounted. Thereby temperature- and pressure-induced transients in f and D can be avoided when, e.g., one liquid is replaced with another. In order to obtain reliable data in conducting salt solutions it is important to pay attention also to capacitive leakage over the crystal. This is taken care of by measuring in the series mode (see above) and/or by having the side of the crystal facing the liquid completely covered with the electrode material [10].

The original setup and measurement chamber briefly described above has later been improved in a number of ways in a commercial instrument (Q-Sense, Göteborg, Sweden) that is now also used in most of our measurements.

1.1.2 Operation of the QCM-D Technique at Elevated Amplitudes

An often raised, but rarely addressed, question with respect to applications of the QCM technique is whether the shear oscillation of the sensor surface influences the adsorption kinetics or binding events being studied. Motivated by this uncertainty, as well as by the possibility of using elevated amplitudes to influence and steer specific biomolecular interactions, as pioneered by Klenerman, at Cambridge University [11], we have in our group further developed the QCM-D technique to operate in dual-frequency mode. In this mode of operation, one harmonic ($n = n_1$) can be utilized for continuous excitation of the QCM-D sensor at resonance at variable driving amplitudes, while a second harmonic ($n \neq n_1$) can be used for combined f and D measurements. By using two harmonics, one acting as a "probe" of surface-binding reactions and the other as an "actuator", elevated oscillation amplitudes can be used to perturb – or activate – binding events in a controlled way, while simultaneously probing the adsorption and/or desorption events in a non-perturbative manner via combined f and D measurements.

It is also worthwhile to note that the technical solution, enabling this mode of operation, is only a minor modification of the original setup, as illustrated in Fig. 4. In brief, to perform combined f and D probe measurements, while simultaneously varying the oscillation amplitude of the crystal in the actuator mode, it is sufficient to add a second signal generator to the original QCM-D setup plus a suitable high- or low-pass filter. In this configuration, one signal generator (#1) is used to excite crystal oscillation at one harmonic, thus providing combined f and D measurements (Fig. 2), while the second signal generator (#2) is operated in continuous mode at either a higher or a lower harmonic. To prevent the second signal generator from interfering with the measured decay signal, a suitable high- or low-pass filter is added between the crystal and the probe. Results obtained from this mode of operation are

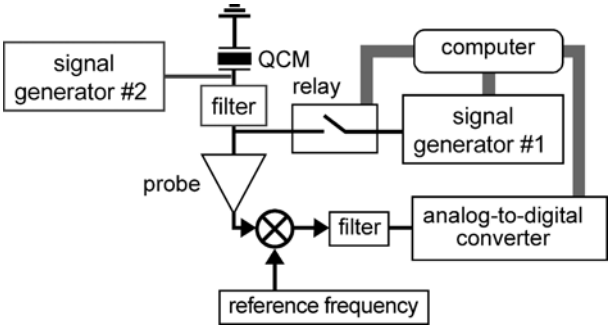

Fig. 4 QCM-D measurements at dual frequencies, with one acting as probe and one as actuator

shown for proteins, lipid vesicles, and colloidal particles in [12]. The most important conclusion from that work is that in most cases there is no detectable influence of the crystal oscillation on interfacial events being studied, at the driving voltages used in typical QCM measurements. Another relevant result from that study is that, at elevated oscillation amplitudes, particles with a diameter of some tens of nanometers become influenced. Current work by us and others will tell in the coming years what potential this approach has for the QCM-D technique to simultaneously influence and follow binding events, and is not further discussed in this overview.

1.1.3 Theoretical Modeling of the QCM-D Response

In probing biomolecular interactions, the information contained in combined f and D measurements is more or less critically dependent on the analyzed system. In most antigen–antibody applications, for example, both the sensing template and the captured molecules are often relatively small and rigid proteins. In such situations, the probed films become quite rigid (low D), and the linear relation between the change in frequency and coupled mass (Eq. 1) is a safe assumption. However, one must be aware that also in the case of small and rigid proteins, water will be hydrodynamically trapped within the film. This means, in turn, that an estimation of the coupled mass in terms of number of interacting molecules requires appropriate means to calibrate the system. Although this must not violate the validity of relative comparisons between different systems analyzed with QCM alone, important information is certainly achieved by operating the QCM technique in parallel with complementary techniques, such as (i) optical techniques like ellipsometry [6, 13, 14], optical waveguide laser spectroscopy [15] or surface plasmon resonance [16, 17], (ii) scanning probe microscopy [18–21], or (iii) techniques engaging external molecular labels such as radio labeling [22], the

latter being, to the best of our knowledge, the first study demonstrating the discrepancy in mass uptake obtained using the Sauerbrey relation and the correct mass for systems probed in a liquid environment.

As the structural flexibility and size of the analyzed systems increase, as is the case for DNA, lipid-based assemblies, hydrogels, bacteria, living cells etc., information from multiple techniques as well as from combined f and D measurements, becomes increasingly important. First, the information provided from f and D measurements, when combined with appropriate theoretical modeling, gives a means to correct for the failure of the linear relation between changes in f and coupled mass. Second, information about changes in energy dissipation is a requirement in order to quantify and separate the viscoelastic components (shear viscosity and elasticity) of the probed films using the theoretical representations available.

In the model most often used to represent QCM-D measurements of viscoelastic films, probed in either gas or liquid environments, the films are represented by a Voigt element, characterized by a complex shear modulus:

$$G = G' + iG'' = \mu_f + i2\pi f \eta_f = \mu_f(1 + i2\pi f \tau)\,, \tag{5}$$

where μ_f is the elastic shear (storage) modulus, η_f is the shear viscosity (loss modulus) and $\tau (= \eta_f/\mu_f)$ is the characteristic relaxation time. The film is further represented by a uniform thickness, δ_f, a density, ρ_f, (referred to as effective hydrodynamic thickness and density, respectively). The film is positioned between the QCM electrode on one side and either gas or a semi-infinite Newtonian liquid on the other side, under no-slip conditions (i.e., the film is assumed not to slip at the film–electrode interface). In this case the change in the resonant frequency, Δf, and the dissipation factor, ΔD is:

$$\Delta f = \frac{\mathrm{Im}(\beta)}{2\pi t_q \rho_q} \tag{6}$$

and

$$\Delta D = -\frac{\mathrm{Re}(\beta)}{\pi f t_q \rho_q} \tag{7}$$

where

$$\beta = \xi_1 \frac{2\pi f \eta_f - i\mu_f}{2\pi f} \frac{1 - \alpha \exp(2\xi_1 \delta_f)}{1 + \alpha \exp(2\xi_1 \delta_f)} \qquad \alpha = \frac{\frac{\xi_1}{\xi_2}\frac{2\pi f \eta_f - i\mu_f}{2\pi f \eta_l} + 1}{\frac{\xi_1}{\xi_2}\frac{2\pi f \eta_f - i\mu_f}{2\pi f \eta_l} - 1}$$

$$\xi_1 = \sqrt{-\frac{(2\pi f)^2 \rho_f}{\mu_f + i2\pi\eta_f}} \qquad \xi_2 = \sqrt{i\frac{2\pi f \rho_l}{\eta_l}}$$

and where δ_f is the film thickness; ρ_f and ρ_l the density of the film and the bulk liquid, respectively; η_f and η_l the viscosity of the layer and the bulk li-

quid, respectively; and μ_f is the elastic modulus of the film. For an aqueous environment, ρ_l and η_l are $\sim 1.0\,kg\,m^{-3}$ and $1.0\,Ns\,m^2$, respectively.

In this section we will illustrate the model by theoretically comparing the situations when a viscoelastic film is sensed in a gaseous or liquid environment. Figure 5 shows the predicted changes in f and D (for a 5 MHz crystal) versus film thickness for a typical viscoelastic film with $\rho_f = 1.0 \times 10^3\,kg\,m^{-3}$, $\eta_f = 1.0 \times 10^{-3}\,Ns\,m^{-2}$ and $\mu_f = 1.0 \times 10^5\,N\,m^{-2}$, probed in air and water. Also displayed in this plot is the predicted change in f according to the Sauerbrey relation (Eq. 1) versus thickness for a rigid film with the same density.

At not too high a film thickness ($< \sim 200$ nm) in air (Fig. 5a), it is seen that direct conversion, via the Sauerbrey relation, of the induced change in f by this type of film would be reliable. For thicknesses 200–500 nm it would lead to a slight overestimation of the thickness (or mass). Although not obvious from this plot, the magnitude of this deviation depends critically on the viscoelastic properties and thickness of the film, as previously carefully treated by Lucklum et al. [23].

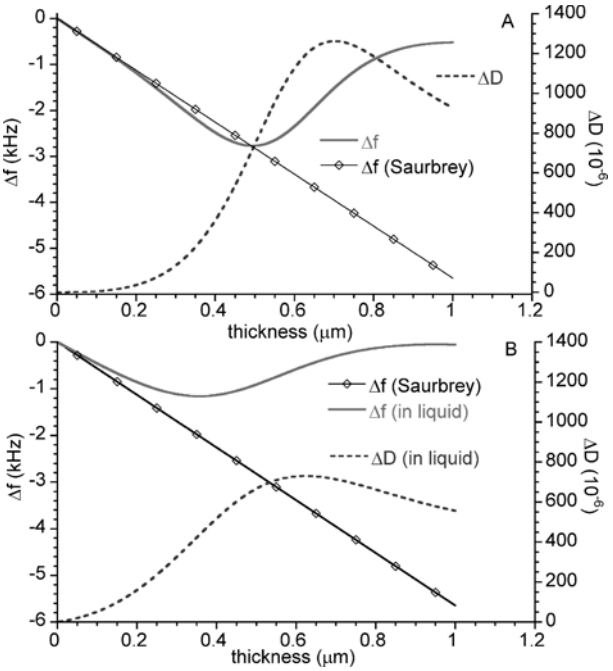

Fig. 5 Changes in f (*solid line*) and D (*dashed line*) at $n = 1$ for a 5 MHz crystal in contact with a viscoelastic film characterized by a homogeneous thickness, viscosity, and elasticity of $1\,g\,cm^{-3}$, 30 mPa s, and 1 MPa, respectively, and a thickness varying between 0 and 1 μm. In **a**, the medium is air. In **b**, the medium is water. Also shown is the frequency shift according to the Sauerbrey equation (Eq. 1) for the same film (*open diamonds*)

Turning now to the situation when a viscoelastic film is contacted between the crystal and a bulk liquid, we see in Fig. 5b the predicted changes in f and D (for a 5 MHz crystal) versus film thickness, according to the model for the same film as described above, but now contacted (under no-slip conditions) between the sensor surface and an aqueous environment. Note that in this case, direct use of the Sauerbrey relation would be reliable only up to a few tens of nanometers and then lead to an *underestimation* of the deposited mass, for all thicknesses (Sect. 2.1). In fact, and in contrast to the situation described above with air, direct use of the Sauerbrey relation on thin ($< \sim 100$ nm) viscoelastic films probed in an aqueous environment generally leads to an underestimation of the coupled mass. This behavior can be qualitative understood as follows: When the oscillatory motion of the crystal penetrates through the viscoelastic layer and then couples to the liquid phase, the superimposed contributions to the total frequency shift from the coupling between the crystal and the solution (which for a bare 5 MHz crystal in an aqueous solution is typically – 793 Hz), becomes reduced when the adsorbed film is strongly dissipative. This, in turn, (over)compensates any increased mass-load due to the film itself. For thicker films, this effect is reduced, and, as a consequence, the situation starts to resemble that of a viscoelastic film probed in gaseous environment (see above). Also note that in Fig. 5b, the induced energy dissipation for small thicknesses ($< \sim 500$ nm) is significantly larger than for the same film probed in air.

It is also worthwhile to point out that when the thickness is increased further, film resonance is induced, reflected as a change in sign of ΔD and Δf versus thickness. Note, in particular, that a situation is possible where a film induces essentially no change in frequency but there is still a significant induced damping (see below).

2 QCM-D Technique for Biorecognition Studies

Besides the potential of the QCM-D technique to provide unique information about the viscoelastic properties of analyzed systems, one of the major benefits is its compatibility with essentially any type of substrate material. In principle all materials that can be either evaporated or deposited by other means (spin coating, electrodeposition, spray coating etc.) as sufficiently thin (typically 1 nm to 10 μm) films are compatible with QCM analysis. This has, in turn, allowed detailed studies of biorecognition reactions extending far beyond those relying on thiol–gold chemistry, for which the surface plasmon resonance (SPR) technique is ideally suited. This statement, as well as the reasoning concerning structural information contained in combined f and D measurements, will be illustrated in the following sections by highlighting

a number of frequently cited studies that illustrate the potential of the QCM technique.

2.1 Analysis of Biospecific Interactions

The development of affinity sensors for studies of biospecific interactions has in the past decades attracted substantial attention in connection with research efforts directed at gene analysis, the detection of genetic disorders, antibody-based diagnostics, tissue matching, drug development etc. Early steps in this direction were taken in the mid-1990s by Okahata and coworkers (see Chap. 10 in this volume) at Tokyo Institute of Technology, Japan, who used the QCM technique to probe DNA immobilization and sequence-specific DNA hybridization [24], later extended by the same group to, for example, studies of template-directed DNA synthesis [25]. The prime merit of the QCM technique to probe DNA templates originates essentially from the fact that properly oriented DNA on a planar interface adopts a structure capable of coupling a substantial amount of water [26]. In fact, up to 90% of the measured mass originates in these situations from coupled water, which in turn makes the technique more sensitive than refractive-index based optical techniques measuring a response merely proportional to the molecular weight of biomacromolecules. In addition, since both the amount of coupled water and the viscoelastic properties vary if the structure of immobilized DNA changes, combined f and D measurements have proven valuable for the determination of, for example, the optimal conditions for DNA hybridization reactions [16, 27] and structural changes induced upon binding of small drug molecules [28]. Hence, surface-immobilized DNA constitutes a very instructive example illustrating the added value of the theoretical modeling introduced in Sect. 1.1.3, including the further added value of parallel analysis using complementary methods.

2.1.1 QCM-D for Studies of DNA

In this section, we describe how combined QCM-D and optical (e.g., SPR, ellipsometry etc.) analysis can be used to determine (i) the water content, and hence the effective density, (ii) changes in effective thickness, δ_f, and (iii) the viscoelastic components: shear viscosity, η_f, and shear elasticity, μ_f, of thin adsorbed films, composed of biomolecules. Also highlighted in this section is the observation that, besides providing information about the viscoelastic components, this type of analysis also helps to correct for shortcomings of the Sauerbrey relation (Eq. 1) for systems inducing high damping (D). These issues are illustrated in this overview using a single

model system: hybridization of fully complementary DNA to immobilized single stranded biotin-modified probe DNA (b-DNA). However, it is emphasized that this approach and the general conclusions are applicable for essentially all systems compatible with both QCM and optical techniques (see below).

The formation of the DNA sensor template is schematically illustrated in Fig. 6, also displaying a typical QCM-D measurements (Δf and ΔD at two harmonics ($n = 3$ and $n = 7$) versus time) upon exposure of a SiO_2 surface to (i) a biotin-doped lipid vesicle solution followed by subsequent addition of (ii) streptavidin, (iii) biotin-modified 15-mer single stranded DNA, and finally (iv) hybridization with fully complementary DNA. (QCM-D for studies of supported lipid bilayer formation is presented in Sect. 2.2.1.)

To treat this situation using the Voigt model, it is important to note that the model contains four unknown parameters (thickness, density, shear viscosity, and shear elasticity). This means that measurements providing at least four parameters, and each delivering new information about the desired quantities, are required in order to get an over-determined system. With the

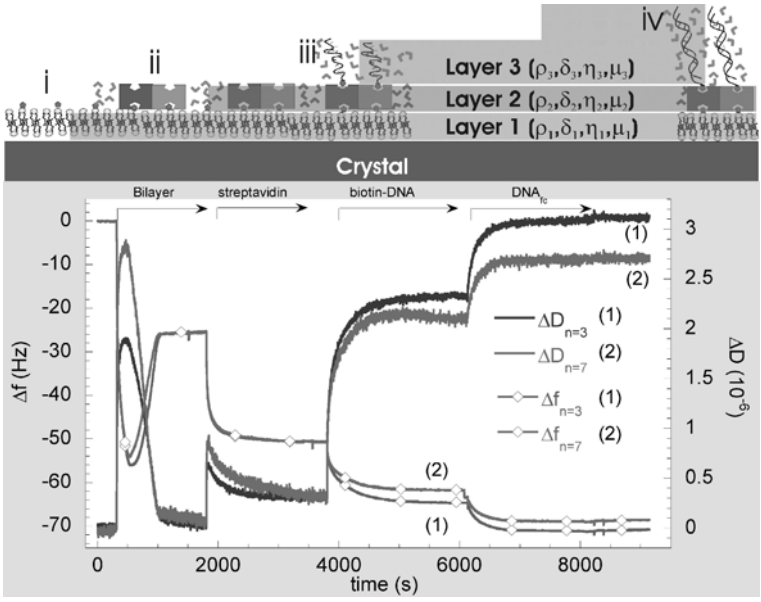

Fig. 6 Changes in f and D measured at two harmonics ($n = 3$ and $n = 7$) of a SiO_2-modified 5 MHz QCM crystal upon subsequent additions of biotin-containing lipid vesicles (*i*), streptavidin (*ii*), biotin-modified single stranded 15-mer DNA (*iii*), and fully complementary single stranded DNA (*iv*). Also shown *at the top* is a schematic representation of the sensing template, illustrating the Voigt-based representation used in the analysis of the data. Note that the DNA film was treated as one layer that undergoes a structural change during hybridization

reasonable assumption that the viscoelastic components for this case do not possess a strong frequency dependence in the MHz region, one can meet the set requirements by measuring at multiple (at least two) harmonics, hence providing (at least) four independent experimental parameters (two f values and two D values). Using appropriate fitting algorithms, it was possible to provide a unique theoretical representation of the three layers, as summarized in Table 1 together with SPR data on the same system [16]:

Note in particular that although the thickness, $d_{\text{effective}}$, is listed in Table 1, the Voigt model alone is not capable of making a unique determination of *both* the effective density, $\rho_{\text{effective}}$, and $d_{\text{effective}}$. In fact, to provide a unique fit, the density must be known or guessed, which in the case of biomolecules probed in an aqueous environment corresponds to an uncertainty varying between $\sim 1.0\,\text{g cm}^{-3}$ (= water) and $\sim 1.5\,\text{g cm}^{-3}$. Although the density can generally be estimated to better than 20%, this leads inevitably to some uncertainty in the provided parameters. It appears, however, that independent of the value of the effective density, the product of the density and the thickness (the coupled mass) remains the same, i.e., the coupled mass is conserved in the model. This means, in turn, that the coupled mass, Δm_{QCM}, can always be accurately determined and compared with that provided using Eq. 1, as listed in *italics* in Table 1, irrespective of the inbuilt uncertainty about the correct value of the effective density. In this particular case, the Voigt model provides essentially the same mass as that obtained using Eq. 1 for the layers that induce low damping (i.e., the supported lipid bilayer and streptavidin) while in the case of DNA, which induces high damping, the mass is significantly underestimated by Eq. 1. This nicely illustrates the importance of theoretical analysis of the QCM response in order to arrive at a correct mass uptake in situations when high damping is present. Furthermore, knowing the acoustic mass, the amount of hydrodynamically coupled water sensed by QCM can

Table 1 Analysis of the SPR and QCM-D responses in Fig. 6

Immobilization step	Δm_{SPR} (ng cm^{-2})	Δm_{QCM} (ng cm^{-2})	η_{f} (mPa s)	μ_{f} (MPA)	$d_{\text{effective}}$ (nm)
Supported lipid bilayer	320	442 *442*	> 20	> 1	4.1
Streptavidin	200	447 *442*	82	0.28	3.4
Biotin–DNA	23	329 *245*	1.8	0.19	3.1
DNA–duplex	36	477 *354*	2.0	0.19	4.5

The numbers in *italics* refer to the Sauerbrey mass

be obtained by comparing the QCM mass uptake by that obtained through a parallel analysis based on measurements of changes in interfacial refractive index using ellipsometry or SPR, for example. In essence, the mass of coupled water equals $\Delta m_{QCM} - \Delta m_{SPR}$ since, to a good approximation, a change in refractive index, which can be used to estimate Δm_{SPR}, is proportional to the number and molecular weight of the adsorbed biomacromolecules. From the comparison between the mass uptake using QCM and SPR listed in Table 1, two major conclusions can be drawn: (i) the amount of hydrodynamically coupled water correlates with increased damping and (ii) the effective film density can now be estimated with high accuracy:

$$\frac{\Delta m_{QCM}}{\rho_{effective}} = \frac{\Delta m_{SPR}}{\rho_{biomolecule}} + \frac{\Delta m_{QCM} - \Delta m_{SPR}}{\rho_{water}} . \tag{8}$$

With the effective density estimated, the Voigt modeling can now be repeated, but in this case providing a much more accurate determination of both the effective thickness:

$$d_{effective} = \frac{\Delta m_{QCM}}{\rho_{effective}} \tag{9}$$

and the viscoelastic components (Table 1). Note, in particular, that in the case of DNA, which couples a large amount of water, the shear viscosity is much closer to that of water (~ 1.0 mPa s) than in the case for the stiffer films. In fact, we arrive in this analysis at values which are very close to those obtained for a DNA system using shear-mode operated surface force apparatus, which operates at a frequency several orders of magnitude lower [29]. This indicates that the assumption of a weak frequency dependence of the viscoelastic components is reasonable, as also verified in QCM-D studies utilizing up to seven harmonics [16].

2.1.2
QCM-D for Studies of Protein–Protein Interactions

At about the same time as the QCM technique started to be used for DNA hybridization studies, investigations of immunoreactions utilizing antibody–antigen interactions started to appear in the literature, see e.g. [30], references therein, and papers citing this work. Since in these cases fairly rigid films (i.e., films inducing low ΔD values) are formed, the added value of QCM measurements compared with for example SPR-based analysis is, with respect to analysis of binding kinetics, not that obvious. However, there is a risk that the amount of hydrodynamically coupled water might still vary with coverage. This means, in turn, that in an analysis of binding kinetics, severe misinterpretations can still be made. This is so because the response in f will in such cases vary in a non-linear and unknown way as the number of bound molecules increases or decreases. This was recently ver-

ified for streptavidin binding to a supported biotin-modified lipid bilayer. To provide information about the variation in the amount of coupled water not only at saturated coverage, as listed in Table 1, QCM-D and SPR were operated in parallel under identical flow geometries. In the case of streptavidin, the mass of coupled water per mass of bound molecule varied from a factor ~ 7 at low coverage to ~ 1.5 at saturated coverage (Fig. 7), signaling that a traditional analysis of binding kinetics would not be applicable in this case.

It should be pointed out that this must not be the general case, since in the actual case streptavidin is likely to form a two-dimensional (2D) crystalline arrangement as the coverage increases. Such structural rearrangements would lead to significant changes in the layer properties, as also verified from ΔD data (see the second addition in Fig. 6). Based on the observation that high damping correlates with high water content, we may actually speculate that if there is a variation in the ratio between ΔD and Δf during a binding reaction, it might be taken as a "warning sign" for the use of traditional means of analyzing binding kinetics – also in cases when the damping is sufficiently low not to significantly violate the validity of the Sauerbrey relation. If this suspicion turns out to be true, which remains to be proven with additional model systems, combined f and D measurements are critical not only in order to correct the mass uptake or to provide additional information about the viscoelastic components, but also in order to arrive at a correct interpretation of binding kinetics for the systems under investigation. It is in this context worthwhile to mention that recent comparisons between QCM-D and SPR in the case of DNA immobilization and hybridization did not signal a non-linear variation in the water content [31]. Similarly, recent work focused on protein–protein and protein–drug interactions display kinetics in good agreement with the expected behavior [32].

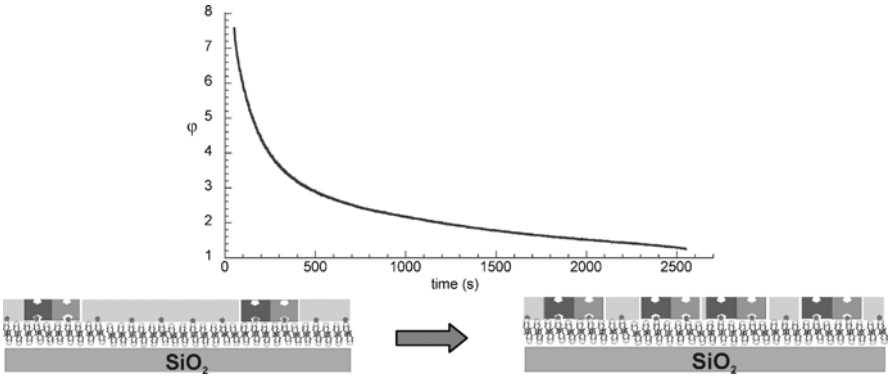

Fig. 7 Coupled water mass per adsorbed biomolecule mass, φ, versus time for streptavidin binding on top of a biotin-modified lipid bilayer

However, in the case of template-directed DNA synthesis, the situation seems more complicated [33], as is also most likely the case for many other situations. Hence, it is fair to state that combined f and D measurements must be considered critical in order to arrive at a proper interpretation of kinetic data.

2.2
Studies of Artificial (Biomimetic) Supported Cell Membranes

Artificial mimics of the natural cell membrane have emerged as extremely important model systems for studies of the natural cell membrane and its components, which are essential for the integrity and function of cells in all living organisms, and also constitute common targets for therapeutic drugs and in disease diagnosis. Early progress in QCM-based analysis of supported artificial cell membranes was made by Janshoff and coworkers, now at Gutenberg University Mainz, as summarized in [4]. It is fair to state, however, that the full potential of using the QCM technique in studies of the formation of supported bilayers became clear when combined f and D measurements were used to analyze the system [34].

2.2.1
Supported Lipid Bilayer Formation on SiO_2

By having a SiO_2 surface evaporated on the QCM electrode, exposed to a buffer solution, which is subsequently exchanged to a vesicle suspension, it was, in a single experiment, possible to discriminate between adsorbed intact lipid vesicles and a planar supported bilayer (see first addition in Fig. 6). While intact vesicles, due their high water content and flexible nature, induce large energy dissipation and mass change, a supported membrane induces negligible energy dissipation and a comparatively smaller mass change, which is in perfect agreement with that expected for a hydrated planar supported bilayer. Hence, it was possible, by using POPC vesicles of ~ 25 nm diameter, to conclude that spontaneous supported bilayer formation occurs via a precursor state of adsorbed intact vesicles, which at a critical coverage are spontaneously transformed into a complete and fluid bilayer [34]. However, in the early work, which relied on QCM-D measurements alone, it was not possible to separate the *mass contribution* from adsorbed vesicles and bilayer *during* the bilayer formation process. To achieve such separation, additional information was required. Using combined SPR and QCM-D measurements under identical flow conditions, a precise separation of the two components could indeed be made [35], as shown in Fig. 8.

In Fig. 8a, the mass uptake estimated from QCM-D data is compared with that obtained using SPR, yielding a measure of the variation in the amount of coupled water versus time. With this multiparameter information, in combi-

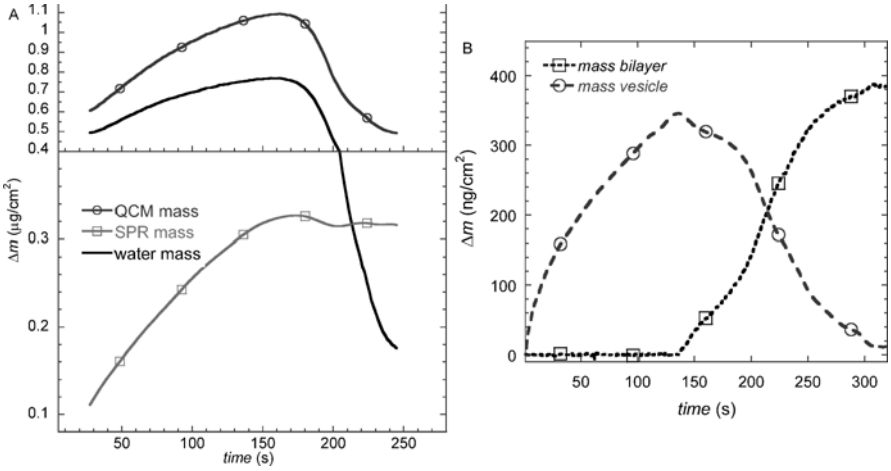

Fig. 8 **a** Changes in mass (*open circles*), obtained through a Voigt-based analysis of combined f and D measurements at multiple harmonics, and SPR mass (*open squares*), obtained through an analysis of changes in interfacial refractive index. The difference between the QCM mass and the SPR mass corresponds to the amount of coupled water sensed by QCM (*solid line*). **b** Separation of the contribution to the total mass uptake from adsorbed non-ruptured vesicles (*open circles*) and planar bilayer patches (*open squares*) versus time was made possible, as detailed in [35]

nation with changes in D (Fig. 6) the mass, and hence coverage, of adsorbed vesicles could be separated from that of planar lipid bilayer (illustrated in Fig. 8b). These data were corroborated by quantitative AFM data, imaging the relative fractions of intact vesicles and bilayer as a function of total lipid coverage [36].

Several groups have performed similar multitechnique studies, where the recent works by Brisson and coworkers at Bordeaux University, France, deserve special attention. They compared QCM data with AFM [19, 37] studies and even ellipsometry [18] to elucidate different stages during the vesicle-to-bilayer transition process, and also studied membrane-assisted protein 2D crystallization, as schematically illustrated in Fig. 9 [38]. While robust solutions for parallel integration of the QCM and various optical techniques appears more and more frequent in the scientific literature, promising means of combining QCM and AFM has been made recently [21, 39]. When this combination is further improved, providing high resolution imaging without scarifying high sensitivity in the QCM recording, a very important need will definitely be met.

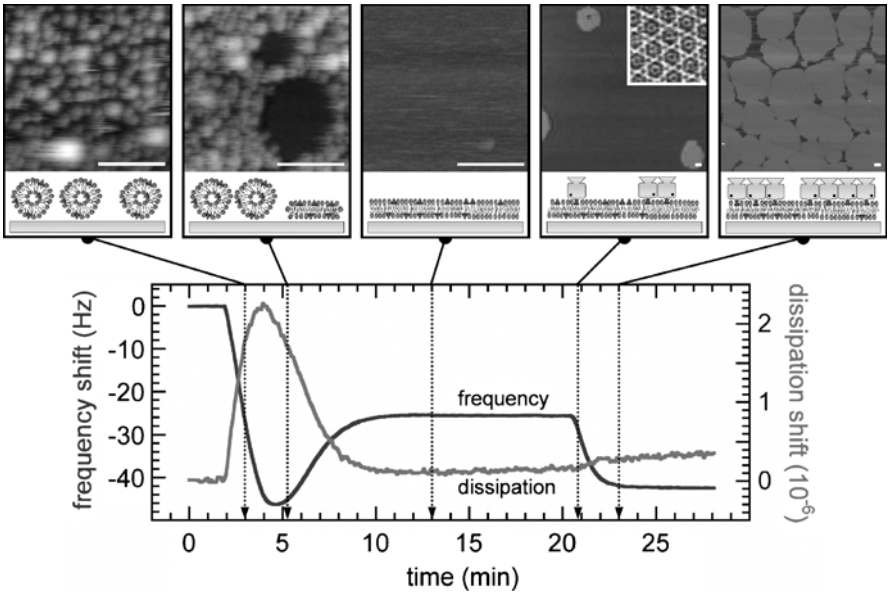

Fig. 9 Formation of a supported lipid bilayer (2–12 min) is followed by the specific adsorption of the protein annexin A5 (> 20 min). AFM allows probing the local structure of intermediates in 2D self-organization processes with nanometer resolution. Images (from *left* to *right*): intact lipid vesicles on a silica support; coexistence of vesicles and patches of a supported lipid bilayer (SLB); a complete SLB; small ordered domains of annexin A5 (the protein's 2D crystalline structure is resolved in the *inset*) on a mica–SLB; close to complete coverage with 2D crystalline domains. *White bars* in the AFM images correspond to 200 nm. The figure is reproduced from [45]

2.2.2 Arrays of Tethered Supported Lipid Vesicles

The strength of the QCM technique to distinguish between adsorbed lipid vesicles and planar supported lipid bilayers, and the opportunity offered by the technique to measure interfacial reactions on substrates other than gold, was recently demonstrated by us [40] and others [41] in connection with studies related to development of sensor arrays, using different types of functionalized lipid assemblies. Textor's Biointerface Group at ETH, Zürich, utilized QCM sensor crystals with either TiO_2 or SiO_2 coatings to evaluate the response of patterned substrates composed of these two materials [41]. We used the same approach for patterns of Au on SiO_2. In this way, we were able to find conditions where the Au regions of the pattern could be modified with single-stranded DNA, while the surrounding SiO_2 area was modified with a highly inert supported lipid bilayer. Using lipid vesicles modified with single-stranded DNA, fully complementary to those immobilized on the

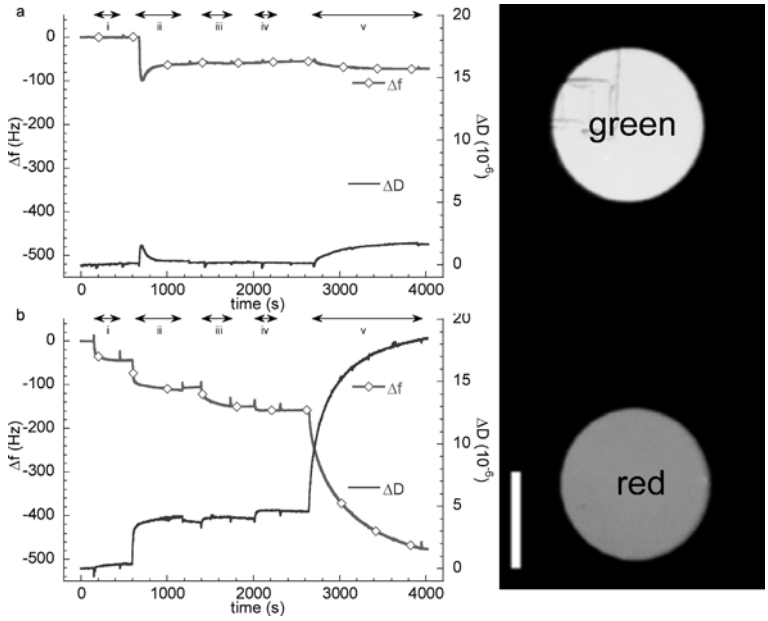

Fig. 10 Subsequent additions of biotin–BSA (*i*), lipid vesicles (*ii*), NeutrAvidin (*iii*), single-stranded biotin–DNA (*iv*), and lipid vesicles modified with fully complementary DNA (*v*) to **a** SiO_2-coated and **b** Au-coated QCM crystals. Note that there is no adsorption of biotin–BSA on SiO_2, while the efficient binding of biotin–BSA on Au significantly reduces vesicles adsorption to the Au-coated surface. Similarly, the bilayer formation renders the SiO_2-coated surface inert to subsequent additions of DNA and vesicles. The micrograph shows sequence-specific sorting of two differently fluorescently labeled DNA-modified vesicles to spots modified with different DNA sequences

substrate, this template was shown to be capable of sequence-specific and site-selective immobilization of different types of lipid vesicles to different DNA spots (Fig. 10).

We believe that this approach of handling membrane proteins on solid supports constitutes a promising route for analytical strategies aimed at analysis of membrane proteins and consequently also for the QCM-D technique in the development of patterned surfaces for array-based analysis of biorecognition events.

2.2.3
Probing Viscoelastic Films that Approach Resonant Conditions

Adsorbed or tethered lipid vesicles induce relatively high damping (Figs. 6, 9, and 10). However, a Voigt-based analysis, in order to correct the apparent mass to obtain the correct mass, shows that the underestimations using the Sauerbrey relation are generally less than 20%. In contrast, if multiple

layers of vesicles are formed, there is evidence of resonant effects between the oscillator and the adsorbed film (Fig. 11) [42], which is quite a complicated situation.

Note, in particular, that as the film thickness increases upon formation of subsequent lipid vesicle layers, the change in f changes sign, while the change in D becomes smaller. This is in very good agreement with the theoretical prediction for a viscoelastic film reaching a condition where film resonance is excited (Fig. 5), as analyzed in detail in [42]. Similarly, in a recent work aimed at designing peptide sequences displaying high specificity to inorganic materials, high selectivity was demonstrated towards phages carrying a peptide sequence specific for TiO_2. The main observation leading to the conclusion of high selectivity was a large change in D, while essentially no response was observed in f, as illustrated in Fig. 12 [43]. Interestingly, if this response is compared with that of multilayers of vesicles, or the theoretical prediction in Fig. 5, it is clear that films in certain thickness regimes are expected to display exactly this phenomenon: high damping, but essentially no change in frequency. Although a theoretical analysis is required before a conclusive statement can be made in the latter example, we consider this interpretation very likely. Hence we emphasize, with these systems as instructive examples,

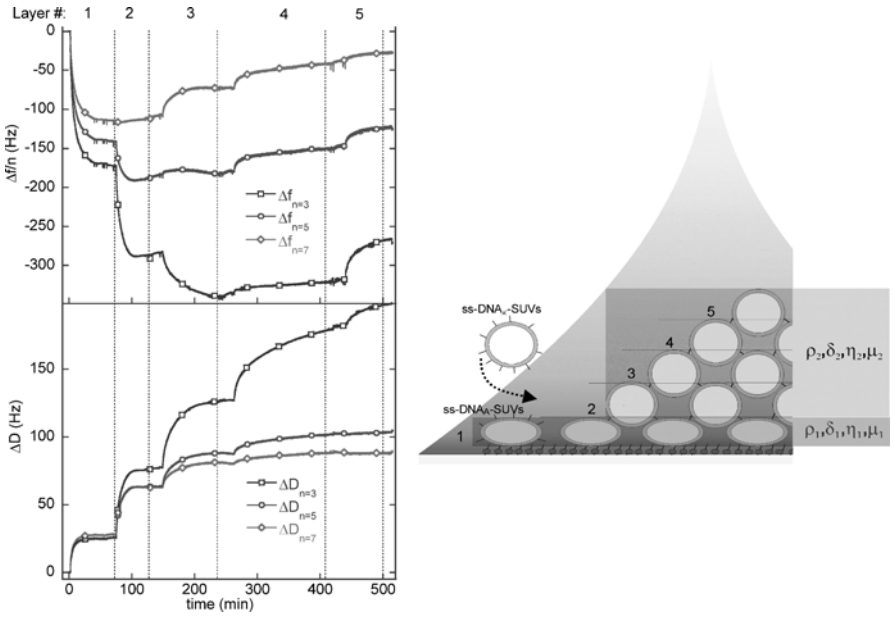

Fig. 11 *Left*: Changes in f and D measured at $n = 3$, 5, and 7 upon subsequent formation of multiple lipid vesicle layers provided via hybridization of vesicles modified with complementary DNA sequences. *Right*: Cartoon illustrating the lipid vesicle multilayer formation

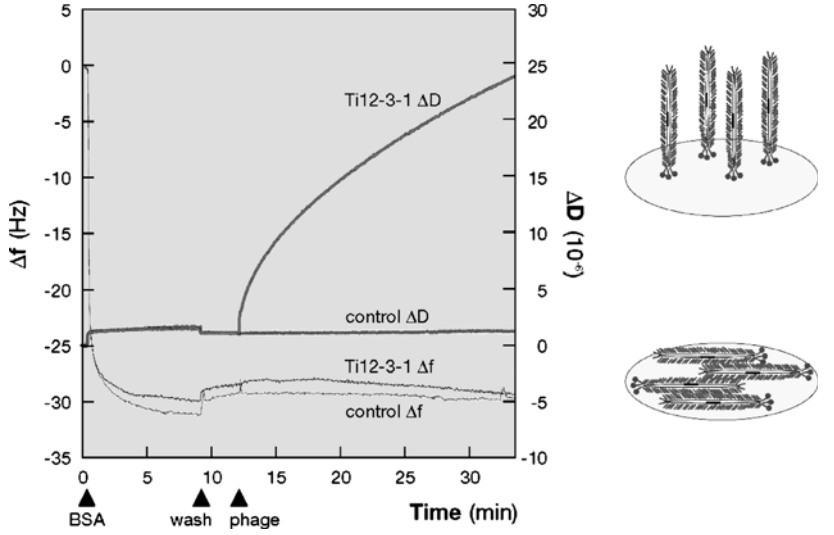

Fig. 12 Changes in f and D versus time during incubation of a peptide-carrying phage and the control phage (which displays no peptide). Note the significant increase in D for the peptide-displaying phage, while no detectable change is observed if the peptide is not present

the usefulness of combined f and D measurements for studies of complex systems (such as virus particles, bacteria, and cells), which are not easily analyzed using alternative techniques and which often require special surface conditions not necessarily easy to achieve with many other techniques. The unique feature of the QCM-D technique is, in this context, its ability to explore property changes in the sample film via changes in its viscoelastic response.

3 Conclusions and Outlook

The relatively recent technical and theoretical improvements (summarized above) and the associated understanding of the involved processes have broadly eliminated the early obscurity and skepticism connected with liquid-phase applications of the QCM technique. This skepticism was founded on examples of large deviations from the Sauerbrey relation, and strange (as perceived at that time) responses to mass loads with very viscous films. Concerns about the interpretation of QCM data were raised when operation of the technique in aqueous solutions was young [44]. Since then, the theoretical developments and associated deeper quantitative and conceptual understanding of more and more complex systems have removed most of the skepticism.

Understanding of the mutual response between a viscoelastic film and the periodic shear motion of the sensor surface, combined with technical advances allowing simultaneous f and D measurements at several harmonics have in fact turned the technique into one of the most important tools both for fundamental biologically oriented surface science and for a variety of biotechnology applications. This does not mean, however, that everything is understood. There are still experimental and theoretical challenges left, especially for more complex and heterogeneous systems. One such example is when and if slip occurs between the adsorbed film and the QCM-D electrode surface, or within the adsorbed film. Another very relevant example is how to treat and interpret the influence of gradients in density and the viscoelastic properties of adsorbed films.

Since the QCM technique has now reached a state where several robust commercially available systems exist and where, in parallel, theoretical models have been developed that help in quantifying the measured quantities into physically meaningful parameters, it is quite likely that the popularity of the technique will continue to increase and that it soon will become a standard instrument in all research groups addressing questions related to biointerfaces and biomacromolecular recognition, and also for other solid–liquid interface studies. A promoting factor for such development is that the technique is ideally suited to be combined with complementary techniques: both optical techniques, such as SPR and ellipsometry, and electrochemical techniques, such as impedance spectroscopy, fluorescence microscopy, AFM etc. As progress is made within molecular biology, deeper and deeper information of the analyzed systems will be required, and since biorecognition kinetics and dynamics constitute essential and fundamental cornerstones in this progress, parallel integration of multiple techniques relying on different physical principles is likely to play a key role in future efforts within these research disciplines. The QCM technique will certainly be one of them.

References

1. Sauerbrey G (1959) Zeitschrift für Physik 155:206
2. Lu C, Czanderna AW (1984) Applications of piezoelectric quartz crystal microbalances. Elsevier, Amsterdam
3. Nomura T, Minemura A (1980) Nippon Kagaku Kaishi 10:1621
4. Janshoff A, Galla HJ, Steinem C (2000) Angew Chem Int Ed 39:4004
5. Rodahl M, Höök F, Krozer A, Brzezinski P, Kasemo B (1995) Rev Sci Instr 66:3924
6. Domack A, Prucker O, Ruhe J, Johannsmann D (1997) Phys Rev E 56:680
7. Rodahl M, Hook F, Fredriksson C, Keller CA, Krozer A et al. (1997) Faraday Discuss 107:229
8. Bandey HL, Hillman AR, Brown MJ, Martin SJ (1997) Faraday Discuss 107:105
9. Rodahl M, Kasemo B (1996) Rev Sci Instr 67:3238
10. Rodahl M, Höök F, Kasemo B (1996) Anal Chem 68:2219

11. Dultsev FN, Ostanin VP, Klenerman D (2000) Langmuir 16:5036
12. Edvardsson M, Rodahl M, Kasemo B, Hook F (2005) Anal Chem 77:4918
13. Tjarnhage T, Puu G (1996) Colloids Surf B: Biointerfaces 8:39
14. Höök F, Kasemo B, Nylander T, Fant C, Sott K, Elwing H (2001) Anal Chem 73:5796
15. Voros J (2004) Biophys J 87:553
16. Larsson C, Rodahl M, Hook F (2003) Anal Chem 75:5080
17. Caruso F, Furlong DN, Kingshott P (1997) J Colloid Interface Sci 186:129
18. Richter RP, Brisson AR (2005) Biophys J 88:3422
19. Richter R, Mukhopadhyay A, Brisson A (2003) Biophys J 85:3035
20. Huang E, Zhou FM, Deng L (2000) Langmuir 16:3272
21. Choi KH, Friedt JM, Frederix F, Campitelli A, Borghs G (2002) Appl Phys Lett 81:1335
22. Muratsugu M, Ohta F, Miya Y, Hosokawa T, Kurosawa S et al. (1993) Anal Chem 65:2933
23. Lucklum R, Behling C, Hauptman P (1999) Anal Chem 71:2488
24. Okahata Y, Kawase M, Niikura K, Ohtake F, Furusawa H, Ebara Y (1998) Anal Chem 70:1288
25. Niikura K, Matsuno H, Okahata Y (1998) J Am Chem Soc 120:8537
26. Höök F, Ray A, Norden B, Kasemo B (2001) Langmuir 17:8305
27. Su XD, Wu YJ, Robelek R, Knoll W (2005) Langmuir 21:348
28. Pope LH, Allen S, Davies MC, Roberts CJ, Tendler SJB, Williams PM (2001) Langmuir 17:8300
29. Cho YK, Kim S, Lim G, Granick S (2001) Langmuir 17:7732
30. Minunni M, Mascini M, Guilbault GG, Hock B (1995) Anal Lett 28:749
31. Su XD, Wu YJ, Knoll W (2005) Biosens Bioelectron 21:719
32. Godber B, Thompson KSJ, Rehak M, Uludag Y, Kelling S et al. (2005) Clin Chem 51:1962
33. Stengel G, Hook F, Knoll W (2005) Anal Chem 77:3709
34. Keller CA, Kasemo B (1998) Biophys J 75:1397
35. Reimhult E, Larsson C, Kasemo B, Hook F (2004) Anal Chem 76:7211
36. Reimhult E, Zach M, Hook F, Kasemo B (2006) Langmuir 22:3313
37. Richter RP, Brisson A (2004) Langmuir 20:4609
38. Richter RP, Him JLK, Tessier B, Tessier C, Brisson AR (2005) Biophys J 89:3372
39. Zhou C, Friedt JM, Angelova A, Choi KH, Laureyn W et al. (2004) Langmuir 20:5870
40. Svedhem S, Pfeiffer I, Larsson C, Wingren C, Borrebaeck C, Höök F (2003) Chem Bio Chem: 339
41. Rossetti FF, Bally M, Michel R, Textor M, Reviakine I (2005) Langmuir 21:6443
42. Graneli A, Edvardsson M, Hook F (2004) Chem Phys Chem 5:729
43. Sano KI, Shiba K (2003) J Am Chem Soc 125:14234
44. Ward MD, Buttry DA (1990) Science 249:1000
45. Richter RP (2004) The formation of solid-supported lipid membranes and two-dimensional assembly of proteins. A study combining atomic force microscopy and quartz crystal microbalance with dissipation monitoring. Bordeaux University, Talence

Springer Ser Chem Sens Biosens (2007) 5: 449–479
DOI 10.1007/5346_035

Published online: 8 July 2006

Resonant Acoustic Profiling (RAP™) and Rupture Event Scanning (REVS™)

Matthew A. Cooper

Akubio Ltd., Cambridge Science Park, Cambridge CB4 0GJ, UK
mcooper@akubio.com

Abstract Following the release of widely available commercial instruments in the 1990s, researchers have driven the development of biosensor-based methods for profiling and screening of small molecule and proteinaceous therapeutic drug candidates. Medicinal chemists have in turn demanded faster and more accurate assays for characterisation of drug candidate interactions with target receptors, serum proteins and side-effect profiling receptors. In response to this challenge, Akubio Ltd. (Cambridge, UK) has been developing an advanced label-free detection platform, resonant acoustic profiling (RAP™). This evolution of the basic QCM approach has the potential to change the way assays are performed and to generate novel information on molecular interactions. Key attributes covered in this chapter include the ability to multiplex to high numbers of resonators, the addition of robust interfacial surface chemistries, fully automated sample handling and sample processing, disposable microfluidic cassettes with submicrolitre dead volumes, and more sensitive detection electronics.

Akubio has also developed a sensitive and economical method to directly detect particulate analytes. The technique, which we term rupture event scanning (REVS™), is based on control of the amplitude of oscillation of an acoustic wave device on which the analytes have been captured. In this chapter, example applications of RAP™ for proteins

and small molecules and REVS™ for virus detection are presented. The physical forces involved in the processes are also discussed.

Keywords Surface chemistry · Microfluidics · Affinity · Kinetics · Force

Abbreviations

BAW	Bulk acoustic wave
BSA	Bovine serum albumin
EDC	1-Ethyl-3-[3-dimethylaminopropyl]carbodiimide hydrochloride
GDH	Glucose dehydrogenase
IL-1β	Interleukin 1-beta
ITC	Isothermal titration calorimetry
Ms IgG	Mouse immunoglobin type G
NHS	*N*-Hydroxysuccinimide
PBS	Dulbecco's modified phosphate buffered saline
QCM	Quartz crystal microbalance
QCRS	Quartz crystal resonance sensing
RaM-FC	Rabbit anti-mouse (Fc-specific) immunoglobin
RAP™	Resonant acoustic profiling
REVS™	Rupture event scanning
SPR	Surface plasmon resonance
Tween-20	Polyoxyethylenesorbitan monolaurate

1 Resonant Acoustic Profiling

1.1 Benefits of Label-Free Technology

Over the past two decades the benefits of label-free analyses have begun to make an impact on their use as mainstream research tools in many laboratories [1, 2]. Label-free biosensors do not require the use of detection labels (fluorescent, radio or colorimetric) to facilitate measurements. Detailed information on an interaction can be obtained during analysis whilst minimising sample processing requirements and assay run times [3]. Unlike label- and reporter-based technologies that simply confirm the presence of the detector molecule, label-free techniques can provide direct information on analyte binding to target molecules, typically in the form of mass addition or depletion from the surface of the sensor substrate [4]. However, these technologies have failed to gain widespread acceptance due to technical constraints, low throughput, high user expertise requirements and cost. Whilst they can be powerful tools in the hands of a skilled user evaluating purified samples, they are not readily adapted to everyday laboratory use where simple-to-understand results on high numbers of samples are the norm.

Resonant acoustic profiling (RAP™) from Akubio (Cambridge, UK) provides researchers with the ability to perform accurate real-time, label-free characterisations on both purified and crude samples in an easy to use format. RAP™, which is based on piezoelectric quartz crystal technology, measures the build-up of molecules on the surface of an oscillating crystal and provides real-time binding information on the binding interactions. The piezoelectric effect was first noted by the Curie brothers in 1880 [5]. Today, acoustic devices based on quartz crystal resonators are found in electronic devices such as watches, computers and televisions, with over a billion units mass-produced each year. Application to biological samples became possible when suitable oscillator circuits for operation in liquids were developed [6, 7]. As molecules interact with immobilised receptors on the surface of a quartz crystal, there is a concomitant modulation of the acoustic resonance of the crystal. This, in turn, results in modulated electrical signal that can be analysed using standard digital signal processing techniques [8]. The signal indicates not only the presence of the analyte but also the specificity and affinity for a surface-bound receptor. When combined with a flow-based microfluidic chip, kinetic parameters and complex half-lives can also be quantified. Additional evaluations of the viscoelastic properties of binding events, through analysis of parameters such as motional resistance, may provide unique data relevant to structural properties and confirmation changes associated with molecular interaction [9]. The simultaneous measurement of these parameters creates an acoustic profile of a molecular interaction, giving a high level of information about a binding event on a routine basis.

1.2 Literature Trends

There has been continued growth in the number of publications referencing the term "quartz crystal microbalance" or "QCM" in which a thickness shear mode bulk acoustic wave resonator is used to probe biological and chemical interactions in life sciences research. As alluded by other contributors to this volume, the term "microbalance" is not strictly accurate: many examples of non-gravimetric responses of acoustic wave devices to analyte binding have been reported in the literature [10–15]. Nevertheless, the terms QCM, QCRS ("quartz crystal resonance sensing") and BAW ("bulk acoustic wave") can be cross-referenced with terms such as "biosensor" and "analyte" to ensure that the vast majority of publications in the field are captured. Following this approach, it is immediately obvious that the number of publications that involve the use of QCM has increased rapidly since the mid-1980s (Fig. 1a). Many of the separate hardware components that make up an acoustic biosensor are commercially available from a number of electronics companies: a lock-in amplifier, a frequency synthesiser, a power supply and a quartz crystal holder. This provides a low barrier to entry for the academic or industrial re-

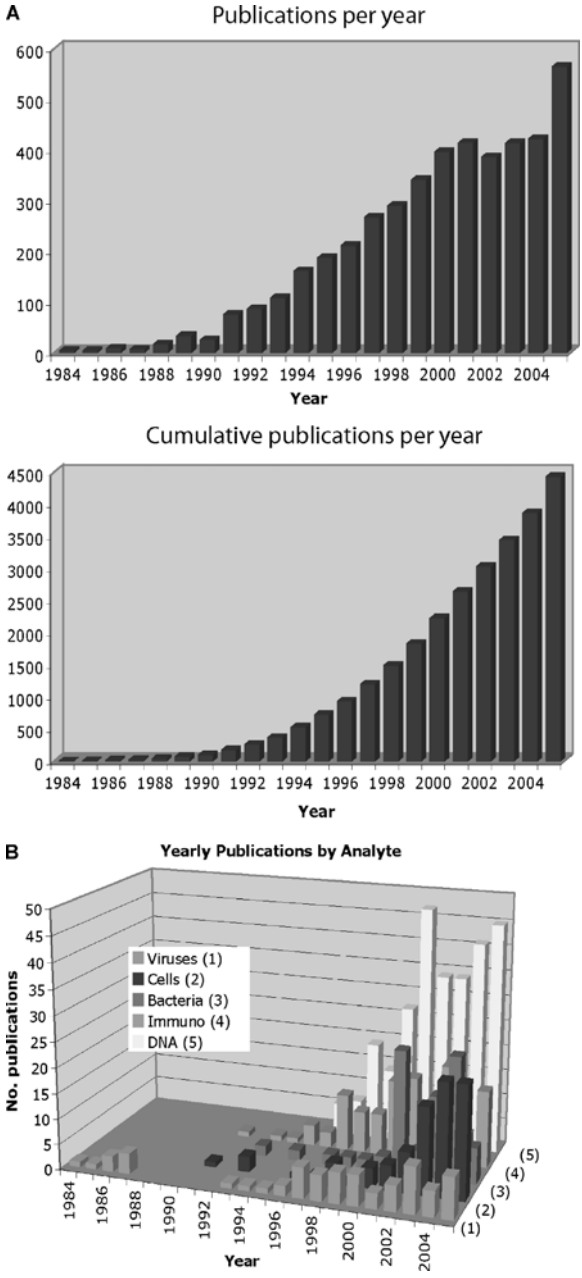

Fig. 1 QCM publications. **A** Yearly cumulative number of publications found using an ISI Web of SCIENCE® search for the term "quartz crystal microbalance" in the title, keyword or abstract. **B** Yearly number of publications found using an ISI Web of SCIENCE® search for the term "quartz crystal microbalance" cross referenced using the terms "DNA", "immunoassay", "bacteria", "cell" or "virus"

Table 1 Published limits of detection for selected clinically relevant immunoassays

Analyte	Matrix	Sensitivity	Refs.
African swine fever virus	Serum	Ag 1 $\mu g\,mL^{-1}$ IgG 0.2 $\mu g\,mL^{-1}$	Uttenthaler 1998 [23]
Anti-*T. gondii* IgG	Blood, serum	1 : 5500	Wang et al. 2004 [24]
Anti-*T. pallidum* IgG	Serum	75–900 mIU	Aizawa et al. 2001 [25]
Complement C4	Serum	0.1–10 $\mu g\,mL^{-}1$	Hu et al. 1998 [26]
C-reactive protein	Serum	10–70 $\mu g\,mL^{-1}$	Aizawa et al. 2001 [16]
Der p (house dust mite) IgE	Serum	0.15 IU mL^{-1}	Su et al. 2000 [27]
Fibrinogen	Serum	10 $\mu g\,mL^{-1}$	Aizawa et al. 2003 [28]
Niacinamide	Serum, urine	1 nM	Long et al. 2001 [29]
Total IgE	Serum	5–300 IU mL^{-1}	Su et al. 1999 [30]
Transferrin	Serum	160 ng mL^{-1}	Wu et al. 2000 [21]

Table 2 Published limits of detection for selected clinically relevant bacteria

Analyte	Matrix	Sensitivity (cfu/mL)	Refs.
S. epidermidis	Growth medium	100	Bao et al. 1996 [31]
L. monocytogenes	Milk	250 000	Minunni et al. 1996 [32]
C. trachomatis	Urine	260 ng mL^{-1}	BenDov et al. 1997 [17]
S. typhimurium	Buffer	530 000	Ye et al. 1997 [33]
S. typhimurium	Growth medium	990 000	Park et al. 1998 [34]
S. typhimurium	Milk	3 200 000	Park et al. 2000 [35]
S. paratyphi A	Growth medium	170	Fung et al. 2001 [36]
T. pallidum	Serum	10–600 TU	Aizawa et al. 2001 [37]

searcher, when compared to the expense and expertise required to assemble an optical platform (which usually require sophisticated CCD cameras, processing software, optical filters, optical interfaces, lasers etc.). As a result, from 1990 to 2000 the number of publications involving QCM has grown semi-exponentially; the rate of growth slowing slightly from 2000 to 2004 (Fig. 1a).

This period has also seen an increase in the number of publications that describe the detection and quantification of clinically relevant analytes [16–22], (Fig. 1b). Published limits of direct detection (LOD) for analytes present in serum, blood or urine are typically in the range 0.1–10 $\mu\,gL^{-1}$ (1). Whilst these LODs can meet, or surpass the clinically relevant LODs for many analytes, there are numerous other examples where $pgmL^{-1}$ or even $fgmL^{-1}$ detection sensitivity is required for accurate diagnosis. However, it is notable

that these data were generated on "home built" QCM systems often using very basic receptor attachment chemistries.

There has been a steady growth in the number of published papers describing detection of clinically relevant bacteria [36, 38–42] (Table 2 and Fig. 1b) and, in the last 5 years, there has been a rapid growth in the number of publications using acoustic biosensors to analyse mammalian cells [43–51]. In the latter application, a variety of cell types have been immobilised on quartz resonators coated with appropriate attachment chemistries. Here the cell forms an active part of the biological transducer component of the sensor, as bulk viscoelastic changes in the cell are also detected via the quartz resonator. This approach has been employed to monitor interactions between cells and the adherent surface, as well as the cellular response to a variety of exogenous stimuli. Both the magnitude and kinetics of the response can be followed, as detection occurs in real-time and does not require fluorescent, chemiluminscent, quantum dot or other reporter labels.

The number of publications using acoustic sensing to measure hybridisation of nucleotides, particularly single-stranded DNA (ssDNA), has grown dramatically since 1996 (Fig. 1b). Recent work has shown that it is possible to sensitively and specifically detect genetically modified organisms and even single base-pair mismatches from PCR-amplified contaminated foodstuffs and pooled patient sera [52–56]. The ability to probe for pathogen nucleic acid, pathogen antigen and pathogen-specific host antibodies provides extra levels of assay redundancy, giving greater confidence in the results. In time this capacity should enable the development of very robust and precise pathogen detection systems that give information on pathogen copy number, antigen level and immunological host response.

1.3 RAP♦*id*™ System

The breadth of application areas described above is significant, with numerous published papers that describe the detection of nearly all classes of clinically relevant analytes. However, it is surprising that these data have almost exclusively been generated using "home built" QCM systems, often with insufficient attention to surface chemistry and assay reproducibility. A widely available and robust acoustic detection system that can generate reproducible data for the above classes of analytes could be of great benefit to life sciences research, clinical diagnostics, environmental sensing and homeland defence communities. In response to this challenge we are developing RAP™ systems that incorporate a number of key technical advances compared to the prior art. We have produced high frequency resonators that possess high merit or *Q* factors (a measure of the piezoelectric device's ability to convert electrical energy into kinetic energy). This increases the detection sensitivity [57] and also improves assay reproducibility. These resonators incorporate a parallel

reference control, which enables analyte to be passed simultaneously over both "active" and "control" receptors. Real-time subtraction of control data from active data further improves the robustness of the assay.

There have been major advances in the field of microfluidics that enable sophisticated devices to be developed, tested and ultimately released to the market over a much shorter time scale than was possible a decade earlier. As quartz is a piezoelectric material, it is highly sensitive to flexural, shear and pressure changes. These artefacts are undesirable in a system designed to measure a specific response to analyte. To address this potential problem, we have combined a proprietary stress-free mounting system for the quartz crystal with a microfluidic lateral flow device with a dead volume of less than one microlitre. This ensures that the detector response is sensitive principally to analyte binding. It also enables a relatively small (< 30 microlitre) volume of liquid to be delivered and removed from the resonant sensing area rapidly and efficiently with minimal sample dispersion or sample cross-contamination (Fig. 2). RAP™ experiments described in this paper were conducted using manually operated or automated two- and four-channel instruments (Akubio, Cambridge, UK). The instruments applied the principles of QCM, in that a high frequency voltage was applied to a piezoelectric crystal to induce the crystal to oscillate, and its resonance frequency was monitored in real time. The two-channel instruments comprised a pair of oscillating crystal sensors mounted in parallel microfluidic flow cells, allowing sample to be flowed across two surfaces simultaneously. As sample is flowed across "control" and "active" sensors, binding to the "active" sensor is measured as a reduction in the oscillation frequency, with the "control" sensor acting as a subtractive sample reference. The RAP™ instruments were fitted with a thermally stable sensor mounting block providing temperature control, and with microfluidic and electrical connections to the pair of piezoelectric sensors. Buffer flow was maintained with two sy-

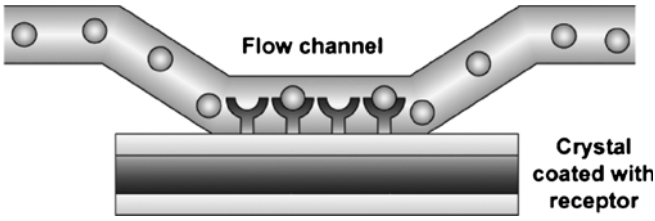

Fig. 2 Microfluidic biosensor chip. Pictorial representation of a piezoelectric bioassay: a piezoelectric acoustic wave device (such as a quartz crystal resonator) is coated with a selective, passivating layer to which an analyte-specific receptor can be immobilised. Liquid containing the analyte of interest is then passed across the surface using appropriate microfluidics, which results in selective capture of the analyte. This additional bound material in turn modulates resonance of the acoustic wave device, which is transformed into an electrical signal due to the piezoelectric effect

ringe pumps (Tecan UK, Reading, UK) under software control (Akubio). Microfluidics comprised separate flow paths to individual flow cells, combined with a common flow path split to address both flow cells simultaneously. Interchange between the different flow paths was either by manually or electronically operated valves (Akubio). Sensors comprised standard gold-coated quartz wafers, with a carboxylic acid-terminated linker layer coating to provide a surface for protein immobilisation, mounted in an acrylic cassette (Akubio).

1.4 Linker Chemistry

The interface between the biosensor surface and the chemical or biological systems to be studied is a vital component of all surface-sensitive sensor systems. Receptors must be attached to some form of solid support whilst retaining their native conformation and binding activity. This attachment must be stable over the course of a binding assay and, in addition, sufficient binding sites must be presented to the solution phase to interact with the analyte. Most importantly, the support must be resistant to non-specific binding of the sample matrix, which could mask the analyte-binding signal. Many receptor-coupling strategies utilise a chemical linker layer between the sensor base interface (e.g. a gold layer) and the biological component to achieve these ends. The termini of these molecules can be derivatised with molecules that possess suitable chemical reactivity for receptor capture (e.g. -epoxy, -carboxyl, -amino, -biotinyl, -nitrilotriacetic acid) [58–60]. The receptor is normally immobilised on the surface, and the binding partner (analyte) is allowed to bind to this surface from free solution. However, it is also possible to configure solution competition assays in which the analyte is immobilised on the surface and competes with solution-phase analyte for receptor.

Selection of the correct coupling chemistry requires careful consideration of: (a) the resultant orientation of receptor, (b) its local environment on the surface, (c) the stability of the linkage under the conditions used to regenerate the surface, and (d) possible effects of the coupling chemistry on components of the binding interaction. We have employed a carboxylic acid-terminating linker layer together with carbodiimide-mediated amine coupling (e.g. to surface lysine residues or *N*-terminal residues on a proteinaceous receptor). If immobilisation is performed at low pH, the amine terminus of the receptor is likely to be more reactive than the gamma-amino group of any lysine residues, in which case amine coupling can give rise to more ordered surface orientation. A control receptor (e.g. BSA or non-specific IgG) can be coupled to a control resonator surface, and the active receptor is coupled to an adjacent resonator surface. Note that it is also possible to couple sulfhydryl-containing receptors or thiolated oligonucleotide probes using chemically selective cross-linking reagents such as pyridinyldithioethanamine (PDEA)

or 3-(2-pyridinyldithio)propionic acid *N*-hydroxysuccinimide ester (SPDP) to achieve an even higher degree of receptor orientation homology.

1.5 RAP™ Assays

After the immobilisation of "control" and "active" receptors, the resultant "sensor chip" can then be stored for future use, or used directly after receptor immobilisation. In a typical RAP™ assay (Fig. 3) at $t = 0$ s, buffer was contacted with the receptor via the microfluidic device. At $t = 60$ s a solution of analyte (in this case mouse IgG) in the running buffer was passed over the active surface (rabbit anti-mouse-Fc) and the control surface (mouse IgG). As the analyte bound to the active receptor, the additional mass and viscoelastic load on the resonator resulted in a change in the resonance signal (depicted here as a negative change in series resonance).

For this simple bimolecular association, $A + B = AB$, the process was assumed to be pseudo first order with no interaction between separate receptor molecules. The dissociation rate is derived from:

$$R_t = R_{t_0} e^{-k_d(t-t_0)}, \tag{1}$$

where R_t is the response at time t, R_{t_0} is the response at time t_0 and k_d is the dissociation rate constant. The association rate constant can be derived using

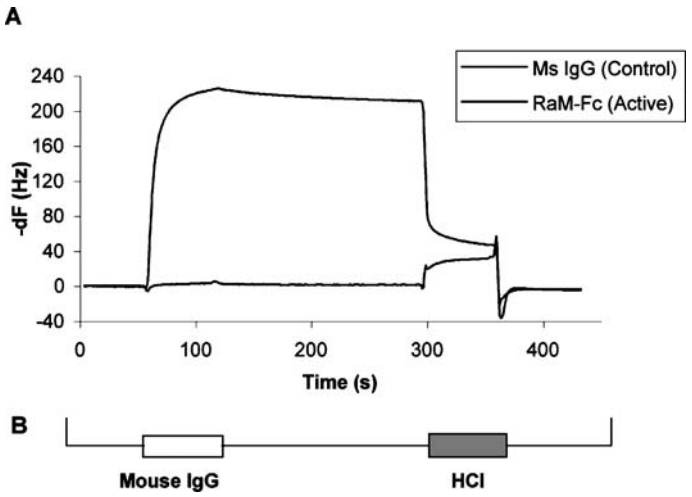

Fig. 3 Typical RAP™ assay with binding and regeneration. **A** Binding of Ms IgG to RaM-Fc active and Ms IgG control sensor surfaces. *Top line* indicates the frequency response generated by binding of Ms IgG to RaM-Fc and the *bottom line* indicates the frequency response generated by minimal binding to the control Ms IgG surface. **B** Schematic representation of sample and regeneration solution injections

the equation:

$$R_t = \frac{k_a\ CR_{max}\left(1 - e^{-(k_a\ C + k_d)t}\right)}{k_a\ C + k_d}, \tag{2}$$

where R_{max} is the maximum response (proportional to the amount of immobilised ligand), C is the concentration of analyte in solution and k_a is the association rate constant. Analysis of the association phase of the binding curve gives directly the observed association rate (k_{obs}). If the concentration of the analyte is known, then the association rate constant of the interaction (k_a) can be determined. Conversely, if the kinetic parameters for an interaction are known (i.e. fixed for a given receptor–analyte interaction), it is possible to derive the active concentration of an analyte in a sample.

Affinities were then calculated from the ratio of k_a/k_d and also from analysis of equilibrium binding levels at varying analyte concentration. By measuring the signal attained at equilibrium as a function of analyte concentration, affinities can be determined from a Scatchard analysis using the equation:

$$\frac{R_{eq}}{C} = K_a R_{max} - K_a R_{eq}, \tag{3}$$

where R_{eq} is the response at equilibrium and K_a is the association constant ($1/K_d$). A plot of R_{eq}/C versus R_{eq} has a slope of $-K_a$.

In the example shown in Fig. 3, at $t = 240$ s the mouse IgG solution was replaced by buffer and the receptor–analyte complex was allowed to dissociate. Analysis of this data can gave the dissociation rate constant (k_d) for the interaction. Many complexes in biology have considerable half-lives, thus a pulse of a regeneration solution (in this case an acid wash followed by a basic wash) was used at $t = 240$ s and $t = 360$ s to disrupt binding and regenerate the free receptor. The entire binding cycle can be repeated many times at varying concentrations of analyte to generate a robust data set for global fitting to an appropriate binding algorithm. The affinity of the interaction was then calculated from the ratio of the rate constants ($K_d = 1/K_a = k_d/k_a$) and confirmed by a non-linear fitting of the response at equilibrium versus varying concentration of analyte.

1.6 Myoglobin

Myoglobin is a 17 kDa cytoplasmic protein found in muscle cells that binds and stores oxygen. Normal levels of myoglobin in blood are very low ($< 100\ ng\ mL^{-1}$). Following muscle damage (e.g. cardiac ischemia), myoglobin is released into the blood and can rise to $> 1000\ ng\ mL^{-1}$ immediately after a myocardial infarction, and can remain high ($\sim 500\ ng\ mL^{-1}$) for some time afterwards. Myoglobin detection in blood is therefore a good diagnostic indicator of preceding and ongoing cardiac disease and damage [61]. We used

a mouse anti-myoglobin antibody, previously captured onto a rabbit anti-mouse-Fc (RaM-Fc) surface to measure binding of varying concentrations of human recombinant myoglobin in real time (Fig. 4a).

Varying concentration of myoglobin in the sample would give varying response levels at equilibrium, which would enable generation of a standard curve for analyte concentration. However, it can be seen from Fig. 4a, that at lower concentrations of myoglobin considerable contact time would be required to reach an equilibrium level. In addition, in a "real world" diagnostic application the sensor is likely to be used only once, and the level of receptor activity may vary upon shipping and storage, which would result in variable equilibrium binding levels. Hence, analyte concentration can be more accu-

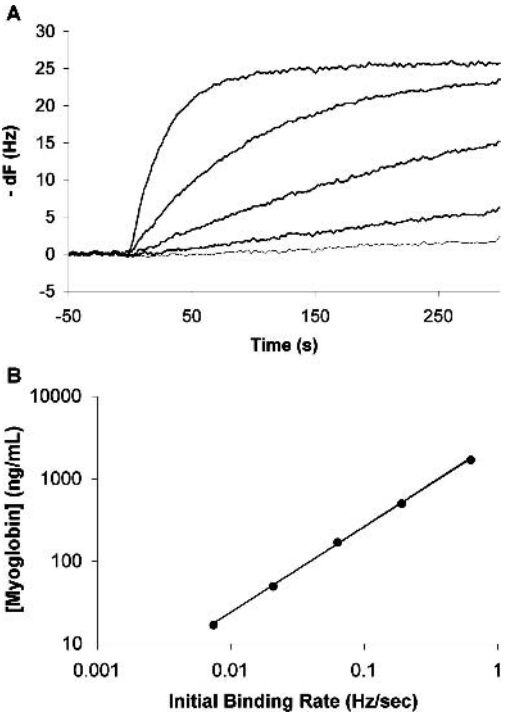

Fig. 4 Myoglobin concentration assay. **A** Binding of recombinant human myoglobin to mouse anti-myoglobin antibody, previously captured onto a RaM-Fc surface. Binding curves for five different standard myoglobin concentrations (equivalent to 100, 30, 10, 3 and 1 nmol L^{-1}) are shown overlaid and synchronised to the start of each myoglobin injection. Correction for signal drift due to the off-rate of the captured antimyoglobin antibody was performed by subtraction of the response from injection of buffer only. **B** Myoglobin concentration–response calibration curve, generated by plotting the initial binding rate for the set of standard concentrations. Estimates of myoglobin concentration in unknown samples were calculated by linear interpolation from the calibration curve with an accuracy of 0.5–15% over the concentration range tested

rately and rapidly determined by analysing the rate of binding of myoglobin to the antibody, and comparing the measured observed association rate with a data set calibrated to analyte concentration (Fig. 4b). This enabled the concentration of myoglobin in the sample to be determined in under 6 min.

1.7 Interleukin 1-Beta

Members of the interleukin-1 (IL-1) family have clear therapeutic and diagnostic potential: the IL-1 agonists, IL-1α and IL-1β, are induced by central nervous system injury, whilst peripheral or central administration of the IL-1

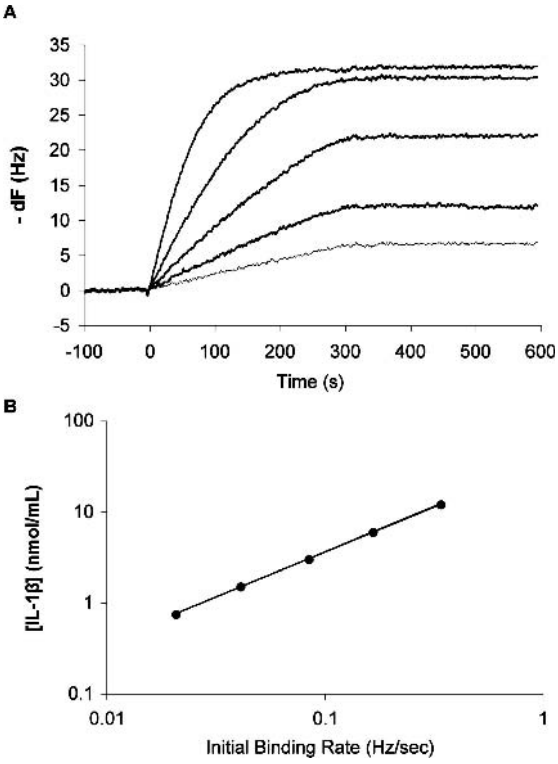

Fig. 5 Interleukin 1-beta concentration assay. **A** Binding of human IL-1β to mouse anti-IL-1β antibody, previously captured onto a RaM-Fc surface. Binding curves for five different IL-1β concentrations are shown overlaid, synchronised to the start of each IL-1β injection. Data have been normalised by subtraction of the response to injection of buffer alone, to correct for the off-rate of the captured anti-IL-1β antibody. **B** IL-1β concentration–response calibration curve. The initial binding rate for each IL-1β concentration was calculated as for the myoglobin concentration–response calibration curve (Fig. 4)

antagonist, IL-1ra, reduces the extent of the damage by more than 50%. The mechanism of action of these cytokines is the subject of intense research [62]. IL-1β is a 17.3 kDa protein that is found in serum, mucosa and in pleural effusions of different etiologies. It has been suggested as a diagnostic marker in the differential diagnosis of several pleural diseases [63]. It has also been found at consistently raised levels in normal appearing mucosa from patients with Crohn's disease, potentially providing evidence for a sustained immune stimulation in Crohn's disease in the absence of patent inflammation [64]. We used a mouse anti-IL-1β antibody, previously captured onto a RaM-Fc surface to bind to varying concentrations of human IL-1β (Fig. 5a).

As in the case for myoglobin, analyte concentration was more accurately and rapidly determined by analysing the rate of binding of IL-1β to the antibody, and comparing the measured observed association rate with a data set calibrated to analyte concentration (Fig. 5b). This also enabled the concentration of IL-1β in the sample to be determined in under 6 min.

1.8 Glucose Dehydrogenase

Glucose dehydrogenase (GDH) is a key initial enzyme in the energy production process that uses nucleotide cofactors to "activate" monosaccharide sugars as a prelude to their subsequent breakdown into pyruvate to enter the Krebs cycle. Nicotinamide adenine dinucleotide phosphate ($NADP^+$, 765 Da) is the preferred cofactor, nicotinamide adenine dinucleotide (NAD^+, 663 Da) will act as a lower activity cofactor, and flavine adenine dinucleotide (FAD, 830 Da) will not bind nor act as cofactor. Preferred monosaccharide substrates for the enzyme are glucose and galactose (180 Da). Other monosaccharides (e.g. fructose, 180 Da) and disaccharides (e.g. maltose, sucrose, 342 Da) cannot act as substrates.

Glucose dehydrogenase was coupled to a carboxylic acid terminating linker layer using standard carbodiimide amine coupling as described earlier. BSA was coupled in a similar manner to a second sensor surface to be used as a passive control. $NADP^+$, NAD^+ and FAD were then independently serially diluted and injected across the GDH "active" and BSA "control" surfaces for 1 min. The complexes were then allowed to dissociate for 1 min until pre-binding baseline levels were attained (Fig. 6).

From simple visual inspection of the magnitude of the binding response of the different cofactors, a rapid estimate of ranking affinity can be made: $NADP^+ > NAD^+ >$ FAD. The equilibrium binding constant, K_D, for $NADP^+$ binding to GDH, was calculated from analysis of equilibrium binding levels resulting from injection of threefold dilutions of $NADP^+$. The average response during the "plateau" phase of binding was plotted against $NADP^+$ concentration, and these data were fitted to a sigmoidal single site binding model to give a K_D of 2.8 mM. This demonstrates that RAP™ can be applied

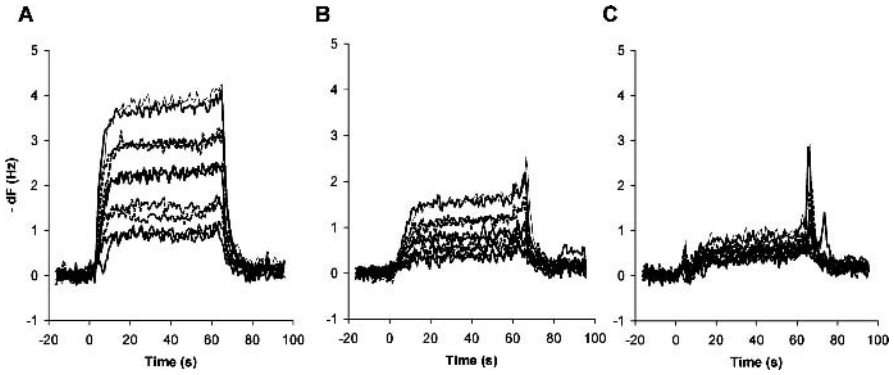

Fig. 6 Enzyme cofactor screening. Binding of preferred substrate, poor substrate, and non-preferred adenine-nucleotide cofactors to the metabolic enzyme GDH. **A** NADP (765 Da, preferred substrate) binding shows a clear equilibrium concentration–response relationship. **B** NAD (663 Da, metabolite) shows a lower equilibrium binding level, and compressed concentration–response relationship. **C** FAD (830 Da, non-preferred substrate) shows very low levels of equilibrium binding

to the accurate determination of cofactor affinities for an enzyme in real time in less than 20 min.

1.9 Automation

Scheduled for full commercial launch in 2006, the first instrument from Akubio, employing resonant acoustic profiling technology, the RAP♦*id*-4 (Fig. 7), integrates the RAP™ detection technology with a continuous flow microfluidic liquid delivery system, a thermal control unit, and automated sample

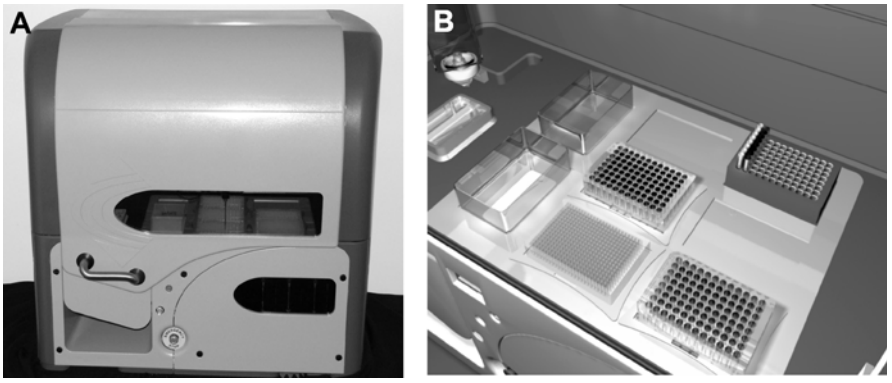

Fig. 7 RAP♦*id*-4™ system (*left*) and view of the sample rack and injection interface (*right*)

handling. Fitted with four individually addressable sensors, the instrumentation can provide specificity, affinity and kinetic characterisations for more than 200 samples per day. The system is capable of working in a variety of different solvents and in complex biological mixtures. For example, interactions can be studied in solutions containing up to 10% DMSO, in cell lysates, and in cell culture media.

1.10 Challenges for Label-Free Technologies

All optical label-free detection methods ultimately measure changes in dielectric constant or refractive index of a solution in close proximity to the surface of the sensor substrate. Whilst they are powerful techniques under extremely well controlled conditions, the advantages are often minimised when trying to apply these methods in routine analysis procedures. As optical methods rely on proximity-based detection, any analyte that is within the evanescent sensing field (typically 300 nm for most SPR devices) is detected as "bound". This is the case whether it physically bound to the receptor or simply in close proximity to the surface of the sensor. In contrast, RAP™ measures only those materials that are acoustically coupled to the sensor surface, i.e. binding-based detection rather than proximity-based detection. The process of measuring refractive index changes with optical methods to infer mass changes imparts a number of other intrinsic limitations, in particular the masking of binding events that occurs in sample environments that have variant refractive indices. In cases where the molecules to be tested have been solubilised in organic solvents, or are components of a crude cell lysate, culture medium or a serum sample, optical based techniques often are incapable of measuring associated binding events without extensive calibration or sample preparation procedures. Thus, one notable advantage of acoustic detection over more established optical label-free detection is the relative insensitivity of acoustics to changes in solvent. When running samples containing DMSO, optical detection systems suffer from large bulk refractive index shifts that arise from the disparate properties of the organic solvent and the running buffer. For example, the dielectric constant of water is 80, whereas for DMSO it is 40 (a difference of 100%). To normalise for these large bulk effects, a calibration routine using known serial dilutions of DMSO in running buffer is normally run a the beginning, middle and end of a screening panel [65]. In contrast, acoustic systems are not effected by refractive index changes, but are instead sensitive to bulk effects dominated by viscosity and density of the solvent; more specifically the square root of the viscosity:density product [14]. For water, this value is 0.99, whereas for DMSO it is 1.10 (a difference of only 11%).

1.11 Theoretical Considerations

The possibility of using quartz crystal resonators as quantitative mass measuring devices was first explored by Sauerbrey. The decrease of the resonant frequency of a thickness shear vibrating quartz crystal resonator, having AT or BT cut, was found to be proportional to the added mass of the deposited film. The derivations of Kanazawa and others when one face of a quartz crystal resonator is in contact with a liquid, and the calculation of penetration depth is dealt with elsewhere in this volume. Brown et al. [66] have attempted to extend the theory to accommodate polymeric or other finite viscoelastic layers acoustically coupled to the rigid quartz crystal and a rigid "ideal mass layer". This situation is analogous to a biological receptor layer coupled covalently to a rigid, high shear modulus chemical linker layer (Fig. 8). Brown

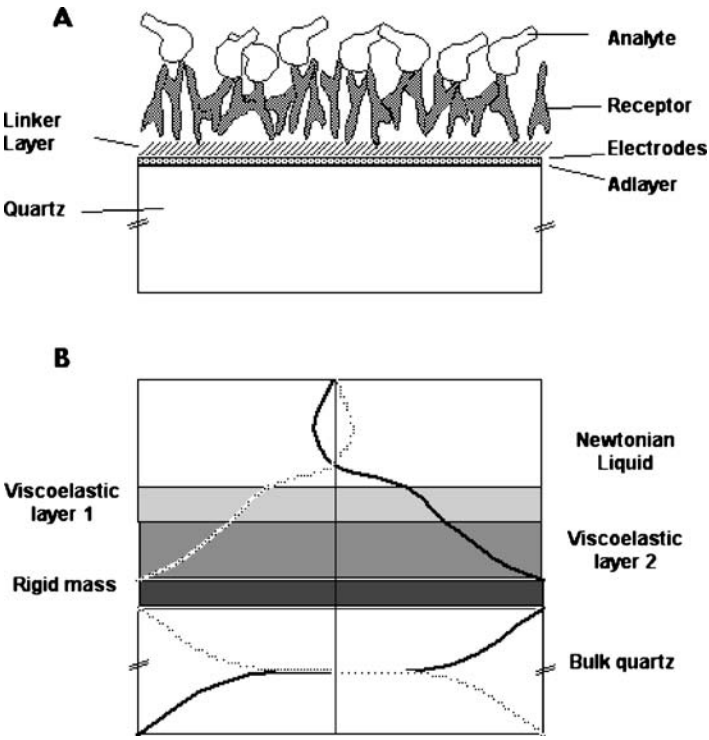

Fig. 8 Idealised model of acoustic attenuation. **A** Diagrammatic representation of a thickness shear mode bulk acoustic wave resonator, coated with a rigid metal adhesion and electrode layer, a rigid chemical linker layer, a finite viscoelastic antibody receptor layer, a second adherent finite viscoelastic analyte layer, and finally a Newtonian liquid. **B** An idealised model of acoustic attenuation from bulk quartz through the above layers of varying viscosity, density, and shear modulus

et al. considered a finite viscoelastic layer (of thickness h_f, density r_f and shear modulus $G = G' + jG''$. The latter value, G, is the complex shear modulus where G' and G'' are the layer storage and layer loss moduli respectively.

These layers are then exposed to a bulk liquid (of viscosity η_L and density ρ_L) (Fig. 8). For these layered components, it is possible to derive the surface mechanical impedances:

$$Z_M = j\omega\rho_s \tag{4}$$

for the ideal/rigid mass layer (in Akubio's the chemical linker layer), where r_s is the mass per area contributed by the linker layer:

$$Z_F = \sqrt{\rho_f G}\tan h(\gamma h_f) \tag{5}$$

for the viscoelastic film (biological film), where γ is the shear wave propagation constant ($\gamma = j2\pi f_0(r_f)^{1/2}$) and $j = \sqrt{-1}$:

$$Z_L = \sqrt{\frac{2\pi f_o \rho_L \eta_L}{2}}(1 + j), \tag{6}$$

for the liquid layer (semi-infinite Newtonian liquid), and finally:

$$Z = j2\pi f_o \sqrt{\rho_f G}\frac{Z_L \cos h(\gamma h_f) + \sqrt{\rho_f G}\sin h(\gamma h_f)}{\sqrt{\rho_f G}\cos h(\gamma h_f) + Z_L \sin h(\gamma h_f)}, \tag{7}$$

where Z is the impedance for the composite system. Note that the impedance measured by the resonator is *not* simply the sum of those for individual layers, as for each layer there will be an acoustic phase shift, which causes a transformation of the impedance contributed by layers more distant from the resonator. In addition this model does not accommodate the typically inhomogeneous layers that exist in reality in biological systems (e.g. a hydrated protein layer), or changes in distribution of mass induced by varying matrix conditions and analyte binding.

When layers of a material of differing density and viscosity to the liquid (such as a protein film) are deposited at the surface–liquid interface, then there is a contribution from both the bulk liquid and from the added material that has displaced liquid and mechanically coupled to the interface. In this case the penetration depth can be defined as:

$$\delta = (1 - \chi_p)\sqrt{\frac{\eta_L}{\pi f_o \rho_L}} + \chi_p \sqrt{\frac{\eta_L}{\pi f_o \rho_f}}, \tag{8}$$

where η_p and ρ_p are the liquid viscosity and density, respectively, and χ_p is the fraction of the volume within the penetration depth occupied by protein. This could be extended to encompass both a receptor layer and analyte layer as shown in Fig. 8 if necessary. Integrating the mole fraction of protein/water in combination with the definition of a composite impedance (Eq. 7), we can

derive:

$$Z = \chi_p j 2\pi f_o \sqrt{\rho_f G} \frac{(1-\chi_p) Z_L \cos h(\gamma h_f) + \sqrt{\rho_f G} \sin h(\gamma h_f)}{\sqrt{\rho_f G} \cos h(\gamma h_f) + (1-\chi_p) Z_L \sin h(\gamma h_f)}. \quad (9)$$

In the case of a resonator coated with a linker chemistry, we can thus model a rigid (high shear modulus) linker layer with a coupled viscoelastic receptor layer, followed by binding of a viscoelastic analyte. The latter interaction is the most difficult to model as the impedance matching and acoustic transmission of the penetrative wave between the receptor layer and analyte layer will depend not only on the density, viscosity and shear modulus of the binding analyte, but also on the affinity of the interaction (van der Waals interactions, hydrogen bonds, induced dipole interactions etc. etc.), and conformational changes in the receptor that may be induced by analyte binding. Fortunately, pure mass responses can be calculated in buffered solutions via SPR measurements, whilst layer thickness can be determined by a combination of dry film ellipsometry measurements and hydrated liquid phase dual polarisation interferometer measurements. In addition, the contribution of viscosity and density to the acoustic load can be deconvoluted via measurement in varying concentrations of buffered glycerol in which the buffer is constituted from H_2O, or from D_2O.

1.12 Current and Future Applications of RAP™

Any system that utilises a highly sensitive transducer such as piezoelectric quartz to measure molecular interactions must possess a variety of integrated technical controls to facilitate the highest level of sensitivity, accuracy and precision. Previous attempts to exploit this detection method in a commercial format have been limited by poor sample delivery mechanics, inadequate thermal controls, and the lack of a multisensor analysis platform. The development of proprietary electronics, fitting algorithms and a low-stress mounting system for the sensor has enabled Akubio to integrate microfluidic delivery together with automated liquid handling in the RAP♦*id* system. Ease of use is further facilitated by a number of simple-to-use coupling chemistries for attachment of target proteins to the sensor surface, and flow-chart-based assay design software.

These features, together with the ability to directly analyse samples in crude matrices means RAP♦*id* could be a useful tool for the protein therapeutic and antibody engineering sectors. RAP♦*id* can directly determine active antibody concentration, interaction specificity, cross reactivity, affinity and dissociation rates/half lives during the early stage development of drug candidates. Later in the pipeline, the technology can also be applied to a fuller kinetic characterisation of the products and interactions with the therapeutic targets and side-effect profilers. The technology may also be applicable in

downstream manufacturing processes where the quantification of production and purification yields in a timely and accurate manor is critical.

In the past, acoustic detection has been used to characterise interactions with peptides [67, 68], proteins and immunoassay markers [16, 17, 19, 20], oligonucleotides [54, 55], bacteriophage [57, 69], viruses [70, 71], bacteria [36, 38, 39] and cells [43–46, 50, 51]. The technology can thus be applied to an extremely wide range of biological and chemical entities. This suggests that one of the most promising applications may be acoustic cell-based screening in which live cells or cell membrane fragments form an active part of the sensor. This would potentially enable pathway-based screens to be carried out on cells to identify or confirm modulators of disease pathways, then mode-of-action assays to be performed with purified receptors; both with a same label-free technique.

2 Rupture Event Scanning

The analysis of molecular interactions is an integral part of many processes in the fields of diagnosis, life sciences and drug discovery. Diagnostic and pharmaceutical companies spend many millions of dollars to screen compounds for receptor binding in vitro during the initial phase of the development of new drugs, and to screen for pathogens which cause human, animal and plant diseases. Rapid diagnosis of bacterial and viral infections is of paramount importance for disease prognosis and prompt administration of appropriate therapy. It is also important to accurately monitor bacterial and viral load in order to determine the efficacy of drug treatment. Traditional methods of diagnosis involve direct culture techniques that are time-consuming, prone to problems of contamination, and may take days or weeks to give a result. Immunoassays such as antibody ELISA are more rapid, but have limited sensitivity and generally are used only to detect the antibodies produced following infection, rather than the infectious agent itself. Oligonucleotide-based assays, which detect pathogenic DNA or RNA, are very sensitive, but are expensive and require considerable experimental skill, as the genetic material must be isolated before nucleic acid amplification [72]. These methods can provide valuable early results in some situations, but in many cases local facilities are not available and specimens are often transported to central reference laboratories for testing. Hence, there is a real need for methods that rapidly detect and identify pathogens, especially those organisms that cause life-threatening infections such as meningitis and septicaemia.

The majority of molecular screening in diagnosis, drug discovery and the life sciences is carried out by interrogating a sample with some form of electromagnetic radiation: radio waves, microwaves, infrared, visible light, ultraviolet light, X-rays or gamma radiation. The most widely utilised screens

require some type of radio or fluorescent labelling to report the binding of a ligand to its receptor. This labelling step imposes additional time and cost demands, and can in some cases interfere with the molecular interaction by occluding a binding site, leading to false negatives. Fluorescent compounds are invariably hydrophobic and in many screens background binding is a significant problem, leading to false positives. Ideally a screen should be universally applicable, label-free, sensitive, economical and rapid.

We have developed a new method of detecting analytes, which we term rupture event scanning or REVS™ [73]. The technology enables rapid, label-free determination of interaction affinities, both in buffered solutions *and* in complex biological fluids. Potential applications range from the diagnosis of clinical infections to the screening of libraries for receptor binding and the quantitation of molecular interactions in general. The detection technology does not utilise any form of electromagnetic radiation, but instead records vibrational excitation in a substrate caused by disruption of molecular interactions. To induce a molecular complex of moderate affinity to break apart requires accelerations many orders of magnitude higher than the forces due to gravity. These very high forces can be imparted on an analyte by using an acoustic wave device, such as a quartz crystal resonator. In contrast to other quartz crystal biosensing applications (quartz crystal microbalance or quartz crystal resonance sensing), REVS™ technology does not only use the quartz resonator as a sensor, but takes advantage of the active surface of the resonator and its influence on systems adhered to it. However, REVS™ technology and our experimental set-up are also compatible with standard frequency and resistance shift measurements [74–76]. By monitoring the change in resonant frequency and resistance of the crystal, which occur upon adsorption of analytes to the surface, quartz crystal resonators can be used together with appropriate surface chemistry and fluidics to detect the adsorption of proteins, oligonucleotides, cells and other analytes to surface-bound receptors [77]. This allows the label-free determination of interaction affinities and kinetics in real time. In this short review the capabilities of REVS™ detection will be demonstrated using the herpes simplex virus as a model system.

2.1 Controlled Applied Force

As the magnitude of an applied electric field applied to a piezoelectric material is increased, the amplitude of oscillation increases and there is increasing acceleration of analytes adhered to the surface. This in turn results in an increasing force exerted by the surface on the analytes, which ultimately causes rupture of the bonds attaching the analytes to the surface (Fig. 9). Due to its piezoelectric properties the quartz crystal can be used to detect the excitation of vibrations in the substrate produced by bond rupture, which are converted into an electrical signal. The signal indicates not only the pres-

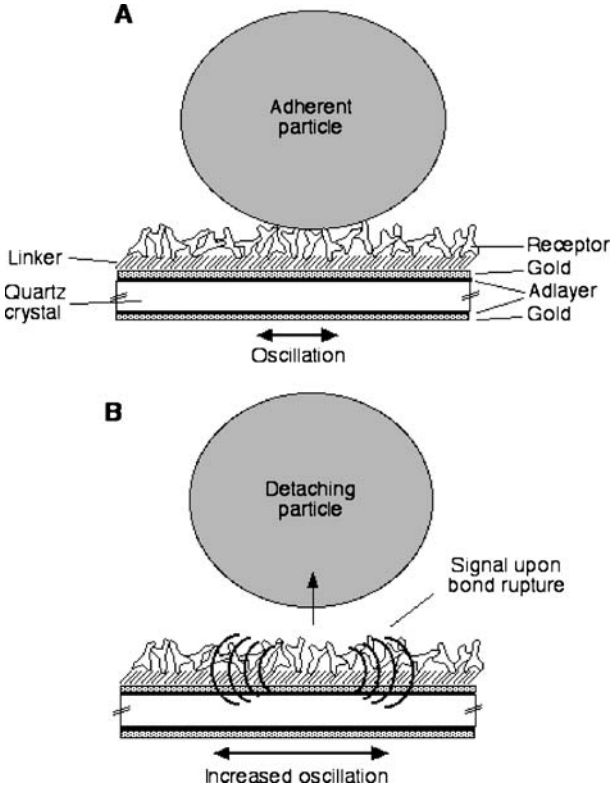

Fig. 9 REVS™ assay. **A** An AT-cut quartz crystal was coated successively with a chromium layer, a gold layer, a chemical linker layer, and a receptor that mediated specific attachment of the particle. The crystal was then transversely oscillated by applying a RF voltage at the main resonant frequency to the gold electrodes on either side of the disc. **B** Increasing the applied voltage results in a transverse oscillation of greater amplitude which, in principle, leads to greater inertial forces between the particle and the surface and concomitant deformation of the surface and the particle. Ultimately the bond between particle and receptor surface breaks and vibrations in the quartz are excited. These vibrations can be detected by using the quartz as a sensitive microphone. Note that the figures are not to scale

ence of the analytes but also the number of analytes present and their affinity for a surface-bound receptor. The scanning process requires minimal sample preparation, works well in buffered solutions *and* in complex biological fluids such as serum, and takes only minutes to perform.

The magnitude of excited vibrations is proportional to the number of analytes present over at least six orders of magnitude, right down to the level of a single particle, with a weight of only 80 fg, in 1 μL of fluid. This corresponds to a mass sensitivity of 80 fg mm^{-2} (8×10^{-14} g mm^{-2}) [73]. In comparison, traditional frequency change quartz crystal biosensors have a detection

limit in the order of 1 ng mm^{-2} (10^{-9} g mm^{-2}), whilst the best surface plasmon resonance optical biosensors can detect a mass change of 1 pg mm^{-2} (10^{-12} g mm^{-2}). The latter technique does not work well in complex fluids such as undiluted serum, as there is significant non-specific binding of materials such as serum proteins to the sensor surface.

The resonators used for REVS™ are commercially available polished AT-cut quartz discs with a diameter of 8.25 mm and a main resonant frequency at 14.3 MHz. The electrodes consist of a 3 nm thin chromium adhesion layer and between 40–80 nm of evaporated gold. The gold electrodes are covered with a chemical linker layer to which the desired receptors are attached. A signal generator is used to drive the quartz crystal at its fundamental resonant frequency, or at a higher overtone. During one scan the drive level is increased from 0 to 10 V. The response of the quartz at three times the fundamental frequency is fed via a filter into a lock-in amplifier and analysed using a signal generated by a second amplifier as reference. A more detailed description can be found in reference [78].

2.2 Detection of Herpes Simplex Virus

Rupture event scanning is a useful addition to existing techniques, as it combines the specificity and versatility of ELISA with the sensitivity of PCR [79]. The ability to include antibodies as a capture reagent adds a critical advantage to the technique, as it can build on the wide availability and tremendous knowledge base of monoclonal antibodies against viruses and bacteria [80]. The application of REVS™ for viral diagnosis has been validated with herpes simplex virus (HSV), which causes recurrent mucosal infections of the eye, mouth and genital tract. It also causes life-threatening generalised infection in the new-born and, more rarely, a fatal encephalitis in adults [81]. Rapid and sensitive detection of HSV is not a major public health issue except in the case of herpes encephalitis, where rapid detection of virus particles in cerebrospinal fluid is a prerequisite for appropriate chemotherapy. HSV is, however, a relatively fragile enveloped virus particle, sensitive to heat and desiccation, and is therefore a reasonable surrogate for many viruses of clinical importance such as HIV, hepatitis viruses B and C, and influenza.

For specific detection of HSV the viral samples were incubated for 40 min on the antibody-coated quartz crystals, washed with phosphate buffered saline solution (PBS) and then scanned under PBS from 0–10 V. A sharp peak at approximately 7.4 V with a signal strength of 450 arbitrary units was detected for a surface coated with HSV specific antibodies, whereas no signal was detected on surfaces coated with antibodies to which HSV does not bind (Fig. 10). This demonstrates that REVS™ only detects specifically bound viruses. A second scan of the driving voltage from 0–10 V immediately following the first gave no peaks, indicating that the viruses had been

detached from the surface. To confirm that the interaction between virus and surface was specific, control experiments were carried out using a modified herpes simplex virus missing the protein to bind to the antibody on the surface. The interaction was also specifically blocked by pre-incubating the

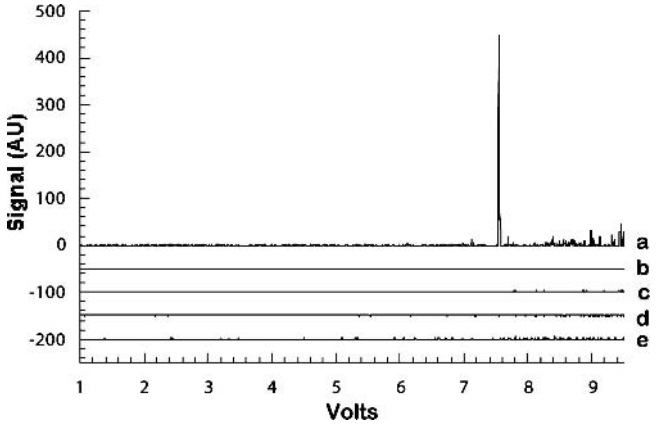

Fig. 10 Herpes simplex virus detection. Validation for specific detection of herpes simplex virus using REVS™: **a** 500 000 HSV (gD^+) virions incubated on a surface coated with an HSV receptor (anti-gD monoclonal antibody), **b** the same number of HSV virions on a surface with a receptor to which HSV does not bind (control bovine IgG), **c** genetically modified HSV (gD^-) on HSV receptor surface, **d** HSV on a soluble gD-blocked HSV receptor surface, **e** HSV in blocking solution (anti-gD monoclonal antibody) on HSV receptor surface. The traces have been displaced from zero on the y-axis for clarity

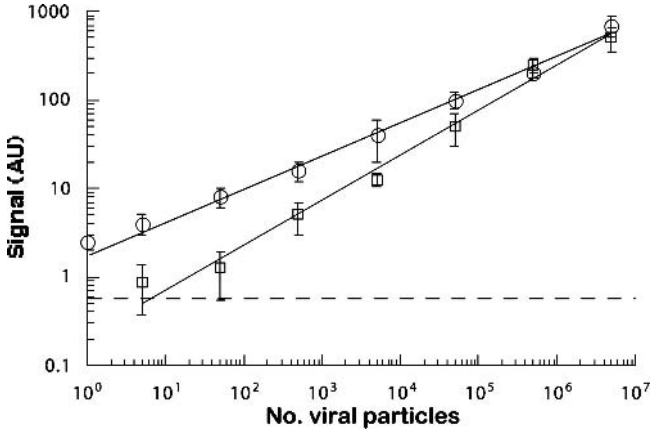

Fig. 11 Limits of detection for REVS™. Signal linearity with particle numbers. Serial tenfold dilutions of HSV1 gD^+ in PBS a sample volume of either 1 μL (*open circle*) or 40 μL (*open squares*) incubated for 40 min at room temperature on a quartz crystal coated with an HSV specific antibody. The *dashed line* represents the noise floor

antibody surface with the protein responsible for HSV binding (surface blocking) and by using HSV pre-incubated with antibodies before deposition on the antibody-covered quartz surface (solution blocking). In all cases no signal was observed (Fig. 11), confirming that REVS™ is an accurate method to detect specifically bound analytes.

To determine the sensitivity limits of detection, a HSV sample was serially diluted in phosphate buffered saline solution. The REVS™ signal specific for detachment of HSV was log-linear with the number of viruses over six orders of magnitude using a 1 μL sample (Fig. 11). The signal intensity using a 40 μL sample volume was approximately fivefold lower than that obtained using a 1 μL sample. This is believed to be due to a slower diffusion of virions to the surface in the larger sample volume, which results in a lower amount of captured virus on the sensor surface when the same incubation period is used with the larger sample volumes.

2.3 Theory

REVS™ is a novel detection and measurement method very different to classical quartz crystal resonant sensing (QCRS), which typically involves measurement of changes in frequency and resistance of the resonator. Whereas in QCRS the resonator is a passive transducer of binding events at the solution–surface interface, in REVS™ the resonator plays an active role in forcing bond rupture and then also detecting modulations in the resonance of the crystal induced by this event. Whilst we have a basic understanding of the processes involved in REVS™, we acknowledge that much more experimental and theoretical work is needed to fully understand the nature of the detachment event and signal generation. Long- and short-range interactions between molecules are central to the dynamic behaviour of biological systems. These interactions have traditionally been examined in great detail using thermodynamic approaches. However, the rupture of these interactions is a dynamic process and it is well known that the force required to break bonds depends not only on the affinity of the interactions, but also on the rate at which the force is applied to the interacting molecules [82, 83]. In recent years a variety of instruments have been developed to measure the force between molecules, including glass fibres, optical tweezers, the surface force apparatus and the atomic force microscope (AFM). Of these, the AFM has rapidly become one of the most widely used force measurement instruments due to its ease of use and its commercial availability [84]. AFM measurements are, however, most often carried out on single molecule interactions in which a single bond between two binding partners is broken. REVS™ possesses single molecule sensitivity, however, many of the analytes studied to date (such as viruses and bacteria) present multiple bonds to the surface of the resonator. It is also notable that a discrete, transient signal is observed from detachment events

involving large number of surface-bound analytes. For example, Fig. 9a shows a sharp peak for the detachment of 500 000 virions. These particles possess slightly varying shapes, sizes and, in particular, different numbers of bonds to receptors on the surface. Nevertheless, they dissociate from the surface of the resonator in a very short period giving rise to the high signal to noise peaks observed with REVS™.

For the purposes of this discussion we will assume that, up to the threshold rupture voltage, adherent particles are mechanically coupled to receptors on the surface via short-range molecular forces (i.e. electrostatic, hydrophobic, ion-dipole, Van der Waals interactions etc.). Transient forces due to inherent thermal energy of the bound complexes are by themselves insufficient to break multiple bonds in the short (1 min) assay time of a REVS™ scan; a necessary condition for subsequent dissociation of the particle. In other words, it is highly improbable that multiple antibody–antigen bonds will all rupture simultaneously at room temperature. It should also be noted that biomolecules such as proteins and viruses are stabilised by weak interactions (for example, the free enthalpies for binding of typical antibody–antigen interactions are in the order of $\sim 50\,\mathrm{kJ\,mol^{-}1}$ [85], with detachment forces measured by AFM in the order of 10–200 pN [86, 87]).

Under the force loading on crystal experienced at high driving voltages, some of the bonds between virus and the antibody on the surface of the resonator will be ruptured, and the particle may partially decouple from the surface of the crystal. The resulting increased force on the remaining intact bonds could then lead to an increased rupture rate of the remaining bonds. This positive feedback mechanism can potentially explain the transient characteristic of REVS™ peaks. This is an attractive hypothesis; however, it is also important to consider the case in which the load on the particle may be wholly, or partially, concentrated on one bond at a time, in which case the bonds will rupture in series [87]. It is also possible that the bonds can reform within the timescale of the rupture event.

To calculate the forces imparted on a molecule on the surface of the resonator it is first necessary to determine the displacement amplitude of the resonator. This has been shown to depend linearly on the merit factor and the drive level. For an AT cut quartz resonator it can be calculated from the following relationship:

$$A = 1.4\ Q\ V_{\mathrm{d}}\,, \tag{10}$$

where A is the amplitude of maximal displacement of the thickness shear mode resonator, the factor of 1.4 (pm V^{-1}) is a proportionality constant determined by Borovsky et al. [88], Q is merit factor of the resonator and V_{d} is the driving voltage. Note that this measured proportionality constant is the same as that calculated theoretically by Kanazawa [14]. Within Kanazawa's model the amplitude is interpreted as the average amplitude across the crystal surface. This is expected to be about one half the maximum amplitude

at the centre of the crystal, in view of the approximately Gaussian amplitude distribution [14, 88]. The Q factor in our experiments under liquid has been determined to be 1400–1600, depending on the resonator used. For a driving voltage of 7 V this gives an estimated vibrational amplitude at the centre of the crystal of ~ 15 nm.

If we assume that particles detected using REVS™ are spherical and attached at a point to the surface of the resonator, we can determine the ratio between force applied tangentially to the surface of the particle and acceleration of the surface of the particle. We also assume that sphere is rolling, or pivoting about this attachment point, which we acknowledge is an approximation of the geometry of the virus–antibody interaction. The moment of inertia of the sphere about a central axis, J_s is defined as:

$$J_s = \int r^2 \mathrm{d}m = 2\pi\rho \int_0^{R_s} r^4 \left(\sqrt{R_s - r^2}\right) \mathrm{d}r = \frac{2}{5} M_s R_s^2 , \tag{11}$$

where r is the integrated radius, R_s is the radius of the sphere, M_s is the mass of the sphere, and ρ is the density of the sphere. The acceleration at the centre of the sphere, a_c is defined as:

$$a_c = \frac{F_t}{M_s} , \tag{12}$$

where F_t is applied total force. The angular acceleration ε_s of the sphere is thus defined as:

$$\varepsilon_s = \frac{F_t R_s}{J_s} = \frac{F_t R_s}{\frac{2}{5} M_s R_s^2} = \frac{5 a_c}{2 R_s} , \tag{13}$$

which makes acceleration of surface of the sphere, a_s with respect the acceleration at its centre, a_c:

$$a_s = \varepsilon_s R_s = \frac{5 a_c}{2} , \tag{14}$$

and hence the total acceleration of the surface of the sphere, a_{ts} is:

$$a_{ts} = a_c + a_s = a_c + \frac{5 a_c}{2} = \frac{7 a_c}{2} . \tag{15}$$

In other words, for a sphere pivoting about an attachment point to a surface, the centre of mass of the sphere moves only 2/7th of the distance moved by the surface at full amplitude about the pivot point. The acceleration of a point on the surface of the resonator thus is given as:

$$a = \frac{2}{7} A (2\pi f)^2 . \tag{16}$$

For the 14.2 MHz crystals driven at 7 V employed in our work this gives an acceleration on the surface of 3.4×10^7 m s^{-2} or 3.4 million g! We can estimate the mass of a single virus from knowledge of its molecular weight

($\sim 5 \times 10^8$ Da) which gives the mass of a single virion as 80 fg [81, 89]. Ignoring any contribution from viscous forces in water and treating the virion as a rigid sphere, this then enables us to estimate the force imparted on a virion adhered to the resonator from:

$$F = \frac{2}{7} mA(2\pi f)^2 \tag{17}$$

giving F as ~ 3 nN. This raises the question: is this force sufficient to break bonds typically found in biological systems? Atomic force microscopy has been used to determine the forces involved in single molecule interactions between antibodies and antigens immobilised on planar surfaces, with typical measured values in the order of 10–200 pN [86, 87]. However, the virus used in this study presents multiple receptors on its surface, and will form multiple bonds with several antibodies on the surface of the resonator. Indeed, adhesion to surface-bound receptors in biology is characterised by polyvalent interactions and multiple receptor–ligand interactions, which serve to enhance the affinity, or avidity of an interaction. To determine exactly the number of interacting molecules during each measurement a prior knowledge of the surface density of the immobilised molecules, particle geometry and particle–receptor contact area is required. Surface coverage can be estimated using radio-labelling and fluorescence techniques. However, determination of particle and receptor orientation and the contact area between the two is problematical, and we have not taken this into account in our calculations. It has also been demonstrated that there is a strong dependence in the measured adhesion force between biomolecules and the loading rate (or pulling rate in the case of AFM) [85, 90]. Notwithstanding these effects, it can clearly be seen that the force imparted by the resonator on the adherent virion (3 nN), is sufficient to rupture several bonds between the particle and receptors immobilised on the surface (10–200 pN each).

2.4 Application to Model Clinical Samples

For REVS™ applications using clinical samples, it is necessary to detect viruses in more complex biological fluids, such as serum or cerebrospinal fluid, which contain large quantities of proteins. To test the suitability of the REVS™ technique for use in complex specimens, HSV samples were diluted in calf serum. Peaks were observed in the region of 7.1 V (Fig. 12). The fact that multiple, distinct peaks can be observed in serum may be due to partial non-specific blocking of some antibody binding sites by serum proteins, which could lead to more variations in the number of interactions between the virus and the surface than is the case in PBS.

These results demonstrate that REVS™ technology could potentially be applied to a wide range of more complex biological samples. Quartz crystal

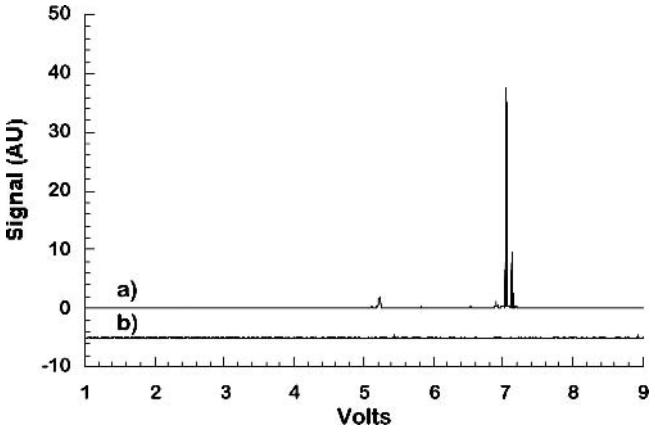

Fig. 12 Detection in neat serum. **a** 1 μL of HSV gD^+ at 5×10^7 particles/mL in calf serum incubated for 40 min on a quartz resonator coated with anti-gD IgG monoclonal antibody, then washed with water and scanned under 10 μL of PBS from 0–10 V. **b** Calf serum only incubated for 40 min on a QCM disc coated with anti-gD IgG monoclonal antibody, then washed with water and scanned under 10 μL of PBS from 0–10 V

resonators have been mass-produced for many years and are relatively inexpensive. The oscillation and detection system is entirely electronic, which results in a direct digital read out without the use of optics, filters, charge-coupled devices or image processing. This makes the instrumentation much simpler and cheaper than is the case with fluorescence, chemiluminescence or evanescent wave-based techniques. The major challenges that lie ahead include the successful integration of the detection technology with fluidics, chemistry, biology, signal processing, and data management. It is possible to multiplex the assay in a variety of ways and also to miniaturise the detector for direct detection in the field or at patient point of care. The label-free nature of the technique should allow rapid assay development with broad applicability to the detection of viruses, bacteria, cells, proteins, oligonucleotides and small molecules. Akubio's acoustic detection technology thus has great potential as a new method for interrogating chemical and biological samples in drug discovery, diagnosis, and the life sciences in general.

Acknowledgements The author wishes to thank all the employees, cofounders and consultants of Akubio Ltd.

References

1. Myszka DG, Jonsen MD, Graves BJ (1998) Anal Biochem 265:326
2. Myszka DG, Rich RL (2000) Pharm Sci Tech Today 3:310
3. Cooper MA (2002) Nature Reviews Drug Discovery 1:515
4. Rich RL, Myszka DG (2005) J Mol Recognit 18:1

5. Curie P, Curie J (1880) C R Acad Sci 91:294
6. Nomura T, Okuhara M (1982) Anal Chim Acta 142:281
7. Auge J, Hauptmann P, Hartmann J, Rosler S, Lucklum R (1995) Sensor Actuator B-Chem 24:43
8. Marx KA, Zhou TA, Montrone A, Schulze H, Braunhut SJ (2001) Biosens Bioelectron 16:773
9. Thompson M, Hayward GL (1997) Proc IEEE Int Freq Control Symp, p 114
10. Ghafouri S, Thompson M (2000) Electroanalysis 12:326
11. Hayward GL, Thompson M (1998) J Appl Phys 83:2194
12. Theisen LA, Martin SJ, Hillman AR (2004) Anal Chem 76:796
13. Arnau A, Jimenez Y, Sogorb T (2001) IEEE T Ultrason Ferr 48:1367
14. Kanazawa KK (1997) Faraday Discuss, p 77
15. Geelhood SJ, Frank CW, Kanazawa K (2002) J Electrochem Soc 149:H33
16. Aizawa H, Kurosawa S, Ogawa K, Yoshimoto M, Miyake J, Tanaka H (2001) Sensor Actuator B-Chem 76:173
17. BenDov I, Willner I, Zisman E (1997) Anal Chem 69:3506
18. Ghourchian HO, Kamo N (1995) Anal Chim Acta 300:99
19. Kurosawa S, Aizawa H, Yoshimoto M (2000) IEEE T Ultrason Ferr 47:1256
20. Percival CJ, Stanley S, Braithwaite A, Newton MI, McHale G (2002) Analyst 127:1024
21. Wu ZY, Shen GL, Xie LJ, Yu RQ (2000) Sensor Actuator B-Chem 71:99
22. Suleiman AA, Guilbault GG (1991) Anal Lett 24:1283
23. Uttenthaler E, Kosslinger C, Drost S (1998) Biosens Bioelectron 13:1279
24. Wang H, Lei CX, Li JS, Wu ZY, Shen GL, Yu RQ (2004) Biosens Bioelectron 19:701
25. Aizawa H, Kurosawa S, Tanaka M, Wakida S, Talib ZA, Park JW, Yoshimoto M, Muratsugu M, Hilborn J, Miyake J, Tanaka H (2001) Mater Sci Eng C-Biomimet Supramol Sys 17:127
26. Hu JM, Pei RJ, Hu Y, Zeng YE (1998) Chinese J Chem 16:219
27. Su XD, Chew FT, Li SFY (2000) Biosens Bioelectron 15:629
28. Aizawa H, Kurosawa S, Tozuka M, Park JW, Kobayashi K, Tanakac H (2003) Biosens Bioelectron 18:765
29. Long YM, Li WF, Nie LH, Yao SZ (2001) J Pharmaceut Biomed 24:361
30. Su XD, Chew FT, Li SFY (1999) Anal Biochem 273:66
31. Bao L, Deng L, Nie L, Yao S, Wei W (1996) Anal Chim Acta 319:97
32. Minunni M, Mascini M, Carter RM, Jacobs MB, Lubrano GJ, Guilbault GG (1996) Anal Chim Acta 325:169
33. Ye JM, Letcher SV, Rand AG (1997) J Food Sci 62:1067
34. Park IS, Kim N (1998) Biosens Bioelectron 13:1091
35. Park IS, Kim WY, Kim N (2000) Biosens Bioelectron 15:167
36. Fung YS, Wong YY (2001) Anal Chem 73:5302
37. Aizawa H, Kurosawa S, Tanaka M, Yoshimoto M, Miyake J, Tanaka H (2001) Anal Chim Acta 437:167
38. Otto K, Elwing H, Hermansson M (1999) J Bacteriol 181:5210
39. Spangler BD, Wilkinson EA (2000) Abstracts of papers of the Am Chem Soc 219: U115
40. Wong YY, Ng SP, Ng MH, Si SH, Yao SZ, Fung YS (2002) Biosens Bioelectron 17:676
41. Pavey KD, Ali Z, Olliff CJ, Paul F (1999) J Pharm Biomed Anal 20:241
42. Pavey KD, Barnes LM, Hanlon GW, Olliff CJ, Ali Z, Paul F (2001) Lett Appl Microbiol 33:344
43. Richert L, Lavalle P, Vautier D, Senger B, Stoltz JF, Schaaf P, Voegel JC, Picart C (2002) Biomacromolecules 3:1170

44. Rodahl M, Hook F, Fredriksson C, Keller CA, Krozer A, Brzezinski P, Voinova M, Kasemo B (1997) Faraday Discuss p 229
45. Fredriksson C, Kihlman S, Rodahl M, Kasemo B (1998) Langmuir 14:248
46. Shinohara H (1999) Electrochemistry 67:280
47. Ebato H, Okahata Y, Matsuda T (1993) Kobunshi Ronbunshu 50:463
48. Gryte DM, Ward MD, Hu WS (1993) Biotechnol Progr 9:105
49. Ebersole RC, Foss RP, Ward MD (1991) Bio-Technology 9:450
50. Braunhut SJ, Marx KA, Zhou T, Warren MC, Schulze HM (1999) Mol Biol Cell 10:64a
51. Wegener J, Seebach J, Janshoff A, Galla HJ (2000) Biophys J 78:2821
52. Mannelli I, Minunni M, Tombelli S, Mascini M (2003) Biosens Bioelectron 18:129
53. Minunni M, Tombelli S, Mariotti E, Mascini M (2001) Fresenius J Anal Chem 369:589
54. Caruso F, Furlong DN, Niikura K, Okahata Y (1998) Colloids Surf B-Biointerfaces 10:199
55. Hook F, Ray A, Norden B, Kasemo B (2001) Langmuir 17:8305
56. Caruso F, Rodda E, Furlong DF, Niikura K, Okahata Y (1997) Anal Chem 69:2043
57. Uttenthaler E, Schraml M, Mandel J, Drost S (2001) Bios Bioelectron 16:735
58. Lahiri J, Isaacs L, Tien J, Whitesides GM (1999) Anal Chem 71:777
59. Sigal GB, Bamdad C, Barberis A, Strominger J, Whitesides GM (1996) Anal Chem 68:490
60. Ernst OP, Bieri C, Vogel H, Hofmann KP (2000) Meth Enzymol 315:471
61. Casey PE (2004) AACN Clin Issues 15:547
62. Gibson RM, Rothwell NJ, Le Feuvre RA (2004) Vet J 168:230
63. Silva-Mejias C, Gamboa-Antinolo F, Lopez-Cortes LF, Cruz-Ruiz M, Pachon J (1995) Chest 108:942
64. Reimund JM, Wittersheim C, Dumont S, Muller CD, Kenney JS, Baumann R, Poindron P, Duclos B (1996) Gut 39:684
65. Frostell-Karlsson A, Remaeus A, Roos H, Andersson K, Borg P, Hämäläinen M, Karlsson R (2000) J Med Chem 43:1986
66. Brown MJ, Hillman AR, Martin SJ, Cernosek RW, Bandey HL (2000) J Mater Chem 10:115
67. Furtado LM, Su HB, Thompson M, Mack DP, Hayward GL (1999) Anal Chem 71:1167
68. Thompson M, Su HB, McGovern M, Kwong K, Mack D (1997) Abstracts of papers of the Am Chem Soc 213:213
69. Hengerer A, Kosslinger C, Decker J, Hauck S, Queitsch I, Wolf H, Dubel S (1999) Biotechniques 26:956
70. Zhou XD, Liu LJ, Hu M, Wang LL, Hu JM (2002) J Pharmaceut Biomed 27:341
71. Susmel S, O'Sullivan CK, Guilbault GG (2000) Enzyme Microb Tech 27:639
72. Higuchi R, Fockler C, Dollinger G, Watson R (1993) Biotechnology (NY) 11:1026
73. Cooper MA, Dultsev FN, Minson T, Ostanin VP, Abell C, Klenerman D (2001) Nat Biotechnol 19:833
74. König B, Grätzel M (1994) Anal Chem 66:341
75. Ballantine DS, White RM, Martin SJ, Ricco AJ, Zellers ET, Frye GC, Wohltjen H (1997) Acoustic wave sensors. Academic, San Diego
76. Ward MD, Buttry DA (1990) Science 249:1000
77. Janshoff A, Galla H-J, Steinem C (2000) Angewandte Chemie 39:4004
78. Dultsev FN, Ostanin VP, Klenerman D (2000) Langmuir 16:5036
79. Saphire EO, Parren PW (2001) Nat Biotechnol 19:823
80. Parren PW, Burton DR (2001) Adv Immunol 77:195
81. Minson AC (1998) In: Mahy BWJ, Collier L (eds) Topley and Wilson's microbiology and microbial infections, vol 1. Arnold, London, p 325

82. Evans E (2001) Annu Rev Biophys Biomol Struct 30:105
83. Evans E (1998) Faraday Discuss, p 1
84. Heinz WF, Hoh JH (1999) Trends Biotech 17:143
85. Evans E, Ritchie K (1999) Biophys J 76:2439
86. Guttenberg Z, Bausch AR, Hu B, Bruinsma R, Moroder L, Sackmann E (2000) Langmuir 16:8984
87. Seifert U (2000) Phys Rev Lett 84:2750
88. Borovsky B, Mason BL, Krim J (2000) J Appl Phys 88:4017
89. Regenmortel MV, Fauquet C, Bishop DHL (2000) Virus taxonomy. Academic, London
90. Merkel R, Nassoy P, Leung A, Ritchie K, Evans E (1999) Nature 397:50

Subject Index

Printing: Krips bv, Meppel
Binding: Stürtz, Würzburg